Assessing Reservoir Depositional Environments to Develop and Quantify Improvements in CO_2 Storage Efficiency: A Reservoir Simulation Approach

Final Report

October 1, 2012–September 30, 2014

Principal Investigator: Roland Okwen
Co-Principal Investigators: Scott Frailey and Hannes Leetaru
Illinois State Geological Survey
Prairie Research Institute
University of Illinois
(217) 244-2869
rokwen@illinois.edu

Report Issued: December 29, 2014

U.S. DOE Cooperative Agreement: DE-FE0009612

The Board of Trustees of the University of Illinois
Sandy Moulton, Director
c/o Grants & Contracts Office
1901 S. First Street, Suite A
Champaign, IL 61820
Illinois State Geological Survey

DISCLAIMER

ABSTRACT

The storage potential and fluid movement within formations are dependent on the unique hydraulic characteristics of their respective depositional environments. Storage efficiency (E) quantifies the potential for storage in a geologic depositional environment and is used to assess basinal or regional CO_2 storage resources. Current estimates of storage resources are calculated using common E ranges by lithology and not by depositional environment.

The objectives of this project are to quantify E ranges and identify E enhancement strategies for different depositional environments via reservoir simulation studies. The depositional environments considered include deltaic, shelf clastic, shelf carbonate, fluvial deltaic, strandplain, reef, fluvial and alluvial, and turbidite. Strategies considered for enhancing E include CO_2 injection via vertical, horizontal, and deviated wells, selective completions, water production, and multi-well injection.

Conceptual geologic and geocellular models of the depositional environments were developed based on data from Illinois Basin oil fields and gas storage sites. The geologic and geocellular models were generalized for use in other US sedimentary basins. An important aspect of this work is the development of conceptual geologic and geocellular models that reflect the uniqueness of each depositional environment. Different injection well completions methods were simulated to investigate methods of enhancing E in the presence of geologic heterogeneity specific to a depositional environment. Modeling scenarios included horizontal wells (length, orientation, and inclination), selective and dynamic completions, water production, and multi-well injection. A Geologic Storage Efficiency Calculator (GSECalc) was developed to calculate E from reservoir simulation output. Estimated E values were normalized to diminish their dependency on fluid relative permeability.

Classifying depositional environments according to normalized baseline E ranges ranks fluvial deltaic and turbidite highest and shelf carbonate lowest. The estimated average normalized baseline E of turbidite, and shelf carbonate depositional environments are 42.5% and 13.1%, with corresponding standard deviations of 11.3%, and 3.10%, respectively. Simulations of different plume management techniques suggest that the horizontal well, multi-well injection with brine production from blanket vertical producers are the most efficient E enhancement strategies in seven of eight depositional environments; for the fluvial deltaic depositional environment, vertical well with blanket completions is the most efficient.

This study estimates normalized baseline E ranges for eight depositional environments, which can be used to assess the CO_2 storage resource of candidate formations. This study also improves the general understanding of depositional environment's influence on E. The lessons learned and results obtained from this study can be extrapolated to formations in other US basins with formations of similar depositional environments, which should be used to further refine regional and national storage resource estimates in future editions of the Carbon Utilization and Storage Atlas of the United States. Further study could consider the economic feasibility of the E enhancement strategies identified here.

TABLE OF CONTENTS

LIST OF TABLES

LIST OF FIGURES

LIST OF APPENDIX TABLES

LIST OF APPENDIX FIGURES

EXECUTIVE SUMMARY

The US Department of Energy, in collaboration with seven Regional Carbon Sequestration Partnerships and 10 American Recovery and Reinvestment Act (ARRA) projects, has identified and classified different geologic depositional environments based on their storage potential through the implementation of 28 CO_2 injection pilot projects. The storage potential and fluid movements within formations are dependent on the unique hydraulic characterization of their respective depositional environments. Storage efficiency (E) quantifies the potential for storage in a formation and can be used to assess basinal or regional CO_2 storage resources, site screening, and determination of monitoring well locations and project area of review.

The objectives of this project are to quantify baseline E ranges and identify E enhancement strategies for eight depositional environments. The eight depositional environments studied include deltaic, shelf clastic, shelf carbonate, fluvial deltaic, strandplain, reef, fluvial and alluvial, and turbidite. Strategies considered for enhancing E include CO_2 injection via vertical, horizontal, and deviated wells, selective completions, water production, and multi-well injection.

Formations were rigorously reviewed and selected from previous reservoir characterization studies, existing geologic models, and available geologic data (log and core data). The geologic models of the selected formations were developed from structure and isopach maps, which were interpreted from cross sections, geophysical logs, core, and outcrop of Illinois Basin (ILB) oil fields and gas storage sites. Depositional environments were interpreted from core and geophysical log data. These geologic models were developed and rigorously reviewed by sedimentary geologists to ensure they closely represent the depositional environment of interest. A rigorous and iterative review process was implemented to ensure that the geologic models and subsequent storage efficiency estimates were not specific to Illinois, USA, but rather represent a typical depositional environment. To define a typical depositional environment, a comprehensive literature review was conducted on other US basins with deposits similar to ILB formations. The US basin formations were compared based on basin type and reservoir characteristics, including complexity (geometry, boundaries, compartments, and potential barriers) and scale (lateral and vertical extent). Findings from the literature review indicate that depositional environments in the cratonic and noncratonic US Basins exhibit similar characteristics but have geologic features that differ in scale. An important aspect of this work is the development of geologic and geocellular modeling that reflects the uniqueness of each depositional environment.

Geologic and petrophysical data from oil fields and gas storage sites were used as constraints in the development of geocellular models; these models were expanded in some cases so that the models were more typical of a specific depositional environment, based on the literature review and field experience. The geocellular models were reviewed to ensure accurate representation of the geologic model and depositional environment of a given formation, before upscaling for flow simulations. To ensure E was influenced only by the depositional environment in question, geocellular models were flattened on a stratigraphic datum.

The general pattern of the depositional environment was repeated in the geocellular models so that E from the numerical models was not adversely influenced by boundary effects that are not geologically constrained. A typical dimension of the reservoir model is 3.2 km by 3.2 km by 12.2 m (2 mi by 2 mi by 40 ft). Instead of having a large number of relatively high pore volume edge

cells to simulate an infinite-acting formation, an analytical aquifer of equivalent thickness was attached to the model's edge gridblocks to avoid pressure boundary effects on estimated values of E. Sensitivity studies were conducted to estimate the average reservoir properties to be assigned to the surrounding aquifer for the system (reservoir model and aquifer), to exhibit infinite-acting behavior. This was achieved by simulating water injection into the formations and comparing the bottomhole pressure of the reservoir simulation to that of an analytical model. Reservoir simulation results indicate that the reservoir-aquifer system exhibits infinite-acting behavior when porosity and permeability of the Carter-Tracy analytical infinite aquifer is equivalent to the arithmetic mean of the formation's porosity and permeability.

Reservoir simulations of CO_2 injection via a vertical well were conducted to determine the baseline E of the eight depositional environments. A Geologic Storage Efficiency Calculator (GSECalc) tool was developed to calculate E and the average CO_2 saturation behind the plume front from simulation output. Estimated E values were normalized to diminish its dependency on relative permeability. CO_2 injection via horizontal and deviated injection wells was also simulated to determine well orientations that can achieve storage efficiencies greater than the baseline E for each depositional environment. Different injection well completion methods were simulated for each depositional system to determine injection and completion strategies that can be implemented to maximize E. Of the eight depositional environments, turbidite has the highest and shelf carbonate has the lowest normalized baseline E values. The estimated average normalized baseline E of turbidite, and shelf carbonate depositional environments are 42.5% and 13.1%, with corresponding standard deviations of 11.3%, and 3.10%, respectively. Some depositional environments have more than one recommended injection strategy because they are statistically equivalent. The horizontal well, multi-well injection with brine production from vertical producers with blanket completions are the most efficient E enhancement strategies for all depositional systems, except fluvial deltaic in which vertical well injection with blanket completions is the most efficient.

This study provides information that can be used to estimate storage efficiency and capacity, thus providing a means to assess the CO_2 storage resource of candidate formations. It improves the general understanding of depositional environment's influence on E in formations with similar lithologies, such that estimates of E do not depend on lithology alone. The lessons learned from this study can be extrapolated to other US basins with formations of similar depositional environments and should be considered in future editions of the Carbon Utilization and Storage Atlas of the United States. Further study could consider the economic feasibility of the E enhancement strategies identified here.

CONTRIBUTORS

The following people wrote text for the geologic characterization section and were responsible for conceptual geologic modeling: Nathan Webb (shelf clastic, deltaic, fluvial deltaic, shelf carbonate, and turbidite), Charles Monson (shelf carbonate), John Grube (shelf clastic, deltaic, fluvial deltaic, and shelf carbonate), Beverly Seyler (shelf clastic, deltaic, fluvial deltaic, and turbidite), Hannes Leetaru (strandplain), and Yaghoob Lasemi (shelf carbonate and reef). Beverly Seyler and John Grube provided the comparison of Illinois Basin depositional environments to depositional environments in other US basins.

James Damico and Nathan Grigsby were responsible for conceptual and geocellular modeling (including core and log analyses).

Christopher Stohr provided assistance with LiDAR and photogrammetry. Megan Seger assisted with photogrammetry.

Roland Okwen, Fang Yang, and Ruisong Zhou were responsible for reservoir simulation.

Damon Garner and Roland Okwen developed the GSECalc tool. Damon Garner provided database support.

Scott Frailey provided reservoir simulation design and interpretation of the results and a technical review of the geologic modeling, geocellular modeling, reservoir simulation, and GSECalc sections.

Daniel Klen provided editing and formatting of the report.

Yu Han and Tayyib Alvi uploaded reservoir simulation output data into the GSECalc for analysis and interpretation.

INTRODUCTION

Saline reservoirs and depleted oil and gas reservoirs, which occur at varying depths and across the globe, have been identified as potential reservoirs for geologic carbon dioxide (CO_2) storage. Through the implementation of 28 CO_2 injection pilot projects in collaboration with the Regional Carbon Sequestration Partnerships and 10 American Recovery and Reinvestment Act (ARRA) projects, the US Department of Energy (DOE) has qualitatively ranked the CO_2 storage potential of these geologic formations based on their depositional environment. The ability to store large volumes of CO_2 depends upon the reservoir storage efficiency, which depends upon depositional environment because it defines the reservoir architecture that influences fluid containment and flow direction (NETL, 2010b). This study examines eight depositional environments that the DOE ranked as possessing medium or high CO_2 storage potential: deltaic, shelf clastic, shelf carbonate, strandplain, reef, fluvial deltaic, eolian, fluvial and alluvial, and turbidite (NETL, 2010b).

Storage efficiency—the ratio of the injected CO_2 volume to the accessible pore volume—provides an estimate of the storage capacity of geologic formations, and thus is an important tool for CO_2 storage resource assessments, site screening, determination of monitoring well locations, and a storage project's area of review. Because the depositional environment defines the reservoir architecture that influences fluid containment and flow direction, storage efficiency (E) is expected to vary from one depositional environment to the other.

The objectives of this project are to quantify baseline E ranges for eight depositional environments and identify strategies for enhancing E. The strategies considered were CO_2 injection via vertical, horizontal, and deviated wells, selective completions, water production, and multi-well injection. The objectives of this study contribute to the National Energy Technology Laboratory's (NETL's) effort to adequately understand and characterize potential storage reservoirs in order to develop tools and procedures to improve storage capacity predictions in geologic systems within a 30% margin of error (NETL, 2012).

Previous studies conducted by IEAGHG (2009) and Goodman et al. (2011) used Monte Carlo simulations to calculate E probability ranges (P_{10}, P_{50}, and P_{90}) by lithology. This study builds on their previous work by considering the different depositional environments of formations with similar lithologies, in attempt to further quantify the CO_2 storage resource of individual formations in addition to regional and national evaluations.

This project attempts to advance efforts made in estimating E ranges from lithology to formation level by building on the depositional environment classifications in NETL (2010b). A Geologic Sequestration and Efficiency Calculator (GSECalc) was developed to calculate E and average CO_2 ($\bar{S}_g$) from simulation output because Nexus and similar commercial simulators do not directly calculate E. The calculated E was normalized to mitigate the influence of relative permeability and to enable application to other basins.

A team of geoscientists and engineers rigorously reviewed and selected Illinois Basin (ILB) formations from an inventory of existing geologic models, previous reservoir characterization studies, and available geologic data (log and core data). Thin sections, core data, and log data of

the selected formations were closely studied to identify their corresponding predominant depositional environments. A comprehensive literature review was conducted on other US Basins with deposits similar to ILB formations. The US Basin formations were compared based on basin type and reservoir characteristics, including complexity (geometry, boundaries, compartments, and potential barriers) and scale (lateral and vertical extent).

Isopach maps and structural tops and bottoms interpreted from wireline log analysis were integrated with core data, outcrops, and information from ILB oil fields and gas storage sites to create conceptual geologic models. Conceptual geologic models were rigorously reviewed (and updated when necessary) by sedimentary geologists until they closely depicted its depositional environment. Wireline logs, isopach maps, core data, and structural tops and bottoms were used to build multiple realizations of three-dimensional geocellular models that depicted the distribution of reservoir properties via geostatistical simulations. The geocellular model realizations were reviewed and the realization that best depicted the conceptual geologic model was selected as the input for reservoir simulations of each formation.

Multiple sets of CO_2 reservoir simulation scenarios using different injection and well completions and plume management strategies were conducted. The GSECalc tool was used to calculate E for each simulation scenario. The performances of each enhancement strategy were compared to the baseline performance to evaluate their viabilities. Procedures for using the GSECalc tool are provided in Appendix 1. Landmark's Nexus software was used to conduct reservoir simulations in this project.

The sections of this report consist of geologic modeling, geocellular modeling, reservoir simulation, and an interpretation of the results. The geologic modeling section discusses the screening, depositional environment classification, and geology of selected ILB formations followed by a comparison to formations in other US Basins. The geocellular modeling section describes the workflow that was used to construct the geocellular models via geostatistical methods. The reservoir simulation section describes how E was estimated from reservoir simulations and how the strategies for enhancing E were evaluated.

GEOLOGIC MODELING

An inventory of all Illinois Basin (ILB) formations with existing reservoir characterization studies, geologic models, geocellular models, and reservoir models was made. Existing reservoir characterization studies were reviewed for data quality and were classified into different depositional environment types. Illinois Basin geologic formations to be considered for new modeling studies were identified. Available core and log data of selected ILB formations were reviewed and analyzed. Illinois State Geological Survey (ISGS) petroleum geologists selected candidates for the deltaic, shelf clastic, shelf carbonate, strandplain, reef, fluvial deltaic, fluvial and alluvial, and turbidite depositional environments (Figure 1; Table 1). Upon review of existing and new ILB reservoir studies, an eolian formation was not identified at the time of formation selection. However, a recent thin section and core analysis study has identified the middle Mt. Simon Formation to be deposited in an eolian environment (Freiburg, 2014).

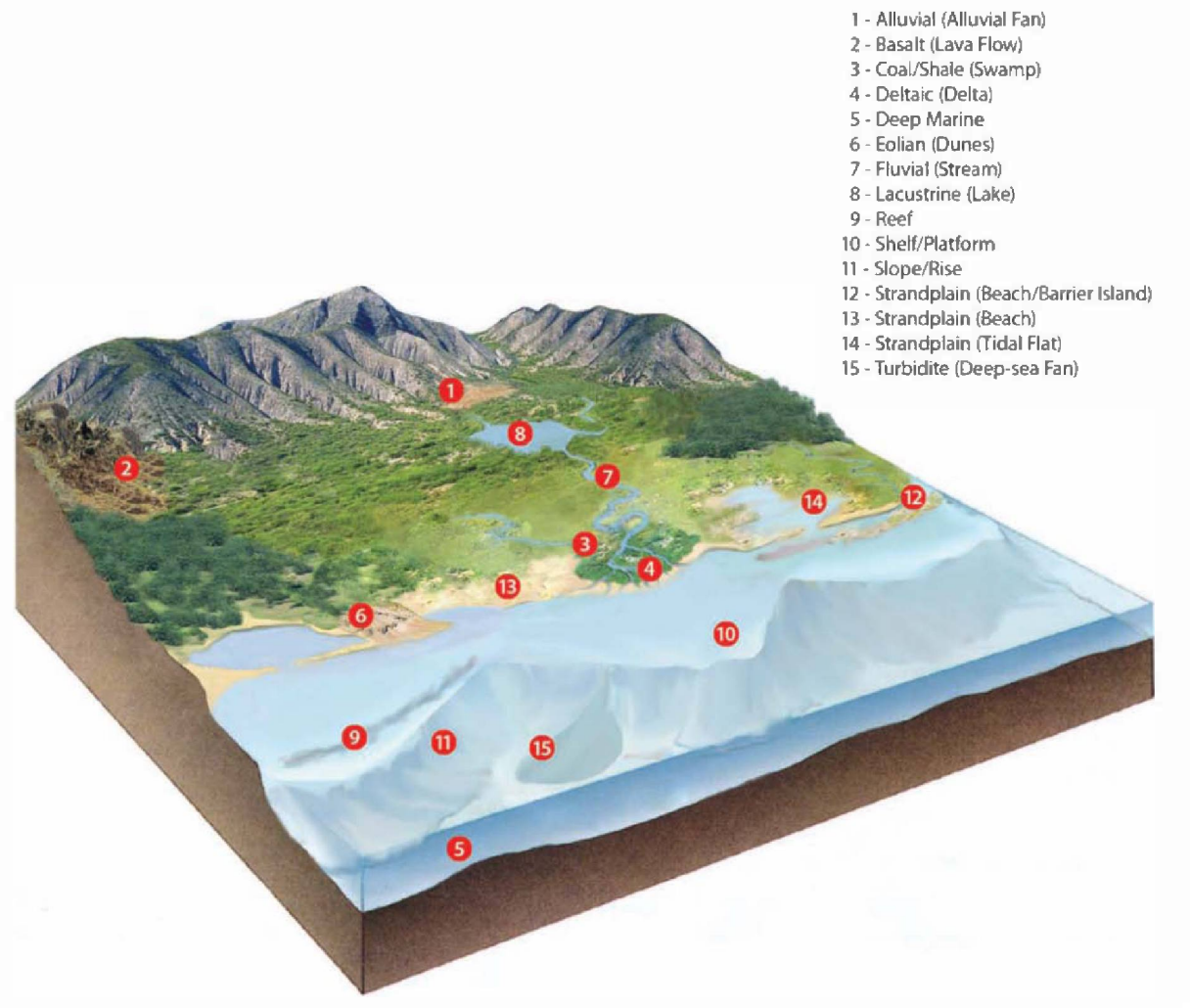

Figure 1 Idealized depositional model of sandstone and carbonate reservoirs (NETL, 2010a).

Table 1 Matrix showing the number of depositional environments under investigation by NETL (modified from NETL, 2010b). Large-scale field tests are defined as CO_2 injection over 1,000,000 tons and small-scale field tests are defined as CO_2 injection less than 500,000 tons. The characterization grouping from NETL (2010b) entails sites where the subsurface has been geologically screened at a location with the potential to inject at least 30,000,000 tons of CO_2. Reservoir potentials were inferred from petroleum industry data and field data from the sequestration program.

Matrix of Field Activities in Different Formation Classes											
Geologic Formation Classes	**High Potential**					**Medium Potential**				**Lower or Unknown Potential**	
	Deltaic	**Shelf Clastic**	**Shelf Carbonate**	**Strandplain**	**Reef**	**Fluvial Deltaic**	**Eolian**	**Fluvial & Alluvial**	**Turbidite**	**Coal**	**Basalt (LIP)**
Large Scale	–	1	–	–	1	3	–	1	–	–	–
Small Scale	3	2	4	1	2	–	–	2	–	5	1
Characterization	1	–	8	6	–	3	3	2	2	–	1

Illinois Basin formations were grouped into classes based on the predominant depositional environment present (Table 2). The eight formation classes in this study are defined according to the definitions given in National Energy Technology Laboratory (NETL; 2010b). Formation classes can be subdivided depending on the particular geology of a reservoir. However, for the purposes of developing guidelines for carbon storage potential, the United States Department of Energy (DOE) defined classes have been used. It is unlikely that any one formation will have a pure depositional system; rather, formations commonly exhibit a mixture of depositional environments with one having a dominating presence in a given area. Therefore, the formation classes given Table 1 should be seen as a guideline for relating carbon dioxide (CO_2) storage potential and depositional environment. Nuances inherent to each depositional environment and formation studied within the ILB are identified.

The existing literature on the reservoir characterization studies, geologic models, and geocellular models of the eight selected formation classes in the ILB was reviewed. The available literature varied for each ILB formation, with some being extensively studied and others with very little previously published studies. The existing literature provides discussion on the discovery and development of the fields and examines the differing interpretations on the structure and stratigraphic relationship of the underlying reservoirs. In this report, informal names given in quotation marks or parentheses are commonly used for these intervals or pay zones in oilfield records or previous literature. This report includes geologic cross sections showing potential reservoir intervals, structure and isopach maps, facies information and interpretations, available core data, and geophysical log information. Furthermore, each reservoir's potential for CO_2 storage was considered. The result of the geologic reservoir characterization is a conceptual model that includes the identification of depositional environment. The conceptual models are used as a basis for geocellular modeling and reservoir simulation.

Table 2 Different formation classes with selected study sites.

Formation Class	Storage Potential (DOE's rating)	ILB Reservoir	Formation	Lithology
Deltaic	High	Lawrence	Bridgeport	Sandstone
Shelf Clastic	High	Lawrence	Cypress	Sandstone
Shelf Carbonate	High	Johnsonville Consolidated	Ste. Genevieve	Limestone
		Miletus	Geneva	Dolomite
Strandplain	High	Manlove	Upper Mt. Simon	Sandstone
Reef	High	Tilden	Racine	Dolomite
Fluvial Deltaic	Medium	Lawrence	Bridgeport	Sandstone
Fluvial and Alluvial	Medium	Illinois Basin–Decatur Project	Lower Mt. Simon	Sandstone
Turbidite	Medium	St. James	Carper	Sandstone

Deltaic and Fluvial Deltaic: Bridgeport Sandstone at Lawrence Oil Field

Lawrence Field Production History and Development

Lawrence Field covers an area of roughly 172 km^2 (66.4 mi^2) in Lawrence County with a few wells extending into Crawford County in southeastern Illinois. The field follows a northwest-southeast trend that begins 16.5 km (10.2 mi) northwest of the village of Bridgeport, Illinois, and extends 14 km (8.7 mi) to the southeast of the village. Discovery of the field occurred in 1906 on the Buchanan Farm (Section 16, T3N, R12W) in Lawrence County, just southeast of Bridgeport. Extensive development of the field commenced in 1907 and 1908. Lawrence is a major oil field in the Illinois Basin; it has produced in excess of 69.3 million m^3 (436 million bbl) of oil from 26 reservoirs since its discovery, ranging from the Middle Pennsylvanian to the Ordovician Galena Group.

In 1906, wildcat drilling in the area led to the discovery of basal Pennsylvanian sandstone reservoirs capable of commercial petroleum production. Development of Lawrence Field began in earnest in 1907–08 (Blatchley, 1913). Primarily developed by the Ohio Oil Company (Marathon), early drilling indicated seven different sandstone pay zones, including three lenses of "Bridgeport" sandstone, Battery Rock (Buchanan) Sandstone, Cypress (Kirkwood/Weiler) Sandstone, Tracey sandstone, and Ste. Genevieve (McClosky) oolites. Records indicate that over 8,200 wells have been completed in the field since its discovery, with some estimates ranging up to 14,000 wells, many of which predate the Illinois Department of Natural Resources regulation program, which started in 1939 (IDNR, 2013). The Mississippian Cypress sandstone and the Pennsylvanian Bridgeport sandstones have proved to be the most prolific reservoirs in the field. There have been nearly 5,000 well completions in the Cypress and over 1,500 wells drilled only to the Bridgeport, with most of the Cypress and deeper wells also being completed in the Bridgeport. Current production is from 3,108 wells as of 2009.

The field was unitized in the mid-1950s for waterflooding, with a majority of the production coming from comingled Cypress and Bridgeport intervals. In the 1970s–1980s, high oil prices prompted interest in the application of enhanced oil recovery techniques. The result was the surfactant-polymer flood (Maraflood) implemented by Marathon in pilot projects, which separately tested the Cypress and Bridgeport reservoirs in different parts of the field (Ver Steeg, 1970; Palmer, 1984). Application of the Maraflood EOR technique proved a technical success, with the 10 ha (25 acre) Bridgeport pilot achieving 34% of residual oil saturation (S_{or}) after primary production and waterflooding (15% PV). However, economic factors, particularly a steep decline in oil prices in the mid-1980s, reduced feasibility, limiting the expansion of the Maraflood beyond the pilot areas.

Lawrence Field is a mature producer. Current production is at a rate of less than 2% oil cut, and it is estimated that recovery thus far is less than 40% of original oil in place (OOIP). For the field, OOIP is likely greater than 0.16 billion m^3 (1 billion bbl) of oil. Using an estimate of 10% tertiary recovery of OOIP yields a potential of greater than 16 million m^3 (100 million bbl) of recoverable oil.

Study Area

The study area within Lawrence Oil Field for the deltaic and shelf clastic (covered in next depositional environment section) geologic models includes roughly 5.5 km^2 (2.1 mi^2) or 546 ha (1,350 acres) in the northern part of field atop the Bridgeport Anticline, mainly Sections 29 and 32, T4N, R12W (Figure 2). The expanded area mapped for the development of the geologic models extends outside of the immediate study area, covering nearly 20.7 km^2 (8 mi^2) or 2,072 ha (5,120 acres), including most of Sections 19, 20, 29, 30, 31, and 32, T4N, R12W, and portions of the surrounding sections. The same wells were used to map both the Pennsylvanian Bridgeport (deltaic) and Mississippian Cypress (shelf clastic) sandstones as both horizons are present in Lawrence Field but occur at different depths. The study area was selected to include areas of two previous DOE sponsored reservoir characterization studies on the potential use of EOR techniques in Pennsylvanian and Mississippian aged sandstone reservoirs (Oltz, 1994; Seyler and Grube, 2012).

For the fluvial deltaic geologic model, a separate study area was chosen to coincide with a channel sandstone body that was identified in a previous study (Seyler and Grube, 2012). This study area includes roughly 3.5 km^2 (1.4 mi^2) or 354 ha (875 acres) along the southeastern edge of the Bridgeport Anticline. This study area mostly passes through portions of Sections 4, 5, and 8, T3N, R12W, and also includes some of the adjoining sections (Figure 2). An expanded area was studied to better define the extent of the channel sandstone body of interest.

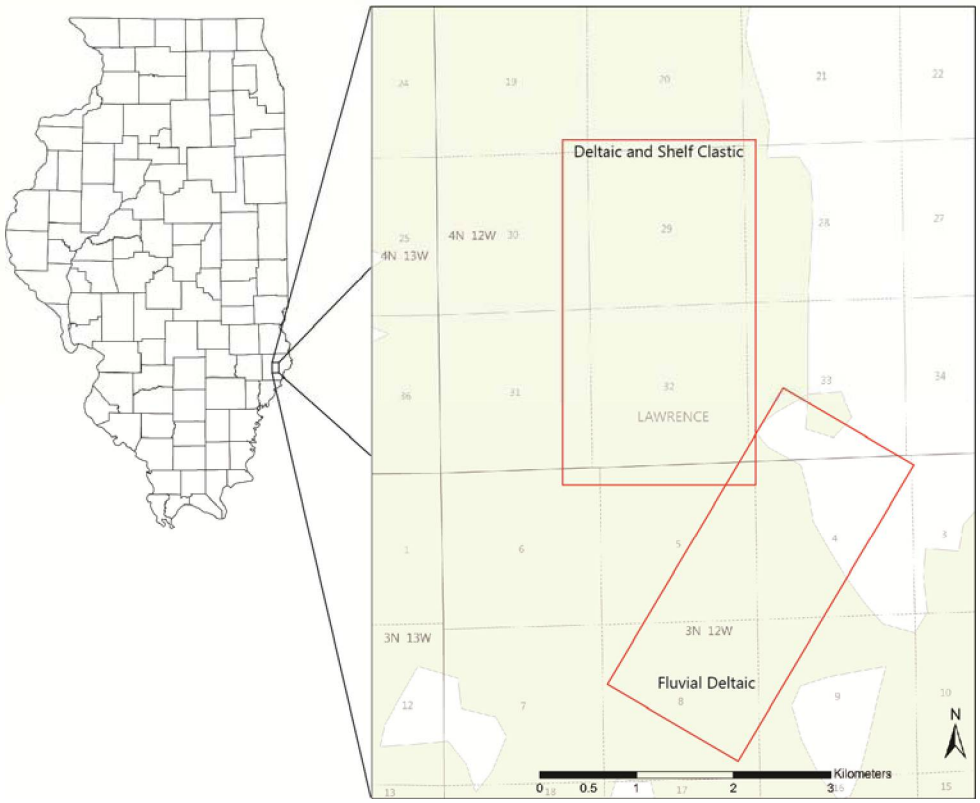

Figure 2 Map showing the locations of the study areas used in the creation of the deltaic, fluvial deltaic, and shelf clastic geologic models in southeastern Illinois. The deltaic and shelf clastic models share the same study area and well control. The main study areas are outlined in red. The study areas are in the Lawrence Oil Field (shaded area).

Geologic Setting

The stratigraphic nomenclature used in this study follows that of Willman et al. (1975). In some instances formal formation names are interchanged with locally used oil industry terms to maintain consistency with previously published reports. All of the formations studied at Lawrence Field fall within the Pennsylvanian and Mississippian Systems.

The stratigraphic units used to map and interpret the Cypress and Bridgeport reservoirs in this study area include the Paint Creek Limestone, multiple Cypress Sandstone subunits, the Beech Creek ("Barlow") Limestone, the Glen Dean Limestone, multiple Bridgeport sandstone subunits, Carrier Mills Shale, and various Middle Pennsylvanian coals (Figure 3). In the study area, the Barlow limestone, Glen Dean Limestone, Carrier Mills Shale, and numerous Pennsylvanian coals are all laterally continuous and useful marker horizons for gross interval mapping.

Structure

Lawrence Field is located on the eastern edge of the Fairfield Basin, the structurally deep part of the Illinois Basin in southeastern Illinois, where it forms along a portion of the LaSalle Anticlinorium. The LaSalle Anticlinorium is composed of a series of anticlines oriented parallel to one another that are generally offset to the west, as the regional anticlinal features extend from their southernmost extent and are expressed in the subsurface in Lawrence County to their northern most extent in LaSalle County, where bedrock anticlinal features can be observed in outcrops.

The Charleston monocline marks the western edge of Lawrence Field as it steeply plunges into the Fairfield Basin. Lawrence Field occupies two structures separated by a saddle: the Bridgeport Anticline (northern structure) and the Lawrenceville Dome (southern structure). Both are a part of the overall La Salle Anticlinorium and are found on top of the Charleston Monocline (Nelson, 1995). To the east of the Bridgeport Anticline and the Lawrenceville Dome lies a gently sloping shelf. A structure map contoured on the base of the Barlow limestone (Figure 4) shows the location of Lawrence Field with respect to these structural features and shows approximately 107 m (350 ft) of closure on the Bridgeport Anticline.

Lawrence Field is broken into two portions based on the two structural elements that form it. To the north is the north-northwest to south-southeast trending Bridgeport Anticline. The Bridgeport Anticline is about 16 km (10 mi) long and 3 km (2 mi) wide with structural closure on the Barlow limestone measuring 67 m (220 ft). To the south is the more circular Lawrenceville Dome that exhibits far less closure. The two structures are separated by a north-northeast to south-southwest trending saddle. Oil accumulation in the field is controlled mainly by structure; however stratigraphy has a significant effect on recovery (Oltz, 1994).

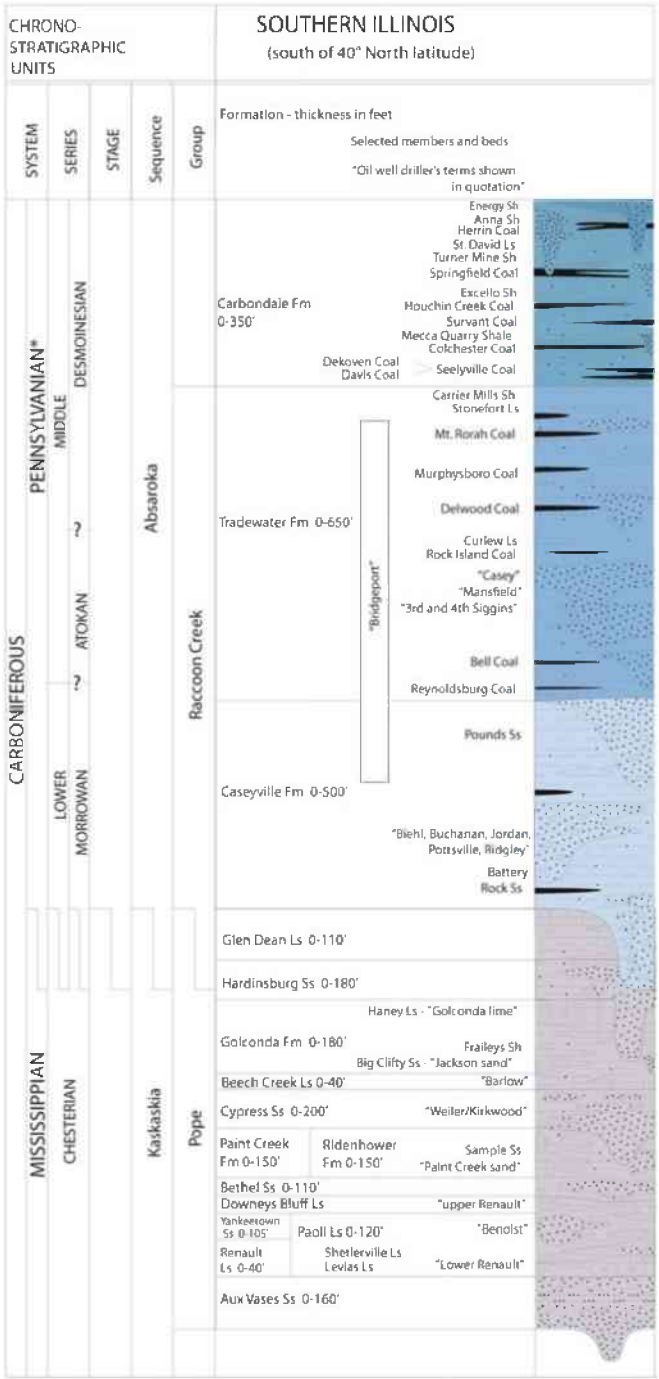

Figure 3 Stratigraphic framework of the Chesterian (Upper Mississippian) and Lower-Middle Pennsylvanian formations in Lawrence Field. The erosional unconformity between the Mississippian and Pennsylvanian Systems is indicated in the figure with a red line; however, Mississippian formations as old as the Barlow limestone have been locally removed by post-Mississippian erosion with later infilling of scoured areas by Pennsylvanian sediments.

A number of key field-wide marker beds were correlated to provide reliable stratigraphic datums for picking tops of reservoir sand bodies. A number of field wide structure maps were completed on many horizons. The Barlow limestone structure map (Figure 4) is shown. The structure maps on the Mississippian Glen Dean Limestone and the base of the Barlow limestone show similar structural closure on the major anticline in the northern portion of the field; however, the stratigraphically higher Glen Dean Limestone structure map shows an area in the structural saddle between the Bridgeport Anticline and the Lawrenceville Dome in Section 8, T3N, R12W, where this marker horizon has been truncated by pre-Pennsylvanian erosion. The stratigraphic relationships of selected mapping horizons are shown in the stratigraphic column in Figure 3.

Mapping Methodology

The basic geologic models were built using a grid of north-south and east-west cross sections. The cross sections were generated using scanned geophysical logs strung together using Geographix software. Gridding algorithms in Geographix were also used to generate contoured structure maps and sandstone isopach maps. The base of the Barlow limestone was used as a stratigraphic datum in picking Cypress subintervals. Net 50% clean sandstone reservoir thicknesses were picked from scanned electric wireline logs using the 50% clean sandstone cutoff between the shale baseline and a thick, clean, and blocky water-wet sandstone. The Fraileys Shale (Figure 3) was used to demarcate the shale baseline, and the basal Pennsylvanian Buchanan sandstone (Caseyville Formation) was used as the 100% clean sandstone.

Thickness data of the net 50% clean sandstone reservoir units were entered into the Geographix mapping software and interpreted. A few thousand well logs were used in the construction of the conceptual geologic models for the Bridgeport (deltaic and fluvial deltaic) and Cypress (shelf clastic) reservoirs. Many of these wells lie outside the immediate study area to help eliminate low data density edge effects in mapping.

Correlation of individual reservoir intervals can be difficult as they can rapidly pinch and swell. Multiple iterations of correlation and isopach mapping are necessary in order to assure that cross-correlations are minimized. If reservoir geometries exhibit an “amoebic” shape rather than a natural form expected from a given depositional environment, then correlations are likely incorrect. This can play a critical role in defining flow units in compartmentalized reservoirs and the implementation of any recovery program for an oil field, particularly secondary and tertiary programs.

Bridgeport Background

Unlike the many Mississippian Formations that have had extensive study in the Illinois Basin, the Bridgeport sandstones have seen markedly less study across the Illinois Basin. Named for the village of Bridgeport in Lawrence County, Bridgeport is an informal term for multiple sandstone reservoirs of Early to Middle Pennsylvanian age which occur across roughly 91.4 m (300 ft) of section in Lawrence Field in southeastern Illinois. Sandstone reservoir bodies of a similar age to the north of Lawrence Field are referred to as Robinson sandstones in Main Consolidated Field in Crawford County and, farther north, the Siggins sandstone reservoirs are found in Siggins Field. All of these informally named sandstones are contained within the lithologically varied Caseyville and Tradewater Formations.

Pennsylvanian sandstones have been productive in the Illinois Basin for over 100 years. Swann and Bell (1958) stated that production from Pennsylvanian reservoirs was nearly 17% of total production in the Illinois Basin through 1955, second only to Mississippian reservoirs in terms of total volume produced. However, their report provided little detail on the character of the reservoirs themselves despite their economic significance. The report mentioned that Pennsylvanian reservoirs were predominantly productive along the structures that make up the LaSalle Anticlinorium; primarily in basal sandstones that immediately overlie the Sub-Absaroka Unconformity at the base of the Pennsylvanian System and in the overlying sandstones when shale does not seal the basal sandstones. Pennsylvanian production outside of the LaSalle Anticlinorium was described as being limited to areas along faults and in basal Pennsylvanian sandstones that immediately overlie Mississippian reservoirs. The report did note that where Pennsylvanian reservoirs occur, they can be prolific producers due to high porosity and permeability values, especially in basal sandstones.

Previous study of the Bridgeport and equivalent sandstones is limited to a handful of early reports and an unpublished thesis from fields along the La Salle Anticlinorium. More recently, studies of the Bridgeport in Lawrence Field include an unpublished dissertation and one DOE funded reservoir characterization project for the application of an alkaline-surfactant-polymer (ASP) flood (Seyler and Grube, 2012).

A report by Rich (1916) touched briefly on the Pennsylvanian strata of Birds Quadrangle in eastern Crawford and Lawrence County. The Lower Pennsylvanian Pottsville Formation (now referred to as the Caseyville and Tradewater Formations) was described as being composed predominantly of sandstone with numerous beds of shale, some thin limestones, and stringers of coal. The Robinson sand was described as the most important oil-producing sandstone in the quadrangle. Rich noted that other Pottsville Formation sandstones below the Robinson were filled with water.

Moulton (1925) described the Bridgeport sandstone at Allendale Field in Wabash County, southeast of Lawrence Field. Here, the Bridgeport sandstones occur 305–335 m (1,000–1,100 ft) deep. The sandstones were described as being composed of fine angular sand grains cemented by tan dolomitic material. Apparently, the permeability of the sandstones in Allendale Field are so high that the small structure on which the field sits is not sufficient to trap oil as water filled the entire sandstone body. Rather, oil is trapped stratigraphically by lithologic variations within the Bridgeport sandstone itself.

In an unpublished manuscript, Fisher (1930) described the Bridgeport sandstones in Lawrence Field. In Lawrence Field, there are a number of different sandstone horizons that are classified as Bridgeport. The lowermost sandstones are generally thicker and, in some areas of the field, coalesce with each other and with the underlying Buchanan sandstone. The upper Bridgeport reservoirs are thinner and more lenticular in character. The sandstones were described as being generally medium grained, although zones of fine and very fine sand do occur, poorly sorted and, in some cases, calcareous. Fisher noted the difficulty in correlating the few marker beds in the area over anything more than short distances.

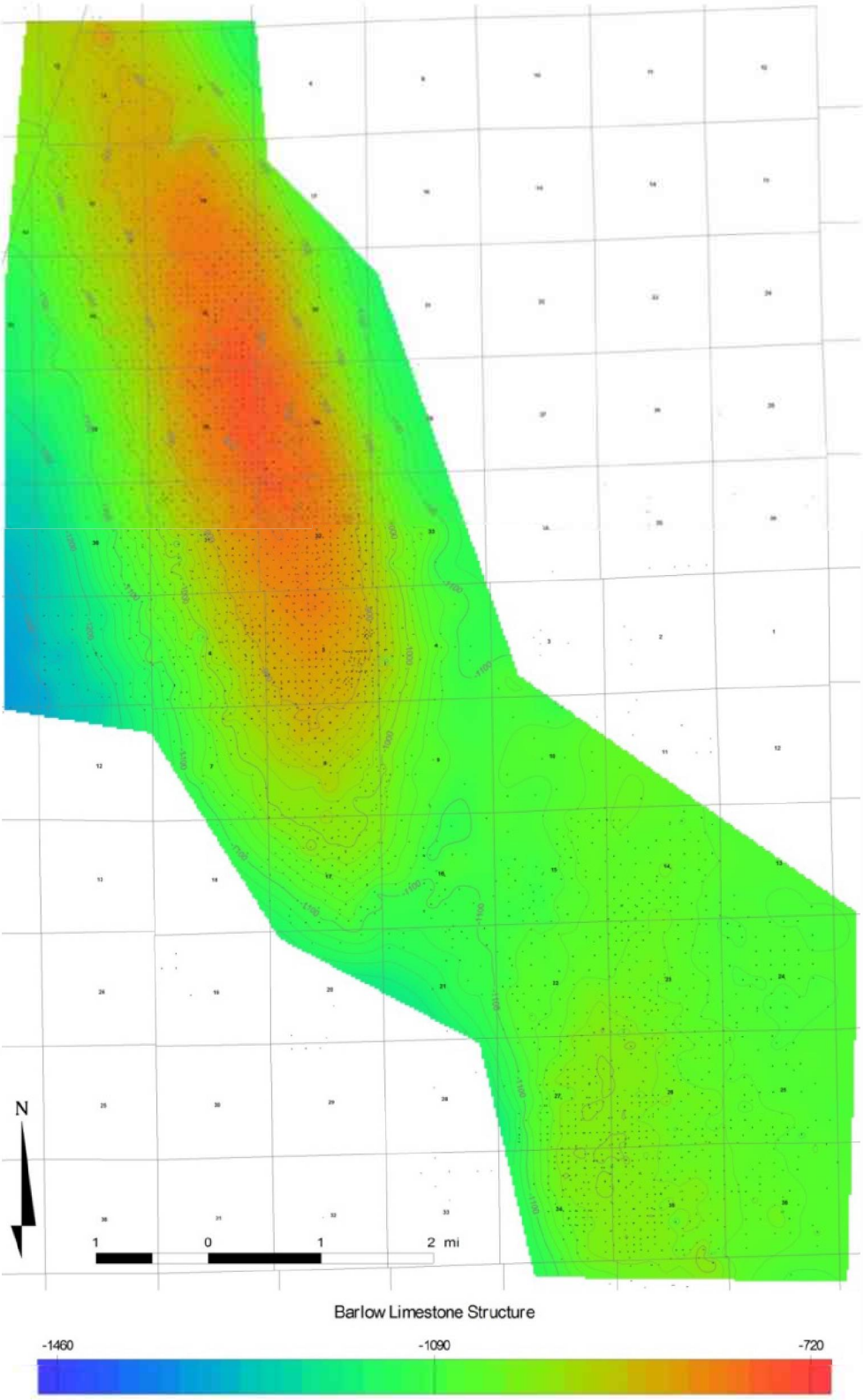

Figure 4 Structure map contoured on the base of the Barlow limestone. Contour interval is 7.6 m (25 ft). The northwest-southeast trending Bridgeport Anticline is shown, as well as the more subtle Lawrenceville Dome to the southeast.

Potter (1956) investigated the Pennsylvanian subsurface geology of Lawrence and Crawford counties to assess the coal resources in the area. The investigation made use of over 1,500 data points from wireline logs to drillers logs and drill hole cuttings using five-foot samples. Potter (1956) described the structural features of the area as the La Salle Anticlinorium entered the area from the north and continued through the central part of the counties. To the west of the anticline, the Pennsylvanian succession thickens rapidly into the deep part of the Illinois Basin. To the east of the Anticline, Pennsylvanian sediments are thinner and lie on a shelf.

Potter (1956) also recognized the presence of the Mississippian-Pennsylvanian unconformity and noted that its presence presented a difficulty in mapping the thickness of the Pennsylvanian interval, especially in Lawrence County, where the massive Mississippian Tar Springs sandstone lies near the unconformity and could easily be mistaken for a basal Pennsylvanian Sandstone. Identification of the unconformity in Crawford County is markedly easier. Potter (1956) also described the nature of the unconformity as it created a basin-wide pattern that was more extensively eroded over active late Mississippian to Early Pennsylvanian structures and that created an integrated system of incised valleys commonly 30–61 m (100–200 ft) deep. In areas of Crawford County, these channels are superimposed across the La Salle structure where they are up to 76 m (250 ft) deep and are generally less than 3–5 km (2–3 mi) wide.

The sedimentary succession that makes up the Caseyville and Tradewater Formations were not differentiated in the study. The Unconformity marked the base of the Caseyville Formation and the Colchester (#2) coal was used to define the top of the Tradewater Formation. Overall combined thickness of the two formations in the area was found to be about 76 m (250 ft) over the crest of the La Salle Anticlinorium, and over 305 m (1,000 ft) in the deep part of the Illinois Basin in southwestern Lawrence County. On the shelf area to the east, thickness of the units ranges from 168 to 213 m (550 to 700 ft).

Potter (1956) described the Caseyville and Tradewater Formation sandstones as being highly irregular, with individual sandstone bodies being only traceable over a few square miles despite thicknesses of over 61 m (200 ft). Potter recognized the application of informal names like Bridgeport, Buchanan, Biehl, Jordan, and Robinson to sandstone reservoirs of limited extent within the Caseyville and Tradewater Formations, but noted that because of the difficulty in tracing the reservoirs over great distances, the utility of the informal names is limited outside of localized areas.

More recently, Lumm (1998) completed a dissertation on the Lower Pennsylvanian and Upper Mississippian strata in Lawrence Field. This study focused on the structural history of the field and the problematic correlation of strata across the Mississippian-Pennsylvanian unconformity. Lumm created gross thickness maps of the sandstones that would traditionally fall into the Bridgeport interval. The maps indicate that individual sandstone bodies within the Bridgeport are extremely variable, with each sandstone body in the study area ranging in thickness from 0 to 46 m (0 to 150 ft) plus. The sandstones are commonly thinner and more lenticular on top of the La Salle Anticlinorium where they reach thicknesses of around 9.1 m (30 ft), except for the lowermost Bridgeport sandstone which can be much thicker. However, all of the sandstones thicken dramatically and often coalesce off the western flank of the structure.

Reservoir Characterization

Stratigraphy

The Caseyville Formation unconformably overlies the sedimentary succession of the Chesterian Series (Upper Mississippian System) in southeastern Illinois (Siever, 1951; Bristol and Howard, 1971). Within the Chesterian, sandstones, siltstones, and shales are interspersed with regionally extensive limestone units that are widely traceable. Above the Tradewater Formation lie the cyclical successions of sedimentary rock of the classic Pennsylvanian Cyclothems (Weller, 1930; Wanless and Weller, 1932) that make up the Carbondale Formation. These cyclothems are punctuated with coal beds such as the Herrin, Springfield, Colchester and Seelyville that, like the Chesterian limestones, are essential marker beds for regional correlation.

Unlike the underlying and overlying formations, the Caseyville and Tradewater Formations are mostly made up of sandstones, siltstones, and shales and generally lack any regionally extensive limestones or coals to act as marker beds for correlation. In fact, the boundary between the two formations is difficult to identify on a lithologic basis because of the lack of variety in the rocks that make up the formations. Caseyville Formation sandstones are typically thickly bedded, medium-coarse grained, and often contain quartz granules and pebbles (Siever, 1951; Willman et al., 1975; Nelson et al., 1991). Tradewater sandstones are generally more lenticular and lack the quartz granules and pebbles indicative of the Caseville Formation. In some instances, widespread, lenticular sandstone bodies are juxtaposed against exceedingly thick and more linear sandstone bodies. In both cases, the discontinuous and commonly stacked sandstones are usually interbedded with grey to black shale and siltstone with occasional localized limestones or coals.

The pre-Pennsylvanian surface was deeply eroded following deposition of Chesterian deposits. Lower Pennsylvanian sediments of the Caseyville Formation were deposited onto the surface and in some instances fill or partially fill valleys that were incised deeply into upper Mississippian strata. The infill of these paleovalleys contributed to the highly complex relationship of sandstone bodies in the Lower Pennsylvanian Caseyville and Tradewater Formations.

The Bridgeport B stratigraphic interval includes the most productive and widespread of the Pennsylvanian reservoirs in Lawrence Field. The Bridgeport B interval falls near the boundary of the Caseyville and Tradewater Formations and contains multiple sandstone bodies that were deposited in multiple depositional environments. Because of high relief substrate (caused by pre-Pennsylvanian erosion), active tectonics, and limited accommodation, nearshore deposits that presumably blanketed the area are commonly truncated by erosion that accompanied frequent subaerial exposure. The result is a confusing mix of older nearshore deposits juxtaposed against younger, more terrestrial deposits in a repeating succession.

Mapping of the sandstone bodies within the Bridgeport B interval was aided by the identification of sequence stratigraphic surfaces. The Bridgeport B interval includes sandstone bodies of two distinct facies and depositional environments: a nearshore, tidally influenced, deltaic facies and a thick, fluvial deltaic channel-fill facies that are juxtaposed against one another in certain areas of the field. An isopach map of sandstone bodies that make up the Bridgeport B interval is a composite of the two depositional facies mentioned above (Figure 5). The Bridgeport fluvial deltaic channel-fill sandstones are mapped as a gross thickness in bright colors and the tidally influenced, deltaic Bridgeport B sandstone bodies are mapped as a net thickness in paler colors

using a normalized spontaneous potential (SP) 50% clean sandstone cutoff. The isopach map is superimposed on a structure map contoured on the base of the Mississippian Barlow limestone with a contour interval of 7.6 m (25 ft). The selected study areas used for the creation of geocellular models were outlined previously (Figure 2).

Deltaic—Bridgeport B

The Bridgeport deltaic facies sandstone occurs on the crest of the Bridgeport Anticline and is most easily defined where it is found in association with the underlying, informally named Beta shale and an overlying unnamed coal. A geophysical log from the Johnson #32 well shows the relationship of the Bridgeport B sandstone lenses with the underlying Beta shale and the overlying coal (Figure 6). Evidence from core and geophysical logs indicate that this is the typical Bridgeport deltaic facies succession. In the study area, Bridgeport B deltaic facies sandstones average approximately 7.6 m (25 ft) thick and trend more or less east-west over the anticline and are shown in pastel colors on the map (Figure 5).

The east-west trending sandstone bodies of the deltaic Bridgeport B are interfingered with nonreservoir siltstones and shales (Figure 7). This nonreservoir facies of the Bridgeport B may have been deposited concurrently with the sandstones in some places, but was almost definitely the result of postdepositional erosion and inactive channel fill in other areas.
The Bridgeport B deltaic sandstone has a sharp contact with the underlying widespread Beta shale that was deposited during a maximum marine transgression. The shale separates the Bridgeport B from a lower lenticular sandstone reservoir. The sharp basal contact of the deltaic sandstone with the underlying shale defines a sequence boundary. Reservoir sandstone in Section 29 and the northern half of Section 32 trends east-west, whereas in the southern half of Section 32 the sandstone takes on a triangular shape and occupies the region between the two thick channel-fill sandstone bodies that trend into Section 5 from the northeast and northwest. The thin, fine-grained, deltaic Bridgeport B facies in the study area was informally divided into three subunits: the B1, B2, and B3 from the base to the top of the unit.

The three Bridgeport sandstones in the study area stack up on top of one another. The lowest Bridgeport B sandstone unit (B1) is more consistent, widespread, and thicker—up to 6 m (20 ft)—than the upper two sandstones units. The B1 sandstone is thicker and better developed than the B2 and B3 sandstones, which can, in some areas, transition out to shale. This is reflected in areas of the isopach map where the net sandstone thickness is less (Figure 5). Much of the Bridgeport B1 is composed of fine-grained, tabular cross bedded and subhorizontal bedded sandstones that show some tidal couplets. The B2 and B3 sandstones are finer grained and are composed of more tidally influenced ripple-bedded facies. Porosity and permeability are greater in the B1 than the overlying B2 and B3 ripple-bedded sandstone facies.

A typical core from the Johnson #32 well shows sedimentary features representative of the Bridgeport B reservoir in Section 32 (Figure 8). The reservoir sandstone is typically fine to very fine grained and fines upwards. The basal contact of the reservoir sandstone with underlying shale is sharp. Tabular cross beds with small clay rip up clasts are common in the B1 sandstone. The reservoir sandstone is punctuated with calcite cemented zones and intervals of lenticular to flaser bedded sandstone that range in thickness from a few inches to around a foot. Flaser and lenticular bedded zones, and to a lesser extent the calcite cemented zones, may create baffles to vertical fluid flow between porous intervals locally, but also extend laterally over a wide area. It

is likely that some baffles, especially calcite cemented zones, do not extend over distance and some vertical communication between the subunits of the reservoir are established. Ripple-bedded sandstone and tidal rhythmites are common in the B2 and B3 sandstone subunits, indicating a tidal influence on deposition.

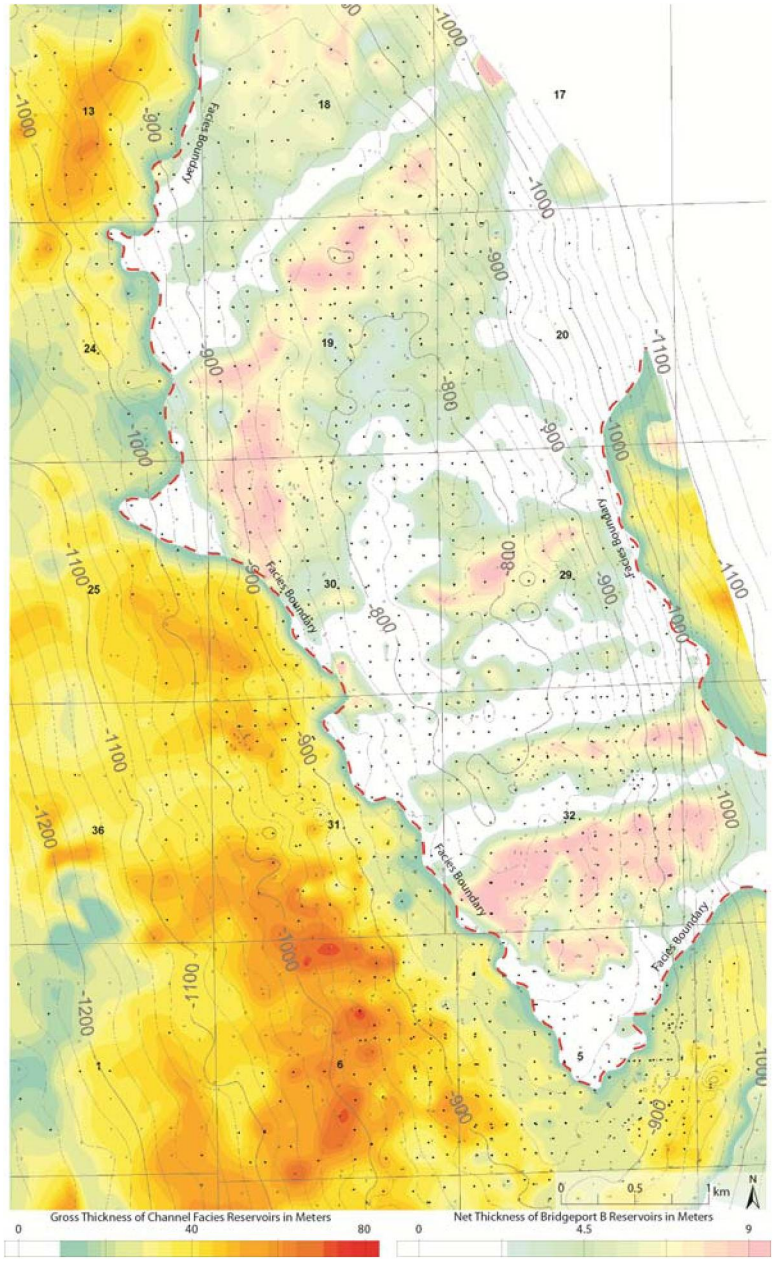

Figure 5 Isopach map of the Bridgeport B and stratigraphically correlative beds, which is a composite of two depositional facies. Bridgeport channel-fill sandstone (bright colors) and nonchannel Bridgeport B (paler colors) are mapped using normalized SP 50% clean data. Structure with a 7.62 m (25 ft) contour interval is on the base of the Mississippian Barlow limestone. In Section 32, Bridgeport B sandstones average about 7.62 m (25 ft) thick and trend more or less east-west over the anticline. Two stratigraphically correlative sandstone intervals up to about 60.96 m (about 200 ft) thick enter Section 5, one from the northeast and one from the northwest, straddling the anticline and converging toward the south.

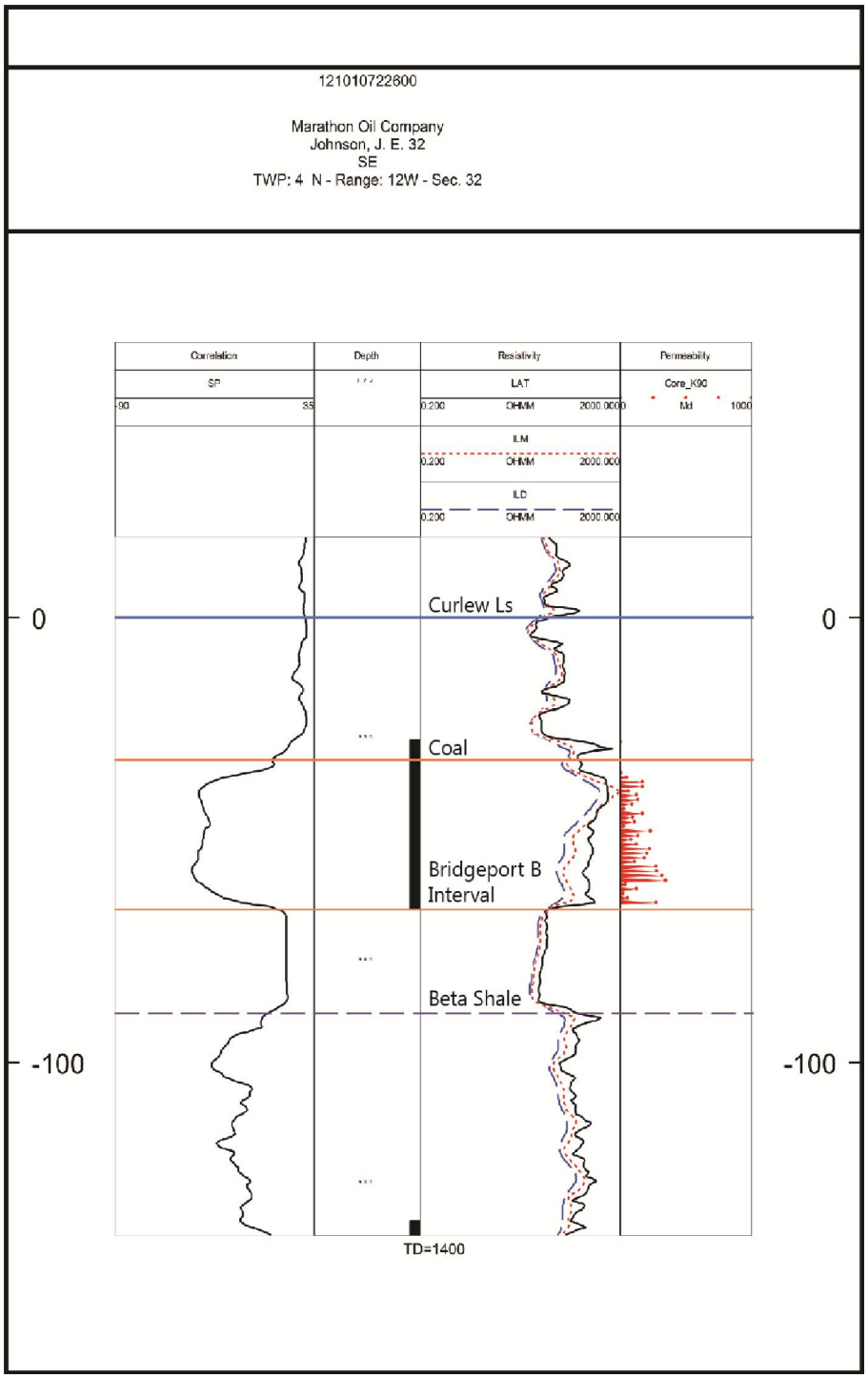

Figure 6 Electric log of the Johnson #32 well indicating cored interval (Figure 8) through a section of the better quality Bridgeport B reservoir in the southern part of Section 32. The deltaic Bridgeport B sandstone can be seen overlying the Beta shale and is capped with coal. Core measured permeability values for the sandstone are plotted in red.

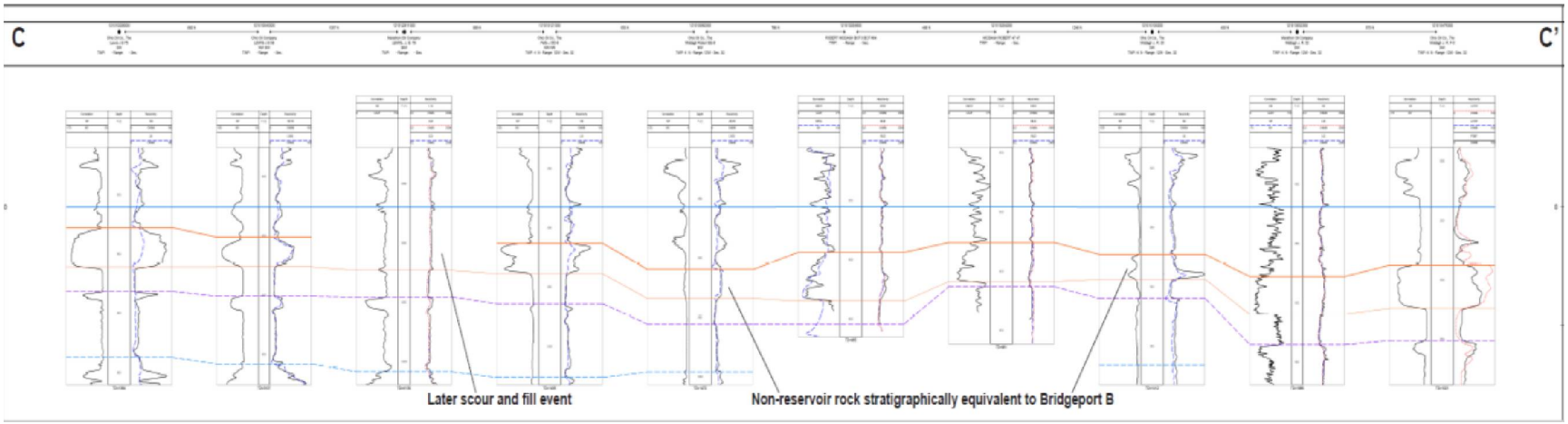

Figure 7 North-south cross section showing small-scale compartmentalization of the Bridgeport B (Figure 5) reservoir. East-west trending reservoir sandstone bodies are underlain by dark grey shale, are overlain by coal and shale, and grade laterally into siltstones, mudstones, and tight sandstones.

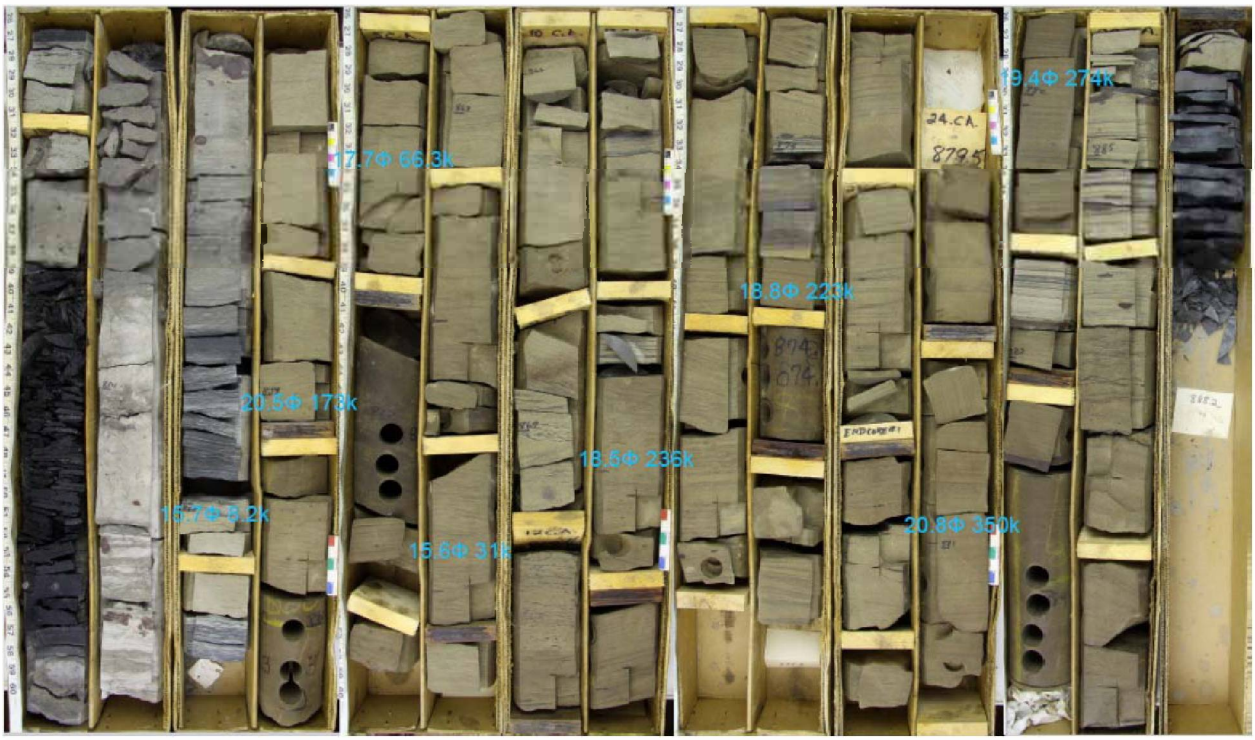

Figure 8 Core from the Johnson #32 well showing typical succession and arrangement of facies of the Bridgeport B in Section 32. The Bridgeport B is underlain by the widespread marine Beta shale. The basal contact of the Bridgeport B sandstone and the Beta shale is erosional and likely constitutes a sequence boundary. The Bridgeport B sandstone averages roughly 9.1 m (30 ft) thick, is mostly medium with some fine-grained sandstone and fines upward. Tabular cross bedded to planar bedded sandstone (about 20Φ 280k) generally makes up the lower portion of the Bridgeport B. The upper portion of the sandstone changes facies to wavy and ripple-bedded (about 17Φ 125k). A sharp contact at 261.4 m (857.5 ft) marks another facies change into lenticular bedded sediments that cap the succession as they transition into rooted sediments that supported the overlying coal. A few inches of dark grey shale on top of the coal indicates the next phase of transgression.

Fluvial Deltaic—Bridgeport Channel

Two thick sandstone bodies up to approximately 61 m (200 ft) thick occupy the same stratigraphic position as the deltaic facies Bridgeport B and enter Section 5, T3N, R12W, one trending from the northeast and one from the northwest, straddling the anticline and converging toward the south. The thick Bridgeport sandstones are mapped in bright colors (Figure 5). This study focused on the eastern of these two sandstone bodies as it was easier to define the physical boundaries of the sandstone body, and it also contained a greater abundance of available core and core analysis data.

The Bridgeport fluvial deltaic channel reservoirs typically occur along the flanks of the Bridgeport Anticline. These channels are interpreted to be younger than the Bridgeport B sequence interval, based on careful correlation of key marker beds and palynological evidence from coals associated with the two sandstones. The channel sandstones are likely related to the depositional sequence overlying the deltaic Bridgeport B sequence, and have incised and removed the sediments that make up the deltaic Bridgeport B section. Thus, where the channels occur, Bridgeport B reservoirs were eroded and replaced (Figure 9).

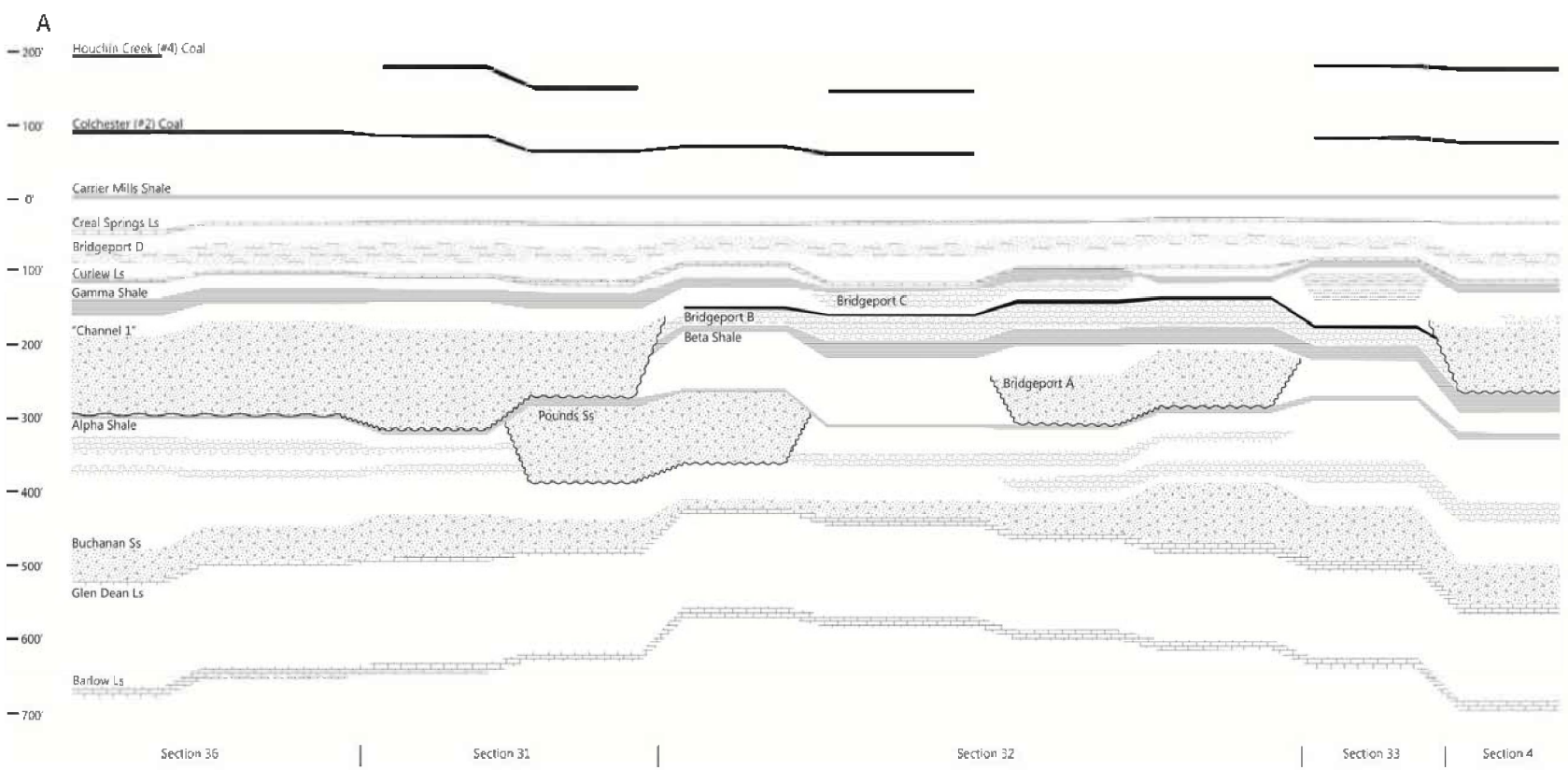

Figure 9 East-west diagrammatic cross section across the Bridgeport Anticline (Figure 5) in the northern part of Lawrence Field that shows the stratal arrangement of lower Pennsylvanian sediments. The Carrier Mills Shale (Figure 3) is the datum. Here, the discontinuous nature of the Bridgeport reservoirs can be seen. The deltaic Bridgeport B is widely traceable in part because of the consistent underlying Beta shale and overlying coal. The Bridgeport B is truncated to both the east and the west by younger Pennsylvanian fluvial deltaic channel-fill deposits

The channels are filled with thick, amalgamated channel-fill deposits of clean, fairly homogeneous, largely medium-grained sandstones that tend to exhibit more estuarine deposition towards the top of this sequence. These stacked Bridgeport fluvial deltaic channel sandstones can reach thicknesses nearing 80 m (262.5 ft) in places. Individual sandstone bodies cover a much larger area and, being more than three times thicker, are larger volume reservoirs that are less confined than the reservoirs of the deltaic Bridgeport B.

The basal fluvial deltaic sandstone contact with the underlying shale is erosive and exhibits a zone containing lag gravel, clay rip-up clasts, and zones of siderite cement. The basal zone is coarse grained but fines upward to medium sand through most of the reservoir. Above the basal zone, alternating sets of cross-bedded and indistinctly bedded sandstone are common. Sandstone beds are generally vertically continuous, lacking the baffles seen in the Bridgeport B. Slumping features are common. The sandstone becomes finer grained near the top of the interval where flaser and lenticular bedding as well as tidal rhythmites are common.

Core showing the typical facies of the Bridgeport channel reservoirs is from the Robins MG-8 well (Figure 10). The core shows sedimentary features common in the thick sandstone in eastern Section 5 and is indicative of channel-fill deposits with rapid deposition followed by limited compaction. Slumping features are common.

Reservoir Lithology and Petrology

Deltaic—Bridgeport B

X-ray diffraction (XRD) analyses of bulk mineralogy are available from fifty samples taken from six cored wells in the fine-grained deltaic sandstone facies of the Bridgeport B in Section 32, T4N, R12W. The sandstone is typically fine to very fine grained has been interpreted as deltaic. Most samples have 90% or greater quartz, making these sandstones quartz arenite. Siderite is most commonly a minor component in these samples at less than 5%; however, there are four samples with 30% or greater siderite. Calcite and dolomite are rarely present in samples from the fine-grained deltaic sandstone facies. Siderite is the most common carbonate present.

The clay mineral fraction most commonly ranges from 3 to 10% siderite; plagioclase and potassium feldspar combined are usually less than 4%, with pyrite/marcasite not present in these samples. Kaolinite is usually the most abundant clay mineral and illite is the second most abundant clay mineral. There are a few examples in shale rich samples where illite is the most abundant clay mineral. Chlorite and mixed layered illite/smectite are the least common clay minerals. Although clay minerals are a minor component they play a major role in preserving porosity by coating many quartz grains, thereby limiting the development of quartz overgrowths.

Thin section microscopy and scanning electron microscopy (SEM) shows that there is some compaction and a high degree of quartz cementation within deltaic Bridgeport B sandstones (Figure 12). Some pores have been enlarged due to dissolution of feldspar grains. The greater the amount of feldspar the greater the opportunity for the development of secondarily enhanced porosity caused by dissolution of feldspar framework grains. Degraded feldspar grains replaced by kaolinite as well as authigenic quartz overgrowths are also common features in this facies.

The greater the amount of quartz overgrowth development the more primary intergranular porosity is filled, resulting in the reduction of porosity and permeability.

Figure 10 Core example of channel fill Bridgeport B stratigraphic equivalent from the Robbins MG #8 well near the Maraflood pilot in Section 5. Sharp scour contact with course rip-up and conglomeratic basal channel lag (approximately 289.56–292 m [950–958 ft]) transitions into very clean tabular cross-bedded sandstone throughout most of the channel facies. Some core shows possible marine indicators in the upper feet of the core (tidal couplets and trace fossils). Channel fill sandstones are generally thicker and have higher permeabilities than their stratigraphic equivalent Bridgeport B deltaic facies sandstones (Figure 11).

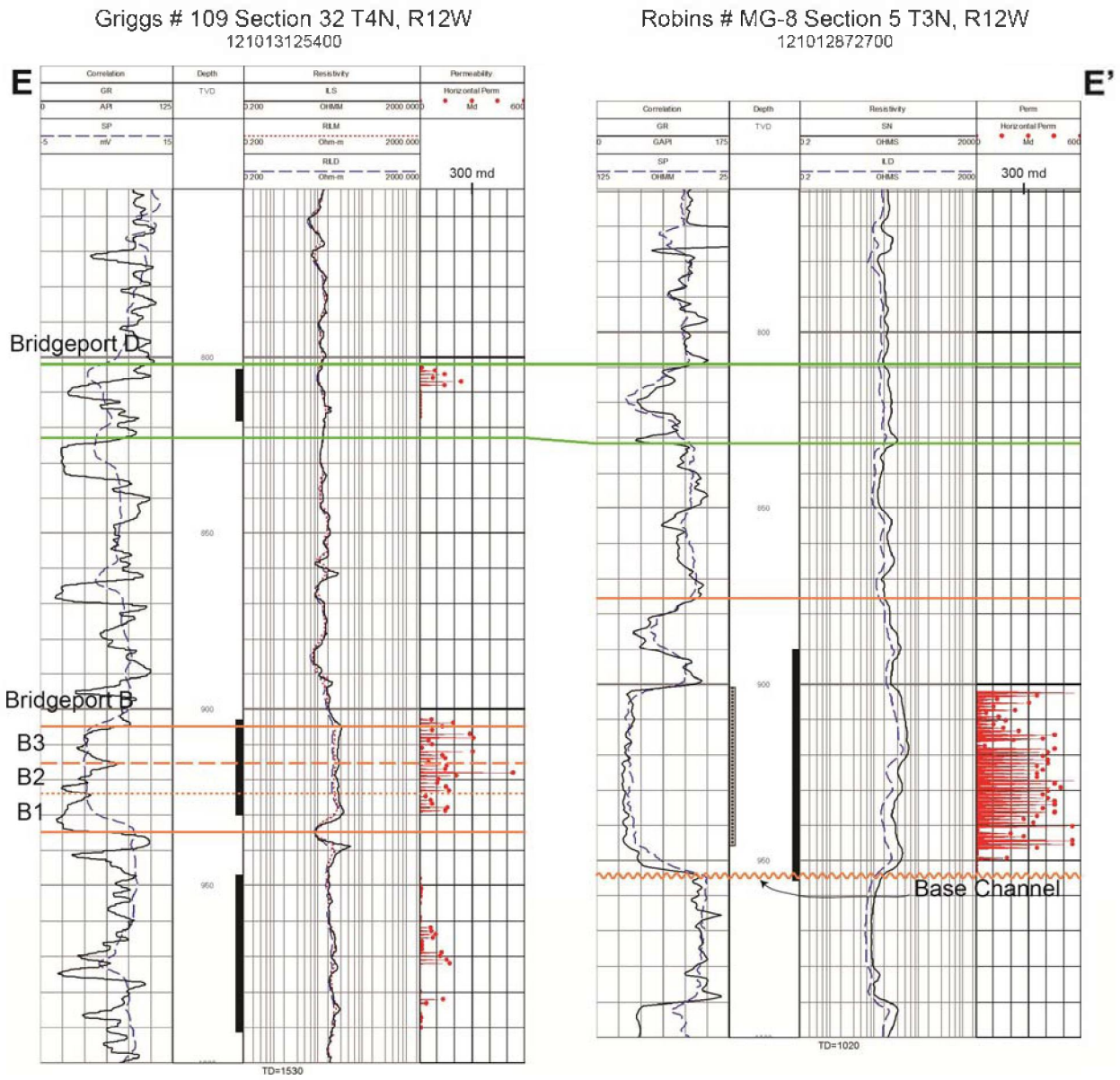

Figure 11 Two well cross section E-E' (Figure 5) shows the two entirely different depositional settings between Section 32 and Section 5. The Griggs #109 well in Section 32 on the left shows the typical stacked Bridgeport B intervals while the Robins #MG-8 well in Section 5 on the right has characteristically thick and blocky channel-fill sandstone. Core permeability is plotted in red on the right side of each log. Average permeability in Section 5 sandstone is 2.8 times greater (3.10×10^{-9} cm^2 [314 md]) than in Section 32 (1.11×10^{-9} cm^2 [113 md]). These wells are separated by about 2 km (1.25 mi), but this rapid change commonly occurs over just a few hundred meters.

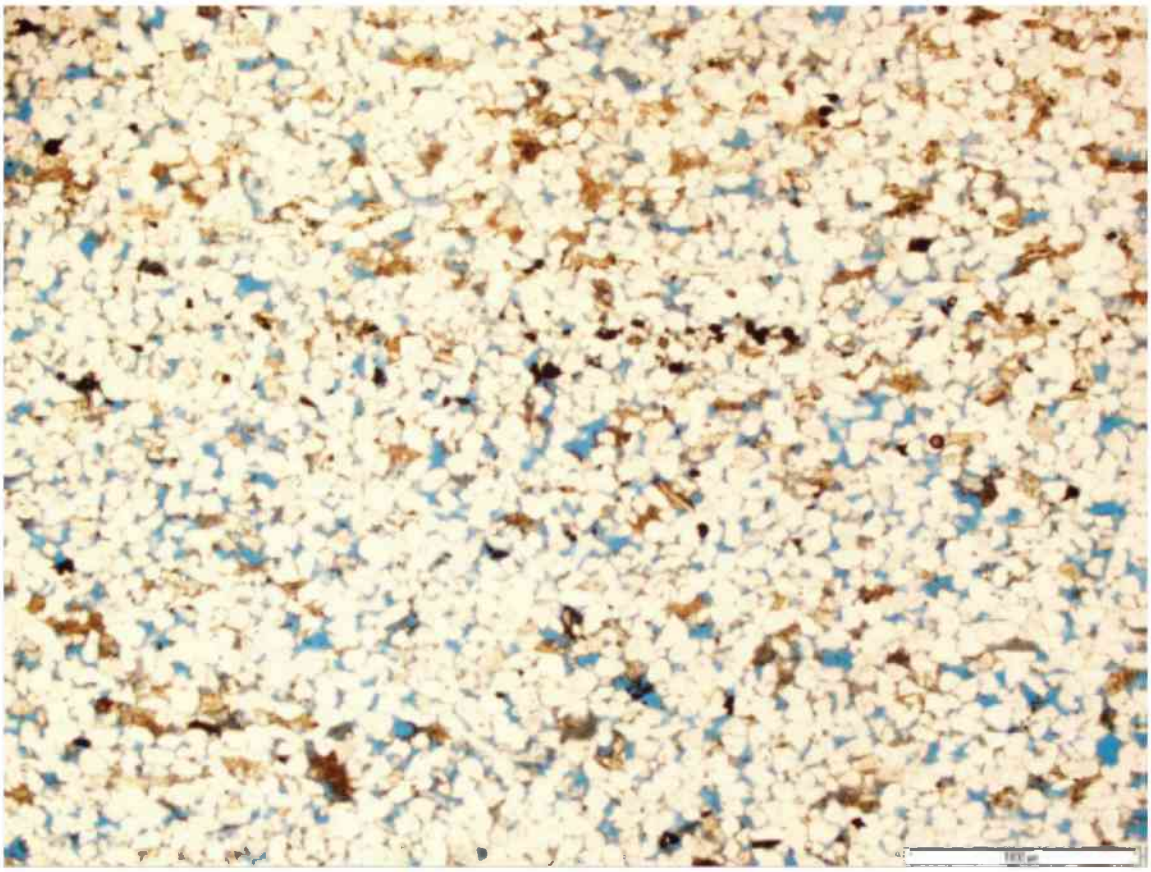

Figure 12 Thin section photomicrograph from the deltaic Bridgeport B sandstone in the Griggs #107 (Section 32, T4N, R12W) well shows fine-grained sandstone. Porosity is 20.3% porosity and permeability is 1.69×10^{-9} cm^2 (171 md). These are common values for this facies. Some fracturing of the sandstone is apparent. Some of the porosity is occluded in this sample by suturing of quartz grains and moderate compaction of ductile grains.

Fluvial deltaic—Bridgeport Channel

XRD analyses of bulk mineralogy and clay mineral fraction are available from samples taken from several wells in the fluvial deltaic channel-fill reservoir sandstones in Section 5, T3N, R12W. Bulk mineralogy analyses identified the relative abundance of clay minerals, quartz, K-feldspar, plagioclase-feldspar, calcite, dolomite, siderite, and pyrite/marcasite. Over 80 samples from core in the channel-fill reservoir sandstones in Section 5 were analyzed. None of the analyzed samples contain enough quartz to be classified as a quartz arenite as all have less than 90% quartz. Pyrite/marcasite is common in a few samples usually located near the base of the channel-fill sequence. Carbonates are the second most commonly occurring minerals in channel-fill sandstones and include calcite, dolomite and siderite with siderite being the most abundant. The amount of siderite ranges from 3 to 35% and is greater than 10% in most samples. Thin section analysis shows that siderite has replaced most of the organic plant material in these sandstones (Figure 13). Feldspar content is relatively low at less than 10% in all samples when K-feldspar and P-feldspar are combined. Some feldspar has degraded to clay minerals.

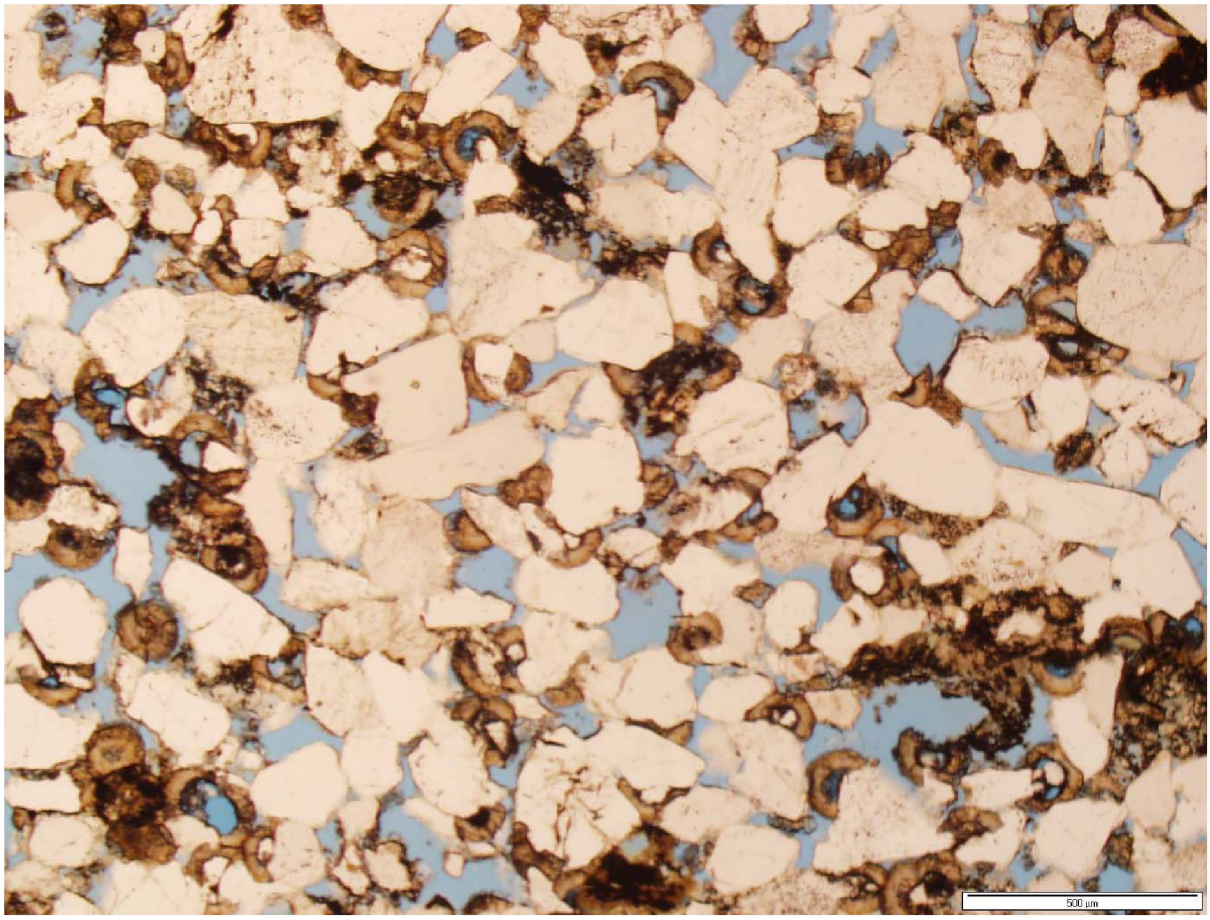

Figure 13 Thin section from 121012871800 Robins ME-10 at a well depth of 284.5 m (933.5 ft) and 5× white transmitted light. Horizontal permeability is 3.80 × 10^{-9} cm^2 (385 md), vertical permeability is 2.88 × 10^{-9} m^2 (292 md), and porosity is 20.5%. Organic material has been replaced by siderite. The intact structure of replaced organic material indicates that this sandstone has undergone little compaction.

The common clay mineral suite consists of kaolinite, chlorite, illite and mixed-layered illite/smectite. Bulk mineral analyses show that total clay mineral content is usually less than 5%. Thin section analyses show that clay minerals are commonly located in pore spaces where they are most likely to come into contact with and react with fluids in the reservoir. The most common clay mineral in most samples is kaolinite with illite being the second most common clay mineral. Chlorite and mixed-layered illite/smectite are the least common clay minerals.

Thin section analysis of some of the samples analyzed with XRD show that quartz sand grains are the most abundant component of most reservoir rock. Sandstones are most commonly cemented by quartz overgrowths with some samples being cemented by siderite that is replacing plant material such as spores. Organic material, such as spores replaced by siderite, are common in some channel-fill intervals. There is also little evidence of compaction resulting in preservation of a large amount of primary intergranular porosity as is indicated by the high core-measured permeability values. The lack of compaction in most intervals of channel-fill sandstone has resulted in excellent reservoir qualities of high porosity and permeability. In contrast, many reservoir samples from the Griggs lease in Section 32, T4N, R12W, show evidence of compaction after deposition resulting in less porosity and permeability.

Porosity and Permeability

The thin stacked sandstone lenses that comprise the deltaic Bridgeport B are much more compartmentalized with much lower permeability and porosity values than the thick blocky fluvial deltaic Bridgeport B channel-fill sandstone. The porosity of the fluvial deltaic sandstones ranges from 18 to 23%, while permeability can reach over 9.86×10^{-9} cm^2 (1,000 md), up to five times the average of the deltaic Bridgeport B sandstones found along the crest of the Bridgeport Anticline. Average permeability of fluvial deltaic sandstone in Section 5 (3.10×10^{-9} cm^2 [314 md]) is 2.8 times greater than the deltaic Bridgeport B sandstone in Section 32 (1.11×10^{-9} cm^2 [113 md]).

The overprint of diagenetic alteration has added to the high degree of variability in these reservoirs, taking place over a geologic time frame that resulted in areas of both enhanced and diminished porosity and permeability. Compaction of grains, particularly in some ripple-bedded intervals within the deltaic facies, has greatly reduced porosity and permeability, diminishing reservoir quality. Cross-bedded sandstones within the fluvial deltaic facies have increased porosity and permeability because of the lack of compaction in channel-fill deposits.

Reservoir Connectivity and Compartmentalization

The deltaic Bridgeport B sandstones in the study area have not been as effectively produced as the channel facies reservoirs in Section 5 because of their more compartmentalized characteristics. Shaly, lenticular bedded intervals within the deltaic Bridgeport B vertically baffle or compartmentalize, while the discontinuous nature of the sandstone lenses tends to horizontally compartmentalize these reservoirs. In the fluvial deltaic Bridgeport channel sandstone facies, it is difficult to correlate preferential flow units within reservoirs with standard mapping techniques using the older style SP-electric logs, which are principally available throughout Lawrence Field, because these sandstones are generally quite homogeneous and have a consistent blocky SP log response that does not lend itself to identifying flow units within the sandstone body. Recent porosity logs and core information have greatly enhanced the ability to delineate reservoir characteristics. In the channel-fill facies, the vertical and horizontal variations within the channel-fill reservoir are relatively minor; this reservoir is more homogenous than most reservoirs in the Illinois Basin.

Depositional Environment

Deltaic Facies

Mapping of the reservoir bodies in Lawrence Field has revealed that the sandstones found in the Bridgeport B interval probably represent at least two different depositional environments. The sandstones of the Bridgeport B deltaic facies are finer grained, more compacted, and are therefore less porous and permeable than the fluvial deltaic channel-fill reservoir sandstones in Section 5, T3N, R12W, and were deposited before the channel-fill sandstones. The Bridgeport B deltaic facies sandstone is commonly fine to medium grained, fining upwards, and has a scoured contact at the base. The sandstone contains common cross-beds in its lower portions, but becomes more ripple bedded upwards with bidirectional current indicators. The sandstone reaches a maximum thickness of about 9.1 m (30 ft) that is fairly consistent across the Bridgeport Anticline, but subsequent channeling in the top has eroded the sandstone along slightly northeast-southwest trends in the study area and replaced it with deposits of nonreservoir siltstones and shales. The sandstone is capped by coal that is widely traceable around the field,

and, along with the extensive underlying dark grey shale, allows for reliable correlation of the Bridgeport B reservoirs.

All these factors imply that the Bridgeport B sandstone could have formed as a tidally-influenced *deltaic* parasequence in an estuarine environment (Figure 14). The Bridgeport B deltaic facies sandstone is deposited over a uniform dark grey shale containing particles of carbonaceous material that likely represents prodeltaic or estuarine muds. Siderite bands and nodules within the shale indicate the presence of brackish water conditions. The shale represents a significant flooding surface. Deltaic sands prograded over the muds along a sharp contact and produced soft sediment deformation features in the form of slickensides in the shale. The lower two thirds or so of the fine- to medium-grained sandstone likely represents the foreset beds of the delta. Because of the low accommodation setting of the basin, the foresets are very low angle. Cross-bedded sandstone is common within the foresets. Shale zones within the sandstone that act to vertically baffle the reservoir represent mud drapes on the foreset surfaces. As sands filled available accommodation, the delta likely switched, moderating the influx of coarse material into the study area as the upper one-third of the sandstone deposit becomes very fine grained and silty. These fine-grained materials exhibit ripple, flaser, and lenticular bedding, with tidal rhythmites, tidal couplets, and bidirectional current indicators, reflecting a tidal influence on deposition. Some burrowing trace fossils were also observed. Accommodation reached zero as subsequent channeling incised into the deltaic sand and filled with silts and clays. Contemporaneous peat swamps formed over the delta top resulting in rooting and the formation of a weak paleosol in the upper part of the Bridgeport B deltaic facies, and the development of about 0.3 m (1 ft) of coal overlying the deltaic deposits just before sea level transgression and the beginning of the next parasequence.

The Bridgeport B deltaic facies is fundamentally a regressive, delta front to lower delta plain deposit with tidal features indicating that it falls along the continuum between river-dominated and tide-dominated deltas (Dalrymple et al., 1992; Bhattacharya, 2006). The Bridgeport B deltaic complex may have formed within an embayment (Dalrymple, 1999). The complexity of this depositional system illustrates the need for detailed mapping of individual sandstone reservoirs and also explains the high degree of variability in reservoir characteristics and geometries over a small area.

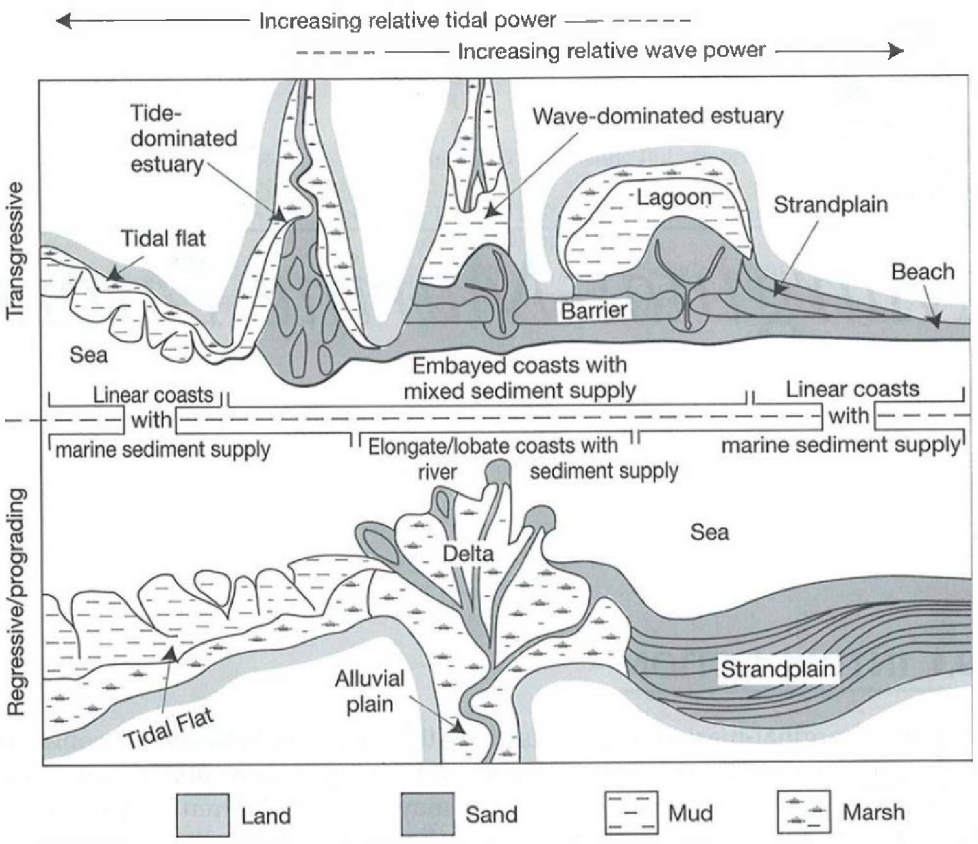

Figure 14 Depositional model of the principle coastal environments of the marginal marine setting (after Boyd et al., 1992, figure 2 used with permission of Elsevier, ©1992 Elsevier B.V). The Benoist sandstone could have formed as the progradation of sands and muds crossed the Illinois Basin from the northwest, with periodic stillstands leading to the accumulation of thick sandstones (middle in lower part of figure). The Bridgeport B sandstone in Lawrence Field could have formed as tidally influenced deltaic deposits in an estuarine setting (upper left in figure).

Fluvial Deltaic Facies

A distinctly different facies of Bridgeport sandstone (described in the "Lawrence Field History" section) is also observed in the field and occupies the same stratigraphic interval as the Bridgeport B deltaic facies. However, these sandstones have been demonstrated to be younger than the sandstones of the Bridgeport B deltaic facies and fill valleys that have been incised through those deposits. Individual channel-fill sandstone bodies can reach thicknesses upwards of 30.5 m (100 ft) and, in some areas of the field, multiple thick valley-fill sandstones seem to be stacked and amalgamated. The valley-fill sandstone exhibits a scoured lower contact with coarse-grained sandstone and rip-up clasts, fines and becomes more estuarine upward, and is often capped with coal. These sandstone bodies usually follow more linear paths at a few different orientations around the field, but tend to be situated along the flanks of the Bridgeport Anticline. Although it occurs in the same stratigraphic position as the Bridgeport B, this sandstone is suspected to have formed during a later scour and fill event. These Bridgeport reservoirs could have formed as stacked braided river deposits in the transitional *fluvial-deltaic* environment (Figure 15).

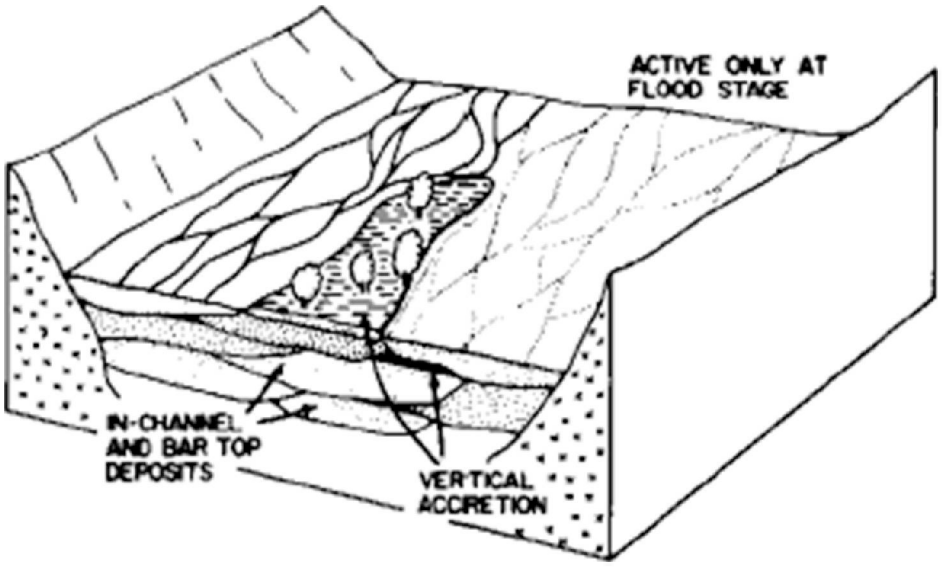

Figure 15 Depositional model of fluvial-deltaic architecture of braided stream deposits (after Walker and Cant, 1984, figure 8 used by permission of the Geological Association of Canada). The thick and sometimes stacked and amalgamated sandstones of the Bridgeport channel facies could have formed in such an environment.

The Bridgeport fluvial deltaic facies was deposited in a coastal plain incised-valley system (Zaitlin et al., 1994) and may be a simple fill incised tributary to a larger trunk valley (Boyd et al., 2006). The Bridgeport fluvial deltaic facies is a fundamentally transgressive deposit likely associated with the cycle or parasequence immediately above the Bridgeport B deltaic facies. The vertical succession of facies is in agreement with those of incised-channel deposits that become estuarine upwards (Figure 16; Clifton, 1982). The valley likely began filling during the lowstand and continued filling during the transgression. Although incised-valley fill successions can be extremely complex, the sediments within the channel in this study area are made up almost entirely of sandstone throughout the majority of the succession that appears blocky on electric logs. Bedding throughout this portion of the channel is largely indistinct with some cross bedding. Truncated surfaces and distorted bedding from soft sediment deformation is also common. Thus, the succession is likely dominantly fluvial with deposition likely outpacing accommodation creation. The sandstone fines upward becoming medium- to fine-grained sand, contains some siderite bands and clasts, and is ripple bedded with some bidirectional current indicators towards the top of the deposit. Here accommodation creation was probably catching up with the rate of sediment deposition with a marine influence starting to become evident. The top of the sandstone is sharply truncated with a sideritic lag which likely represents a transgressive surface where the rate of accommodation creation exceeds that of sediment supply. Only above this transgressive surface, in the upper meter or so of the deposit does it become shaly with lenticular bedding.

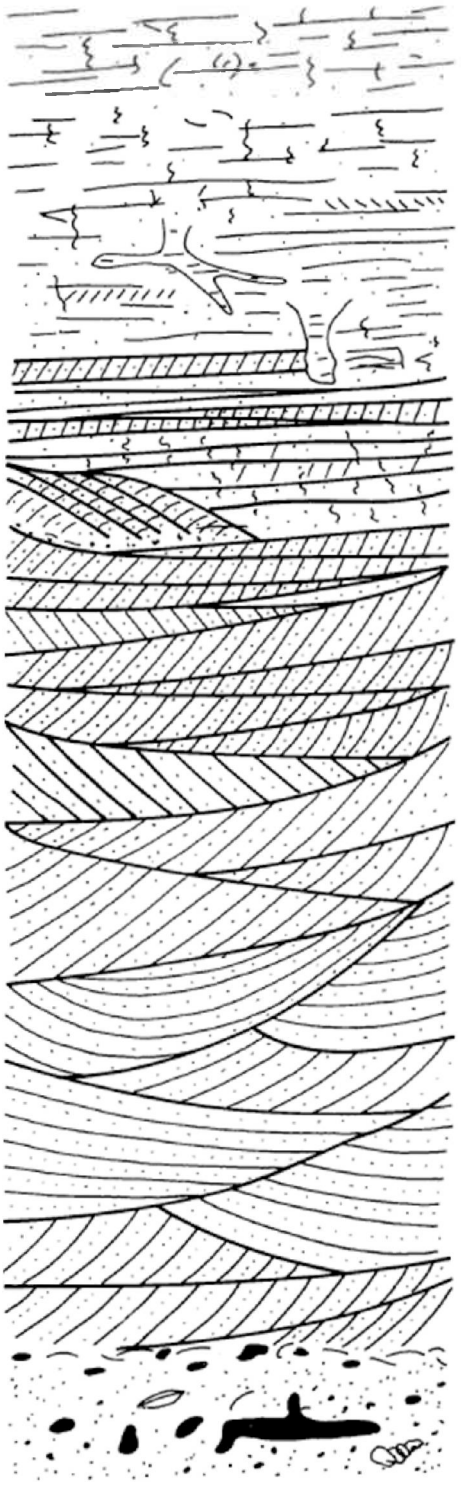

Figure 16 Idealized schematic diagram showing the typical succession of sediments found in an incised-valley fill. The lithologies and sedimentary structures presented here are representative of those found in core of the Bridgeport fluvial deltaic sandstones (after Clifton, 1982).

Shelf Clastic: Cypress Sandstone at Lawrence Oil Field

Cypress Background

The Cypress Sandstone is the most widespread siliciclastic unit and the most prolific producing horizon in the Illinois Basin, with over 0.2 billion m^3 (1 billion bbl) of oil production (Oltz, 1994). As such, the Cypress has undergone study in numerous fields throughout the Illinois Basin, including Herald Field (McDurmitt, 1949), Louden Field (Cluff and Lasemi, 1980), Bartelso Field (Whitaker and Finley, 1992), Tamaroa Field (Grube, 1992), Mattoon Field (Oltz, 1994), Lawrence Field (Oltz, 1994; Udegbunam and Grube, 1995),Xenia East Field (Xu and Huff, 1995), Storms Field (Leetaru, 1996) Richview Field (Grube and Frankie, 1999), as well as in the outcrop belt (Cole and Nelson, 1995).

The Cypress Sandstone is one of the thickest and most persistent Chesterian sandstones. The formation reaches a thickness of 30.5–61 m (100–200 ft) along a northeast-southwest trending belt in the interior of the Illinois Basin in south central Illinois, but thins outward from there (Willman et al., 1975). The formation is commonly quite variable; being composed of thick sandstone in some areas and made up of shale with numerous interbedded, well-cemented sandstone bodies in others. Such a high degree of variability indicates that the reservoirs are often heterogeneous and compartmentalized. Early study of the Cypress in Herald Field indicated that the Cypress could be subdivided into three zones; the uppermost of which being the productive horizon. Although the field is situated on a structure, the Cypress reservoirs' compartmentalized character leads to a degree of stratigraphic control on the entrapment of oil (McDurmitt, 1949). The study also noted the common occurrence of rapid permeability changes within the reservoirs over a few acres and often over just a few feet. As noted in the study, these reservoir characteristics translated to the surface pattern of producing wells; wells drilled atop the structure and expected to be good producers were dry holes, which resulted from drilling into shaly zones or well cemented sandy zones.

In Bartelso Oil Field, in southwestern Illinois, the 30.5-m (100-ft) thick Cypress formation was divided into four sandstone intervals, with each separated by thin shale layers (Whitaker and Finley, 1992). The lowermost sandstone interval studied was typically 12.2–15.2 m (40–50 ft) thick and showed a clean and blocky SP log response. The next sandstone interval up was 3.1–4.6 m (10–15 ft) thick, relatively continuous around the field, and apparently lacking in interbedded shales within the sandstone. This created a more or less homogenous reservoir. The third mapped interval was almost entirely composed of siltstone and shale, containing only localized thin sandstone beds. The uppermost interval was made up of discontinuous, multistoried northeast-southwest trending sandstone bars. Such sandstone lenses, being disconnected, stacked, and separated by thin shale layers, are highly compartmentalized with the persistence of the thin shale layers. Given higher resolution data, this may even allow the mapping of individual compartments or flow units within the larger scale sandstone lenses. Grube (1992) further demonstrated the compartmentalized character of the Cypress in an investigation of the unit at Tamaroa Field. Grube describes the Cypress as containing shales, siltstones, and poorly to moderately well sorted, very fine- to fine-grained sandstones. Some thin bioclastic limestones that grade to calcite cemented sandstones were also observed. The sandstones are thinly bedded and are commonly interbedded with shale. In this study, the Cypress was divided into three main intervals: an upper, middle, and lower interval. As only the

Upper Cypress interval was found to be oil productive, it was further subdivided into four subintervals. Each of the less than 3.1-m (10-ft) thick sandstone subintervals was separated from one another by thin shale, but the lenticular sandstone bodies were observed to coalesce in places. Thickness mapping of the Cypress subintervals of Tamaroa Field revealed northeast-southwest trending bars similar to those mapped in Bartelso Field.

Previous study of the Cypress at Lawrence Field indicates that the formation is predominantly composed of very fine- to fine-grained sandstone and shale (Udegbunam and Grube, 1995). Again, within some of the sandstones are thin beds of sandy limestone to calcareous sandstone. Red and green variegated mudstone was found to overlie the sandstone reservoir in some places. The authors correlated the reservoir sandstones of Lawrence Field to be the equivalent of the Middle Cypress as it is known in other Illinois Basin fields. In Lawrence Field, the Middle Cypress is divided into five subintervals which are all separated by shale and may not all occur in the same well. Thickness of the individual subintervals is commonly less than 3.1 m (10 ft). Reservoir sandstones are described as having thin shale laminations that compartmentalize the reservoir. Sandstone geometries mimic those seen previously, exhibiting elongate, parallel-ridged sandstone bars oriented northeast-southwest.

In Mattoon Oil Field, in southeast central Illinois, the Cypress was observed to be between 20 and 31.4 m (64 and 103 ft) thick and was divided into five subintervals. The subintervals include, in ascending order, Cypress A, a composite Cypress B/C, Cypress D, Lower Cypress E, and Upper Cypress E (Oltz, 1994). The sandstone reservoir subintervals described in Mattoon seem to occupy the whole of the Cypress interval rather than just the Upper or Middle Cypress Formation, as was the case in the Tamaroa and Lawrence Fields, respectively. Thickness of the subunits tends to be no more than 3–3.7 m (10–12 ft), except where the subintervals coalesce, as in the case of the composite Cypress B/C subinterval that reaches thicknesses of 6.1–12 m (20–40 ft). The lithology of the Cypress A was described as being a heterogeneous mixture of shale, sandstone and calcite cemented sandstone, and limestone. The remaining subintervals contain largely very fine to fine grained sandstone and shale. The sandstone bodies typically have ripple laminations and flaser bedding as well as occasional calcite cement, all contributing to a very compartmentalized reservoir. Of the subintervals described, the Cypress B/C and D were apparently the highest quality reservoirs. Thin, interbedded siltstones and shales commonly separate the subunits from one another. Geometries of the mapped sandstone bodies at Mattoon field ranged from discontinuous and irregularly elongate sandstone in the Cypress A; channel-bound, north-south oriented sandstones with distinct lateral lithologic changes in the B/C; more gradational and bar-shaped, north-south trending sandstones in the D; shoestring sandstones oriented northeast-southwest in the Lower Cypress E; and discontinuous lobate sands that thicken and become better developed to the south in the Upper E subinterval. Bar-shaped sandstones tended to be on the order of 3.2–8.1 km (2–5 mi) in length and less than 1.6 km (1 mi) in width.

Xu and Huff (1995) describe the Cypress formation at Xenia Oil Field in south central Illinois as reaching a maximum thickness of 48.8 m (160 ft) and divided the unit into seven different subintervals. The subintervals were numbered 2.5–17.8 cm (1–7 in.) descending order. The Cypress 1–6 subintervals consist of thin sandstone units interbedded with and separated by shale as has typically been seen in other fields. The Cypress 7, however, is made up of a thick

sandstone body with thin shale breaks, and this makes up roughly half the thickness of the overall Cypress Formation. The Cypress 4 subinterval contributed the most to overall Cypress production in the field, but minor production was also attributed to the Cypress 2 subinterval with oil shows in both the Cypress 5 and 6 subintervals. Lithology of the Cypress was typically fine-grained sandstone in the two lowermost subintervals. The Cypress 4 and 5 subintervals were typically fine- to very fine-grained sandstone with low angle cross bedding, while the Cypress 1, 2, and 3 subintervals occasionally had some very fine-grained sandstone but was predominantly composed of siltstone. In terms of sand body geometries, the two lowermost subintervals tend to be elongate in the north-south direction, whereas the five uppermost sandstones tend to form elongate bars trending northeast-southwest. The sandstone bodies in the Cypress 7 and 6 subintervals are large features with dimensions of 5 by 4 km and 5 by 2.4 km (3 by 2.5 mi and 3 by 1.5 mi), respectively. The sandstone bodies that make up the upper subintervals are smaller features with dimensions typically on the order of more than 1.6 km (1 mi) long by 0.53 km (0.33 mi) to 2.4 km (1.5 mi) wide.

In Storms Oil Field, in southeastern Illinois, Leetaru (1996) divides the overall Cypress formation into four different subintervals, including (from top to bottom) the Cypress A1, A2, B, and C. Each of these subintervals was separated by laterally persistent shale. Of these subintervals, the Cypress A1 and A2 were the most productive. The Cypress A was described as being very fine-grained and extensively cemented by calcite. A lack of samples from the lower sandstone subintervals within the Cypress led to a limited description of the lithologic characteristics of the reservoirs. The Cypress C is described as forming two linear sandstone bodies 8 km (5 mi) long by 1.2–2.4 km (0.75–1.5 mi) wide and more than 18.3 m (60 ft) thick, one of which trends north-south and the other northeast-southwest. The Cypress B is composed of four different sandstone units that were not subdivided in the report and were mapped as a composite unit. The resulting isopach map shows no apparent trend to the subinterval. The Cypress A sandstones are up to 4.3 m (14 ft) thick and form elongate, lenticular sandstone bars and are typically oriented northeast-southwest.

The Cypress sandstone was studied in Richview Oil Field in southwest central Illinois by Grube and Frankie (1999) where the formation reaches a maximum thickness of 33.5 m (110 ft). Overall lithology of the formation is described as consisting of mainly sandstones and shales with thin siltstones and mudstones, along with calcareous sandstones that grade to limestones. The report also noted the presence of variegated green and red mudstones, carbonaceous shale, and impure coal above the reservoir sandstones. The Cypress was divided into four subintervals; in ascending order, they are the Cypress A, B, C, and D sandstones. Shales, ranging in thickness from 0.3 m (1 ft) to several tens of feet thick, were described as separating the reservoir sandstone bodies. The Cypress A sandstone is equivalent to the Lower Cypress interval and has seen limited productive value in the field. Cypress A sandstone bodies are up to 12.2 m (40 ft) thick. Separating Cypress A and Cypress B is a shale interval that is typically 3.1 m (10 ft) thick. Drill cuttings show that it commonly contains red to green variegated mudstones as well as rare coal near the top. The Cypress B and C sandstone subintervals are the most prolific producers in the field and are generally separated by 0.3–1.2 m (1–4 ft) of shale, though in some places the shale pinches out and the sandstone bodies coalesce. These subintervals are lenticular and stacked in a manner similar to the Cypress at Tamaroa field. The Cypress B has elongate, northeast-southwest trending sandstone bodies up to 7.6 m (25 ft) thick that extend over 5 km (3

mi) in length and 0.40–0.53 km (0.25–0.33 mi) in width. Cypress C sandstone bodies reach a thickness of 6.1 m (20 ft), exhibit a northeast-southwest trend, and are geographically coincident with the underlying Cypress B sandstone bodies. The Cypress D is separated from the underlying C subinterval by shale that, again, is shown to contain red to green variegated mudstones as well as rare coal near the top. The D subinterval sandstone directly underlies the Barlow limestone in Richview field. The D has abundant shale partings and wavy laminations and forms 1.8-m (6-ft) thick lenticular sandstone bodies that trend northeast-southwest.

In addition to the numerous oil field studies that have been conducted on the Cypress Sandstone in the Illinois Basin, the Cypress has also been studied in outcrop (Cole and Nelson, 1995). It was again recognized in this report that the Cypress can be divided into three intervals. The Lower Cypress interval was described as being generally sandstone, the Middle Cypress composed generally of shale with some interbeds of siltstone and sandstone, and the Upper Cypress as being another interval of sandstone. The Lower Cypress was described as the dominant interval in the Cypress formation, commonly making up two thirds to three fourths of the overall thickness of the Cypress. Thick sandstone was common with occasional laminae of shale and siltstone. The authors also recognized the presence of red and green variegated mudstone as well as coal and carbonaceous shale in the Middle Cypress interval. The upper Cypress was described as containing generally thin bedded sandstones with interbeds of shale and siltstone and occasional lenses of thick sandstone. In the areas of the outcrop belt where the Cypress Formation thins on either side of the trend of thick Cypress described by Willman et al. (1975), the formation is largely composed of shale with some lenses of sandstone and common red to green variegated mudstones. The sandstones described in outcrop were typically very fine-grained to fine-grained and moderately well sorted.

The Cypress Formation is typically overlain by the Barlow limestone along a sharp contact that is easily identified on wireline logs. However, in some areas of the Illinois Basin, channeling in the top of the Cypress is known to occur, with the channels being often filled with sandy to shaly limestone. In these areas, the channelized limestone facies is known as the False Barlow and increases the overall thickness of the overlying Barlow limestone (Cluff and Lasemi, 1980). Where they occur, these channels make correlation of subintervals within the Cypress more difficult, since they scour out portions of the previously deposited Cypress Formation sediments. In reviewing the many studies that have been conducted on the Cypress Formation in the past, some definite trends emerge that should aid in the future study of the formation. First, the overall Cypress Formation can be generally divided into three broad informal intervals: the Lower, Middle, and Upper Cypress. Productive zones are found throughout the Cypress Formation but occur more commonly in the Middle and particularly the Upper zones. Sandstone subintervals within the Cypress often occur in elongate bar geometries, especially in the Middle and Upper Cypress intervals.

Reservoir Characterization

Stratigraphy

The Cypress Sandstone is a part of the Pope Group in the Upper Mississippian Chesterian Series. Chesterian strata are comprised of cycles of mostly siliciclastic rock punctuated by widespread thin limestones. The Cypress Sandstone is underlain by the Ridenhower Limestone, a widespread limestone that can be correlated across much of the Illinois Basin. The Cypress is directly

overlain by the Barlow limestone, a thin limestone marker horizon that is a prominent basin-wide strata commonly used for constructing contoured structure maps. The stratigraphic relationships of the Cypress Sandstone with overlying strata are shown in Figure 17.

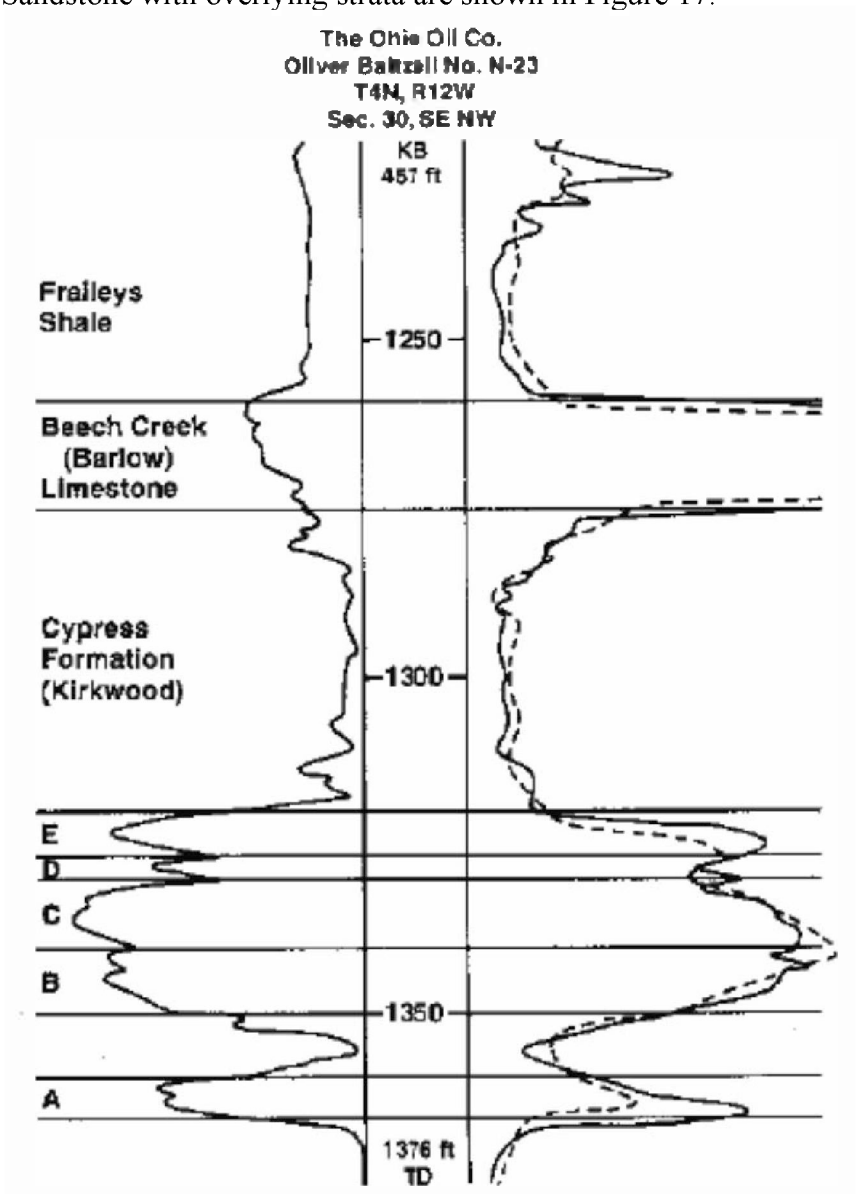

Figure 17 Type log from the Baltzell #N-23 well in the southeast-northwest of Section 30, Lawrence Field, showing the Cypress Sandstone stacked intervals "A" through "E". The Cypress Sandstone on this log shows a typical lower, thick, in part shaly, sandstone, with the upper part of the formation being generally shaly with occasional thin beds of sandstone. The Barlow limestone is easily recognized on geophysical logs and is used in regional mapping.

The Cypress Sandstone falls within the Lower Chesterian strata, located above the transition from the Middle Mississippian Valmeyeran carbonates. There are approximately ten cycles of alternating siliciclastics with widespread thin limestones in the Chesterian Series. In total these cycles have a maximum thickness of approximately 426.7 m (1,400 ft) and are bounded at the base by Valmeyeran Series carbonates and truncated at the top by the Pennsylvanian System

along the sub-Absaroka unconformity. Each Chesterian cycle is usually less than 30.5 m (100 ft) thick and represents between 500,000 and 1 million years of deposition if each cycle represents approximately equal periods of time.

Cypress Sandstone reservoirs in the study area are similar to those observed in numerous other fields around the Illinois Basin. A type well log from the study area shows several stacked sandstone lenses in the Cypress Sandstone (Figure 17). The stacked intervals of the Cypress Sandstone have been correlated around the study area and are named, from bottom to top, the A, B, C, D, and E subintervals. The SP trace on the electric logs from the 1940–50s characteristically "amplify" the deflection between the cleaner reservoir sandstone lenses and the shaly sandstone breaks. Very characteristic within the Cypress, and many other sandstone bodies within the Mississippian and Pennsylvanian section, is a 3.1 m (10 ft) genetic thickness tendency of units that is probably a function of available accommodation versus the influx of sediment into the intracratonic Illinois Basin, where subsidence was minimal under the prevailing conditions. The sandstone lenses commonly coalesce, thus increasing the overall thickness of the reservoir compartment. The "10 foot rule" can be a very useful tool for correlating these thinly bedded units in cratonic settings. The individual Cypress sandstone intervals have a lenticular, tidal shoal geometry where each shoal defines discrete reservoir flow units.

Isopach maps of the 50% clean sandstone for the Cypress B, C, D, and E intervals were contoured by hand in Sections 19 and 30, T4N, R12W, in an earlier unpublished study. These hand contoured maps all show northeast–southwest-oriented sandstone bodies. The D and C intervals are among the most laterally continuous of the Cypress Sandstone lenses in Lawrence Field. Sandstones units with similar sedimentary features and directly analogous to the Cypress units in the study area have been interpreted as linear tidal shoals.

A series of isopach maps of the Cypress Sandstone in the expanded study area were constructed using the 50% clean sandstone normalized SP curves on geophysical logs for the entire Cypress interval including the B, C, D, and E intervals. An isopach map of the total middle Cypress, 50% clean normalized SP sandstone thickness map of the study area is shown in Figure 18. This map combines sandstones in the B, C, D, and E intervals and has a contour interval of 1.5 m (5 ft). These units are all interpreted to be tidal shoal deposits that are analogous to those found in modern high tidal range settings. The elongated shoals are oriented in a northeast-southwest direction. The basal Cypress A interval appears to be a genetically distinct depositional facies that is less permeable and therefore is, more commonly, nonproductive.

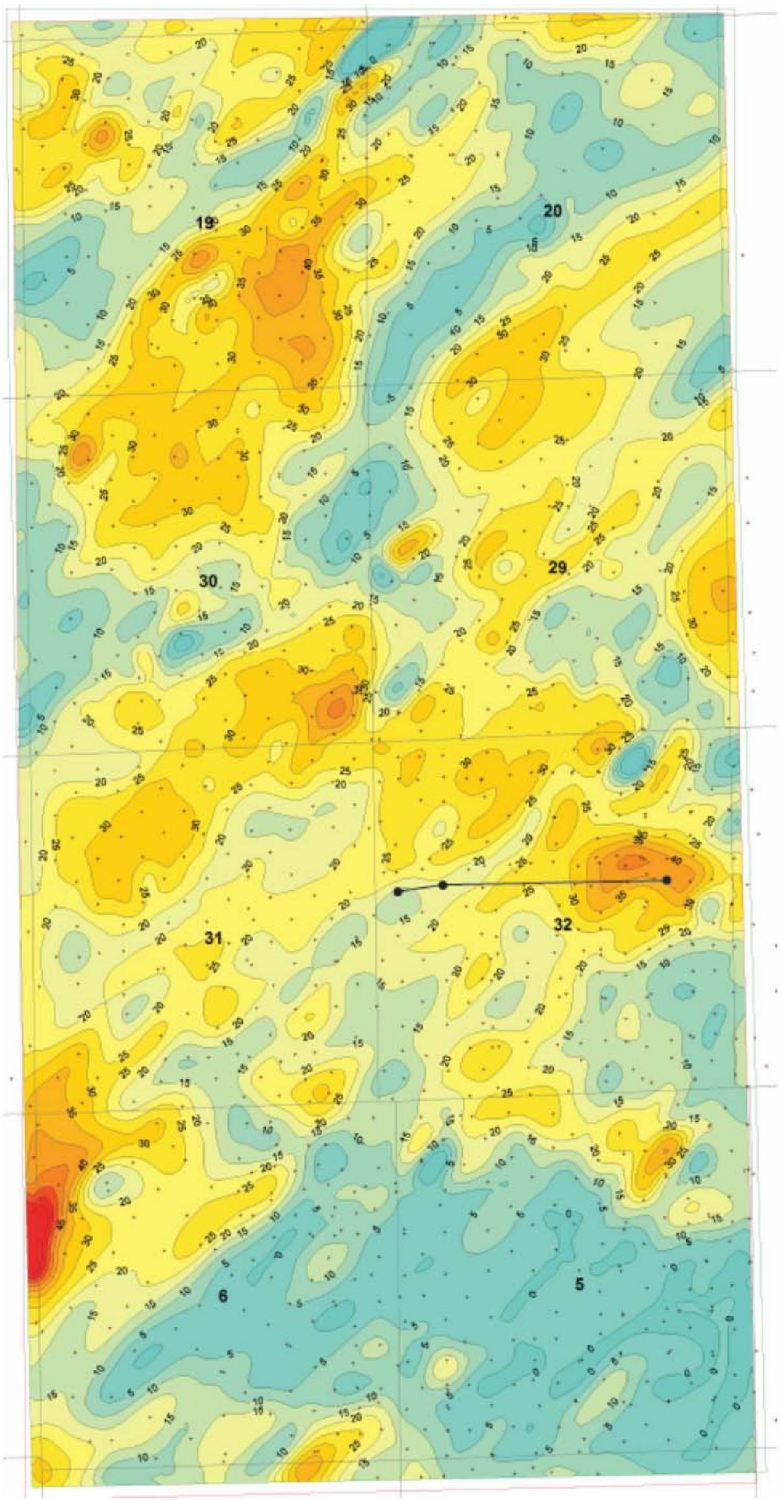

Figure 18 Total middle Cypress, 50% clean normalized SP sandstone thickness map of the study area. This interval includes the B, C, D, E intervals, which make up the Middle Cypress. These units are all interpreted to be tidal shoal deposits that are found in modern high tidal range settings. Note the elongated, shoal geometry trending northeast-southwest.

Reservoir and nonreservoir facies were observed and described in core from the study area and adjacent parts of Lawrence Field. Figure 19 shows typical reservoir and nonreservoir facies encountered in the Cypress. The reservoir facies observed in this representative core are the same as those observed in other Cypress core from around the field. The ripple-bedded facies (green bar) is the least porous and permeable of the three reservoir facies. It also exhibits a high degree of variability in porosity and permeability ranging from 5 to 18% porosity and 9.86×10^{-11} to 1.48×10^{-9} cm^2 (10 to 150 md) permeability. The massive (structureless) obscurely bedded facies (red bar) possesses the best porosity and permeability values, the parallel/subparallel bedded tidal rhythmites (yellow bar) also possess very good porosity and permeability, the ripple-bedded facies (green bar) possess good to poor porosity and permeability. The nonreservoir flaser/wavy/lenticular bedding facies is indicated by a purple bar and the nonreservoir calcite cemented sandstone facies is indicated by a light blue bar.

Legend listing characteristics and illustrating the color code for reservoir and non-reservoir facies.

CYPRESS SANDSTONE RESERVOIR FACIES

Mottled or obscured bedding: (excellent porosity and permeability)
Grain size fine grained
Sorting poorly sorted to well sorted
Composition quartz grains, small amount of clay minerals and feldspar grains

Parallel laminated tidal rhythmites: (usually good to excellent porosity and permeability)
Grain size fine grained
Sorting well sorted
Composition quartz grains, small amounts of clay minerals and feldspar grains

Ripple bedded/herringbone: (good to poor porosity and permeability dependent on amount of clay sized ductile grains)
Grain size fine – very fine grained
Sorting well sorted
Composition quartz grains, feldspar grains, laminae of ductile clay sized grains

NON RESERVOIR FACIES

Calcite cemented sandstone: (little to no porosity and permeability)
Grain size fine-very fine
Sorting well sorted
Composition quartz grains, calcite cement

Flaser bedded: (little to no porosity and permeability)
Grain size Alternating layers of shale and fine grained sandstone
Sorting well sorted
Composition sandstone quartz and small amount of feldspar grains; mud drapes/clay

Figure 19 Core of entire middle Cypress from the Griggs #107 well in the southeast-northeast of Section 32 with general lithofacies assignments coded by color. The Cypress A interval is included below shale but does not include facies characterization. Core is dominantly wavy laminated, ripple-bedded sandstone with ubiquitous wispy shale lamina. Tidal couplets and tidal generated herringbone ripple beds are common sedimentary features. The uppermost 2.4 m (8 ft), the D interval, is a mottled, poorly sorted massive (structureless) facies and has the best reservoir porosity and permeability. This is possibly a bioturbated facies. A common lithology noted is a calcite cemented sandstone that is generally less than 0.3 m (1 ft) thick. These beds likely act as baffles or boundaries to fluid flow. Meteoric water percolation that leaches and reprecipitates carbonates during subaerial exposure of shoals is suggested as the source of these cemented beds.

Reservoir Lithology and Petrology

XRD of the bulk mineral and clay mineral fractions of 98 Cypress Sandstone samples from eleven cored wells were completed. Quartz is the most common mineral found in Cypress reservoir sandstones and usually makes up greater than 90% of samples. Carbonates are usually a minor component of samples at less than 1%. Calcite cemented intervals, however, contain less than 90% quartz with pores in these samples filled with 10–20% iron-rich calcite. Clay minerals range from 1–8% in most sandstone samples. Potassium and plagioclase feldspars are also minor components of reservoir sandstones usually making up 1–4% of most samples. However, these feldspars likely made up a larger proportion of the original rock (up to 10%) before many of the detrital grains were degraded by dissolution during diagenesis (**Error! Reference source not found.**). Trace amounts of pyrite/marcasite were detected in some samples, usually less than 1%. Siderite was only rarely detected and when present was less than 1%. Clay minerals in sandstone samples are diagenetic and formed as the result of dissolution of feldspar grains. Diagenetic clay minerals commonly occur in pores where they may react with reservoir fluids.

XRD analysis shows that most Cypress reservoir samples with good core-measured porosity and permeability values contain less than 2% clay minerals and less than 4% feldspars and have very high quartz content, with thin section and SEM analysis showing that many pores are partially lined with diagenetic clay minerals that are likely derived from degraded feldspar grains. This complicates the mineralogical associations within the sandstone and is a factor in the response of these sandstones to fluids introduced for reservoir treatments in conjunction with enhanced oil recovery. The degradation and dissolution of feldspars have enhanced porosity and permeability but have also lined many pores with diagenetic clay minerals such as Fe-rich chlorite, kaolinite illite, and mixed layered illite-smectite.

Petrographic examination of thin sections, SEM/EDX, and XRD analyses of Cypress samples from the ripple-bedded reservoir sandstone facies show that these sandstones are very fine grained and are highly cemented by quartz overgrowths (Figure 20 and **Error! Reference source not found.**). Thin section point count analyses and XRD mineralogical analyses show that most Cypress Sandstone samples are composed of approximately 95% quartz, less than 1% K-feldspar, less than 3% plagioclase feldspar, less than 2% clay minerals and less than 1% other minerals. A common feature of the ripple-bedded facies is porous laminae alternating with finer grained nonporous laminae (Figure 20). Wispy shale partings are common in this facies and separate nonporous, tightly cemented, very fine-grained sandstone from porous intervals. The most common diagenetic clay mineral in the ripple-bedded facies is Fe-rich chlorite. Numerous sand grains in the scanning electron photomicrographs are coated by chlorite (Figure 21). Several stages of Fe-rich chlorite precipitation are evident in this sample. The bottom left photomicrograph (Figure 21) shows quartz overgrowth precipitated over chlorite clay minerals. The bottom right photograph shows a grain completely coated by chlorite and an area occupied by a degraded feldspar grain with diagenetic chlorite and illite.

XRD and thin section analyses of the massive (structureless), possibly bioturbated reservoir facies show amounts of quartz, feldspar, and clay minerals similar to those measured in samples from the ripple-bedded facies of 95% or greater quartz, 3% or less feldspar, and 2% or less clay minerals. Thin section examination shows that samples from this facies are less tightly cemented by quartz overgrowths, are more porous, possess greater amounts of intergranular porosity, and

are more poorly sorted than samples from the ripple-bedded facies. The mineralogical difference between the two facies is in the clay mineral suite. The clay minerals in the bioturbated facies consist primarily of kaolinite, with lesser amounts of illite and Fe-chlorite. Some XRD analyses of bioturbated samples contained no mixed layered illite/smectite. The predominant clay mineral in this facies is kaolinite, which can be an abundant pore filling and pore lining mineral. XRD analyses of Cypress Sandstone samples show that the kaolinite clay minerals are diagenetic and well crystallized. The kaolinite in the Cypress Sandstone occurs as vermicular or book-like stacks of plates. SEM/EDX analyses confirm the vermicular and booklet morphology findings.

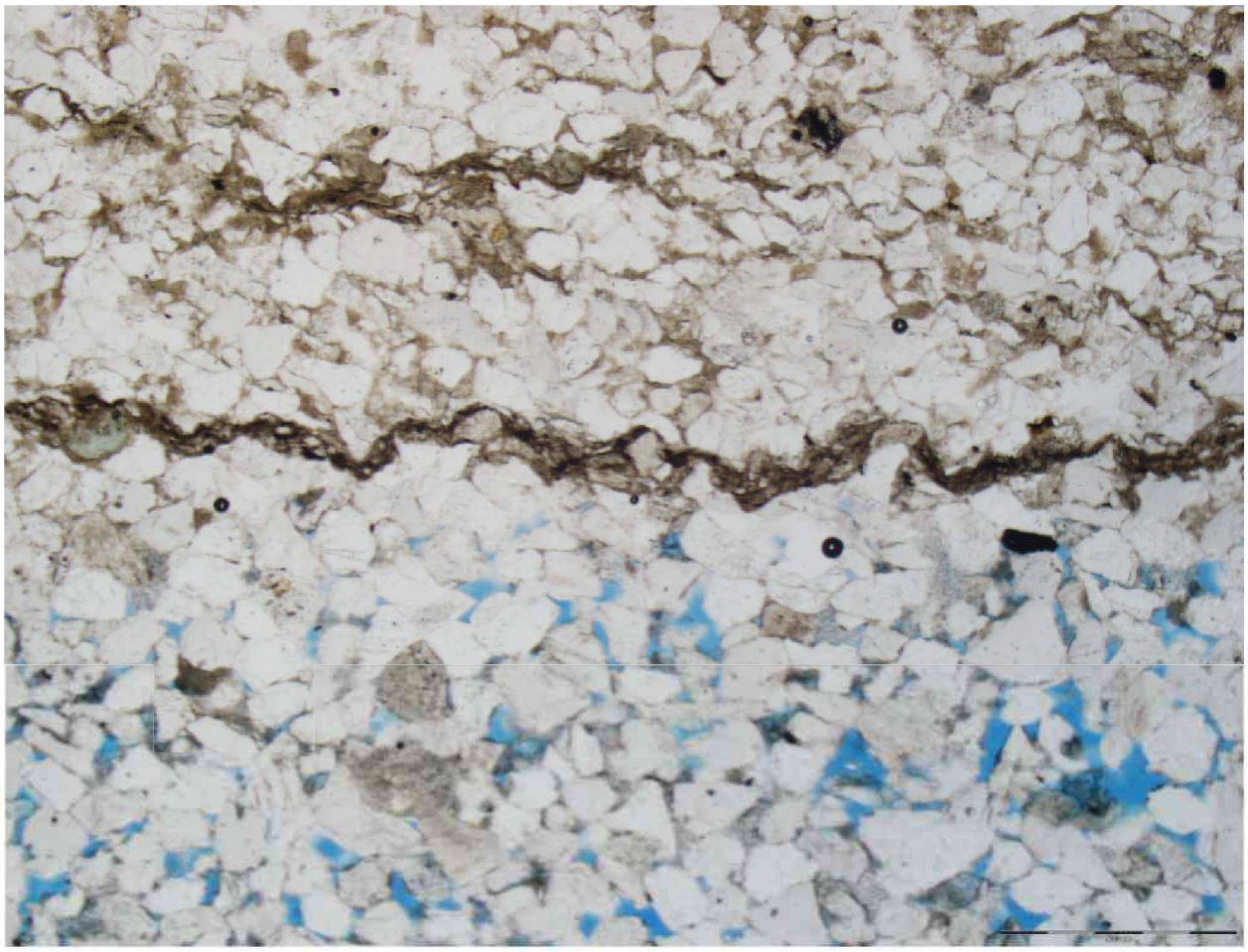

Figure 20 Example from the Griggs #107 at 443 m (1453.4 ft) shows porous laminae alternating with nonporous laminae. Porosity is highlighted by medium-blue stained epoxy. A clay laminae parting separates the nonporous tightly cemented fine-grained sandstone from the porous sandstone.

Calcite cemented intervals a few centimeters (inches) up to 1 m (3 ft) thick are found in some Cypress Sandstone lenses and can be useful marker horizons for correlating geophysical logs. XRD analysis of these intervals shows that they contain 80% or less quartz and 17–20% calcite. Thin sections of calcite cemented sandstone intervals show that intergranular porosity of approximately 18% has been filled by iron-rich carbonate cement. These carbonate cemented intervals have little to no porosity and permeability, and can form permeability barriers where they are laterally extensive.

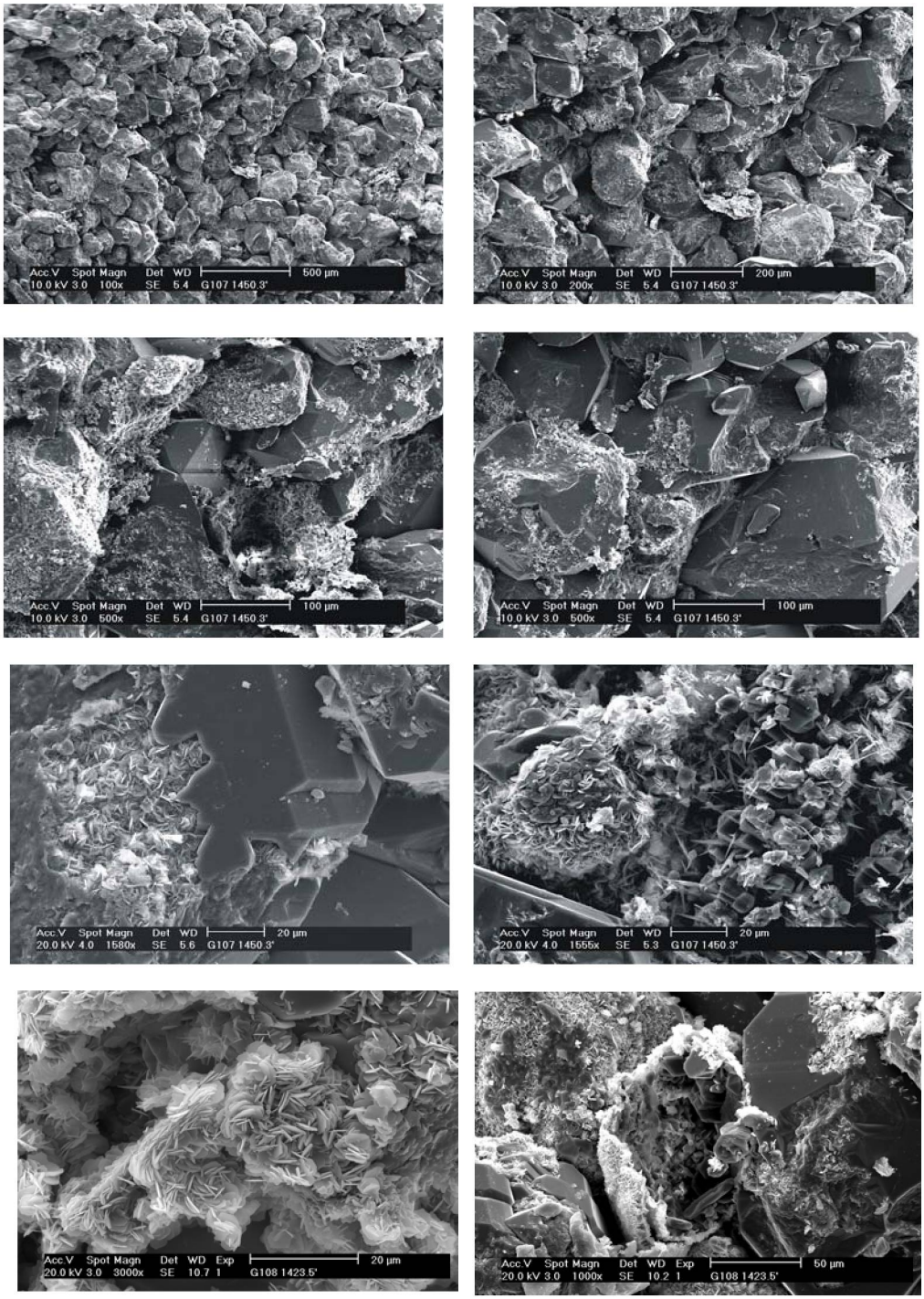

Figure 21 Cypress Sandstone sample from the Griggs #107 well. Cypress Sandstone is fine grained and cemented by quartz overgrowths. The most common diagenetic clay mineral in the Cypress Sandstone is Fe-rich chlorite. Numerous sand grains in the photographs are coated by chlorite. Several stages of Fe-rich chlorite precipitation are evident in this sample. The second from bottom left photograph shows quartz overgrowth precipitated over chlorite clay minerals. The bottom right photograph shows a grain completely coated by chlorite and an area occupied by a degraded feldspar grain with diagenetic chlorite and illite.

Porosity and Permeability

Three different reservoir facies with different flow unit characteristics were identified in Cypress Sandstone reservoirs in cores from the study area in Lawrence Field with two of the facies likely representing the highest quality reservoirs in the formation. The most common reservoir facies consists of ripple-bedded, fine- to very fine-grained sandstone with occasional occurrences of herringbone cross-bedding and tidal couplets. The ripple-bedded reservoir facies has core measured porosity values ranging from 16 to 19% and core measured permeability values most commonly in the 9.86×10^{-10} cm^2 (100 md) range. A second less common reservoir facies consists of massively (structureless) bedded, possibly bioturbated, poorly sorted, fine-grained sandstone. Core measured porosity commonly exceeds 20% and permeabilities are commonly greater than 1.97×10^{-9} cm^2 (200 md) in this facies. This facies has the highest core-measured porosity and permeability values observed in Cypress Sandstone reservoirs in the study area.

Reservoir Connectivity and Compartmentalization

The tidally influenced depositional setting of the Cypress Sandstone has introduced a high level of reservoir compartmentalization. Petrographic examination also shows differences between reservoir facies that increase reservoir complexity and introduce production obstacles on a microscopic scale. Both reservoir facies contain clay mineral suites that can be highly reactive to fluids introduced for enhanced oil recovery treatments. Although the volume of clay minerals is relatively low, they are most commonly located in pores where they are likely to come in contact with fluids introduced for treatments. Because these reservoirs are located in close proximity to one another, the presence of Fe-rich chlorite and, to a lesser degree, illite and mixed layered illite/smectite in pore spaces should be taken into consideration.

While compartmentalization is evident in all the targeted sandstones, some sandstones exhibit a directional orientation that must be considered in reservoir development. Effective implementation of flooding in the study area should take into account compartment orientation that is dictated by depositional trends and type and location of permeability barriers. Reservoir characterization of Cypress Sandstone lenses show that these sandstones contain intervals of highly variable vertical permeability. Interpretation of the Cypress Sandstone interval in cross sections in Section 32, T4N, R12W, suggest that permeability barriers are subtlety reflected on geophysical logs but likely play a major role in compartmentalization of these reservoirs. Intervals with very high permeability may be susceptible to channeling. The Mississippian Cypress Sandstone may be complexly compartmentalized than either of the previously described Bridgeport sandstones. Mineralogy of the pores is complex with diagenetic clay minerals including Fe-rich chlorite, illite, mixed-layered illite/smectite and kaolinite playing a major role in the response to fluids introduced during drilling and treatment. Although the major component is quartz as both a grain composition and cementing agent, it is not necessarily the major component in pore mineralogy.

Depositional Environment

Interpretations for the depositional environment exhibited by the Cypress Formation (described in "Cypress Background") are as numerous and varied as the researchers who have investigated the fields listed above. What is clear is that multiple depositional environments are probably represented by the different reservoir geometries seen in the Cypress Formation in different fields. The most common geometry mapped in the upper portion of the Cypress is that of the

lenticular sandstone bars with a typical northeast-southwest orientation, which were observed in every studied field. The recent study of Lawrence Field showed similar northeast-southwest trending stacked sandstone bodies roughly 1.6 km (1 mi) long, 0.8 km (0.5 mi) wide and up to 3.1 m (10 ft) thick that were interpreted to be tidal shoals (Seyler and Grube, 2012). The general consensus seems to be that the sandstone bars were deposited as shelf sands in a large, embayed region with a potentially high tidal range. Off's (1963) model for deposition of tidal ridges in the Gulf of Korea (Figure 22) could be an analog for the deposition of the Cypress Sandstone; although, in many cases, the Cypress is believed to have been deposited closer to the shoreline. The lower portion of the Cypress, when it does not exhibit the common northeast-southwest trending sandstone bodies could be interpreted as having been deltaic deposits within an estuarine channel.

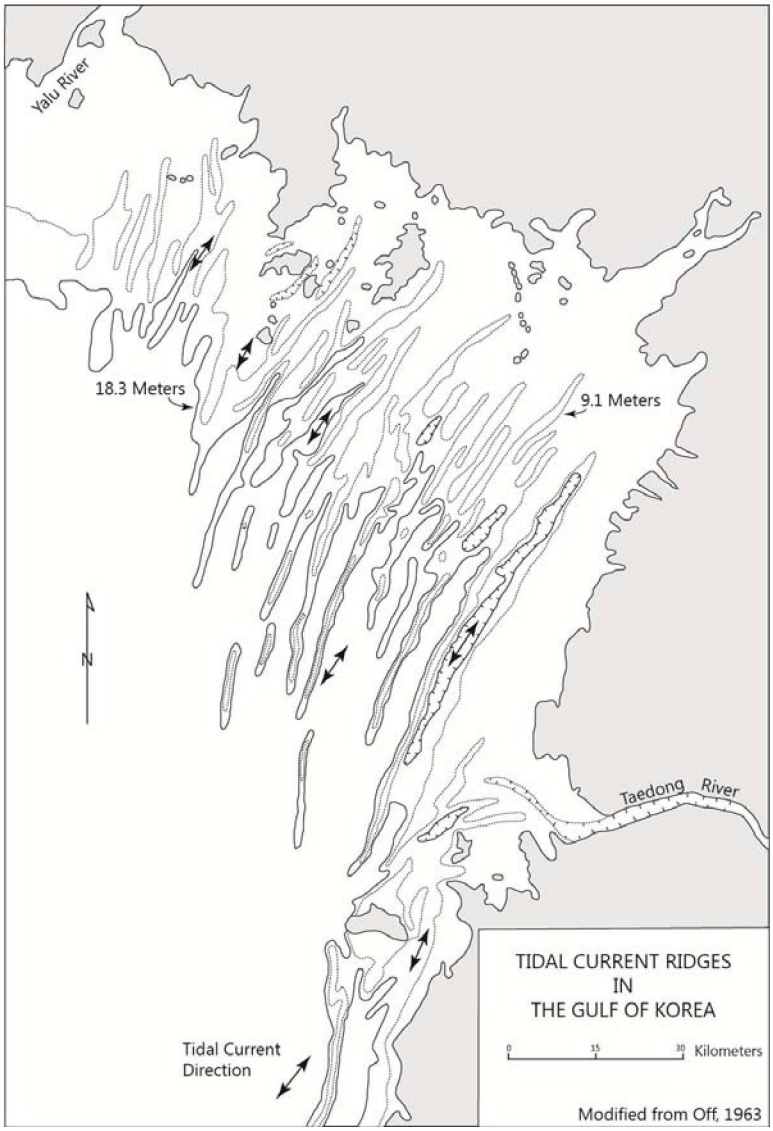

Figure 22 Depositional model for elongate tidal sand ridges in the Gulf of Korea (after Off, 1963, figure 1 used by permission of the American Association of Petroleum Geologists whose permission is required for further use, AAPG©1963). This modern model is likely analogous to the deposition of Cypress Sandstone bars in the Illinois Basin during the Chesterian.

Shelf Carbonate: Ste. Genevieve Limestone at Johnsonville Consolidated

Johnsonville Consolidated (Figure 23) is located in the Fairfield Basin (the deep central part of the Illinois Basin) in west-central Wayne County, southeastern Illinois, several miles west of the Clay City Anticline and immediately west of the Bogota-Rinard Syncline (Nelson, 1995). There are smaller adjacent Johnsonville fields—Johnsonville North, West, and South—but this study focuses on Johnsonville Consolidated, which was discovered in 1940. The Johnsonville Consolidated Field produces from the Mississippian Ste. Genevieve Limestone ("McClosky" and "O'Hara" reservoirs) and Aux Vases Sandstone. This review focuses on the Ste. Genevieve Limestone because it is considered to represent a shelf carbonate deposit at the Johnsonville Consolidated Field.

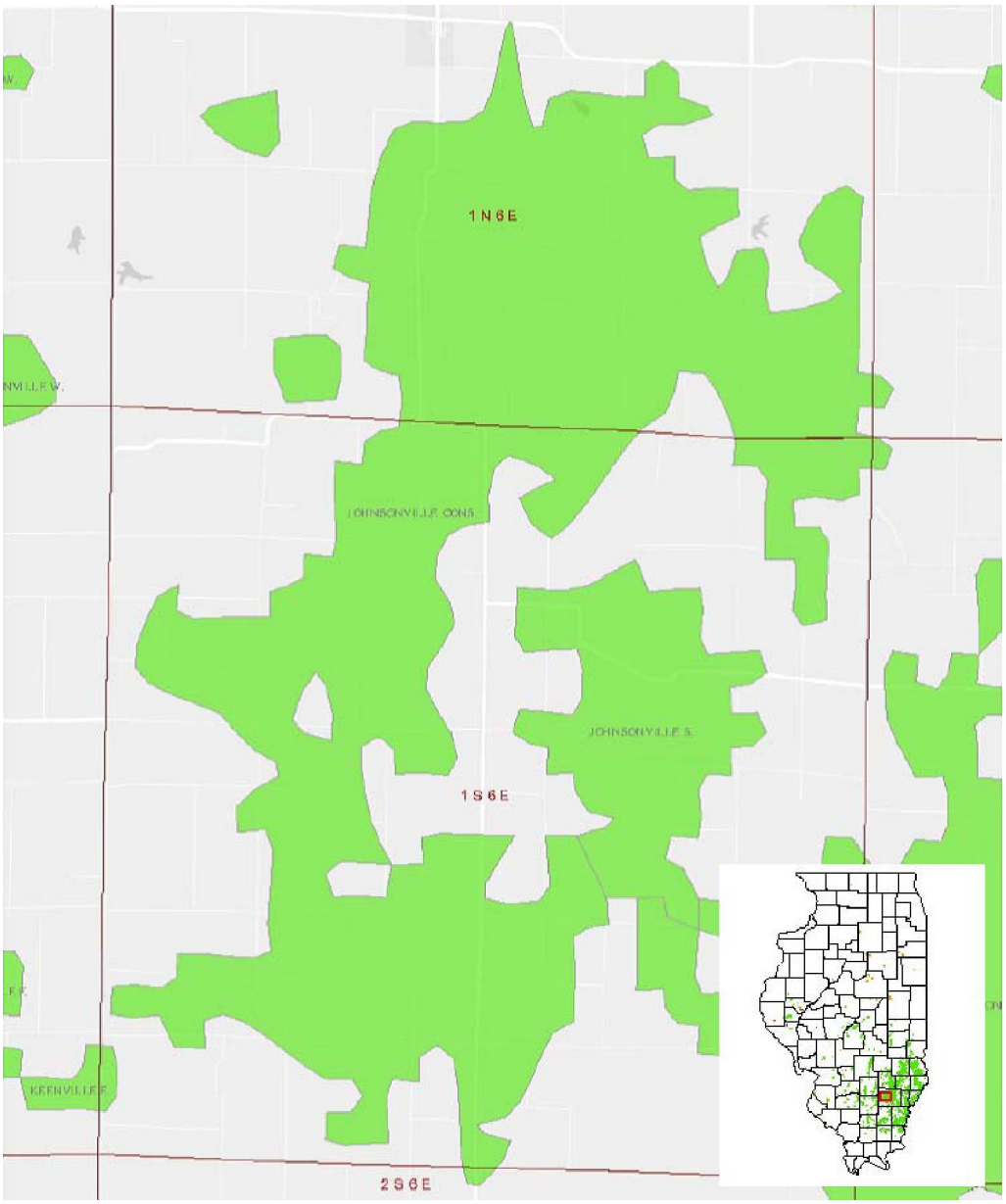

Figure 23 Map showing the boundaries of Johnsonville Consolidated Field (Wayne County, Illinois) and adjacent fields (Source: http://maps.isgs.illinois.edu/iloil/). The map scale is 1:72,224.

Johnsonville Consolidated Production History and Development

A recent study put the volumetric OOIP of Johnsonville Consolidated Field at 12.6 million m^3 (79 million stb) or 20.4 thousand m^3 (128 thousand stb) with 48% oil recovery (MGSC, 2005). Production at the field began in 1940 with completion of the Dickey #1 well (initial production 1.6 m^3/d [10 bopd]) into the Mississippian "McClosky" (Ste. Genevieve) and accelerated the following year with completion of the high-yield Hilliard #1 (initial production 383 m^3/d [2,406 bopd]). The latter is centrally located on the crest of the dome which constitutes the main structure at Johnsonville Consolidated (Figure 24). Production from the "Lower O'Hara" began in 1943, and total production from these two zones at Consolidated was in excess of 3.8 million m^3 (24 MMbbl) within about eight years of completion of the Hilliard #1 (Cassin, 1949). Other Mississippian production followed in 1960–61 (Salem and St. Louis), 1980 (Ullin), and 1995 (Cypress), although the McClosky still has by far the largest number of well completions in the area (ILOIL, 2009). An "accidental waterflood" in late 1947—that is, a water well leak that stimulated production—constituted the first (albeit inadvertent) application of secondary recovery techniques at Johnsonville Consolidated (Cassin, 1949). Deliberate waterflooding at the primary Johnsonville Unit began in 1956. Cumulative production at the end of 2009 was an estimated 9.78 million m^3 (61.5 MMbbl; ILOIL, 2009).

Geological Background

The Ste. Genevieve was deposited near the end of the Kaskaskia II Subsequence during a time of warm, near-equatorial shallow marine conditions in the Illinois Basin (Devera et al., 2010). The placement of the Meramecian (Valmeyeran)/Chesterian boundary in the ILB, and hence the exact age of the Ste. Genevieve, has been the subject of considerable debate. Lane and Brenckle (2005) and Devera et al. (2010) consider the Ste. Genevieve to be the basal unit of the Chesterian Series (uppermost North American division of the Mississippian Subsystem), although other recent publications (Huff and Seyler, 2010) follow the example of earlier workers by categorizing the unit as Valmeyeran (the middle series of the Mississippian in the ILB). The boundary between the Meramecian and the Chesterian falls at about 335 Ma in the upper Visean global stage (the stage which corresponds to the traditional Middle Mississippian; Davydov et al., 2012).

The Ste. Genevieve is a largely carbonate unit with some minor clastic intervals. Ooids and coral and algae fossils indicate warm, shallow-shelf depositional conditions; at the time of deposition, this part of the Illinois Basin was located at 5–15 degrees south latitude (Smith et al., 2001). Eolian deposits have also been reported as a minor nonmarine facies (Hunter, 1993; Parrish, 2005). Members recognized by current workers include the basal Fredonia, in which oolitic limestones and grainstones alternate with finer grained limestones and dolomites; the "Spar Mountain Sandstone," which is actually shaly in this area (Leetaru, 2000); and the top Karnak Limestone Member. The distinctive log signature of the layer of shale or shaly sand overlying the Fredonia at most wells made it a convenient marker bed for correlation and mapping in this study (Figure 25). This layer is located 0–3 m (0–10 ft) above the top ooid grainstone and constituted the entirety of the Spar Mountain in much of the mapped area, although Spar Mountain intervals containing thin limestone or sandy layers were found at some wells.

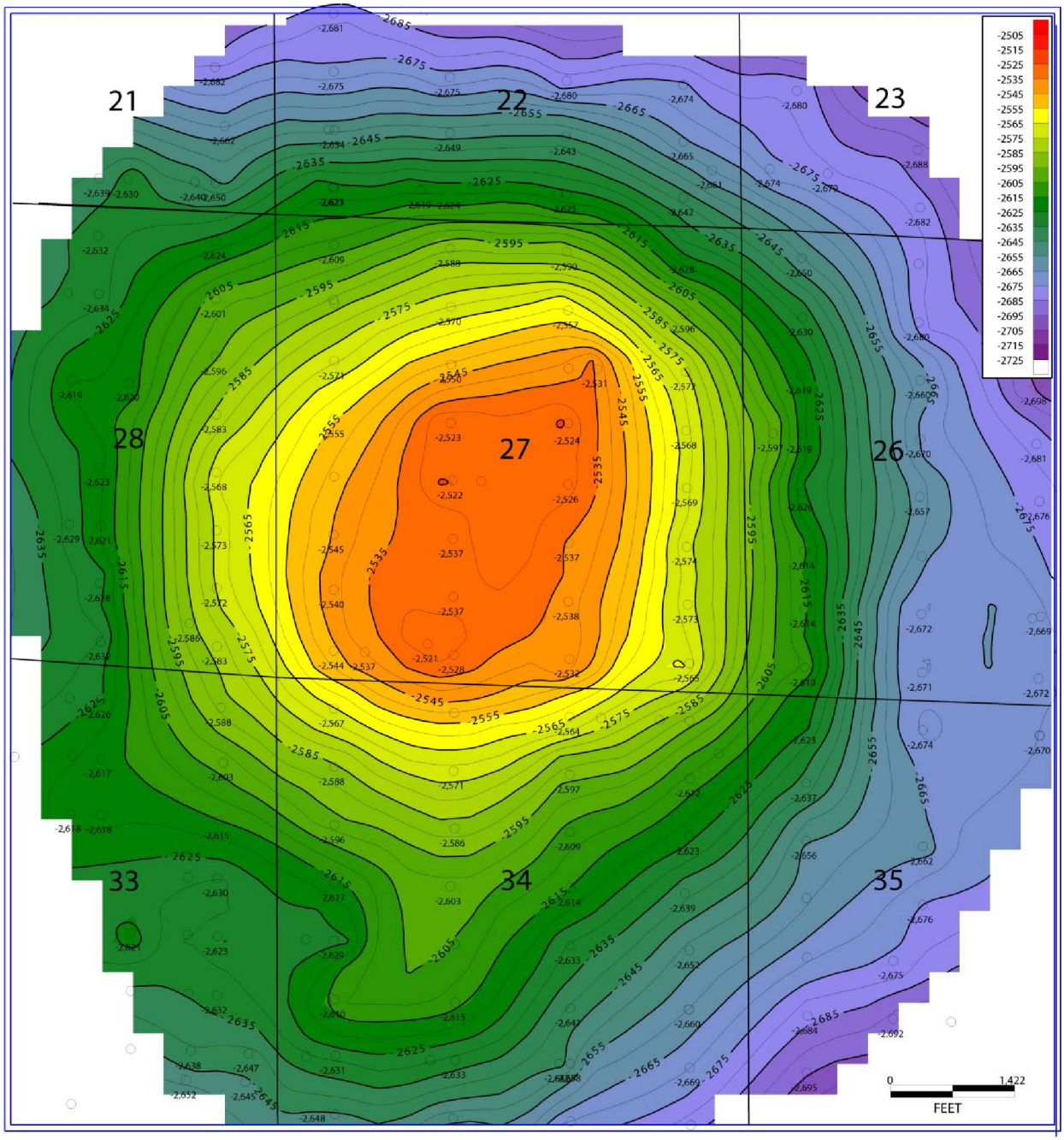

Figure 24 Johnsonville Dome structure in Wayne County, IL, T1N R6E, defined here by the top of the Fredonia Member of the Ste. Genevieve Limestone. Contour interval 1.5 m (5 ft). Larger numbers shown are section numbers.

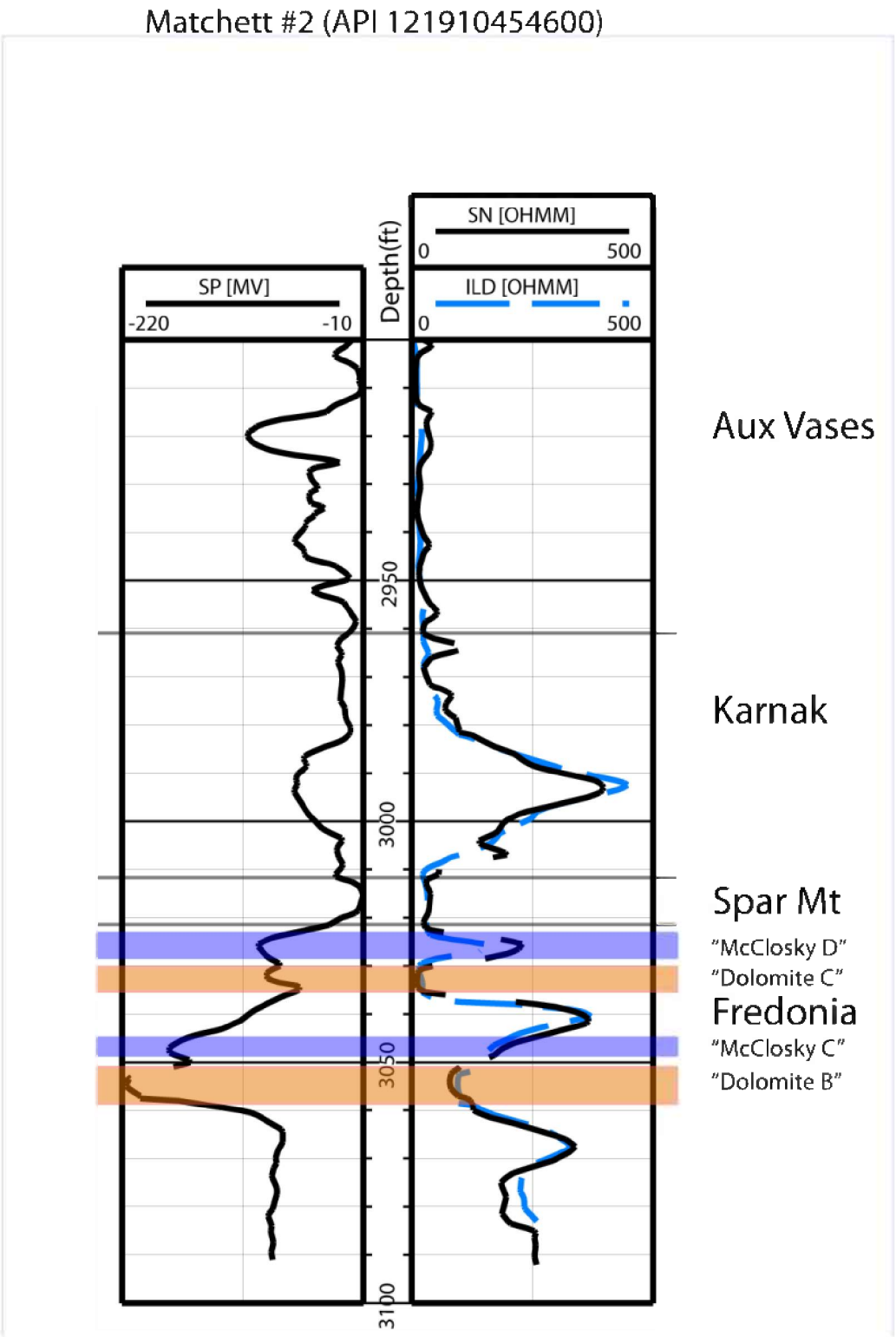

Figure 25 Log section for Matchett #2 well, (API 121910454600) at Johnsonville Consolidated oil field, showing characteristic log signatures of Ste. Genevieve carbonate members. As noted by Bandy (1993), oil-saturated dolomites exhibit the lowest resistivity compared to ooid grainstones and nonpermeable limestone, and both grainstones and dolomites exhibit SP deflection. Not all grainstones or dolomite layers are found at every well, hence the absence of "Dolomite A" and "McClosky B" and "A".

The full Ste. Genevieve interval is typically 46–61 m (150–200 ft) thick but may achieve a maximum thickness of 122 m (400 ft; Devera et al., 2010). The Fredonia ranges from a few meters thick to over 80 m (262 ft) in different parts of the ILB. Distinguishing the contact between the Ste. Genevieve and the underlying St. Louis can be difficult. Prominent chert content in the St. Louis is sometimes used to differentiate the two, but the Fredonia can also be cherty (Nelson et al., 2002). Willman et al. (1975) recommended putting the contact "below the lowest prominent oolitic bed"; this indicates a Fredonia thickness of approximately 23 m (75 ft) at Johnsonville, although in some wells the oolite zones are confined to the top 9 to 12 m (30 to 40 ft). This may simply reflect the irregular size and spatial distribution of the shoals, or it may indicate that the Fredonia and the St Louis are intertongued (also suggested by the appearance of cherty beds only about 12 m [40 ft] below the top Fredonia at the Hilliard #1 well [API 121910031900]), or both.

Cassin (1949) noted the existence of a circular, 5-km- (3-mi-) diameter dome with 36 m (120 ft) of closure on the Ste. Genevieve at Johnsonville Consolidated Field. The structure was named the Johnsonville Dome by Nelson (1995), who mentioned the possibility that the dome is "a reef-drape structure analogous to those associated with numerous Silurian pinnacle reefs in Illinois," possibly associated with a fault and corresponding horst block. This followed the suggestion of Whitaker and Treworgy (1990), who mapped the Johnsonville Dome as an expression of buried "isolated Valmeyeran reefs" in the deeper Salem and Ullin limestones. A thick crinoidal interval of Ullin in the Greathouse #1 well (API 121910050901) was identified as a possible expression of such a reef by Cassin (1949). This structure probably would have had some topographic expression on the Mississippian seafloor and thus would have influenced deposition.

Reservoir Facies and Correlation

The Fredonia at Johnsonville Consolidated predominantly produces from oolite bodies, but dolomitic layers are also productive at some wells.

Oolite shoals in the Ste. Genevieve (Figure 26) have collectively yielded several hundred million barrels of oil across the Illinois Basin, accounting for a significant percentage of Illinois production (Huff and Seyler, 2010). Productive intervals in the Ste. Genevieve at Johnsonville include the "McClosky Oolite" of the Fredonia Limestone Member (the primary productive interval); the Spar Mountain (mostly shaly or carbonate here, but with scattered "Rosiclare" sandy intervals); and the "O'Hara," a part of the Karnak Limestone Member (Huff and Seyler, 2010). The productive McClosky zones are found at some 762–823 m (2,500–2,700 ft) below sea level, which is a favorable depth for storage of CO_2 as a supercritical fluid. Three major McClosky oolite intervals—referred to as (from deepest to shallowest) the McClosky D, C, and B—are modeled here, although thin deeper intervals are known to occur at some wells. Microcrystalline dolomite layers are also common in the Fredonia at Johnsonville and yield oil at some wells, similar to other fields with Ste. Genevieve production, such as North Bridgeport (Choquette and Steinen, 1985).

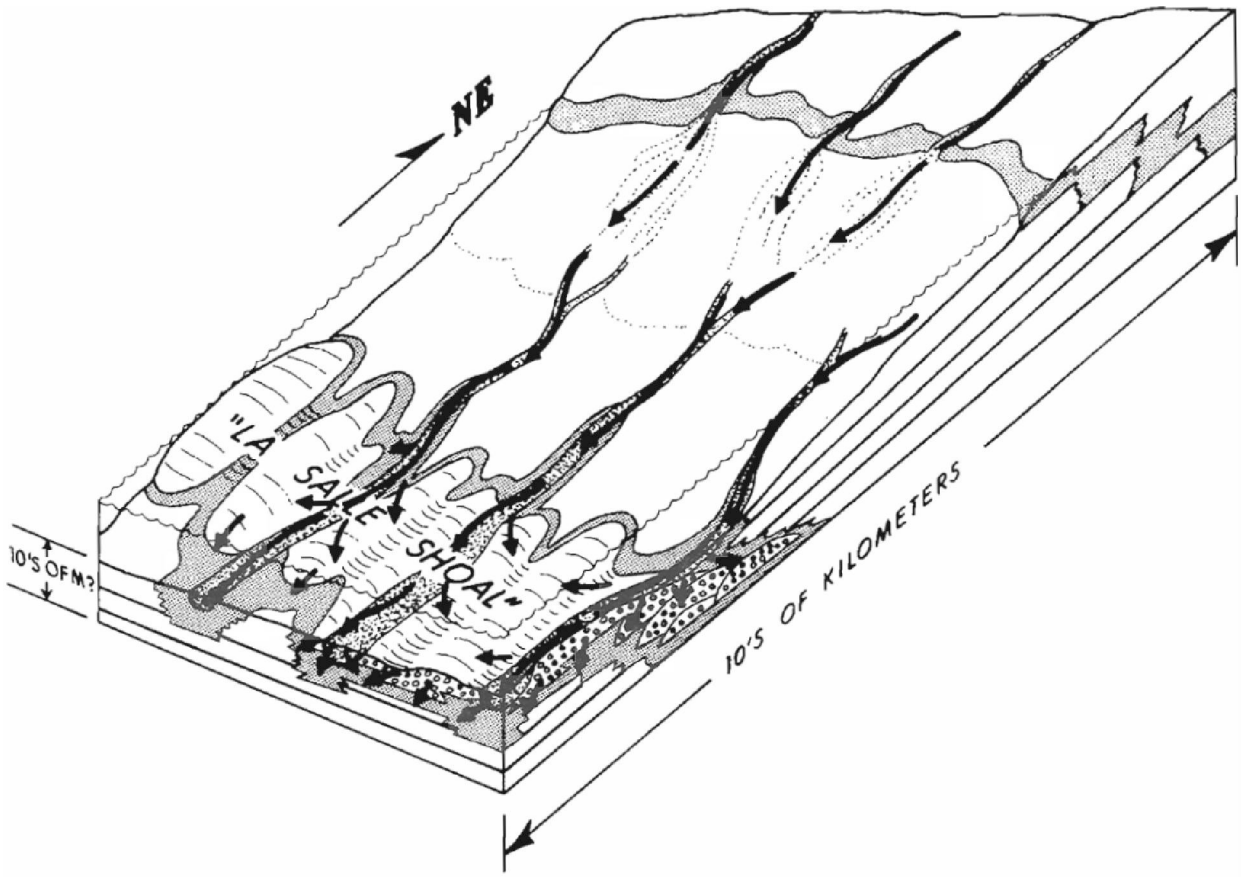

Figure 26 Generalized model of Ste. Genevieve oolite deposition in the Illinois Basin (after Cluff and Lineback, 1981, figure 23 used with permission of SEPM [Society for Sedimentary Geology]). Paleoshoreline is to the north and is roughly perpendicular to the ooid bars, which are oriented northeast-southwest.

Fredonia oolite shoals are typically bar-shaped (i.e., relatively long and narrow), often with flat or convex-upward geometry, and are vertically juxtaposed but horizontally staggered (*en echelon)*. They may occur as parallel or subparallel swarms (Cluff, 1986; Devera et al., 2010).

A typical McClosky oolite shoal is less than 0.4 km (0.25 mi) wide, 3.2 km (2 mi) long, and 3.0 m (10 ft) thick (MGSC, 2005) and may cover as few as six or eight wells (J. Grube and B. Seyler, personal communication, 2013), although thicker and broader oolite bodies are not uncommon and probably represent vertical and/or lateral coalescence of multiple shoals (Figure 27). Keith and Zuppann (1993) noted that modern oolite bodies can show preferential orientation either along or perpendicular to depositional strike. The former orientation (parallel to depositional strike and slope break, in a northwest-southeast direction in the ILB) is created by currents moving along the shoreline, while the latter (along depositional dip, in a northeast-southwest direction) is the product of water moving in and out of tidal channels. The latter process is generally considered the dominant type in ILB Mississippian deposits (Gibson, 2001), but both of these primary orientations, as well as orientations between these end members, can be found within the same depositional regime. The McClosky C isopach map (Figure 27) created for this study shows both shoal orientations, either in isolation or coalescing. This is broadly in keeping with the findings of an earlier study (MGSC, 2005).

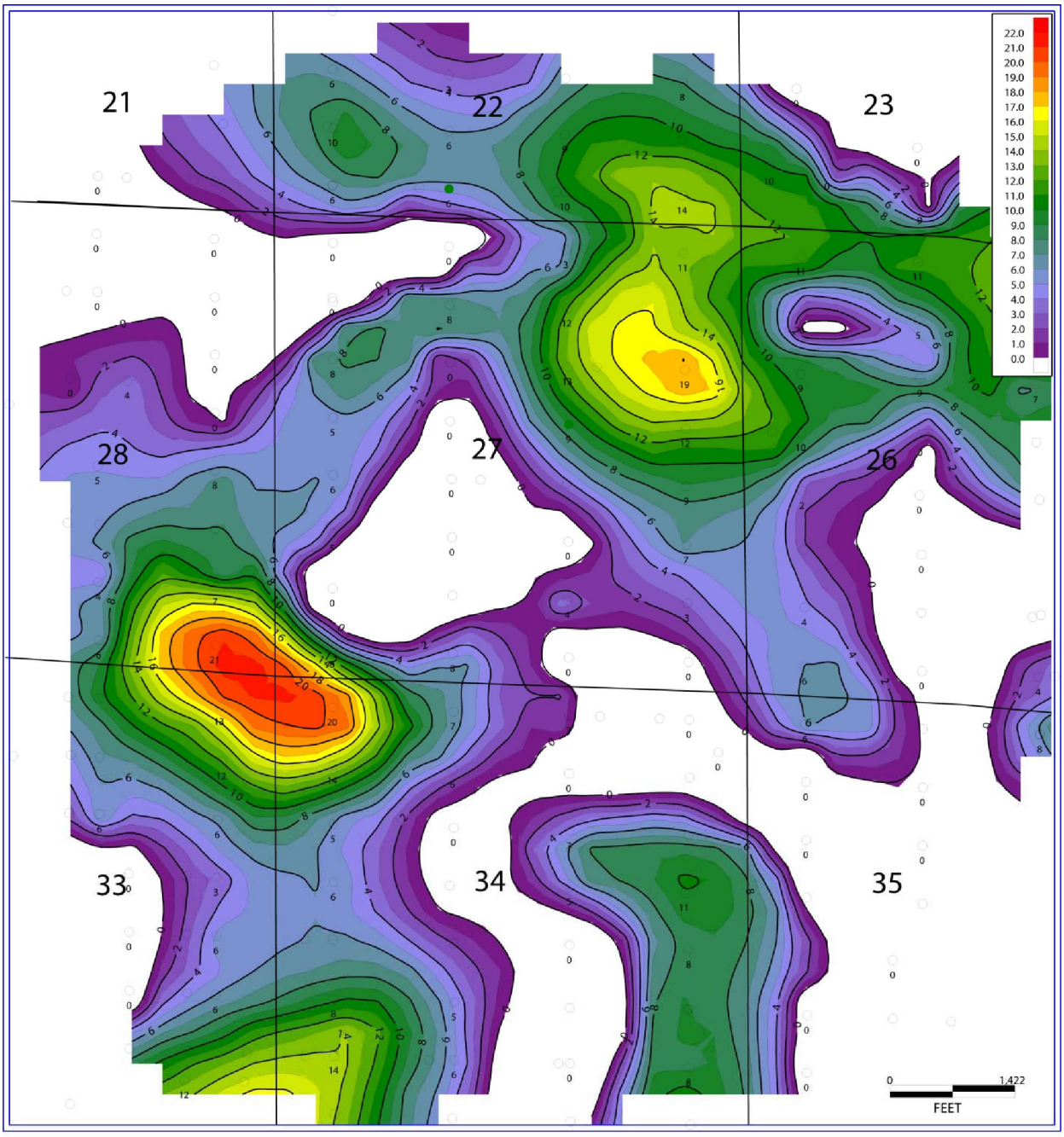

Figure 27 Net thickness of "McClosky C" oolite shoals. Thickness is in feet and the contour interval is 0.6 m (2 ft).

Fredonia oolite reservoirs are created by a combination of stratigraphic trapping (lithofacies change) and structural trapping (Choquette and Steinen, 1985). Overlying fine-grained sediments trap petroleum within the "shoals." Cluff (1986) and Gibson (2001) noted two different internal facies within the bars themselves—a core of clean oolite grainstone enclosed by nonporous oolite packstone—as well as an interbar facies of fossiliferous wackestone and lime mudstone. In many cases, basal portions of the ooid shoals are dolomitized, as are interbar facies (Gibson,

2001). Microporosity between dolomite crystals sometimes accommodates oil accumulation. The dolomite reservoir at this location closely underlies the "McClosky C," but appears to have a reciprocal thickness relationship with it in some parts of the field, suggesting that the dolomite layers represent dolomitized interbar mudstones.

Figure 28 shows a photomicrograph of a sample taken from a productive dolomite (good permeability, good oil saturation and low water content on well log) from the Matchett #2 well (API 121910454600). An average porosity of 25.6% was calculated for this sample via phase analysis. Coarse dolomite rhombs on the order of 200 microns in maximum length (from vertex to opposite vertex) were present in this interval, but the crystals are mostly fine to medium (e.g., 30 microns or less) according to the classification of Lucia (1999).

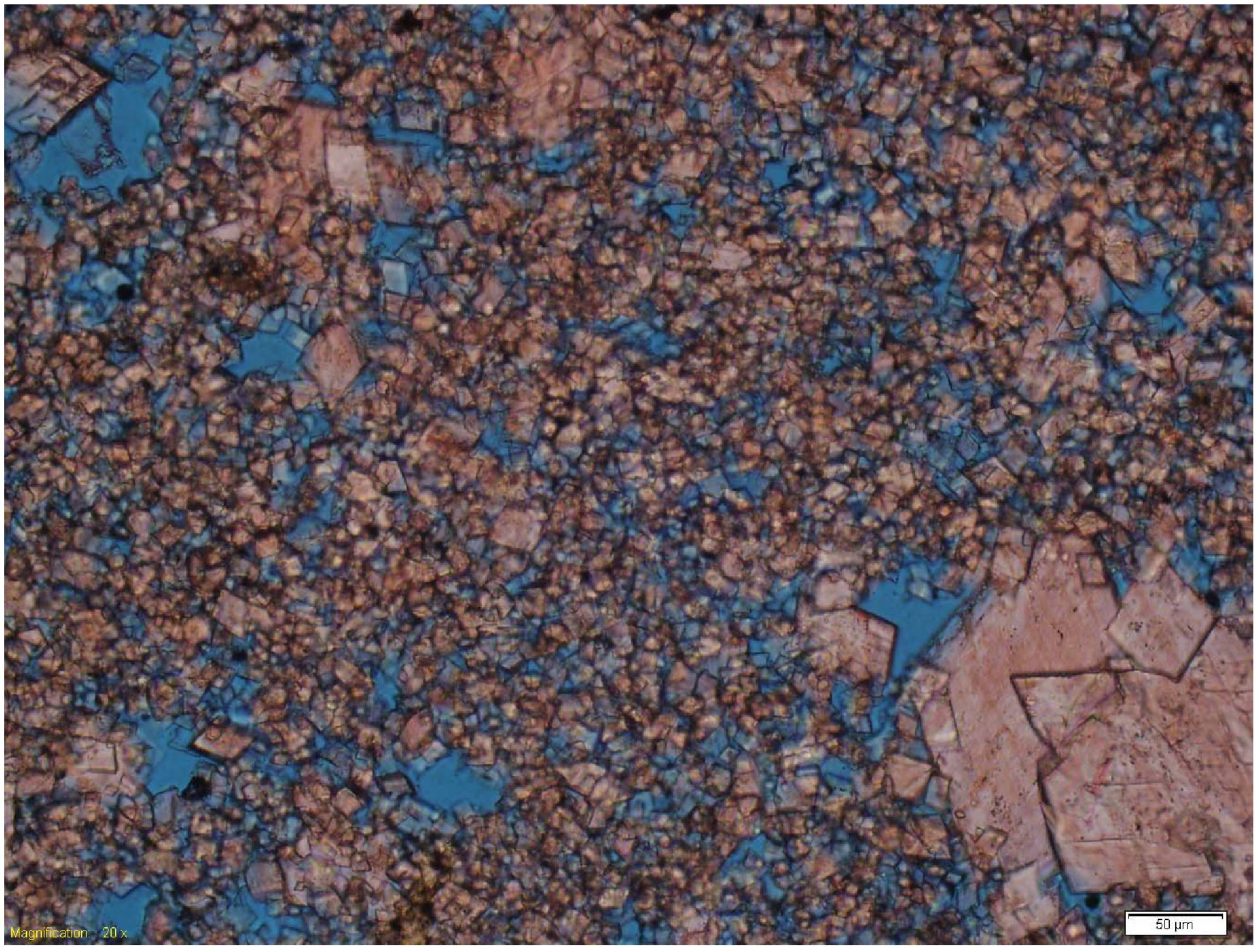

Figure 28 Photomicrograph of a sample from a productive dolomite zone at the Matchett #2 well on Johnsonville Consolidated Field.

Modern oolites can have porosities upwards of 40% and permeabilities of tens of thousands of millidarcies, but typical values for oolitic limestones are on the order of 10–20% porosity, with permeabilities in the tens to hundreds of millidarcies (Keith and Zuppann, 1993). Permeabilities approaching 9.86×10^{-8} cm^2 (10,000 md) have been reported for Mississippian oolites in the Illinois Basin (Choquette and Steinen, 1993), but such high values are anomalous; average permeabilities of 9.86×10^{-8} to 2.47×10^{-9} cm^2 (100 to 250 md) are more likely to be

representative of ILB oolites (Choquette and Steinen, 1993; Manley et al., 1993). Multiple core analyses in ISGS files showed isolated permeabilities as high as 4.93×10^{-8} to 5.92×10^{-8} cm^2 (5,000–6,000 md), but these were considered atypical and most likely the result of fractures. Initial porosity-permeability transforms were unduly influenced by these high values and yielded permeability distributions that were considered unrealistic by the geologic modelers, so a more conservative relationship was imposed to bring mean reservoir permeability down to 2.08×10^{-9} cm^2 (211 md; see the "Geocellular Modeling" section for further discussion).

While porosity and permeability can be high in Ste. Genevieve oolite lenses, intergranular diagenetic calcite fill greatly impacts reservoir quality in some instances (Seyler, 1986). (See Figure 29 for an example of porosity partially occluded, but not seriously impacted, by intergranular diagenetic calcite at Johnsonville.) Ste. Genevieve oolite zones may show bimodal porosity, i.e., microporosity within the ooids as well as macroporosity between them; some examples of this are in evidence at Johnsonville (Figure 30), but intergranular porosity was dominant in the two oolite zones that were sampled.

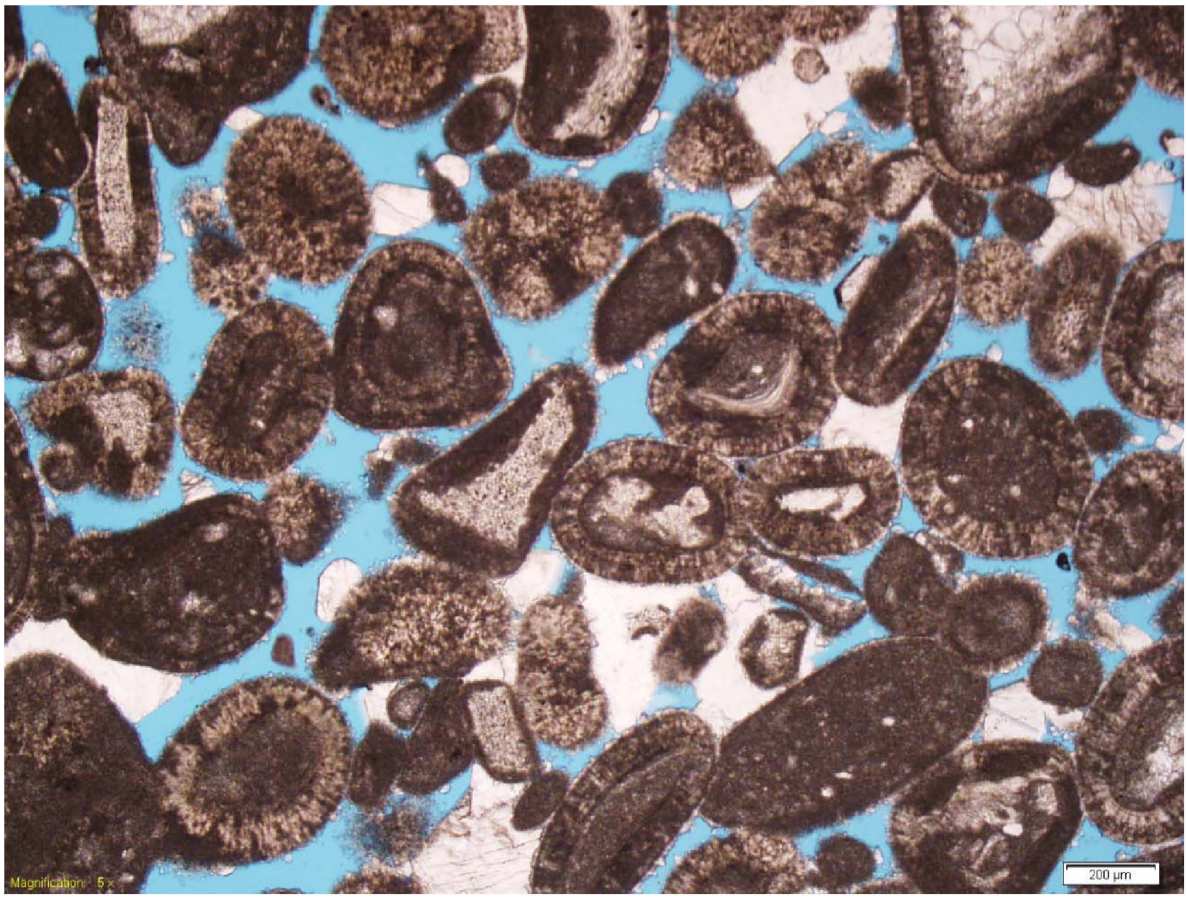

Figure 29 Photomicrograph of an ooid grainstone from a reservoir zone at Johnsonville Consolidated Field, showing porosity partially occluded by calcite overgrowths.

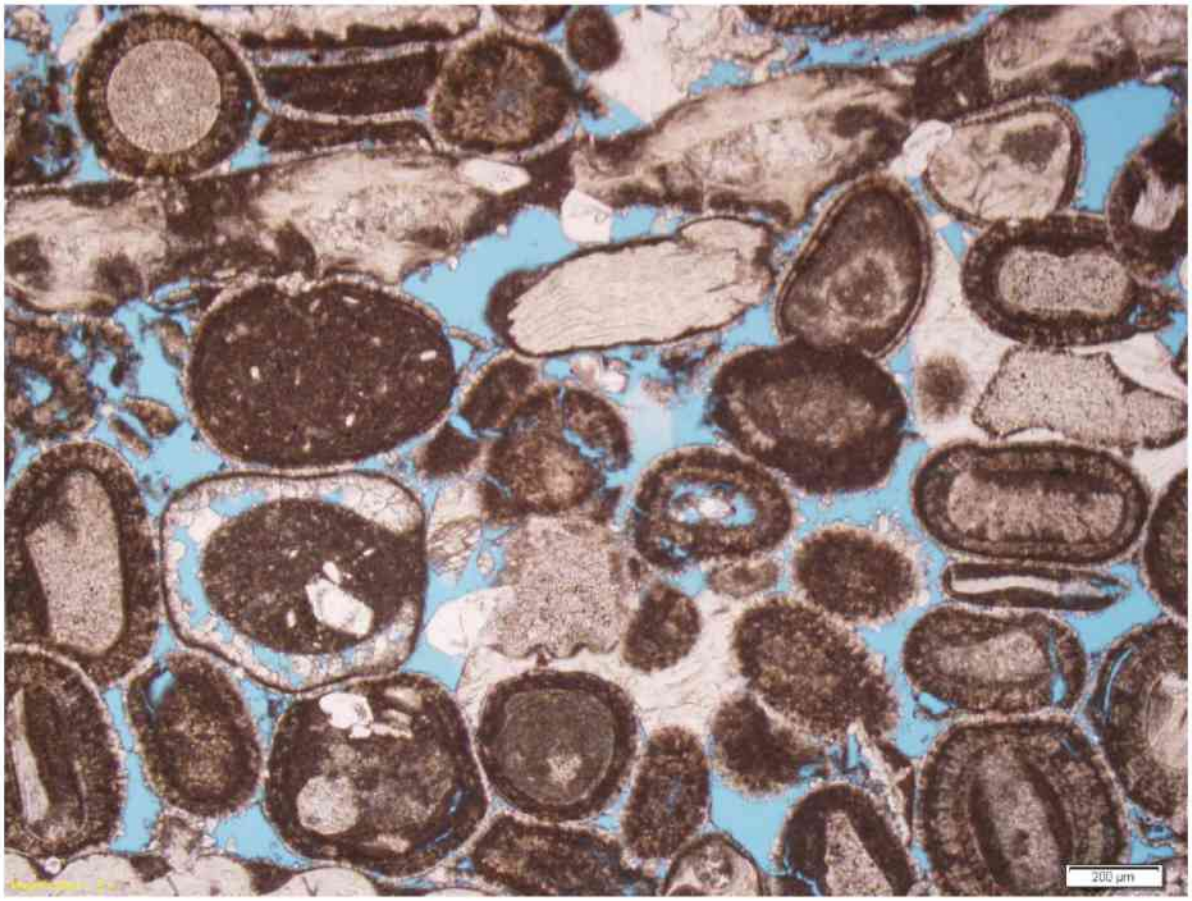

Figure 30 Photomicrograph of an ooid grainstone from a reservoir zone at Johnsonville Consolidated Field, showing minor intragranular porosity.

Ste. Genevieve oolite shoals are notoriously difficult to map and correlate due to their irregular thicknesses and shapes, abrupt transitions to interbar facies, and relatively short and narrow dimensions, i.e., small enough to readily pinch out between wells at typical ILB pattern sizes (Zuppann, 1993; Nelson et al., 2002). Although data and well logs from Johnsonville were generally honored in the construction of these models, representation of a typical shelf carbonate depositional environment was the primary goal; thus, at wells where correlations were ambiguous, interpretations that were most compatible with the depositional environment model (e.g., maximum shoal thickness of 3–5 m [10–15 ft], but shoals sometimes stacking) were favored. Thick reservoir intervals which appeared continuous on well logs were divided between multiple McClosky zones if logs from adjacent wells seemed to support this interpretation, although thicknesses of over 6 m (20 ft) have been reported in the literature (Zuppann, 1993) and were permitted locally if logs from adjacent wells provided no grounds for dividing the interval among two different mapped layers. Lithological notes on old well logs for Johnsonville Consolidated often show thin permeable limestone layers persisting between (and seemingly correlative with) major shoals, but these are generally nonproductive (Y. Lasemi, personal communication, 2014) and were excluded from net isopachs. Similarly, zones marked as dolomitic in lithological notes on geophysical logs were widely distributed (Figure 31) but good pay was far more localized (Figure 32).

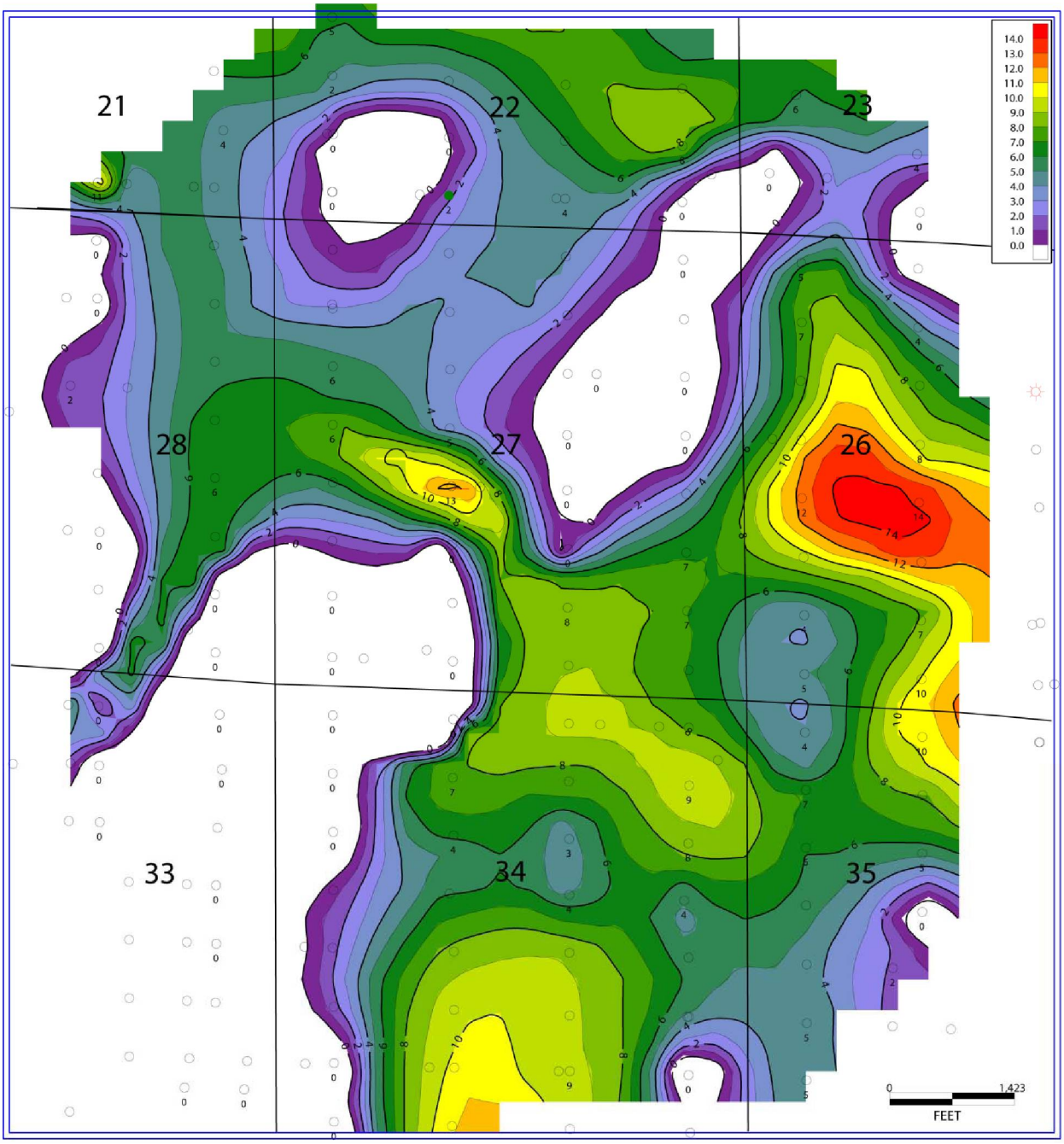

Figure 31 Gross isopach map of a portion of the "Dolomite B" zone at Johnsonville Consolidated Field. The contour interval is 0.6 m (2 ft).

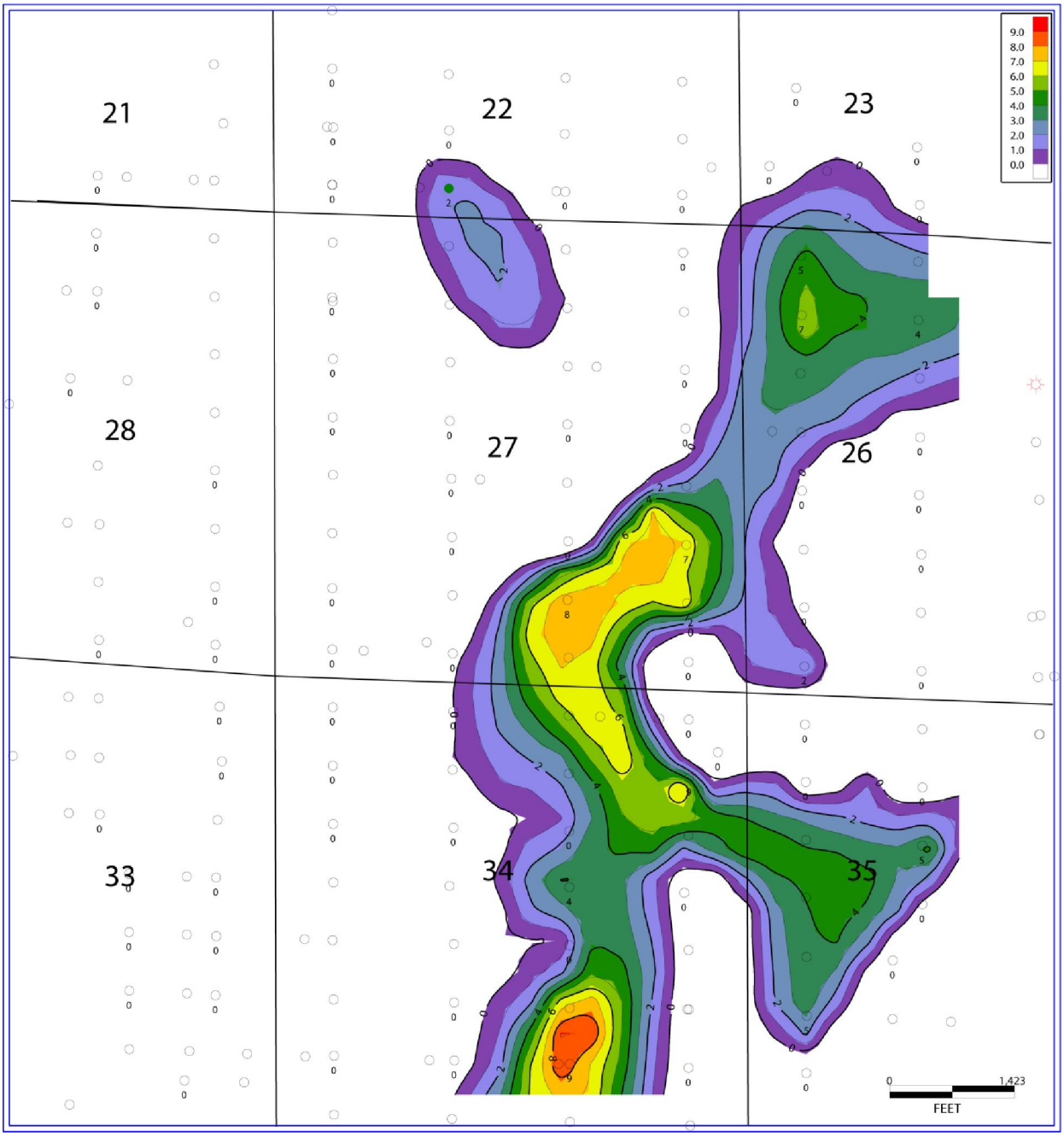

Figure 32 Net isopach map of a portion of the "Dolomite B" zone at Johnsonville Consolidated Field. The contour interval is 0.6 m (2 ft).

Depositional Environment

The Johnsonville "McClosky" reservoir bodies were probably deposited in shoals and tidal channels in a shallow marine shelf to lagoonal setting, possibly on the flanks of a syndepositional topographic expression of a buried reef (ooid accumulations tended to be thicker off-center of the structure). Subaerial exposure of sediments in these shallow waters may have occurred periodically, permitting dolomitization of lagoonal, and/or interbar lime muds.

Shelf Carbonate: Geneva Dolomite at Miletus Oil Field

Geneva Dolomite Production History and Development

The Geneva Dolomite reservoir in the Miletus Oil Field (Figure 33) was first drilled in the early 1980s, but the initial well was determined to be noncommercial and was abandoned. In late 1996, a second attempt was made to drill an exploratory well into the Geneva Dolomite. The second attempt was successful during fall 1996 when the Ceja Corporation Basset No. 3 was deepened into the Middle Devonian Geneva Dolomite and completed open-hole for 25.1 m^3/d (158 bopd) of production. Ceja Corporation subsequently developed the Geneva reservoir in Miletus Field by drilling additional wells. The combined monthly production and cumulative production graphs (Figure 34) show a sharp increase in annual and cumulative production of more than 0.3 million m^3 (2 million bbl) of oil over a period of 2.5 years. Monthly and cumulative production graphs from the Ceja Corporation Church No. 5, Hogan No. 2, Keller No. 2, and Basset No. 3 wells show very high monthly rates of production, some exceeding 1,590 m^3 (10,000 bbl) of oil (Figure 35). Each of these wells produced more than 31,800 m^3 (200,000 bbl) of oil between late 1996 and mid-2000. These data illustrate the high productivity potential of good-quality Geneva Dolomite reservoirs.

The Geneva Dolomite is commonly the basal member of the Middle Devonian Grand Tower Limestone in much of the Illinois Basin. Prolific Geneva Dolomite reservoirs are associated with shelf carbonates sediments in Illinois oil fields. A study of Geneva Dolomite reservoirs at the Miletus, Raccoon Lake, Sandoval, Patoka, and St. James oil fields (Figure 33) shows that pronounced structural closure, fracturing, and formation of secondary porosity through dolomitization and dissolution are associated with reservoir development and entrapment of petroleum (Seyler et al., 2003). Examination of cores from Geneva Dolomite reservoirs in Illinois and quarry exposures in Indiana show the rock to be a brown, vuggy, and sucrosic dolomite. Indications are that postdepositional dolomitization combined with dissolution of fossil material of Geneva carbonates is a viable mechanism to explain the enhanced porosity, permeability, and brecciation found in Geneva Dolomite reservoirs. Much of the information in this report is taken from or based on Seyler et al. (2003).

Reservoir Characterization

Stratigraphy and Facies Relationships

The Geneva Dolomite is widely exposed in quarries located near the Geneva outcrop belt in Indiana (Perkins, 1963; Leonard, 1996). The description of the Geneva Dolomite in these quarries, examination of continuous core from two recently drilled Geneva wells, and core biscuits from wells in several neighboring fields aided in the determination of stratigraphic relationships within the Grand Tower and Jeffersonville limestones. Likewise, these components aided in the interpretation of facies and diagenetic alterations that occurred to create the highly porous and permeable sucrosic dolomite of the Geneva.

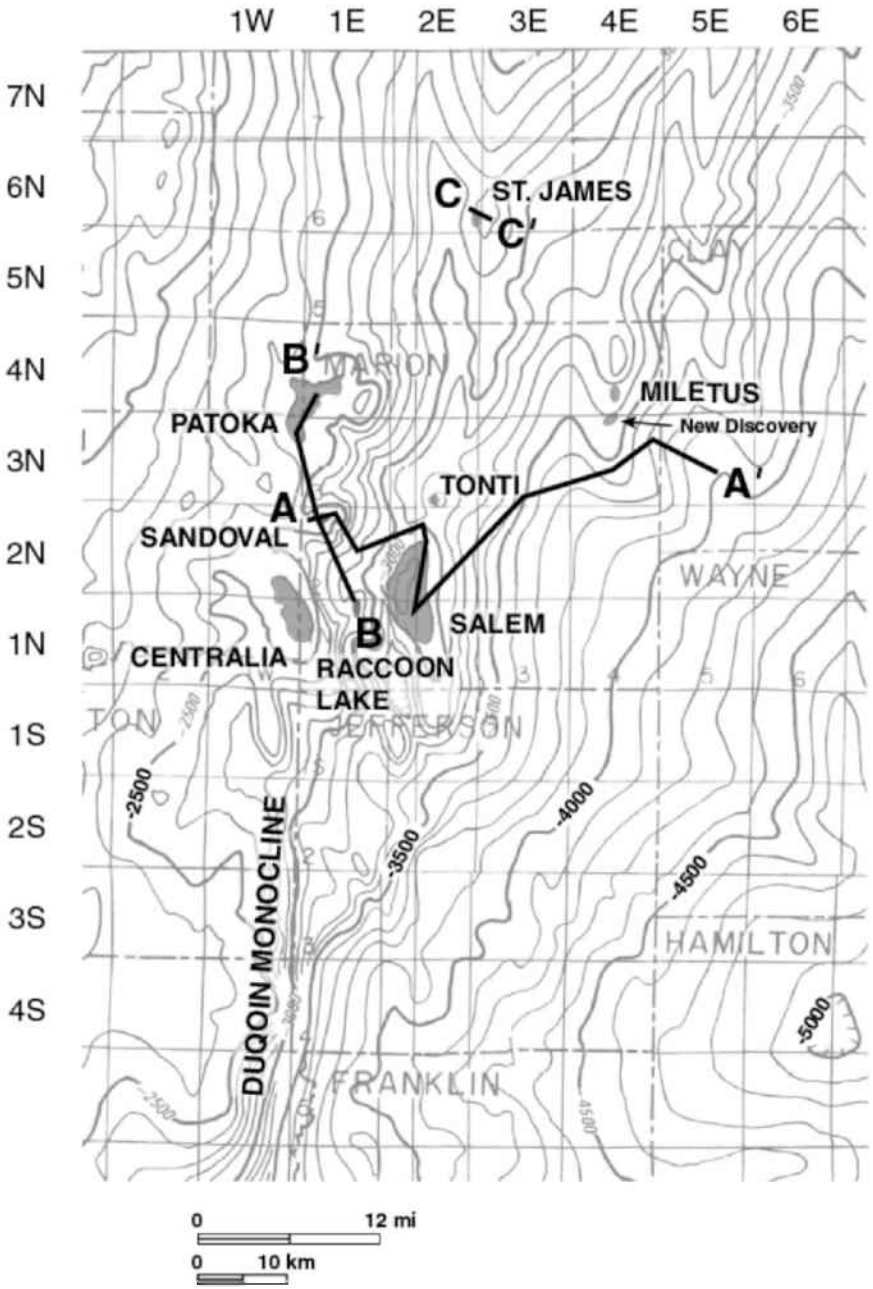

Figure 33 Structure map contoured on the base of the New Albany Shale. Contour interval is 30.5 m (100 ft). Cross section locations and selected Geneva Dolomite reservoirs are shaded in gray. The "New Discovery" arrow is the location of the prolific Stephen A. Forbes State Park 2002 Geneva discovery (Seyler et al. 2003; modified from Cluff et al., 1981).

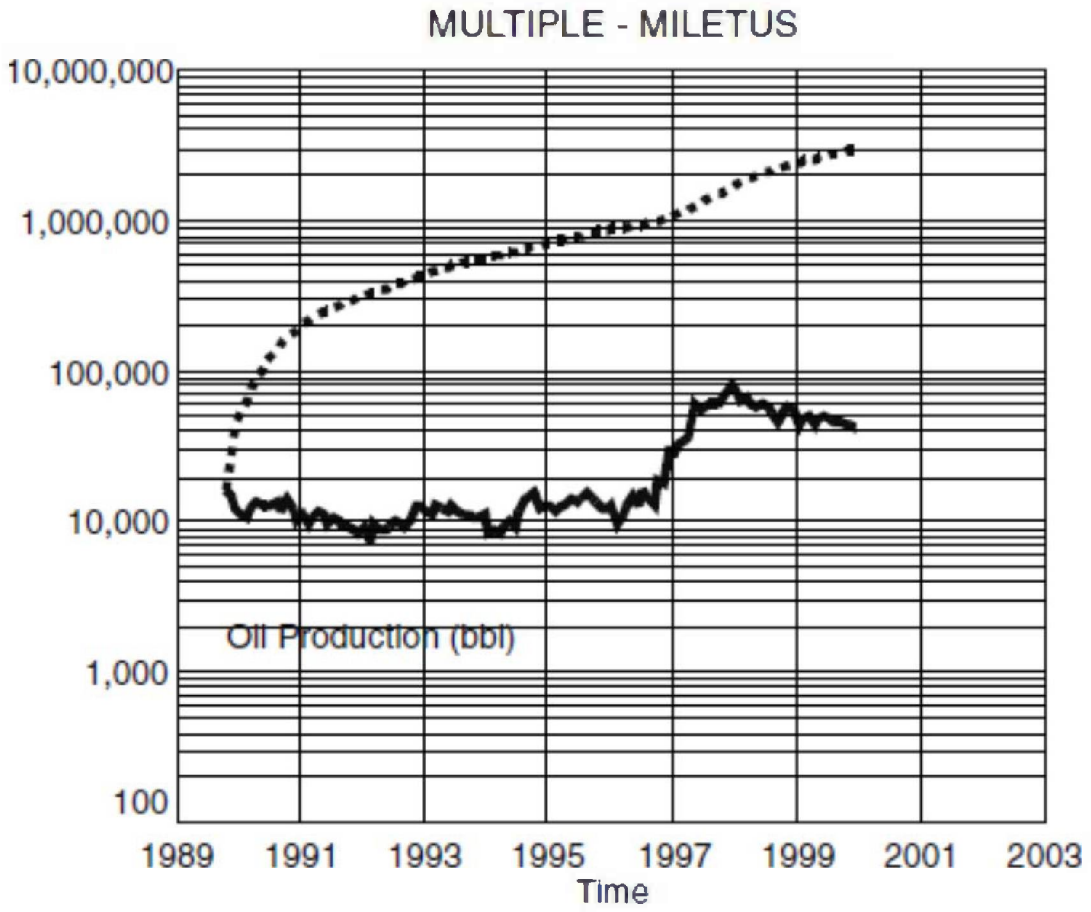

Figure 34 Combined graphs of the monthly production (solid line) and cumulative production (dashed line) from the Geneva Dolomite reservoir in Ceja Corporation wells in the Miletus Field. The graphs show a sharp increase of over 0.3 million m^3 (2 million bbl) of oil in annual and cumulative production over a period of two and one-half years (December 1996 to June 2000; unpublished data from the IHS Energy Group; Seyler et al., 2003).

The Geneva Dolomite has been considered to be a facies of the Grand Tower Limestone in Illinois and the Jeffersonville Limestone in Illinois and Indiana (Figure 36; Meents and Swann, 1965; Droste and Shaver, 1975). Thin Dutch Creek Sandstone locally underlies the Geneva Dolomite in the study area. Sandy dolomite intervals are common within the Geneva Dolomite formation. Both the Grand Tower and Jeffersonville consist of a pure, fossiliferous southern limestone facies (commonly biostromal and/or biohermal) and a northern dolomite facies (Schwalb, 1955; Meents and Swann, 1965; Droste and Shaver, 1975; Devera and Fraunfelter, 1988). The limestone facies primarily occurs in the southern portion of the Illinois Basin, including its extension into west-central Indiana. The dolomite facies primarily occurs in the central to northern portion of the Illinois Basin (Meents and Swann, 1965; North, 1969). The dark brown, sandy dolomite of the Geneva occurs at the base of the dolomite facies of the Grand Tower and Jeffersonville Limestone.

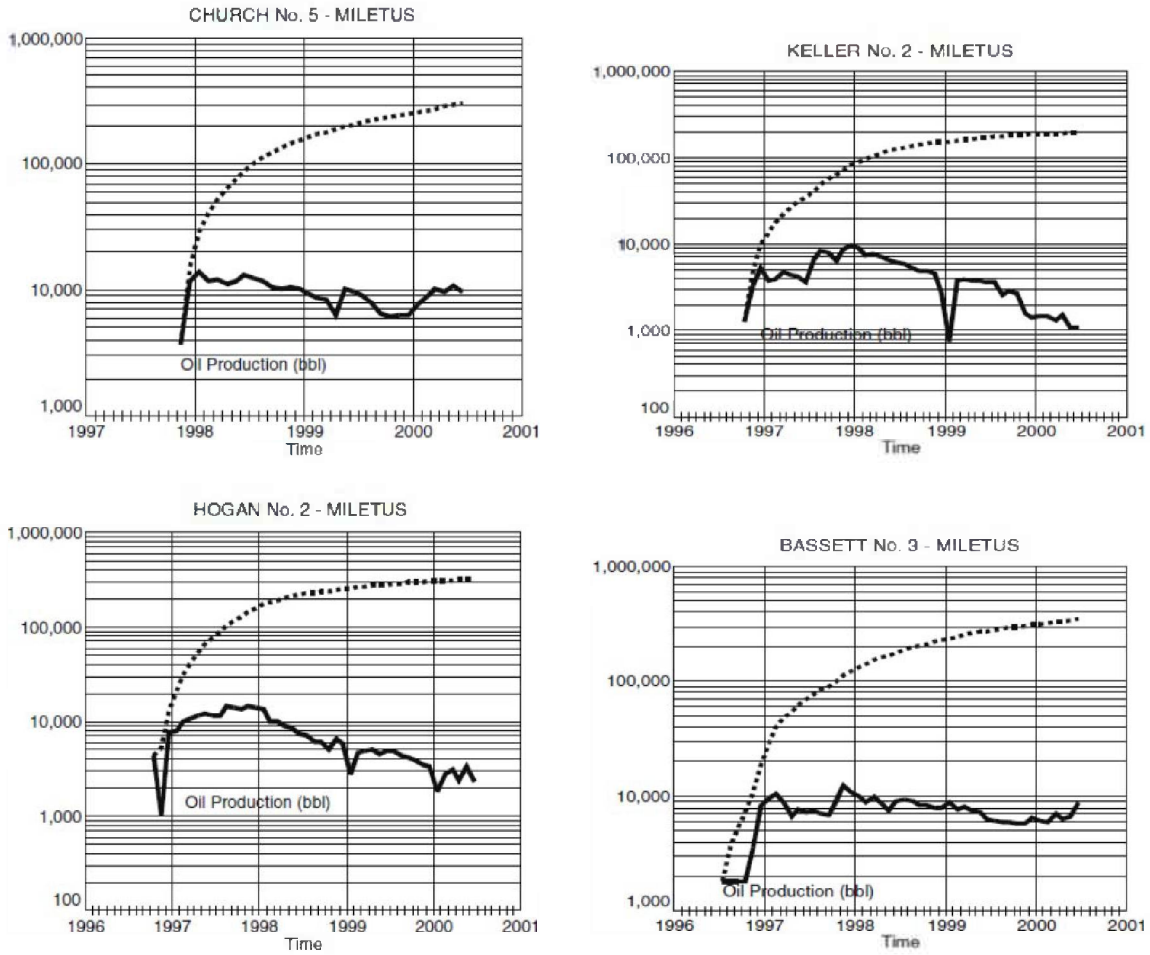

Figure 35 Combined graphs of the monthly production (solid line) and cumulative production (dashed line) from the Ceja Corporation wells in the Miletus Field: (a) Church No. 5, (b) Hogan No. 2, (c) Keller No. 2, and (d) Basset No. 3. These highly productive Geneva Dolomite wells show very high monthly rates of production, some exceeding 1,590 m^3 (10,000 bbl) of oil per month. Each of these wells produced from 31,800 to over 47,700 m^3 (200,000 to over 300,000 bbl) of oil between late 1996 and June 2000. Note the low decline rate for some of these wells (unpublished data from IHS Energy Group; Seyler et al., 2003).

The Geneva Dolomite is buff to dark brown but oxidizes into pale tan, cream, and even white in near-surface exposures (Droste and Shaver, 1975). Its distinctive brown color has been attributed to organic material disseminated within the rock (Schwalb, 1955). When samples are dissolved in hydrochloric acid, this organic material floats to the surface. In most places, the color darkens toward the base, although in some areas the reverse is true (Schwalb, 1955). Quartz sand grains "floating" in the carbonate are present throughout the Geneva but are especially common near the base. The dolomite is massive to thin bedded and granular and vuggy for the most part. The Geneva has a bioclastic and pelletoidal texture (packstone to grainstone); common molds and casts of branching and solitary corals, stromatoporoids, some brachiopods, bivalves, gastropods, and ostracodes make up this texture (Droste and Shaver, 1975).

Subsurface distribution of the Geneva Dolomite forms an arcuate belt that curves northwest from the outcrop to west-central Indiana and bends to the southwest from Clark and Edgar Counties in Illinois, extending as far as Montgomery, Bond, and Clinton Counties (Figure 37). The Geneva ranges from 0 to 15 m (0 to 50 ft) thick in central Illinois but is thicker in some local areas (Schwalb, 1955). Studies of well cuttings from recently drilled wells show that the Geneva locally may be up to 27 m (90 ft) thick. In central and west-central Indiana, the Geneva forms a semicircular body ranging in thickness from 0 to 18 m (0 to 60 ft).

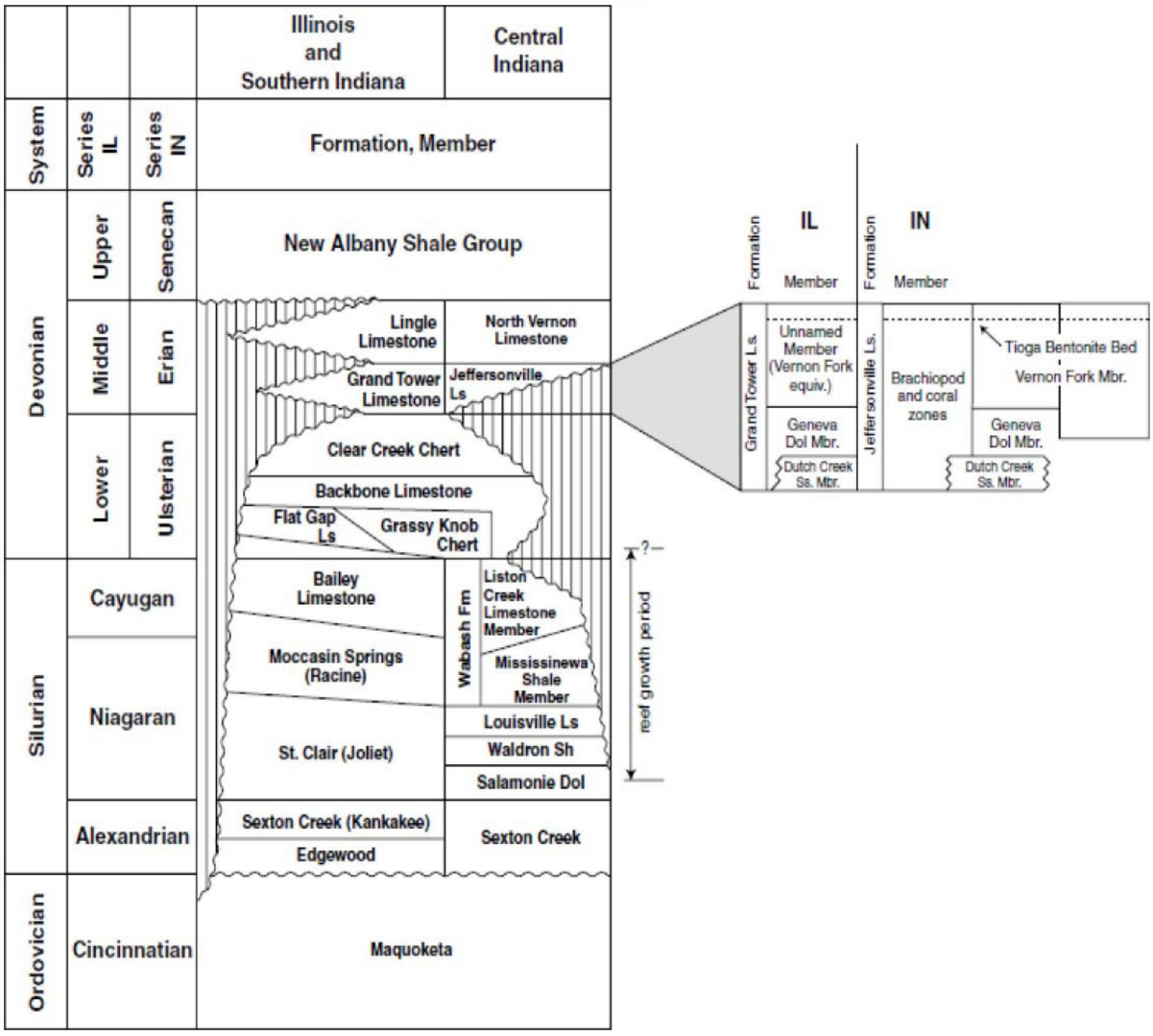

Figure 36 Correlation and nomenclature of the Devonian and Silurian sections of the stratigraphic column in Illinois and Indiana (Seyler et al., 2003; modified from Droste and Shaver, 1987; Droste et al., 1975).

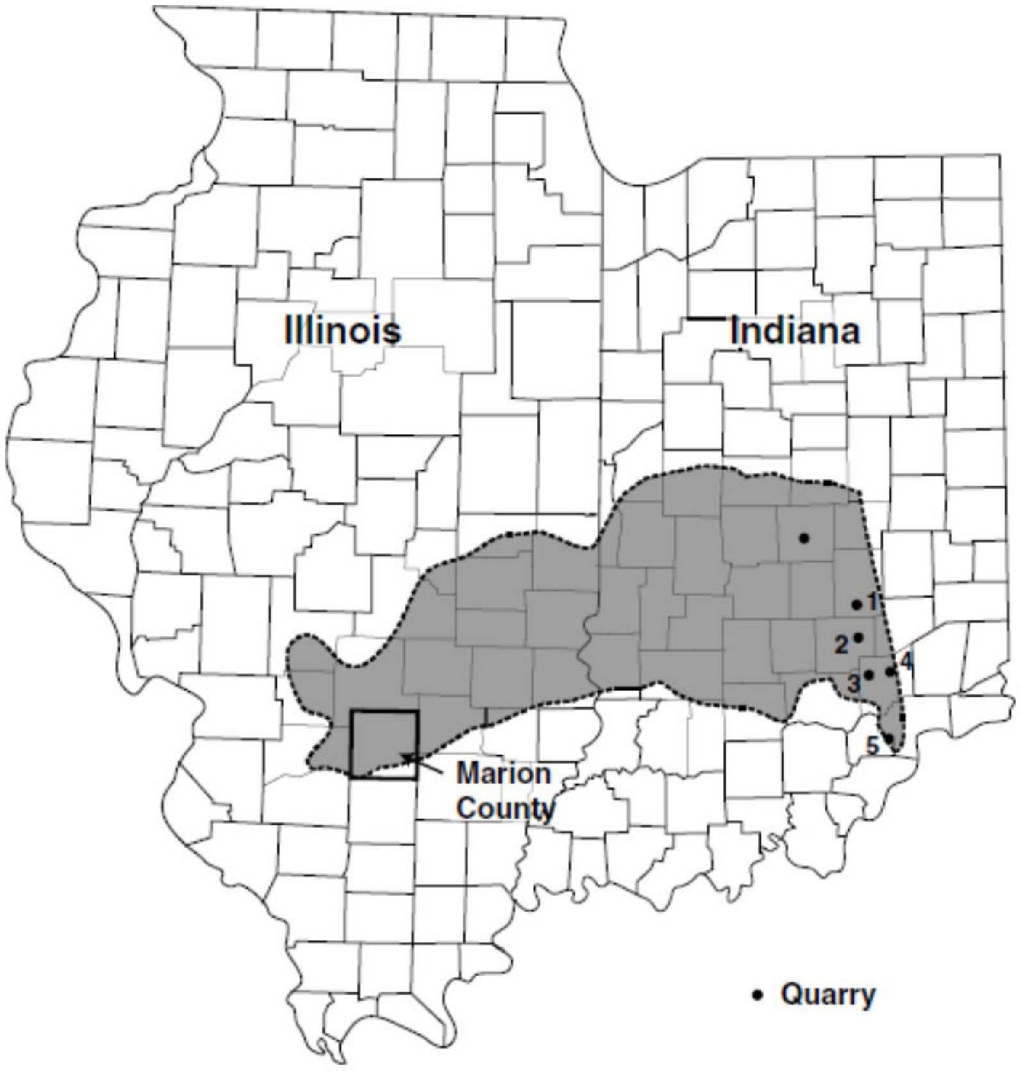

Figure 37 Distribution of the Geneva Dolomite in Illinois and Indiana. The Geneva reaches a maximum thickness of about 27 m (90 ft) in east-central Illinois; thins to zero in southern Marion County, Illinois; and outcrops in a series of quarries (numbered 1 through 5) in southeastern Indiana, where it is 6.1 to 9.1 m (20 to 30 ft) thick (Seyler et al., 2003; modified from Perkins, 1963, figure 2 used by permission of the Geological Society of America; Schwalb, 1955).

The Geneva conformably overlies the Dutch Creek Sandstone, where it is present at the base of the Grand Tower. However, in many places, the Geneva uncomfortably overlies Lower Devonian to Middle Silurian strata that increase in age from south to north in Illinois (Meents and Swann, 1965). The stratum underlying the Middle Devonian Grand Tower Limestone in the southern part of Marion County is the Lower Devonian Clear Creek Chert. In the northern part of Marion County, the Upper Silurian-Lower Devonian Bailey Limestone directly underlies the Grand Tower Limestone.

The Geneva Member is overlain by a somewhat thicker section of lighter-colored dolomite. The dolomite above the Geneva has been referred to as the "laminated beds," "laminated zone,"

"chalk beds," or "fine-grained dolomite of the Jeffersonville" in Indiana (Droste and Shaver, 1975) and the "unnamed," "light-colored dolomite above the Geneva," or "the northward facies of the Grand Tower" in Illinois (Schwalb, 1955; Meents and Swann, 1965; Collinson, 1967; North, 1969). Droste and Shaver (1975) named the unit above the Geneva Dolomite the Vernon Fork Member for the central and west-central Indiana Jeffersonville facies. Subsurface data suggest that the Geneva interfingers with the Vernon Fork dolomite in Indiana (Droste and Shaver, 1975) and its equivalent unit in Illinois (Schwalb, 1955; Meents and Swann, 1965). The Geneva is correlated with the lower part of the Middle Devonian Vernon Fork and, therefore, with the lower part of the Grand Tower Limestone of southern Illinois (Schwalb, 1955; Meents and Swann, 1965; North, 1969; Devera and Fraunfelter, 1988).

Abundant and diverse fossil allochems in the Geneva suggest deposition within a normal marine environment. The overlying Vernon Fork Member and its equivalent in Illinois, however, appear to have been deposited in shelf lagoon and tidal flat environments that were periodically subjected to subaerial exposure, as indicated by the presence of mud cracks (Perkins, 1963; Lasemi, 2001). In such restricted shallow-water settings, evaporation of seawater could have formed the magnesium-rich solutions that may have been responsible for formation of the dolomites in the Grand Tower and Jeffersonville limestones (Droste and Shaver, 1975; Lasemi, 2001). The boundary between the normal marine Geneva Dolomite and the overlying restricted marine Vernon Fork Member marks a transgressive-regressive transition. However, biostratigraphically, there is no significant time break along this boundary (Norby, 1991), and there has been no unequivocal evidence thus far indicating major subaerial erosion.

The sub-Kaskaskia unconformity separates the Upper Silurian and Lower Devonian strata from the Middle Devonian strata. Truncation of the Upper Silurian through Lower Devonian strata formed an eroded surface on which the Middle Devonian Geneva Dolomite and Dutch Creek Sandstone Members of the Grand Tower were deposited (Devera and Fraunfelter, 1988; Devera and Hasenmueller, 1991).

Structure

The Upper Devonian New Albany Shale is a widespread and consistent formation that is useful for structural mapping in the Illinois Basin. A structure map contoured on the base of the New Albany Shale reflects structural relationships of the Geneva Dolomite (Figure 33). Pronounced structural closure, as great as 30.5 m (100 ft), is associated with oil production from the Geneva Dolomite. Much of this structure is tectonic; but, in some cases, the closure is caused or enhanced by the drape of younger Middle Devonian strata over Silurian reefs (Bristol, 1974). Some of the most prolific Geneva wells are associated with the postulated underlying Silurian reefs. This postulate is related to enhanced structural closure in the strata overlying the reef, which is a function of differential compaction. Fractures within the Geneva beds may have resulted from differential compaction. Reef-induced paleostructure (Droste and Shaver, 1975) may have influenced Geneva deposition by offering sites suitable for growth of bioherms and the ensuing diagenetic alteration of these carbonates, resulting in improved reservoir porosity and permeability. Structure caused by differential compaction of the fine-grained sediments flanking the rigid core of a Silurian reef has been documented throughout the entire overlying stratigraphic section and can even be detected in structural highs in the overlying Pennsylvanian coals (Whitaker, 1988). Many of these reefs also have topographic expression at the surface that may be located by present-day drainage patterns (Whitaker, 1988).

Geneva Dolomite production is also associated with structures induced by tectonism. Production from anticlinal closure at the St. James, Salem, and Centralia Fields indicates that pronounced structural closure from tectonic deformation is sufficient to trap petroleum in the Geneva Dolomite. However, the most prolific production is from highly porous and permeable Geneva Dolomite draped over pinnacle reefs. A number of uplifted fault blocks in the Illinois Basin have coincidental reef structures, indicating that Silurian reefs may have preferentially developed atop pre-existing structural highs (Davis, 1991).

Geneva Dolomite Quarries and Outcrops

A series of quarries was examined in the Geneva outcrop belt in east-central Indiana that extends for 113 km (70 mi) in a north-south direction (Figure 37). The Geneva is 6.1 to 9.1 m (20 to 30 ft) thick here and is quarried for construction aggregate. The fossil content, crystal size, zonation of dolomite crystals, color, staining, porosity, and permeability of the Geneva observed in Indiana quarries are all similar to the prolific reservoirs in Illinois. The Geneva Dolomite shows widespread porosity in both cores and quarries. Geophysical logs from Indiana and Illinois show that porous zones in the Geneva are widespread throughout the subsurface. The distribution of similar facies and porous zones from central Indiana to south-central Illinois suggests possible connectivity across the entire region. The outcrop region of Indiana may serve as a recharge area for the active water drive that is characteristic of the Geneva Dolomite reservoirs throughout the Geneva fairway. These characteristics indicate that the Geneva Dolomite fairway in Illinois and Indiana may prove to be an extensive CO_2 sequestration target.

North Vernon Quarry

The North Vernon Quarry is located near North Vernon, Indiana (number 4 in Figure 37). The highly porous, sucrosic Geneva Dolomite Member is over 6.1 m (20 ft) thick and is overlain by the Vernon Fork Member of the Jeffersonville Limestone (Figure 38a). The late-stage mineralization by cavity-filling, white, sparry, calcite, which is prevalent in the Meshberger and other quarries, is not common in this quarry. Most Geneva vugs in the North Vernon Quarry are not affected by the late-stage calcite mineralization and remain open. Although dolomitization has obscured the direct fossil evidence, remnants of large coral heads and stromatoporoids are common in this quarry, indicative of a biostrome or a biohermal buildup within a biostrome depositional environment. Figure 38b shows a 2.4 m (8 ft) thick bed that includes empty vugs created by the dissolution of large 0.3 × 0.46 m (1 ×1.5 ft) coral heads and stromatoporoids. Partially dissolved smaller colonial corals and other marine fossils were also observed in the quarry walls (Figure 38c). The matrix surrounding the vugs is composed of highly porous, brown sucrosic dolomite. Dissolution of the larger coral heads is more complete than that of the smaller branching corals and other marine fossils found in the matrix. The Geneva Dolomite in the North Vernon Quarry very closely resembles the Geneva Dolomite in cores from reservoirs in Marion County, Illinois. The quarry walls show how abundant these organisms were at the time of deposition as is illustrated in Figure 39, a conceptual model of a biostromal depositional environment.

Scott Quarry, Southern Indiana

The Scott Quarry is number 5 in Figure 39. The Geneva Dolomite equivalent strata in this quarry contain a profusion of fossils (Figure 40) including large unaltered coral heads, stromatoporoids, and an abundance of other fossils types. The matrix surrounding the intact fossils is a brown,

slightly dolomitic limestone (Figure 40). The Geneva Dolomite equivalent in this quarry is 4.6 m (15 ft) thick and lacks the visible porosity that is present in the quarries to the north. These strata most closely resemble the Geneva Dolomite observed in core samples from the Sandoval Field in Marion County, Illinois. The change from the visibly porous and permeable dolomite observed in the North Vernon Quarry to the highly fossiliferous limestone in the Scott Quarry is due to less dissolution of fossils and less dolomitization in the more southern extent of the Geneva Dolomite equivalent strata.

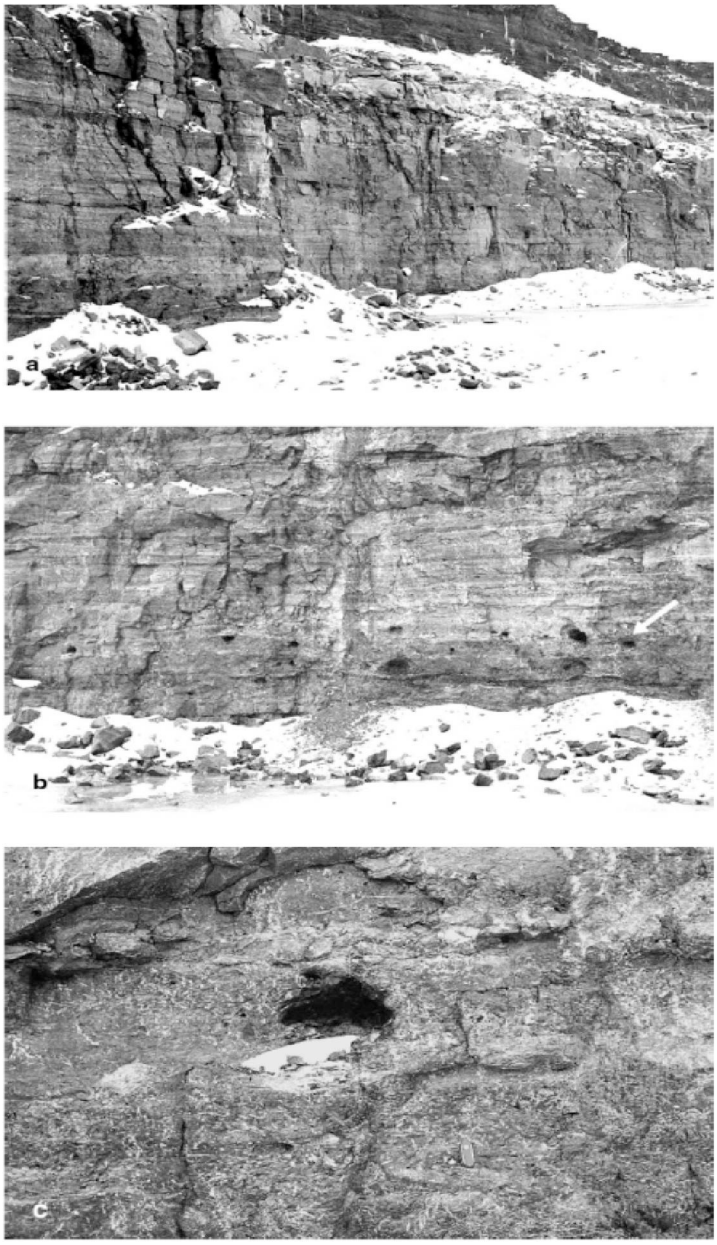

Figure 38 (a) North Vernon Quarry near North Vernon, Indiana (number 4 in Figure 37). Highly porous, sucrosic Geneva Dolomite is over 6.1 m (20 ft) thick and is overlain by the Jeffersonville Limestone. (b) Row (at arrow) of large, empty vugs in the Geneva Dolomite. The highly porous dolomite contains many vugs created by dissolution of marine fossils, including colonial corals and stromatoporoids. (c) Close-up of vug from photo (b) showing detail of smaller branching corals and other marine fossils. The branching corals are the ubiquitous white areas in the rock (Seyler et al., 2003).

Figure 39 Depiction of the biotic assemblage that thrived on the shallow marine shelf environment that was present across the Illinois Basin during Middle Devonian time. The bioclastic remnants of this assemblage form a widespread biostrome that is the fabric of the Grand Tower and Jefferson limestones and the diagenetically transformed Geneva Dolomite (Seyler et al., 2003; modified from Greb et al., 1993, cover photo used with permission of the Kentucky Geological Survey).

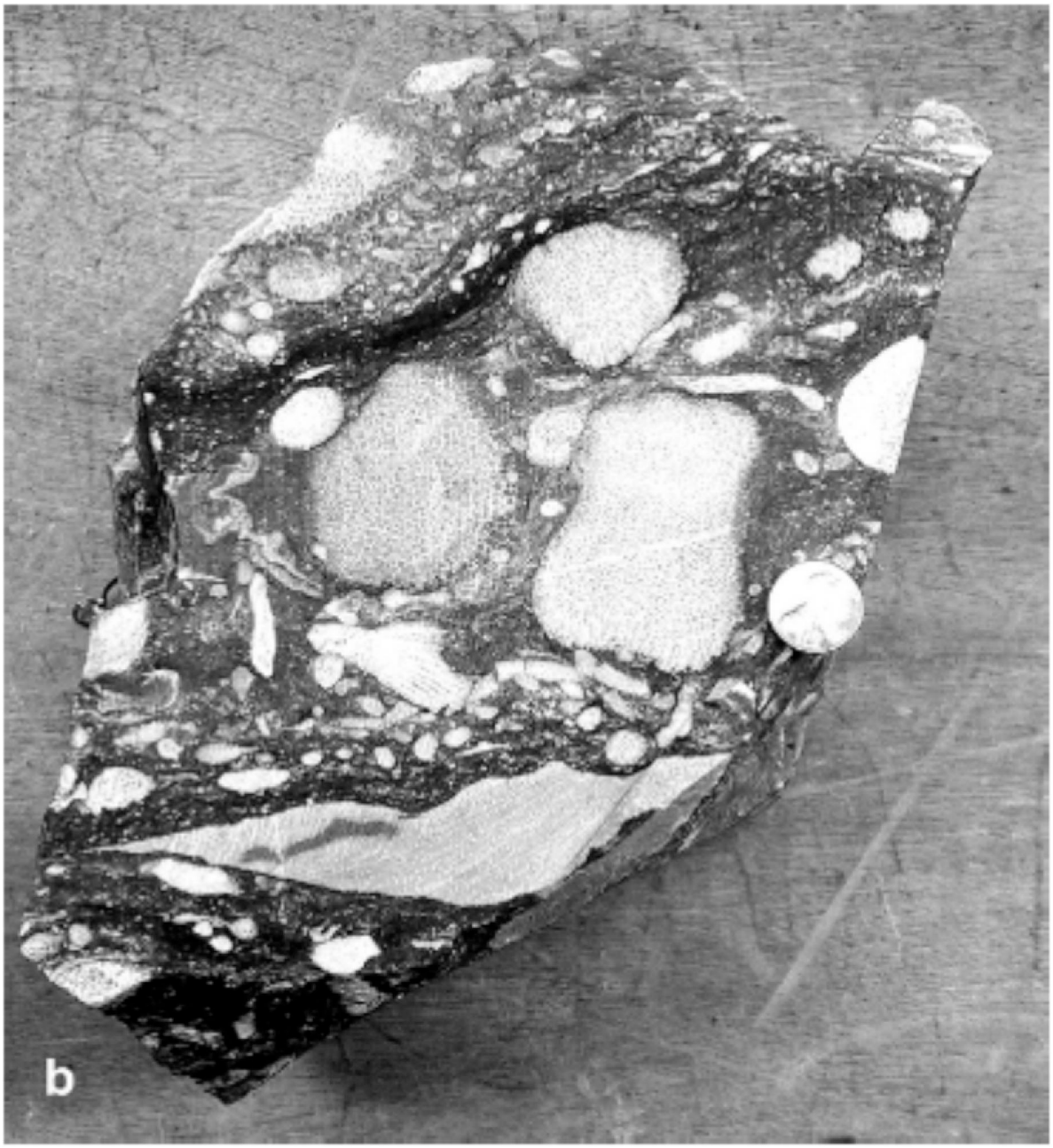

Figure 40 The biostromal facies of the Jeffersonville Limestone is shown on these 20 cm (8 in.) wide slabbed rock samples, which were collected from the Scott Quarry near Jeffersonville, Indiana (Figure 37, number 5). The Jeffersonville Limestone, considered to be equivalent to the Geneva Dolomite, has not been altered by dolomitization and dissolution (Seyler et al., 2003).

Regional Setting of Geneva Dolomite Reservoirs in Illinois

A substantial amount of petroleum production from the Geneva Dolomite comes from the northern half of Marion County, Illinois. Locations of many of these fields, including the most recent discovery near Miletus Field, are shown in Figure 33. In many instances, anticlinal closure combined with drape over underlying pinnacle reefs is the hydrocarbon-trapping mechanism in

the Geneva Dolomite reservoirs, and deep-seated structures likely formed the foundation for the growth of pinnacle reefs during the Silurian (Davis, 1991) because the corals and other reef building organisms thrived in the shallower water found at structurally high locations. Structural noses along major anticlines are potential sites for structural closure and hydrocarbon entrapment in the Geneva Dolomite. The St. James Field, located along the southern nose of the Louden Anticline, is an example of recently discovered production from closure along a structural nose (Figure 33). Portions of these structural noses may also have been potential sites for growth of Silurian pinnacle reefs if the same feature was structurally high during the Silurian. Increasing evidence suggests that many major structural features in the Illinois Basin have a history of episodic movement through Paleozoic time (Davis, 1991; McBride and Kolata, 2000).

A west-east stratigraphic cross section A–A′ (Figure 33) crosses Marion County, Illinois, where several prolific Geneva Dolomite oil reservoirs have been found (Figure 41). This section crosses Sandoval Field, which produces from the highly porous Geneva Dolomite that is draped over a Silurian reef. Eastward along the section, the Salem Field produces from two different horizons in the Middle Devonian. The cross section also shows that the lower Mississippian Chouteau Limestone, a marker horizon in some areas of the Illinois Basin, thickens to the east of the DuQuoin Monocline (Figure 33). The Upper Devonian New Albany Shale and Middle Devonian carbonates also thicken to the east of the Duquoin Monocline, which suggests that the DuQuoin Monocline was a structurally high feature during deposition of these strata and a likely site for accumulation of biohermal carbonates in the Devonian.

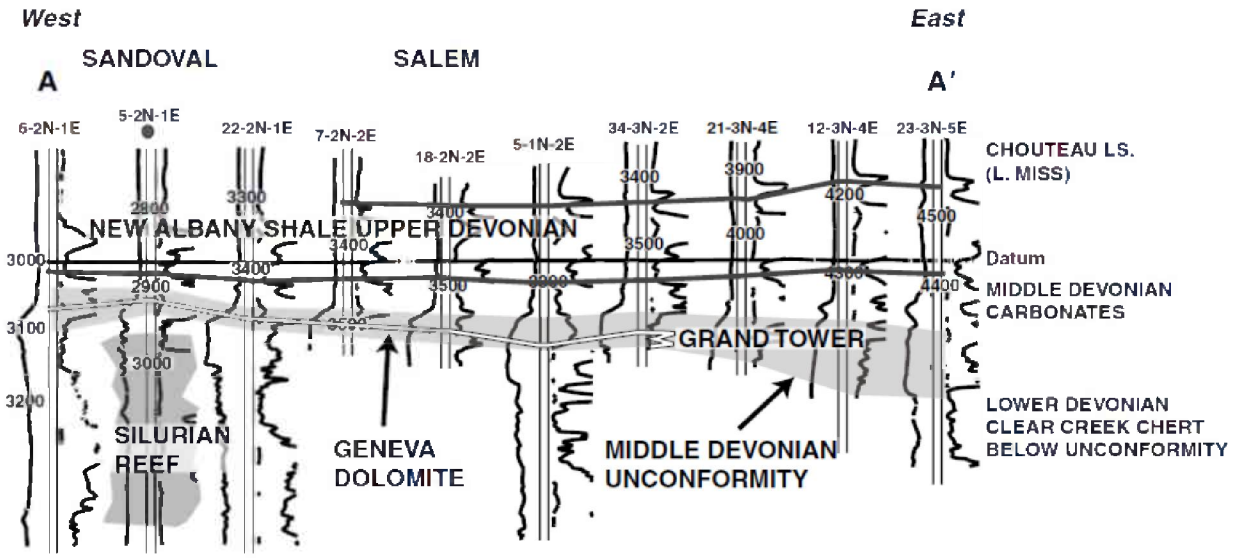

Figure 41 West-east stratigraphic cross section (Figure 33, A–A′) in Marion County. Lower Mississippian Chouteau Limestone thickens eastward of the DuQuoin Monocline (Figure 33). The Upper Devonian New Albany Shale and Middle Devonian carbonates also thicken eastward. Sandoval field produces from porous Geneva Dolomite draped over a Silurian reef (Seyler et al., 2003).

A north-south cross section, B–B′ (Figure 33), from Raccoon Lake through Sandoval, South Patoka, and Patoka Fields, shows the Geneva Dolomite thickening from south to north (Figure 42). The Raccoon Lake Field is located near the southern limit of the Geneva Dolomite. The cross section (Figure 42) also shows an increase in thickness of Middle Devonian carbonates

above the Geneva Dolomite from south to north. This increase may be due to the Lower Devonian Clear Creek Chert unconformity, which underlies the Middle Devonian Geneva Dolomite in the southern half of Marion County, Illinois. Structural cross section C–C′ (Figure 33 and Figure 43) through the Geneva Dolomite reservoir at the St. James Field in southern Fayette County, Illinois, shows a well-developed zone of highly porous Geneva Dolomite immediately underlying the dense, bioclastic grainstone in the Grand Tower Limestone. Core of the Geneva Dolomite reservoir, starting at a depth of 1,040 m (3,411 ft) in the Smail No. 25 well shown in this cross section, is a brown, sucrosic, highly porous, and permeable dolomite with large amounts of moldic porosity caused by dissolution of fossil fragments. This core has a permeability ranging from 8.87×10^{-10} to 4.19×10^{-9} cm^2 (90 to 425 md), with an average of 2.47×10^{-9} (250 md). The porosity ranges from 19 to 24% (average 20%) in a fine- to medium-grained, crystalline dolomite.

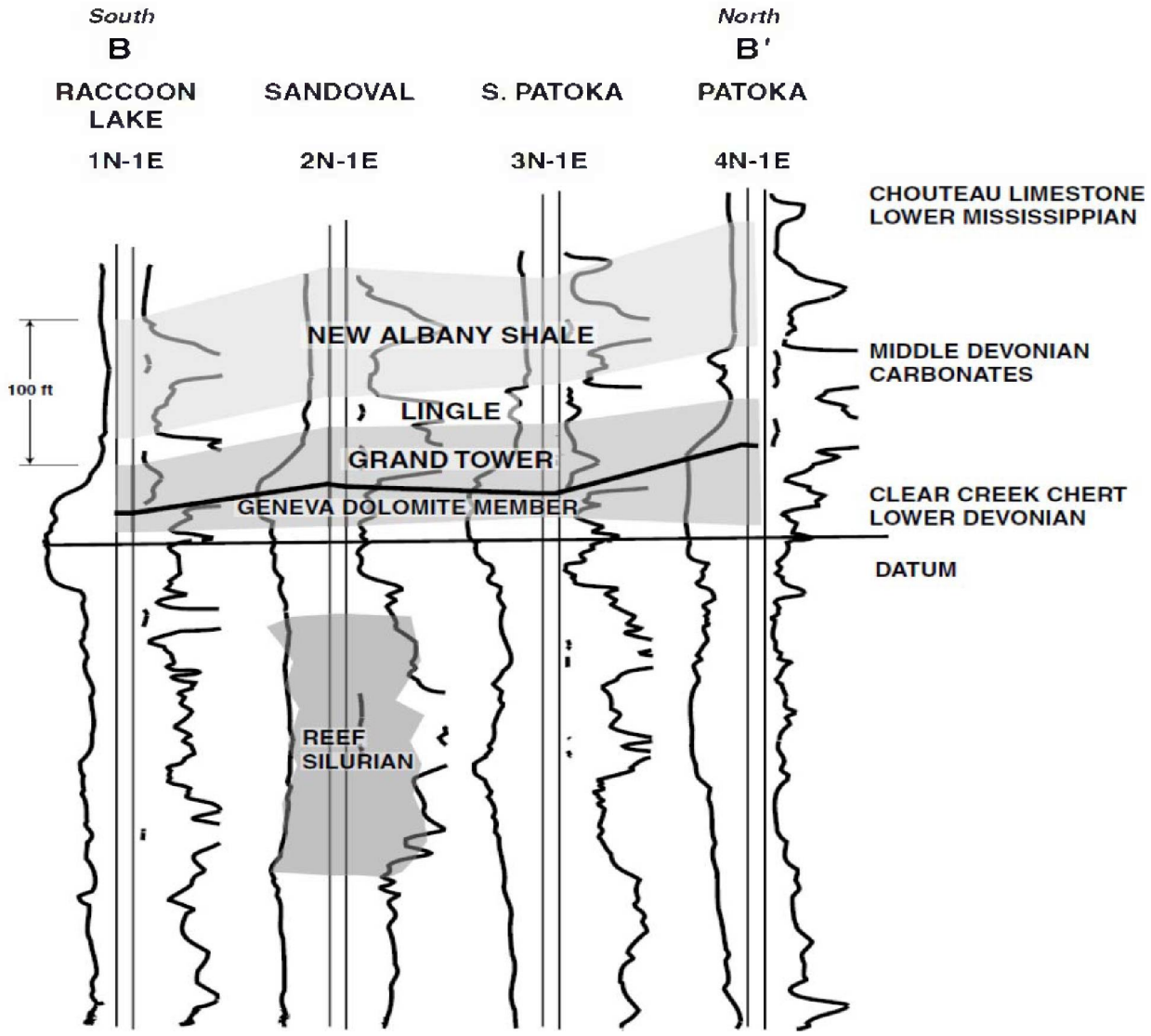

Figure 42 Stratigraphic cross section (Figure 33, B–B′) from the Raccoon Lake Field to the Patoka Field in Marion County. Pinnacle reefs underlie the Raccoon Lake and Sandoval Fields. The Grand Tower Limestone thickens from south to north (Seyler et al., 2003).

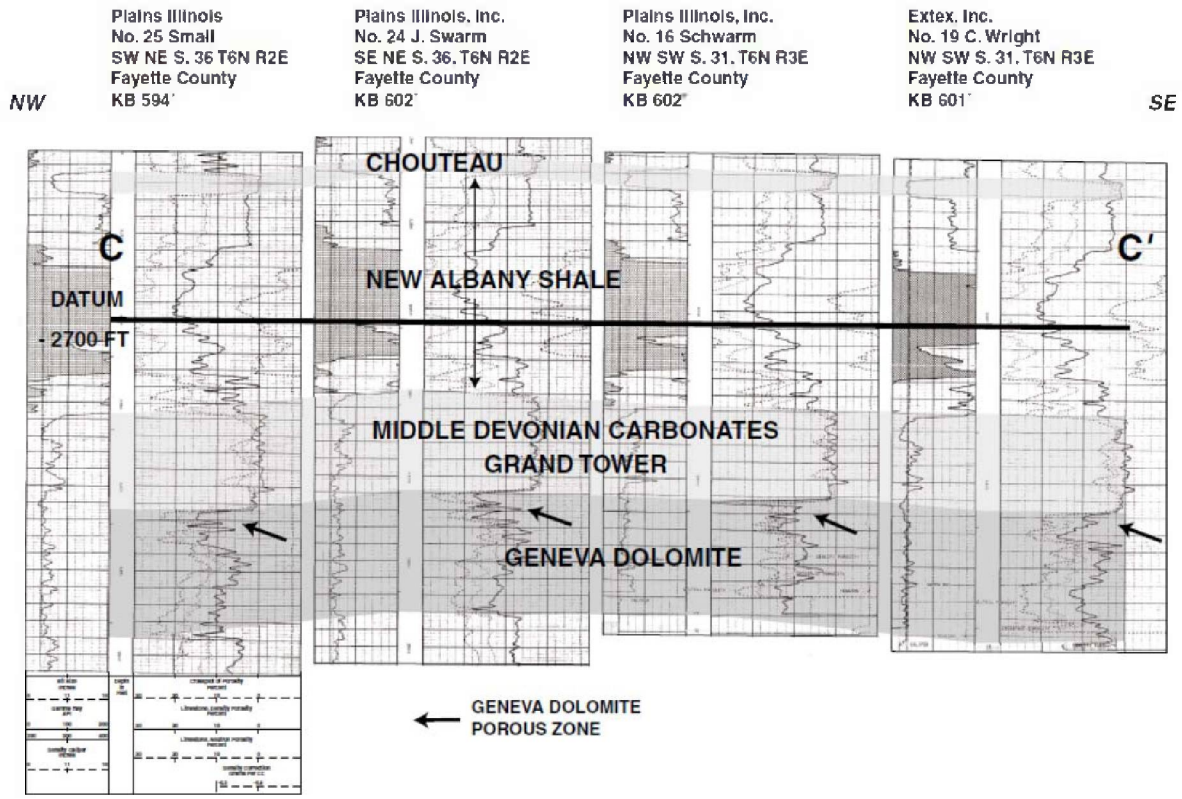

Figure 43 Structural cross section (Figure 33, C–C′) of the Geneva Dolomite reservoir at the St. James Field in southern Fayette County, Illinois. This field is 21 km (13 mi) northwest of Miletus Field. Included in the cross section is the Plains, Illinois, Smail No. 25 (well No. 1), which was cored through the Geneva reservoir. This section shows a well-developed zone of highly porous dolomite (at arrows) immediately underlying dense, bioclastic grainstone in the Grand Tower Limestone. This upper contact of the Geneva Dolomite with the Grand Tower Limestone is abrupt across the field (Seyler et al., 2003).

Geneva Dolomite at Miletus Oil Field

A structure map on the top of the Geneva Dolomite porosity zone at Miletus Oil Field is shown in Figure 44. The field lies on an anticlinal feature with 18 m (60 ft) of closure on the top of the Geneva. The structure has a steep east flank and becomes more subtle in the shallower horizons, indicating recurrent movement of the structure through time. Details of the closure on the Geneva horizon show an arcuate geometry that possibly reflects an underlying atoll-like Silurian reef. Geneva production has been established in Section 27, 28, and 33, T4N, R4E. The most productive wells correlate with the maximum closures on the top of the Geneva (Figure 44).

An isopach map of the Middle Devonian carbonates overlying the Geneva Dolomite at Miletus Oil Field (Figure 45) shows that the pronounced thinning of these carbonates coincides with the crest of the structure shown on the structure map of the Geneva Dolomite (Figure 44). The thinning of the section over the structure could be the result of compensating deposition over a paleohigh that was induced tectonically, by an underlying Silurian reef, or by a combination of the two. The stratigraphic section over Silurian pinnacle reefs is commonly thinner than the section adjacent to the reefs in the Illinois Basin.

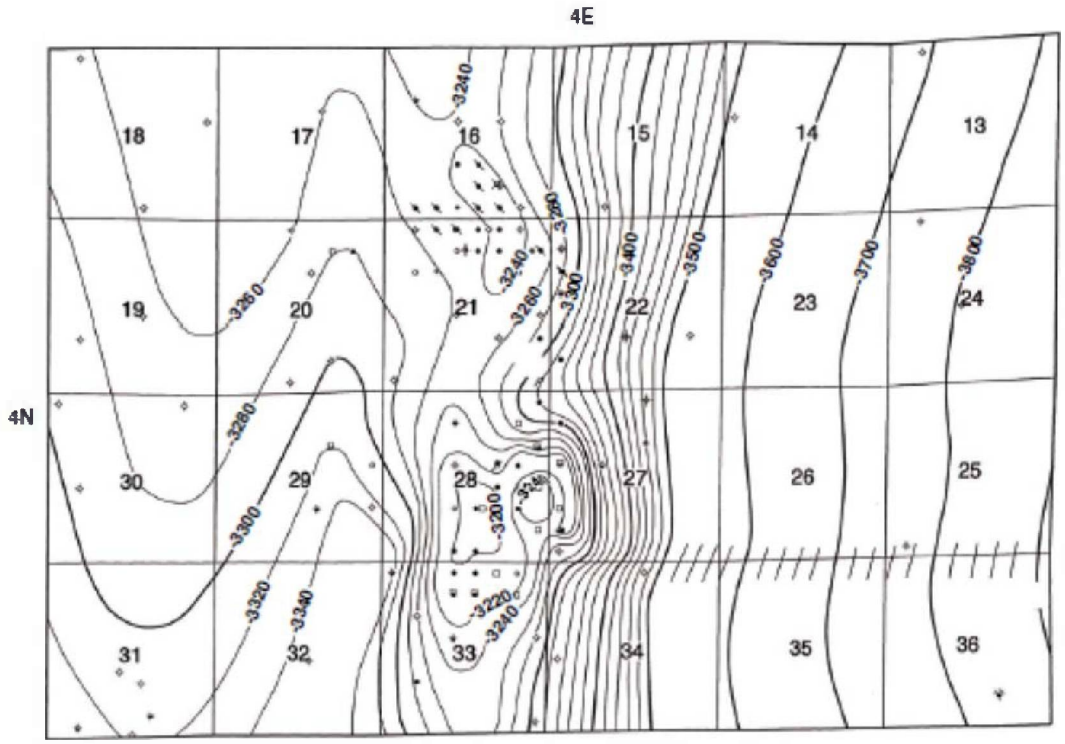

Figure 44 Structure map on the top of the Geneva Dolomite porosity at the Miletus Field. The field lies on a pronounced nose with closure of approximately 18 m (60 ft). The Geneva Dolomite is productive in the southern portion of the field, specifically in sections 27, 28 and 33 (Seyler et al., 2003).

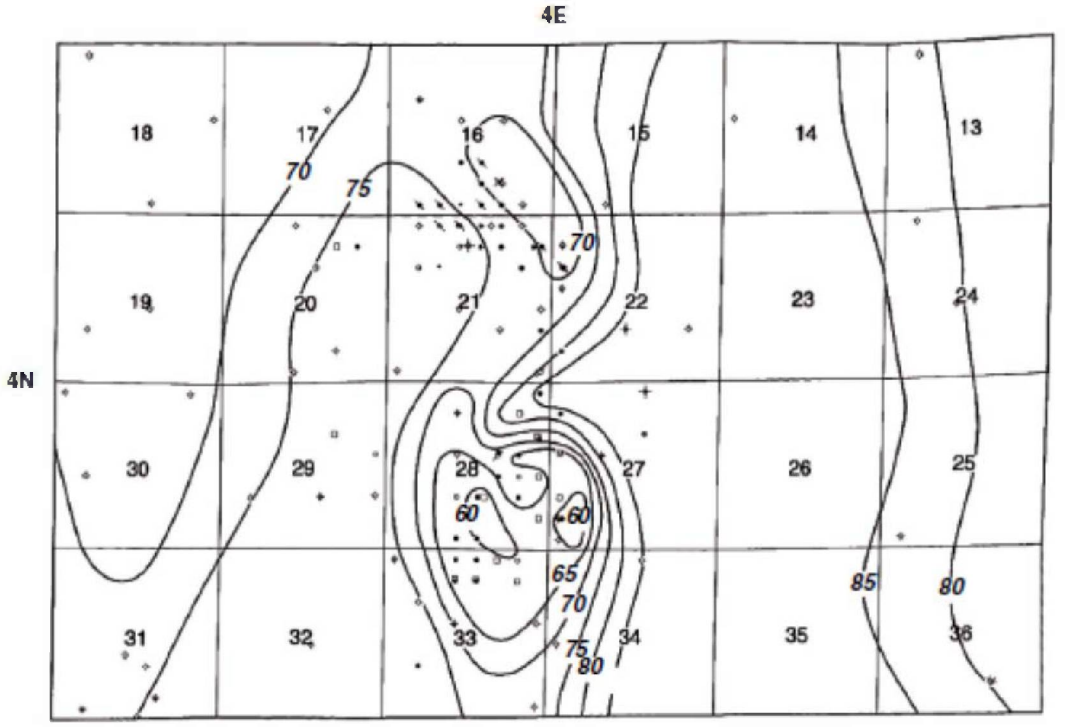

Figure 45 Thickness map of the Middle Devonian carbonates overlying the Geneva Dolomite at the Miletus Field. A pronounced thinning of these carbonates coincides with the crest of the structural nose shown on the structure map in Figure 44 (Seyler et al., 2003).

The density-neutron log of the Hogan No. 2 well in Section 28 is shown in Figure 46. The Middle Devonian carbonates start at a depth of 1,131 m (3,712 ft) and are 20 m (65 ft) thick at this well. The top of the Geneva Dolomite starts at 1,151 m (3,777 ft). For many wells, crossplot density-neutron porosity of the Geneva interval averages approximately 15%; porosity spikes exceed 20%.

Dolomitization

The dolomite of the Geneva and overlying units formed from replacement of limestone sediments, as indicated by the common presence of dolomitized bioclastic allochems in the Geneva and of dolomitized algal structures and scattered dolomitized fossil allochems in the overlying units. The Geneva Dolomite occurs at the base of the northern dolomite facies of the Grand Tower and Jeffersonville limestones in central Illinois and west-central Indiana. The northern dolomite facies of the Grand Tower and Jeffersonville also includes a microcrystalline dolomite facies that overlies the Geneva. This microcrystalline dolomite was named the Vernon Fork Member in Indiana (Droste and Shaver, 1975). The close resemblance between the distribution of the Geneva Dolomite and that of the Vernon Fork dolomite of the Jeffersonville Limestone in Indiana and its equivalent in Illinois suggests a genetic relationship (Perkins, 1963). Therefore, any mechanism that dolomitized the Geneva sediment must also explain dolomitization of the overlying unit.

Droste and Shaver (1975) suggest that dolomitization occurred in a supratidal sabkha (evaporitic) environment within a highly saline, magnesium-rich pore water system. Although tidal flat conditions prevailed during deposition of the Vernon Fork dolomite, the sabkha dolomitization model as envisioned by Droste and Shaver (1975) cannot adequately explain the formation of over 45.7 m (150 ft) of combined dolomite of the Geneva and the overlying unit. In sabkha environments, the magnesium-calcium ratio of the pore fluid increases through evaporation and precipitation of calcium carbonates and calcium sulfates. The amount of dolomite formed in such environments is, however, very small and restricted only to the upper 0.9 to 1.5 m (3 to 5 ft) of sediments. In addition, any dolomite formed from a highly saline brine, generated within the sabkha environments, appears to be a direct precipitate (Machel and Mountjoy, 1986; Hardie, 1987) rather than a replacement of pre-existing sediments, a conclusion supported by scanning electron microscopy (Lasemi et al., 1989).

Mixing zone dolomitization, although extensively suggested as the mechanism for dolomitization of many carbonates in the 1970s and 1980s, has now been largely discounted (Machel and Mountjoy, 1986; Hardie, 1987). The very slow rate of dolomite precipitation (because of the ordered nature of dolomite crystals) relative to calcite dissolution would mean that dolomite could not precipitate in significant quantities in a mixing zone (Machel and Mountjoy, 1986; Hardie, 1987). As in the sabkha environment, the amounts of dolomite formed in mixing zones are small and texturally different from the ancient massive, replacement dolostones. At low temperatures, replacement dolomite requires long reaction times; as a result, mixing-zone dolomitization may occur only below major unconformities. However, many shallowing-upward cycles and even major unconformities with exposure surfaces lack dolomite (Machel and Mountjoy, 1986).

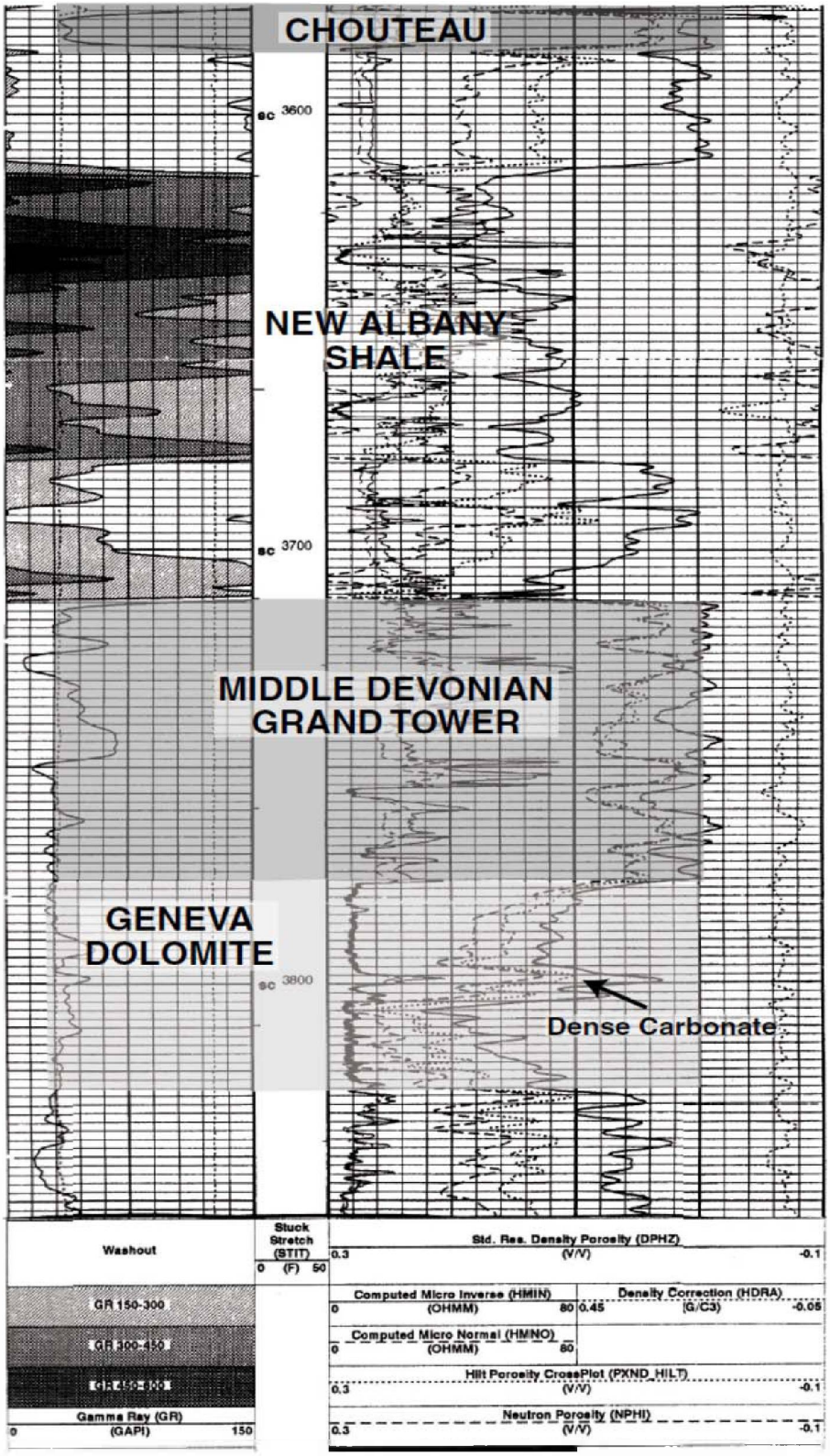

Figure 46 Geophysical log of the Ceja Corporation Hogan No. 2 well in the Miletus Field in Section 28, T4N, R4E. This well has produced over 47,700 m^3 (300,000 bbl) of oil since its discovery in 1996 through June of 2000. Note the well-developed porosity in the Geneva Dolomite (16–19%; Seyler et al., 2003).

Another dolomitization model commonly applied to dolomite sequences associated with evaporates is the seepage-reflux model (Adams and Rhodes, 1960). Here, extensive evaporation results in hypersaline brine with a high magnesium-calcium ratio through precipitation of gypsum. The dense and hot, highly alkaline and magnesium-rich brine is capable of percolating through porous and permeable underlying carbonate sediments, which results in extensive dolomitization. Unfortunately for this mechanism, there is no evaporite deposit associated with the Geneva Dolomite and the overlying Vernon Fork Member or its equivalent in Illinois. A few thin brecciated laminae and minor calcite pseudomorphs after gypsum in the dolomite above the Geneva (Perkins, 1963) suggest the minor deposition of evaporites, but not enough to explain the formation of thick, widespread dolomite. Furthermore, as in the sabkha model, a highly saturated, hypersaline brine created during seepage-reflux would most likely have led to precipitation of dolomite rather than the replacement of pre-existing carbonate sediments.

A variation of the reflux model as suggested by Simms (1984) is now favored by many as an effective mechanism for dolomitization in modern and ancient carbonate platforms that experienced hydrographic restriction. In this model, during a long residence time, the seawater trapped on the platform top fluids becomes progressively concentrated by evaporation (even in humid climates) to greater than normal salinities. The slight difference in the density of the water on the shallow platform and that of the pore water generates a long-term, vertical fluid flow system that is capable of causing large-scale dolomitization of platform sediments. Hypersaline conditions are not required, and the lack of evaporates does not preclude dolomitization through reflux. This flow system is potentially large scale, affecting rocks over a region of thousands of square miles to depths of 305 m (1,000 ft) or more (Simms, 1984), assuming no aquicludes (such as evaporites or clay beds) prevent downward flow. If long-lived, such a flow system can produce massive replacement dolomite that cuts across formation boundaries (Hardie, 1987).

Hydrographic restriction occurred in shallow lagoonal and tidal flat settings that developed over the Vandalia Arch. According to Workman and Gillette (1956), the Vandalia Arch was a depositional high during deposition of the Grand Tower and Jeffersonville limestones that trended northeast-southwest from the Clinton County area in southwestern Illinois to the Indiana state line in Edgar and Clark Counties. Distribution of the Geneva and the overlying units of the Grand Tower and Jeffersonville indicate that the arch extended into west-central and central Indiana. The New Albany Shale thins over the position of this arch. Because of a lack of evidence indicating tectonic influence, Cluff et al. (1981) rejected the term "Vandalia Arch" and informally referred to the area of thin New Albany as the "central thin" (Nelson, 1995). However, the dolomitization of the Grand Tower Formation suggests the use of the term Vandalia Arch. Evaporation of seawater in restricted lagoonal and tidal flat settings on the arch could have formed denser fluids that percolated through the underlying carbonate sediment. The reflux began toward the end of the Geneva deposition and continued through deposition of the overlying Vernon Fork Member of the Jeffersonville in Indiana and its equivalent unnamed unit of the Grand Tower in Illinois. The lack of evaporites indicates that the environment was not hypersaline. Deposition of over 30.5 m (100 ft) of carbonates with features that indicate deposition under restricted marine conditions in the Grand Tower and Jeffersonville limestones over the Geneva Dolomite suggests that such a flow system could have persisted for a relatively long time.

Depositional Environment

The Geneva Dolomite Member is recognized as a highly dolomitized facies of the Grand Tower Limestone in Illinois and the Jeffersonville Limestone in Indiana. A fossiliferous, open-marine carbonate shelf environment, partly biostromal to biohermal facies containing abundant corals and stromatoporids in the Grand Tower and the Jeffersonville, correlates and is comparable with the brown, vuggy, porous, and permeable zone that characterizes the best reservoir interval of the Geneva Dolomite. The shape, size, and distribution of fossils in the Grand Tower and Jeffersonville match the shape, size, and distribution of the moldic or vuggy porosity of the Geneva Dolomite Member, although dolomitization and dissolution have partially to totally obscured the original fossil content in the Geneva.

Strandplain: Upper Mt. Simon Sandstone at Manlove Gas Storage Field

Manlove Gas Storage Field Background

In northern Illinois, the Cambrian Mt. Simon Sandstone (Figure 47) is a permeable and porous formation that is used for natural gas storage by utilities in Illinois. Manlove Gas Storage Field is defined by a closed anticline in the Cambrian Mt. Simon Sandstone, a quartz sandstone aquifer about 1,190 m (3,900 ft) underground with a sealing caprock formed by the overlying Cambrian Eau Claire Formation. The field, located in Champaign County, Illinois (Figure 48) and about 209 km (130 mi) south of Chicago, began operation in 1966. It has a storage capacity of 4.33 billion m^3 (153 Bcf) and is operated by Integrys Corporation. Manlove Field is called an "aquifer gas storage reservoir" because the Mt. Simon Sandstone was generally water-bearing before injection of natural gas that was brought to the site by pipeline. Once injected, part of the gas volume, called "working gas," is withdrawn and delivered to market to meet peak use requirements. Gas remaining in the reservoir provides pressure and is called "cushion gas" or "base gas." The information in this section is largely taken from or based on Morse and Leetaru (2005).

At Manlove, digital log and core analysis data from approximately 330 wells were acquired directly from the operating company; 175 of these wells reached the Mt. Simon Sandstone. The major formation boundaries and internal correlation markers were picked primarily using the Vshale log, which is based on the gamma ray trace. Porosity was calculated conventionally from neutron and density logs and calibrated against core data. Wells with only gamma ray neutron logs that had gas-affected values were not used in this study. Two cores that passed through the entire gas storage interval at Manlove Field were described in detail and the sedimentary environments interpreted. Samples from the different facies in the cores were thin sectioned and examined with a SEM as well as with standard transmitted polarized light petrography. The thin sections from the cores were point-counted at 300 points per slide to determine mineralogical variations in the Mt. Simon Sandstone.

SYSTEM	GROUP	FORMATION
Ordovician	Maquoketa	Brainard
		Ft. Atkinson
		Scales
	Galena	Kimmswick
		Decorah
	Platteville	
	Ancell	Joachim
		St. Peter
	Praire du Chien	Shakoppee
		New Richmond
		Oneota
		Gunter
Cambrian	Knox	Eminence
		Potosi
		Franconia
		Ironton-Galesville
		Eau Claire
		Mt. Simon
Precambrian		

Figure 47 Stratigraphic column of Ordovician through Precambrian rocks in Illinois.

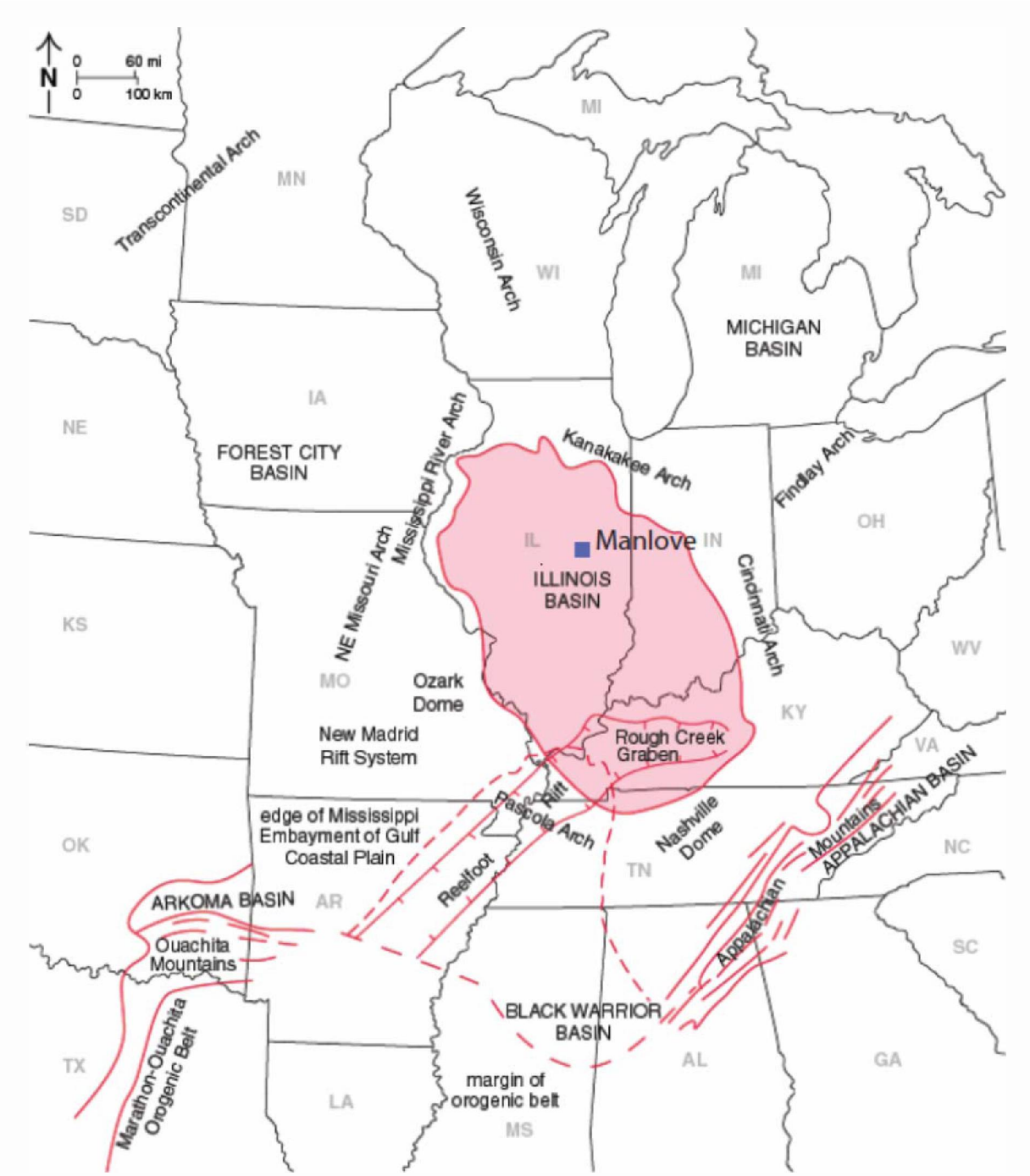

Figure 48 Regional map showing the location of Illinois Basin and important regional tectonic features. The Manlove gas storage project and is also labeled (Morse and Leetaru, 2005).

Structure

In order to define the structure of the field with detail, shallower formation tops, such as the Galena Group (Figure 47), were mapped in addition to those of the Mt. Simon Sandstone. The field had numerous shallow wells that had been used to define the structure of the reservoir. Log tops from all the wells were compiled, and structure maps for the top of the Galena Group (Ordovician) and the top of the Mt. Simon Sandstone (Figure 49) were prepared with the structure of the deeper maps conforming to the details of the shallower structure. This structure map of the top of the Mt. Simon and a three-dimensional (3-D) diagram of the area (Figure 50) illustrate the north-south oriented, asymmetrical, doubly plunging anticline. Gas is stored to an elevation of about –994 m (–3,260 ft), filling a vertical closure of approximately 45 m (150 ft). At this elevation, the area under closure is approximately 73 km^2 (28 mi^2; Buschbach and Bond, 1974).

The field has a steep west flank and a gentle east flank (Figure 50). The spill point lies in the northeast part of the field. The Mt. Simon Sandstone is about 1,220 m (4,000 ft) deep in this field and has an average porosity of 12% and an average permeability of 9.86×10^{-10} cm^2 (100 md).

Stratigraphy

The Mt. Simon Sandstone consists of stacked clean sandstone units capped with thin interbeds of fine-grained sandstone, siltstone, and shale. These interbeds produce an indentation in the gamma ray log curve and generally cannot be correlated across the field or even in an adjacent well drilled 201 m (660 ft) away. Only one marker unit, the L120, could be traced across the field (Figure 51 and Figure 52).

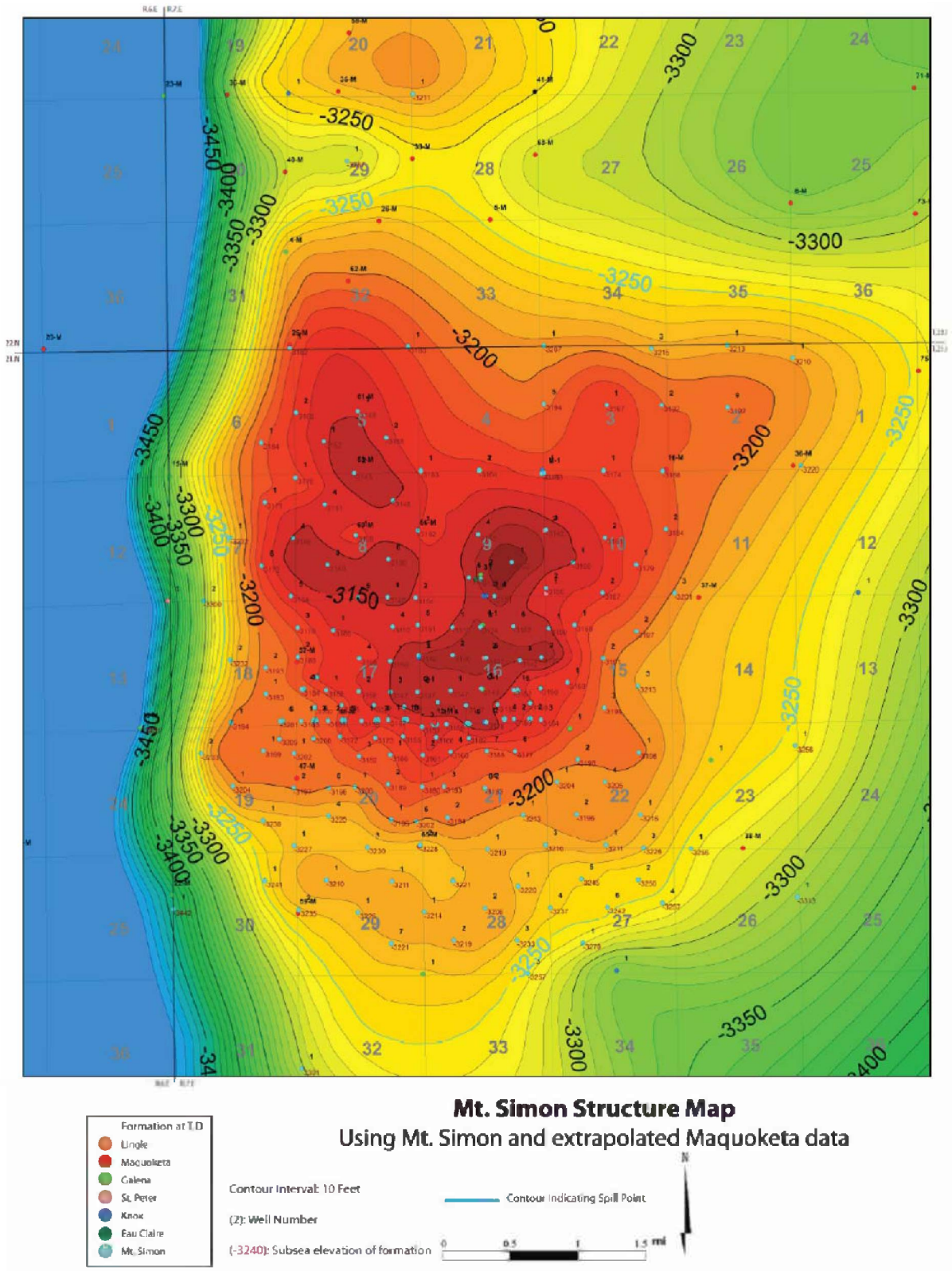

Figure 49 Structure map of the Mt. Simon Sandstone at Manlove Field. The locations of Mt. Simon Sandstone wells are indicated by number. The structure conforms to the shape developed from the Galena level.

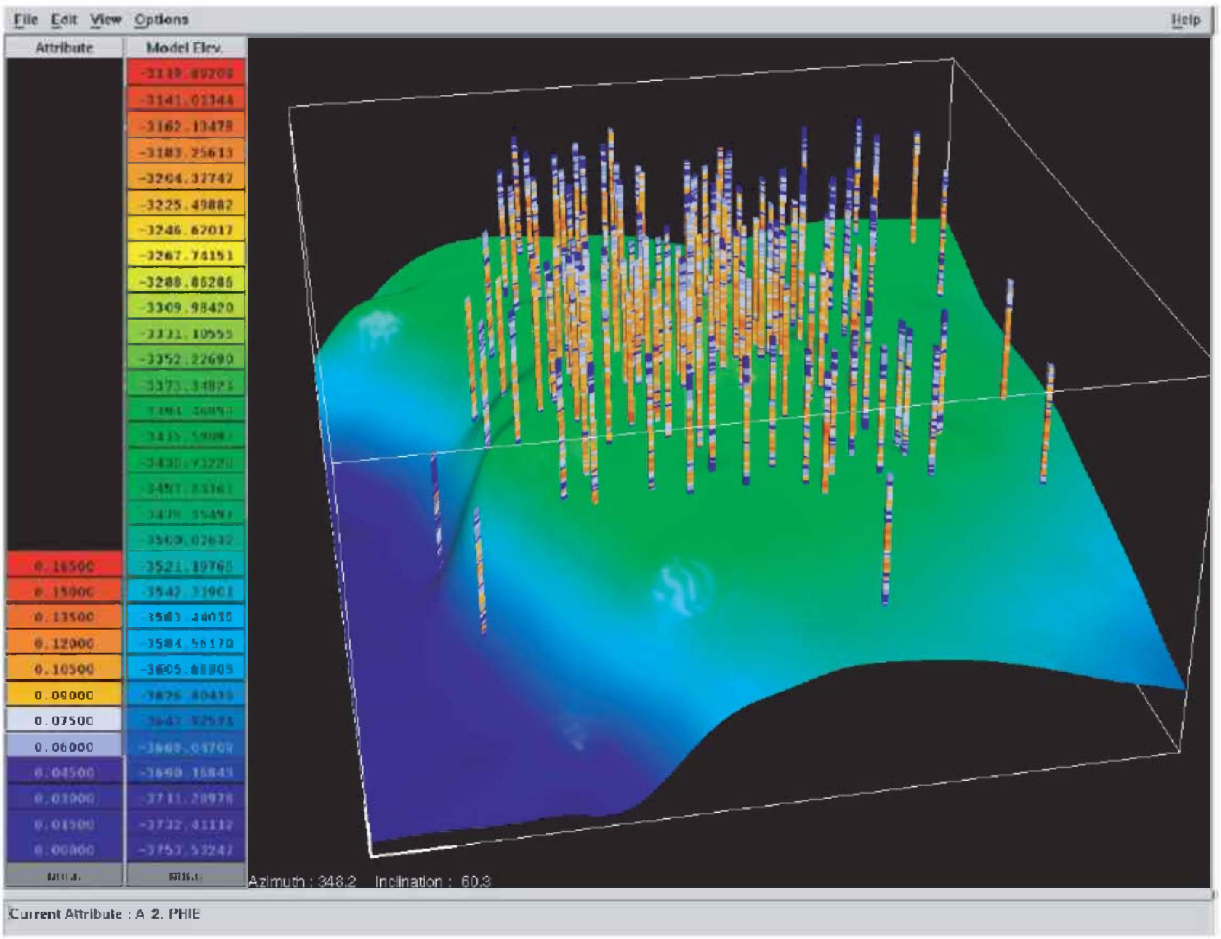

Figure 50 3-D view of the Mt. Simon well control at Manlove Field. There were 121 wells used to construct the 3-D porosity model. The surface shown is the L120 marker.

Petrography

The Mt. Simon Sandstone contains a wide range of grain sizes and minerals. The reservoir sandstones examined in the cores consist of clean, well-sorted, and medium to very coarse grains of quartz cemented by quartz overgrowths. Pores are large and smoothly lined by this cement. Fine to very fine grained sandstones and less well-sorted sandstones contain significantly more relatively unaltered K-feldspar grains than the coarser sandstones. K-feldspar in the Mt. Simon Sandstone occurs only as fine to very fine grains. These grains have angular, euhedral outlines indicative of diagenetic feldspar overgrowths. No plagioclase feldspar was seen.

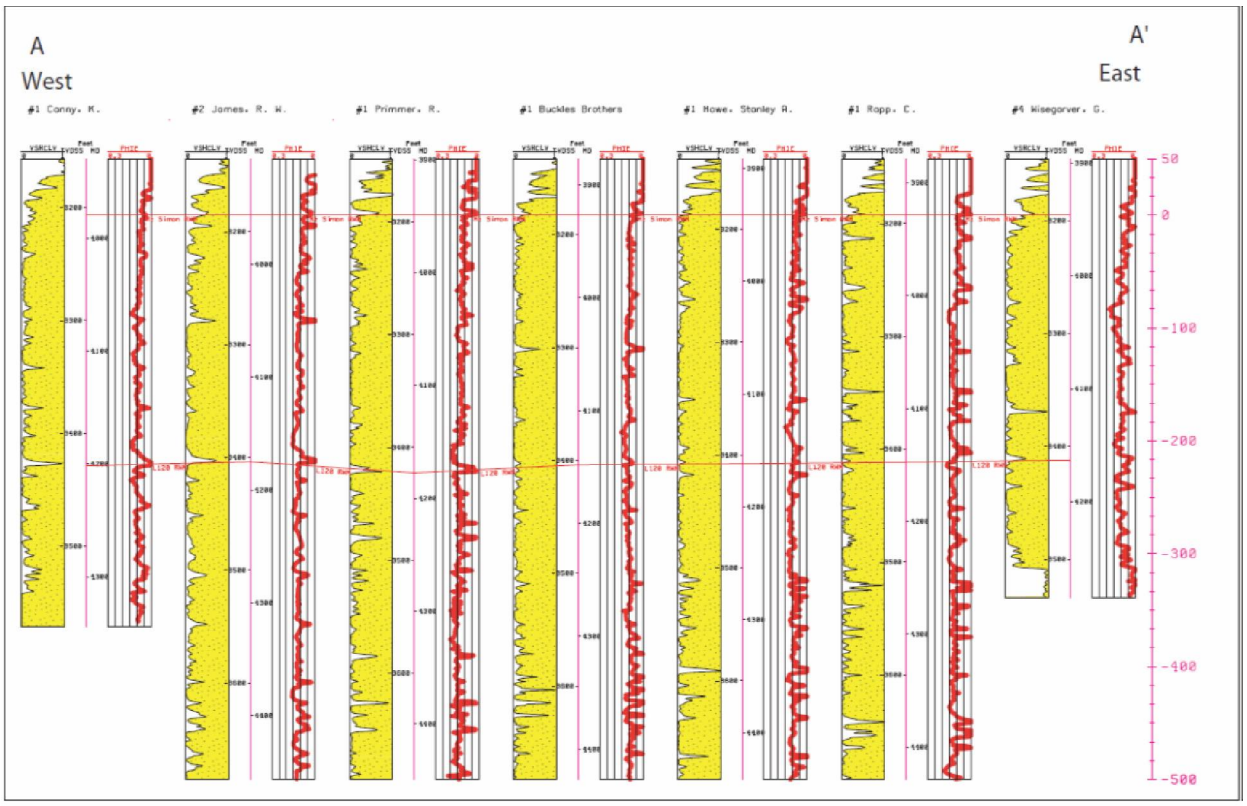

Figure 51 East-west stratigraphic log cross section of Manlove Field. Vshale and calculated porosity for each well are shown with the lateral correlation of the top of the Mt. Simon and the L120 marker shale.

Depositional Environment

The depositional environment for the upper part of the Mt. Simon Sandstone, interpreted from the cores at Manlove Field, was probably a coastal setting composed of barrier bars, fine-grained tidal flat sediments, and cross-bedded, meandering tidal channel and tidal bar deposits (Figure 53). The presence of Skolithos and Planolites burrows in these deposits indicates marine influence. The cross-bedded sandstone facies is interpreted as a shallow subtidal deposit formed by meandering tidal channels and subaqueous tidal delta bars. Clay-drape laminae on some of the cross-bedded sandstone beds are characteristic of a tidal regime in which clay settles out of suspension during slack water periods of a tidal cycle or during neap tides of the lunar cycle. Clay intraclast lags indicate reworking of previously deposited thin shale beds and their transportation for short distances in laterally migrating channels. The bioturbated sandstone facies with Skolithos burrows was formed in high-energy settings, such as tidal-delta bars or tidal channels, with coarse-grained substrates that are constantly being reworked by tidal currents and suspension-feeding infauna.

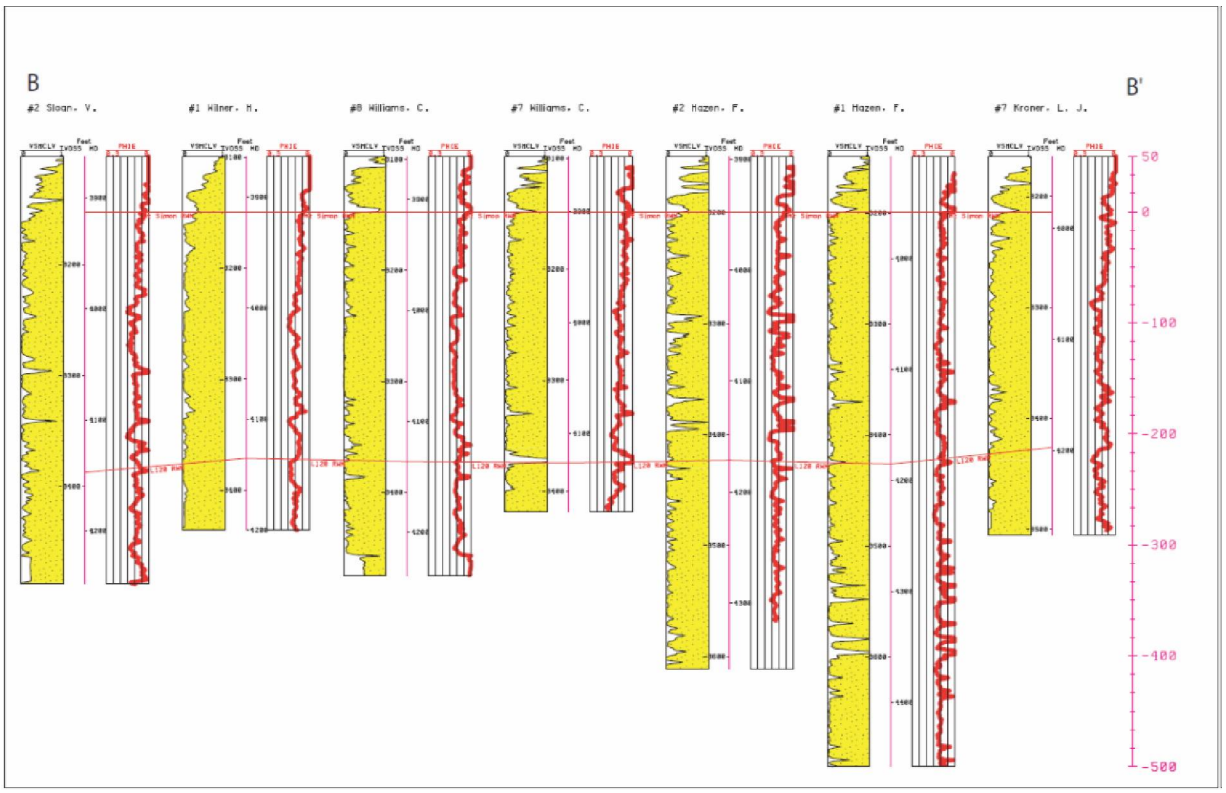

Figure 52 North-south stratigraphic log cross section of Manlove Field. Vshale and calculated porosity for each well are shown with the lateral correlation of the top of the Mt. Simon and the L120 marker shale.

Long-shore currents from bottom to top in this diagram (Figure 53) bring in sediment from an alluvial system that is outside the model area. Tidal channels cut through the lagoonal area and have sinuous paths. Thin intertidal sand flats and mud flats rim the lagoon. Progradation of the barrier lagoon-flat system creates laterally continuous barrier sands, discontinuous channel sands, and dissected intertidal sand and mud flats. Additionally, laterally continuous bar-shaped sandstones cut by discontinuous channel sands have been mapped in the Mt. Simon Sandstone at Manlove Field, and core photos show the presence of laminated shale facies, including those that alternate with beds of very fine sandstone (Figure 54 and Figure 55). A reasonable interpretation of the data suggests that the upper Mt. Simon Sandstone is part of a prograding, and in some places retrograding, strandplain/barrier island system.

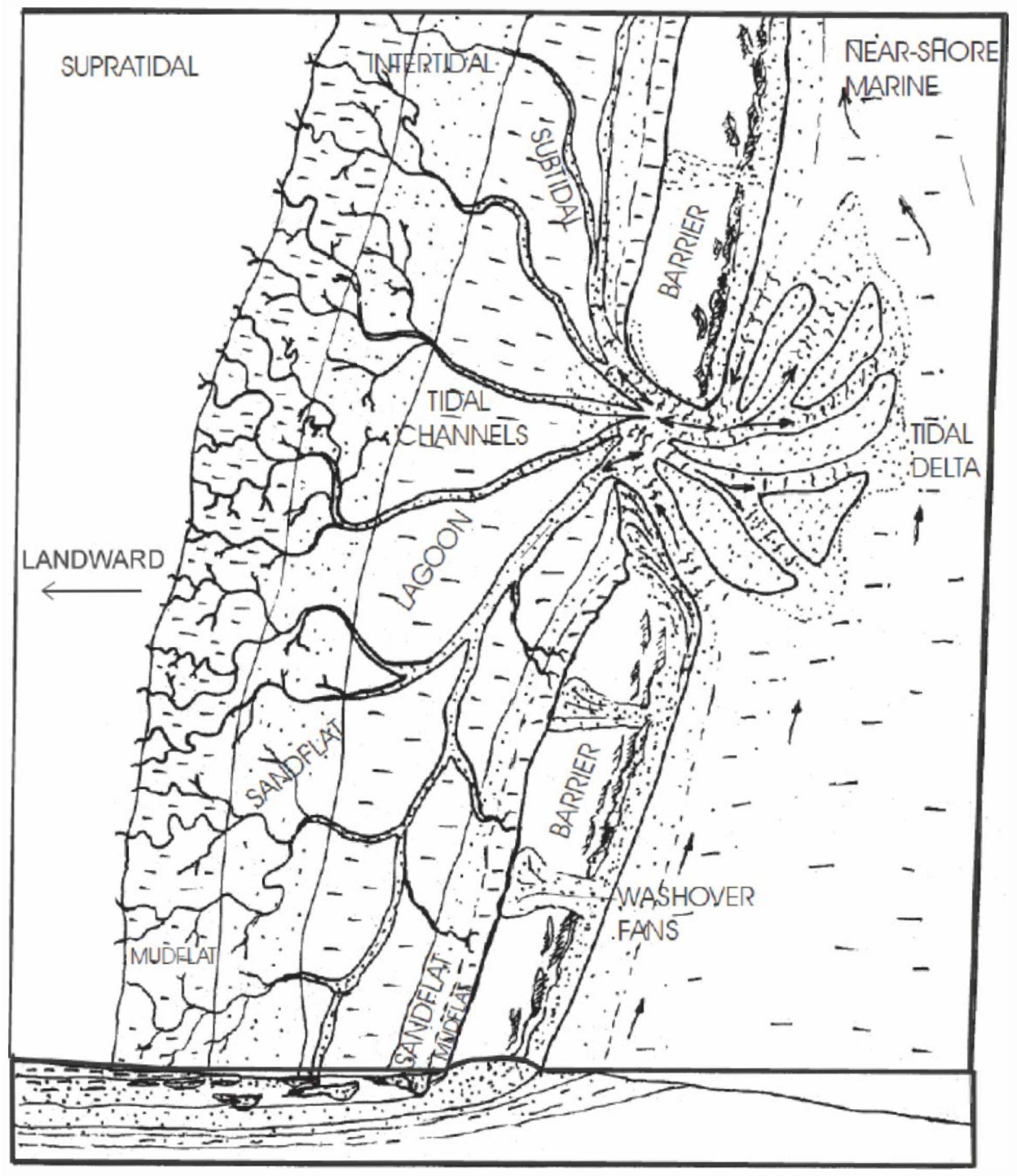

Figure 53 Depositional model block diagram for Manlove Field (after Morse and Leetaru, 2005). A general barrier-lagoon-tidal flat model is shown here. Exiting from the major tidal channel system separating the barriers is an ebb-tidal delta deposit. Long-shore currents from bottom to top in this diagram bring in sediment from an alluvial system that is outside the model area. Tidal channels cut through the lagoonal area and have sinuous paths. Thin intertidal sand flats and mud flats rim the lagoon. Progradation of the barrier-lagoon flat system creates laterally continuous barrier sands, discontinuous channel sands, and dissected intertidal sand and mud flats.

A.
Hazen #5, 4105'

C.

J Williams #4, 4030'

B.

J Williams #4, 4197'

Figure 54 Core photograph of cross-bedded sandstone facies. This medium to coarse-grained, cross-bedded sandstone is the primary reservoir facies. Cross-beds may be tabular- (A) or trough- (C) shaped. (B) The bases of the cross-beds may have some quartz granules. The thickness of the tabular cross-bed sets range from 30 to 100 cm (1 to 3 ft). Trough cross-bed sets typically are only 5 to 15 cm thick (2 ½ to 6 in.). Core from the Hazen #5 and J. Williams #4 wells.

Figure 55 Core photograph of bioturbated sandstone facies. Vertical *Skolithos* burrows in medium to coarse sandstone may obliterate most of the original stratification. These burrows are formed from filter feeders that live a high energy substrate and intercept food from the moving water that lies above. Core from the Hazen #5 and J. Williams #4 wells.

Reef: Moccasin Springs Formation at Tilden Oil Field

Tilden Oil Field Production History and Development

The Tilden Field produces from prolific limestone or dolomitized limestone reservoirs that occur in the upper part of the Silurian succession. It is located in the southwest part of a carbonate reef bank, just north of the deep area of the Illinois Basin (Figure 56).

Tilden Oil Field was discovered in 1951 when Jet Oil Co. drilled No. 1 C. Easdale well in the NW1/4 of section 16, T4S, R5W, Randolph County, Illinois. However, completion data for this well was not released until October 1952. The field was found by subsurface mapping; the discovery well was drilled on a coal structural high to the Silurian, the top of which was reached at 653.2 m (2,143 ft). The well was drilled to a total depth of 679.1 m (2,228 ft); a porous limestone interval was encountered in the Moccasin Springs formation at 673.6–676.0 m (2,210–2,218 ft), and was completed with an initial production of 10 m^3/d of oil (65 bopd) after an acid treatment. During early stages of development, the upper part of the formation was drilled, and as much as 39.6 m (130 ft) of pay was encountered. In most wells, the pay was found in the top 18 m (60 ft) of the formation. The formation was generally cored and wells were completed open-hole with 757–3,785 L (200–1,000 gal) of mud acid treatment. Initial production of over 95.4 m^3/d of oil (600 bopd) was reported for some wells.

Following the early field development, the deepening of some wells led to production increases in the late 50s and 60s. Oil production peaked again in the 80s through 90s when the deepening of additional wells and the drilling of new wells (Figure 57) resulted in the discovery of new productive and compartmentalized reservoirs in the middle part of the Moccasin Springs Formation. The entire section was cased and perforated at producing intervals. The perforated intervals were treated with acid and hydraulic fracturing was conducted in low porosity zones. Average treatment consisted of 227,125 L (60,000 gal) of gelled water/nitrogen foam and 27–36,288 kg (60–80,000 lbs) of 20/40 or 12/20 mesh sand with initial production of 3.2–6.4 m^3/d (20–40 bopd; Baker and Carlisle, 1992).

A total of 58 wells have been completed, 40 wells are currently producing, and the field has produced over 0.87 million m^3 (5.5 million bbl) of oil. The reservoirs are compartmentalized with varying lateral and vertical extent. Both primary and secondary porosity have played an important role; cave travertine, banded calcite, and caliche zones in a number of cores suggests multiple episodes of sea level fall and formation of secondary dissolution porosity (Baker and Carlisle, 1992).

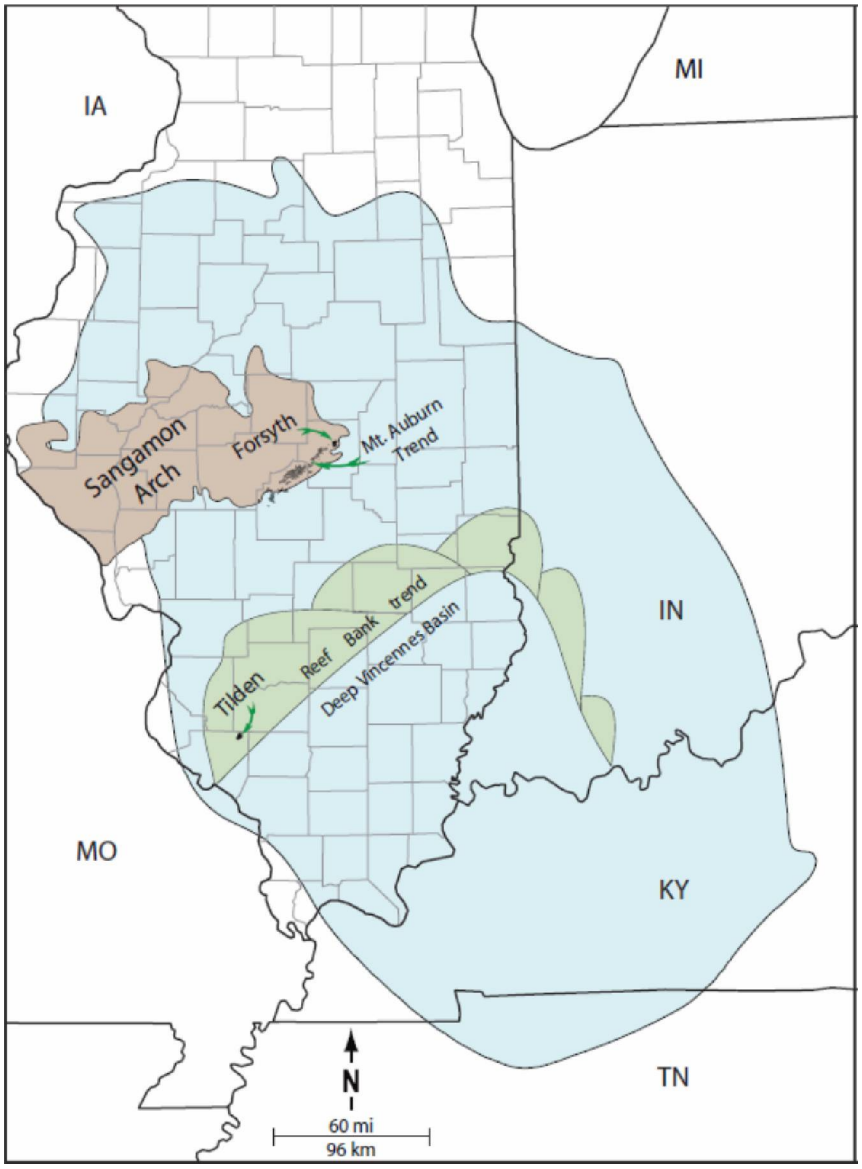

Figure 56 Location of the Illinois Basin (in light blue; Buschbach and Kolata, 1991) and the Sangamon Arch in west central Illinois (in brown; Whiting and Stevenson, 1965) in the northwest area of the Illinois Basin. The Tilden Field is located in the southwest of the known pinnacle reefs bank trend, which marked a slope break in southern Illinois and southwestern Indiana (Droste and Shaver, 1980, 1987), separating the gently sloping ramp from the deep Vincennes Basin in the southern part of the Illinois Basin during Silurian time (modified from Lasemi et al., 2010).

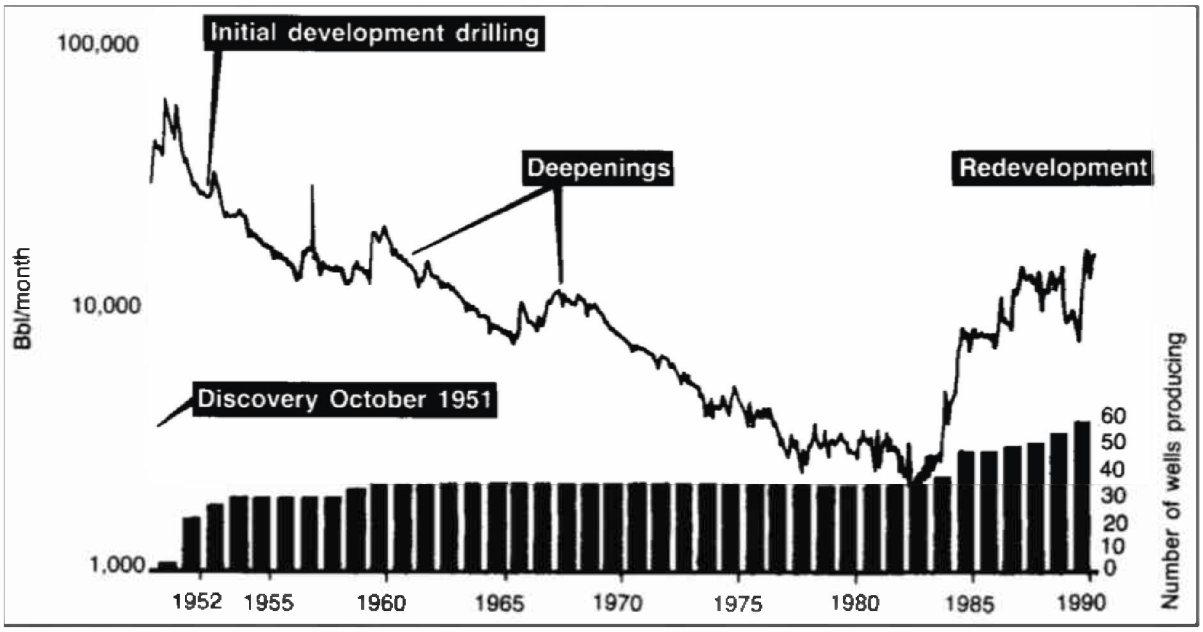

Figure 57 Tilden Field production decline curve showing stages of field development and production history since its discovery through 1990 (Baker and Carlisle, 1992, figure 3 used with permission of Oil and Gas Journal).

Geological Background

During Silurian time, a gently sloping, shallow, marine carbonate ramp covered central Illinois, and a broad northeast-southwest trending structure, the Sangamon Arch (Figure 56), existed in west Central Illinois (Whiting and Stevenson, 1965). In southern Illinois and southwestern Indiana, however, a platform margin, the Terre Haute reef bank (Figure 56) marked a slope break that was facing the deep Illinois Vincennes Basin (Droste and Shaver, 1980, 1987).

In Tilden Field, the Lower and Middle Devonian deposits are absent (Figure 58), and Silurian carbonates are overlain by the Upper Devonian to lowermost Mississippian organic-rich New Albany Shale Group (Whiting and Stevenson, 1965; North, 1969). The Silurian System has been the subject of several lithostratigraphic classifications (Willman and Atherton, 1975; Droste and Shaver, 1987). In this report, the stratigraphic classification of Willman and Atherton (1975) for western and southern Illinois has been adopted to identify the Silurian deposits of the study area. The Silurian System encompasses the Lower Silurian Alexandrian and the Middle Silurian Niagaran Series, which consist mainly of limestone and dolomite. The upper part of the Niagaran succession may consist of several dolomite or limestone reservoirs. The succession is over 198 m (650 ft) thick in Tilden Field (Figure 58) and consists of the St. Claire Formation and the overlying Moccasin Springs Formation. The Moccasin Springs Formation is mostly characterized by layers of limestone, dolomite, silty argillaceous limestone/dolomite, and shale that vary in thickness from place to place.

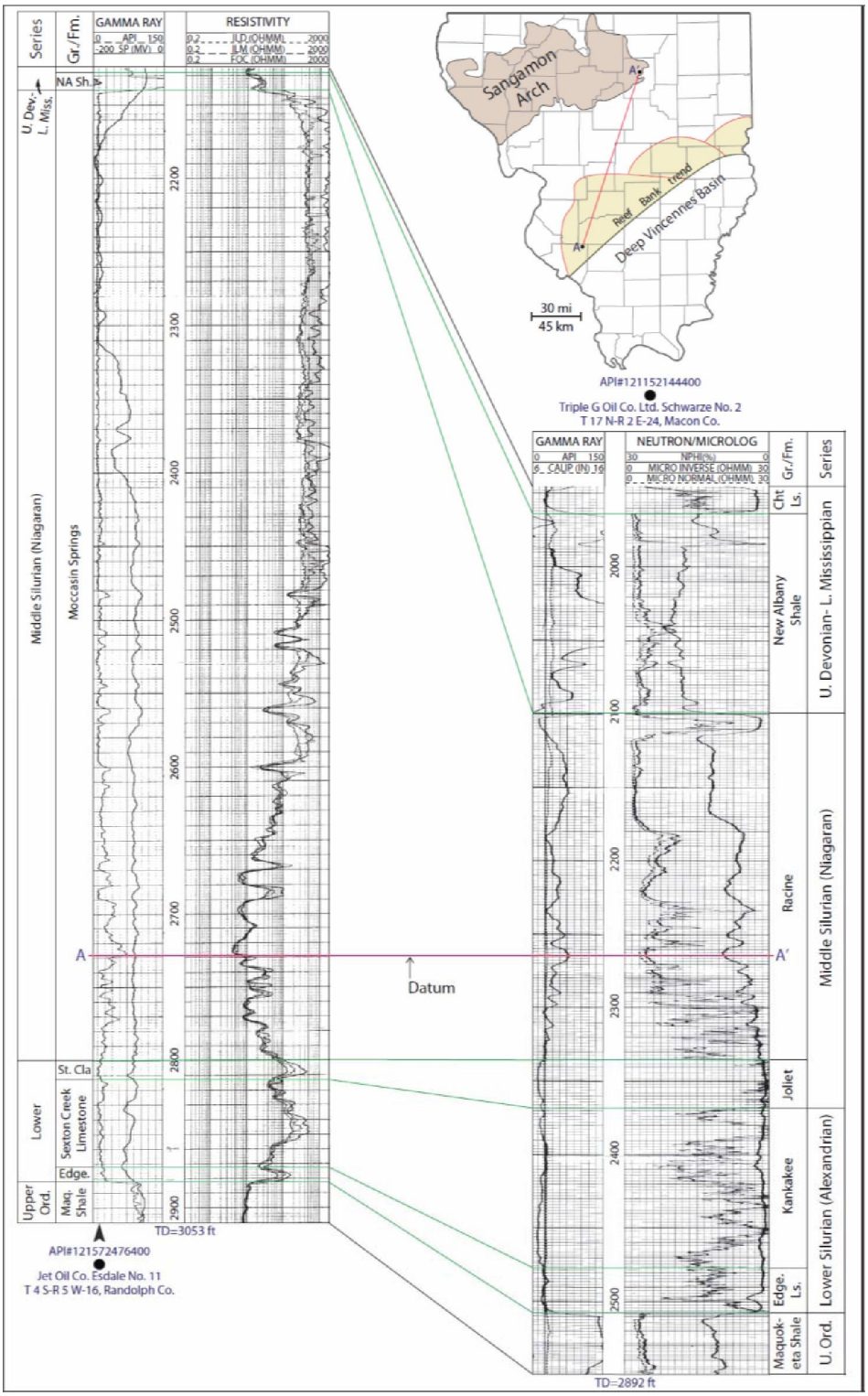

Figure 58 Southwest-northeast cross section from Forsyth to Tilden showing stratigraphic nomenclature and lateral variations of the Silurian deposits. Edge.: Edgewood; Cht Ls.: Chouteau; Dev.: Devonian; Gr.: group; Fm.: formation; Maq.: Maquoketa; Miss.: Mississippian; NA Sh.: New Albany; St. Cla.: St. Claire; Ord.: Ordovician.

Reservoir Facies and Depositional Environment

The producing horizons in the Tilden Field are reef reservoirs that occur in the upper and middle parts of the Moccasin Springs Formation. Exploration for Silurian reefs in Illinois started in 1946 when Lowenstam (1946) recognized the Marine Field in Madison County as being a reef producer. As shown in Figure 56, the Tilden Field is within the southern Illinois reef belt, which comprises a number of individual or coalesced pinnacle reefs. A Silurian pinnacle reef is defined as an isolated carbonate structure that has the shape of a dome or slightly elongated dome, with a diameter of less than 3.2 km (2 mi) and thickness of 91.4–304.8 m (300–1,000 ft; Bristol, 1974).

The Tilden structure was erected by reef-building organisms, which formed two closely spaced and topographically raised, rigid, and massive structures (reef core and reef flank facies) above the bedded muddy inter-reef deposits during deposition. The structural contour map on top of the Silurian deposits (Figure 59) indicates over 30.5 m (100 ft) of closure and two interconnected and slightly elongated dome structures typical of pinnacle reefs. The clean carbonate facies in the productive areas of the field is mainly composed of reef building organisms dominated by corals and stromatoporoids. The gamma ray and resistivity log signatures show a characteristic blocky, cylindrical-shape body (reef core and reef flank deposits) as opposed to less resistive argillaceous inter-reef deposits (Figure 60 and Figure 61). Similar to Marine Oil Field (Lowenstam, 1949), the Tilden reef is composed of pure carbonate (mainly limestone) with coral and stromatoporoid skeletons being the main skeletal component. It is a stratigraphic trap that is capped by organic-rich New Albany Shale, Chouteau Limestone, and Borden Siltstone (Figure 61).

The known productive reefs in Illinois are up to 213 m (700 ft) thick (Lowenstam, 1949; Bristol, 1974). They are almost entirely developed along the northeast-southwest trending platform margin that was facing the deep Vincennes Basin (Figure 62; Shaver et al., 1978; Droste and Shaver, 1980, 1987). Reef-building metazoans typically build laterally and vertically along the platform margin, where nutrient supply is abundant and depositional energy is very high (Wilson, 1975; James, 1983; Flügel, 2010).

The Niagaran pinnacle reefs in the Illinois Basin are similar to the extensively studied prolific reefs of the Middle Silurian Niagara Formation in the Michigan Basin, which form a rim of pinnacle reef bank up to 19 km (12 mi) wide facing the central deep basin (Gill, 1985; Droste and Shaver, 1985; Catacosinos et al., 1991; Grammer, 2013).

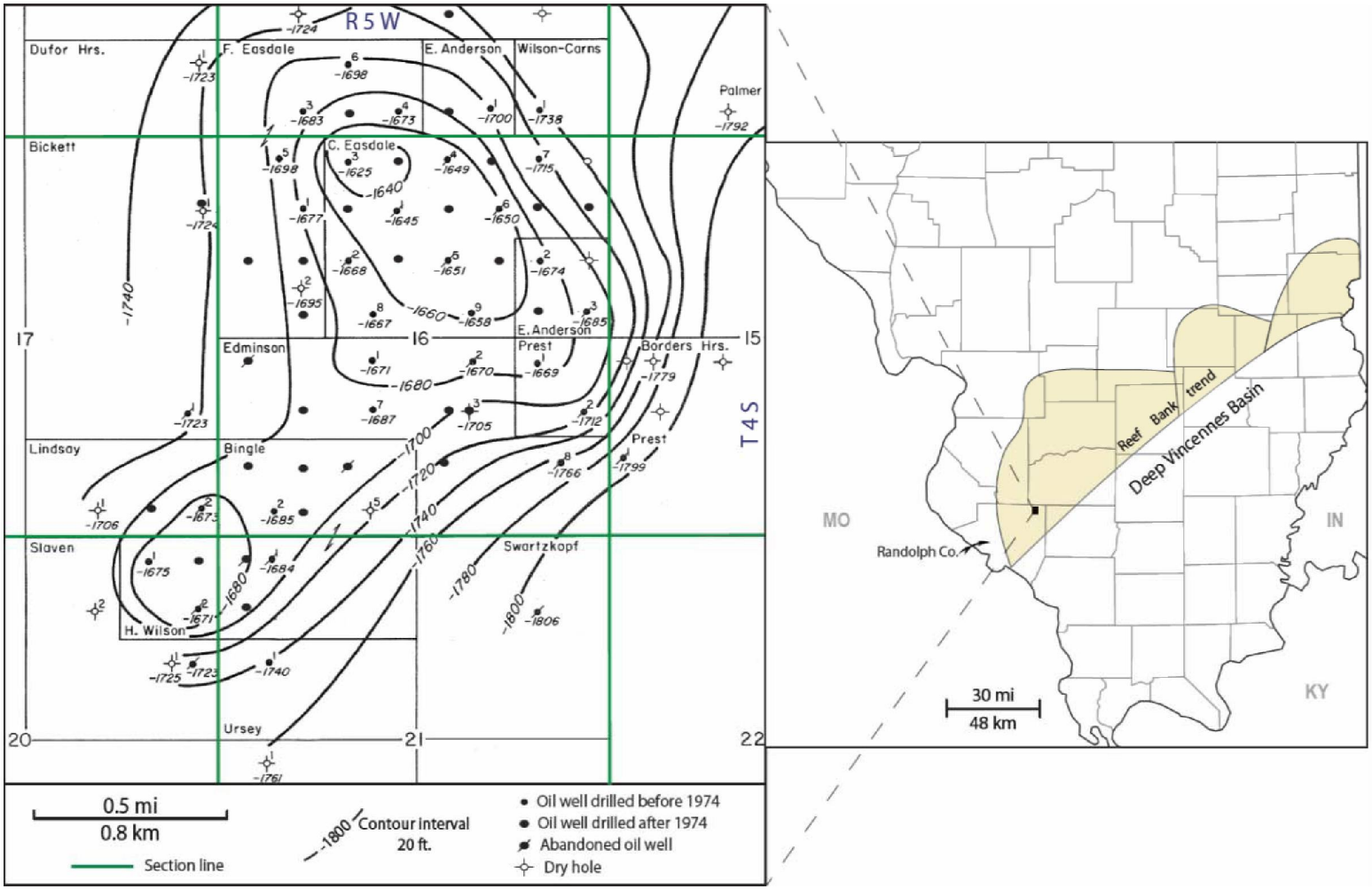

Figure 59 Structure contour map of the Silurian rocks in Tilden Field (modified from Bristol, 1974) showing two slightly elongated dome shape reef structures with over 30.5 m (100 ft) of closure. Cross sections across the field (Figure 60 and Figure **61**) indicate that the reef structures change laterally to deeper marine inter-reef facies.

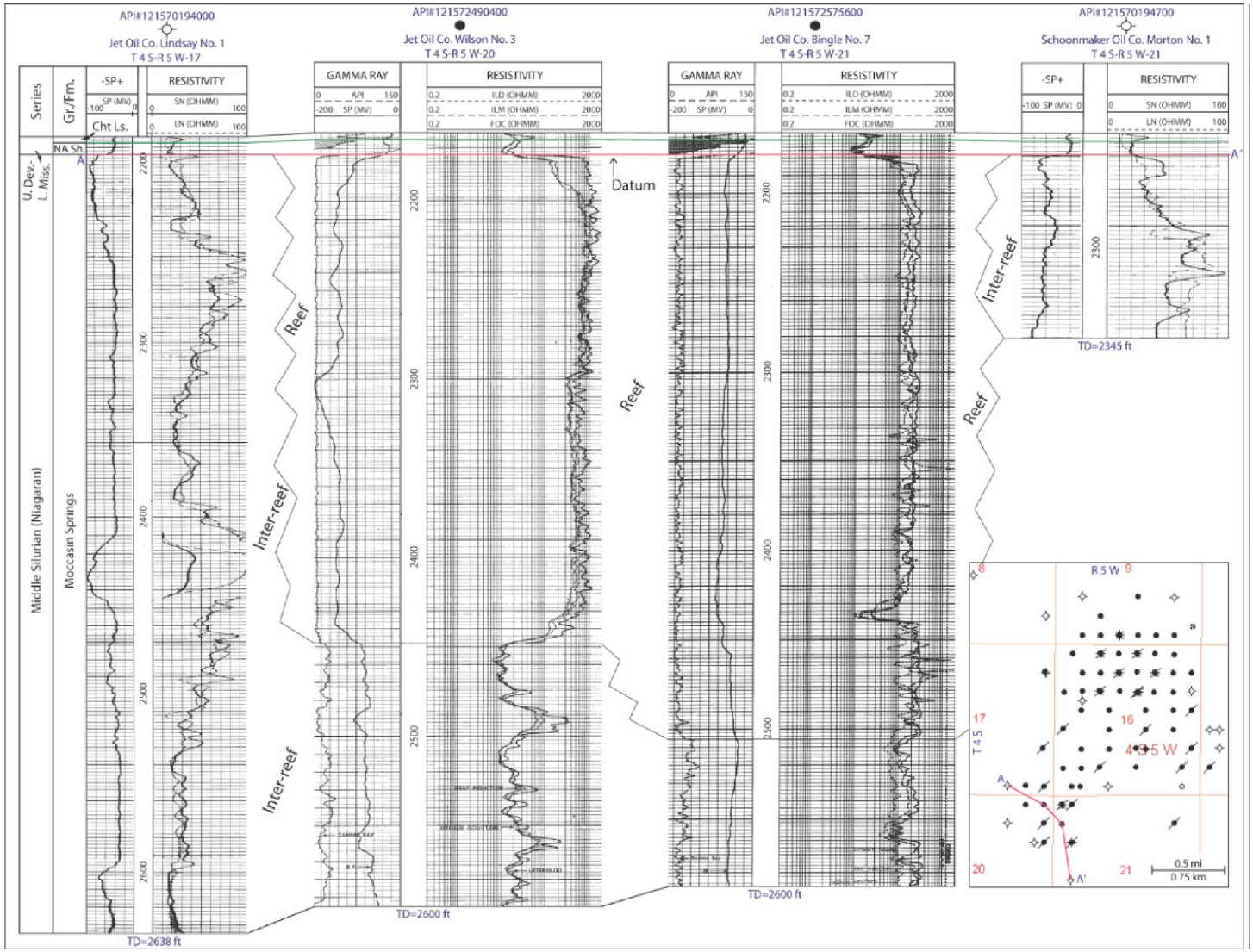

Figure 60 Cross section AA' across the southwest portion of Tilden Field showing lateral facies change from reef core and reef flank facies to shale and shaley limestone inter-reef facies towards the northwest and southeast. Note the clean limestone of the reef facies with cylindrical gamma ray and resistivity log signatures. Datum (labeled AA') is the base of New Albany Shale Group. Cht Ls.: Chouteau Limestone; Dev.: Devonian; Gr: group; Fm.: formation; Miss.: Mississippian; NA Sh.: New Albany.

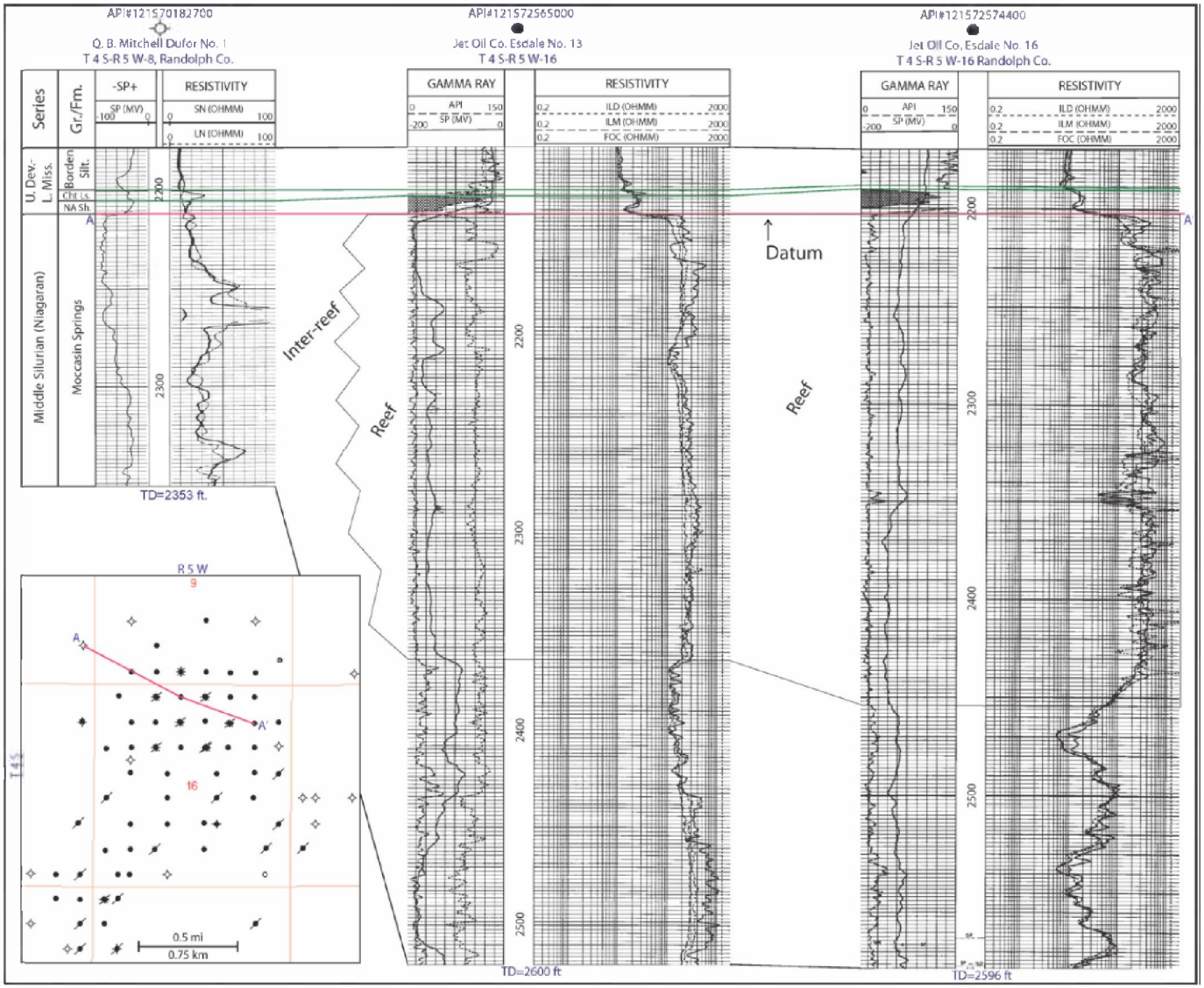

Figure 61 Cross section AA' across the northeast portion of Tilden Field showing the reef core and reef flank facies that change to shale and shaley limestone inter-reef facies toward the northwest within the Moccasin Springs Formation. Datum (labeled AA') is the base of New Albany Shale Group. Cht Ls.: Chouteau Limestone; Dev.: Devonian; Gr: group; Fm.: formation; Miss.: Mississippian; NA Sh.: New Albany.

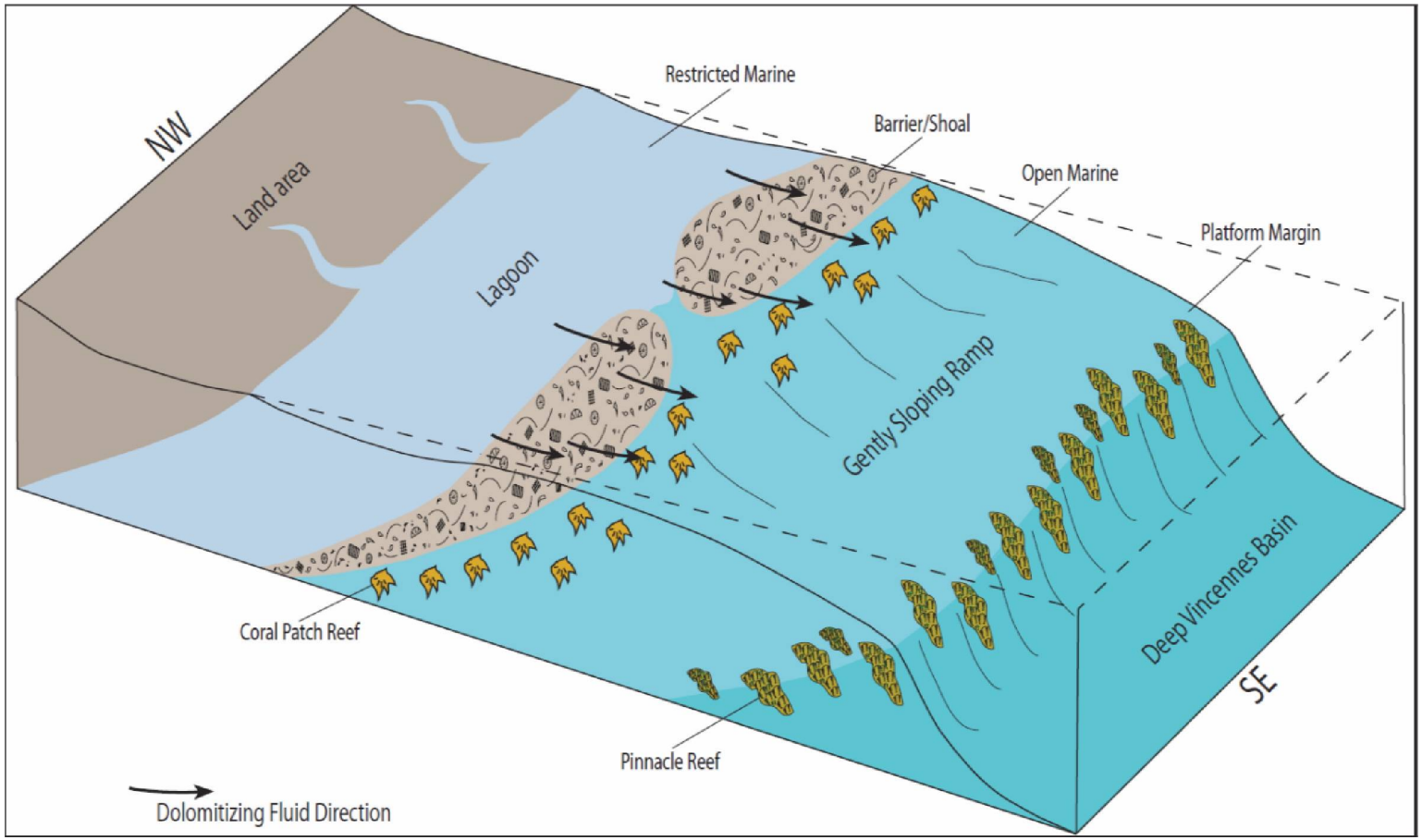

Figure 62 Generalized depositional model that depicts the distally steepened ramp of the Illinois Basin during Middle Silurian (Niagaran) time. Small coral patch reefs developed seaward of the bioclastic ramp margin barrier/shoal environment, and large pinnacle reefs were mainly restricted to the outer ramp margin. A narrow reef bank marks a slope break in southern Illinois and southwestern Indiana, separating the gently sloping ramp from the deep Vincennes Basin in the southern part of the Illinois Basin (Droste and Shaver, 1980, 1987). The depositional facies of the inner ramp (restricted lagoon and tidal flat facies) are absent due to the upper contact of the Niagaran deposits and the complete removal of the Silurian rocks towards the northwest in the Mississippi Arch area (Lasemi et al., 2010).

Fluvial and Alluvial: Lower Mt. Simon Sandstone at the Illinois Basin–Decatur Project

Illinois Basin–Decatur Project Background

The Illinois Basin–Decatur Project (IBDP) is a large-scale carbon capture and storage (CCS) demonstration project managed by the Midwest Geologic Sequestration Consortium (MGSC). IBDP is injecting 1 million tonnes (1.1 million tons) of carbon dioxide in the Upper Cambrian Mt. Simon Sandstone over three years at a rate of 1,000 tonnes (1,102 tons) per day. The Mt. Simon Sandstone can be subdivided into three major units with different geologic and diagenetic histories that have a profound effect on reservoir quality. At the IBDP site, the top of the Mt. Simon Sandstone is overlain by 100 m (300 ft) of tight silt and shale in the Eau Claire Formation, which forms a seal that prevents possible migration of CO_2 into the overlying strata. At IBDP, the best reservoir quality rocks are in the fluvial dominated braided river system in the lower most Mt. Simon Sandstone, where the average porosity is 22% and permeability is 1.97×10^{-9} cm^2 (200 md), respectively.

The Mt. Simon Sandstone is possibly one of the most important carbon sequestration targets in the United States. In the Illinois Basin, the Cambrian-age Mt. Simon Sandstone (Figure 63) can be over 792 m (2,600 ft) thick (Figure 64), with portions of the Mt. Simon having excellent reservoir properties.

SYSTEM	GROUP	FORMATION
Ordovician	Maquoketa	Brainard
		Ft. Atkinson
		Scales
	Galena	Kimmswick
		Decorah
	Platteville	
	Ancell	Joachim
		St. Peter
	Praire du Chien	Shakoppee
		New Richmond
		Oneota
		Gunter
Cambrian	Knox	Eminence
		Potosi
		Franconia
		Ironton-Galesville
		Eau Claire
		Mt. Simon Sandstone
Precambrian		

Figure 63 Stratigraphic column of Ordovician through Precambrian rocks in Illinois.

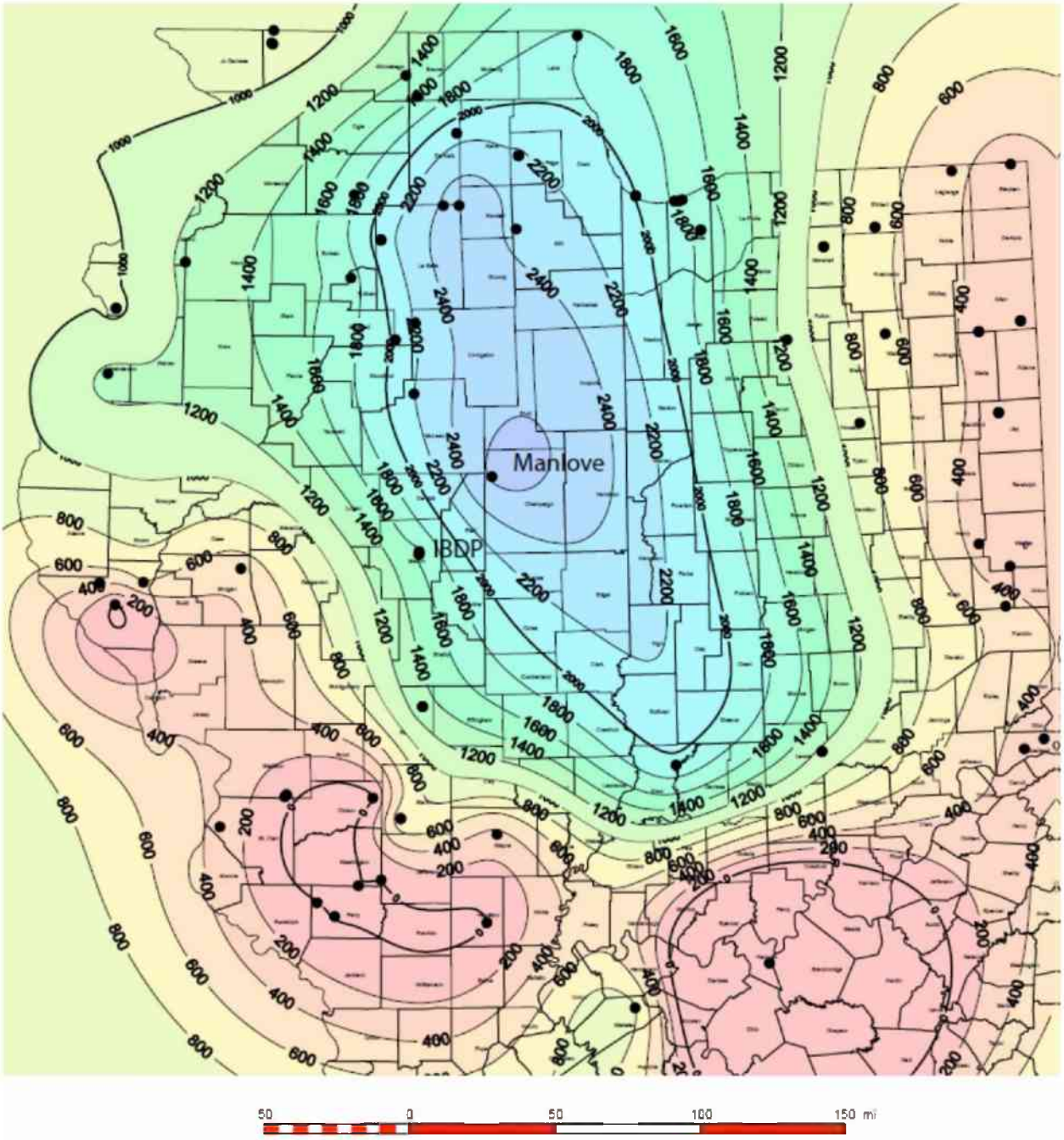

Figure 64 Thickness of the Mt. Simon Sandstone in the states of Illinois, Indiana, and Kentucky. Red areas highlight areas where the Mt. Simon Sandstone is either thin or was not deposited. Contour interval is 61 m (200 ft).

The best reservoir quality occurs in the lower Mt. Simon Sandstone, with an average porosity of 22% and permeability of 1.97×10^{-9} cm^2 (200 md). Individual intervals can have porosities as high as 28% and permeabilities of over a darcy. Beginning November 15, 2011, there has been continuous injection of about 1,000 tonnes (1,102 tons) of CO_2 per day into the lower Mt. Simon reservoirs. As of June 3, 2013, the total injected CO_2 is over 500,000 tonnes (551,155 tons).

Methods

The reservoir characterization of the Mt. Simon Sandstone at the IBDP site is based on petrophysical and stratigraphic analysis of three recently drilled wells. The well data were integrated with 3-D seismic reflection data by using wireline logs and two zero offset vertical seismic profile (VSP) data. Two of the wells, the ADM CCS No. 1 and the ADM Verification No. 1, well were drilled 330 m (1,000 ft) apart, whereas the third well, ADM Verification No. 2 well, was approximately 1,500 m (5,000 ft) from Verification No. 1 well (Figure 65). In addition to a full suite of logs, the CCS No. 1 well acquired 20 m (60 ft) of whole core from the Mt. Simon Sandstone; the Verification No. 1 well had over 200 m (600 ft) of whole core from the Eau Claire and Mt. Simon Sandstone; and Verification No. 2 well recovered 60 m (200 ft) of whole core, spanning major divisions of the formations. Detailed stratigraphic and petrographic descriptions were made of the Mt. Simon Sandstone core and the interpretations were integrated with wireline log data and petrophysical properties, such as porosity and permeability.

Porosity values from wireline logs were calculated using the Schlumberger Elemental Analysis (ELAN) interpretation process. The program was also used to compute a probabilistic volume of all the minerals and fluids, including summation of all fluids, irreducible water, and bound water. This process also allows the accurate determination of pore space that would be affected by CO_2 injection and is designated as PIGN (inter-granular porosity), which includes the free fluids plus the irreducible fluids.

Regional Geology

The Mt. Simon Sandstone is a thick succession of primarily very gently dipping to flat lying Cambrian-age sandstones, siltstones, and conglomerates (Figure 64); it comprises the lower part of one of the major depositional units within the North American mid-continental deposition successions referred to as the Sauk sequence (Sloss, 1963). In the Decatur area, there is a pre-Mt. Simon interval that can be recognized by its lower porosity and vertical burrows identified within core. This pre-Mt. Simon Sandstone has not been recognized elsewhere in the Illinois Basin. The basement rocks below the contact are a strongly altered rhyolite.

The Mt. Simon Sandstone varies from dominantly well-sorted, fine- to coarse-grained sandstone to poorly sorted conglomerates and minor siltstones and mudstones. There are no observed carbonate intervals or evaporates. The predominant cementation component is quartz. The primary seal for the Mt. Simon Sandstone sequestration reservoirs is the overlying Eau Claire Formation. In central Illinois, the lower portion of the Eau Claire is primarily siltstone to shale and the upper part is dense carbonates in central Illinois; however, further south it becomes a carbonate and in the Missouri area is referred to as the Bonneterre Dolomite (Bell et al., 1964).

Lithofacies of the Lower Mt. Simon Sandstone

All three wells in the IBDP area are drilled into the top of the Precambrian basement, which is composed of rhyolite (Figure 66). The ADM Verification No. 2 well also penetrated lower layers of granodiorite and granite. Above the Precambrian is a burrowed pre-Mt. Simon siliciclastic unit that is distinct when compared to the overlying non-marine Mt. Simon Sandstone. The Mt. Simon Sandstone can be subdivided into three major intervals consisting of a Lower, Middle, and Upper Mt. Simon and is overlain by the Eau Claire Formation. This report only discusses the fluvial system of the lower Mt. Simon.

Figure 65 Basemap of the IBDP study area.

Lower Mt. Simon

Fine- to coarse-grained sandstone and conglomeratic facies (Figure 67) that have excellent reservoir and injection capabilities dominate the lower Mt. Simon Sandstone. Interbedded within these strata are some low porosity and permeability, siltstones, and mudstones. The lower Mt. Simon can be divided into four distinct depositional facies characterized by changes in the rock lithofacies and changes in the geophysical log signatures.

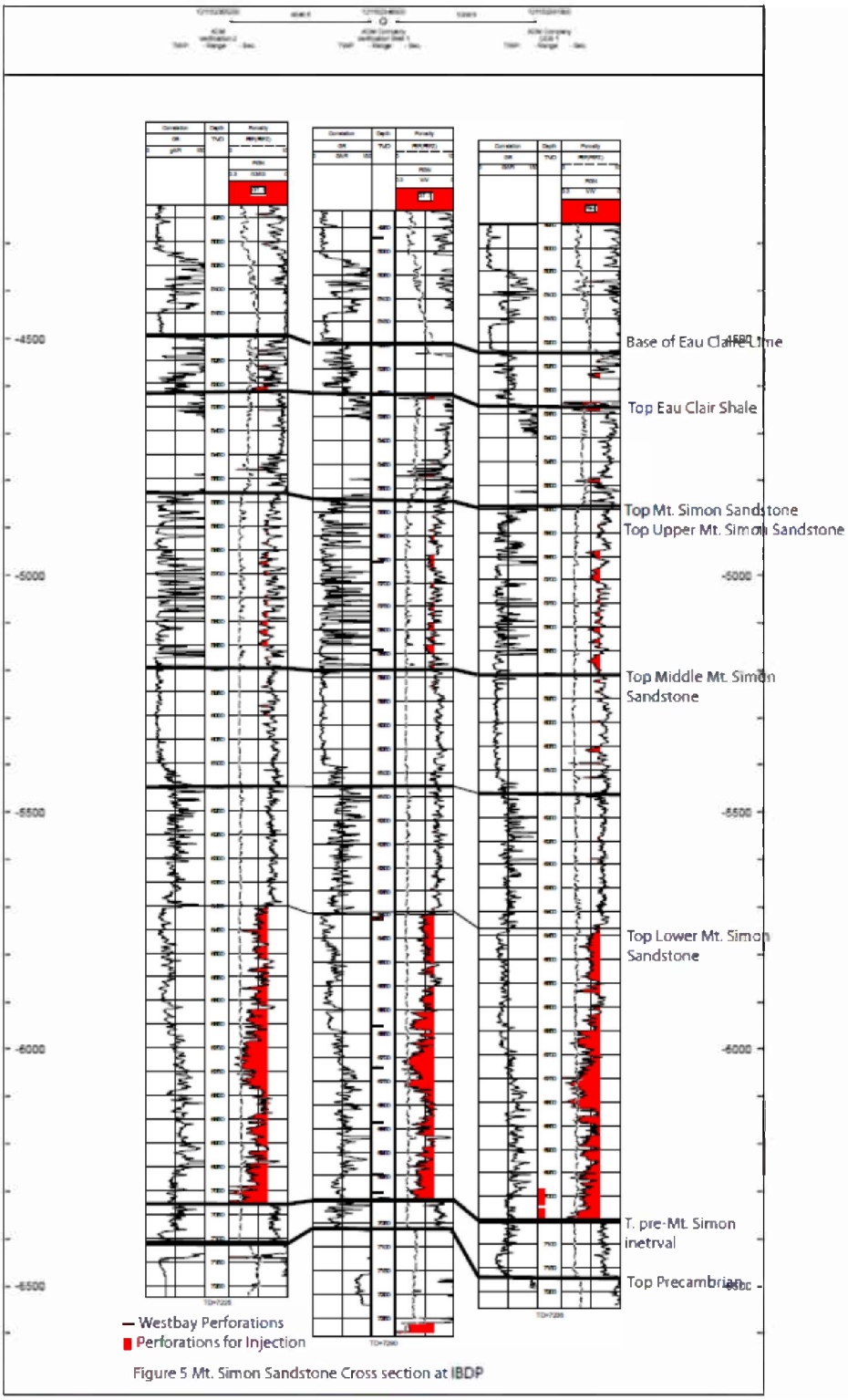

Figure 66 Structural cross section of the Mt. Simon Sandstone across the IBDP study area. Three sub intervals of the Mt. Simon are shown along with the Eau Claire Formation, the pre-Mt. Simon interval, and the basement. Reservoir quality of the Mt. Simon Sandstone is illustrated by the porosity logs. The porosity cutoff (red shaded area on the porosity curve) is 10%. The gamma ray log illustrates the heterogeneity of the Mt. Simon facies.

Figure 67 Poorly sorted conglomerate from the lower Mt. Simon Sandstone acquired from Verification Well #2 (measured depth of 2,119 m [6,952 ft]). Pebbles consist of quartz and k-feldspar. The horizontal permeability is 2.22×10^{-9} cm^2 (225 md), vertical permeability is 2.37×10^{-9} cm^2 (240 md), and porosity is 17%.

The first facies, found in the lowest part of the Mt. Simon Sandstone, is composed primarily of pink-tan to light maroon, poorly sorted, cross-bedded sandstone and granule to pebble conglomerates that are often friable. The lithology is mostly sub-arkose, sub-lithic arenite, and arkose wacke with dominantly well rounded, coarse-grained strata. However, grain size ranges from fine sand to pebbles. Fining upward sequence, erosional surfaces, and pebble lags are common. Sub-angular intraclasts of light-green clayey siltstone and maroon basement rhyolite are common. Porosity is largely primary framework porosity; however, secondary porosity enhancement, as a result of k-feldspar dissolution, is common, but not a major contributor to the total porosity. Occluding clay cements lining detrital grains and pore throats are a major control on porosity destruction, whereas authigenic quartz cement and grain compaction is a minor control.

The second facies is dominantly moderate to well-sorted medium to fine-grained sandstone that is planar to cross-bedded and sometimes massive. Fining upward sequences are common. The sandstones are classified as subarkose to sublithic arenites. Trace green clay laminae are dispersed throughout. Grains are commonly well rounded, moderately unconsolidated, and exhibit clay minerals as the dominant cement. Quartz cements are trace to moderate throughout.

The third facies comprises the upper most section of the lower Mt. Simon Sandstone and is composed of fine-grained, planar finely laminated and low-angle cross-bedded sandstone (Figure 68). The lithology is mostly subarkose to quartz arenite with dominantly sub-angular to sub-rounded very fine- to fine-grained sand. Porosity is dominantly controlled by primary grain framework. Trace to moderate amounts of authigenic quartz, moderate amounts of clay, and traces of authigenic k-feldspar occlude pore throats.

The fourth facies is composed of finely laminated to ripple-laminated mudstone, siltstone, and very fine-grained sandstone. These deposits are not a major constituent of the lower Mt. Simon Sandstone, but occur sporadically and are interbedded within the first and second facies and are typically from 0.3 to 1.8 m (1 to 6 ft) thick. Intraclasts of similar siltstone lithology occur throughout the first facies and second facies.

Interpretation

Sandstones and conglomerates of the lower Mt. Simon Sandstone (facies 1) are interpreted to have formed in a fluvial braided river system. The conglomerates near the base of the Mt. Simon Sandstone were deposited in a distal alluvial fan. Some of the more poorly sorted conglomerates may even represent debris flow (alluvial fans) deposits, which were sourced from numerous nearby Precambrian paleotopographic high areas.

The massive to stratified medium- to fine-grained sandstone strata (facies 2) that form the bulk of the lower Mt. Simon Sandstone represent deposits formed during ephemeral sheet flood events on a low relief distal fan or sandy braid plain. Beds of planar to cross-bedded, moderately well sorted, and fine to medium sandstone with mudstone intraclasts are common in modern and ancient fluvial deposits. The planar strata are commonly interpreted to have formed under upper flow regime conditions (high flow rates in shallow water). These types of representative strata have been interpreted to be a prevegetative fluvial style produced by sheet floods or stream floods (Long, 1978).

Figure 68 Fine- to medium-grained, cross-bedded eolian sandstone in the lower Mt. Simon from the ADM Verification Well #2 (measured depth of 2,126 m [6,974 ft]). The horizontal permeability is 1.40 × 10^{-9} cm^2 (142 md), vertical permeability is 1.42 × 10^{-9} cm^2 (144 md), and porosity is 22%.

The finely planar laminated and low-angle cross-bedded, fine to medium, well-sorted sandstones (facies 3) are likely eolian deposits formed in low relief portions of the Illinois Basin by reworking of the fluvial strata. Because these intervals are thin and interbedded with fluvial deposits, reworking on a sand sheet, rather than forming in a large dune field, is envisioned. In the Precambrian, there were no land plants that would bind the soil material; therefore, during any dry period, the wind could rework the finer grained fluvial sands and redeposit them as thin eolian strata.

The fourth facies is interpreted as being deposited in a flood plain to shallow ephemeral playa ponds. However, thin mudstone and clay laminae may be overbank deposits. There are occasional clasts of mudstone throughout the sandstone, and conglomerate facies that are likely remnants of these deposits that were eroded out. These floodplain or playa deposits would have a low preservation potential and could be easily reworked by both eolian and fluvial processes on the braid plain.

Depositional Environment

The lower Mt. Simon strata are dominated primarily by braided river, alluvial fan, playa, and eolian deposits. Present day fluvial geologic analogs may not be as relevant because the Mt. Simon Sandstone was deposited before the advent of vascular plants. The importance of vegetation on bank stability has been demonstrated by Smith (1976) who observed that nonvegetative sediment can be up to 20,000 times less stable than comparable sediments containing plant roots. The lack of land plants tends to produce fluvial systems that formed by the development of broad plains. It is also important to note that in a braided river system the predominant deposition is that of coalescing channel bars. The presence of numerous conglomerate beds are commonly deposited under conditions associated with flash floods. Modern flash floods include sheet wash, which is broad flows a few centimeters thick; sheet floods that are several kilometers wide and 4 to 16 cm (1.6 to 6.3 in.) deep; and stream floods that are less than 1.5 m (4.9 ft) deep and up to 4.8 km (3 mi) wide. These could occur on alluvial fans or lower gradient areas of arid basins. In modern arid river settings, the presence of dense vegetation tends to break up sheet flows, which produces turbulent flows in small channels. This would not have been the case in the Cambrian. Even in semihumid to humid environments, sheet floods might be expected to be the most common depositional mechanism. In fluvial systems with rapid water infiltration, there would most likely be deposition of massive beds or beds with poorly defined laminations.

The interbedding of eolian planar laminae, which are formed by migrating wind ripples, and low angle cross-beds composed of well-sorted, fine- to medium-grained sand, formed by small dunes with coarser, rippled, and cross-bedded fluvial deposits, suggest periodic flooding and drying of the sediment. Red colored sediments are typical in more arid environments.

The Role of Topography on Deposition

During the initial reconnaissance analysis of the targeted Mt. Simon and Eau Claire Formations intervals, it was determined that earlier structural development may have impacted deposition of these intervals.

Seismic data suggests that in some areas of Illinois there are more than 609 m (2,000 ft) of paleotopographic relief on the base of Mt. Simon Sandstone (Leetaru and McBride, 2009). There

is approximately one degree of regional stratigraphic dip at the IBDP area. This suggests that the mapping of the top of the pre-Mt. Simon interval surface, which has a good seismic reflector, could readily illustrate the paleotopography just before deposition of the Mt. Simon Sandstone. Mapping the top of the pre-Mt. Simon interval shows an unconformity with 61 m (200 ft) of topographic relief (Figure 69). The map of the top of the pre-Mt. Simon interval surface shows an apparent east-west trending valley with a hill with 30.5 m (100 ft) of relief above the valley floor.

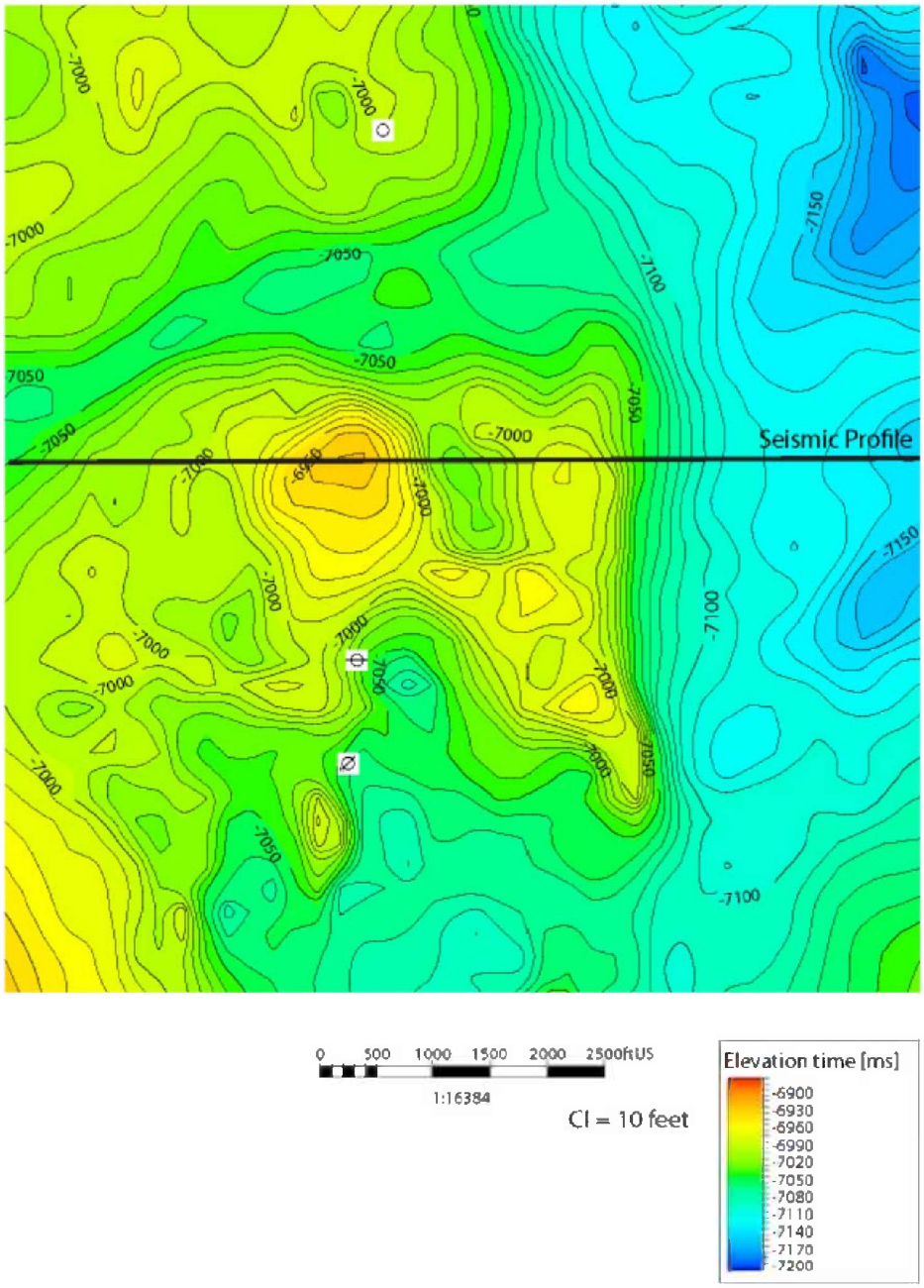

Figure 69 Structure map of the top of the pre-Mt. Simon interval seismic reflector over the 3-D seismic survey area of the IBDP. The map shows the topography of the base of the Mt. Simon Sandstone.

Turbidite: Carper Sandstone at St. James Oil Field

St. James Field Production History and Development

St. James Field in Fayette County, Illinois, covers an area of a little more than 1,618 ha (4,000 acres). Following discovery in 1938, early production from the field came primarily from the Cypress Sandstone. A test of the Carper sandstone was conducted on a well drilled in 1962, but due to a bad cement job, the test showed noncommercial production from the horizon and the Carper was subsequently overlooked. In 1982, a second well was drilled 201 m (660 ft) to the north of the earlier well and established commercial production from the Carper. The field is situated over a small dome on an unnamed southward plunging anticlinal nose that extends south of the Louden Anticline (Nelson, 1995).

Carper Background

The Carper sandstone reservoirs in the Wilberton, St. James, and St. Paul oil fields in Fayette County Illinois have been interpreted as turbidites, which were deposited as deep-water sediments adjacent to the Borden Siltstone (Mississippian) delta in southern Illinois. The Borden Siltstone is lower Valmeyeran (Early to Middle Mississippian) in age; mapping in the subsurface shows that it is a tongue shaped body, extending in a southwest direction across central and southern Illinois (Figure 70; Swann et al., 1966). The Borden Siltstone is 122 to 213 m (400 to 700 ft) thick and was deposited in water that was 152 to 213 m (500 to 700 ft) deep. Turbidites in the Borden Siltstone are composed of very fine-grained quartz sandstone that is well sorted and exhibits graded bedding (Lineback, 1968).

Mapping of the Borden Siltstone interval between the underlying Kinderhookian (Early Mississippian) Chouteau Limestone and the overlying Valmeyeran carbonates illustrates a large area of deeper-water clastics deposition than is normally associated with the Illinois Basin (Figure 71). The Borden Siltstone contains large volumes of shale, particularly in the lowermost portions of the formation near the contact with the Chouteau Limestone. The Springville Shale that separates the Carper D sandstone from the underlying Chouteau Limestone has been interpreted as deep-water shale by Lineback (1966).

The Carper sandstone consists of extremely fine-grained sandstone, ranging in thickness from 0 to 30.5 m (0 to 100 ft). The Carper sandstone occurs in isolated lenses located near the base of the Borden Siltstone with 6.1 to 15 m (20 to 50 ft) of dark shale separating it from the underlying Chouteau Limestone. These stratigraphic relationships are shown in the cross section in Figure 71. The Chouteau Limestone directly overlies the Devonian New Albany Shale, a black, organic-rich shale that is possibly the major source rock in the Illinois Basin.

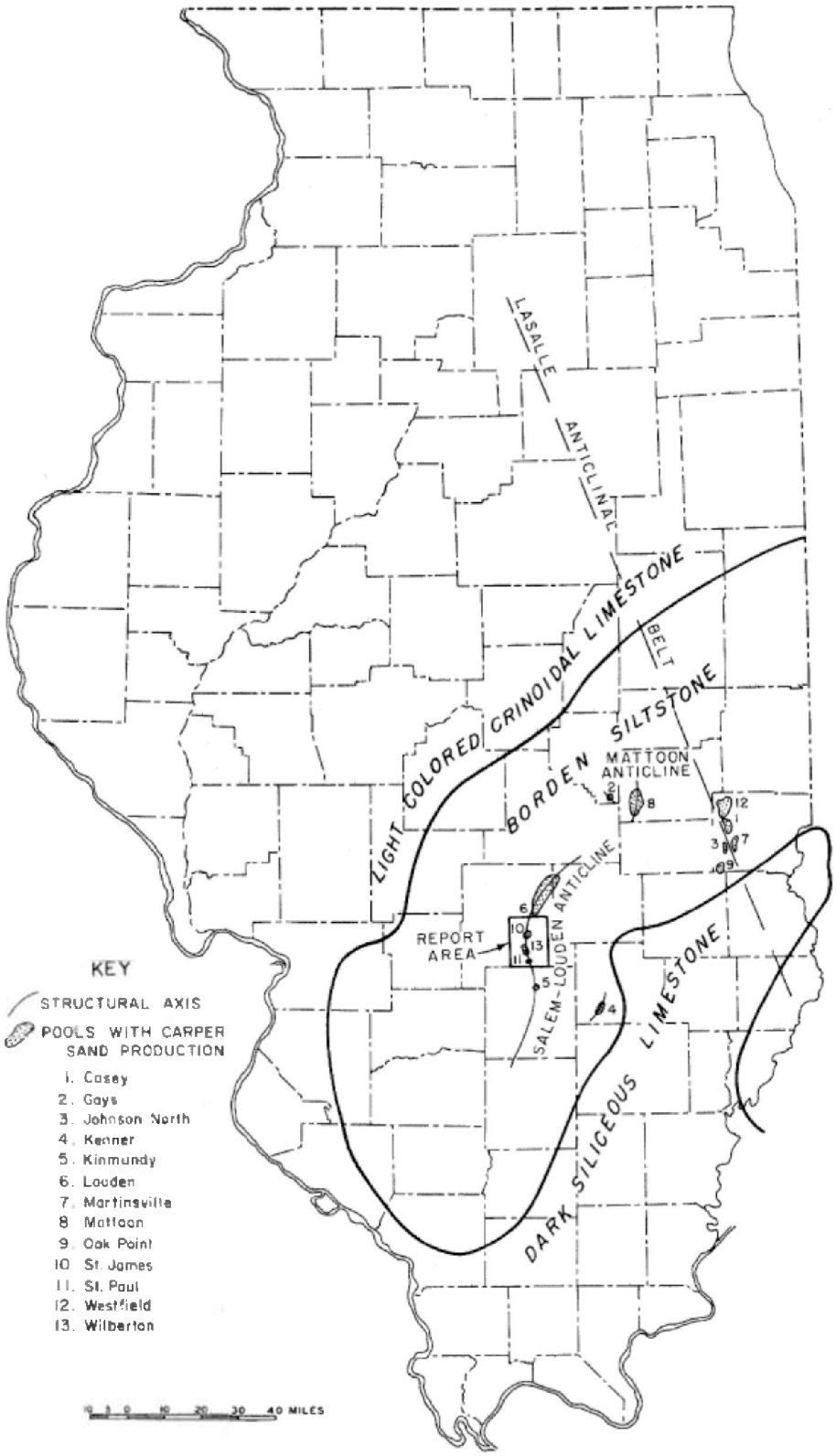

Figure 70 Map showing areal extent of Borden Siltstone (after Stevenson, 1964).

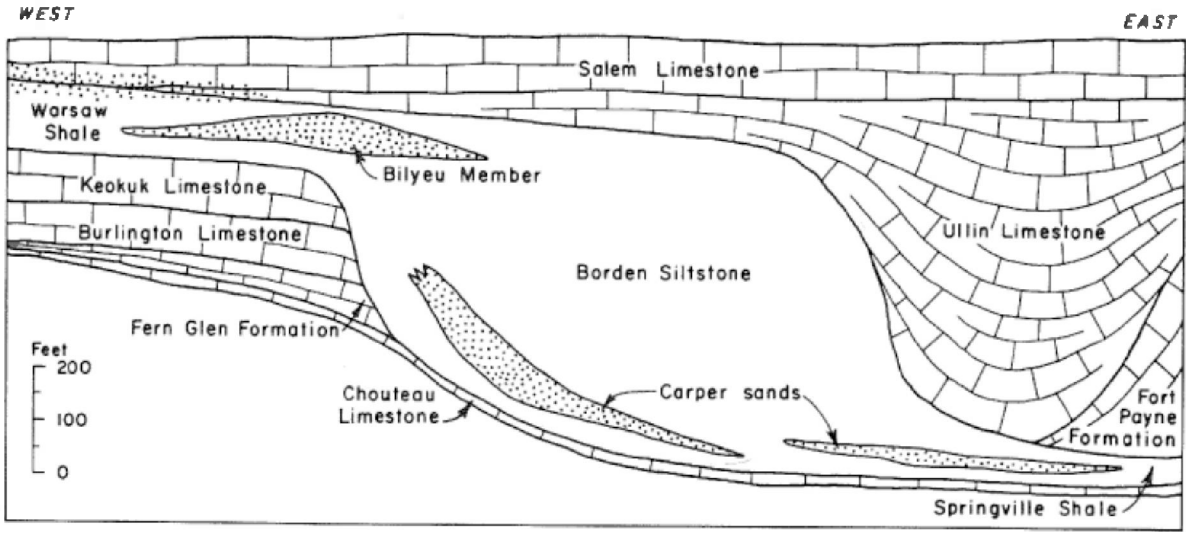

Figure 71 Regional cross section illustrating stratigraphic and vertical relationship of Carper sandstone bodies within the Borden Siltstone (after Lineback, 1968).

The Borden Siltstone has been interpreted as a deltaic deposit, extending across east-central and southwestern Illinois with the source of sediments located far to the northeast (Figure 72). Maps showing the location and direction of the major sediment sources for sandstones in the Borden delta system are shown in Figure 72. Previous research mapped the Borden Siltstone delta using electric log characteristics, where topset, foreset, and bottomset beds were identified within the delta (Lineback, 1968). A series of five separate sandstone accumulations comprise the Carper A, B, C, D, and E sandstones. These discontinuous sandstone bodies are made of extremely fine-grained sandstone and are located near the base of the Borden Siltstone in some areas of central and east central Illinois and near the top in others (Figure 71; Lineback, 1968). Carper sandstones are sandy facies located within finer grained dark shales that make up the bottomset beds of the Borden delta. The sand accumulated on the foreset slope of the Borden Siltstone delta off the mouths of major distributaries (Lineback, 1968). Sand and other clastics were moved downslope in turbidity currents that carried the sand across the pro-delta plain and eventually deposited it as submarine fans.

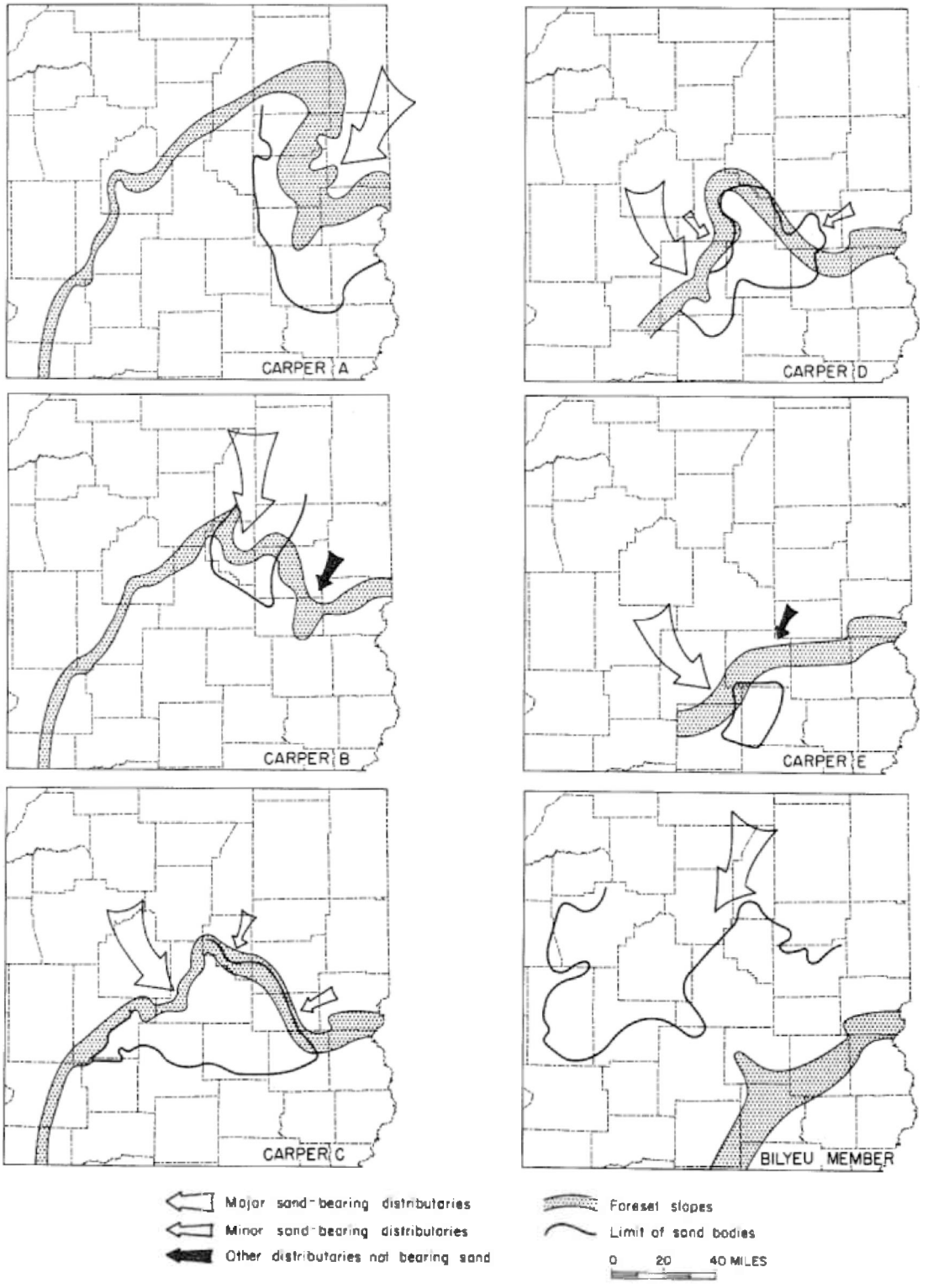

Figure 72 Series of maps showing shifting directions of depositional sources for Carper A, B, C, D, and E sandstones (after Lineback, 1968).

Carper sandstone bodies located in the lower portion of the Borden Siltstone are localized and usually fan shaped. The geometry of Carper sandstone deposits are lenticular in transverse cross sections; however, in longitudinal cross sections, the bottom surface slopes upward with respect to the base of the Borden Siltstone in one direction and slopes downward, closer to the base, in the other. Downslope, the geometry of Carper sandstone bodies thin and pinch out. Upslope, the sandstone body may thicken (Figure 71; Lineback, 1968). Several Carper sandstone bodies were recognized and mapped in the Borden Siltstone. Interpretation of deposition by turbidity currents was based on the geometry of mapped Carper sandstone bodies, their stratigraphic position, and graded bedding of the lowermost bottomset sandstone bodies (Lineback, 1968). Maps of Carper sandstone bodies show that most have one primary sediment source, with a few having additional secondary sediment sources as shown in Figure 72 from Lineback (1968). These maps illustrate several episodes of turbidite submarine fan deposition within the Borden Siltstone.

The Carper A, B, C, D, and E sandstones, as well as the Bilyeu member, were mapped in previous studies (Figure 72; Lineback 1966, 1968; Swan et. al., 1965). The Carper A sandstone (Figure 73) is the oldest, thickest, and most extensive of the Carper sandstones. The Carper A is the coarsest grained Carper sandstone and represents the earliest and most extensive buildup of turbidite deposits within the Borden Siltstone. The Carper B sandstone (Figure 74) is less extensive, but does contain massive sandstone beds that can be more than 76.2 m (250 ft) thick with few interbedded shales. The Carper B sandstone shows a shift to the northwest in sediment source. The Carper C sandstone shows another westward shift in sediment source. The Carper C sandstone is a fan-shaped deposit that attains a thickness of over 42.7 m (140 ft) in a localized area, thinning in its distal margins (Figure 75). Several individual lobes were recognized by Lineback (1968) during mapping. The Carper C sandstone produces oil in the Louden Field in Fayette County. The thick portions of the Carper C sandstone are made up of a complex amalgamation of many sandstone beds, while thinner areas contain no more than three sandstone lenses. The Carper D sandstone is relatively widespread (Figure 76) and attains a thickness of approximately 30.5 m (100 ft) in a few localized areas of Fayette County, Illinois. The Carper D produces oil in the St. James, Wilberton, and St. Paul Fields in Fayette County. The cross section in Figure 77 shows the relationship of the Carper D and Carper C sandstones as well as the shale underlying the sandstone bodies in Fayette County. The Carper D sandstone is interpreted as having a higher silt and mud content than the other Carper sandstones, based on its high SP and unusually low resistivity on electric logs. The Carper E sandstone is the least extensive of the Carper sandstone deposits (Figure 78) and attains a maximum thickness of 33.5 m (110 ft).

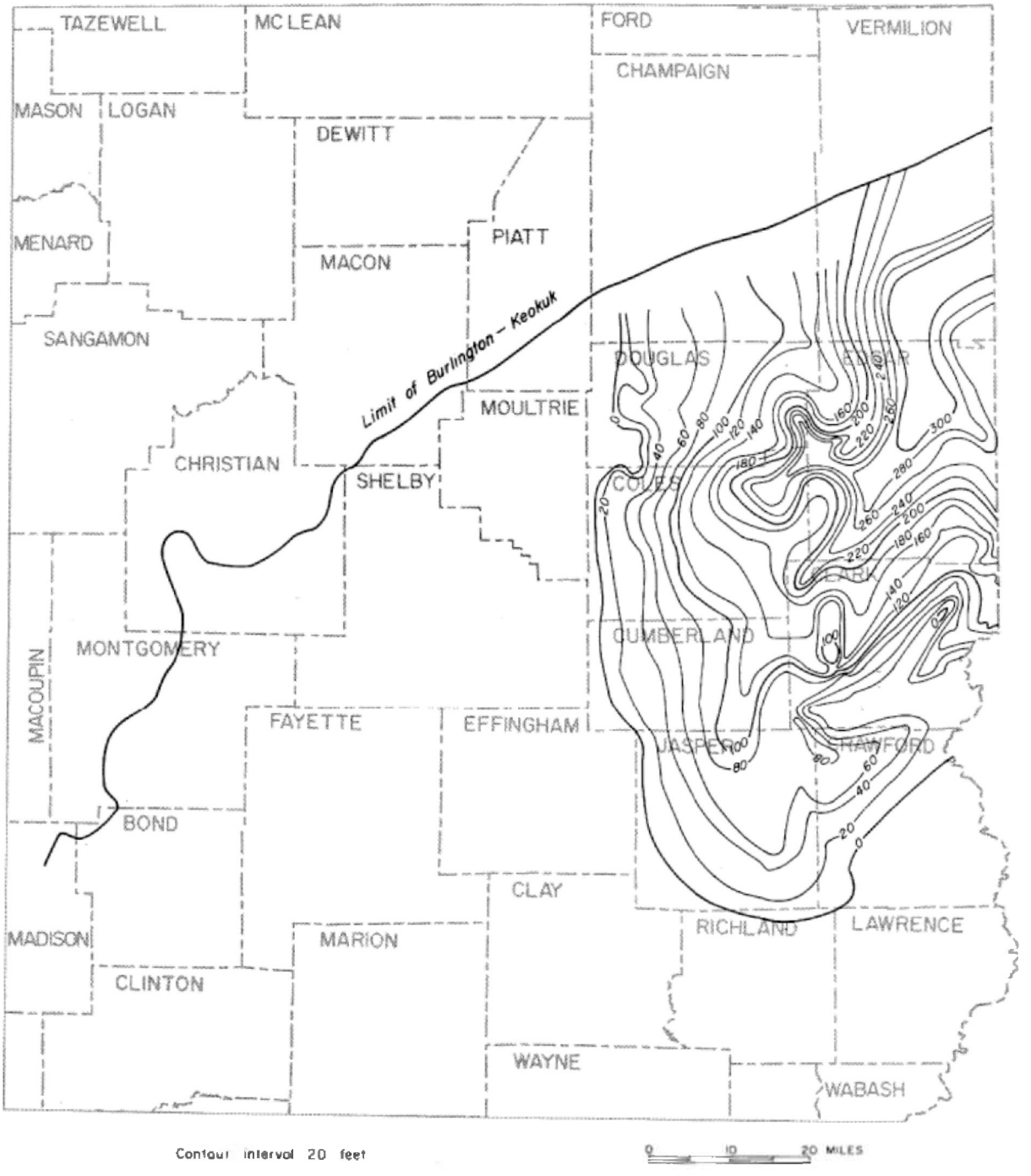

Figure 73 Isopach of Carper A sandstone (after Lineback, 1968).

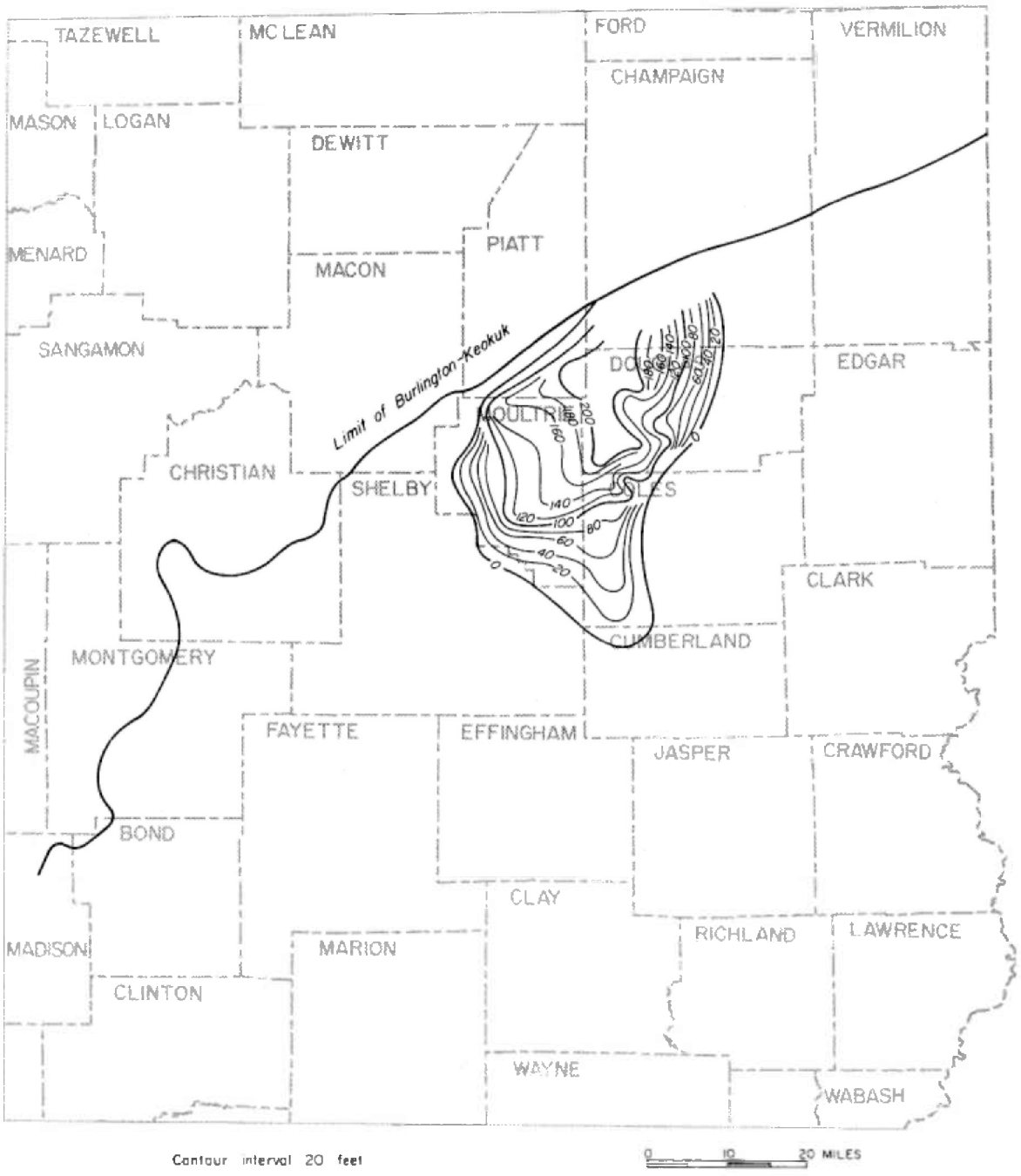

Figure 74 Thickness of the Carper B sandstone (after Lineback, 1968).

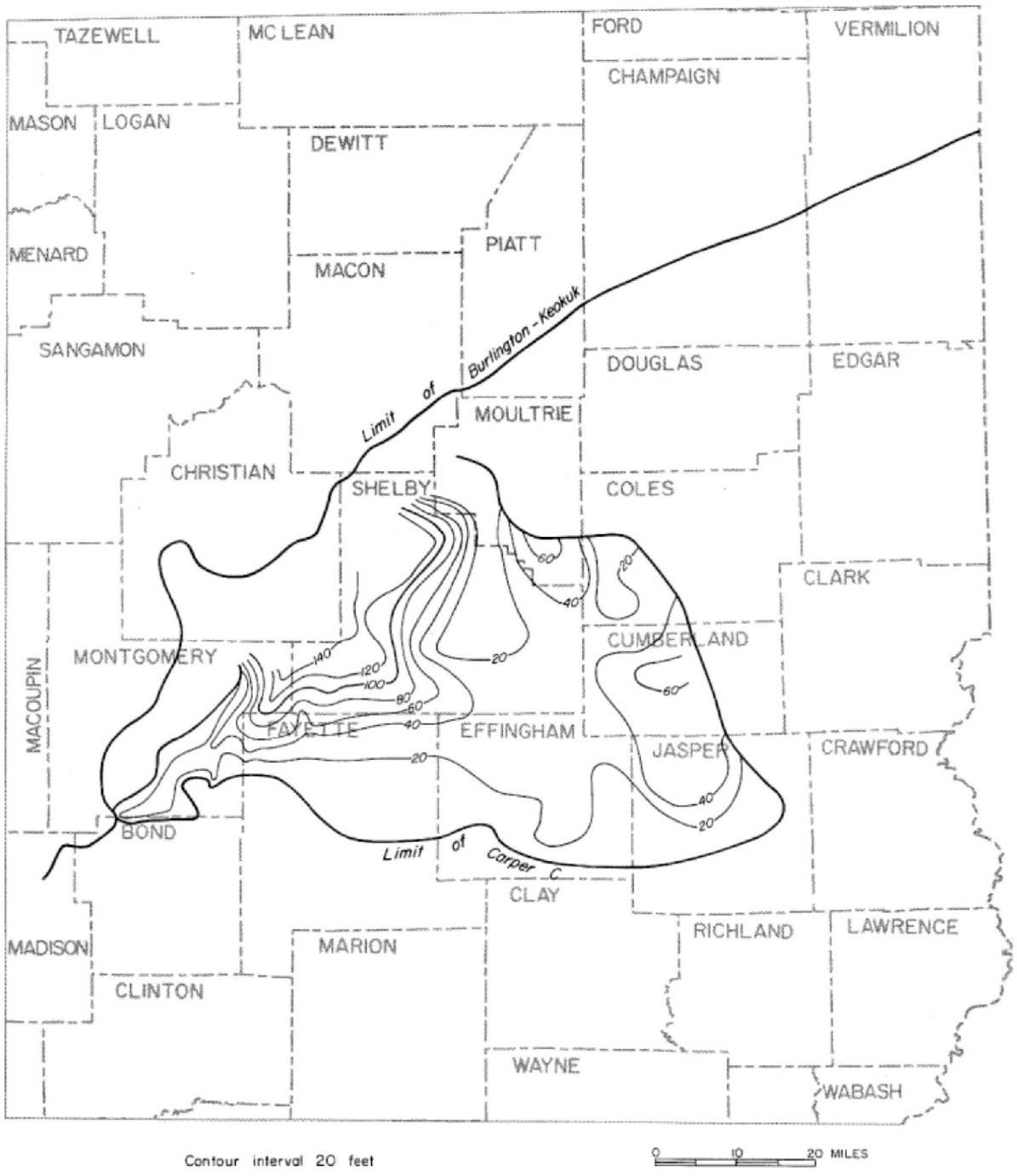

Figure 75 Thickness of the Carper C sandstone (after Lineback, 1968).

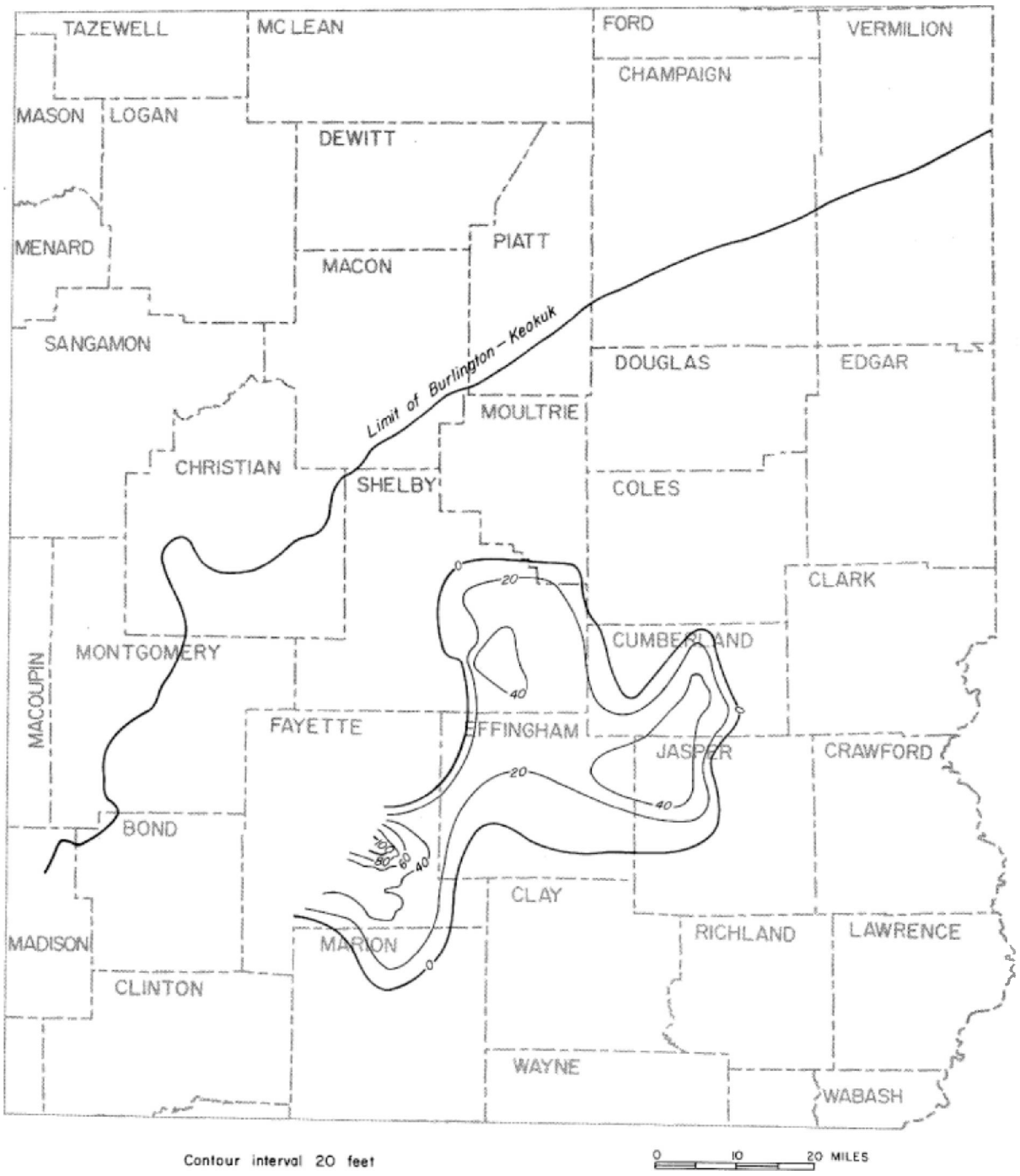

Figure 76 Thickness of the Carper D sandstone (after Lineback, 1968).

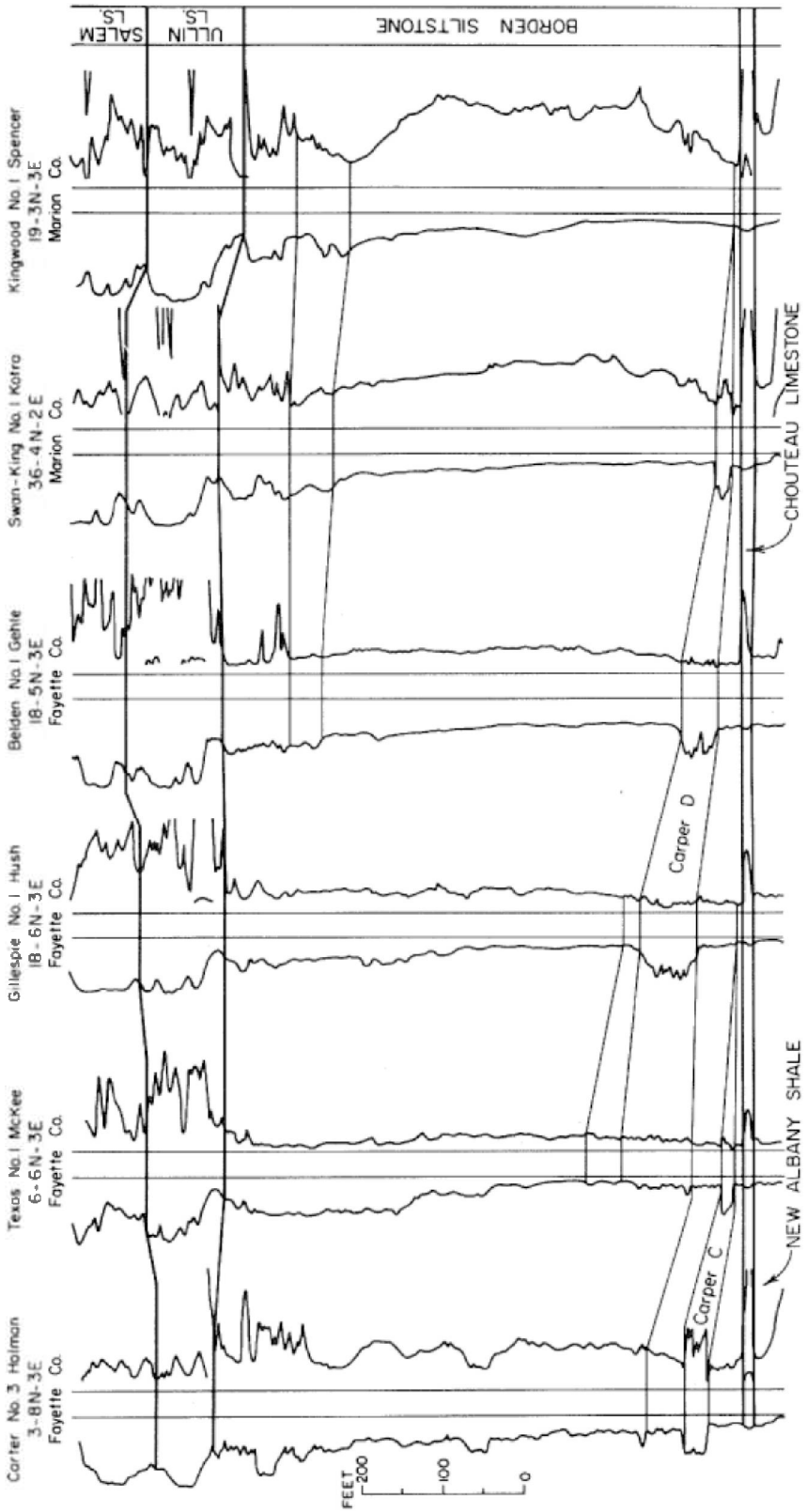

Figure 77 Cross section of Carper D Sandstone Fayette County (after Lineback, 1968).

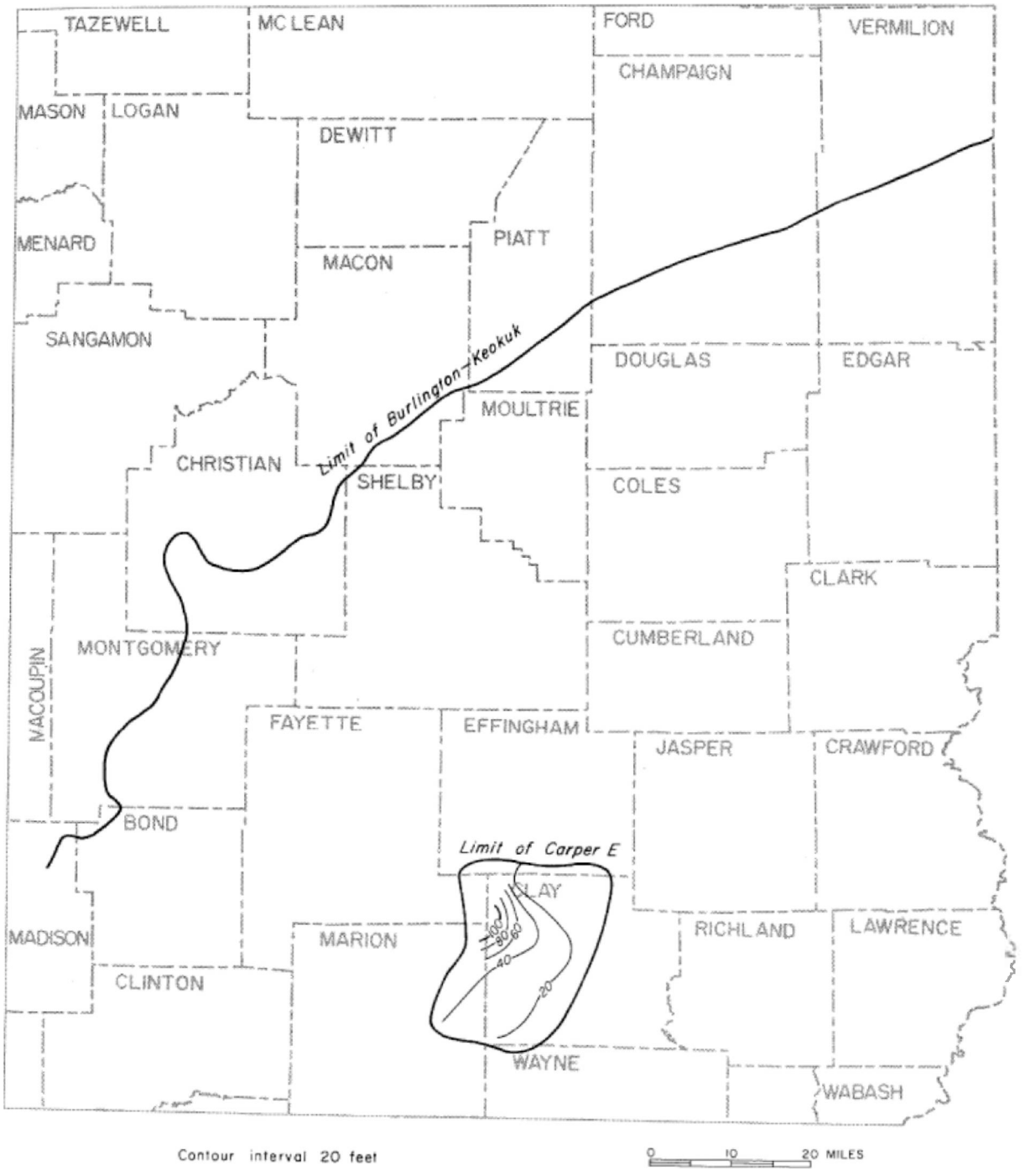

Figure 78 Thickness of the Carper E sandstone (after Lineback, 1968).

Study Area

The study area within St. James Oil Field includes roughly 303 ha (750 acres) of the oil field (Figure 79). The area mapped for the development of a geologic model includes part of Sections 25 and 36, T6N, R2E, and Sections 30 and 31, T6N, R3E, with portions of some surrounding sections. This study area was selected to include an area of more modern drilling into the Carper sandstone and includes some core analysis data. The geophysical logs in the study area include a mix of 1960s vintage electric logs with 2000s vintage gamma ray–neutron/density logs. The older logs are more common in the northern half of the study area, and the newer logs are more common in the southern half. A number of the older logs do not penetrate the entire thickness of the Carper sandstone as wells were commonly drilled to total depth within the formation. The more recently drilled wells with modern log suites capture the entire formation.

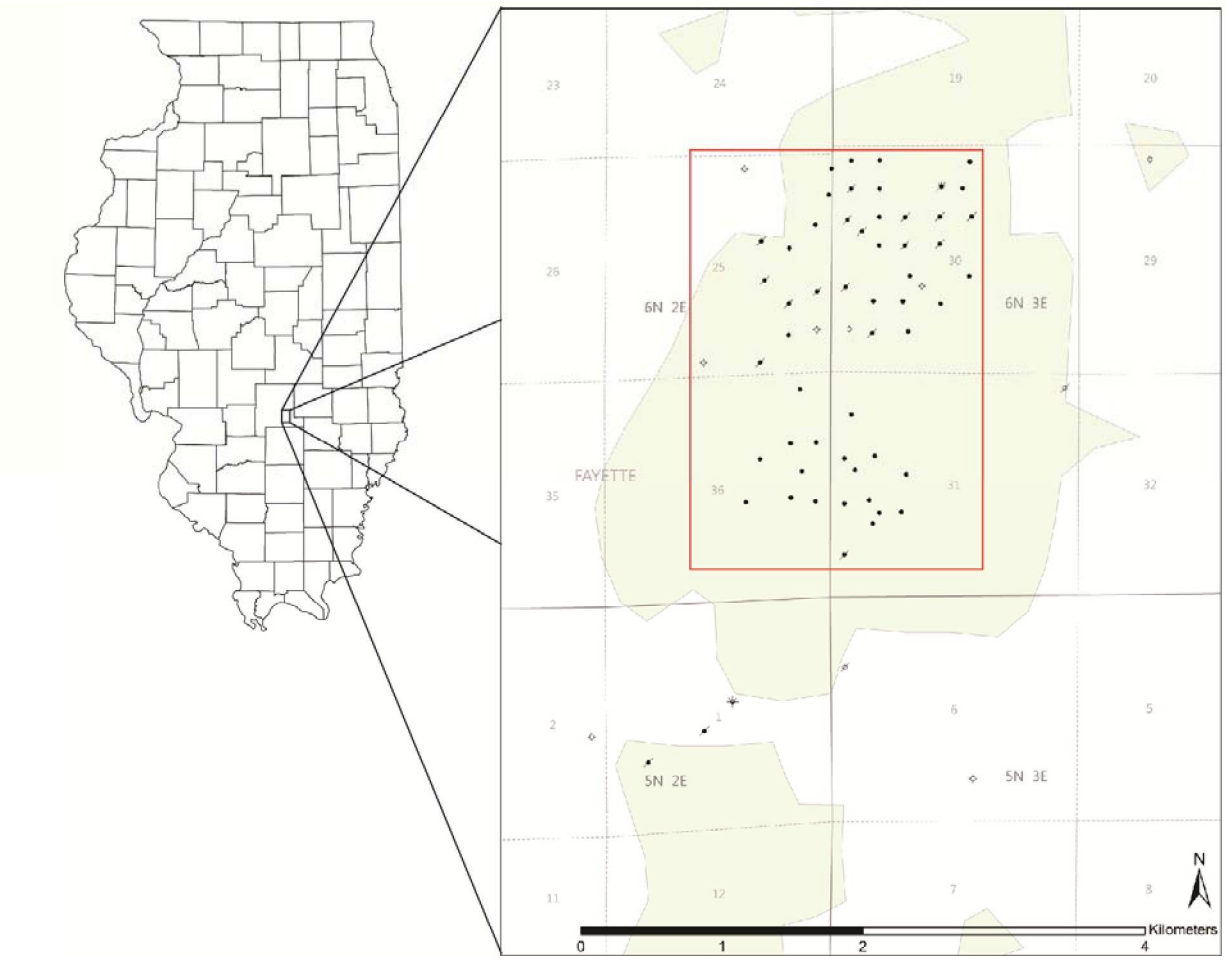

Figure 79 Map showing the location of the study area in south-central Illinois. The main study area is outlined in red and all wells used to construct the geologic model are shown on the map. The study area is in the southern part of the St. James Oil Field (shaded). The northern part of the Wilburton Oil Field extends into the southern part of the map.

Structure

The St. James Oil Field lies within the Louden-Salem anticlinal belt at the southern end of the Louden Anticline. There is pronounced closure in the St. James Oil Field located on the crest of a slightly elongated, southward-plunging dome (Stevenson, 1964), called the St. James Dome (Nelson, 1995), that coincides with relatively thick deposits of Carper D sandstone, resulting in a combination structure-stratigraphic trapping mechanism for the oil reservoir. The structure is 4.5 km (3 mi) long and 3 km (2 mi) wide with about 12 m (40 ft) of closure (Nelson, 1995). The study area falls a few kilometers (miles) to the south of the area of maximum closure in the southern part of St. James Field. A structure map contoured on the base of the Chouteau Limestone shows about 7.62 m (25 ft) of structural closure within the study area (Figure 80).

Stratigraphy

The Carper sandstone occurs within the Borden Siltstone (Figure 81). In St. James Field, on average more than 152 m (500 ft) of Borden Siltstone overlies the Carper. The Carper sandstone reservoir ranges in thickness from about 12 to 34 m (40 to 110 ft). The Carper thins southward somewhat uniformly, thinning roughly 5.7 m/km (30 ft/mi; Figure 82). This trend supports previous mapping of the Carper D which shows St. James field very near the source of sediment at the shelf edge. Underlying the Carper is the Springville Shale, which ranges in thickness from 12 to 15 m (40 to 50 ft) and also thins somewhat to the south. The Springville Shale rests atop the roughly 3.1 m (10 ft) thick Chouteau Limestone, a regional marker bed that was used as a stratigraphic datum in this study.

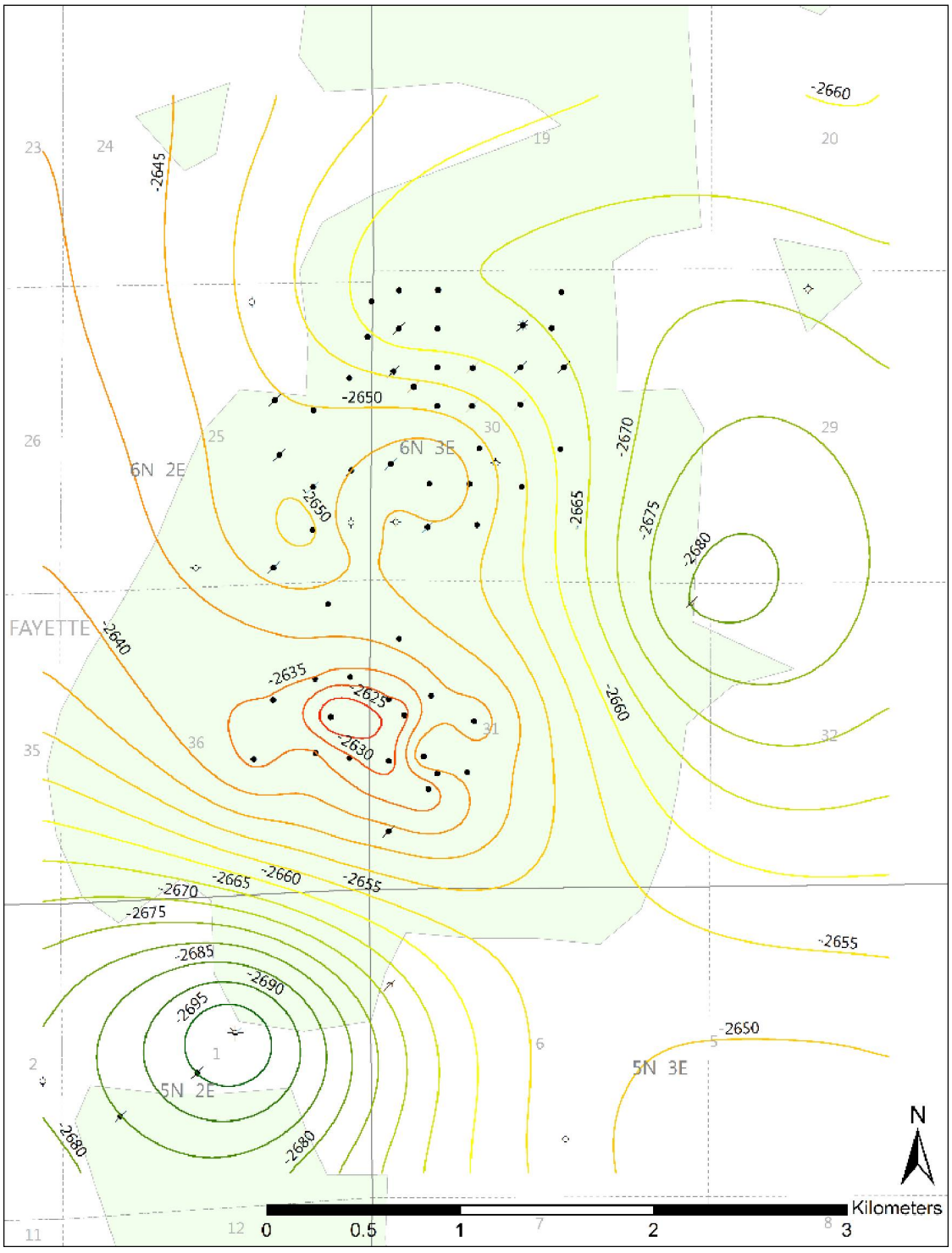

Figure 80 Structure contour map on the base of the Chouteau Limestone, a regional marker horizon underlying the Carper sandstone and used as a stratigraphic datum in this study. Elevations are in feet. Contour interval is 1.52 m (5 ft). The location of a north to south cross section is also shown on the map (Figure 82).

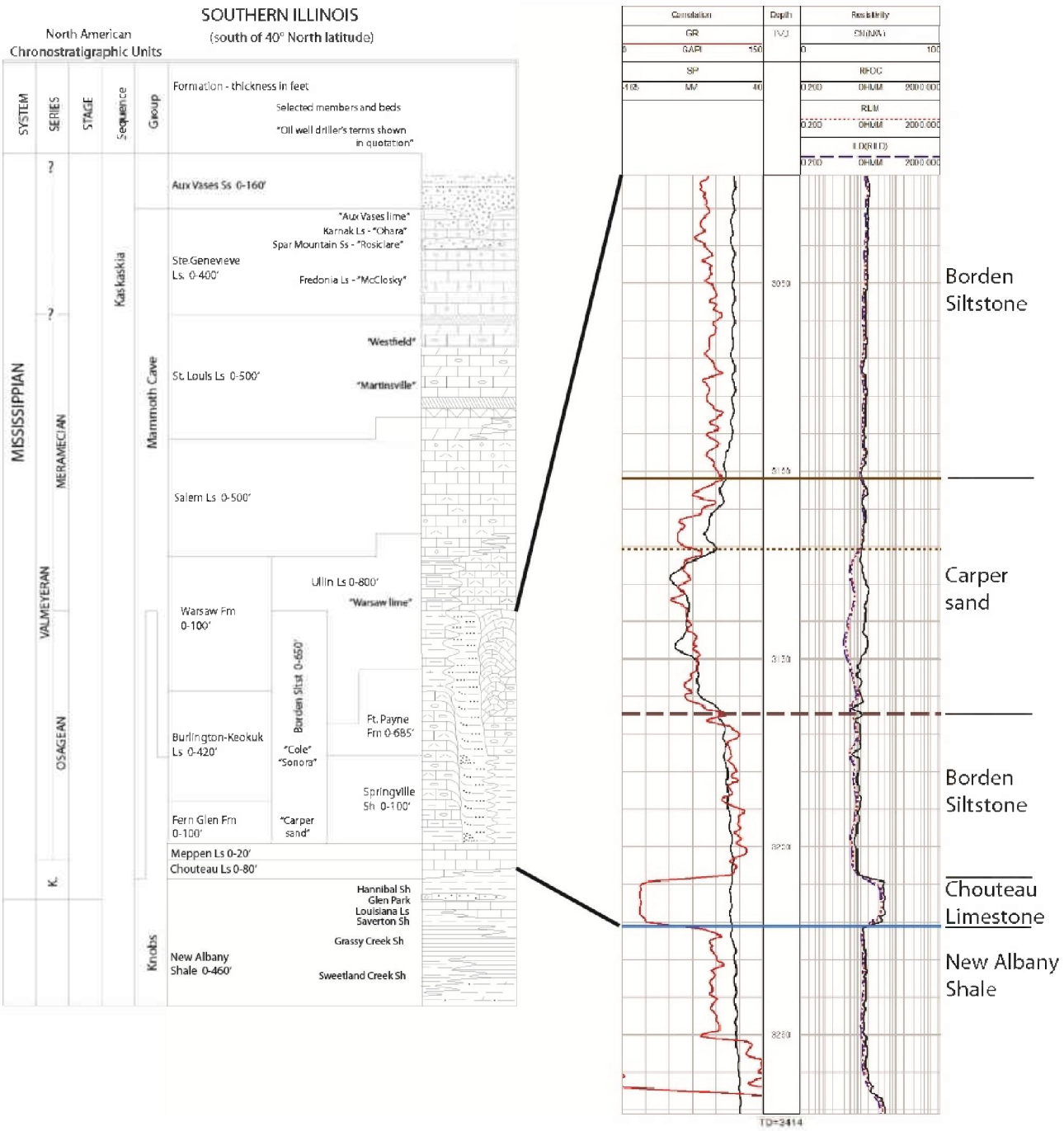

Figure 81 Left: Portion of the generalized stratigraphic column for Illinois. Rocks below the New Albany Shale and above the Aux Vases Sandstone are not shown. Formal formation names are listed along with gross thicknesses of the formations. Oil industry terms are listed in quotes. Right: Type log of the Kistler Unit 19 Well (API 120512794100) showing the interval that was used to map the Carper sandstone reservoir in St. James Field

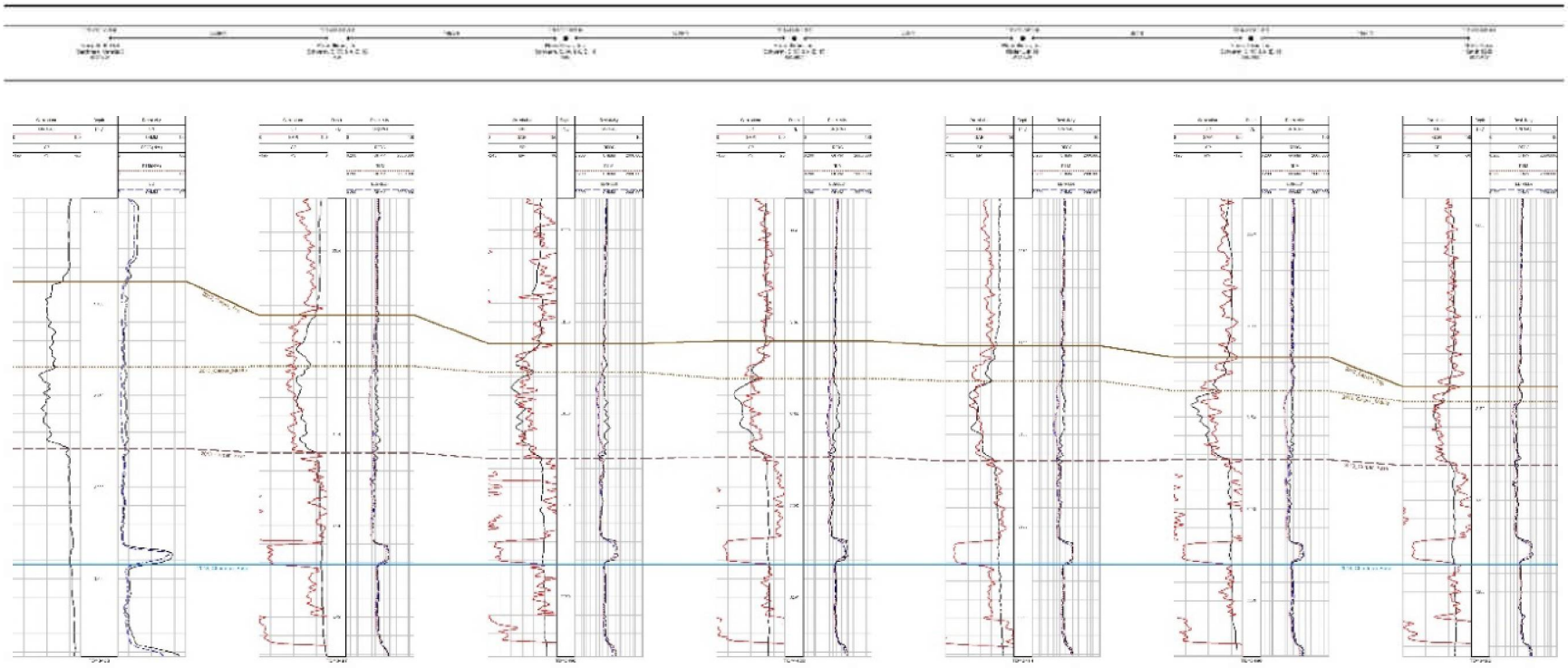

Figure 82 North-south cross section through St. James Field (Figure 80). The Carper sandstone itself appears to contain a single consistent break on the logs, generally about two-thirds of the way up from the base of the unit, even as the gross thickness of the Carper thins from the north (left) to the south (right). The break does not appear significant and as such the Carper was mapped as a single unit in the study area (Figure 83). Stratigraphic datum is the base of the Chouteau Limestone.

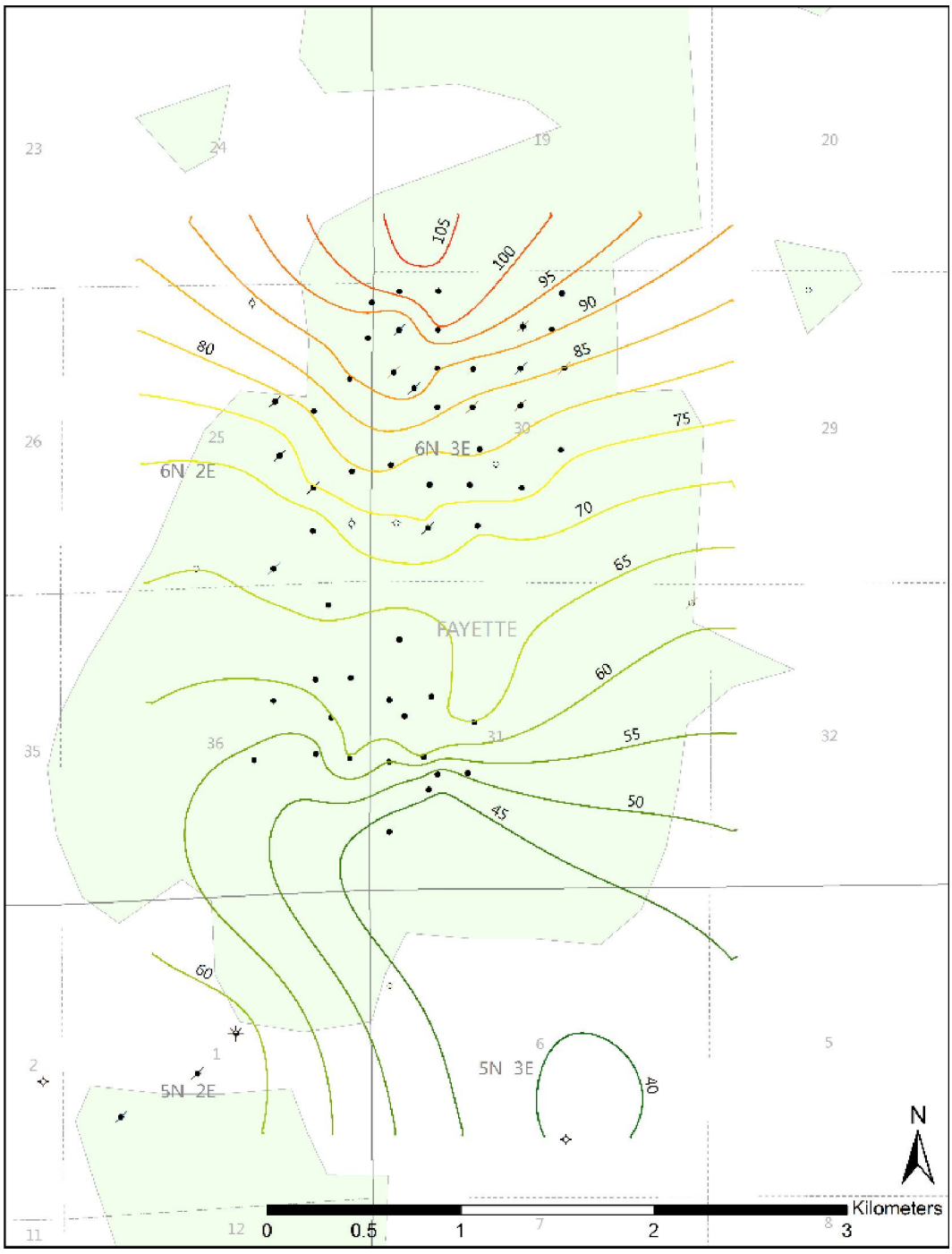

Figure 83 Gross thickness map of the Carper sandstone. Regular thinning of the Carper from north to south is shown as the formation gets progressively more distal from its sediment source at the shelf edge. Contour interval is 1.5 m (5 ft).

Reservoir Lithology and Petrology

Four cores that penetrate the Carper sandstone were described from oil fields in the vicinity of St. James Field. Some old core descriptions were also available for cores that were taken early in the development of St. James Field, but are no longer available. The lithologies and sedimentary structures observed were very similar amongst all the core. Texturally, the Carper consists of very fine-grained sandstone interbedded with silt and shale. Planar bedding, flame structures, and shale rip-up clasts are common. The sandstone is almost always calcareous, exhibiting a slow dolomitic reaction. The two most common minerals identified in thin sections of the Carper sandstone in the St. James Oil Field are extremely fine-grained quartz and dolomite cement (Stevenson, 1964).

Porosity and Permeability

In the productive portions of the Carper D sandstone, core measured porosities commonly range from 13 to 18%. Permeabilities are very low and usually average only about 9.86×10^{-12} cm^2 (1 md). Fracture treatments with several thousand gallons of water and several thousand pounds of sand are typical completion practices in producing intervals.

A number of cores were taken from the Carper sandstone early in the development of St. James Field. No continuous cores remain today, but laboratory analyses of Carper sandstone core from five wells in the area were available. This data amounted to 89 core analysis data points from the Carper. Data analysis of the five total cores from the Carper sandstone showed that porosity ranged from 2.8 to 21.0% with an average of 13.2%. Permeability values from these same samples ranged from 0 to 2.76×10^{-10} cm^2 (0 to 28 md) with an average of 1.35×10^{-11} cm^2 (1.37 md).

Reservoir Connectivity and Compartmentalization

Examination of Carper sandstone core from central Illinois and logs in St. James Field indicates that, as a reservoir, the Carper likely has better lateral communication than vertical communication. Core studies indicate well defined graded bedding, with repeating fining upward sediment packages as thin as about 10 cm (3.94 in.) or so. These regular, horizontal shaly interbeds are likely laterally persistent over large areas given the nature of the mode of deposition. Geophysical log responses in the Carper show numerous thin shale breaks within the sandstone interval. While these breaks are not significant enough features to be reliably correlated around the field, they are a common feature of all wells.

Depositional Environment

The Carper sandstone in St. James Field was most likely deposited as a mud/sand-rich submarine fan; a type of turbidite deposit (Reading and Richards, 1994; Figure 84). This interpretation supports the work of researchers who had previously interpreted the Carper as such. The generally fine-grained, mud-rich lithology that makes up the Carper is consistent with what would be expected in a cratonic basin setting with a large fluvial input (Bouma, 2000). The very fine-grained sand to silt texture of the Carper indicates that the sediment followed a long transport route along a low gradient fluvial system in which coarser sediment was left behind before its deposition along the shelf edge and later remobilization as a submarine fan (Bouma, 2000). Carper sandstone bodies occur within the Borden Siltstone with grain sizes up to very fine sand being most common.

The Carper sandstone represents the turbidite deposits of a basin floor fan, deposited as part of the lowstand systems tract. The Carper unconformably overlies hemipelagic mud deposits of the Springville Shale along a sequence boundary.

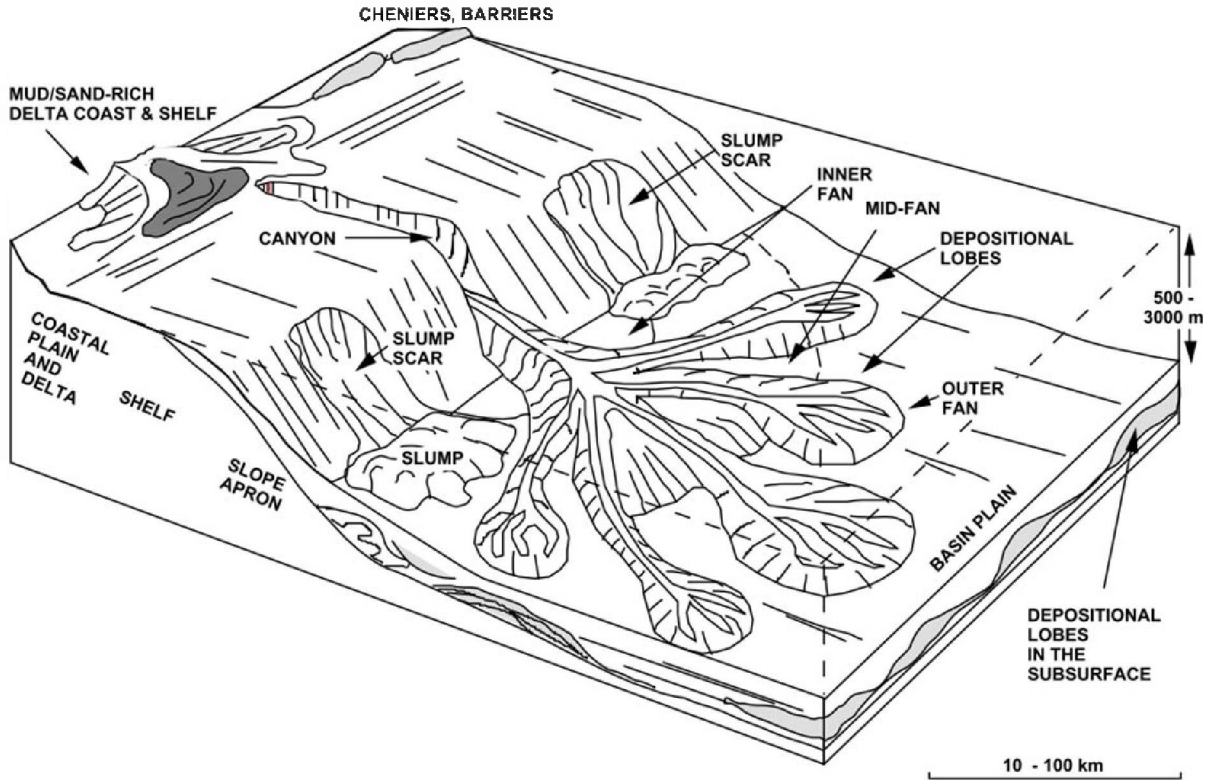

Figure 84 Depositional model of a mud/sand-rich submarine fan (after Reading and Richards, 1994). The Carper D sandstone at St. James Field is thought to be quite proximal to the point-source of sediment for the fan and thus would be positioned in the vicinity of the inner fan. Within the Carper D lobe, but more distal from the source, the reservoirs may become more compartmentalized. This is likely because the more distal fan area would receive fewer pulses of coarser grained sediment. The coarser reservoir sediment would also be separated by thicker silts and muds.

Turbidites are associated with clastic deposition in deeper-water submarine settings, such as continental shelves and slopes. Turbidity currents are a means of transporting large amounts of clastic sediments into these deeper-water submarine environments beyond deltaic settings. Clastics deposited by turbidity currents were described initially by Bouma (1962), who recognized five distinct divisions in cyclic sediments deposited by turbidity currents. These deposits are typically called Bouma Sequences (Figure 85). An erosional contact is part of the lowermost unit in the cycle, commonly made up of conglomerate that is usually in a sandy matrix. The second division in the cycle is plane parallel, bedded coarse- to medium-grained sandstone, followed by cross-bedded sandstone and then ripple-bedded sandstone or silty sandstone. The sequence is capped by the fifth and final division of parallel laminated siltstone and shale. The five divisions in this fining-upward sequence are usually designated by letters A, B, C, D, and E from bottom to top. The vertical succession of sedimentary structures with an overall fining-upward sequence is typically deposited by turbidity currents that can carry large

amounts of clastics in suspension. The first sediments deposited are the coarsest grained component of the sediment load and are deposited during the highest energy flow regime. As the energy of the turbidity current gradually dissipates, increasingly finer grained clastics are deposited with very fine-grained sand and silt being deposited in cycle D under low energy regime conditions. The finest grained clay-sized clastics are deposited in the final waning phases of very low energy, resulting in the entire Bouma Sequence being capped by shale laminae of the E division. Complete Bouma Sequences containing all five divisions are rare.

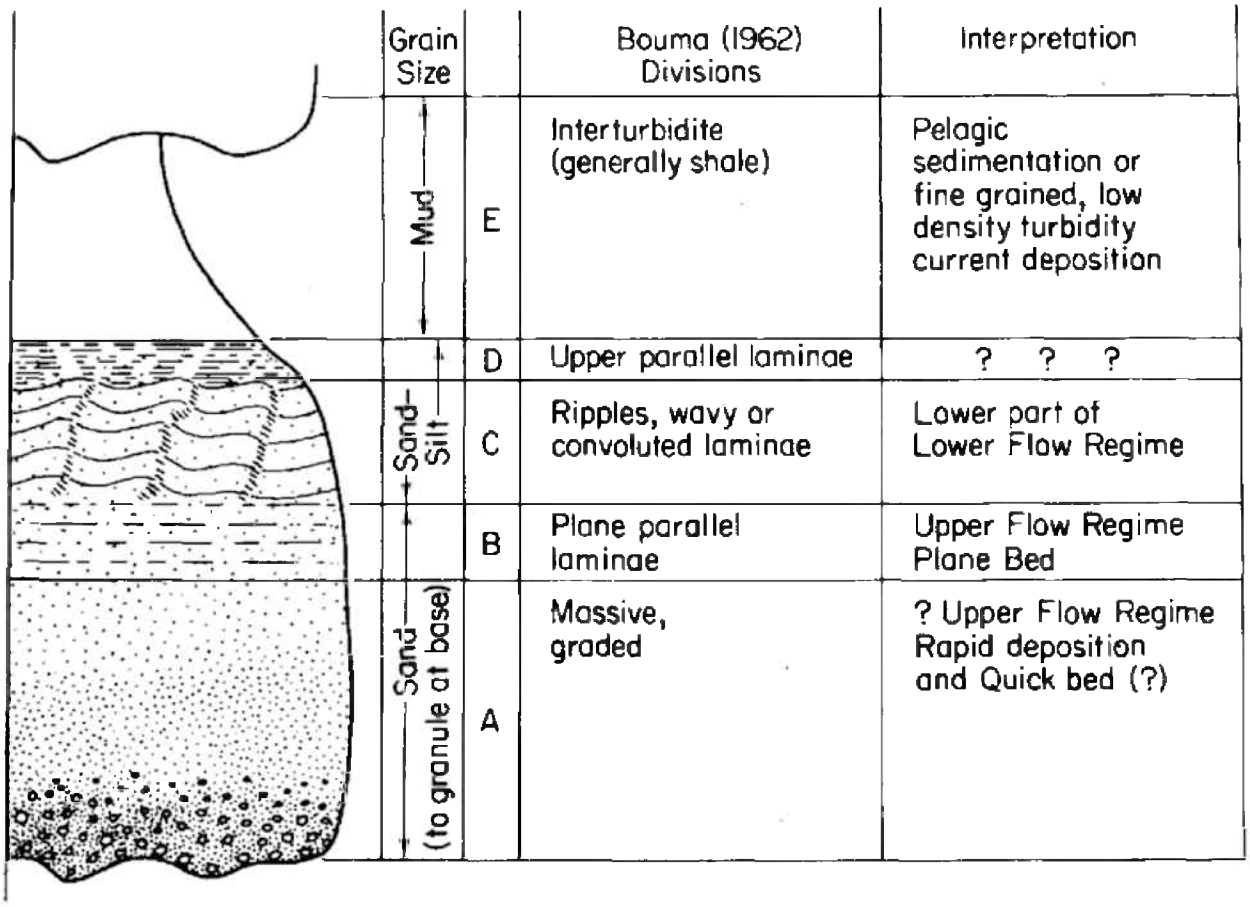

Figure 85 Idealized Bouma Sequence showing the five divisions with interpretations for each. Some of the lower divisions are commonly missing in turbidite deposits of the Carper sandstone (after Middleton and Hampton, 1973).

It is common for the lower divisions in the Bouma Sequence to be missing. This was the case of core from the Carper sandstone for the studies completed by Lineback (1966; 1968) and Stevenson (1964), as well as those currently available near St. James Field from the Shell Oil C. C. Ford #1 well (API 120510174800) in Section 31, T5N, R3E, in Fayette County, Illinois (Figure 86). The lowermost A division that would contain sole marks at the erosional contact and coarse-grained conglomerates in the classic Bouma cycle is missing. However, sedimentary structures, such as parallel laminated fine-grained sandstone, shale clasts, and graded bedding associated with the B, C, and D divisions of the Bouma sequence, are present in Carper sandstone core near St. James Field (Figure 87a and 87b). The core is underlain by the black

Springville Shale (Figure 86, Figure 87a, and 87b). The cored interval of the Shell Oil C.C. Ford #1 is shown on the log in Figure 86. The Carper D sandstone in this well is approximately 12 m (40 ft) thick. Only core from the lower 2 m (8 ft) of the sandstone was available; the lowest portion of the sandstone is made up of extremely fine-grained sandstone and silt that is separated from the main body of the Carper sandstone by a two foot interval of laminated shale and alternating shale and siltstone. Most of the core is the Springville shale that underlies the Carper sandstone, where there is an erosional contact. The presence of larger rip-up clasts of consolidated rock, flame structures, and sharp upper contacts with finer grained intervals (Figure 87a and 87b) are also indications of mass grain flow, which is also associated with deeper-water sedimentation.

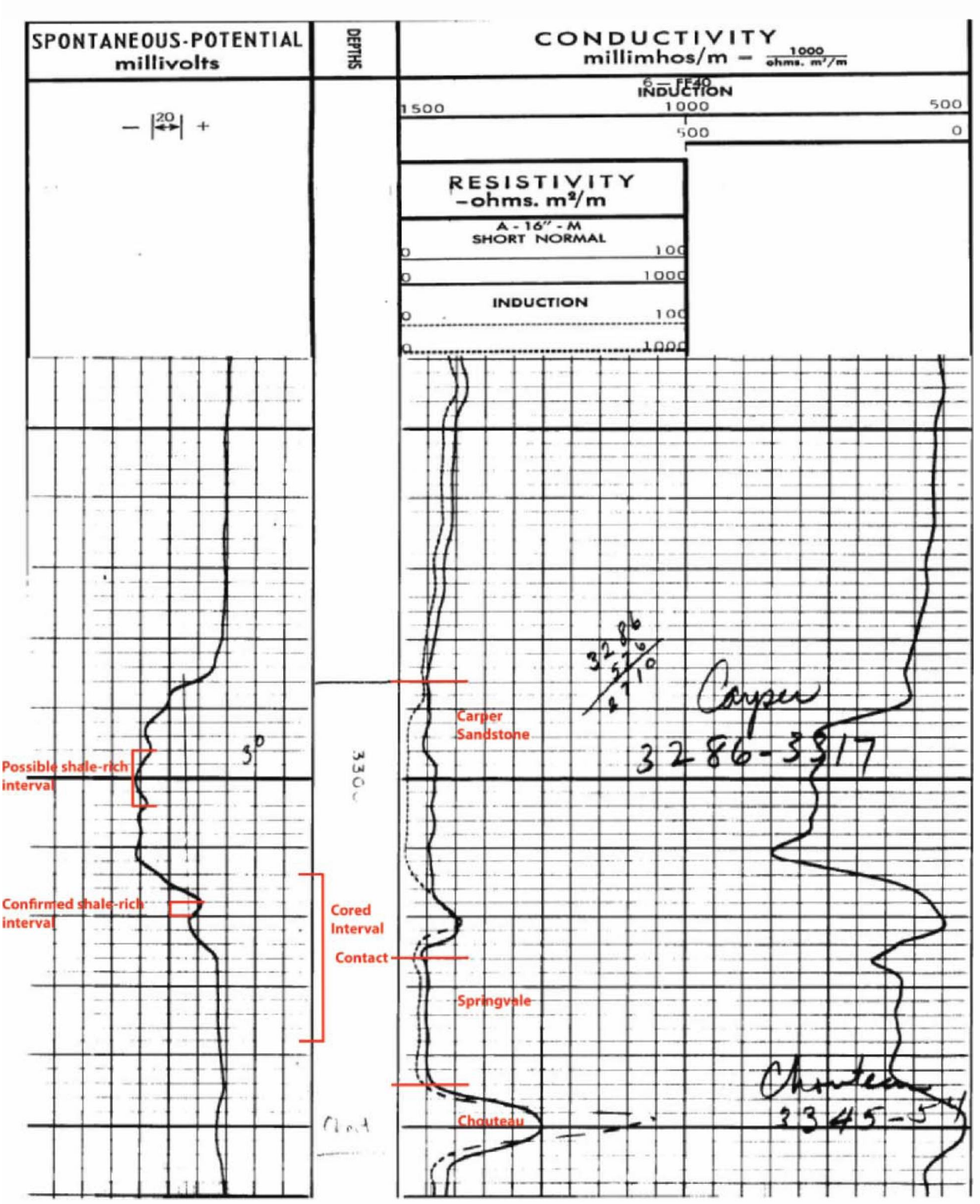

Figure 86 Geophysical log from Shell Oil C. C. Ford #1 Fayette County. Cored interval is of the lower most portion of the Carper Sandstone, and it consists mostly of underlying shale. There is a 0.61-m-thick (2-ft-thick), shale-rich interval separating the lowest very fine-grained sandstone to siltstone.

120510174800 – 31-5N-3E, Fayette Co., C.C. Ford #1, Core Number 14421, Depth 3314-3338'

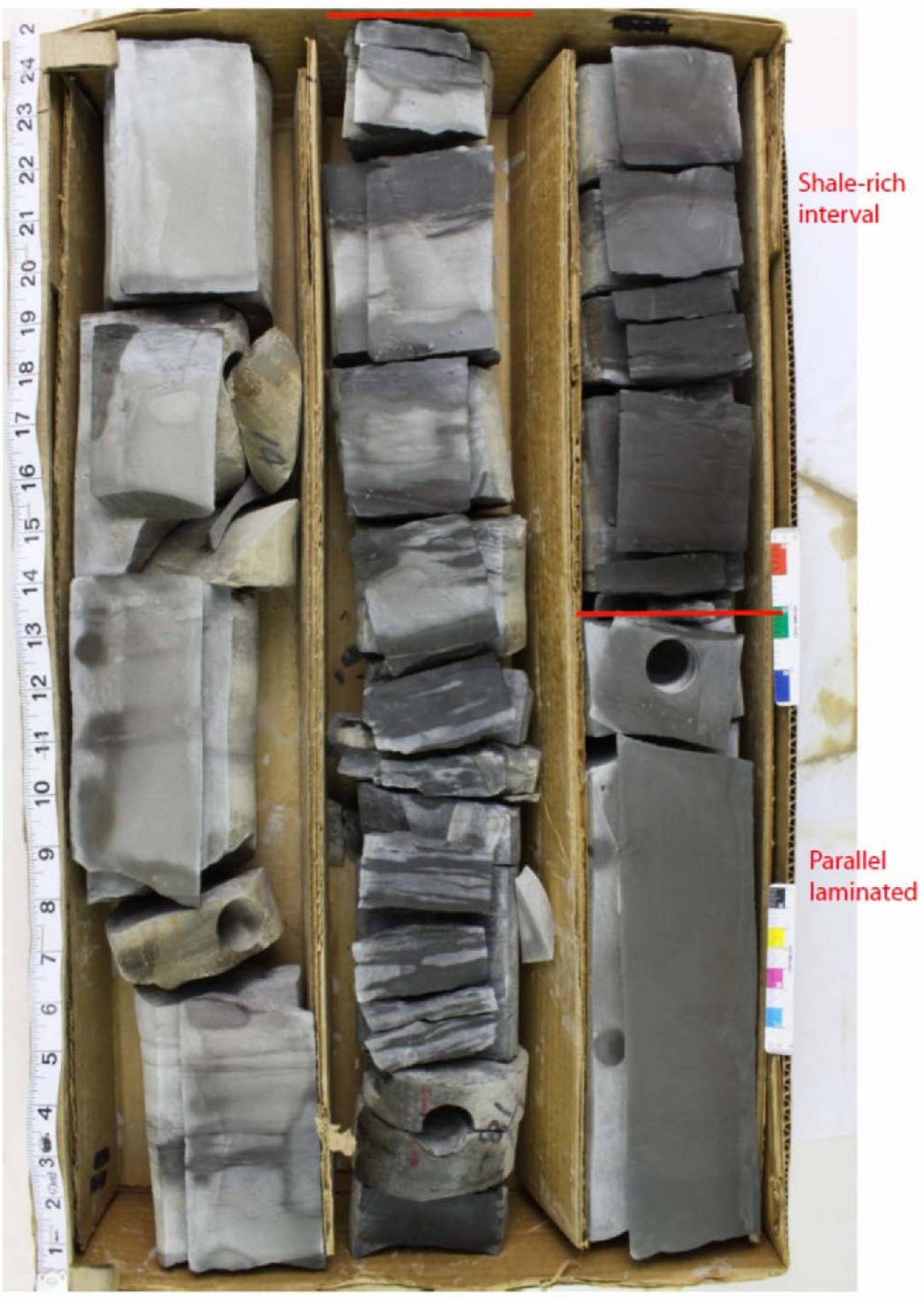

Figure 87a Core from Shell Oil C. C. Ford #1 Well taken at a depth of 1,010–1,012 m (3,314–3,320 ft). The top of the core is in the upper left and the bottom is in the lower right. The photograph shown is of Illinois State Geological Survey core. The center column and top right column within the red lines are the shale-rich interval. The bottom right column below the red line shows the parallel lamination.

Figure 87b Core from Shell Oil C. C. Ford #1 well Fayette County taken at a depth of 1,010–1,012 m (3,314–3,320 ft). The top of the core is in the upper left and the bottom is in the lower right. Some small shale interclasts can be seen within the sandy intervals. The photograph shown is of Illinois State Geological Survey core. The red line marks the contact spot noted on the geophysical log in Figure 86.

Comparison of Illinois Basin Formations to Formations in Other US Basins

The ILB is an interior cratonic basin with the following factors influencing siliciclastics deposition and carbonate accumulation in potential host reservoirs for CO_2 storage: gentle low gradient sea floor, low rate of subsidence relative to the rate of sedimentation, and a thin vertical interval to accommodate influxes of sediment. These conditions are in large part responsible for the distribution, geometry, size, compartmentalization and complexity of reservoirs in the ILB. Other interior cratonic basins in the United States with similar reservoir characteristics include the Williston, Michigan and Forest City basins. Most of the 36 basins identified in the United States by the United States Geological Survey (USGS), while not categorized as interior cratonic basins, exhibit similar depositional environment settings. These basins have numerous sandstone and carbonate reservoirs that were deposited in fluvial and alluvial to submarine environments that are potential candidates for CO_2 storage. The basin type is not a major criterion in selecting reservoirs for CO_2 storage. However, basin type does play a role in reservoir complexity and scale, including lateral and vertical extent of reservoirs available for CO_2 storage. Sandstone and carbonate reservoirs in some US basins and their depositional environments will be compared to those in the ILB. In general, CO_2 storage has the potential to be broadly applied to many reservoirs in the United States. The main factor influencing successful application of CO_2 storage is adapting to specific conditions of individual reservoirs. Detailed reservoir characterization and knowledge of individual reservoir geometries, boundaries, compartments, and potential barriers to fluid flow are important in determining suitability of reservoirs for CO_2 storage.

The USGS Geologic Carbon Dioxide Storage Resources Assessment Team (2013) identified 36 US basins that have potential for CO_2 storage in clastic and carbonate formations. The USGS assessment provides a detailed analysis of the methodology developed and used by its researchers to estimate approximate storage capacities in each of the identified 36 US basins. Figure 88 lists the basins in the United States and the USGS estimate of their individual potential CO_2 storage capacities. The Illinois Basin has one of the highest potential CO_2 storage capacities in the United States (Figure 88).

A map of the eight major US regions and the basins included in these regions is shown in Figure 89. Virtually all of the basins contain formations with depositional environments that are similar to the depositional environments of one or more of the ILB reservoirs discussed in the report presented here. According to NETL (2010b), studies of reservoirs attributed to the following depositional environments have been completed in earlier Phase II, Phase III and American Recovery and Reinvestment Act programs: fluvial, fluvial deltaic, shelf carbonate, reef, shelf clastic, fluvial and alluvial, strandplain/barrier island, and turbidite (Table 3).

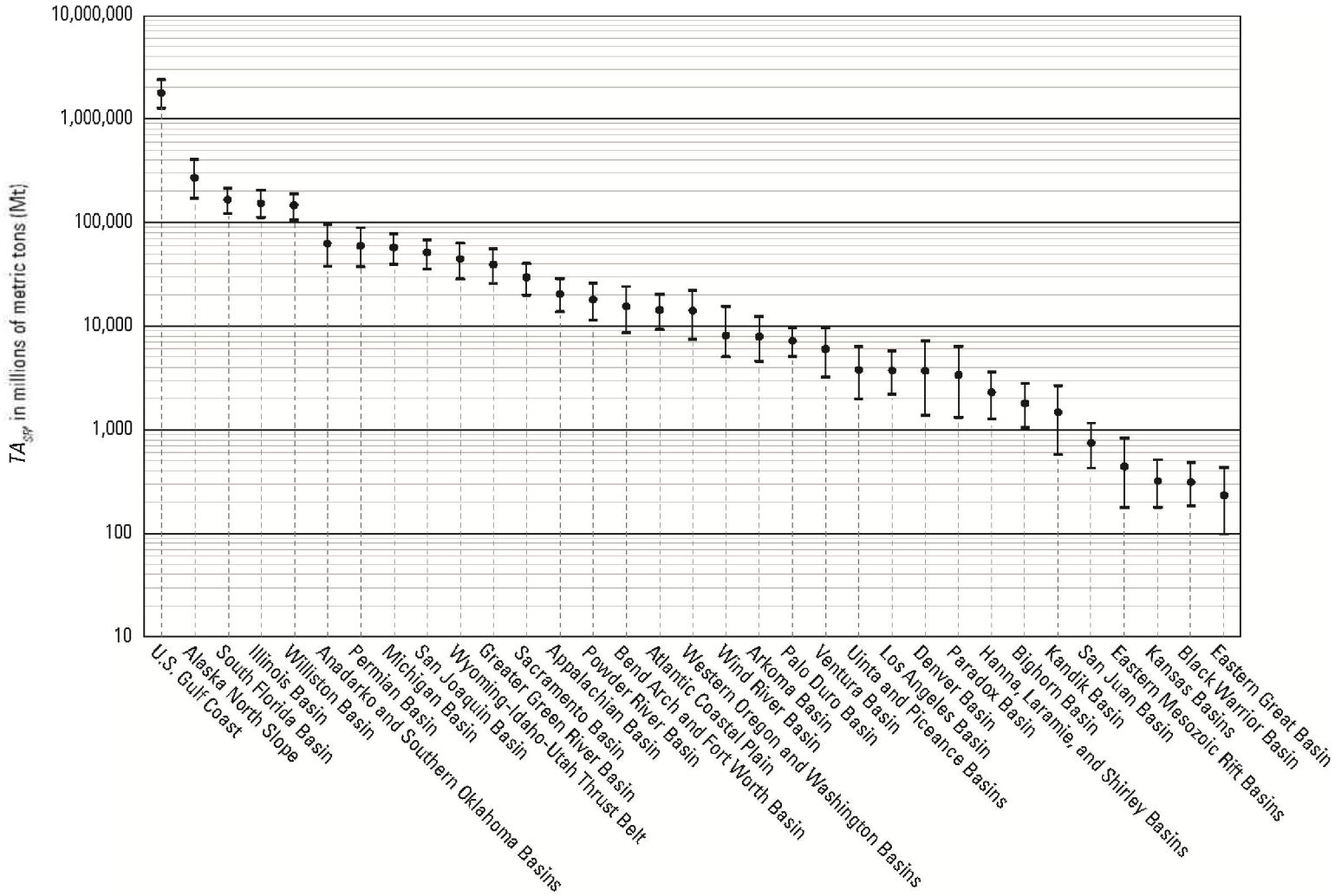

Figure 88 Estimated ranges of technically accessible CO_2 storage resources (TA_{SR}) in tonnes (Mt) for evaluated basins in the United States (USGS, 2013; base map from Jarvis, 2008). Center dots represent the mean estimate. The lower boundary represents the P_5 percentile and the upper boundary represents the P_{95} percentile.

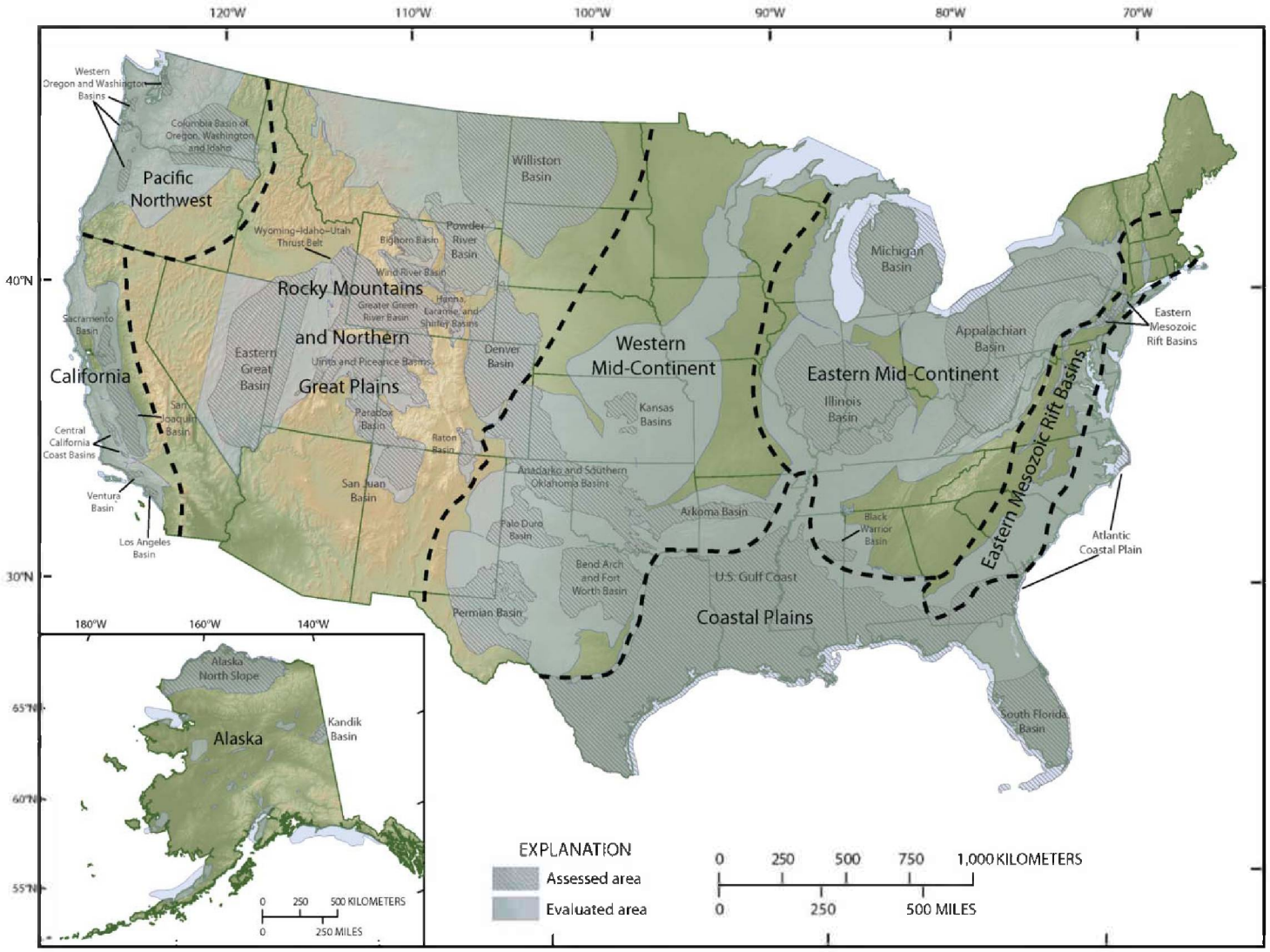

Figure 89 Map of the United States that shows regions evaluated as CO_2 storage resources (USGS, 2013).

Table 3 Examples of some US basins or geologic areas and the associated formations that are covered in this comparison according to the DOE depositional formation classification.

Formation Class	Formation(s) and Groups	Region	Formation Class	Formation(s) and Groups	Region
Shelf Clastic	Tapeats Sandstone	Colorado Plateau	**Strandplain**	Mt. Simon; St. Peter	Illinois Basin
Shelf Clastic Shelf Carbonate	Hamilton; Martinez	Sacramento Valley Basin		Fleming Group	Gulf of Mexico Basin
	Desert Creek; Ismay	Paradox Basin		Pico; Puente	Los Angeles Basin
Shelf Carbonate Fluvial Deltaic	Naco; Martin	Colorado Plateau		Pottsville; Parkwood; Hartselle	Black Warrior Basin
	Knox	Michigan and Illinois Basins		Dakota; Entrada	Green River Basin
	Arbuckle	Ozark Plateau		Tensleep	Rock Springs Uplift
	Bangor; Tuscumbia	Black Warrior Basin		upper Mt. Simon	Michigan Basin
	Madison; Bighorn	Powder River Basin	**Reef**	Cisco-Canyon	Permian Basin
	Paluxy; Tuscaloosa	Gulf Coast Basin	**Fluvial and Alluvial**	Tuscaloosa	Gulf Coast Basin
Fluvial Deltaic	Domengine	Sacramento Valley Basin		Stockton; Passaic	Newark Basin
	Fleming Group	Gulf of Mexico Basin	**Turbidite**	Fleming Group	Gulf of Mexico
				Puente	Los Angeles Basin

The chart in Figure 88 shows the range estimated by the USGS for technically accessible storage resources of CO_2 in each of 36 assessed US basins. Estimates are in millions of tonnes. According to this chart, those basins with the greatest CO_2 storage capacity in descending order are the US Gulf Coast, Alaska North Slope, South Florida Basin, Illinois Basin, Williston Basin, Anadarko and Southern Oklahoma Basins, Permian Basin, Michigan Basin, San Joaquin Basin, Wyoming-Idaho-Utah Thrust Belt, Greater Green River Basin, Sacramento Basin, Appalachian Basin, Powder River Basin and the Bend Arch and Fort Worth Basin (Table 4; USGS, 2013).

Sources of information used to describe some examples of sandstone and carbonates deposited in various depositional environments in basins across the United States include the USGS basin assessments for petroleum resources. The USGS completed assessments of conventional oil and gas resources in all US basins in 1995. These assessments were updated starting in 2002 to include unconventional and under developed resources. Some of the information in this section is from the series on National assessment of United States oil and gas resources published in 1995 by the USGS (Gautier et al., 1995). Each basin or province in the United States was treated separately and published in a series for a national assessment of oil and gas resources in the United States. Many of the individual reports on each of the 36 basins in the United States discuss and identify depositional environments for some of the major producing horizons and potential producing strata as reported in previous studies. These reports are useful in identifying major categories of depositional environments and are most appropriate when used on an individual field or small-scale basis because depositional environments can change or transition within the same formation over lateral, vertical distances, or both. Additional information for this compilation was gathered from the series of atlases published in the 1990s, cataloguing the major gas reservoirs in US basins (Bebout 1992, 1993; New Mexico et al., 1993). The emphasis of these atlases is on the major gas-producing carbonate and sandstone reservoirs in the United States.

Descriptions of some sandstone and carbonate reservoirs deposited in various depositional environments in basins across the United States are given in the following sections. These descriptions include reservoirs in noncratonic basins representative of regions across the United States, including the Alaska North Slope, South Florida Basin, mid-Continent Basins US, Gulf, Rocky Mountain Basins and California Basins. Descriptions of reservoir sandstones and carbonates in cratonic basins and their depositional environments are also included in the following sections.

Table 4 Example list of 13 basins from the USGS (2013) evaluation of US basins showing formations with the greatest capacity for CO_2 storage.

Assessment Unit	Formations and Groups
US Gulf Coast	Norphlet Formation; Smackover Formation; Haynesville Formation; Sligo and Hosston Formations; Cotton Valley Group; Rodessa Formation; James Limestone; Frederickson Group; Rusk Formation; Washita Group; Tuscaloosa and Woodbine Formations; Navarro; Taylor and Austin Groups; Carrizo Sand and Wilcox Group; Queen City Sand; Yegus and Cockfield Formations; Frio and Vicksburg Formations; Lower, Middle, and Upper Miocene
Alaska North Slope Basin	Endicott Group; Beaufortian and Ellesmerian Formations; Lower Torok Formation
South Florida Basin	pre-Punta Gorda; Gordon Pass and Marco Junction Formations; Cedar Keys and Lawson Formations
Illinois Basin	Cambrian Mt. Simon Sandstone; Devonian- and Silurian-age formations
Williston Basin	Deadwood and Black Island Formations; winnipegosis Formation; Interlake Formation; and the Bighorn Group; Three Forks Formation and the Jefferson Group; Kibbey Formation; Madison Group; Minnelusa Group
Anadarko and Southern Oklahoma Basins	Lower Paleozoic Groups; Hunton Group and Misener Sandstone; Mississippian units; Lower Virgilian; Chase and Council Grove Groups
Permian Basin	Lower Paleozoic strata; Permian units
Michigan Basin	Ordovician and Cambrian; Salina Group; Middle Silurian Composite
Wyoming-Idaho-Utah Thrust Belt	Paleozoic strata; Nugget Sandstone
Greater Green River Basin	Paleozoic strata; Nugget Sandstone; Hilliard; Baxter and Mancos Shales; Mesaverde Group
Sacramento Basin	Winters Formation; Starky Sands of the Moreno Formation; Mokelumne River Formation
Appalachian Basin	Ordovician and Cambrian strata; Clinton; Medina and Tuscarora Formations; McKenzie; Lockport; Newburg Formations
Powder River Basin	Minnelusa and Tensleep Sandstone; Fall River and Lakota Formations; Frontier Sandstone; Turner Sandy Member; Parkman Sandstone Member

Noncratonic Basins

Eastern US Gulf of Mexico Coast (US Gulf Coast)

There are numerous plays in a wide variety of depositional environments in the central and eastern coast of the Gulf of Mexico. One major play is the Upper Miocene of the Louisiana Gulf Coast, where there is a series of major sandstone reservoirs interpreted as proximal deltaic and distal deltaic sandstones. The Upper Miocene proximal deltaic sandstone reservoirs have significant potential storage capacity and are characterized by thick sandstones separated by much thinner intervals of shale. Pennsylvanian Bridgeport B sandstone reservoirs in the ILB are commonly proximal deltaic deposits that show tidal influence. Iola Field has proximal deltaic sandstone reservoirs in the Benoist sandstone.

Reservoirs in the Frio Sandstone of the Louisiana Gulf Coast have also been interpreted as distal–deltaic and slope depositional environments. These deposits share similarities with the ILB Mississippian Carper Sandstone that is being modeled at St. James Field. The Carper Sandstone is interpreted as turbidite, although it has some characteristics of submarine channels. Reservoirs in the Cockfield Formation are interpreted as marine-shelf sandstones. Sandstones in the Cockfield are relatively thin for the US Gulf Coast and are discontinuous and locally distributed. This results in facies changes that control the distribution of reservoirs. These characteristics are similar to those found in shelf sandstones of the Cypress Formation in Lawrence Field in Illinois.

Reservoir sandstones in the Wilcox Group of Louisiana and Mississippi have been interpreted as being deposited in fluvial, deltaic and shallow marine environments. Fluvial and deltaic processes deposited reservoirs composed of very fine- to fine-grained sandstone. Reservoirs in the fluvial and deltaic subplay are generally found in narrow, elongate sand bodies. These sandstones are locally distributed and have been interpreted as channel and chenier sandstones deposited on a delta plain (Galloway, 1968). The ILB upper Mt. Simon sandstones are categorized, in part, as strandplain deposits. The strandplain has similar depositional characteristics to chenier plain deposits, although the chenier muds and organics are not present.

Reservoir sandstones in the Wilcox shallow marine sandstone subplay are composed of very fine- to fine-grained sandstones. Some reservoirs in this subplay were deposited in offshore bar complexes, which vary from poorly sorted lower shoreface sandstones to well-sorted upper shoreface deposits.

Cretaceous Plays

Austin-Taylor-Navarro Groups form a shallow marine sandstone subplay. These Upper Cretaceous strata were deposited in open marine or shelf conditions.

The Upper Tuscaloosa shallow marine sandstone is another Cretaceous subplay that was deposited in shallow seas during transgressive and regressive cycles. Reservoir sandstones are composed of fine- to medium-grained sandstone that may be locally glauconitic. Illinois Basin Cypress Sandstone tidal shoals at Lawrence Field were deposited on the shallow shelf, similar to these Cretaceous depositional settings.

The Lower Tuscaloosa fluvial to shallow marine sandstone is another Cretaceous play. Reservoir sandstones in the Lower Tuscaloosa in Mississippi and Louisiana were deposited in major fluvial-deltaic systems. Subplays include the Lower Tuscaloosa updip fluvial-deltaic sandstones that were deposited in a fluvial system of meandering stream channels. There are also shallow marine facies in some Lower Tuscaloosa sandstone reservoirs. Pennsylvanian Bridgeport channel sandstones, like those at Lawrence Field, have fluvial characteristics that can be meander- or braided-type channel deposits. Sequence stratigraphic overprint can cause a complex relationship of both fluvial types and can juxtapose these with deltaic and shallow marine deposits.

The Hosston-Sligo Sandstone plays are located in the Mississippi Interior Salt Basin. Hosston sandstones were deposited in a wide range of depositional environments: tidal flat, fluvial, deltaic, prodelta, and nearshore marine. Reservoir quality siliciclastics change from gravel and coarse-grained sandstone in the north portion of the Interior Salt Basin to medium- to fine-grained sandstone in the south. Some of these reservoirs are fluvial-deltaic with fining upward sequences in logs and consist of medium-grained, cross-bedded sandstone. These thick sandstones have been interpreted as channel-fill alluvial deposits (Thomson, 1978). Fine-grained delta front and marine sandstone facies are located down dip of the coarse-grained reservoirs.

The Hosston Sandstone of north Louisiana and south Arkansas is another play that consists of siliciclastics deposited in fluvial-deltaic and shallow marine environments. Sandstone reservoirs in the Hosston Formation were formed in a terrigenous clastic wedge that thickens from Arkansas southward into Louisiana. Two major fluvial systems contributed to the clastic wedge, and the Hosston Formation in this play is thick. The primary reservoirs in the Cotton Plant Field, located in the North Louisiana Salt Basin, consist of fluvial-deltaic, fine- to medium-grained sandstones.

Trinity Group Carbonates are a play in the Sabine Uplift (located in north Louisiana and south Arkansas). Ooid and skeletal grainstones are carbonate shelf deposits in the Sligo and Rodessa formations of the Trinity Group. Porous carbonate grainstones are the primary reservoir facies in this play. Carbonate shelf ooid reservoirs are common in the Mississippian Ste. Genevieve formation in the ILB. The Trinity Group subplay in the North Louisiana Salt Basin includes various types of carbonate grainstone reservoirs in the Sligo Formation. Grainstone reservoirs in some fields such as the Panther Creek and Black Lake are made up of mollusk and ooid grainstones.

The Hosston Formation and Cotton Valley Group Sabine Uplift play consists primarily of siliciclastics. Reservoir sandstones in the Hosston Formation include fluvial and fluvial-deltaic deposits. Fluvial deposits include thick braided-stream sandstones that grade into deltaic and marine facies.

The Cotton Valley Group consists mostly of sandstones deposited in fluvial-deltaic facies that are part of the ancestral Mississippi River delta system. There are also areas of wave-dominated deltas and regions of shallow marine and nearshore marine sandstones, including barrier bar and strandplain deposits.

Jurassic Plays in the US Eastern and Central Gulf of Mexico

The Upper Jurassic shallow marine carbonate and sandstone play and the Upper Jurassic carbonate shallow marine play, including the Smackover, Buckner and Haynesville equivalents, are major reservoirs with large amounts of potential CO_2 storage capacity. The primary reservoir facies in these carbonate plays are ooid grainstones deposited in very shallow marine bar complexes. These reservoirs have similarities to ooid grainstones in the Mississippian Ste. Genevieve Formation in the ILB where the Johnsonville Field in Illinois is an example, where porosity is largely intergranular and burial depths are relatively shallow.

North Alaska Basin (Alaska North Slope)

According to the USGS assessment of the Northern Alaska Province (001), there are seven confirmed play types in the North Alaska Basin (Bird, 1998). One play is found in the Cretaceous and Tertiary reservoir rocks deposited in marine and nonmarine deltaic environments consisting of sandstone, siltstone, shale and conglomerate of the Nansushuk Group and Sagguaniktok Formation and uppermost parts of the Torok and Channing Formations. Reservoirs in these formations are sandstone and siltstone. Shoreline sandstones are found in the Mississippian Cypress and the Cambrian upper Mt. Simon sediments and are common in many of the clastic deposits in the ILB.

The Brookian turbidites are located in the Torok and Channing Formations and are composed primarily of marine shale and siltstone. Individual reservoirs are toe slope or basin plain turbidites. Reservoir bodies are relatively thin at 30.5 m (100 ft) or less and laterally discontinuous. Mississippian Carper Sandstones are interpreted to be turbidite sediments in the ILB.

The Barrow Arch Beaufortian Play is another major play in the North Alaska Basin. The Beaufortian sequence consists of Jurassic and Early Cretaceous sandstone reservoirs. The most important reservoir rocks are shallow marine shelf sandstones of the Kuparuk Formation, which are in the same category as some of the Mississippian Cypress Sandstones in the ILB.

The Barrow Arch Ellesmerian play consists of Mississippian to Triassic sandstone reservoirs and Mississippian and Pennsylvanian carbonates. The stratigraphic intervals included in the play are the Endicott, Lisburne, and Sadlerochit Groups; the Shublik Formation; and Sag River Sandstone. Sandstone reservoirs are more abundant than carbonate reservoirs with the most important occurring in nonmarine to shallow marine sandstones in the Sadlerchit Group.

Ellesmerian–Beaufortian clastics play consists of sandstone reservoirs Permian to Early Cretaceous age. These sandstones were deposited primarily in shallow marine environments with lesser amounts of fluvial sandstone and turbidite sandstone reservoirs. Fluvial sandstones are found in the ILB Pennsylvanian and Mississippian sedimentary rocks including Bridgeport and Cypress formations.

The Endicott play is made up of reservoir rocks in the Mississippian-age Endicott Group that consists of fluvial to shallow-marine quartzose sandstone and conglomerate.

The Fold Belt Play consists of Cretaceous and Tertiary sandstone reservoirs in the northern portion of the Brooks Range. Stratigraphic units in this play include the Nanushuk Group, the Torok, Sagavanirktok, and the Canning Formation. Sandstone reservoirs in these stratigraphic units represent deltaic, shallow marine and turbidite depositional environments.

South Florida Basin

Reservoirs in the South Florida Basin consist almost entirely of carbonates that range in age from the Upper Jurassic to the Lower Cretaceous. The Sunniland tidal shoal is one play type in the South Florida Basin. The reservoir facies in the Sunniland Formation consists of isolated fossil-shell hash (skeletal grainstones) in the warm shallow marine-shelf setting of the eastern portion of the basin during the latter part of the Early Cretaceous. These shoal mounds were later subareally exposed and dolomitized. In the ILB, Assumption Field is a good example of a shallow marine-shelf, skeletal grainstone reservoir that is middle Devonian in age.

Williston Basin Madison (Mississippian) Play

The Williston Basin is a large interior cratonic basin located primarily in North Dakota, South Dakota, Montana, and Canada (Peterson, 1995). Most reservoirs are in carbonate sediments. The Madison play is the largest conventional reservoir unit in the Williston Basin. The play consists of intervals of porous carbonate reservoirs associated with argillaceous or nonporous lateral carbonate facies and overlain by evaporitic or argillaceous seals. Reservoirs in the Madison play are composed of both limestone and dolomite. In the Mission Canyon and Charles Formations, depositional environments include carbonate algal-oolitic, crinoidal or bioclastic banks similar to the Johnsonville Field oolitic shoals in the ILB.

The Red River (Ordovician) play is another significant play in the Williston Basin. Reservoirs are found in dolomite and dolomitic limestone bioclastic buildups and tidal-flat dolomites. Similar to the Devonian Geneva Dolomite shallow shelf dolomite found at Miletus Field in the ILB. The Red River (Ordovician) Play can be separated into several cyclic intervals.

Sandstone production in the Williston Basin is from the Pennsylvanian-age Tyler Formation. Siliciclastics in the upper unit of the Tyler Formation have been interpreted as being deposited as a barrier island complex in a prograding delta environment (Sturm, 1982). The Tyler Formation produces oil from barrier island as well as channel fill sandstones located in southwestern North Dakota.

Anadarko and Southern Oklahoma Basins

The Wolfcampian shallow shelf carbonate play includes carbonates in the Chase and Council Grove Groups. These are cyclically deposited dolomitized limestones in the Chase Group. Carbonate reservoirs in the Chase Group were deposited in nearshore, shallow-marine, and arid supratidal settings. Reservoir quality carbonates are composed of grainstones that contain algal-coated grains which have been extensively dolomitized.

Pennsylvanian and Mississippian Plays

Pennsylvanian-age plays in the Anadarko-South Oklahoma Basin include alluvial-fan and fan-delta siliciclastics, the Virgilian deltaic sandstone, the Desmoinesian fluvial-deltaic sandstone and shallow marine limestone, Atoka marine sandstone, the Morrow sandstone, and the Springer marine sandstone.

The Pennsylvanian alluvial-fan and fan-delta clastics in the Anadarko Basin are a time transgressive sequence of Early Pennsylvanian- (late Morrowian) through Early Permian- (Wolfcampian) age reservoirs that have been subdivided into three subplays, based on differences in lithology and petrophysical properties. Reservoirs were deposited as alluvial fans, fan deltas, or a combination of both, emanating from mountains in the Amarillo-Wichita region. Coarse clastics eroded from these mountains formed alluvial fans and fan deltas. Alluvial deposits in this subplay are similar to alluvial deposits at Manlove Field in the Lower Mt. Simon of the ILB. The Upper Morrow chert-conglomerate subplay is another subplay dominated by alluvial fan deposits. Alluvial fan reservoirs in this play are chert conglomerates that were deposited adjacent to the Amarillo-Wichita Mountains. The distribution of these deposits is erratic. Some of these conglomerates were deposited in distributary channels that are generally straight and have widths that rarely exceed 1.6 km (1 mi) (Shelby, 1980). Much of the porosity in these reservoirs is secondary and averages 14.5%. Permeabilities average 1.97×10^{-11} cm^2 (2 md). Porosity and permeability are limited by pore and calcareous cements and clays that plug pores.

The granite wash subplay consists of reservoirs derived from Precambrian granite eroded from the Amarillo-Wichita Mountains. There are both alluvial-fan and fan-delta deposits that are major reservoirs.

The Virgilian deltaic sandstone subplay contains reservoirs deposited during a period of repeated regressions and transgressions in the Late Pennsylvanian. A siliciclastic wedge was deposited during each regressive period. The Tonkawa is a major reservoir in this play and was deposited in a deltaic complex that forms well defined delta lobes (Busch, 1974).

The Missourian shallow marine sandstone subplay consists of sandstone reservoirs deposited on an open-marine shelf as linear sand ridges or offshore bars and has been interpreted as subtidal ridges with inter-bar areas of depressions and intertidal flats separating bars (Baker, 1979). Isopach maps of sandstone bodies show a series of subparallel elongate sand bodies oriented in a northeast-southwest direction. The Cypress Sandstone reservoirs at Lawrence have similar characteristics.

The Pennsylvanian-age Desmoinesian fluvial-deltaic sandstone and shallow marine limestone play is divided into two subplays: the Lower Desmoinesian fluvial-deltaic sandstone and the Upper Desmoinesian shallow marine limestone. Most of the reservoirs in the Lower Desmoinesian subplay are located in the Cherokee Group and were deposited in a fluvial-deltaic depositional system that existed across much of the Anadarko Basin. Deltas prograded into the basin from the southwest.

The Morrow Sandstone in the Anadarko Basin and Hugoton Embayment is divided into three subplays: (1) the Lower Morrow shallow marine sandstone, (2) the Upper Morrow fluvial and deltaic sandstone and (3) the Upper Morrow estuarine and shallow marine sandstone. The Lower Morrow shallow marine sandstone subplay contains the greatest number of reservoirs in the Morrow Sandstone. Lower Morrow sediments were deposited on an unconformable eroded surface that was exposed and eroded before deposition of the Morrow Sandstone. Reservoir

quality sandstones in the Lower Morrow have been interpreted as marine siliciclastics deposited following a major transgressive event. Beach, barrier island, and offshore marine facies occur in the Lower Morrow.

Reservoirs in the Upper Morrow fluvial and deltaic sandstone subplay consist primarily of valley fill sandstones. Some of these reservoirs resemble the fluvial channel-fill reservoir in the Bridgeport Sandstone in Lawrence Field in the Illinois Basin.

The upper Mississippian Chester shallow marine carbonate play is located in the Anadarko Basin and the Hugoton Embayment in Kansas. These carbonates were deposited on a shallow marine shelf where ooids and grainstones were deposited under high energy conditions. These elongate bars are composed of ooid grainstone; intergranular porosity is developed within the bars. They are interpreted as being deposited in a belt of tidal bars oriented perpendicular to the shelf edge. These elongate bars are similar to the Ste. Genevieve reservoir in the Johnsonville Field; however, they are much larger than the oolite shoals found in the ILB.

Rocky Mountain and Northern Great Plains

This region contains numerous basins with carbonate and sandstone formations that have large capacities for CO_2 storage. These basins include the Powder River, Bighorn, Wind River, Greater Green River, Uinta, Paradox, Denver, and San Juan. Much of the Cretaceous interior seaway is also located in the Rocky Mountain and Northern Great Plains region.

Carbonates of the Mississippian Madison Group are a major host of reservoirs in the central Rocky Mountain region. Cyclic shallow marine carbonate deposition of the Madison Group developed on a carbonate ramp that was more than 644 km (400 mi) wide and 1,529 km (950 mi) long. The Madison Group is a regressive unit that progrades from east to west; facies represent a shallow marine environment that became more restrictive through time. The Whitney Canyon-Carter Creek Field shows a continuum of facies from open marine shelf to shoal to subtidal-inner shelf and finally to evaporitic mud flat, the most landward facies. The main porosity zone encompasses shoal through inner shelf facies similar to those found in the ILB Ste. Genevieve play and the Geneva Dolomite at Miletus Field.

Denver Basin

The major reservoir horizons in the Denver Basin include the Sussex (terry) and Shannon (Hygiene) Sandstones, Codell Sandstone, Niobrabra Chalk, D Sand, and the Muddy (J) Sand. The Cretaceous Sussex and Shannon Sandstones are major reservoir units in the Pierre Shale Formation in the Denver Basin and the Power River Basin. The Pierre Shale was deposited in an epicontinental sea that covered large portions of the Great Plains States. The Sussex (Terry) member and the Shannon (Hygiene) member both consist of marine shelf deposits composed of upward coarsening sequences of interbedded sandstones, siltstone and shales. They were deposited in a north-south trending complex of shallow marine bars. The best reservoir qualities are found in cross-bedded, fine- to medium-grained offshore marine bars, deposited in the high energy, upper portion of offshore marine deposits. These reservoirs resemble the Cypress Sandstone reservoirs at Lawrence Field as do other areas of the ILB, although the Cypress has more tidal characteristics than the Sussex and Shannon sandstones.

The Lower Cretaceous Muddy (J) Sandstone is a major reservoir unit in the Denver Basin and the Powder River Basin. The equivalent of this sandstone is found throughout most of the area covered by the Cretaceous epicontinental sea. The J sandstone in the Denver Basin has been divided into two sandstone members, the Fort Collins and the Horsetooth. The Fort Collins member is a fine-grained, upward-coarsening sandstone deposited in delta front and nearshore marine environments. The overlying Horsetooth member is composed of fine- to medium-grained, well-sorted, cross-bedded sandstones that were deposited in fluvial and estuarine channels. A major sequence boundary separates these two members causing unrelated depositional environments to be juxtaposed. This is a very common occurrence in the ILB, particularly in the Mississippian Cypress Formation and Pennsylvanian Bridgeport deposits found in Lawrence Field.

San Juan Basin

There are six plays in the San Juan Basin are mostly located in New Mexico. These plays include the Fruitland Formation, Pictured Cliffs Formation, Mesaverde Group, Gallup, Tocito and Mancos Formations, and the Dakota and Dakota-Morrison Formations. Reservoirs in the Pictured Cliffs Formation were deposited in a coastal barrier island environment during the Late Cretaceous. The lower Pictured Cliffs Sandstone contains mudstone and upward coarsening sandstones interpreted as shelf muds and shoreface sands. Sandstone reservoirs in the Upper Pictured Cliffs Formation have a blocky pattern response in well logs. Reservoirs are interpreted as being deposited in a wave-dominated delta as barrier-strandplain facies.

The Mesaverde Group is a play in coastal barrier island sandstones. Major reservoirs in the Mesaverde Group were deposited in coastal barrier bar and beach ridge environments. These depositional environments are common to the ILB depositional settings. The Benoist sandstone at Iola Field displays many of these siliclastic depositional settings. The previously mentioned Cypress and Bridgeport sandstones are similar to many of these Cretaceous and Jurassic sandstones and their related depositional settings. The Upper Mt. Simon at Manlove Field displays coastal depositional environments, including barrier-strandplain, while the Lower Mt. Simon has fluvial braided stream deposits similar to the Morrison Formation.

Dakota and Dakota—Morrison Formations

The Dakota and Morrison Formation play in the San Juan Basin consists of sandstone reservoirs deposited in fluvial, deltaic, and marine shelf sand environments during the Lower Cretaceous and Jurassic. Depositional environments vary within the formation and are dependent on the vertical location within the stratigraphic sequence as well as the geographic location within the San Juan Basin. The Upper Jurassic Brushy Basin member of the Morrison Formation contains coarse-grained fluvial sandstone reservoirs. Reservoirs in the Lower Cretaceous Burro Canyon Formation are coarse-grained to conglomeratic, fluvial sandstones deposited on an alluvial plain by an eastward flowing system of streams. In the eastern portion of the San Juan Basin marine sandstones merge into fluvial sandstones in the Dakota Formation.

Frontier Formation

The Upper Cretaceous Frontier Formation is a widespread siliciclastic unit that hosts sandstone reservoirs in a large variety of depositional environments spread across several Mid-Continent basins, including the Greater Green River where the fluvial-deltaic subplay is located, the Wind River Basin where the nearshore marine sandstone subplay is located, and the Powder River

Basin where the reworked transgressive subplay and marine shelf sandstone subplay is located. Major Frontier Formation fluvial-deltaic sandstone reservoirs are found in the Green River Basin where the best quality reservoirs were deposited in channel facies. The nearshore marine subplay of the Frontier Formation is well developed in the Salt Creek Field in the Powder River Basin Wyoming. The nearshore marine sandstone in the Salt Creek Field was deposited as a discrete, offshore marine sandstone bar with a north-south orientation. The reservoir sandstone in this field is encased in marine shale. The Frontier Formation in the Rocky Mountain basins is also very similar to the range of depositional settings associated with the Cypress, Benoist, and Bridgeport sedimentary deposits.

Upper Cretaceous Plays

The Western Interior Cretaceous Seaway was a narrow epicontinental sea that extended from the Gulf of Mexico to the Arctic and was the site for the deposition of several thousand feet of Upper Cretaceous siliciclastics. These sediments were deposited in environments varying from fluvial, deltaic, and marine shelf. Deposition over the broad region and the great vertical thickness) resulted in numerous sandstone geometries, including submarine fans, delta front sands, offshore shelf bars, barrier bars, point bars, a broad spectrum of deltaic complexes, fluvial deposits and eolian deposits. The Mississippian Carper Sandstone at St. James Field in the ILB is categorized as a turbidite, which resembles submarine fans or debris flows found in the upper Cretaceous of the Rocky Mountains basins.

Michigan Basin

The Michigan Basin, an interior cratonic basin, is largely confined to the state of Michigan (Dolton, 1995). Although most reservoirs are in carbonate rocks, some reservoirs are hosted in the Devonian-age Berea Sandstone. In the Michigan Basin, Salina and Niagaran rocks of the Silurian period contain highly productive oil and gas reservoirs in reefs and associated structures. Niagara rocks in the subsurface are predominantly dolomites and limestones with scattered regional occurrences of cherty zones and thin shale beds. Reservoirs are found primarily in pinnacle reef complexes a few miles basinward from the thick carbonate bank.

Reefs, reef-associated sediments, and biostromes occur in the Salina-Niagara Group. Most reefs in the subsurface are coral-algal-stromatoporoid mounds. Reservoir porosity is developed by preferential solution of coral skeletons and invertebrate remains from the fossiliferous rock. Dolomitization of limestone reefs frequently plays an important role in the development of porosity. Pinnacle reefs are major reservoirs in Silurian-age rocks in the Illinois Basin and are modeled in Tilden Field.

California Basins Monterey Turbidites

Tertiary basins in California and offshore California provide some excellent examples of prolific turbidite oil production. Multistory, stacked sandstone lenses are common, resulting in thick sequences of oil prone strata. The Stevens Sandstone is a clastic facies of the Miocene Monterey Shale (Clark et al., 1999). The Stevens turbidite complex is a layered, fan-shaped, prograding complex deposited in a slope-basin setting. California Basin turbidite complexes are much thicker than those found in the Illinois Basin, some reservoir characteristics, such as core measured porosity and permeability values, are similar. They also have a relatively high clay content. These characteristics are similar to those found in the Carper Sandstone at St. James Field.

Western mid-Continent—Forest City Basin

The Forest City Basin is an interior cratonic basin where sandstone reservoirs most resemble those found in the Illinois Basin. Most oil reservoirs in the Forest City Basin are located in northeastern Kansas with some located in Nebraska. The main sandstone reservoirs are fluvial-deltaic Pennsylvanian sandstones of Desmoinesian age are similar to the Pennsylvanian reservoirs at Lawrence Field (Charpentier, 1995). Approximately 80% of the oil production in the Forest City Basin is from Desmoinesian sandstone reservoirs. These reservoirs are combination structure-stratigraphic traps. This is a very mature play where the Paola-Rantoul Field was the first significant field with more than 6.5 MM m^3 (41 MM bbl) was discovered in 1882 in Miami County, Kansas.

Summary

Reservoirs researched for CO_2 storage potential in the ILB DEEP study are categorized by the environments that deposited the sediments which form the individual reservoirs. Considering the vast number of comparable depositional settings in the sedimentary rocks throughout the United States, this comparison is a condensed summary of various basins within the United States that show similar depositional environments to those identified in the reservoirs of the ILB DEEP research. While it is recognized that these depositional settings are common to all sedimentary basins, not all depositional settings are identified within every sedimentary formation, nor within every basin.

While the depositional environment categories are limited in number, the variations of sedimentary characteristics and the resultant influences on reservoirs are extensive. For example, deltas are classified as fluvial, wave, tide dominated, or a combination of those, and the trend, geometry and positional relationship of potential reservoirs are dependent on the particular depositional setting. The deltas associated with the ILB Mississippian Cypress Formation show characteristics of a high tidal range influence similar to those found today along the northern coast of Australia or along the southern coast of North Korea in the Yellow Sea. Reservoirs associated with this setting form as linear shoal deposits that trend perpendicular to the shore compared to reservoir deposits that align parallel to the shore, which is commonly associated with wave or low tidal range settings as found in deltaic settings along the southeastern coast of the United States. Fluvial deposits, commonly classified as braided or meander, are another example. Higher gradient rivers that are closer to the clastic source, like the ILB lower Mt. Simon, characteristically have coarser grained sediments, less muds and form anastomosing bar deposits that tend to have better reservoir communication than the point bars found in a meander setting. In general, the commonality of depositional and reservoir characteristics for a particular depositional setting including reservoir geometries, compartmentalization, boundary or baffle types, fluid flow, and spatial relationships of reservoir and nonreservoir facies has been a useful correlation tool that has been successfully applied in the exploration for and development of oil and gas reservoirs, and they should be likewise useful in the evaluation of reservoirs for CO_2 storage.

As an interior cratonic basin, the ILB generally had a low gradient sea floor and a low rate of subsidence relative to the rate of sedimentation. This resulted in a thin accommodation space and accounts for reservoirs that are laterally and vertically very compartmentalized. The compartments are commonly stacked or shingled and individual compartments are generally less

than 3 m (10 ft) thick. While the limiting accommodation conditions that influenced the depositional settings in the ILB resulted in thin, highly compartmentalized reservoirs, a similar depositional environment in another basin with greater accommodation space and sedimentation rate could yield reservoirs that were significantly thicker, more widespread and more conformable. Therefore, given a similar environment of deposition, individual basin characteristics may significantly influence reservoir complexity and scale, including lateral and vertical extent (volume) of reservoirs available for CO_2 storage, while the commonality of many depositional characteristics may remain discernable.

GEOCELLULAR MODELS

The approach to building each geocellular model followed a workflow that uses geostatistical methods to describe the heterogeneity of the formation. The workflow was developed during the course of preparing models for other EOR fields within the ILB and employs the geostatistical geologic-modeling software Isatis by Geovariances Corporation (MGSC, 2009; Frailey et al., 2012a; Frailey et al., 2012b). The geocellular modeling process included the following steps:

1. Data preparation: Geophysical logs were typically used as the basis of the geocellular model. Before modeling, some procedures were usually required to obtain quantifiable data that was consistent between wells, such as normalization or matrix conversion. Exact procedures are detailed under each section for individual fields.

2. Grid creation: A grid was constructed that encompassed the formation within the study area. Any deformation due to tectonic activity was removed from both the data and grids and was returned to the orientation during deposition of the formation. A consistent stratigraphic marker was chosen, usually of marine origin, to serve as a stratigraphic datum for all the data and grids.

3. Geostatistical analysis: Geologists' expertise and well log data were used to construct semivariogram maps to determine the horizontal anisotropy of the depositional environment. Well log data was used to develop experimental semivariograms to quantify the horizontal and vertical spatial correlation of the formation. Models fit to the experimental variograms were used to simulate heterogeneity.

4. Simulation: Stochastic simulation was used to generate multiple realizations of each formation. The different realizations were reviewed by ISGS geologists, who suggested modifications to better match the conceptual geologic model. Once the geologists agreed the model reproduced the reservoir architecture adequately, a single realization was chosen to be input for the reservoir simulation.

5. Petrophysical property transformation: After simulating the proxy data from logs, the models were converted into the desired petrophysical properties, porosity and permeability, by developing a transformation equation via regression of log and core analysis data. Typically, ordinary least squares and total least square (reduced major axis) were applied but the scatter in data resulted in poor correlation for many of the models. Thus, the transform equations were frequently modified to fit the geologists' expected relationships. Vertical permeability was calculated for each cell by multiplying the horizontal permeability by a coefficient of 0.85, which was derived from previous studies of various oil fields (MGSC, 2009; Frailey et al., 2012a; Frailey et al., 2012b).

6. Geocellular model expansion: If CO_2 reached the reservoir model boundaries before the storage efficiency profile stabilized during simulations, then the geocellular model was expanded beyond the area constrained by data coverage to a hypothetical extent, using the initial model parameters and the geologists' input.

7. Upscaling: The initial models used the highest resolution model possible to view the complete architecture of the formation. Upscaling was done only after determining that the important features could be captured with a coarser grid, in order to expedite the reservoir simulation process. Values from multiple cells are averaged into a single, larger cell. The arithmetic mean of porosity, geometric mean of horizontal permeability, and harmonic mean of vertical permeability were used.

Unique characteristics of the different formations and the data available in the study areas required some variation from the procedure; the individual sections below describe variations where necessary. Typically, the differences in available data caused the variations, such as for the fluvial and alluvial model where seismic data was used in place of well log data, or as a result of the lack of data available for expanding models, such as for the fluvial deltaic model where a new set of unconditioned model parameters were used to simulate the expanded model.

Spontaneous Potential Data

Though core analysis data and geophysical log data were both employed when available as the basis for the geocellular model construction, the majority of models relied on data from geophysical logs because of the paucity of core analysis data at the majority of fields. In mature basins like the Illinois Basin, the number of wells logged with modern package suites, such as gamma ray or neutron-density suites, is frequently small or nonexistent. In many of the fields studied, the absence of adequate data coverage from modern log suites required the use of older log suites for the modeling process. After examining the available logs, spontaneous potential (SP) was selected because of their availability and high correlation with permeability.

To compensate for well-to-well variation in SP logs caused by fluid chemistry or other borehole conditions, each well's SP log is normalized by transforming the raw SP into a sandstone-shale ratio (SP_{norm}).
Normalizing the SP log for a specific well is done by picking maximum and minimum observed SP values from formations near the zone of interest in that well. The minimum value represents a shale baseline (SP_{shale}), which is picked in a sand-free, shale zone, and the maximum represents a sandstone baseline (SP_{sand}), which is picked in a brine-saturated, shale-free sandstone that is at least 3.0 m (10 ft) thick, to avoid the effect of adjacent beds. Both are picked as close to the formation as possible to reduce the effect of shale baseline drift as well as differences in fluid chemistry, clay composition, and temperature effects between layers.
The following equation was used to convert the observed values from the raw SP log to SP_{norm}:

$$SP_{norm} = \frac{SP_{log} - SP_{shale}}{SP_{sand} - SP_{shale}} \times -100 \quad (1)$$

For the purpose of this study, the normalization does not necessarily represent an absolute ratio of the sandstone-shale composition of the formation; instead, it is designed to create a consistent scale for comparing the reservoir quality of the formations between wells. The actual values of the normalized SP are relative to the field.

Variography

Experimental semivariograms measure the difference in values as a function of the separation distance between them. They are displayed as a plot of a binned lag distance (on the *x*-axis) vs. variance (*y*-axis). Spatial correlation decreases with increasing separation distance until a distance at which no spatial correlation exists (the range). The manner in which the semivariogram reaches the range describes the transitional behavior of the geology.

Horizontal anisotropy can be detected by looking at the aerial distribution of the variance (a semivariogram map). For this study, warm colors indicate a high degree of correlation. Warm colors preferentially aligning in a direction indicates that the data are more spatially correlated in that direction.

If the semivariogram map detects a trend, multiple directional semivariograms with different parameters are created to describe the anisotropy. If the semivariogram map shows no clear trend, and the geologists agree that the formation has no clear anisotropy, a single omnidirectional semivariogram may be used.

Simulating values requires the semivariogram function to be defined for all distances, so a model semivariogram is created. In most cases, the model semivariogram is fit to the experimental semivariogram data. The geologist inference on the geometry of the formation, as interpreted during development of the conceptual model, is also used guide construction of the semivariogram model. Frequently, the periodicity of the data resulted in unstable or noisy semivariograms, thus the geologist interpretation was relied on more heavily during the model development.

The semivariogram analysis serves two purposes: to detect and measure anisotropy in the architecture of the formation and to serve as input for the stochastic simulation. With regard to the former, this helps to confirm the interpretations developed by the geologists during development of the conceptual model and can also sometimes detect more subtle trends in the geometry that may not be readily apparent. The semivariograms also reflect the level of heterogeneity and compartmentalization of the formation, which allows the different formations to be classified according to anticipated sweep efficiency. In addition, the majority of stochastic simulations are not possible without some type of semivariogram model.

Deltaic: Bridgeport B at Lawrence Field Oil Field

Two models differing in size were constructed for the Bridgeport B, which was classified as a deltaic depositional environment. The original model was based on the isopach maps and other conceptual geologic work. However, CO_2 reached the boundaries of this model before the storage efficiency profile stabilized so a new, expanded model was constructed. The initial model is referred to as the Original Deltaic Model, and the expanded model is referred to as the Expanded Deltaic Model.

The initial structural geocellular grid contained 75 cells in the *x*-direction, 68 cells in the *y*-direction, and 350 layers. Cell spacing of $\Delta x = \Delta y = 30.5$ m (100 ft) and $\Delta z = 0.3$ m (1 ft) resulted in a total surface area of 4.7×10^6 m^2 (5.10×10^7 ft^2) and a volume of 5.07×10^8 m^3 (1.79×10^{10} ft^3).

Structural maps provided by the geologist were used to delineate the top and bottom of the formation. A small coal seam at the top of the formation was used as the stratigraphic datum. Removing structure reduced the number of layers from 350 to 74 and the volume from 5.07×10^8 to 1.07×10^8 m^3 (1.79×10^{10} to 3.77×10^9 ft^3).

Data

A total of 113 normalized SP and 158 digital neutron-density porosity logs were used. The SP_{norm} log data was depth shifted and plotted against depth-shifted, cross plotted neutron-density porosity log data from nearby wells (<15 m [50 ft]). A curve was fit using regression and the resulting equation of the curve was used to transform SP_{norm} into porosity for each well (Figure 90). There was a large amount of scatter in the plots, so the geologist's experience was relied on to select a suitable curve. The resulting porosity-transformed SP logs were combined with available porosity logs to create a combined log data set.

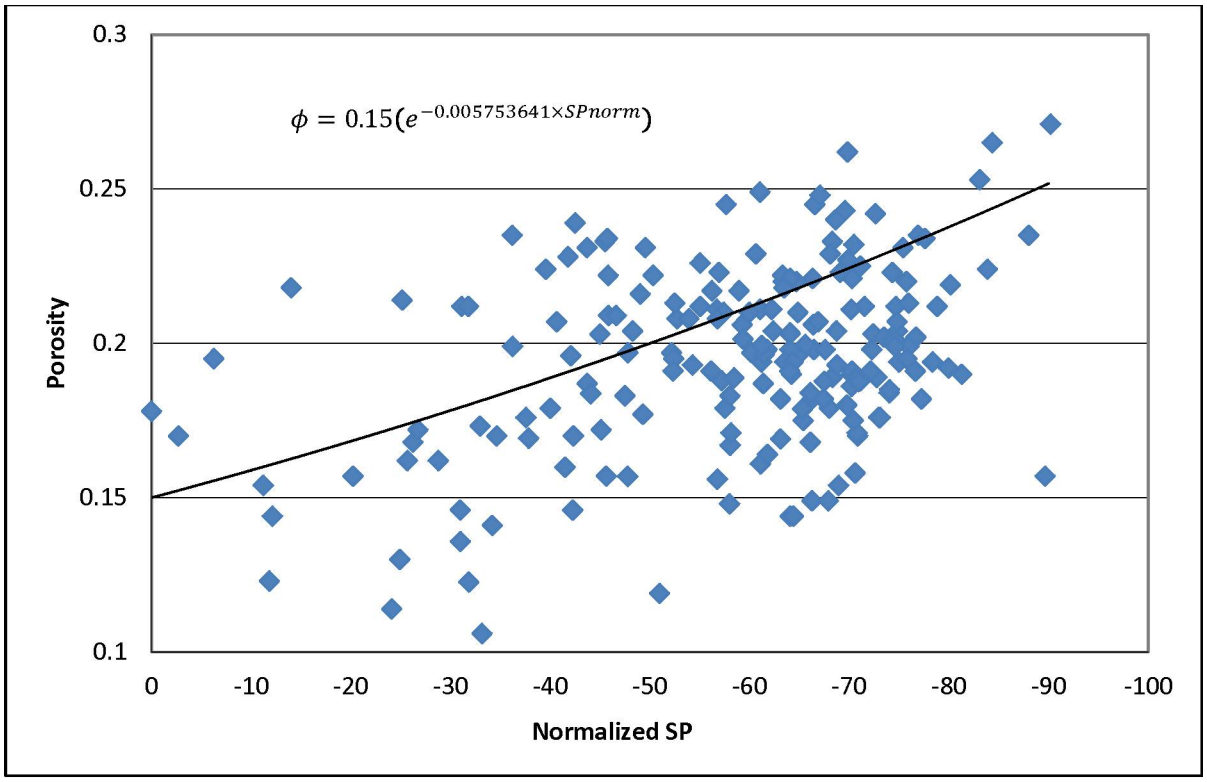

Figure 90 Plot of normalized SP (*x*-axis) vs. porosity (*y*-axis) for the Bridgeport B at Lawrence Field. The equation defining the line was used to transform normalized SP values into porosity in the deltaic model.

Geostatistical Analysis

Semivariogram maps produced by the combined log suite indicated a northeast-southwest trend of N70° (Figure 91). Anisotropy in the horizontal spatial distribution of the data was represented by two experimental semivariograms. One aligned with the direction of maximum continuity (N70°) and one normal to it (N160°). A vertical semivariogram was also developed to capture the vertical transitional behavior. Models fit to the semivariograms had two nested models to

capture the short- and long-range behavior of the geology. The first model had a range of 244 m (800 ft) in the northeast-southwest direction, a range of 152 m (500 ft) in the northwest-southeast direction, a 5 m (16 ft) range in the vertical direction, and a sill of 0.6 (Figure 92). The second model had a range of 2,743 m (9,000 ft) in the northeast-southwest direction, a range of 1,524 m (5,000 ft) in the northwest-southeast direction, a range of 14 m (45 ft) in the vertical, and a sill of 0.3 (Figure 92). Both semivariogram models used spherical structures with a nugget effect of 0.1.

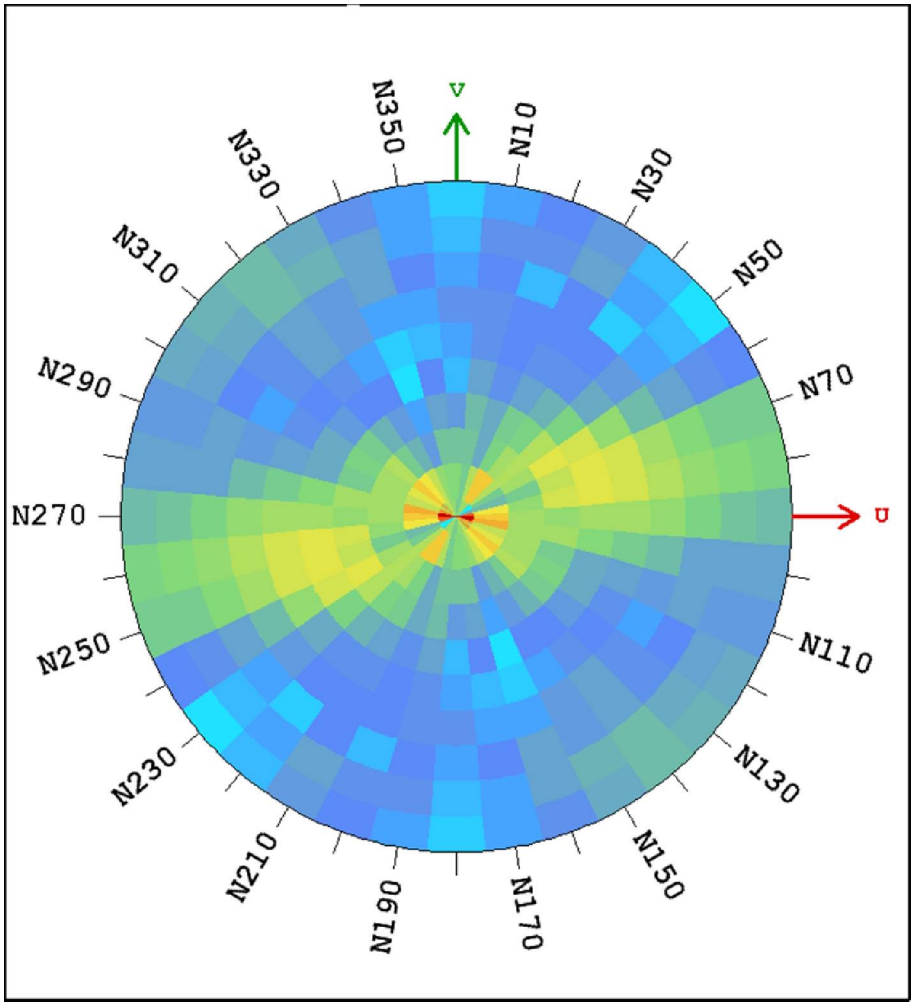

Figure 91 Semivariogram map from the combined log data set for the Bridgeport B at Lawrence Field. Warm colors indicate connectivity. A strong trend in the N70°E direction is clearly visible.

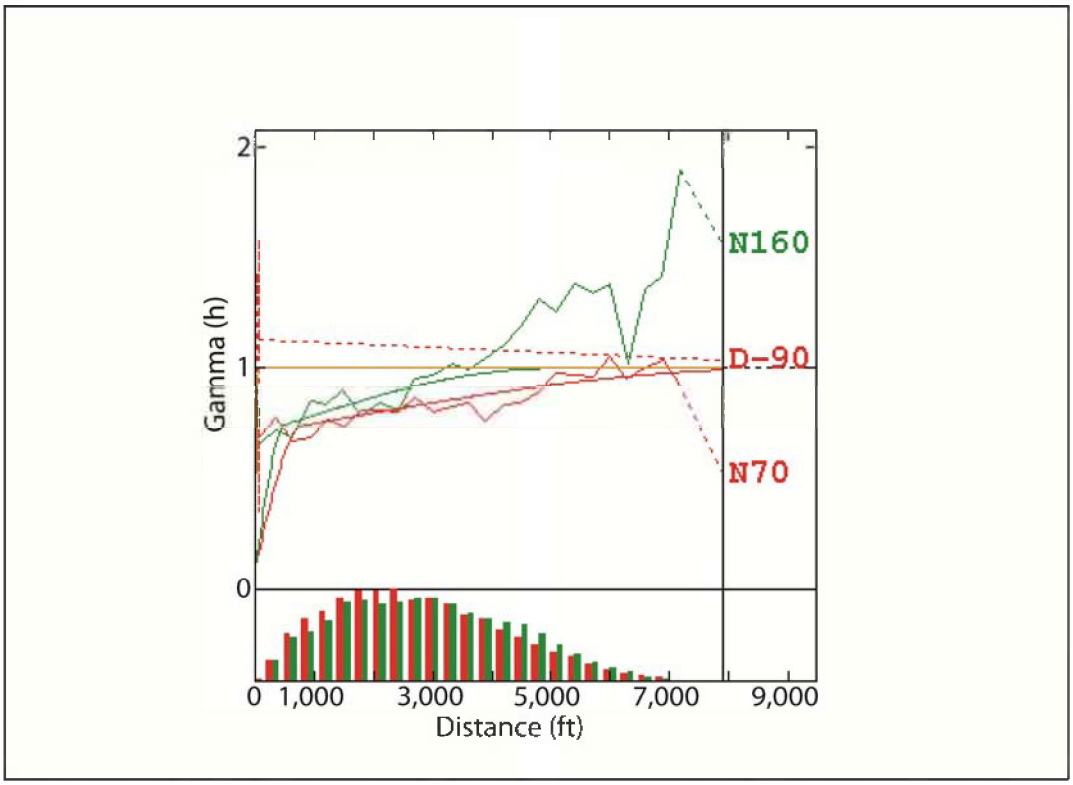

Figure 92 Directional experimental (thin lines) and model (thick lines) semivariograms for the original deltaic model. The red lines are semivariograms aligned with the direction of maximum connectivity (N70°), and the green lines are semivariograms normal to the direction of maximum connectivity (N160°). The longer range in N70° results in a geocellular model with more connectivity in that direction.

Simulation

The semivariogram models were used to simulate the porosity distribution for the Bridgeport B by applying the turning band method (Matheron, 1973; Journel, 1974). The simulations produced 50 unique, equiprobable realizations. The median (P_{50}) of the realizations was considered the most representative of the reservoir architecture and used in reservoir simulations.

Property Transformation

After an acceptable geocellular model of porosity had been constructed, a porosity-to-permeability transform derived from regression analysis of core samples was applied to transform the porosity values into permeability (Figure 93).

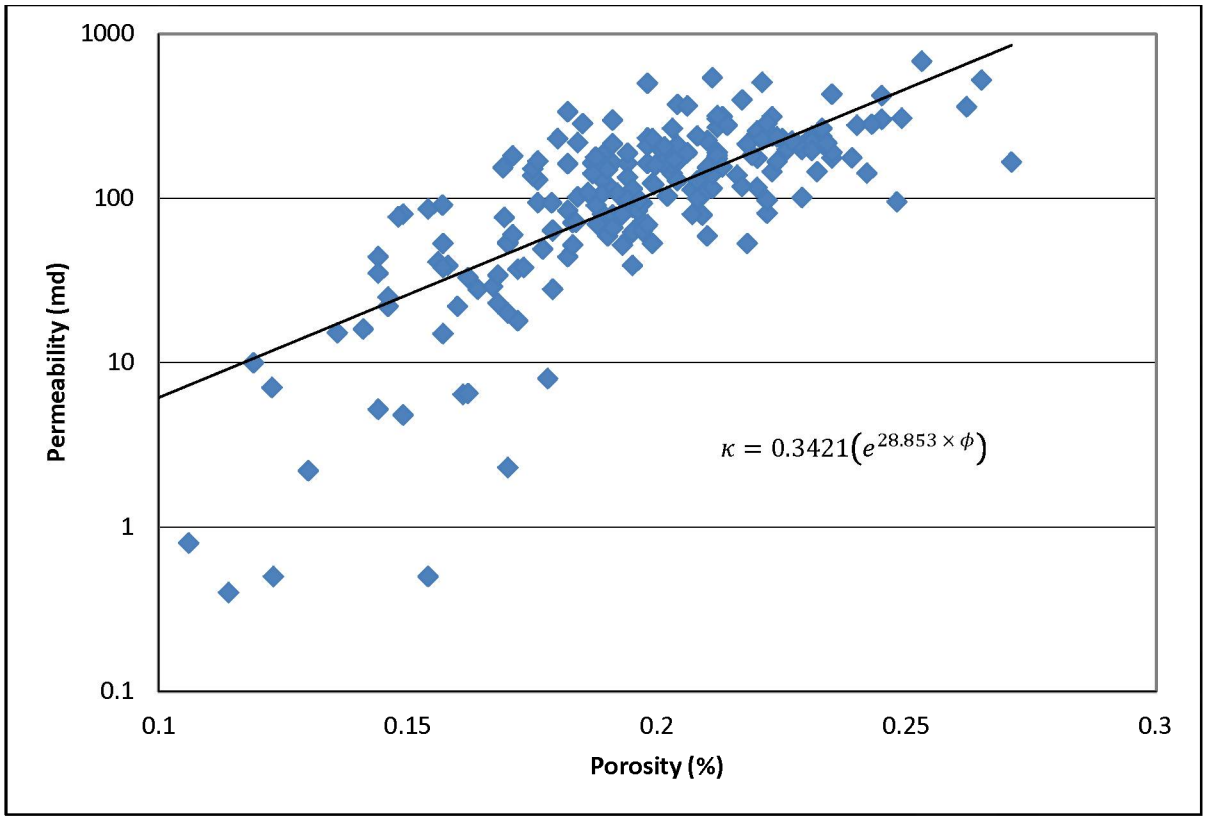

Figure 93 Plot of porosity (*x*-axis) vs. permeability (*y*-axis) from core samples of the Bridgeport B at Lawrence Field. The equation defining the line was used to transform porosity values to permeability.

Model Expansion

The model boundaries were expanded to the maximum lateral extent of the data available. Different realizations of the area were stacked on top of each other to mimic stacked parasequences of deltaic sedimentary strata. The lack in accommodation, which is typical of the ILB during Pennsylvanian time, resulted in relatively thin sandstone bodies when compared to analogous environments in other basins. The stacking of realizations within the geocellular model provided a better representation of the typical thickness of deltaic sandstone bodies. Geologists were consulted to ensure that the expanded geocellular model's architecture was consistent with the characteristics of a deltaic depositional environment.

A new stratigraphic grid with the same grid spacing was developed with 150 cells in the *x*-direction, 152 cells in the *y*-direction, and 138 layers to provide the volume necessary for the desired injection volume. This new grid covered a surface area of 2.12×10^7 (2.28×10^8 ft^2; approximately 4.5 times that of the original grid; Figure 94) and encompasses a volume of 8.92×10^8 m^3 (3.15×10^{10} ft^3; 8.34 times the original grid).

Data from the original vetted model was used in conjunction with an additional 82 digital SP logs from outside the original model domain to condition the simulation (Figure 94). Empirical and model semivariograms (Figure 95) were developed using the new data suite, and turning band simulations were run on the larger grid. The results were vetted, and three realizations deemed representative of a deltaic depositional environment were stacked on top of each other (Figure 96 and Figure 97). Layer thicknesses were upscaled from 0.3 to 0.9 m (1 to 3 ft).

Final Geocellular Model

The porosity and permeability ranges (Table 5) compare reasonably well with the ones determined for the reservoir from the core analyses (Figure 93), especially when considering the oversampling of sandstone in the core analysis data and the effects of upscaling. The distribution of the petrophysical properties in the original deltaic geocellular model (Figure 98 and Figure 99) captured the geometry observed in the thickness maps (Figure 5). The area beyond the data control in the expanded model (Figure 100 and Figure 101) was considered by the geologists to successfully capture the general geometry of a deltaic depositional environment.

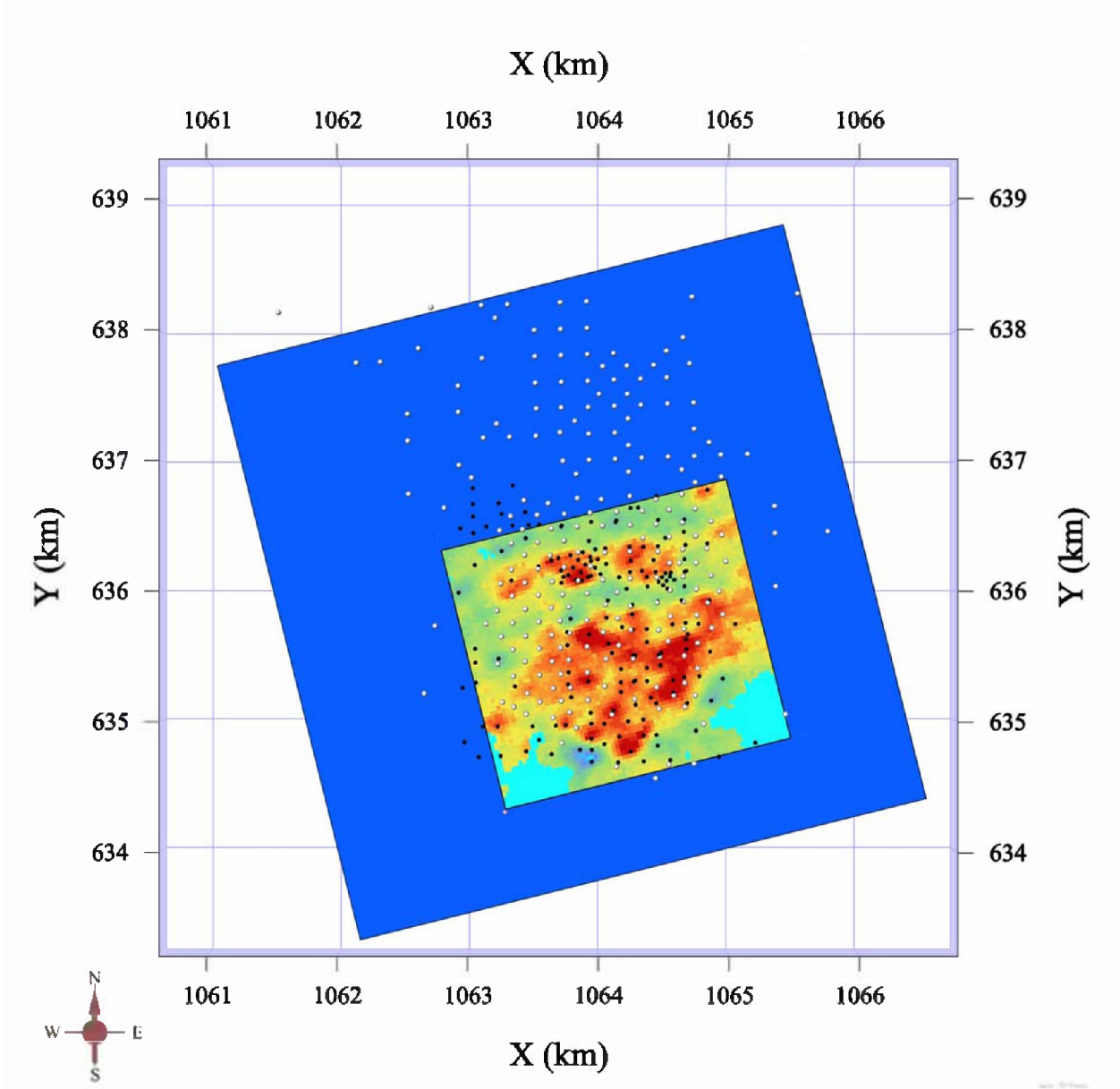

Figure 94 Data used to condition the simulation of the expanded model. The original grid (shown in this example with the porosity model) is the smaller area in the middle; the blue area is the expanded grid. White dots are SP logs and black dots are porosity logs.

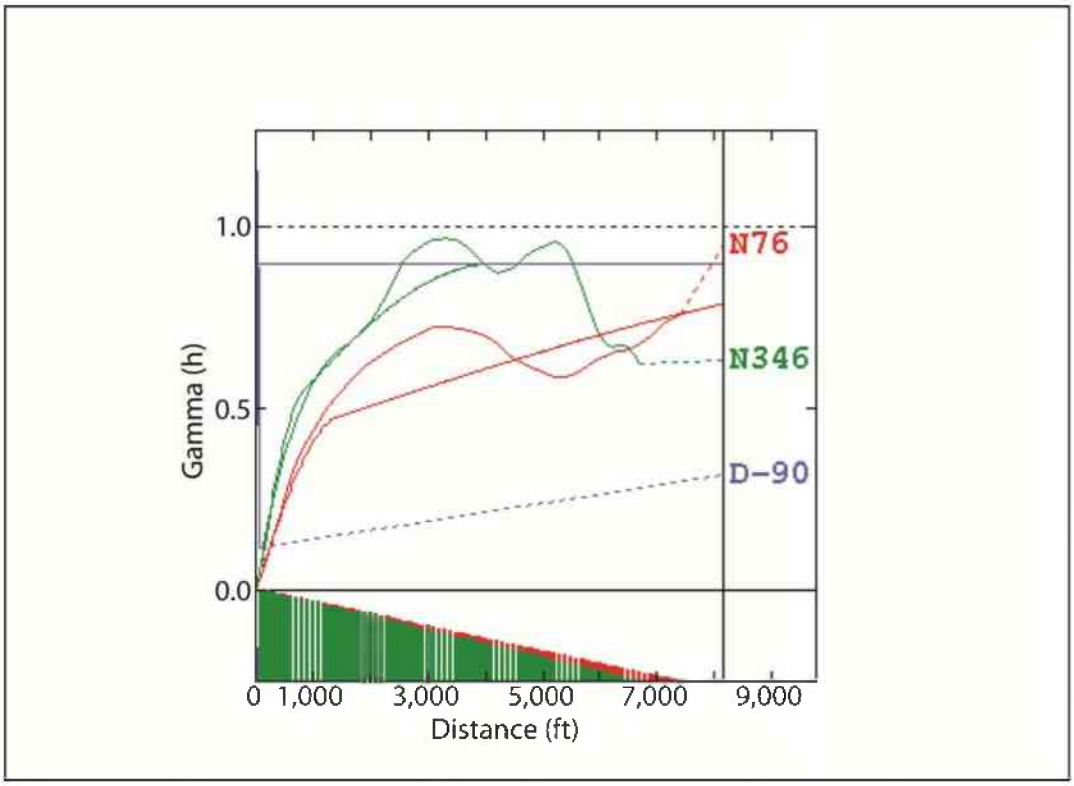

Figure 95 Directional experimental (thin lines) and model (thick lines) semivariograms for the expanded deltaic model. The red lines are the semivariograms aligned with the direction of maximum connectivity (N76°), and the green line are the semivariograms normal to the direction of maximum connectivity (N346°). The longer range in the direction of maximum connectivity (N76°) causes the portion of geocellular model beyond the boundaries of the original model to have more connectivity in that direction.

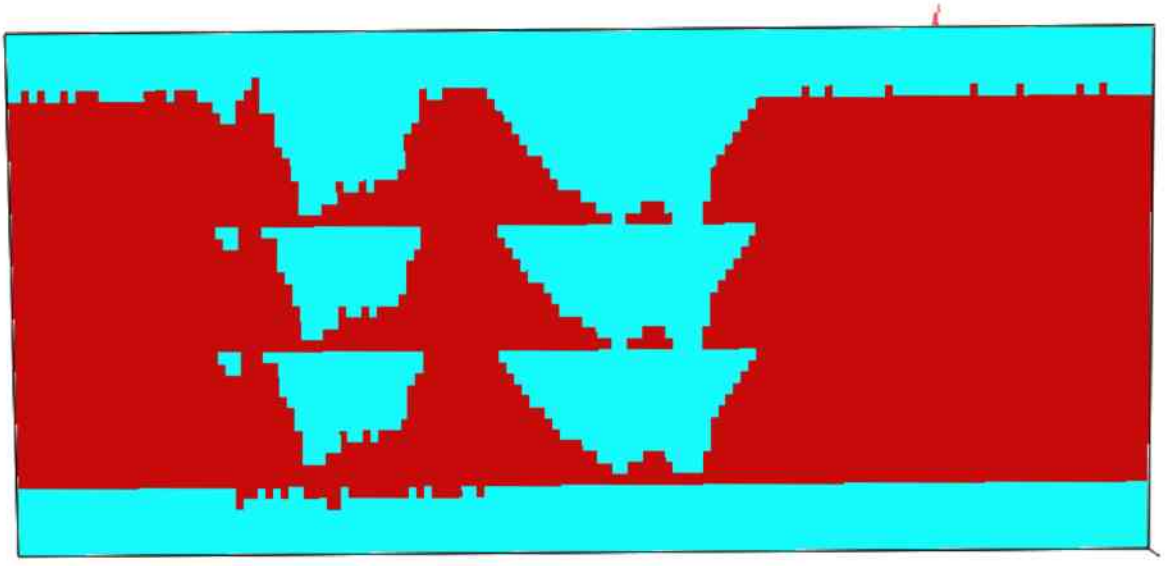

Figure 96 Image of the three individual models stacked on top of each other to form the final geocellular model used in reservoir simulations. The original models are shown in red, and the empty space between them is light blue.

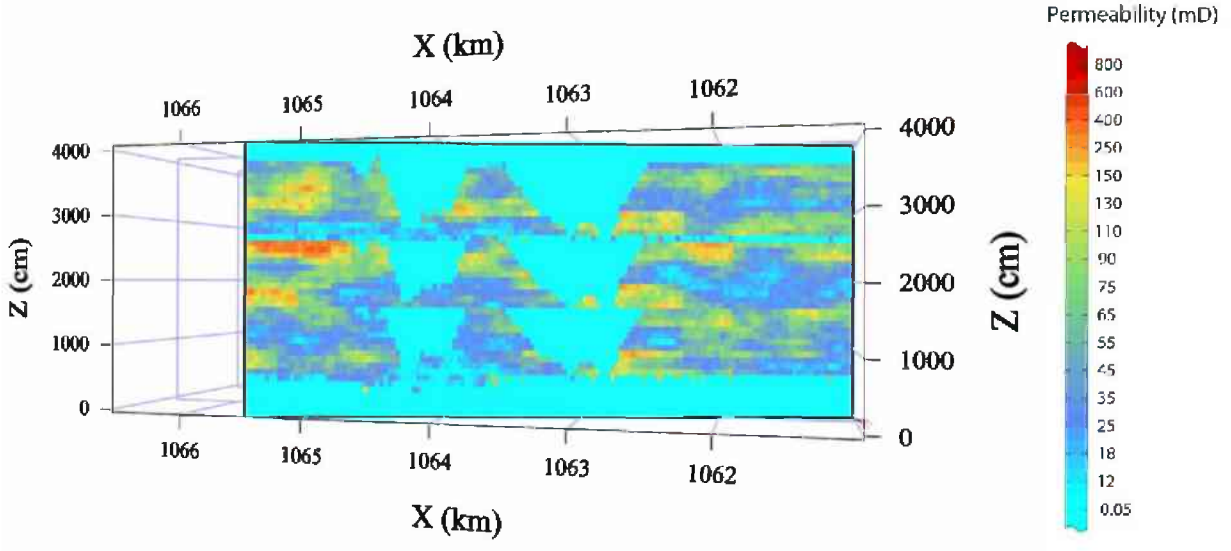

Figure 97 Image of the three individual models stacked on top of each other to form the final deltaic geocellular model used in reservoir simulations. The permeability distribution is shown for individual models, and the empty space between them is shown in light blue.

Table 5 Parameters for the deltaic geocellular model. The reservoir thickness, porosity, permeability, and pore space rows are the statistics after applying a 5% porosity cutoff and represent the higher quality portion of the formation.

Parameter	Bridgeport B Original Model	Bridgeport B Expanded Model	Stacked Bridgeport B Model
Total number of grid cells	377,400	524,400	1,048,800
x-direction	75	150	150
y-direction	68	152	152
z-direction	74	23	46
dx/dy (m [ft])	30.5 (100)	30.5 (100)	30.5 (100)
dz (m [ft])	0.3 (1)	0.9 (3)	0.9 (3)
Area (m^2 [ft^2])	4.74×10^6 (5.10×10^7)	2.12×10^7 (2.28×10^8)	2.12×10^7 (2.28×10^8)
Total volume (m^3 [ft^3])	1.07×10^8 (3.77×10^9)	4.45×10^8 (1.57×10^{10})	8.92×10^8 (3.15×10^{10})
Mean reservoir thickness (m [ft])	9.808 (32.18)	8.699 (28.54)	28.0 (91.8)
Number of defined cells	1.69×10^5	2.40×10^5	6.44×10^5
Total defined volume (m^3 [ft^3])	4.79×10^7 (1.69×10^9)	2.04×10^8 (7.19×10^9)	5.47×10^8 (1.93×10^{10})
Porosity (min/max/mean)	0.01/0.26/0.09	0.01/0.26/0.08	0.01/0.26/0.11
Total pore space	(3.40×10^8)	(1.26×10^9)	(3.46×10^9)
Permeability (min/max/mean) (cm^2 [mD])	4.54×10^{-12}/5.92×10^{-9}/3.82×10^{-10} (0.46/600.13/38.79)	4.54×10^{-12}/5.74×10^{-9}/3.09×10^{-10} (0.46/582.61/31.36)	4.54×10^{-12}/5.74×10^{-9}/3.09×10^{-10} (0.46/582.61/43.32)
Reservoir porosity (min/max/mean)	(0.05/0.26/0.18)	(0.05/0.26/0.17)	(0.05/0.26/0.17)
Reservoir permeability (min/max/mean) (cm^2 [mD])	1.42×10^{-11}/5.92×10^{-9}/8.47×10^{-10} (1.44/600.13/85.95)	1.42×10^{-11}/5.74×10^{-9}/6.71×10^{-10} (1.44/582.61/68.06)	1.42×10^{-11}/5.74×10^{-9}/6.93×10^{-10} (1.44/582.61/70.31)
Reservoir pore space	(3.05×10^8)	(1.22×10^9)	(3.28×10^9)

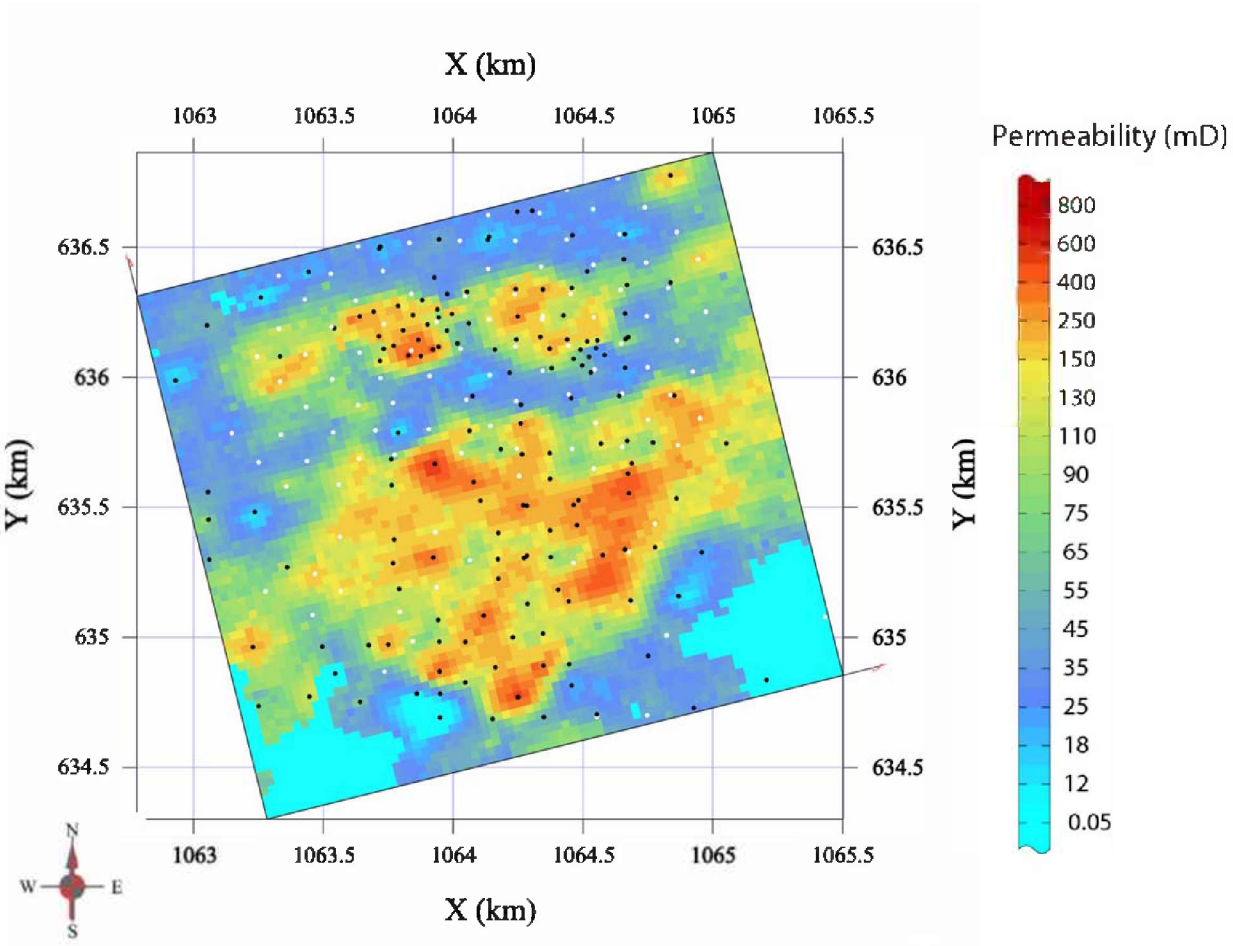

Figure 98 Permeability distribution of the original deltaic model. Black dots represent well locations with porosity logs, and white dots represent well locations with SP logs. The layer shown is 6.4 m (21 ft) below the stratigraphic datum.

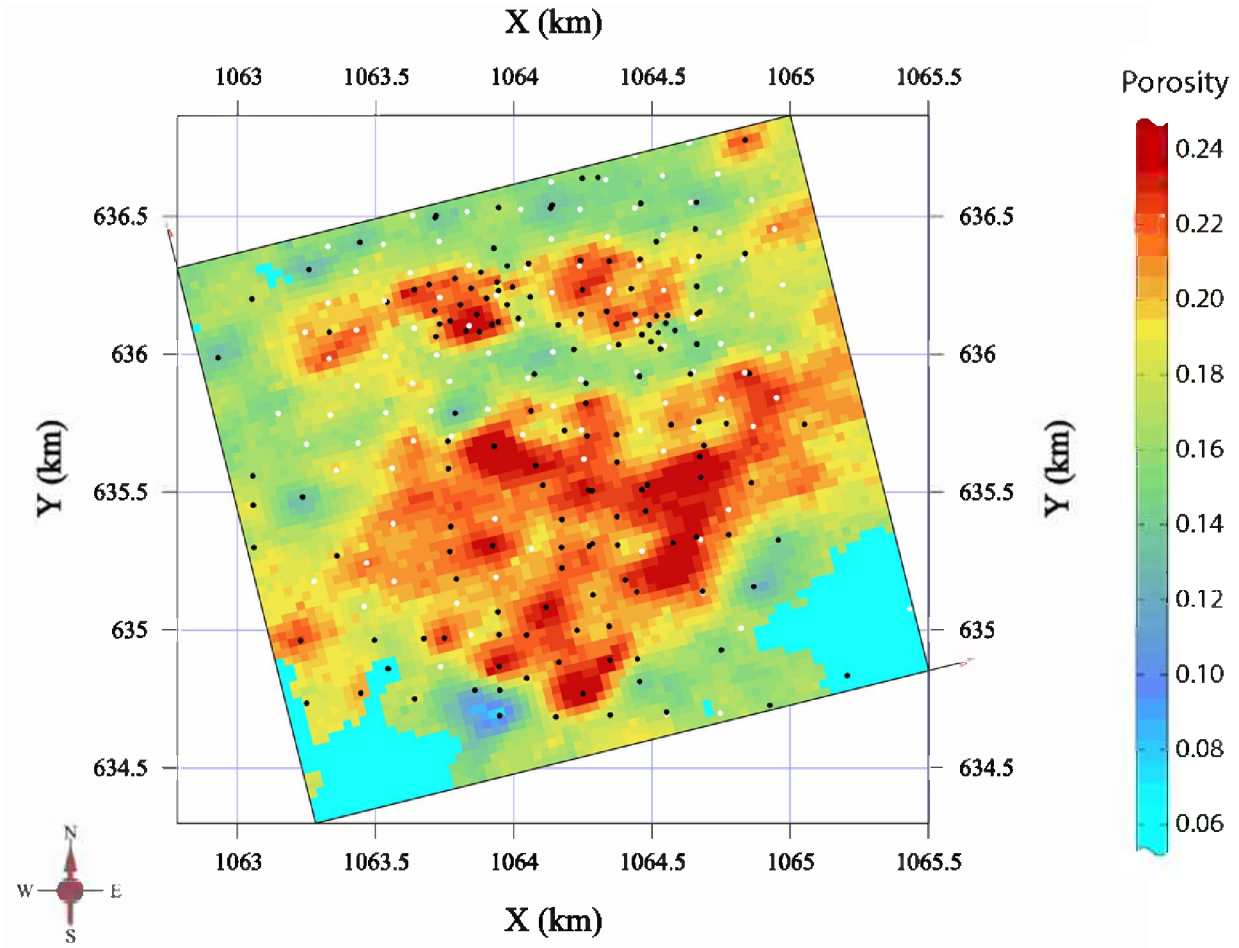

Figure 99 Porosity distribution of the original deltaic model. Black dots represent well locations with porosity logs, and white dots present well locations with SP logs. The layer shown is 6.4 m (21 ft) below the stratigraphic datum.

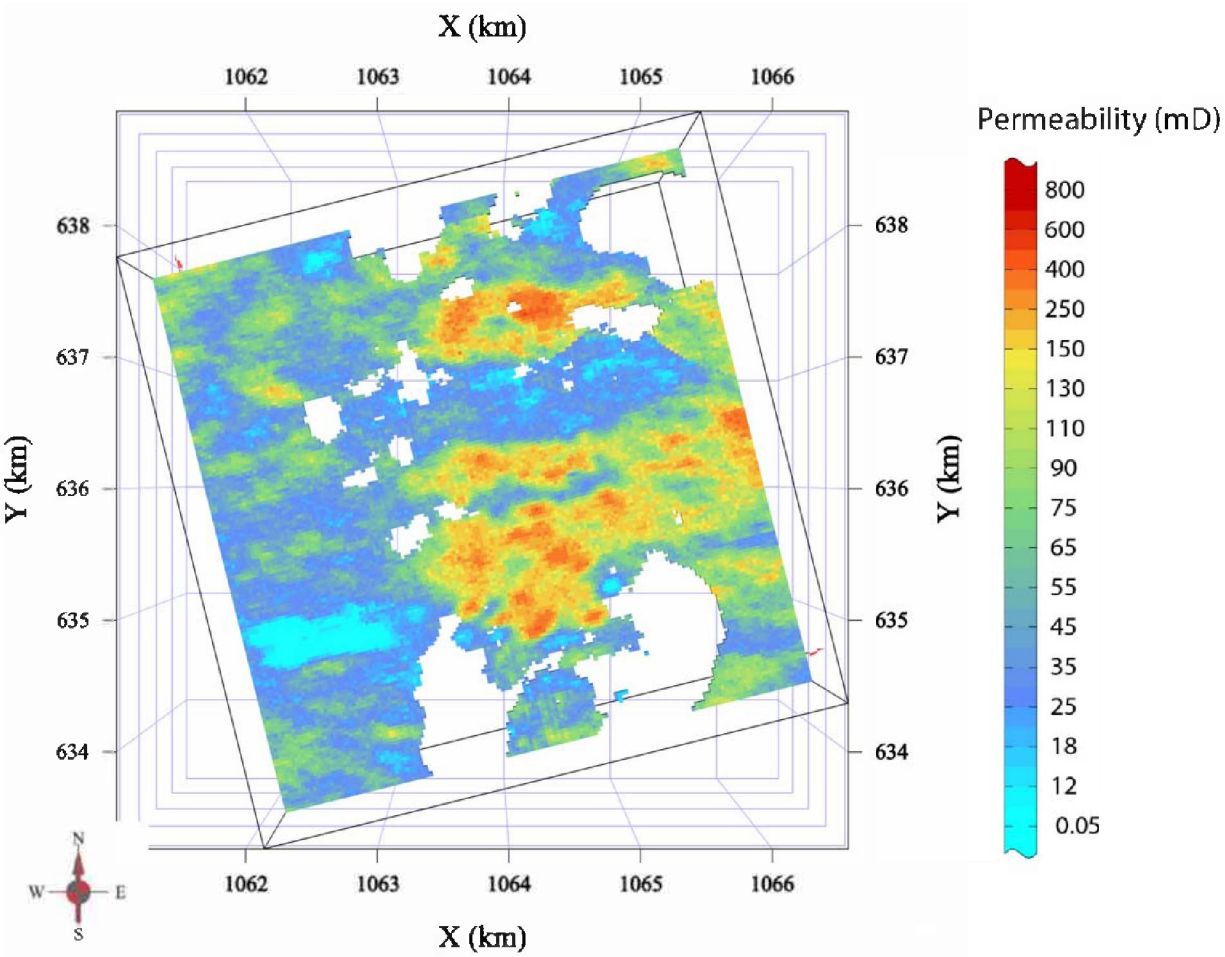

Figure 100 Permeability distribution of the expanded deltaic model. The layer shown is 6.4 m (21 ft) below the stratigraphic datum.

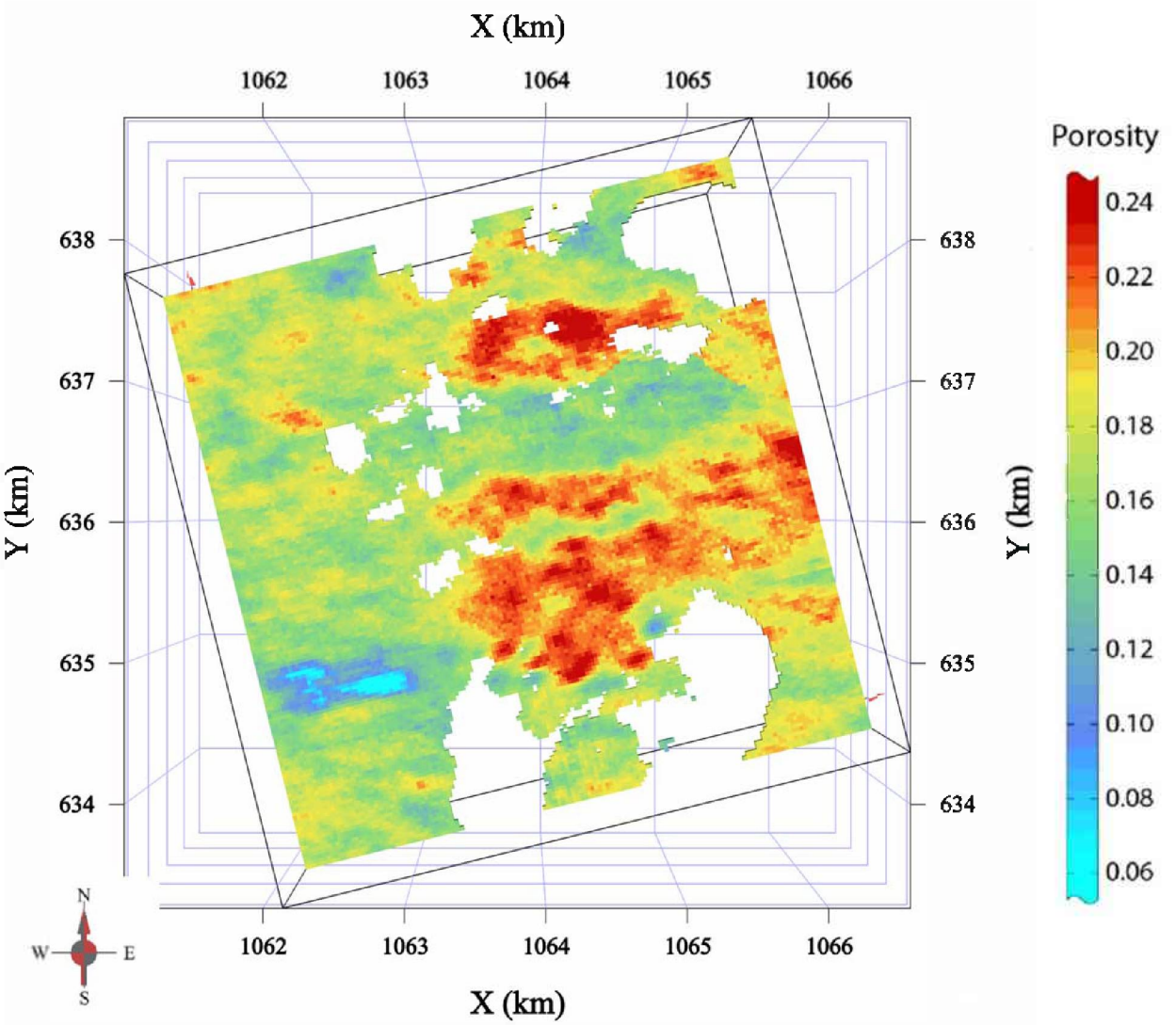

Figure 101 Porosity distribution of the expanded deltaic model. The layer shown is 6.4 m (21 ft) below the stratigraphic datum.

Fluvial Deltaic: Bridgeport Channel at Lawrence Oil Field

The initial model for the Bridgeport Channel at Lawrence Field spanned sections 4, 5, 9, and 8, 3N 12W, Lawrence County, Illinois, and covered a surface area of 614 ha (1,520 ac). This model was expanded significantly after initial reservoir simulations.

Structure was removed from the grid and wells by using a shale marker, described in the geologic characterization section, as a stratigraphic origin. The grid of the initial model contained 56 nodes cells in the *x*-direction, 118 cells in the *y*-direction, and 182 layers. Cell spacing of $\Delta x = \Delta y = 30.5$ m (100 ft) and $\Delta z = 0.305$ m (1.00 ft) resulted in a volume of 1.11×10^9 m^3 (1.20×10^{10} ft^3).

Data

The data available for the model was unusual because of a large amount of core taken and analyzed from this portion of Lawrence Field. Core analysis data was taken at every half foot from 188 wells and resulted in over 3,164 measurements. This data was supplemented by 6 neutron-density logs.

Porosity was the property used for simulation and geostatistical analysis. Based on a comparison of wells with geophysical logs and core, a slight discrepancy was noted between core analysis-derived porosity and log-derived porosity values. To compensate, porosity values from logs were plotted against porosity values from the core analysis and a curve fitted via linear regression (Figure 102). The equation describing the curve was used to transform all porosity values from logs into equivalent core analysis porosity values.

Geostatistical Analysis

Semivariogram maps produced by the combined log suite indicated a northeast-southwest trend of N30° (Figure 103). Anisotropy in the horizontal spatial distribution of the data was represented by two experimental semivariograms. One aligned with the direction of maximum continuity (N30°) and one normal to it (N120°). A vertical semivariogram was also developed to capture the vertical transitional behavior. Models fit to the semivariograms had two nested structures to capture the short- and long-range behavior of the geology. The first used an exponential type, a range of 120 m (400 ft) in the northeast-southwest direction, a range of 61 m (200 ft) in the northwest-southeast direction, a 3.0 m (10 ft) range in the vertical direction, and a sill of 0.45 (Figure 104). The second used a spherical type, had a range of 1,800 m (6,000 ft) in the northeast-southwest direction, a range of 460 m (1,500 ft) in the northwest-southeast direction, a range of 43 m (140 ft) in the vertical, and a sill of 0.3 (Figure 104). A nugget effect of 0.1 was included.

The anisotropy indicated by the geostatistical analysis coincides with the orientation of the northeast-southwest trending channel with paleoflow to the southwest. The alignment of anisotropy in petrophysical properties with the channel orientation is expected and reflects the depositional process that formed the reservoir. The vertical semivariogram had a relatively large range when compared to other models, reflecting the thickness of the reservoir.

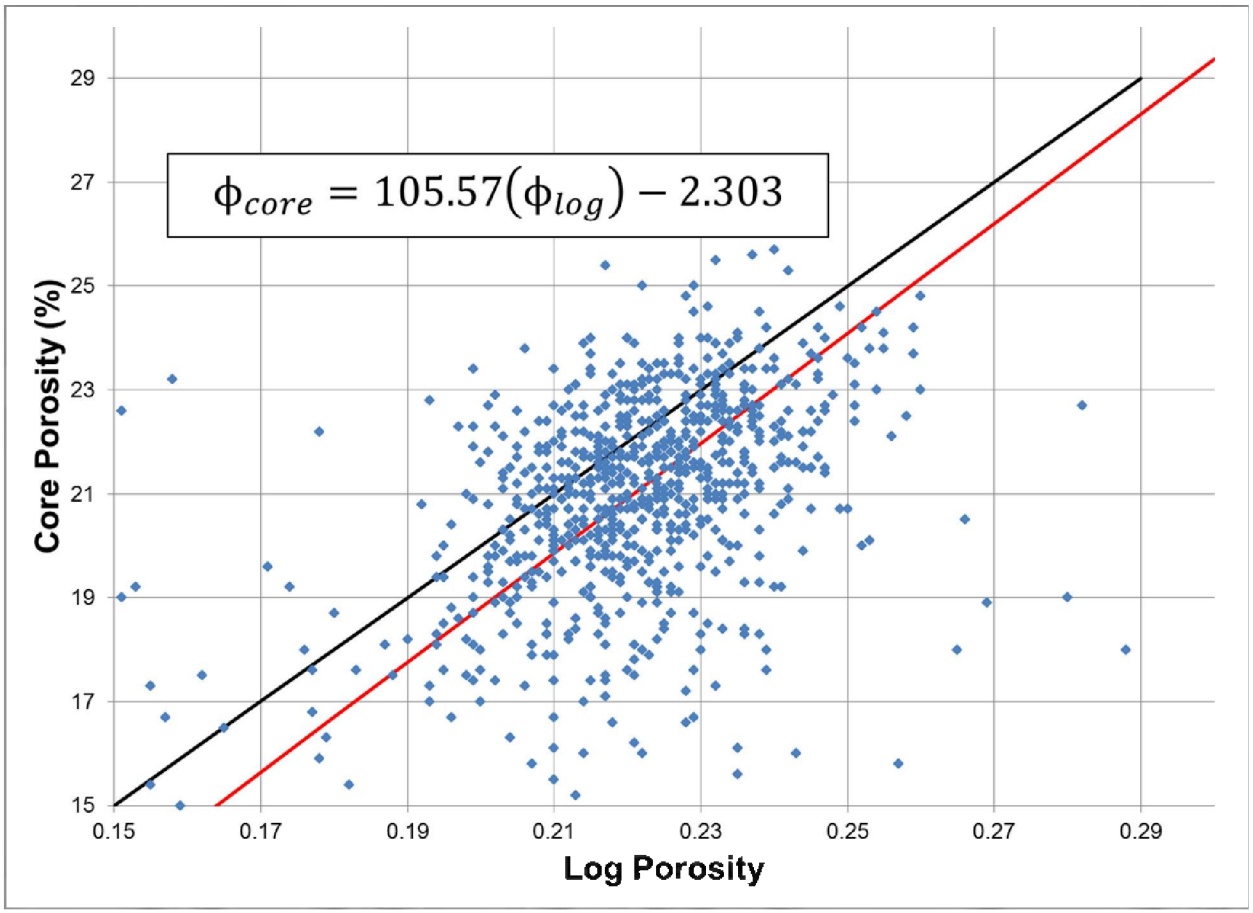

Figure 102 Plot of porosity data from neutron-density logs (*x*-axis) against porosity from core analysis (*y*-axis). A one-to-one line is plotted in black to demonstrate the discrepancy between the two data sources. The red line was fit to the data using linear regression and the resulting equation used to transform log-derived porosity into equivalent core analysis porosity values.

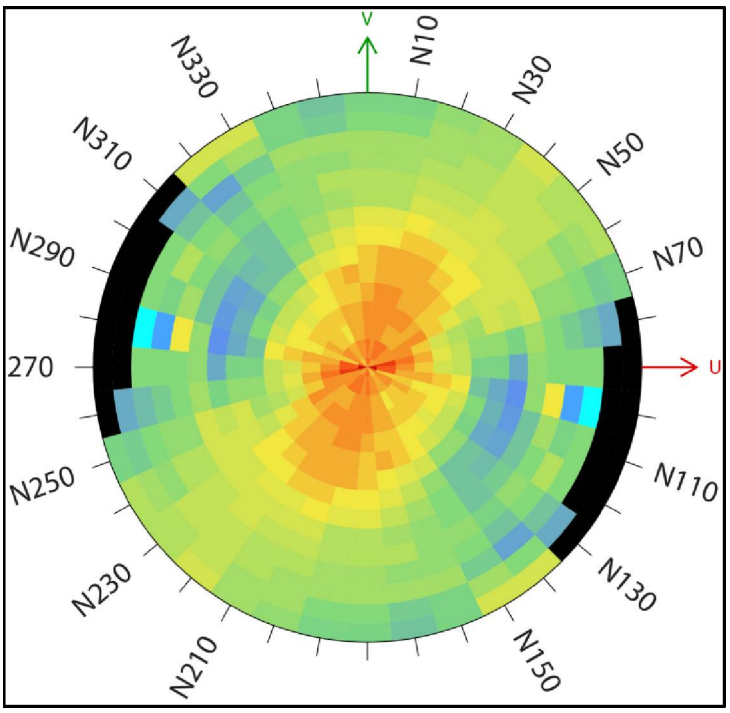

Figure 103 Semivariogram map from the data set for the Bridgeport Channel at Lawrence Field. Warm colors indicate connectivity. A strong trend in the N30° direction is clearly visible.

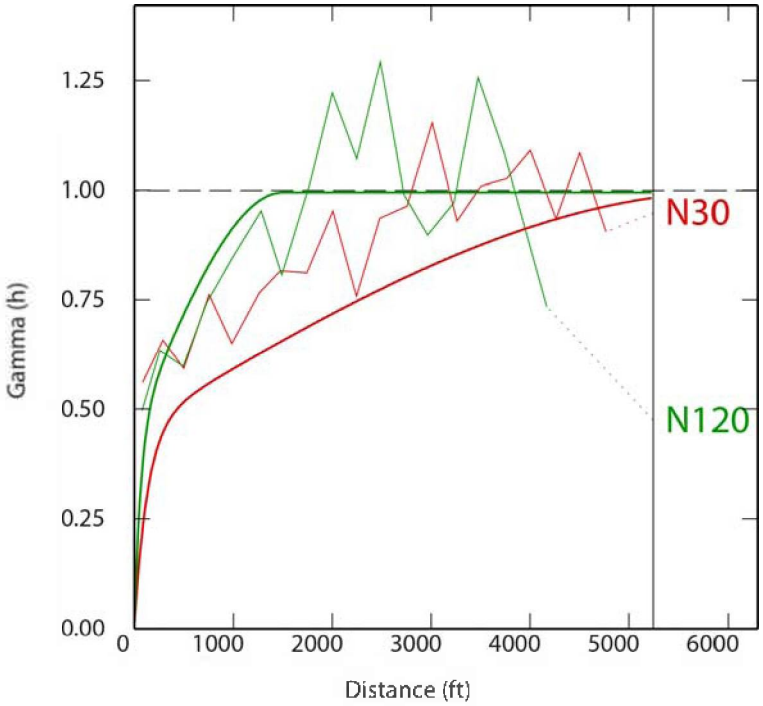

Figure 104 Directional experimental (thin lines) and model (thick lines) semivariograms for the initial Bridgeport Channel model at Lawrence Field. The red lines are the semivariograms aligned with the direction of maximum connectivity (N30°), and the green lines are the semivariograms normal to the direction of maximum connectivity (N120°). The longer range in N30° results in a geocellular model with more connectivity in that direction.

Simulation

The semivariogram models were used to simulate the porosity distribution for the Bridgeport B by applying the turning band method (Matheron, 1973; Journel, 1974). The simulations produced 100 unique, equiprobable realizations. The realizations were reviewed with the project geologist to select the one that replicated the expected distribution of petrophysical properties and considered the most representative of the reservoir architecture for use in reservoir simulations. Layer thicknesses were upscaled from 0.3 to 0.9 m (1 to 3 ft).

Property Transformation

After an acceptable geocellular model of porosity had been constructed, a porosity-to-permeability transform derived from regression analysis of core samples was applied to transform the porosity values into permeability (Figure 105).

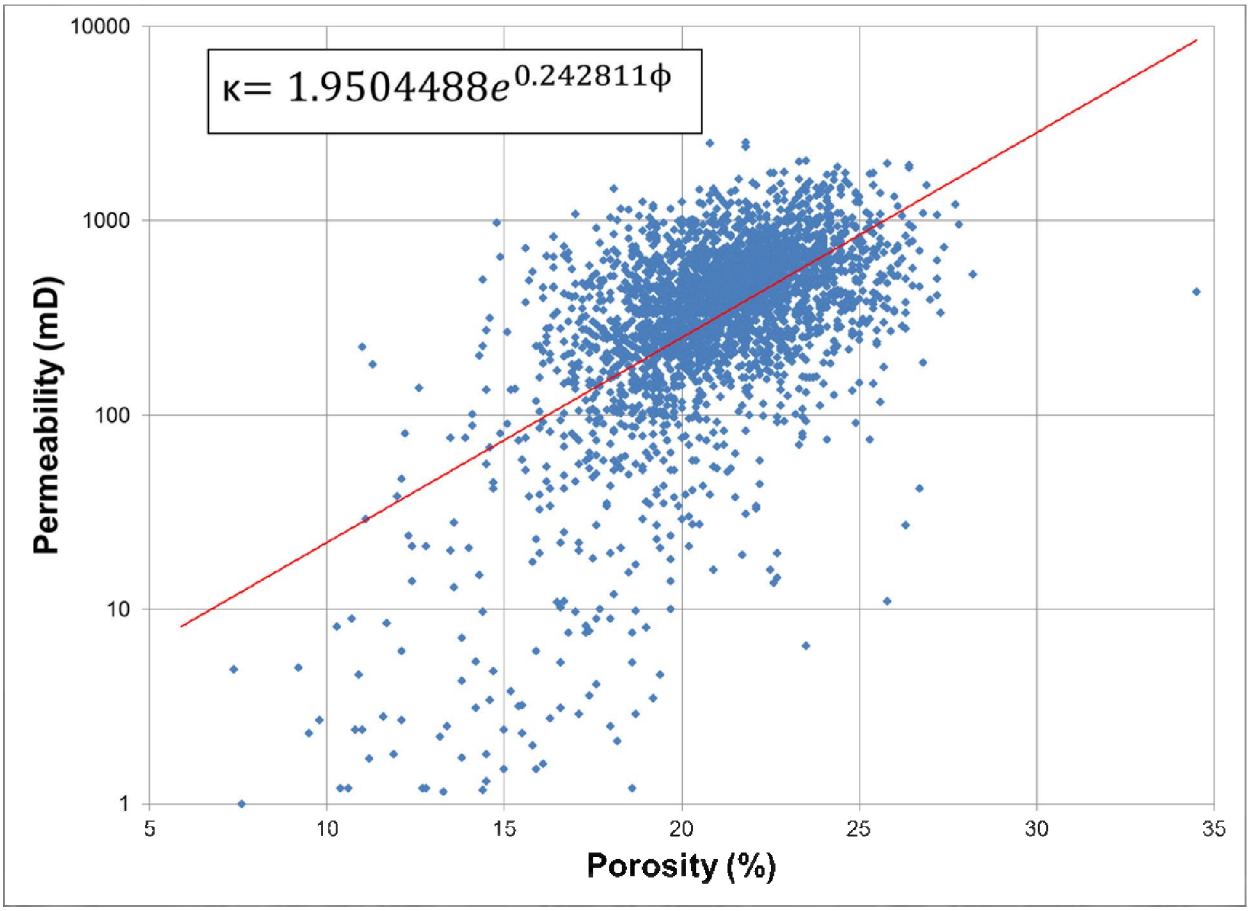

Figure 105 Plot of porosity (*x*-axis) vs. permeability (*y*-axis) from core samples of the Bridgeport Channel at Lawrence Field. The equation defining the line was used to transform porosity values to permeability.

Model Expansion

The initial model was expanded in a manner to match the dimensions of a meandering channel system in a fluvial deltaic environment. This was accomplished primarily by extending the length of the channel. While additional data was available in the northeast to constrain the active model boundaries, the formation is eroded away in the southwest. The structure of the formation in the southern portion was based on geological characteristics of the depositional system and

trends of the existing portions of the formation. Figure 106 shows the isopach used to construct the initial model superimposed over the isopach used for the expanded model. The increase in the scale of the model meant the relevant geologic features could be captured with a coarser grid in the horizontal plane. This also reduced the number of active cells in the reservoir simulation, improving the computational efficiency of the simulations. The Δx and Δy cell spacing was increased to 61.0 m (200 ft) while the layer thickness was maintained at 0.914 m (3.00 ft). The final grid had 52 cells in the x-direction, 211 cells in the y-direction, and 98 layers. In total, the model area was expanded to 4,080 ha (10,100 ac) and the volume was increased to 1.20×10^9 m^3 (1.29×10^{11} ft^3).

The geostatistical analysis determined that the direction of anisotropy in the petrophysical properties was coincident with the orientation of the channel. In the expanded model, the channel orientation is no longer static and instead varies as the channel meanders and bends. The anisotropy of the petrophysical properties was assumed to vary in the same fashion, so a new semivariogram model was needed. The new semivariogram model was based upon the variation of the channel orientation and included four directions in the horizontal axis, N30°, N120°, N235°, and N325°, in addition to the vertical direction. The properties of the new semivariogram model (Table 6) were based on those used for the initial model. The semivariogram and semivariogram models are shown in Figure 107.

The initial model was used as conditioning data for the simulations of the expanded model, thus ensuring the initial model would be honored in the expanded model. No additional core or porosity log data was available. The new semivariogram model was used with turning band simulations to generate a 100 realizations and a single realization was selected from the group using the same criteria that was used to select the initial model.

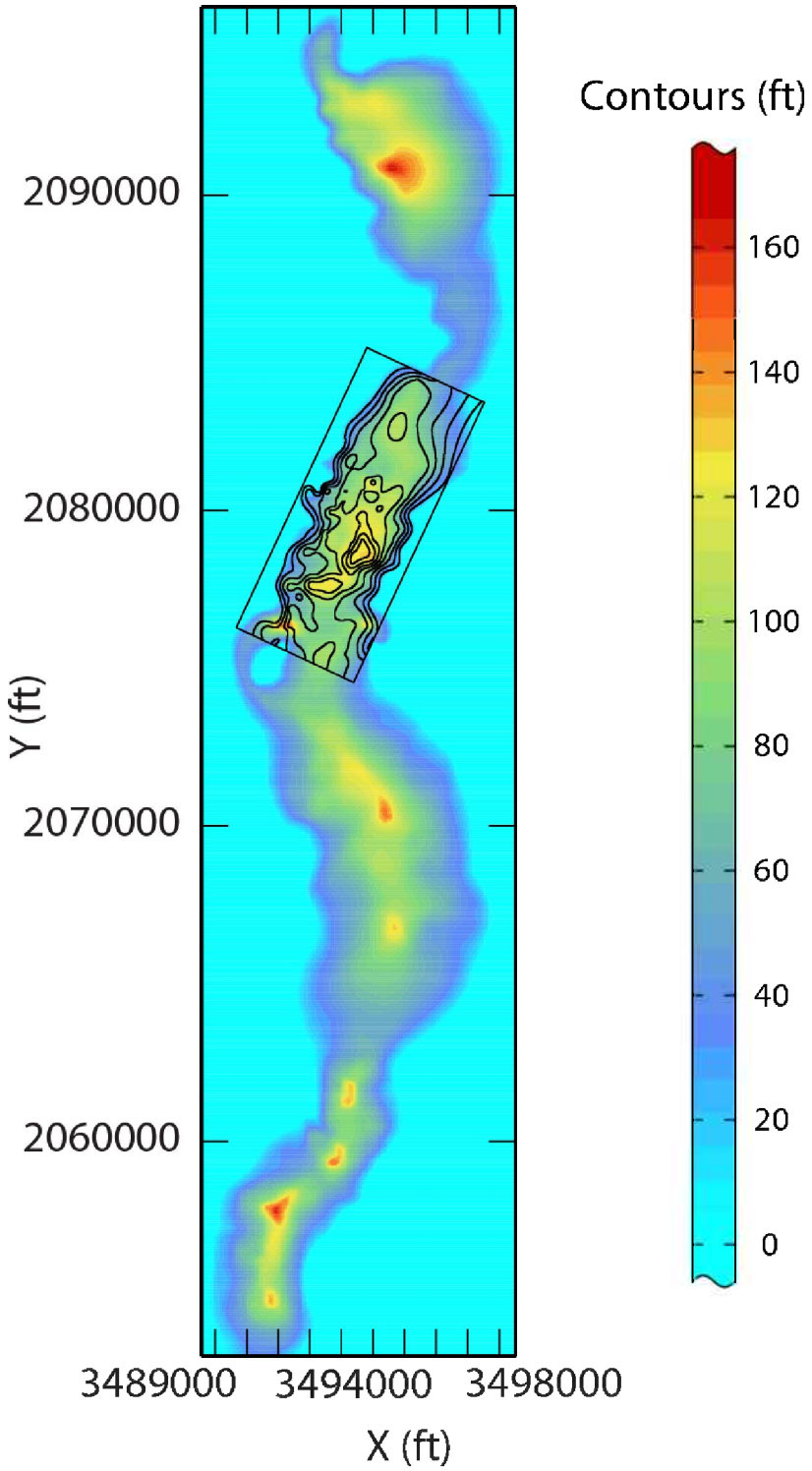

Figure 106 Map with the isopach of the initial model, represented within the inset box by 6.1 m (20 ft) contour lines, overlaying the isopach for the expanded model, represented by color-filled contours.

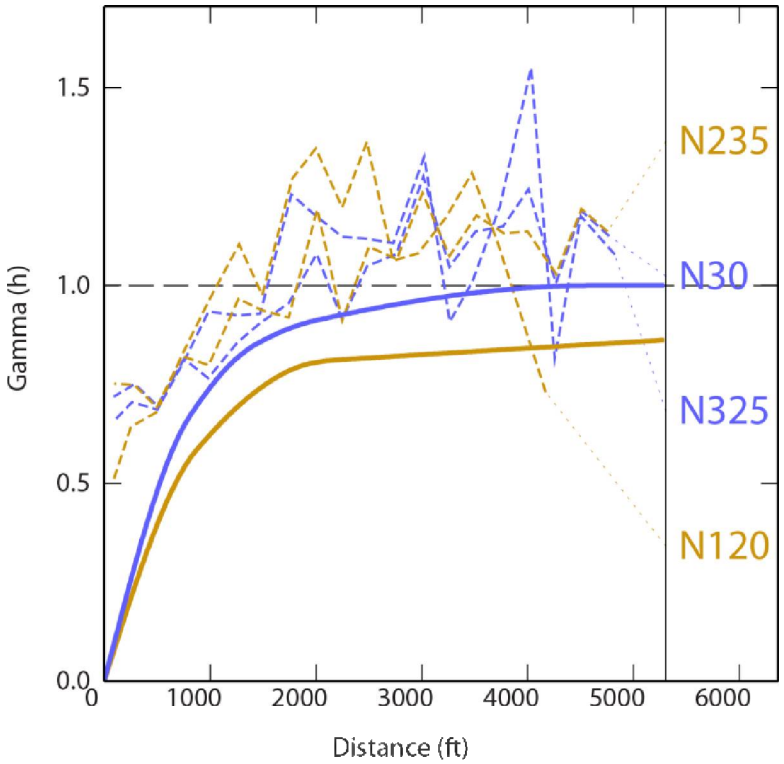

Figure 107 Directional experimental (thin lines) and model (thick lines) semivariograms for the expanded Bridgeport Channel model at Lawrence Field. The purple lines are the semivariograms aligned with the direction of maximum connectivity (N30° and N325°), and the gold lines are the semivariograms normal to the direction of maximum connectivity (N120° and N235°). The longer range in N30° and N325° results in a geocellular model with more connectivity in that direction.

Table 6 Properties of the semivariogram model for the expanded model. A nugget was not used.

Structure Number	Directions	Structure Type	Range (m [ft])	Sill
1	N30°	Spherical	609.6 (2,000)	0.275
	N120°	Spherical	244 (800)	0.275
	Vertical	Spherical	2 (5)	0.275
2	N325°	Spherical	609.6 (2,000)	0.275
	N235°	Spherical	244 (800)	0.275
	Vertical	Spherical	15 (50)	0.275
3	N30°	Spherical	(20,000)	0.225
	N120°	Spherical	609.6 (2,000)	0.225
	Vertical	Spherical	30.5 (100)	0.225
4	N325°	Spherical	(20,000)	0.225
	N235°	Spherical	609.6 (2,000)	0.225
	Vertical	Spherical	61 (200)	0.225

Final Geocellular Model

Figure 108 and Figure **109** show the results of the final geocellular model used for reservoir simulation. Table 7 has a summary of the model properties. The figures illustrate that the reservoir architecture of the initial model area was successfully replicated in the expanded model area. The model effectively captures the behavior of anisotropy in petrophysical properties aligning with the orientation of the channel. In deeper portions of the channel, the porosity and permeability is very low, which is a characteristic of some channel depositional environments.

Table 7 Bridgeport channel final geocellular model parameters. The reservoir porosity, permeability, and pore space rows are the statistics after applying a 5% porosity cutoff and represent the higher quality portion of the formation.

Parameter	Value
Total number of grid cells	1,075,256
x-direction	52
y-direction	211
z-direction	98
dx/dy (m [ft])	61.0 (200)
dz (m [ft])	0.9 (3)
Area (m^2 [ft^2])	4.08×10^7 (4.39×10^8)
Total volume (m^3 [ft^3])	1.20×10^9 (1.29×10^{11})
Reservoir thickness (min/max/mean) (m [ft])	0.914/50.3/21.6 (3.00/165/70.8)
Number of active cells	1.06×10^5
Total active volume (m^3 [ft^3])	3.60×10^8 (1.27×10^{10})
Depth (min/max/mean) (m [ft])	260/348/306 (854/1,142/1,005)
Reservoir porosity (min/max/mean/st.d)	0.013/0.276/0.171/0.045
Total reservoir pore space (m^3 [ft^3])	6.16×10^6 (2.17×10^8)
Reservoir permeability (min/max/mean/median/st.d) (cm^2 [mD])	2.64×10^{-11}/1.57×10^{-8}/1.89×10^{-9}/1.61×10^{-9}/1.46×10^{-9} (2.67/1,590/191/163/148)
Reservoir vertical permeability (min/max/mean/median/st.d) (cm^2 [mD])	1.23×10^{-11}/7.21×10^{-9}/8.01×10^{-10}/6.59×10^{-10}/6.77×10^{-10} (1.25/731/81.2/66.8/68.6)

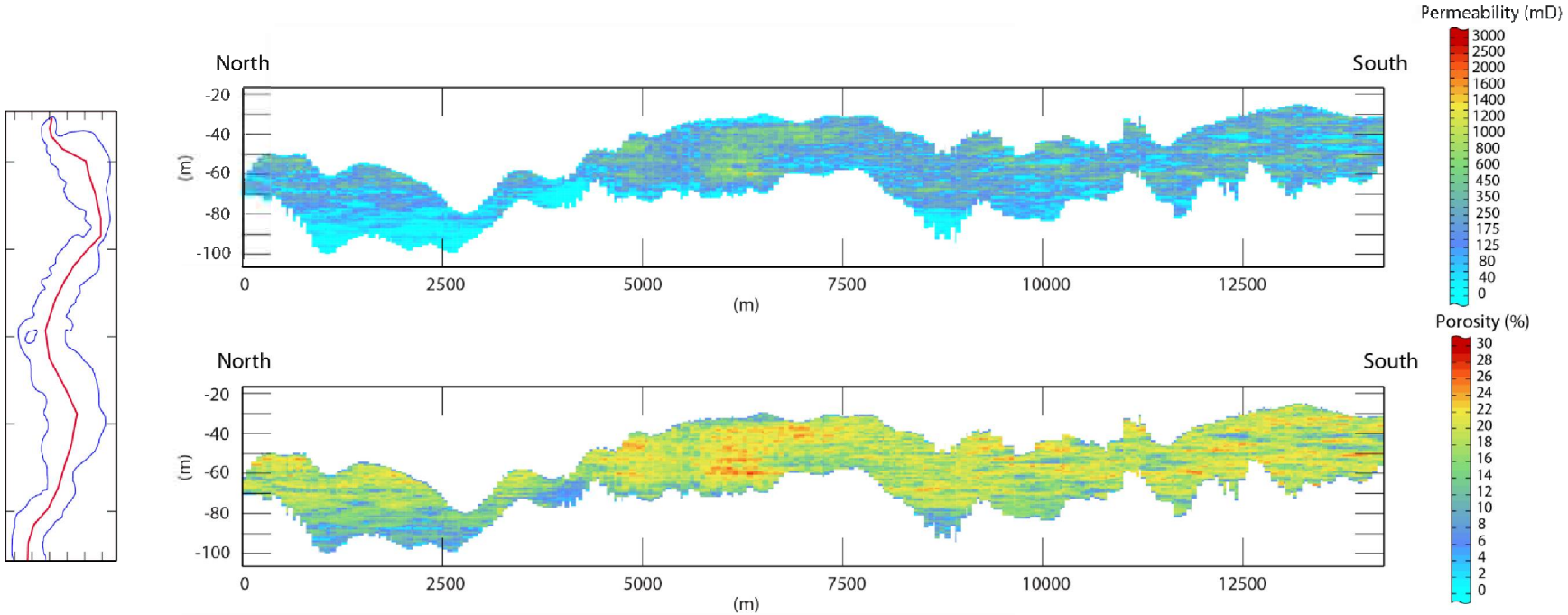

Figure 108 North to south cross section showing the distribution of permeability (top) and porosity (bottom) within the expanded Bridgeport Channel model. The trace of the cross section is shown in the box to the left, which also shows the outline of the channel. The vertical exaggeration is 25×.

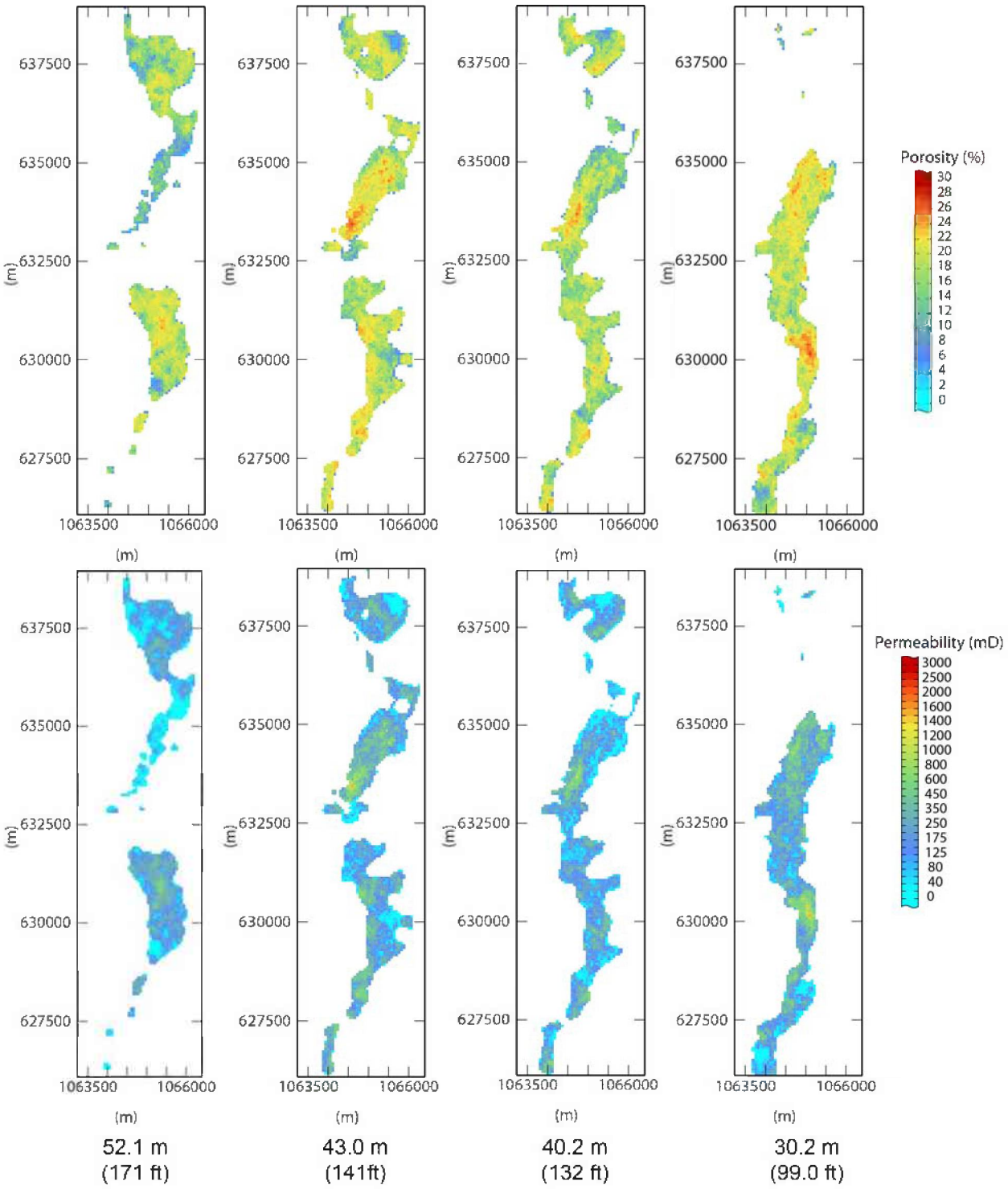

Figure 109 Plan views of layers from the expanded model of the Bridgeport Channel at Lawrence Field that show the distribution of porosity (top) and permeability (bottom) within the expanded model of the Bridgeport Channel at Lawrence Field. The depth from the top of the channel that each pair of images was taken from is listed underneath.

Shelf Clastic: Cypress Sandstone at Lawrence Oil Field

The initial structural geocellular grid contained 155 rows, 155 columns, and 502 layers. Cell spacing of $\Delta x = \Delta y = 30.48$ m (100 ft) and $\Delta z = 0.30$ m (1 ft) resulted in a total surface area of 2.23×10^7 m^2 (2.4×10^8 ft^2) and a volume of 3.40×10^9 m^3 (1.2×10^{11} ft^3). The initial stratigraphic grid contained 139 layers and a volume of 3.34×10^{10} ft^3.

Data for the development of the shelf clastic geocellular model consisted of 127 normalized SP and 119 neutron-density porosity digital logs. A gamma ray cutoff of 60° API was used to filter out porosity log data from the upper shaley interval of the Cypress.

The SP_{norm} log data was depth shifted and plotted against depth-shifted, cross plotted neutron-density porosity log data from nearby wells (<15 m [50 ft]). A curve was fit using regression and the resulting equation of the curve was used to transform SP_{norm} into porosity for each well (Figure 110). There was a large amount of scatter in the plots, so the geologist's experience was relied on to select a suitable curve. The resulting porosity-transformed SP logs were combined with available neutron-density porosity logs to create a combined log data set.

The semivariogram map indicated a trend of N35° (geologist plane; Figure 111). The experimental semivariogram data suggested little difference in ranges for the two directions, so the modeled range was extended in the direction of maximum connectivity to create the desired geometry. The short-range structure had a range of 365.76 m (1,200 ft) in the northeast direction, a range of 182.88 m (600 ft) in the northwest direction, a 3.05 m (10 ft) range in the vertical direction, and a sill of 0.6. The long-range structure had a range of 1,981.2 m (6,500 ft) in the northeast direction, a range of 914.4 m (3,000 ft) in the northwest direction, a range of 9.14 m (30 ft) in the vertical direction, and a sill of 0.3. The semivariogram model used spherical structures with a nugget of 0.1 (Figure 112).

Porosity and permeability data from core analysis records were plotted against each other on a semilog plot and a curve was fit using mean least squares regression. The resulting equation was used to convert porosity into permeability (Figure 113).

The Δx and Δy were upscaled from 30.5 to 61 m (100 to 200 ft) and Δz was upscaled from 0.3 to 0.9 m (1 to 3 ft). The final grid contains 77 rows, 77 columns, and 47 layers.

The porosity and permeability ranges (Table 8) compare reasonably well with the ones determined for the formation from the core analyses, especially when considering the oversampling of sandstone in the core analysis data and the effects of upscaling. The geocellular model was able to successfully capture the lenticular geometry and northeast-southwest trending orientation of the sandstone bodies within the shelf clastic environment seen in this formation (Figure 114–Figure 117).

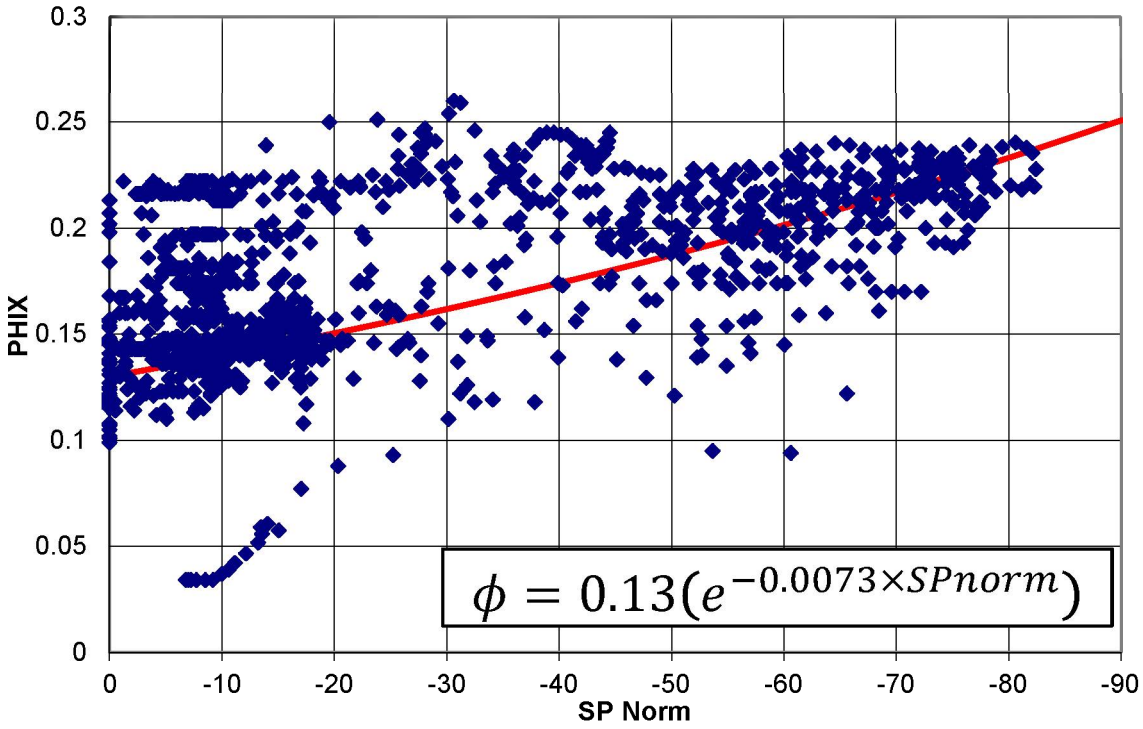

Figure 110 Plot of normalized SP (*x*-axis) vs. porosity (*y*-axis) for the Cypress at Lawrence Field. The equation defining the line was used to transform normalized SP values into porosity in the shelf clastic model.

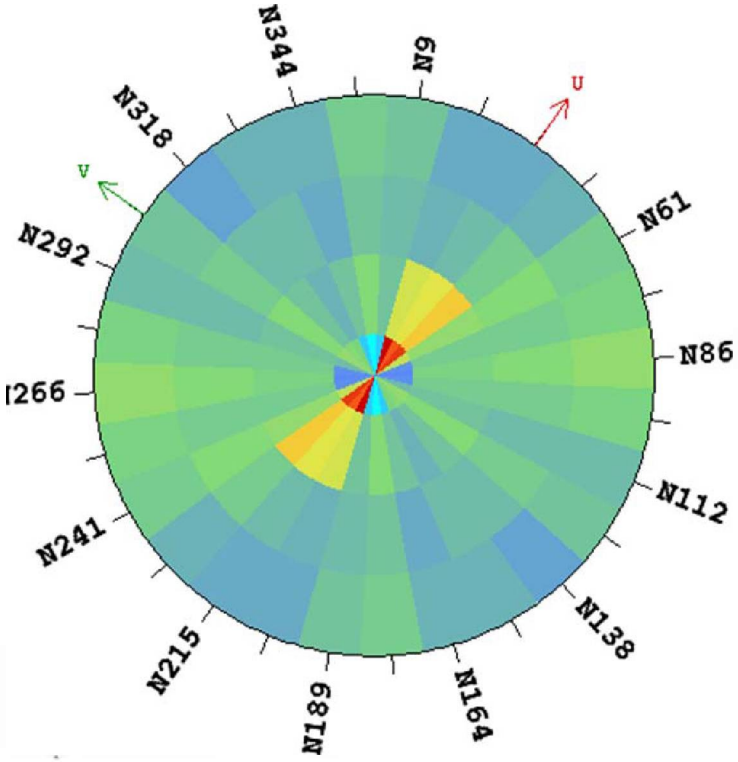

Figure 111 Semivariogram map from the combined log data set for the Cypress Formation at Lawrence Field. A trend in the N35°E direction is visible.

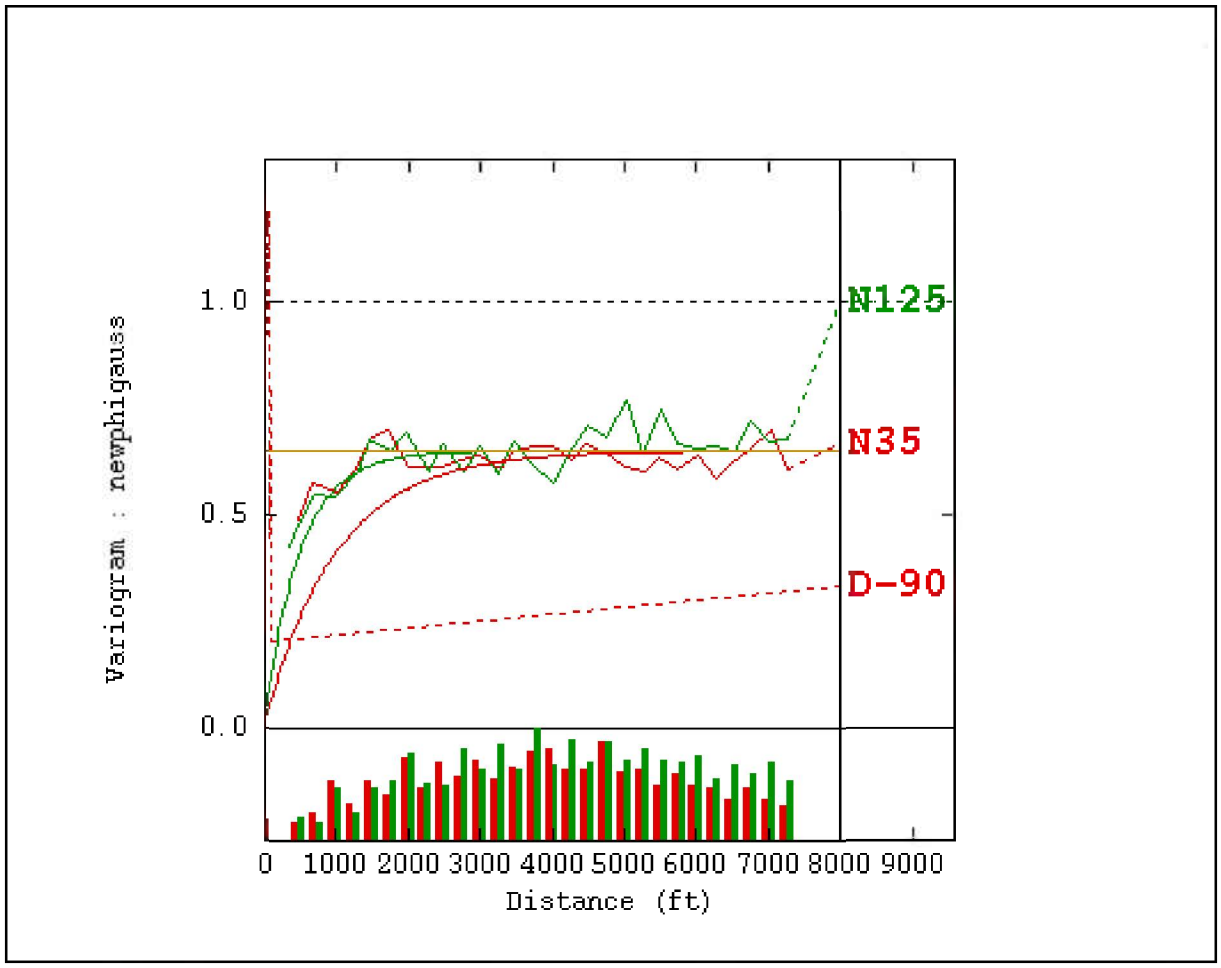

Figure 112 Directional experimental (thin lines) and model (thick lines) semivariograms for the shelf clastic model. The red lines are the semivariograms aligned with the direction of maximum connectivity (N35°), and the green lines are the semivariograms normal to the direction of maximum connectivity (N125°). In this case, the range of the model fit to the direction of maximum connectivity (N35°) was extended to create a model with northeast-southwest trending bodies.

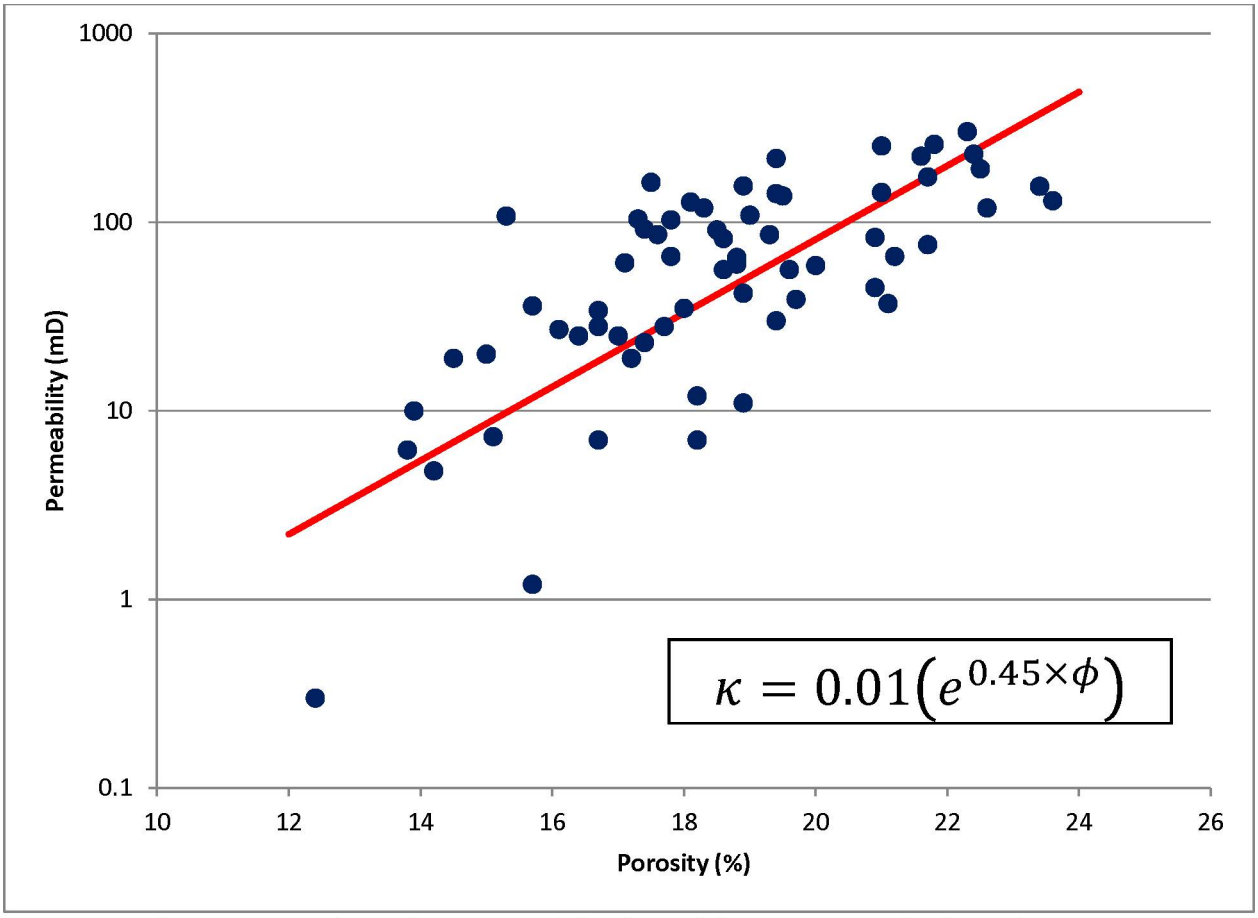

Figure 113 Plot of porosity (*x*-axis) vs. permeability (*y*-axis) from core samples from the Cypress at Lawrence Field. The equation defining the line was used to transform porosity values to permeability.

Table 8 Parameters for the shelf clastic geocellular model. The reservoir thickness, porosity, permeability, and pore space rows are the statistics after applying a 10% porosity cutoff and represent the higher quality portion of the formation.

Parameter	Value
Total number of grid cells	278,663
x-direction	77
y-direction	77
z-direction	47
dx/dy (m [ft])	61.0 (200)
dz (m [ft])	0.9 (3)
Area (m^2 [ft^2])	2.20×10^7 (2.37×10^8)
Total volume (m^3 [ft^3])	9.46×10^8 (3.34×10^{10})
Reservoir thickness (min/max/mean) (m [ft])	0.9/36.6/23.52 (3/120/77.17)
Number of defined cells	1.58×10^5
Total defined volume (m^3 [ft^3])	5.38×10^8 (1.90×10^{10})
Depth (min/max/mean) (m [ft])	231/383.1/307.2 (759/1,257/1,008)
Porosity (min/max/mean/st.d)	0.01/0.25/0.08/0.07
Total pore space	2.68×10^9
Permeability (min/max/mean/median/st.d) (cm^2 [mD])	1.97×10^{-13}/8.09×10^{-9}/1.20×10^{-10}/1.89×10^{-11}/4.76×10^{-10} (0.02/820.14/12.21/1.92/48.31)
Reservoir porosity (min/max/mean/st.d)	0.1/0.25/0.14/0.03
Reservoir permeability (min/max/mean/median/st.d) (cm^2 [mD])	7.49×10^{-12}/8.09×10^{-9}/2.04×10^{-10}/2.20×10^{-11}/6.18×10^{-10} (0.76/820.14/20.71/2.23/62.7)
Reservoir pore space	2.66×10^9

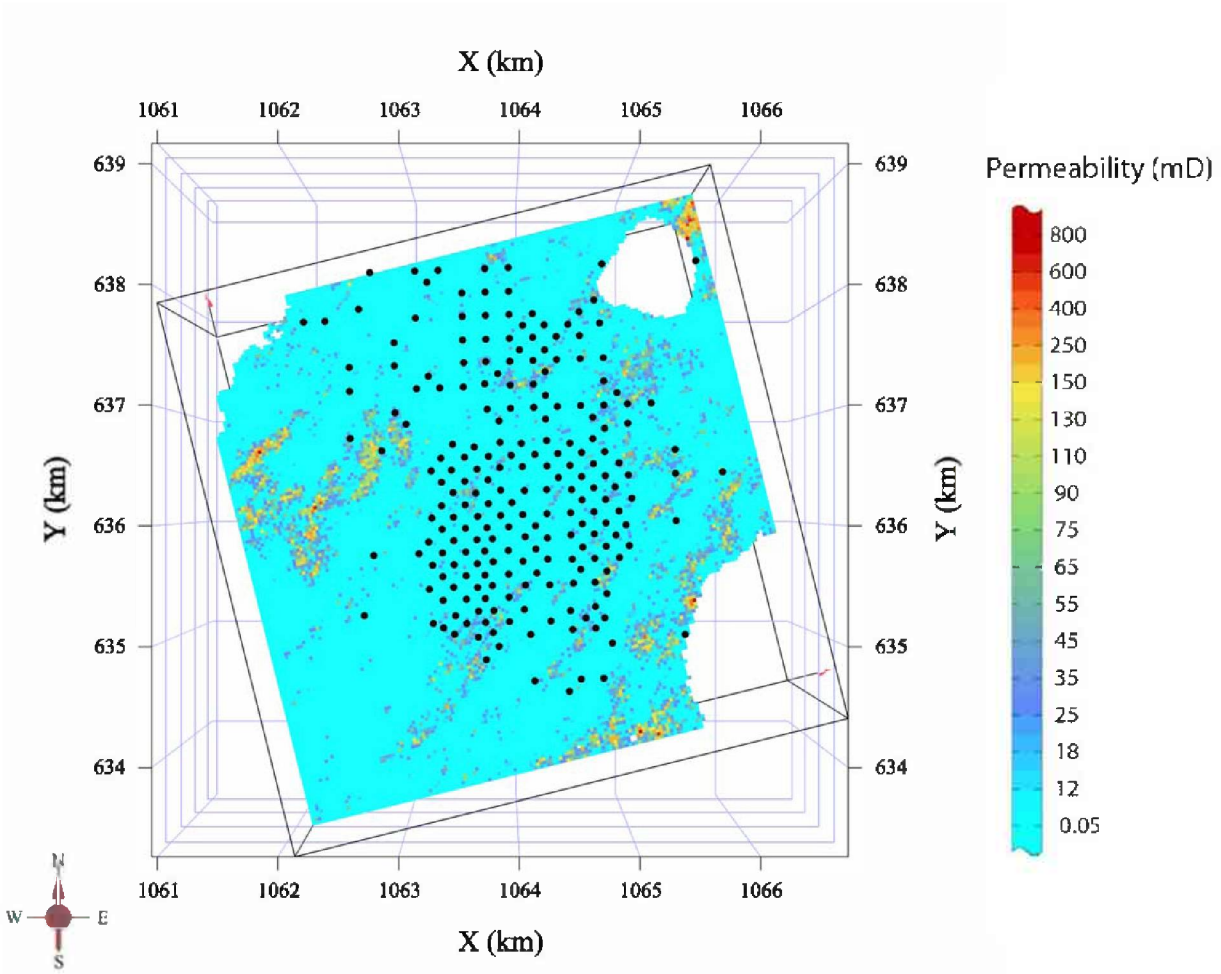

Figure 114 Layer of the permeability distribution from the shelf clastic model. Black dots represent well locations. The layer is 19 m (63 ft) below the top of the Cypress.

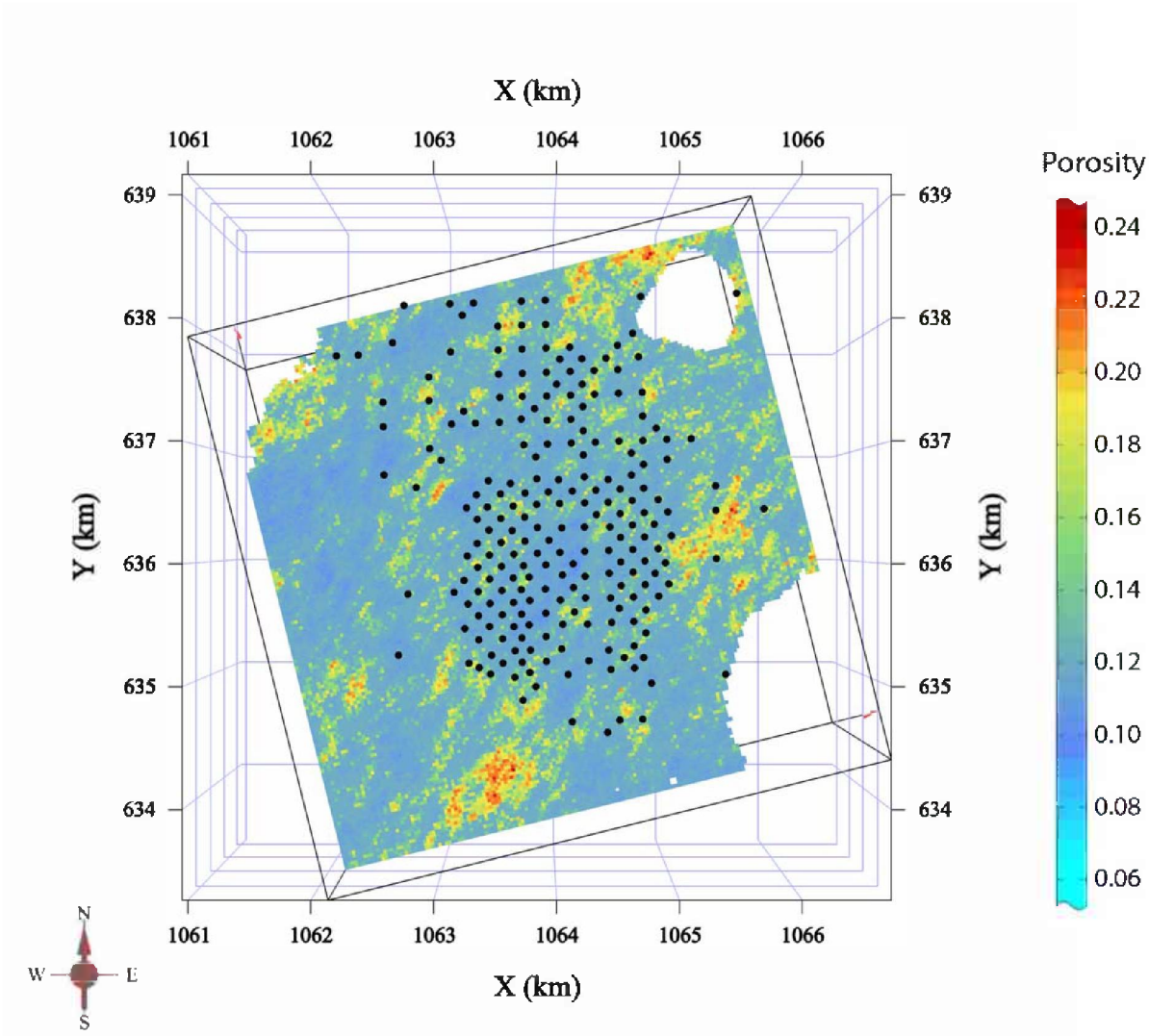

Figure 115 Layer of the porosity distribution from the shelf clastic model. Black dots represent well locations. The layer is 19 m (63 ft) below the top of the Cypress.

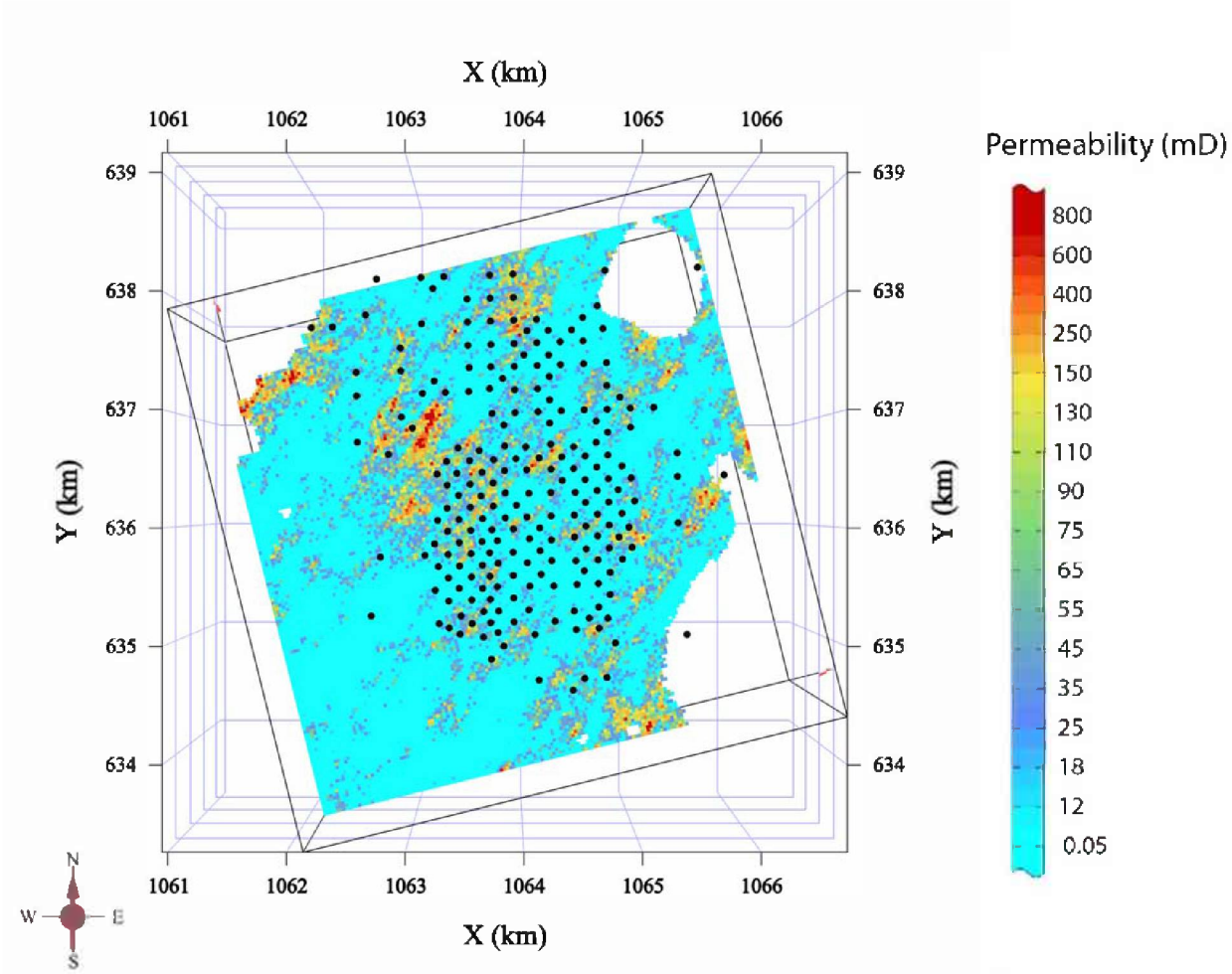

Figure 116 Layer of the permeability distribution from the shelf clastic model. Black dots represent well locations. The layer is 24 m (78 ft) below the top of the Cypress.

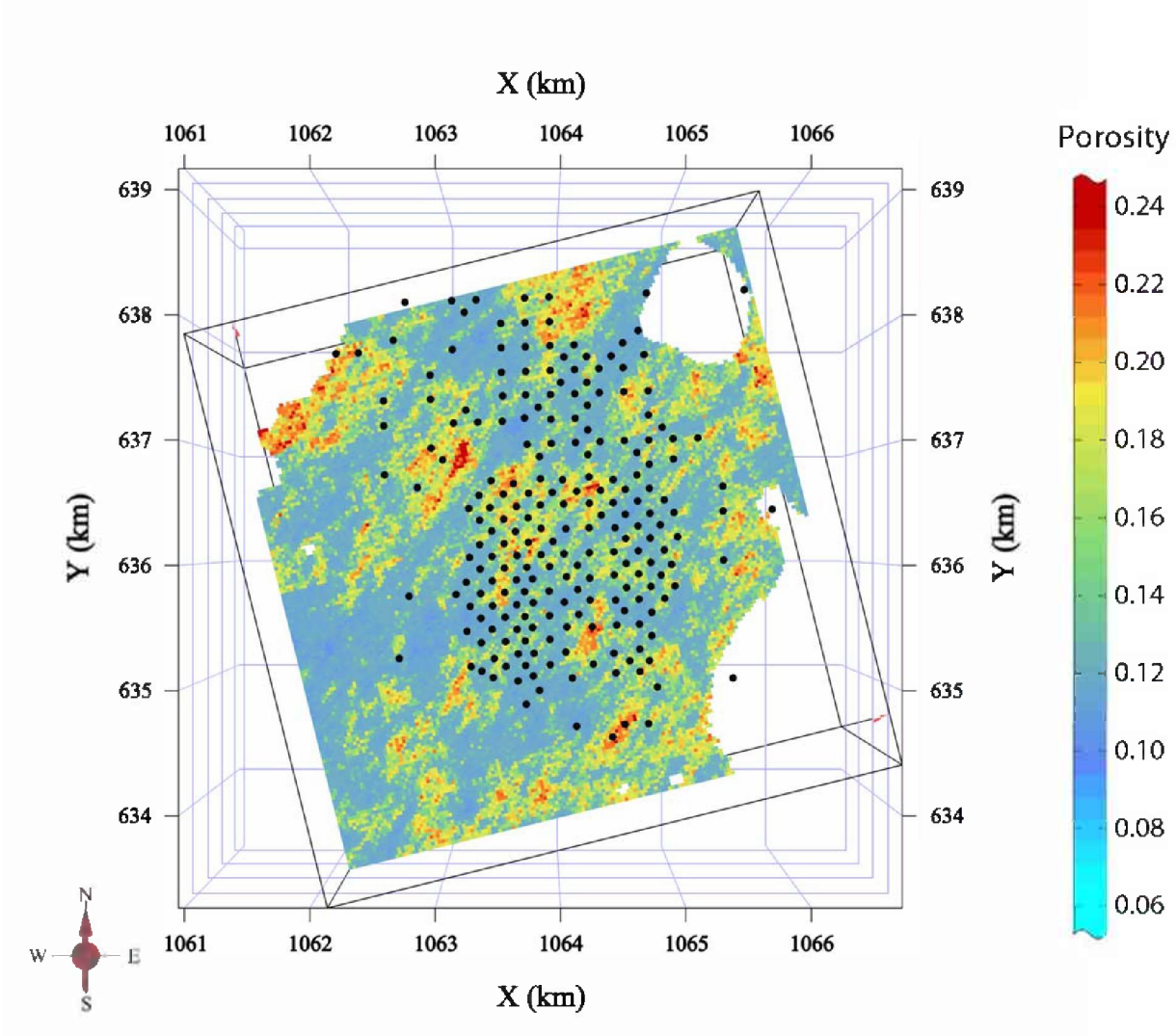

Figure 117 Layer of the porosity distribution from the shelf clastic model. Black dots represent well locations. The layer is 24 m (78 ft) below the top of the Cypress.

Shelf Carbonate: Ste. Genevieve at Johnsonville Consolidated

The initial structural geocellular grid contained 140 rows, 130 columns, and 215 layers. Cell spacing of $\Delta x = \Delta y = 30.48$ m (100 ft) and $\Delta z = 0.30$ m (1 ft) resulted in a total surface area of 1.69×10^7 m^2 (1.82×10^8 ft^2) and a volume of 1.11×10^9 m^3 (3.91×10^{10} ft^3). Structural maps and isopachs provided by the geologist were used to delineate three ooid zones (McClosky D, C B) and a productive dolomite zone (Dolomite B) within the model. The top of the Fredonia (see the "Shelf Carbonate" section of the Geologic Modeling for detail) was used as the stratigraphic datum. The stratigraphic grid had 69 layers and a volume of 3.57×10^8 m^3 (1.26×10^{10} ft^3).

Data for the development of the geocellular model consisted of seven digital neutron-density porosity logs and 87 normalized digital SP logs. Semivariogram maps suggested an isotropic distribution, so SP values were used to construct omnidirectional semivariograms for each zone (Figure 118–Figure 121). The models fit to these semivariograms have the characteristics shown in Table 9.

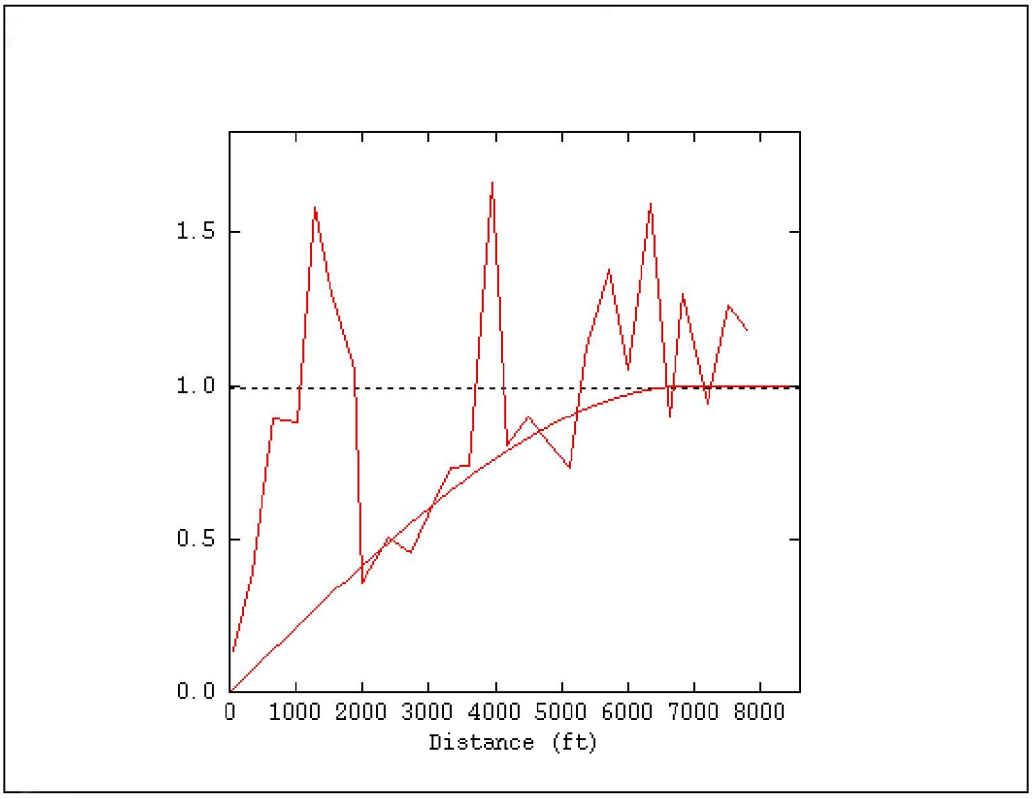

Figure 118 Omnidirectional experimental (thin line) and model (thick line) semivariogram for the McClosky D zone of the shelf clastic model.

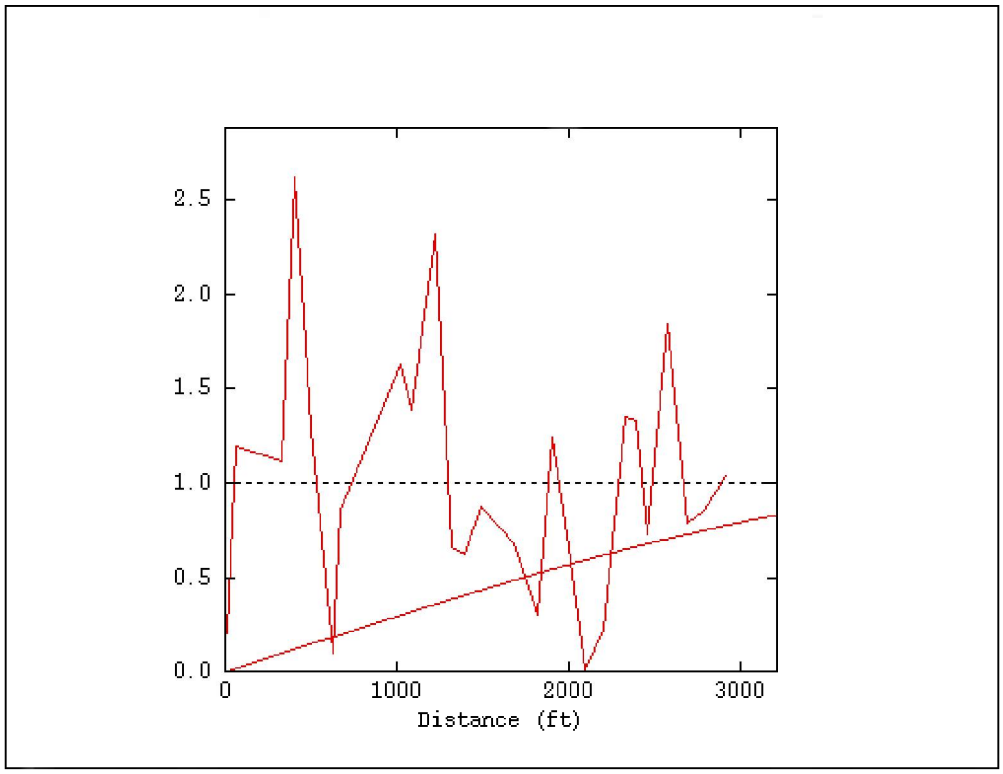

Figure 119 Omnidirectional experimental (thin line) and model (thick line) semivariogram for the McClosky C zone of the shelf clastic model.

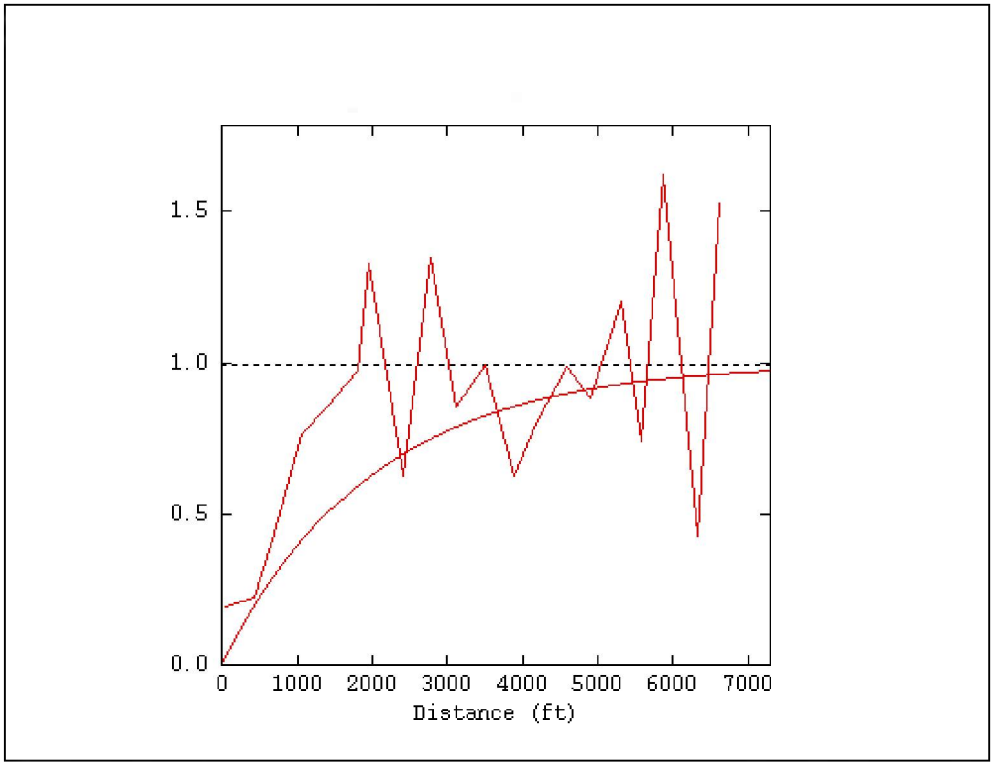

Figure 120 Omnidirectional experimental (thin line) and model (thick line) semivariogram for the McClosky B zone of the shelf clastic model.

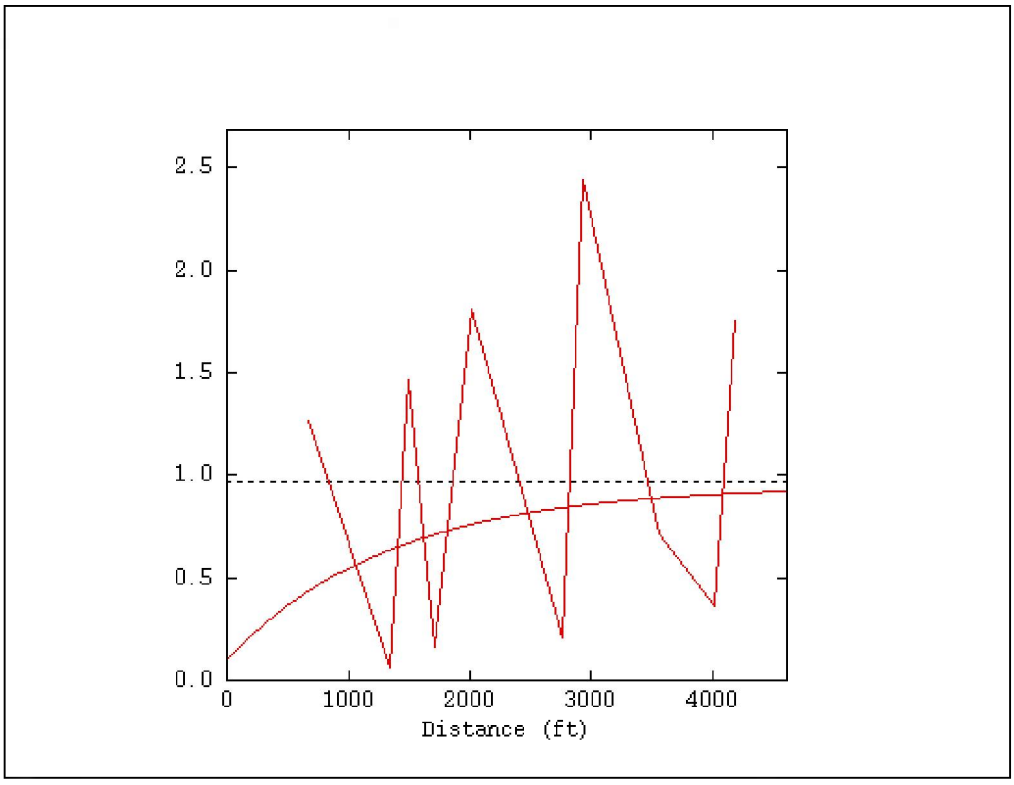

Figure 121 Omnidirectional experimental (thin line) and model (thick line) semivariogram for the Dolomite B zone of the shelf clastic model.

Table 9 Characteristics of the models fit to the semivariograms.

	McClosky D	McClosky C	McClosky B	Dolomite B
Nugget	–	–	0.1	–
Range (x/y; m [ft])	2,134 (7,000)	1,524 (5,000)	1,219 (4,000)	1,829 (6,000)
Range (z; m [ft])	4.6 (15)	9.1 (30)	3.0 (10)	8.2 (27)
Sill	1	1	0.85	1

Simulated SP values were converted to porosity by using a transform derived from the logs that had both SP and porosity data within the McClosky. The SP data was plotted against the porosity data and a curve was drawn (Figure 122). There was a significant amount of scatter, so a curve was selected to produce porosity values in line with the geologist's expectations. The equation defining this curve was used to transform SP values to porosity. Porosity values were converted to permeability by using transform equations derived from the literature (Jennings and Lucia, 2003; Figure 123).

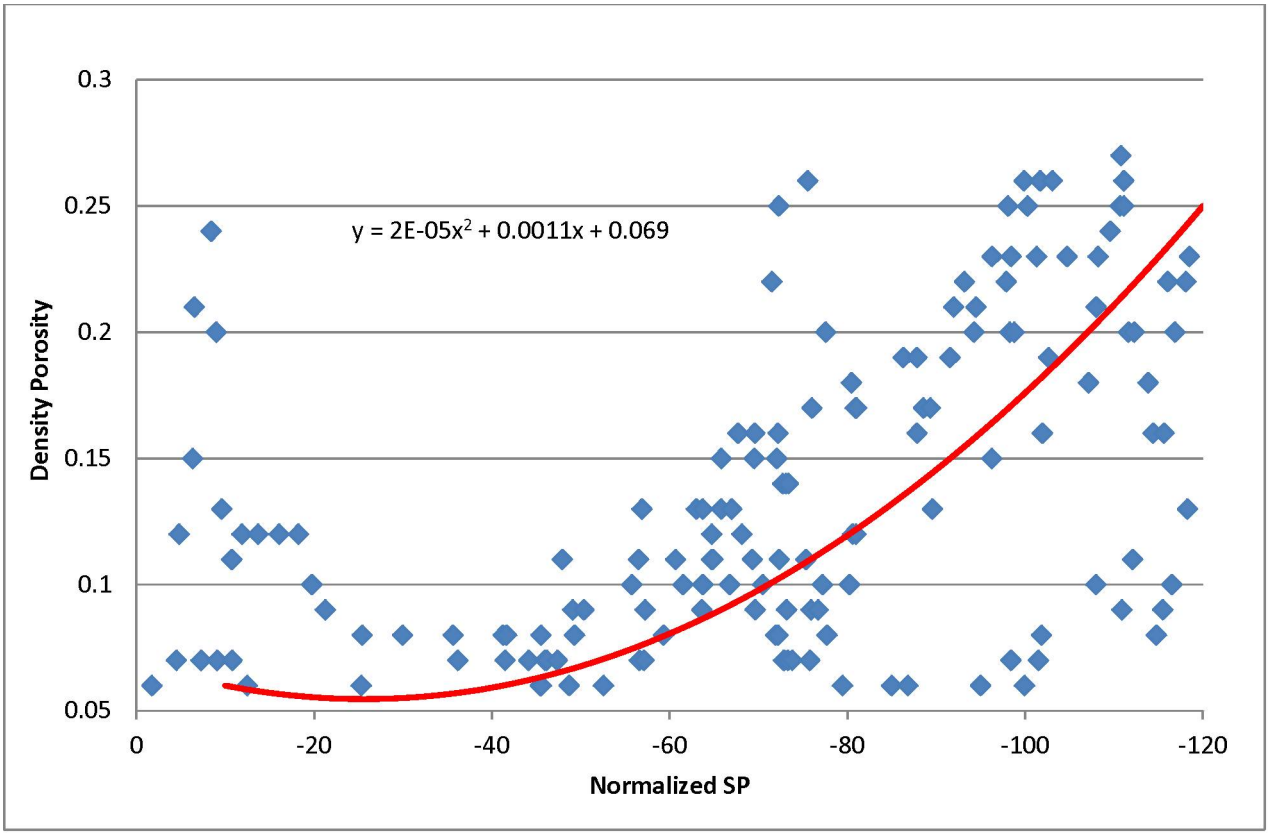

Figure 122 Plot of normalized SP (*x*-axis) vs. density porosity (*y*-axis) for the logs that had both within the McClosky. The equation defining the line was used to transform normalized SP values to porosity. The curve was selected to produce porosity values in line with geologists' expectations.

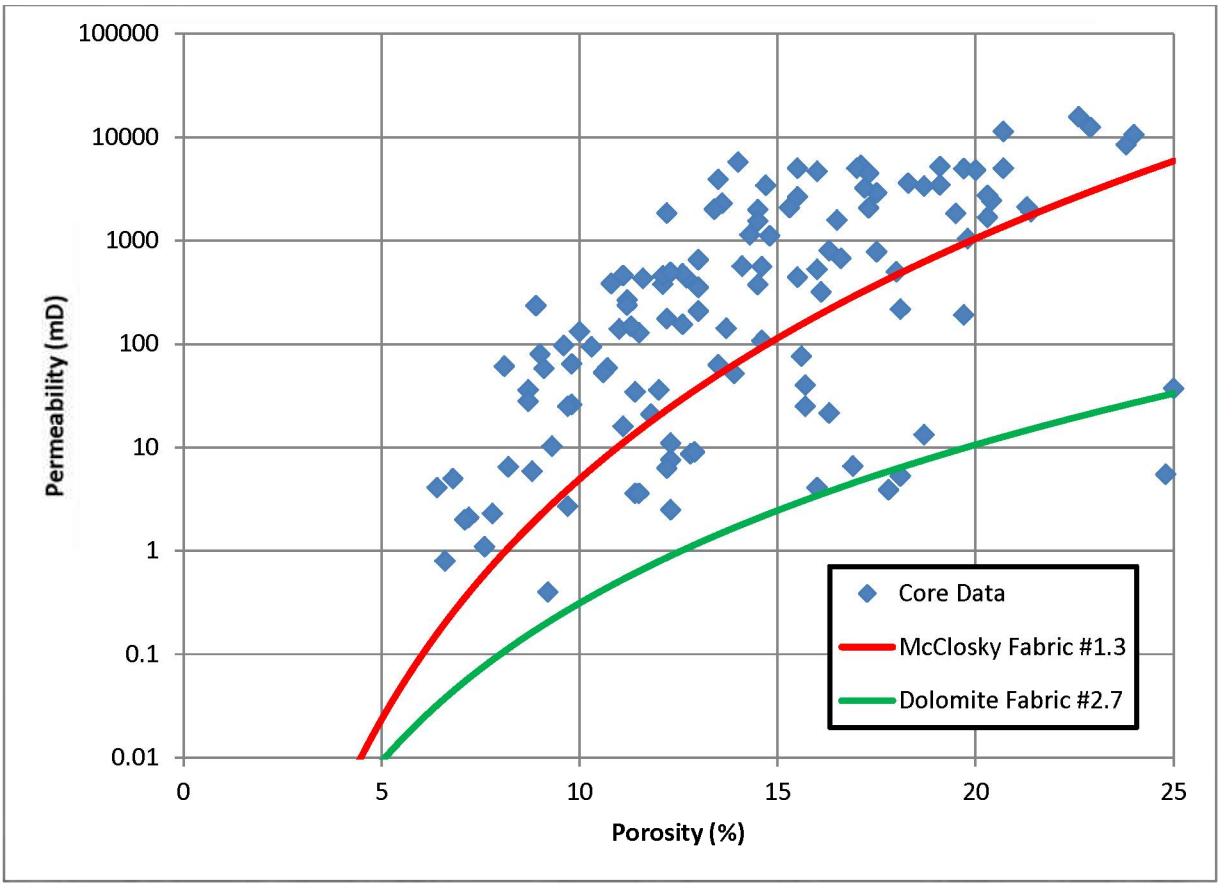

Figure 123 A plot of porosity (*x*-axis) vs. permeability (*y*-axis) data from core analysis reports from the McClosky within Johnsonville Field. The equations defining the lines were used to transform simulated porosity values to permeability within the oolite grainstone (red line) and dolomitic (green line) portions of the model. The lines were adjusted to produce permeability values in line with geologists' expectations.

A rock fabric number of 1.3 was used for the oolite zones. The ooids within the McClosky are considered extremely permeable grainstones (rock fabric number of 1), which is generally supported by the porosity-permeability relationship observed in the available core data (Figure 123). However, it was determined that some very high permeability values were likely the result of fractured plugs, so a more conservative line was imposed. Several rock fabric numbers were evaluated, and it was determined that a fabric number of 1.3 created permeability values in line with the geologist's expectations and followed the trends present in the core data (red line, Figure 123). The equation defining this line is

$$k = e^{19.39} * \Phi^{7.726} \quad (2)$$

A rock fabric number of 2.7 was used to transform the porosity to permeability for the remaining dolomitic areas of the model. Thin sections suggest that the dolomite is medium to fine grained (rock fabric number between 2 and 3). A few data points from the core analysis reports have high porosity and relatively low permeability, which also suggests that a portion of the reservoir has a rock fabric number between 2 and 3. Multiple lines were evaluated, and it was determined that a

fabric number of 2.7 best fit these data points (green line, Figure 123). The equation defining this line is

$$k = e^{10.56} * \Phi^{5.09} \quad (3)$$

The Δx and Δy were upscaled from 30.5 to 61 m (100 to 200 ft) and Δz was upscaled from 0.3 to 0.9 m (1 to 3 ft). The final grid contained 70 rows, 65 columns, and 23 layers (Table 10).

The geocellular model was able to successfully capture the general geometry and compartmentalized nature of the ooid zones found within the McClosky, as well as the sharp contrast between the petrophysical properties of the ooid grainstone and the dolomite (Figure 124–Figure 127).

Table 10 Parameters for the shelf clastic geocellular model. The reservoir thickness, porosity, permeability, and pore space rows are the statistics after applying a 5% porosity cutoff and represent the higher quality portion of the formation.

Parameter	Value
Total number of grid cells	1.05×10^5
x-direction	65
y-direction	70
z-direction	23
dx/dy (m [ft])	61.0 (200)
dz (m [ft])	0.9 (3)
Area (m^2 [ft^2])	1.69×10^7 (1.82×10^8)
Total volume (m^3 [ft^3])	3.57×10^8 (1.26×10^{10})
Mean reservoir thickness (m [ft])	253.2 (77.17)
Number of defined cells	3.82×10^4
Total defined volume (m^3 [ft^3])	1.30×10^8 (4.58×10^9)
Depth (min/max/mean) (m [ft])	766.9/832.1 (2,516/2,730)
Porosity (min/max/mean/st.d)	0.05/0.25/0.07/0.04
Total pore space	2.68×10^9
Permeability (min/max/mean/median/st.d) (cm^2 [mD])	9.86×10^{-14}/5.69×10^{-8}/7.61×10^{-10}/9.86×10^{-14}/3.91×10^{-9} (0.01/5,772/77.14/0.01/397)
Reservoir porosity (min/max/mean/st.d)	0.05/0.25/0.12/0.05
Reservoir permeability (min/max/mean/median/st.d) (cm^2 [mD])	1.97×10^{-13}/5.69×10^{-8}/2.08×10^{-9}/1.57×10^{-11}/6.26×10^{-9} (0.02/5,772/211/1.59/635)
k_z (min/max/mean/median/st.d) (cm^2 [mD])	9.86×10^{-14}/4.84×10^{-8}/5.12×10^{-10}/9.86×10^{-148}/3.04×10^{-9} (0.01/4,906/51.89/0.01/308)
Reservoir k_z (min/max/mean/median/st.d) (cm^2 [mD])	1.97×10^{-13}/4.84×10^{-8}/1.40×10^{-9}/1.08×10^{-12}/4.90×10^{-9} (0.02/4,906/142/0.11/497)

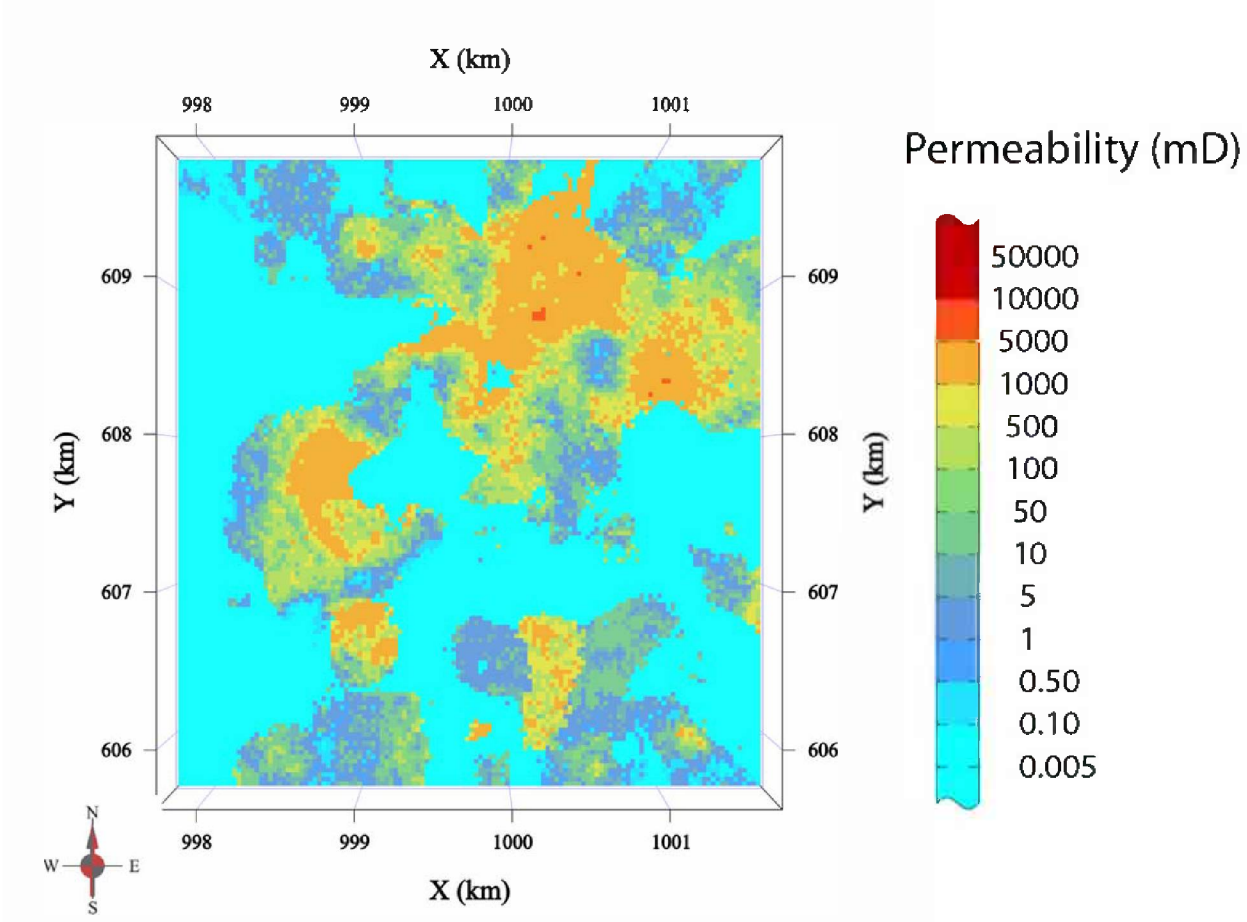

Figure 124 Layer of the permeability distribution from the limestone shelf carbonate model. The layer is 3.7 m (12 ft) below the stratigraphic datum.

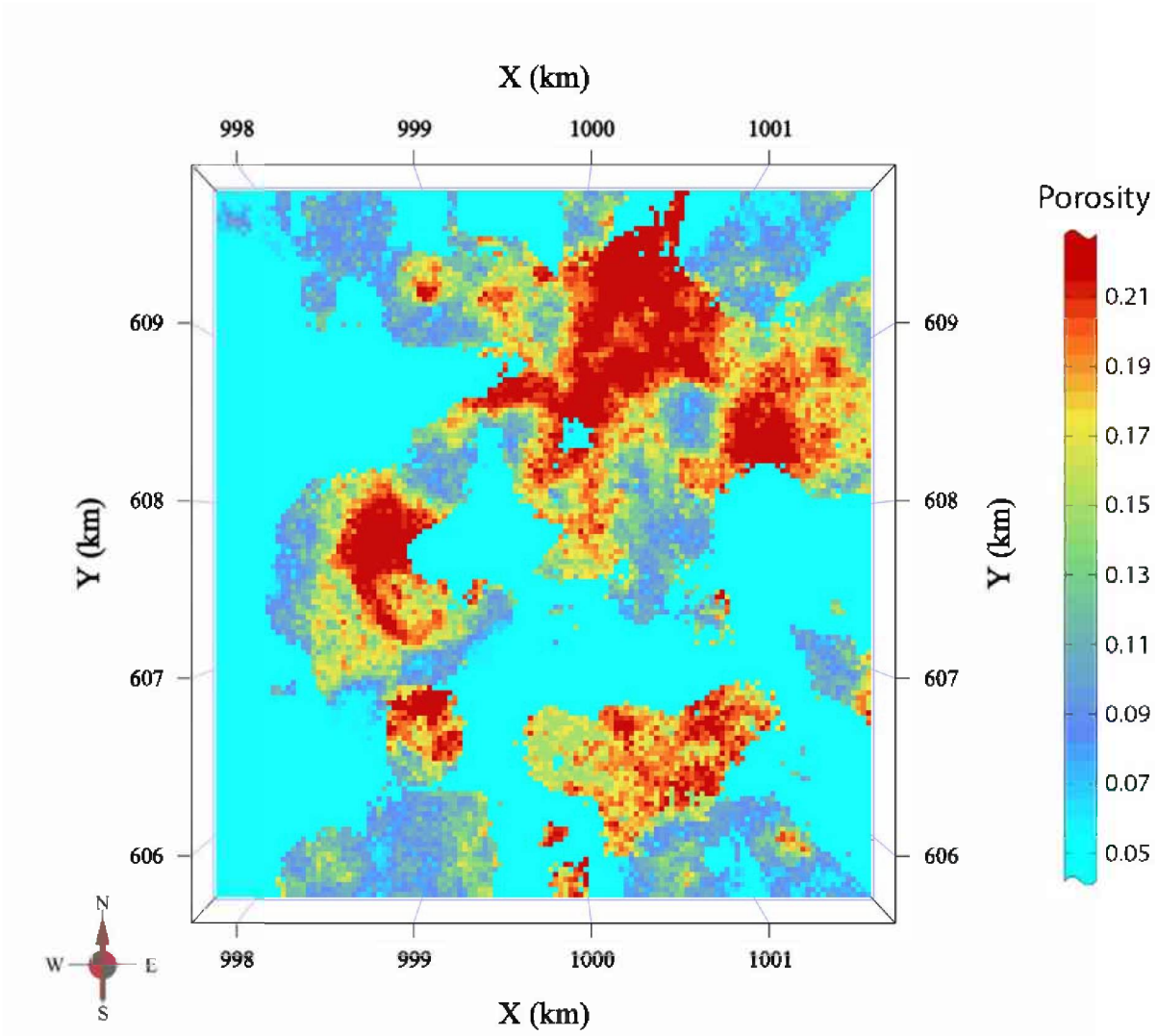

Figure 125 Layer of the porosity distribution from the limestone shelf carbonate model. The layer is 3.7 m (12 ft) below the stratigraphic datum.

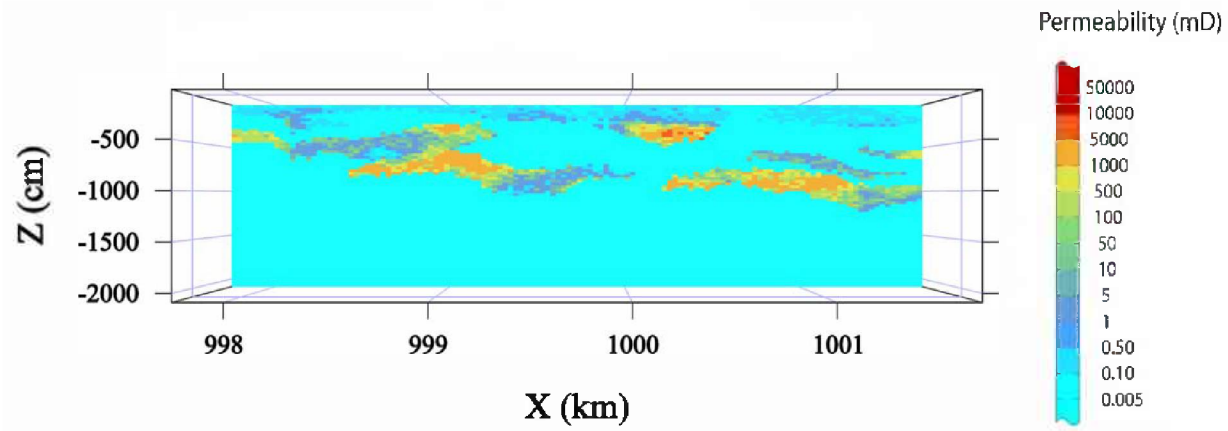

Figure 126 Side view of the permeability distribution from the limestone shelf carbonate model. The layer is 1,250 m [4,100 ft] from the southern boundary with 50× vertical exaggeration.

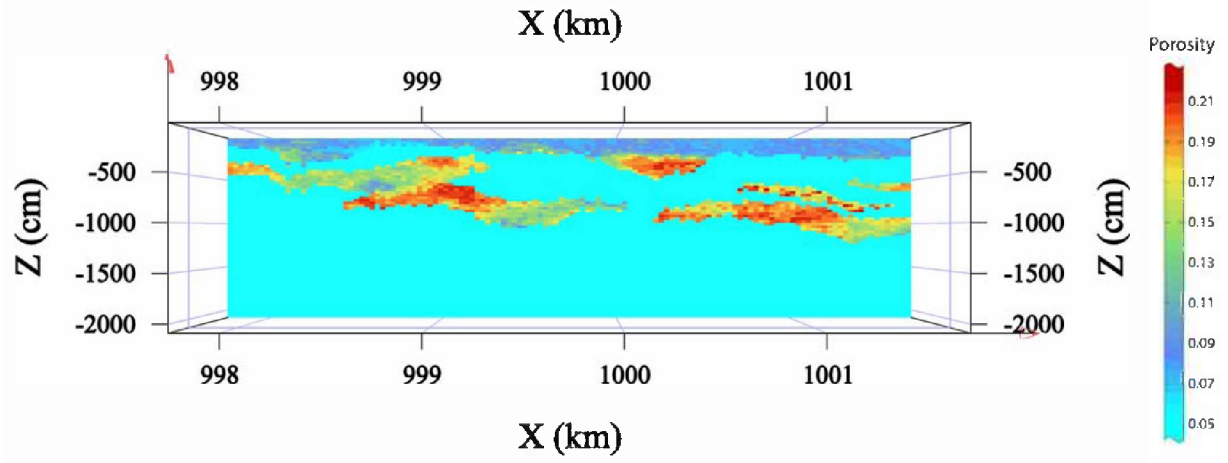

Figure 127 Side view of the permeability distribution from the limestone shelf carbonate model. The layer is 1,250 m [4,100 ft] from the southern boundary with 50× vertical exaggeration.

Shelf Carbonate: Geneva Dolomite at Miletus Oil Field

The original structural grid had 350 rows, 215 columns, and 715 layers. Cell spacing of $\Delta x = \Delta y = 30.48$ m (100 ft) and $\Delta z = 0.30$ m (1 ft) resulted in a total surface area of 6.97×10^7 m^2 (7.5×10^8 ft^2) and a volume of 1.52×10^{10} m^3 (5.38×10^{11} ft^3). To achieve the necessary volume, it was necessary to model the upper dolomite and lower cherty zone separately. Structural maps provided by geologists were used to delineate the boundary between the two zones.

Twenty neutron-density porosity logs were used to develop semivariograms and condition simulations (Table 11). No lateral trend could be detected, so an omnidirectional semivariogram (Figure 128 and Figure 129) was created for each zone.

Table 11 Parameters for the semivariogram models for the dolomite shelf carbonate geocellular model.

	Dolomite	Cherty Zone
Nugget	0.1	0.2
Range (*x*/*y*; m [ft])	2,438 (8,000)	457.2 (1,500)
Range (*z*; m [ft])	6.1 (20)	11 (37)
Sill	0.9	0.8

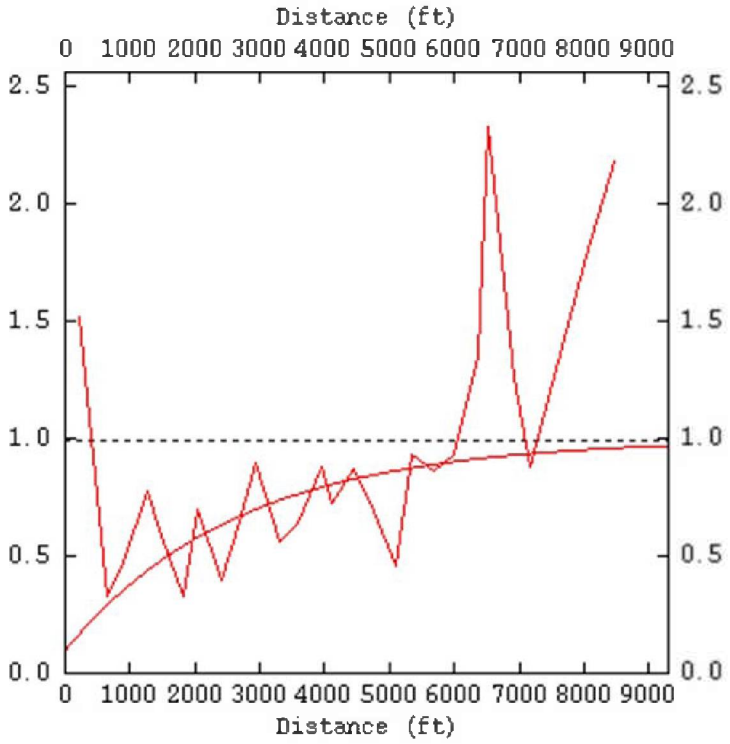

Figure 128 Omnidirectional experimental (thin line) and model (thick line) semivariogram for the upper portion of the dolomite shelf carbonate model. The long range of the semivariogram results in a homogenous distribution of the petrophysical properties.

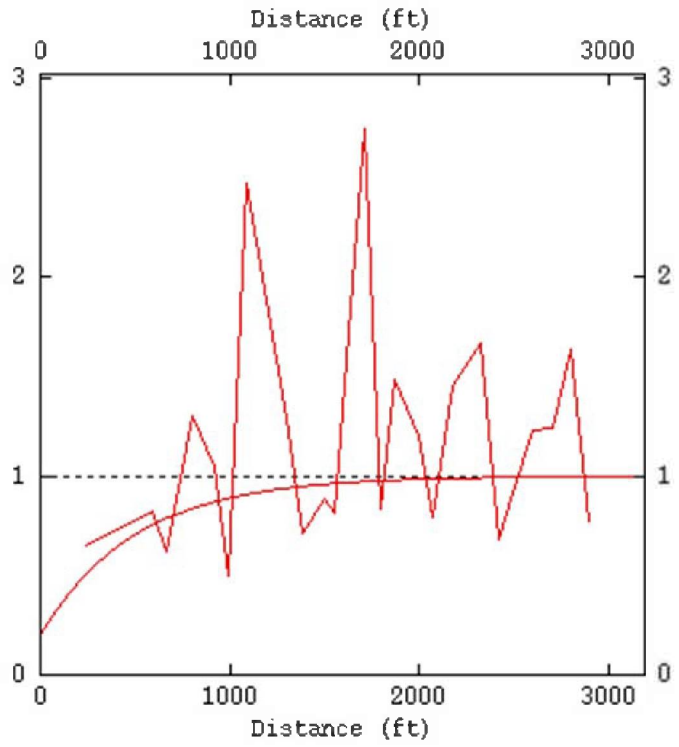

Figure 129 Omnidirectional experimental (thin line) and model (thick line) semivariogram for the lower cherty portion of the dolomite shelf carbonate model. The short range results in a more compartmentalized distribution of the petrophysical properties in the cherty zone.

No core data was available for Miletus Field, so core data from nearby fields (Pakota and Sandoval; Figure 33) were split into cherty and dolomite zones and used to develop porosity-to-permeability transforms (Figure 130) for each zone (Eqs. 4 and 5).

The reservoir transform equation was

$$k = 10^{(phi*0.1869-1.2767)}, \quad (4)$$

and the cherty zone transform equation was

$$k = 10^{(phi*0.2210-3.6694)}. \quad (5)$$

The geocellular model contains the widespread high porosity and permeability typically found in the Geneva dolomite (Figure 131 and Figure 132) as well as the more compartmentalized porous, but less permeable lower cherty zone (Figure 133 and Figure 134). The contrast between the two zones can be seen in a side view (Figure 135 and Figure 136). The modeled porosity and permeability values are within the range of the available core data (Table 12).

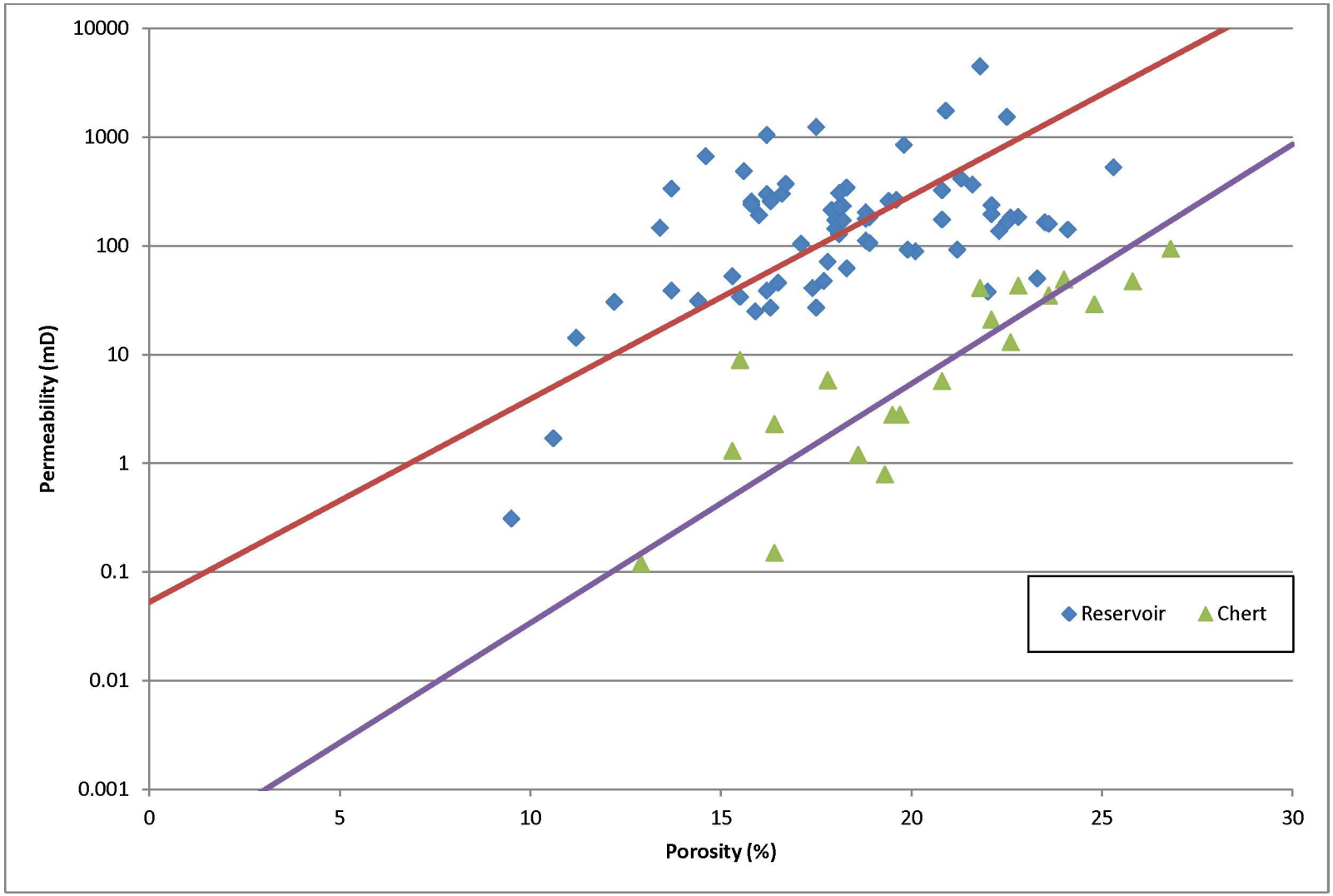

Figure 130 Plot of porosity (*x*-axis) vs. permeability (*y*-axis) data from core analysis reports from the Geneva dolomite at Miletus Field. The equations defining the lines were used to transform porosity values to permeability.

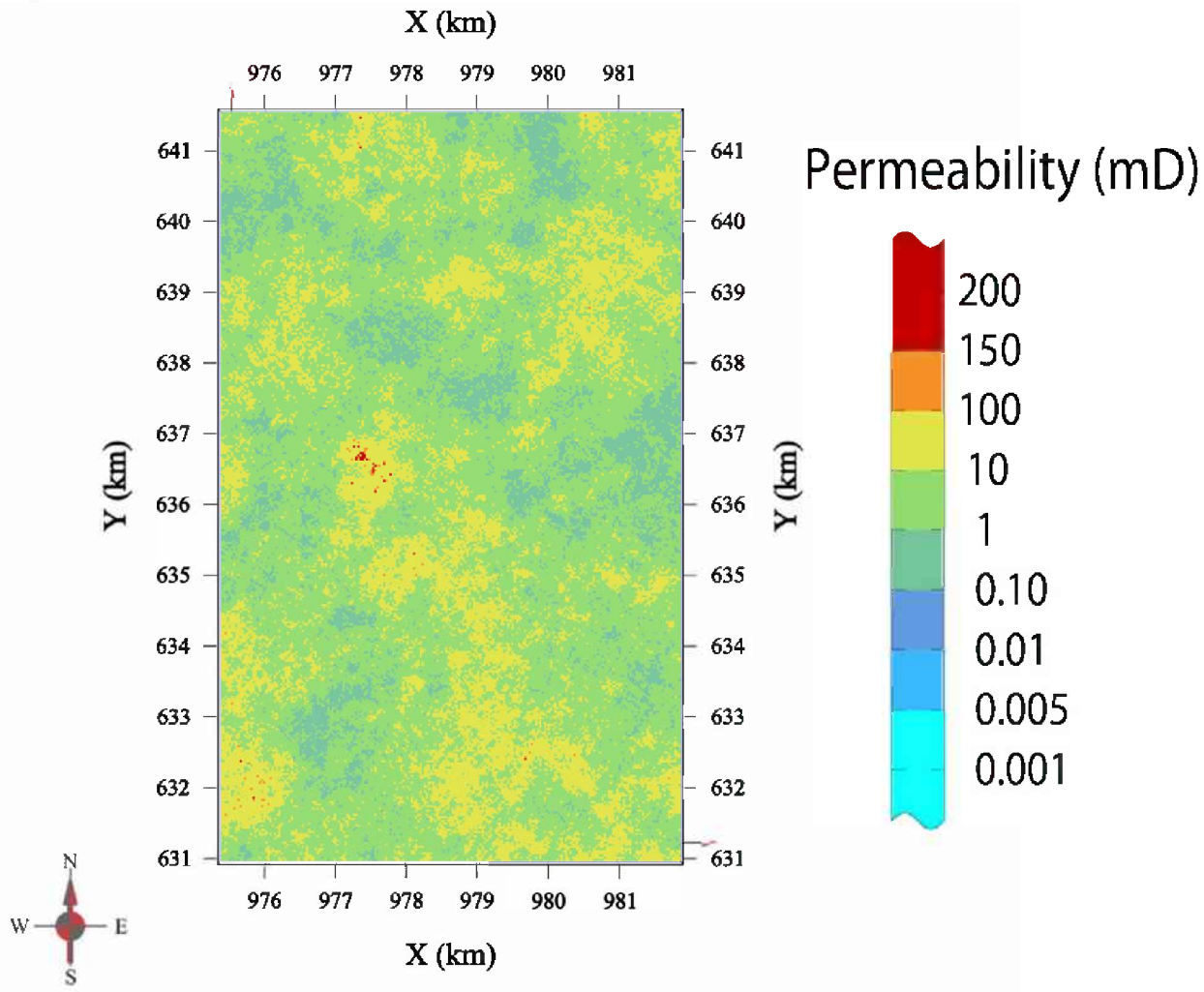

Figure 131 Permeability distribution of the upper reservoir unit for the dolomite shelf carbonate model. The layer is 3.7 m (12 ft) below the stratigraphic datum.

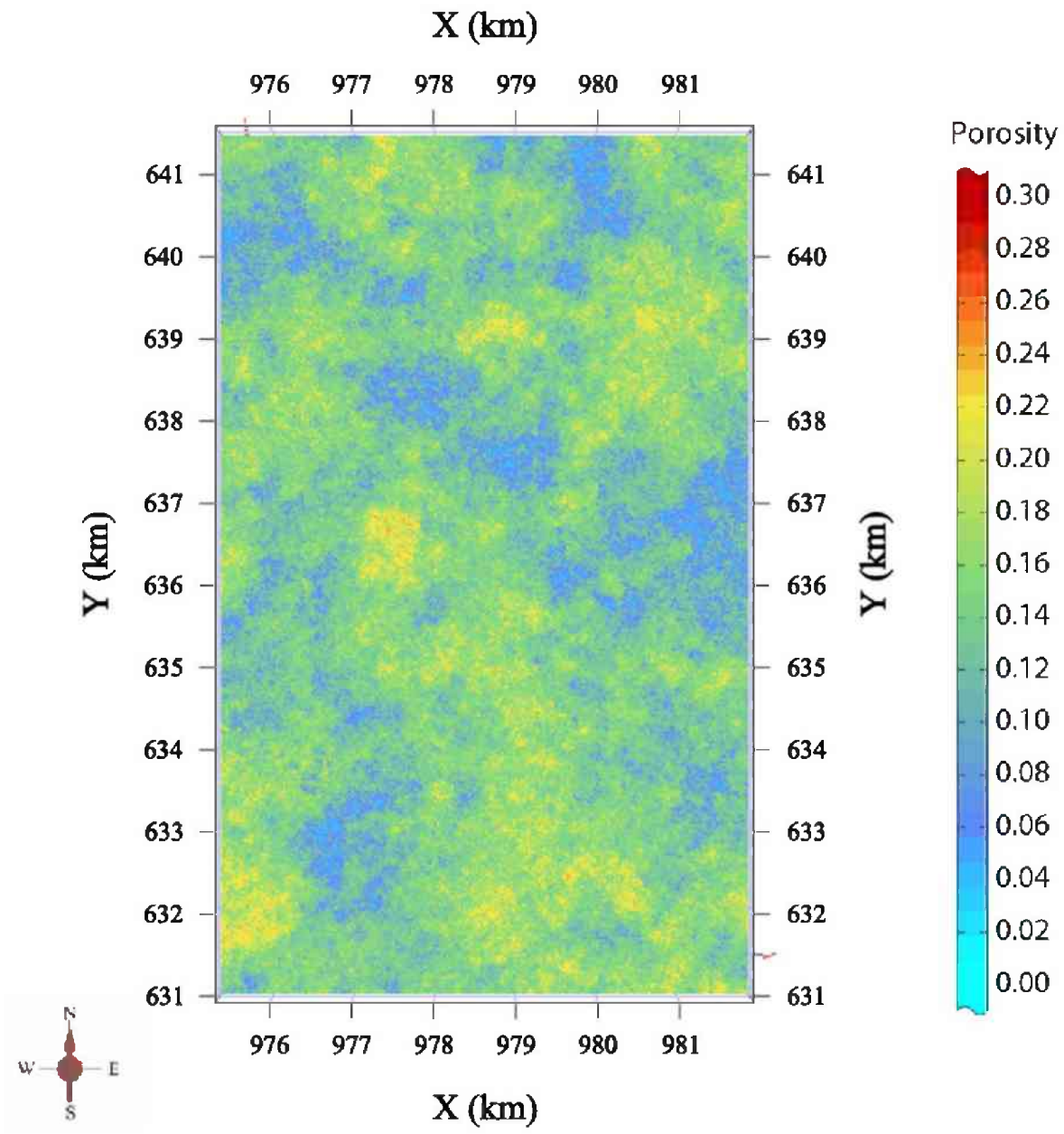

Figure 132 Porosity distribution of the upper reservoir unit for the dolomite shelf carbonate model. The layer is 3.7 m (12 ft) below the stratigraphic datum.

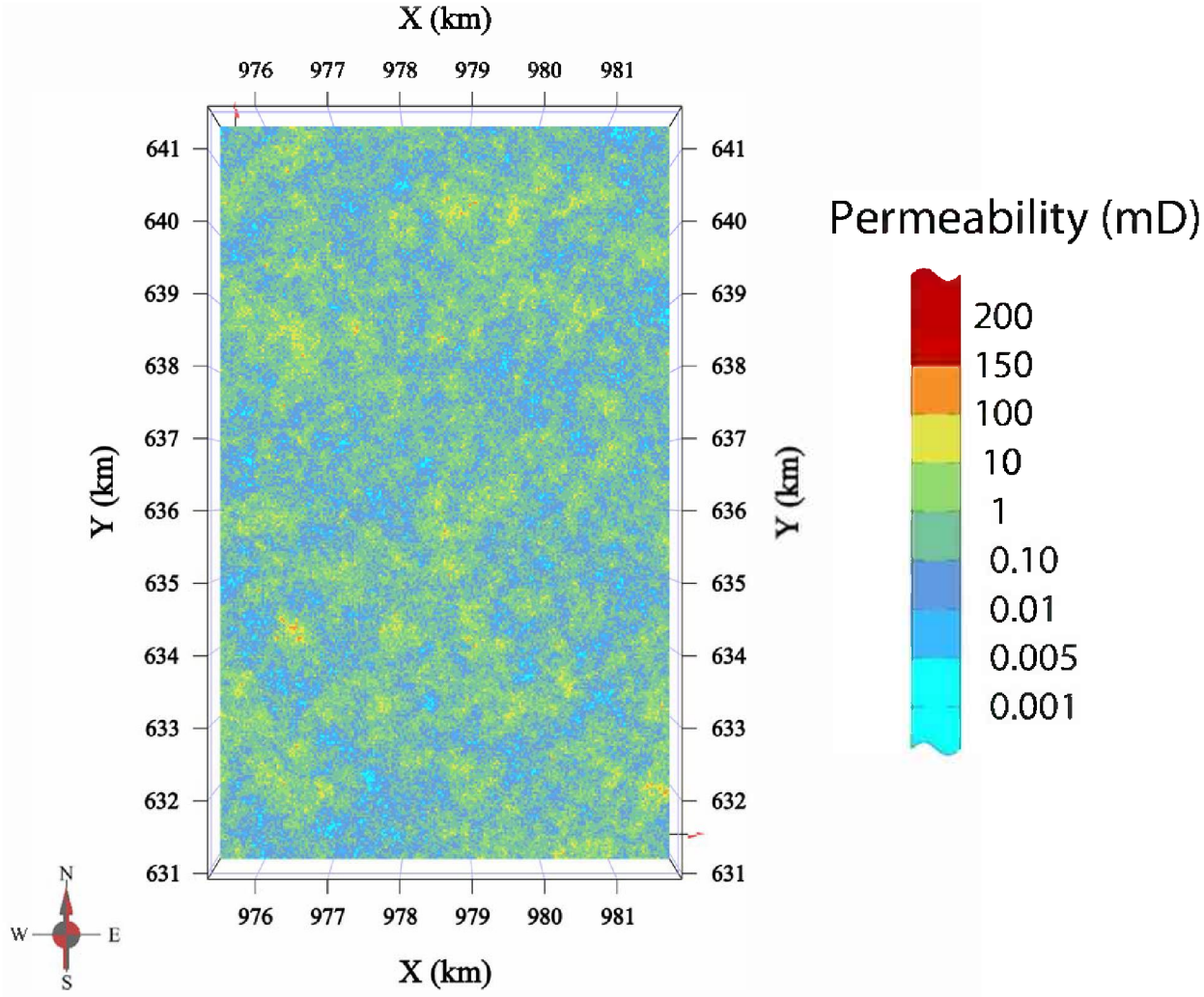

Figure 133 Permeability distribution of the lower cherty unit for the dolomite shelf carbonate model. The layer is 10 m (33 ft) below the stratigraphic datum.

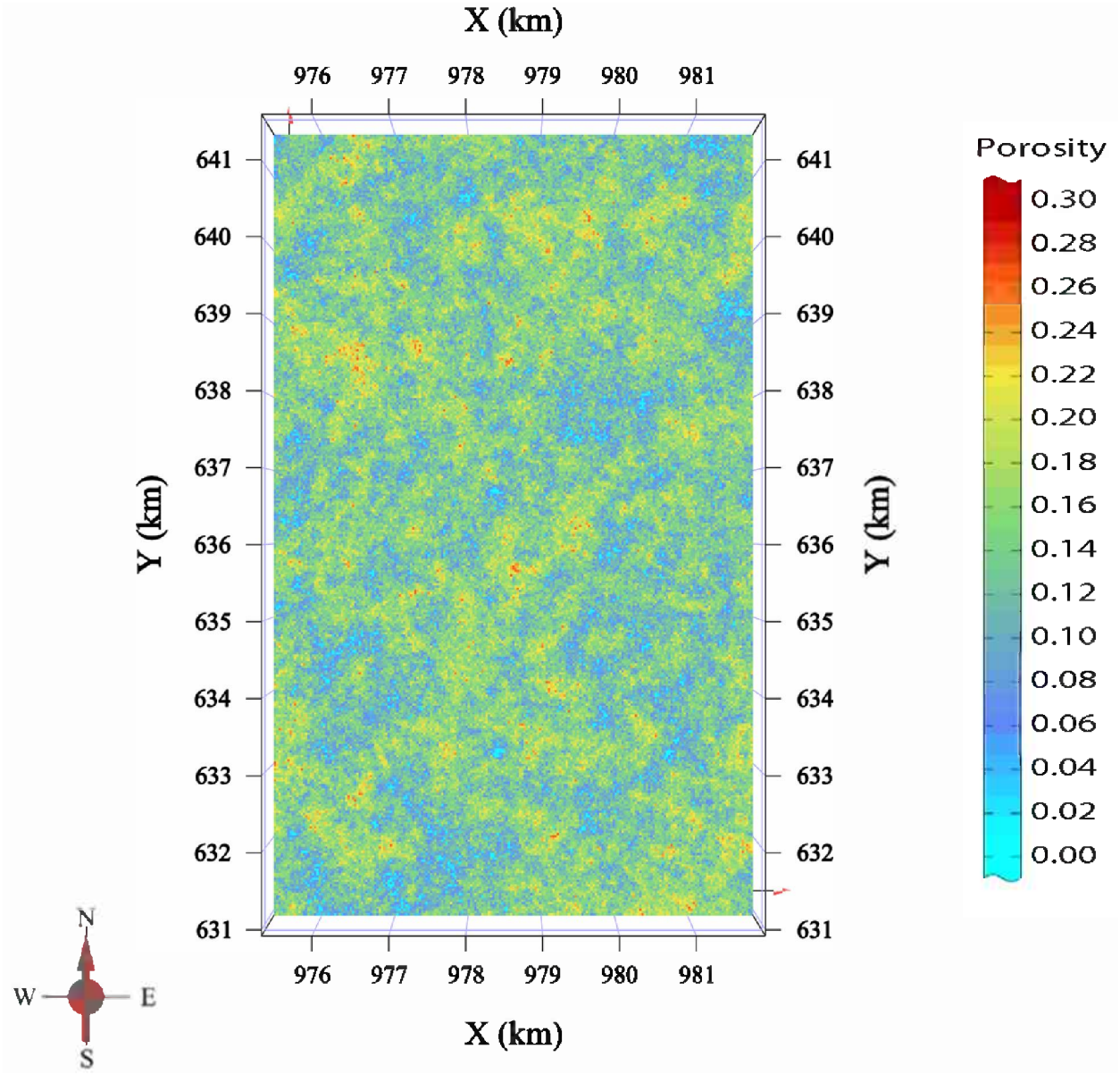

Figure 134 Porosity distribution of the lower cherty unit for the dolomite shelf carbonate model. The layer is 10 m (33 ft) below the stratigraphic datum.

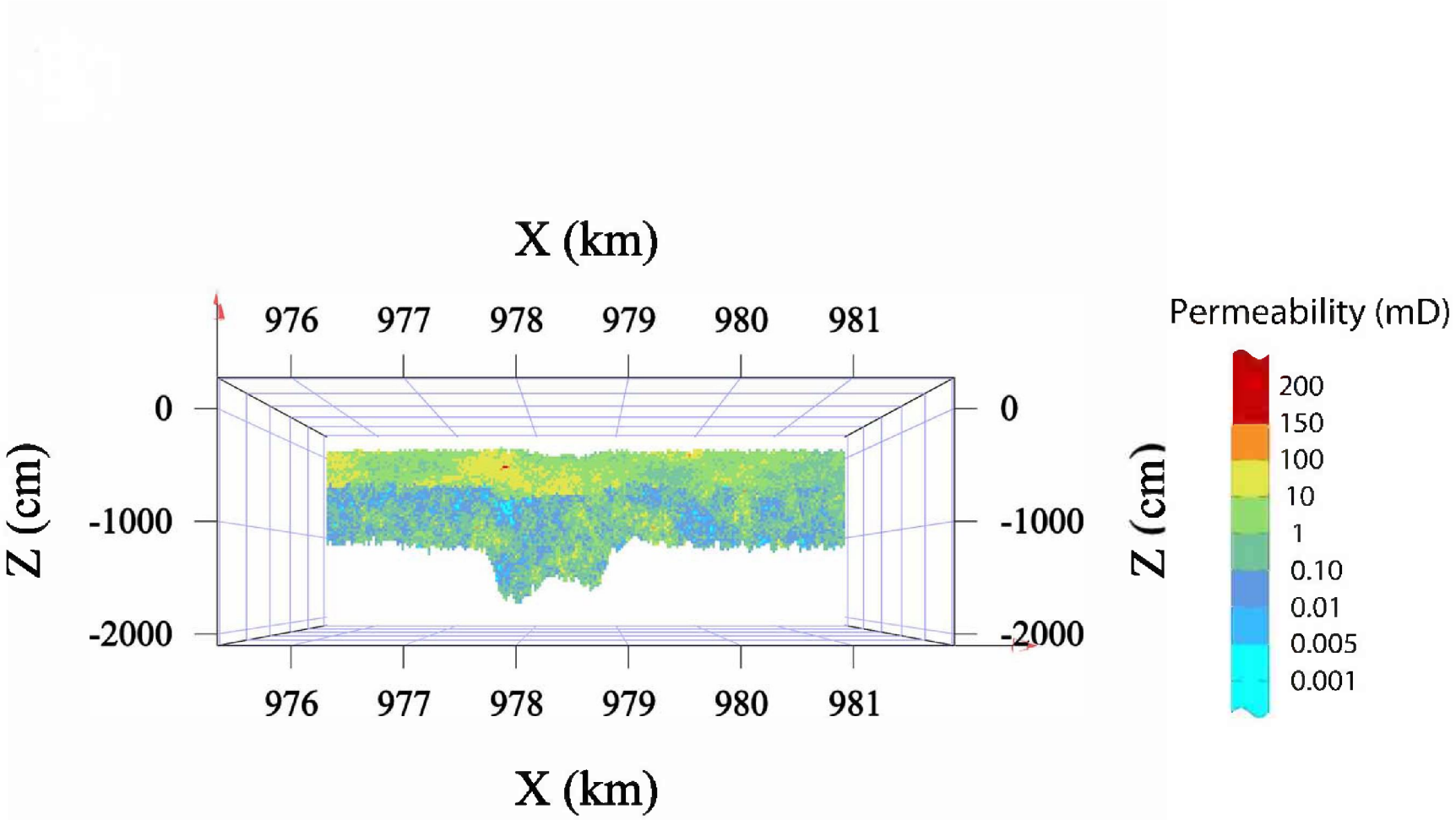

Figure 135 Side view of the permeability distribution of the dolomite shelf carbonate model. The layer is 5,304 m [17,400 ft] from the southern boundary. The upper reservoir zone has better permeability than the lower cherty zone.

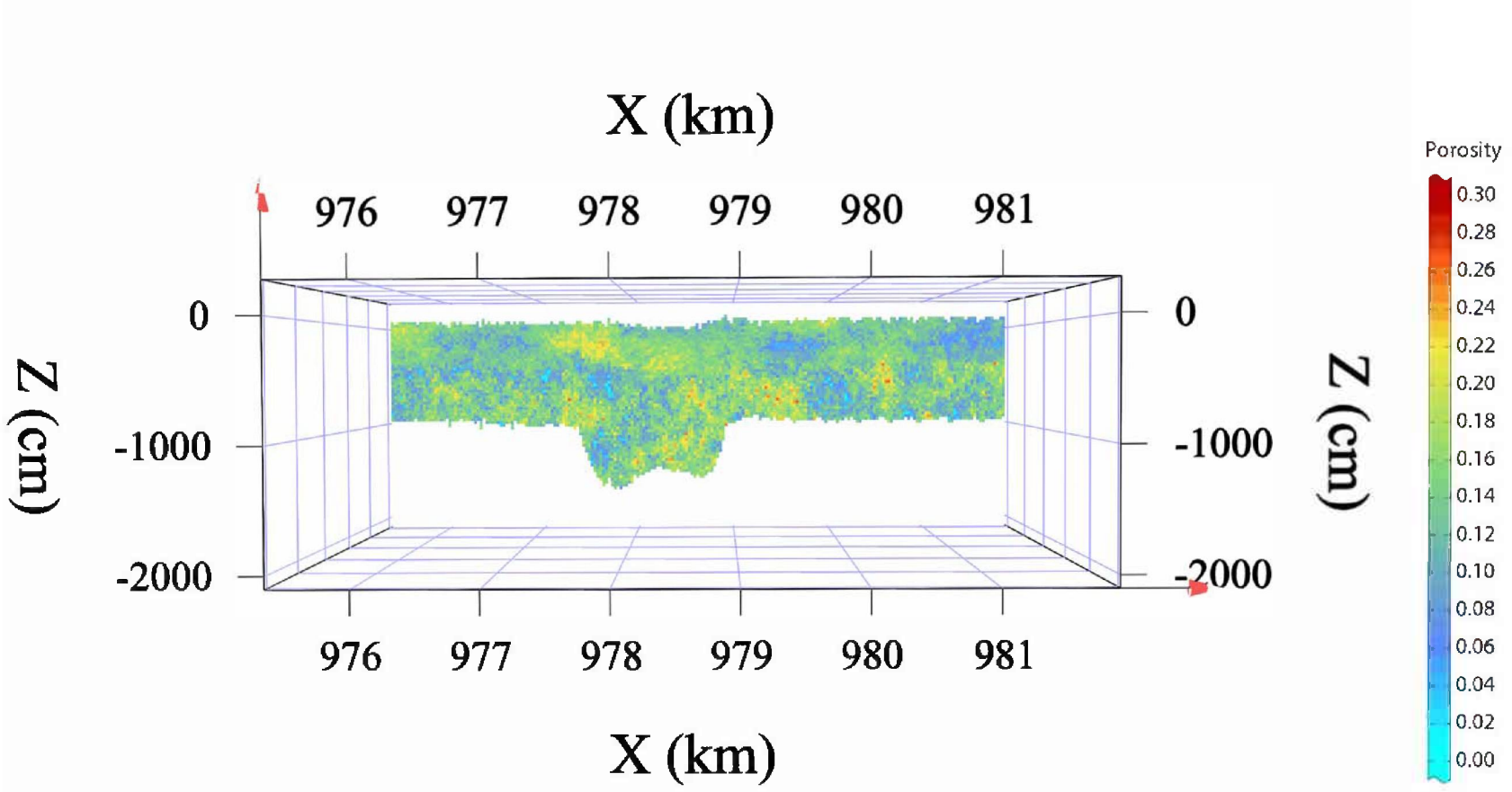

Figure 136 Side view of the porosity distribution of the dolomite shelf carbonate model. The layer is 5,304 m [17,400 ft] from the southern boundary.

Table 12 Parameters for the dolomite shelf carbonate geocellular model. The reservoir thickness, porosity, permeability, and pore space rows are the statistics after applying a 0.1% porosity cutoff and represent the higher quality portion of the formation.

Parameter	Value
Total number of grid cells	1.73×10^6
x-direction	215
y-direction	350
z-direction	23
dx/dy (m [ft])	30.5 (100)
dz (m [ft])	0.9 (3)
Area (m^2 [ft^2])	7.00×10^7 (7.53×10^8)
Total volume (m^3 [ft^3])	1.47×10^9 (5.19×10^{10})
Reservoir thickness (min/max/mean) (m [ft])	9.1/20/14 (30/66/45)
Number of defined cells	1.21×10^6
Total defined volume (m^3 [ft^3])	1.03×10^9 (3.63×10^{10})
Depth (min/max/mean) (m [ft])	974.1/1,140.6/1,057 (3,196/3,742/3,469)
Porosity (min/max/mean)	0/0.27/0.10/0.07
Total pore space	5.19×10^9
Permeability (min/max/mean) (cm^2 [mD])	$0/1.69 \times 10^{-8}/9.16 \times 10^{-11}/1.58 \times 10^{-12}/3.56 \times 10^{-14}$ (0/1,717/9.29/0.16/36.14)
Reservoir porosity (min/max/mean)	0/0.27/0.14/0.035
Reservoir permeability (min/max/mean) (cm^2 [mD])	$0/1.69 \times 10^{-8}/1.31 \times 10^{-10}/5.62 \times 10^{-12}/4.20 \times 10^{-10}$ (0.0/1,717/13.28/0.57/42.6)
k_z (cm^2 [mD])	$0/1.44 \times 10^{-8}/6.50 \times 10^{-11}/7.69 \times 10^{-13}/2.66 \times 10^{-10}$ (0/1,459/6.59/0.078/27)
Reservoir k_z (cm^2 [mD])	$0/1.44 \times 10^{-8}/9.30 \times 10^{-11}/3.16 \times 10^{-12}/3.14\times 10^{-10}$ (0/1,459/9.43/0.32/31.88)

Strandplain: Upper Mt. Simon Sandstone at Manlove Gas Storage Field

The initial model was constructed as part of research related to an early study of carbon sequestration potential of the Illinois Basin (MGSC, 2005) and was subsequently updated for this project. The model covers a large area, nearly all of the sections in TWP, 21N, and RNG, 7E, and spanned a surface area of 6,690 ha (16,500 ac). The grid and data were transformed into stratigraphic space by using the top of the Mt. Simon/base of the Eau Claire as the origin. The grid consisted of 80 cells in the *x*-direction, 100 cells in the *y*-direction, and 75 layers. The grid cell spacing was $\Delta x = \Delta y = 91.4$ m (300 ft) and $\Delta z = 0.914$ m (3.00 ft) resulting in a total grid volume of 1.51×10^{10} m^3 (1.62×10^{11} ft^3). The grid was adequate for capturing the relevant geologic features and was large enough for reservoir simulation purposes, so the grid was unchanged throughout the modeling process.

Data

According to the original study (Rittenhouse, 2005), the model was constructed on the basis of geophysical logs (gamma ray and neutron-density) and core analysis data. The study lists 175 gamma ray logs, 120 neutron-density logs, and 29 core samples. Wells with only gamma ray logs were converted into porosity during an earlier study (Morse, 2003). The model used porosity as the basis of construction because of the larger amount of data and approximately normal distribution.

Geostatistical Analysis

Geostatistical analysis was confined to construction of semivariograms and semivariogram models. An analysis of horizontal anisotropy was not mentioned in the earlier study. One semivariogram was used to represent behavior of porosity in the horizontal plane and one was used to represent the vertical behavior of porosity. An omnidirectional semivariogram model was used to represent both vertical and horizontal trends. The model used a spherical structure type and had a range of 671 m (2,200 ft), a sill of 0.0005, and a nugget of 0.00031. The simple nature of the semivariograms and semivariogram models is possibly a reflection of the homogenous nature of large portions of the formation. Figure 137 illustrates the semivariograms and the semivariogram model.

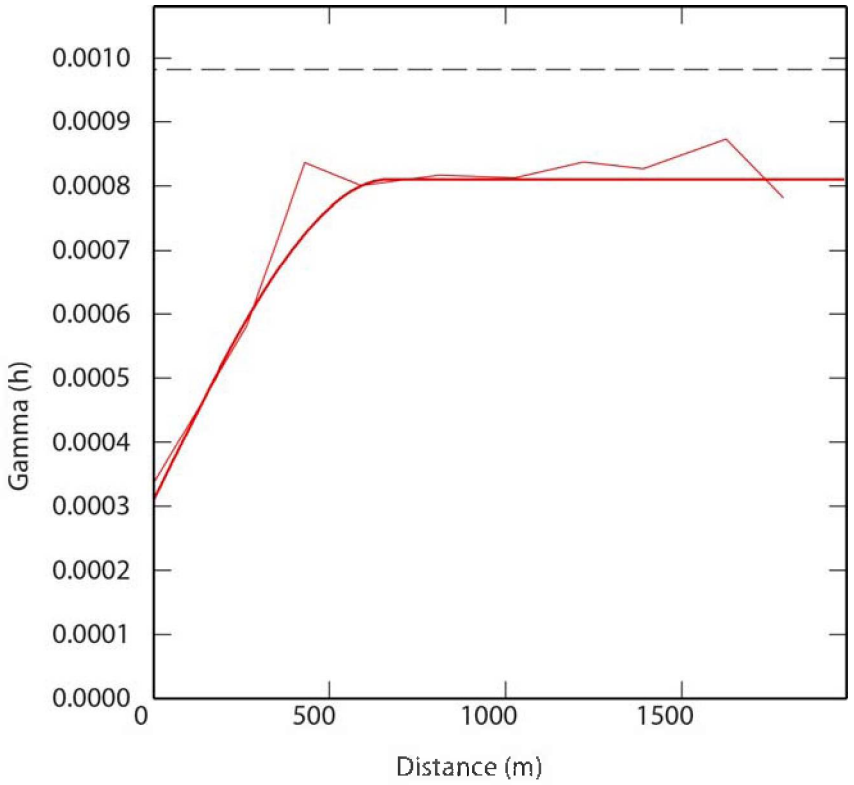

Figure 137 Omnidirectional experimental (thin line) and model (thick line) semivariograms of the Upper Mt. Simon at the Manlove Gas Field.

Simulation

The semivariogram models were used to simulate the porosity distribution for the Upper Mt. Simon by applying the turning band method (Matheron, 1973; Journel, 1974). The simulations produced 35 unique, equiprobable realizations. The simulations were ordered by total pore volume and the median (P_{50}) was selected for reservoir simulation as it was considered most representative of the reservoir architecture.

Property Transformation

After an acceptable geocellular model of porosity had been constructed, a porosity-to-permeability transform derived from regression analysis of core samples was applied to transform the porosity values into permeability (Figure 138).

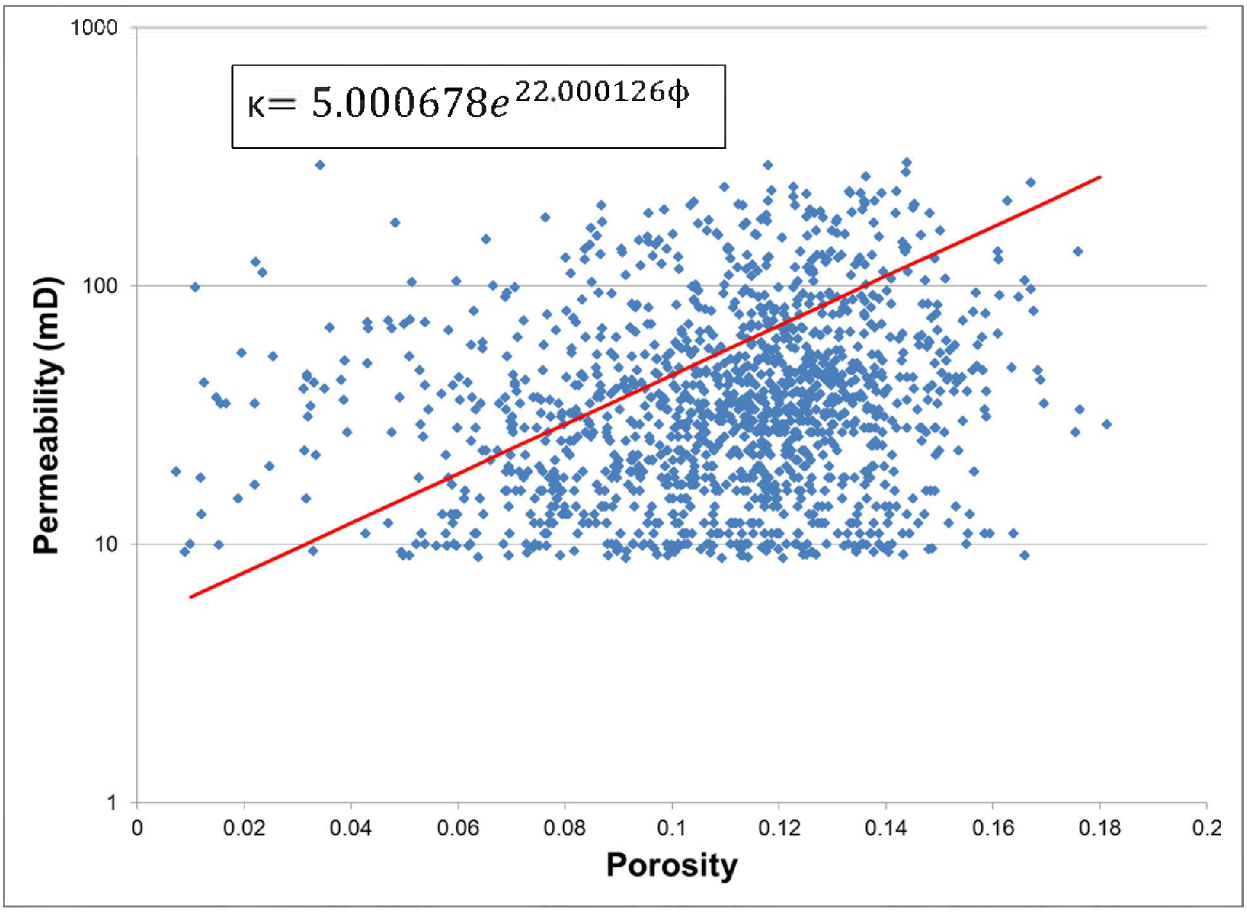

Figure 138 Plot of porosity (x-axis) vs. permeability (y-axis) from core samples of the Upper Mt. Simon at Manlove Gas Storage Field. The equation defining the line was used to transform porosity values to permeability.

Final Geocellular Model

Figure 139–Figure 141 show the results of the final geocellular model used for reservoir simulation. Table 13 has a summary of the model properties. The figures illustrate a distinct change with depth in the petrophysical properties of the Upper Mt. Simon. The upper 15–18 m (50–60 ft) is dominated by low porosity and low permeability rock, while the lower 53.3 m (175 ft) contains noticeably higher porosity and permeability. This change is noted in core samples where the upper portions of the cores are dominated by laminated shales and thin, interbedded sandstone and the lower portions are characterized by 3–4.6 m (10–15 ft) thick intervals of porous, cross-bedded sandstone with fewer occurrences of shales (Morse, 2003). In the plan view images of the model (Figure 141), the shale appears as thin, elongated bodies with a northwest-southeast direction surrounded by high porosity and high permeability rock. This is interpreted as reflection of the strandplain environment, where the shale was deposited in the swales of the strandplain while the sandstone was deposited in the dunes of the strandplain.

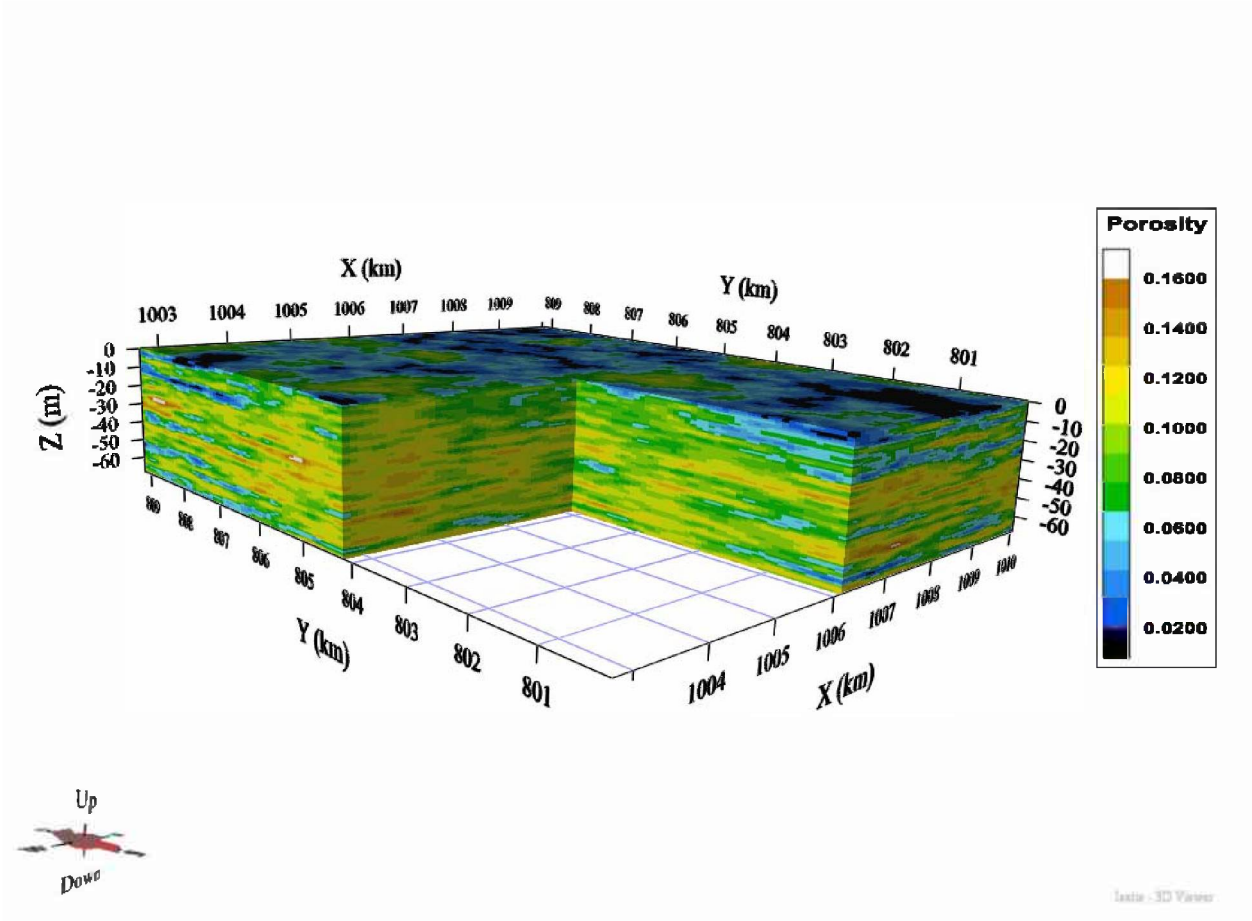

Figure 139 Distribution of porosity within the final model of the Upper Mt. Simon at Manlove Gas Field. Viewpoint is from the southwest looking northeast and vertical exaggeration is 25×. A section of the model in the southwest corner is cut away to show internal architecture.

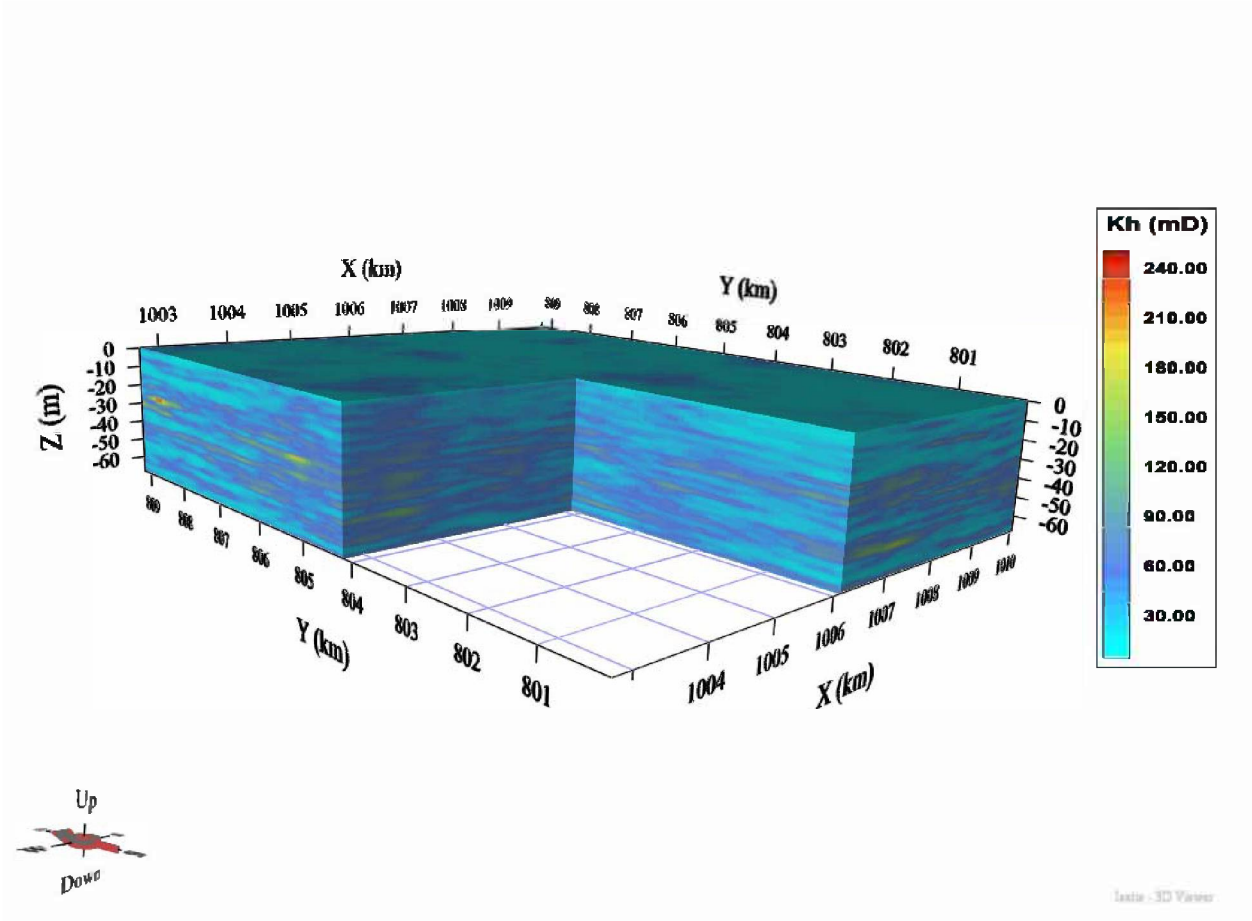

Figure 140 Distribution of permeability within the final model of the Upper Mt. Simon at Manlove Gas Field. Viewpoint is from the southwest looking northeast and vertical exaggeration is 25×. A section of the model in the southwest corner is cut away to show internal architecture.

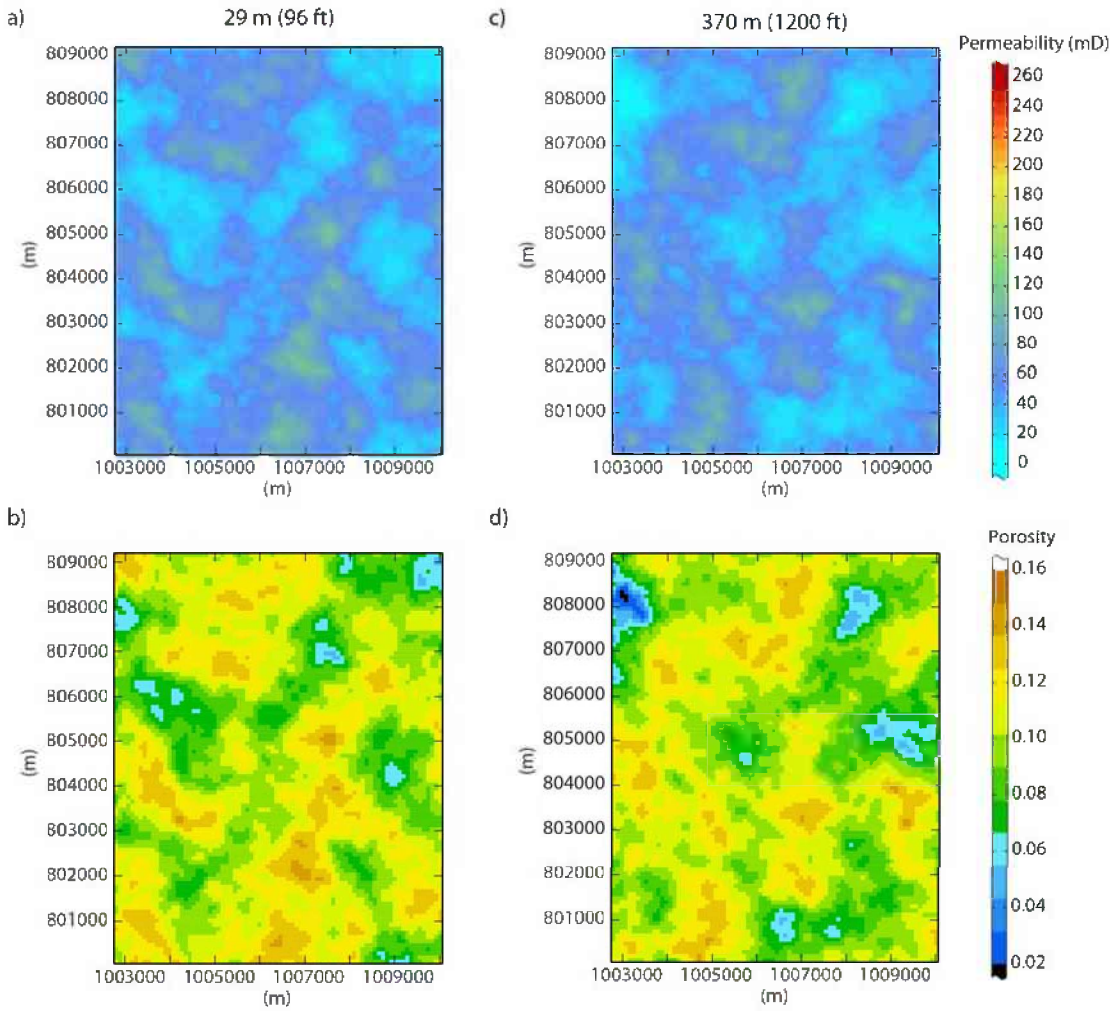

Figure 141 Plan view of the permeability (a and c) and the porosity distribution (c and d) of two layers from the final model of the Upper Mt. Simon at Manlove Gas Storage Field. The images on the left are 29 m (96 ft) from the top of the Mt. Simon and the images on the right are 370 m (1,200 ft) from the top of the Mt. Simon.

Table 13 Parameters for the strandplain geocellular model. No porosity cutoff was used.

Parameter	Value
Total number of grid cells	600,000
x-direction	80
y-direction	100
z-direction	75
dx/dy (m [ft])	(300)
dz (m [ft])	0.9 (3.00)
Area (m^2 [ft^2])	(7.20×10^8)
Total volume (m^3 [ft^3])	1.51×10^{10} (1.62×10^{11})
Porosity (min/max/mean/st.d)	0.00100/0.178/0.0877/0.0240
Permeability (min/max/mean/median/st.d) (cm^2 [mD])	4.94×10^{-11}/2.47×10^{-9}/3.88×10^{-10}/3.53×10^{-10}/2.00×10^{-10} (5.01/250/39.3/35.8/20.3)

Reef: Moccasin Springs Formation at Tilden Oil Field

The initial structural geocellular grid contained 88 rows, 71 columns, and 288 layers. Cell spacing of $\Delta x = \Delta y = 30.48$ m (100 ft) and $\Delta z = 0.30$ m (1 ft) resulted in a total surface area of 5.80×10^6 m^2 (6.25×10^7 ft^2) and a volume of 5.10×10^8 m^3 (1.80×10^{10} ft^3). Isopach maps provided by the geologist were used to split the formation into three zones (A, B, C).

The geocellular model was developed from 25 digital neutron-density porosity logs. Indicator values were assigned to the logs by using a 6% porosity cutoff to separate clean from muddy intervals.

The indicator values were used to construct an omnidirectional semivariogram. The short structure had a range of 3,048 m (10,000 ft) in the *x*-*y* direction, a range of 12 m (40 ft) in the *z* direction, and a sill of 0.11. The long-range structure had a range of 15,240 m (50,000 ft) in the *x*-*y* direction, a range of 30.5 m (100 ft) in the *z* direction, and a sill of 0.1. There was no nugget effect and both structures were spherical. Sequential indicator simulations produced realizations of indicator values for all three zones (Figure 142–Figure 144).

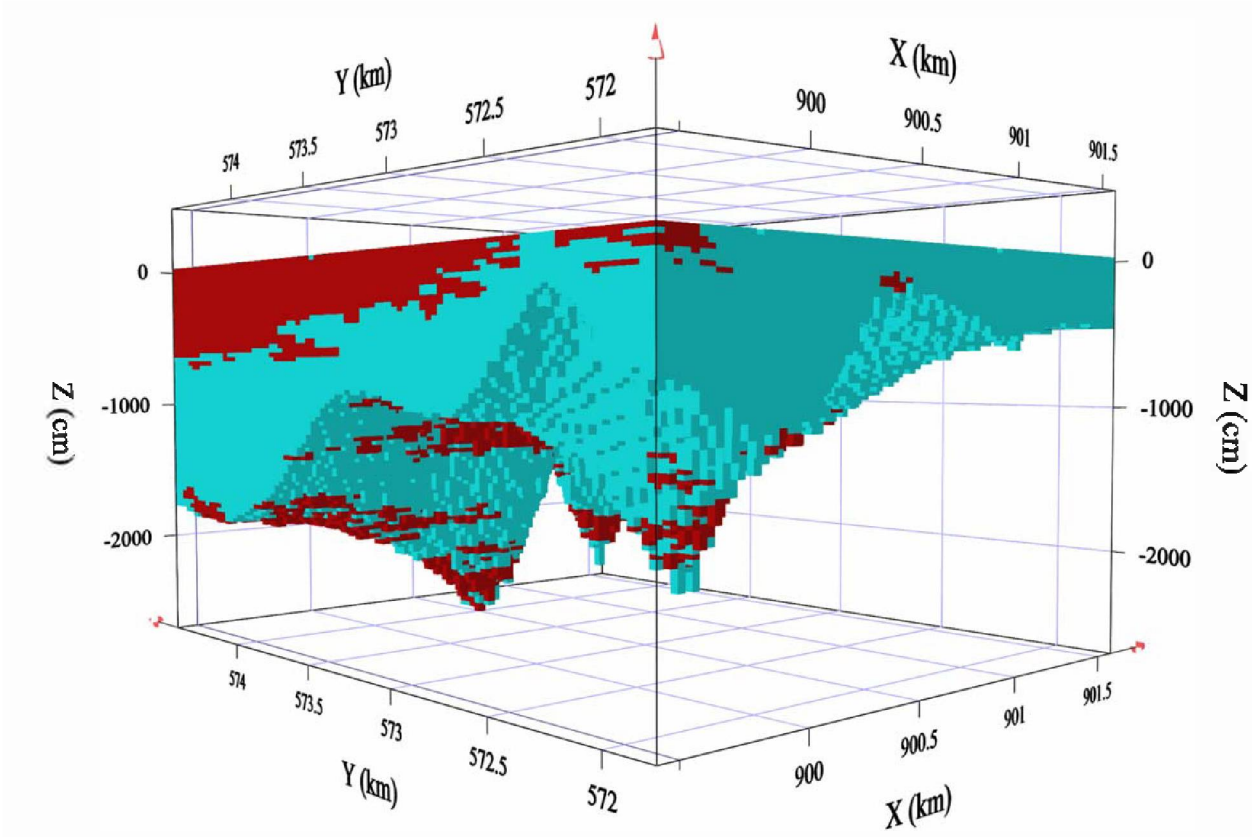

Figure 142 Distribution of the indicator values for the A zone. Red is the clean zones and blue is the muddy zones. Vertical exaggeration is 50×.

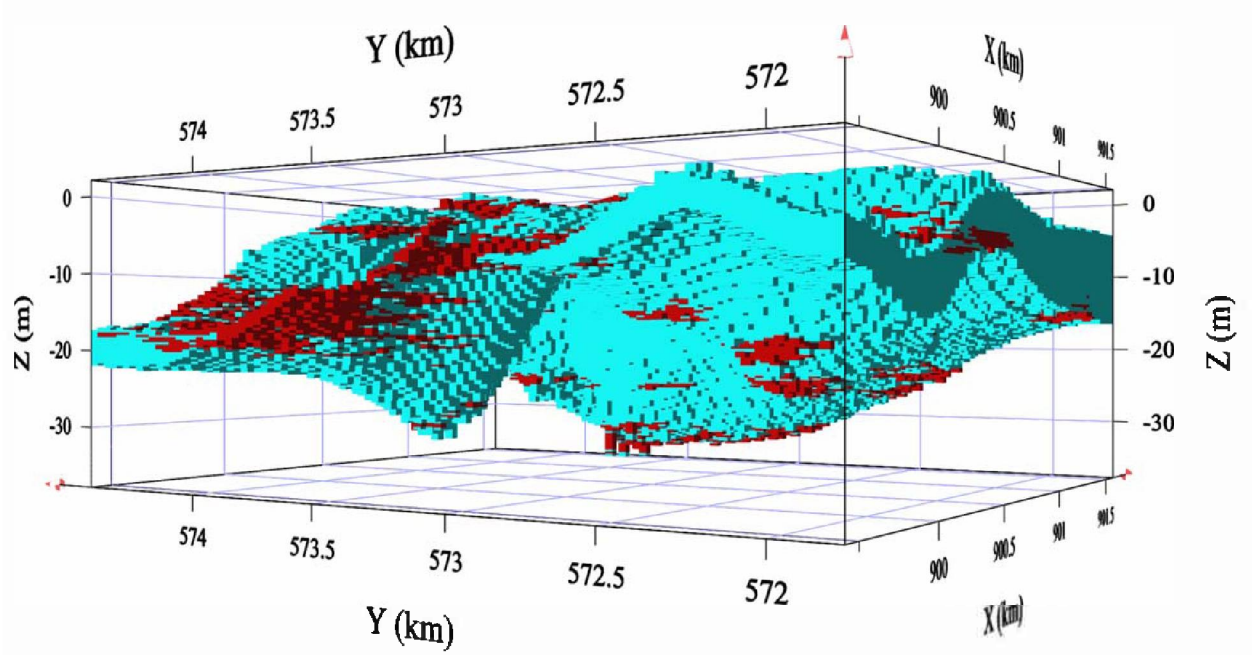

Figure 143 Distribution of the indicator values for the B zone. Red is the clean zones and blue is the muddy zones. Vertical exaggeration is 50×.

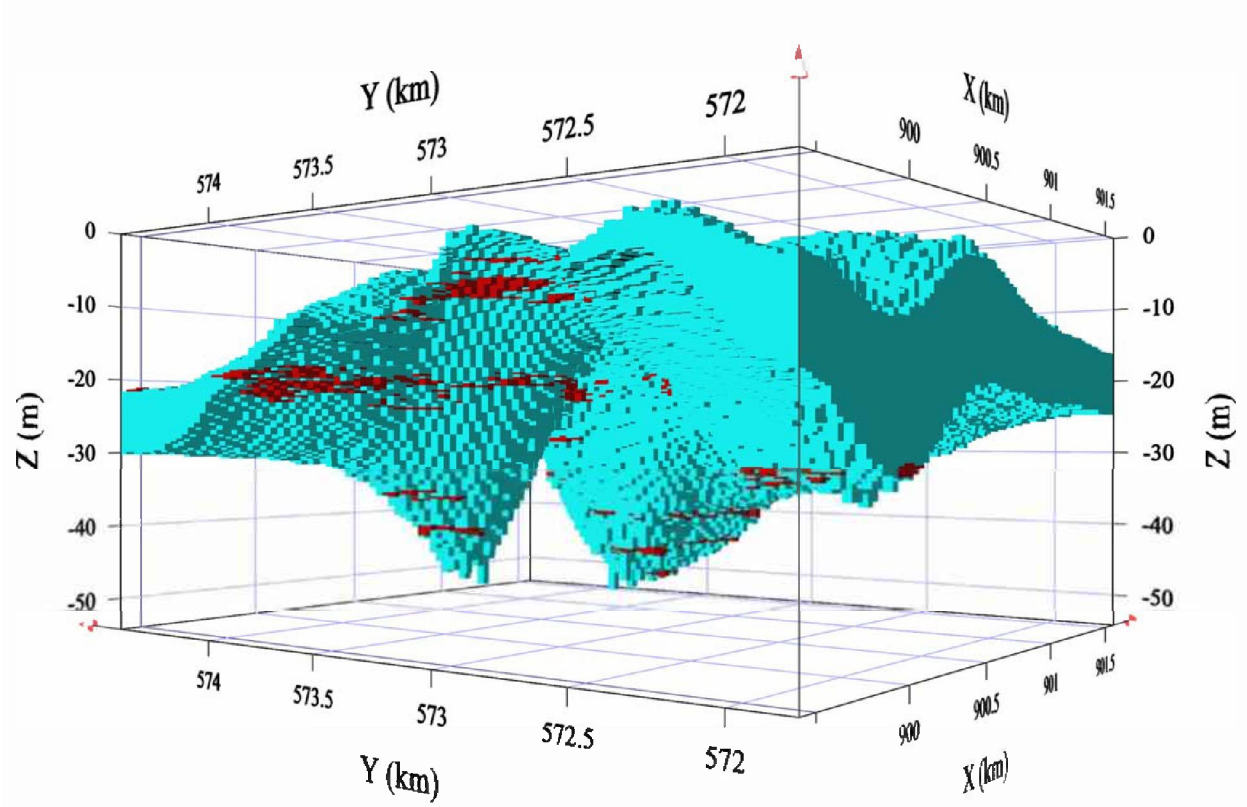

Figure 144 Distribution of the indicator values for the C zone. Red is the clean zones and blue is the muddy zones. Vertical exaggeration is 50×.

An omnidirectional semivariogram was developed for the porosity data. Two Sequential Gaussian simulations were run: one conditioned with porosity data from the muddy inter-reef intervals (0–6% porosity) and one conditioned with porosity data from the clean carbonate intervals (between 6–20%). Clean zones, as delineated by indicator simulations (Figure 142–Figure 144), were filled with porosity values from the simulation conditioned by the 6–20% porosity data, and the muddy zones were filled with porosity values produced by the simulation run with the low porosity (between 0–6%).

Simulated porosity values were converted to permeability by using a transform equation derived from Jennings and Lucia (2003). The rock fabric number was adjusted to 1.3 to create permeability values in line with the geologist's expectations:

$$k = \mathrm{e}^{19.39} * phi^{7.726}. \quad (6)$$

The Δx and Δy were upscaled from 30.5 to 61 m (100 to 200 ft) and Δz was upscaled from 0.3 to 0.9 m (1 to 3 ft). The final grid contains 44 rows, 36 columns, and 57 layers.

The geocellular model (Table 14) was able to successfully capture the compartmentalized nature of the clean facies zones found in this formation (Figure 145–Figure 148). These zones are more connected in the upper zones and became less widespread and less connected with increasing depth.

Table 14 Parameters for the reef geocellular model. The reservoir thickness, porosity, permeability, and pore space rows are the statistics after applying a 0.1% porosity cutoff and represent the higher quality portion of the formation.

Parameter	Value
Total number of grid cells	9.03×10^4
x-direction	36
y-direction	44
z-direction	57
dx/dy (m [ft])	61 (200)
dz (m [ft])	0.9 (3)
Area (m^2 [ft^2])	5.89×10^6 (6.34×10^7)
Total volume (m^3 [ft^3])	3.06×10^8 (1.08×10^{10})
Reservoir thickness (min/max/mean) (m [ft])	2/51.2/25 (6/168/83)
Number of defined cells	4.54×10^4
Total defined volume (m^3 [ft^3])	1.54×10^8 (5.45×10^9)
Depth (min/max/mean) (m [ft])	495.9/582.8/539.5 (1,627/1,912/1,770)
Porosity(min/max/mean/st.d)	0/0.20/0.02/0.03
Total pore space	2.17×10^8
Permeability (min/max/mean/median/st.d) (cm^2 [mD])	$0/1.03 \times 10^{-8}/1.18 \times 10^{-11}/0/1.54 \times 10^{-10}$ (0/1,041.62/1.2/0/15.6)
Reservoir porosity (min/max/mean/st.d)	0/0.20/0.03/0.03
Reservoir permeability(min/max/mean/median/st.d) (cm^2 [mD])	$0/1.03 \times 10^{-8}/2.27 \times 10^{-11}/0/2.17 \times 10^{-10}$ (0/1,041.62/2.3/0/22)
k_z (min/max/mean/median/st.d) (cm^2 [mD])	$0/8.73 \times 10^{-9}/7.89 \times 10^{-12}/0/1.14 \times 10^{-10}$ (0/885.05/0.8/0/11.61)
Reservoir k_z (min/max/mean/median/st.d) (cm^2 [mD])	$(0.00 \times 10/8.73 \times 10^{-9}/1.58 \times 10^{-11}/0/1.61 \times 10^{-10}$ (0/885.05/1.6/0/16.3)

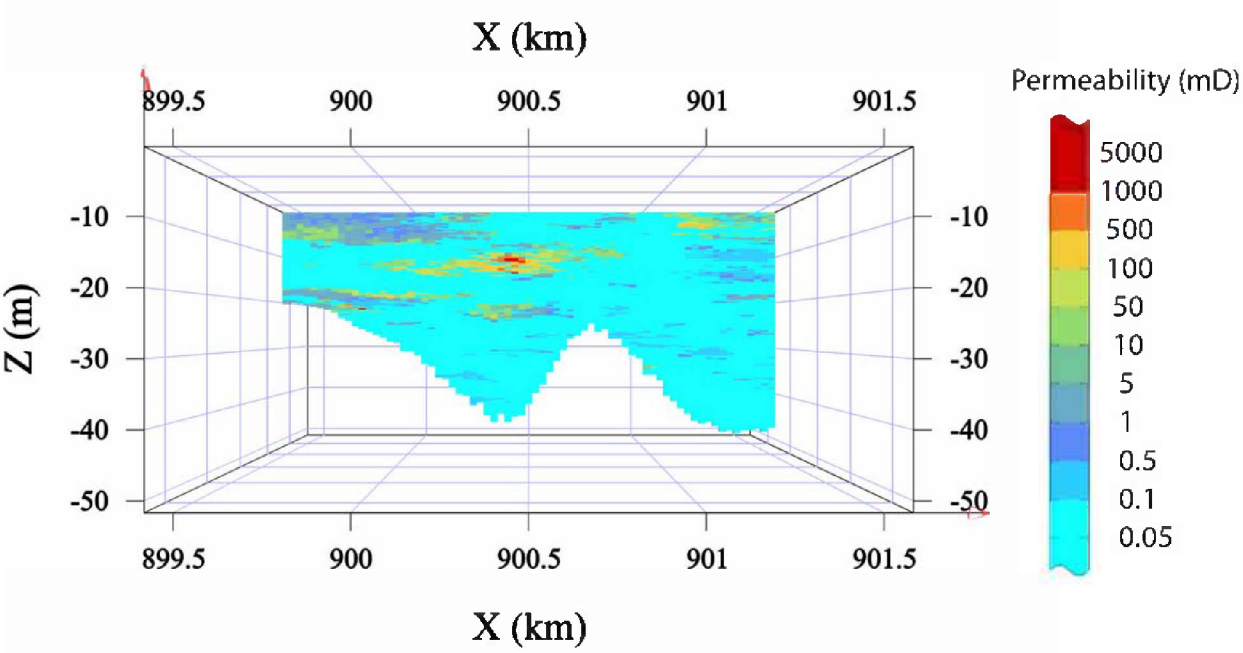

Figure 145 Side view of the permeability distribution for the reef model with structure removed. The layer is 610 m [2,000 ft] from the northern boundary.

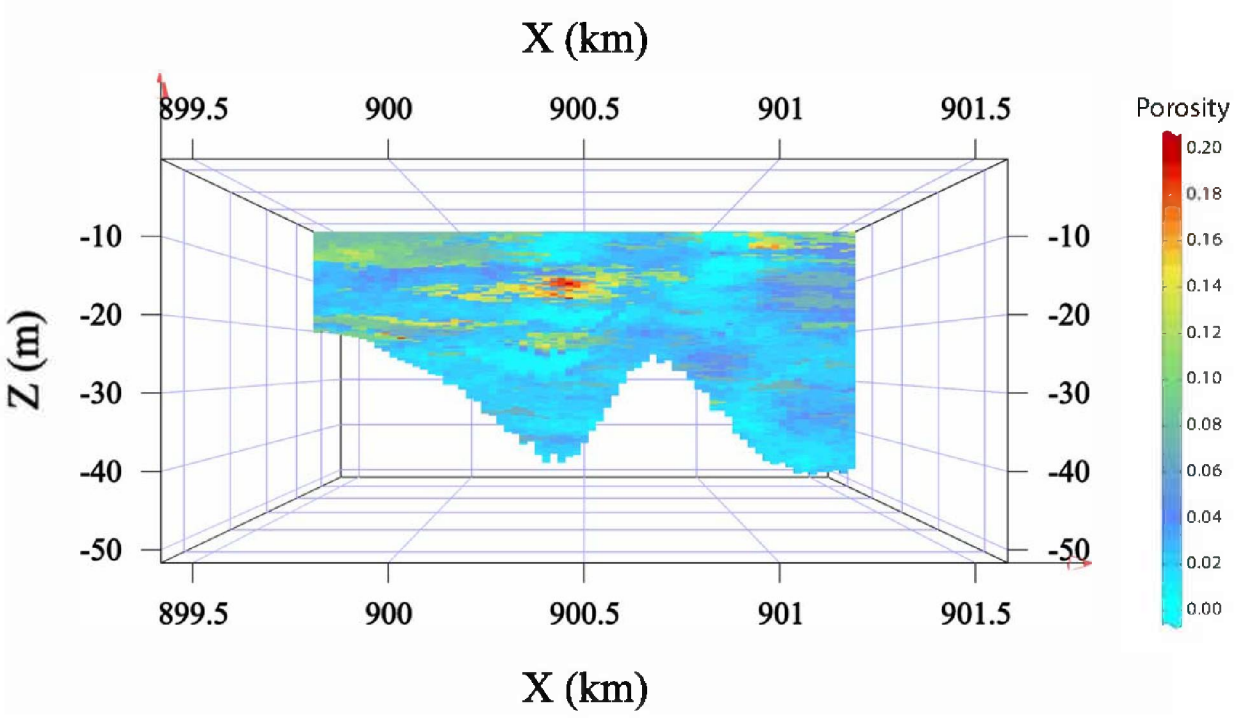

Figure 146 Side view of the porosity distribution for the reef model with structure removed. The layer is 610 m [2000 ft] from the northern boundary.

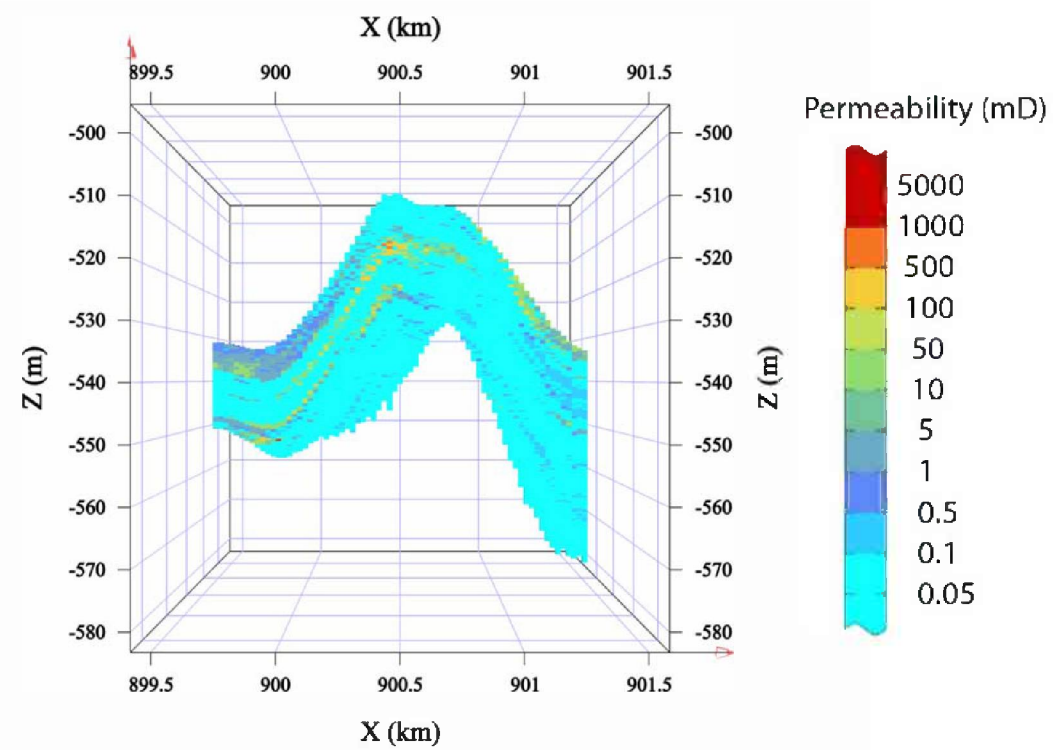

Figure 147 Side view of the permeability distribution for the reef model with structure included. The layer is at 610 m (2,000 ft) from the northern boundary.

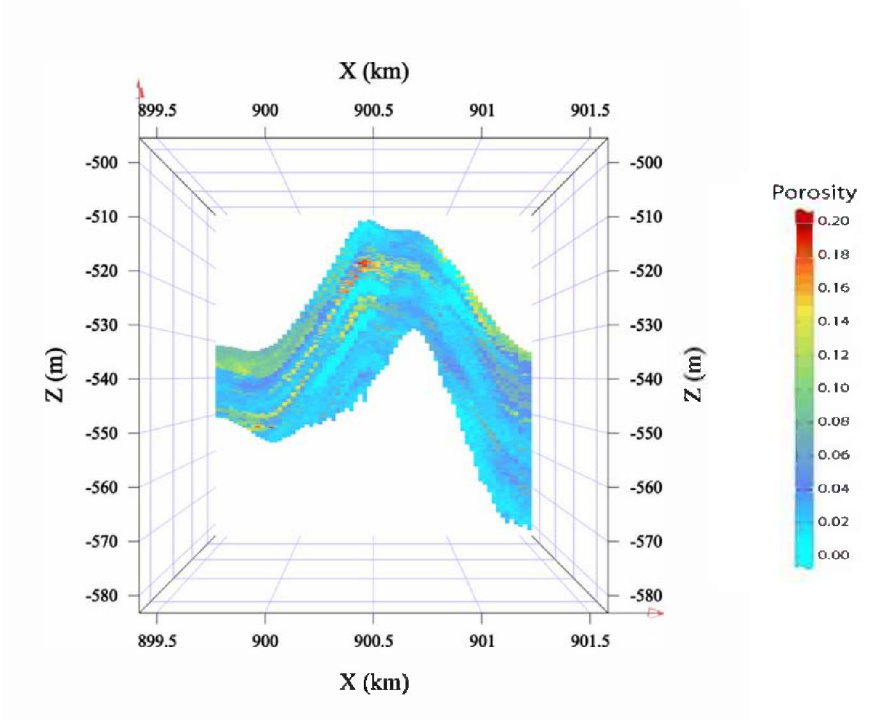

Figure 148 Side view of the porosity distribution for the reef model with structure included. The layer is at 610 m (2,000 ft) from the northern boundary.

Fluvial and Alluvial: Lower Mt. Simon Sandstone at the Illinois Basin–Decatur Project

The Lower Mt. Simon model was constructed by Schlumberger personnel as part of the site characterization study for the test of a deep saline CO_2 injection well (Coueslan et al., 2014). The model was unique compared to the other models in this study in that the model relied on data provided by three-dimensional (3D) seismic surveys. The lower portion of the Mt. Simon, designated as Mt. Simon A, was divided vertically into three zones based on observations from the core and geophysical logs: an Upper Mt Simon A, a dividing zone characterized by low permeability, and a Lower Mt Simon A. Each zone was modeled separately. The model covered a surface area of 3,580 ha (8,840 ac). The grid had 102 cells in the x- and y-directions and 65 layers. The grid cell spacing was $\Delta x = \Delta y = 45.7$ m (150 ft) and used a variable layer thickness with an average of $\Delta z = 2.97$ m (9.74 ft), which resulted in a total grid volume of 3.68×10^{10} m^3 (1.30×10^{12} ft^3). The model did not require any upscaling or expansion.

Data

Couselan et al. (2014) describes the methodology for generating porosity values from seismic data. Porosity data was generated from porosity inversion of the 3D seismic data based on relationships between acoustic impedance, shear impedance, and density. The end result was a 3D cube of data with porosity values described throughout the volume. Geostatistics was employed to fill in areas not covered by the seismic surveys. Permeability was derived from core analysis and advanced well logging suites.

Geostatistical Analysis

Geostatistical analysis was conducted separately on the Upper and Lower zones of the Mt. Simon A. Results of the Lower zone were used for the dividing zone between the Upper and Lower. Semivariogram maps were calculated of the Upper and Lower Mt. Simon A using the porosity cube data to determine the direction of principal directions of horizontal anisotropy (Figure 149). The semivariogram maps indicated a trend slightly to the northwest-southeast direction, N342°. Two semivariograms, one in the N342° direction and one in the N252° direction, were constructed to represent the horizontal anisotropy in the Upper and Lower Mt. Simon A. Vertical semivariograms were also developed to capture the vertical transitional behavior. Models fit to the semivariograms used a single structure. For the Upper Mt. Simon A, the semivariogram model used an exponential type structure, a sill of 0.9999, a range of 549.9 m (1,804 ft) in the northwest-southeast direction, 514.5 m (1,688 ft) in the northeast-southwest direction, and 6.1 m (20 ft) in the vertical direction. For the Lower Mt. Simon A, the semivariogram model used an exponential type structure, a sill of 0.9999, a range of 719.9 m (2,362 ft) in the northwest-southeast direction, 529.1 m (1,736 ft) in the northeast-southwest direction, and 6.1 m (20 ft) in the vertical direction. All models used a nugget of 0.0001. The semivariograms and semivariogram models are illustrated in Figure 150 and Figure 151.

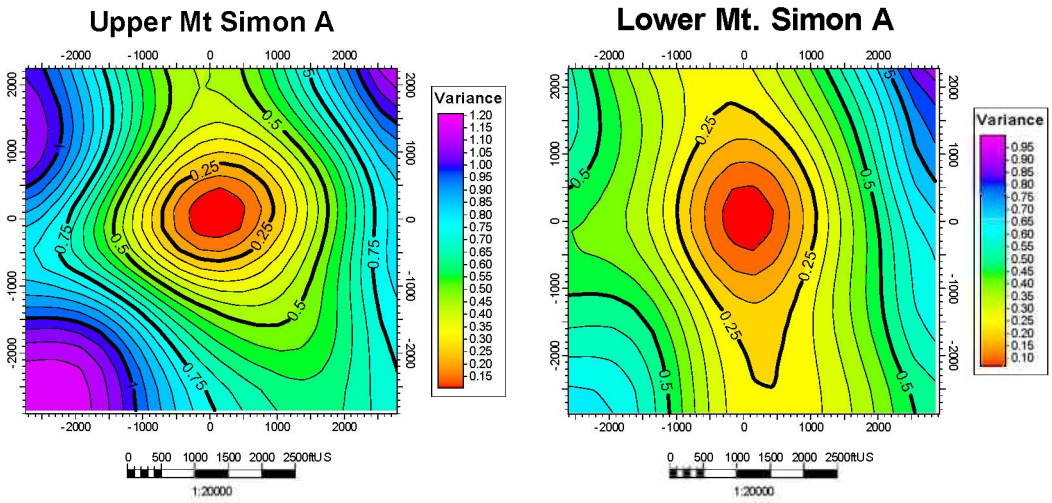

Figure 149 Semivariogram maps of the upper and lower portions of the Mt. Simon A. Warmer colors indicate connectivity.

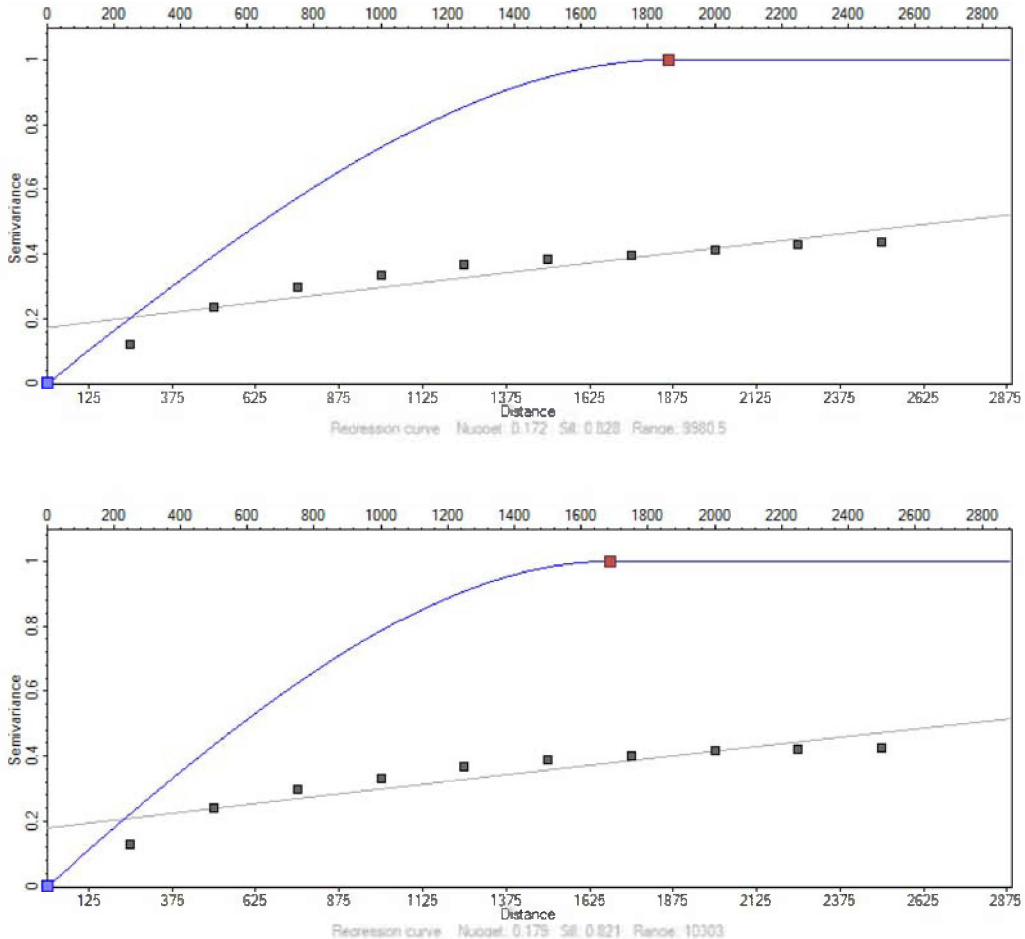

Figure 150 Semivariograms and semivariogram models of the Upper Mt. Simon A. The top image is in the N342° direction, and the bottom image is in the N252° direction. Black squares represent the experimental semivariogram, the red square is the range of the semivariogram model, and the blue line is the semivariogram model.

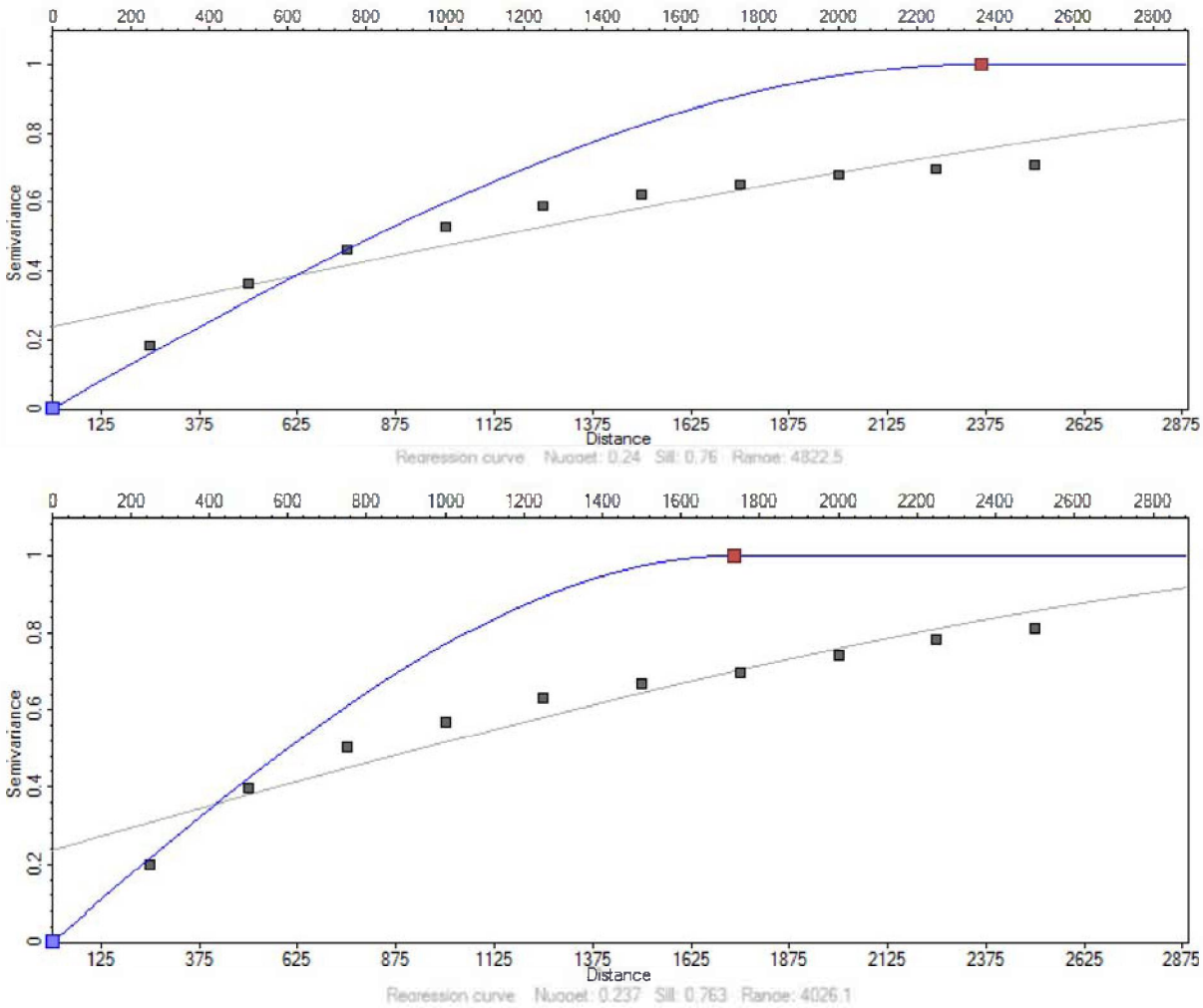

Figure 151 Semivariograms and semivariogram models of the Lower Mt. Simon A. The top image is in the N342° direction, and the bottom is in the N252° direction. Black squares represent the experimental semivariogram, the red square is the range of the semivariogram model, and the blue line is the semivariogram model.

Simulation

The semivariogram models were used to simulate porosity by applying ordinary kriging with the porosity cube as conditioning data. The permeability was co-simulated with porosity using the same semivariogram models by applying multi-Gaussian simulation. The methodology produced a single realization that was reviewed by the project geoscientist and determined to adequately reflect the reservoir architecture.

Final Geocellular Model

Figure 152 and Figure **153** show the results of the final geocellular model used for reservoir simulation. Table 15 has a summary of the model properties. The model reflects the range of heterogeneity in the model with porosity ranging from 0.02 to 0.35 and permeability from 0 to 1.00×10^{-8} cm^2 (0 to 1,016 mD). The figures of the model clearly illustrate the division between the Upper and Lower Mt. Simon A, with the low porosity and low permeability zone dividing the two. The highest permeability and porosity is confined to the very base of the Mt. Simon, which agrees with the findings from the wells and core analysis data. The scale of the reservoir

architecture, as reflected in the ranges of the semivariogram models as well as in the figures of the model, also reflect the large-scale structures found in the interpreted depositional environment.

Table 15 Parameters for the lower Mt. Simon Sandstone model. No porosity cutoff was used.

Parameter	Value
Total number of grid cells	676,260
x-direction	102
y-direction	102
z-direction	65
dx/dy (m [ft])	45.7 (150)
Average dz (m [ft])	2.97 (9.74)
Area (m^2 [ft^2])	3.58×10^7 (3.85×10^8)
Total volume (m^3 [ft^3])	3.68×10^{10} (1.30×10^{12})
Porosity (min/max/mean/st.d)	0.022/0.350/0.168/0.034
Permeability	$0.00/9.87 \times 10^{-8}/6.96 \times 10^{-10}/1.14 \times 10^{-10}$
(min/max/mean/st.d) (cm^2 [mD])	(0.00/1,016/117.79/155.48)

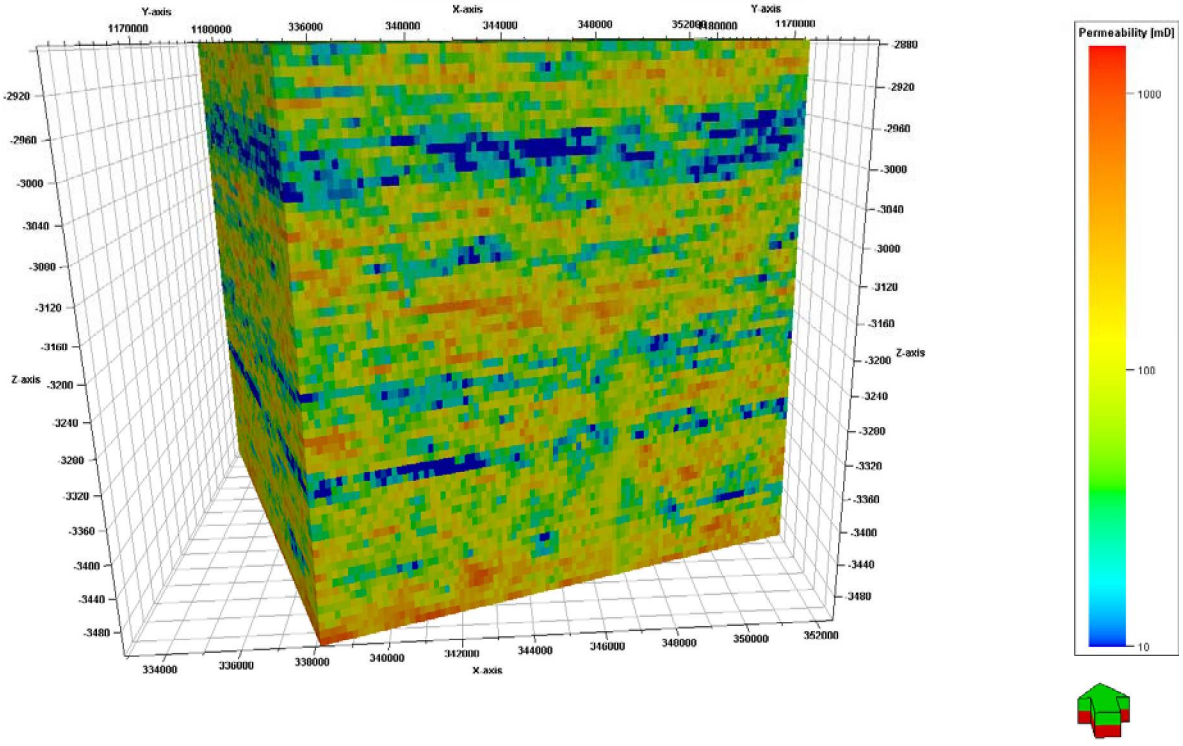

Figure 152 Distribution of the permeability in the final model of Mt. Simon A at IBDP.

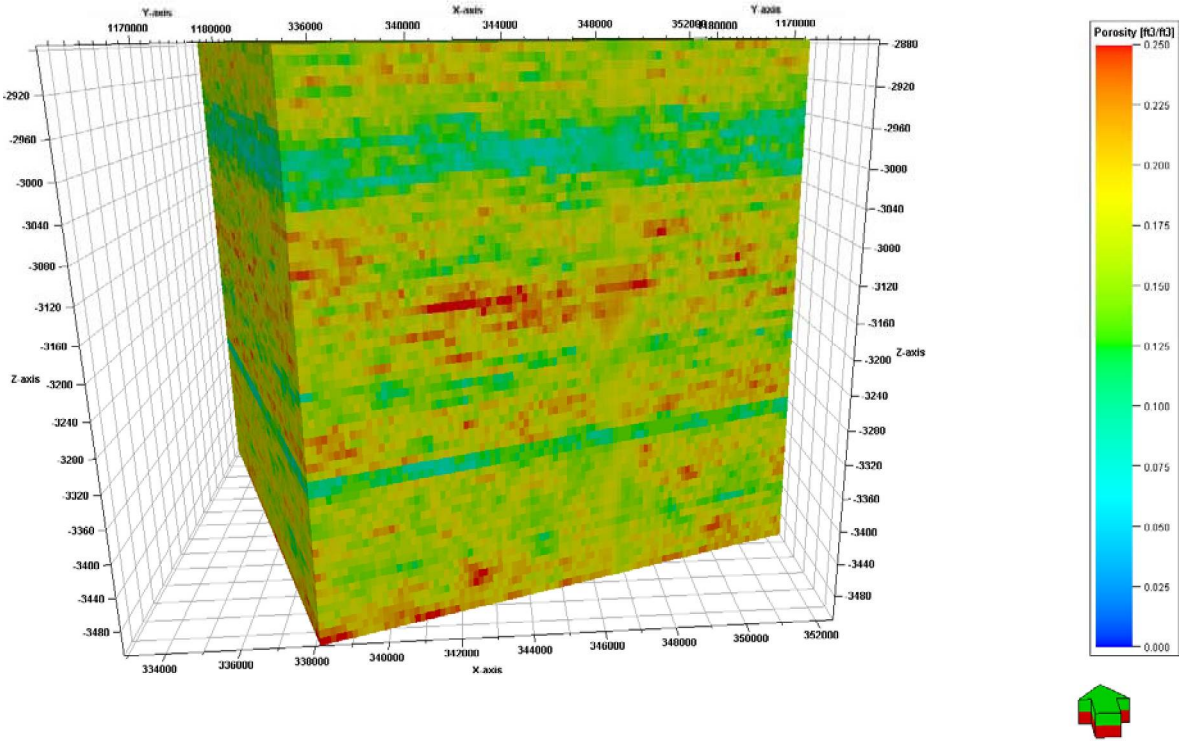

Figure 153 Distribution of the porosity in the final model of the Mt. Simon A at IBDP.

Turbidite: Carper Sandstone at St. James Oil Field

The initial structural geocellular grid contained 190 rows, 150 columns, and 217 layers. A cell spacing of $\Delta x = \Delta y = 30.5$ m (100 ft) and $\Delta z = 0.30$ m (1 ft) resulted in a total surface area of 2.65×10^7 m^2 (2.85×10^8 ft^2) and a volume of 1.75×10^9 m^3 (6.18×10^{10} ft^3). The initial stratigraphic grid contained 112 layers and a volume of 9.03×10^8 m^3 (3.19×10^{10} ft^3).

Data for the development of the turbidite geocellular model consisted of 18 digital, neutron-density porosity logs.

The semivariogram map indicated a strong trend of N145° (geologist plane; Figure 154 and Figure 155). The semivariogram model had a short-range structure with a range of 1,219.2 m (4,000 ft) in the southeast-northwest direction, a range of 609.6 m (2,000 ft) in the southwest-northeast direction, a range of 3.05 m (10 ft) in the vertical direction, and a sill of 0.4. The long-range structure had a range of 21,336 m (70,000 ft) in the southeast-northwest direction, a range of 3,657.6 m (12,000 ft) in the southwest-northeast direction, a range of 9.14 m (30 ft) in the vertical, and a sill of 0.5. The semivariogram model used exponential structures with a nugget of 0.1. The significant difference in ranges between the two directions results in a model with elongated bodies oriented along the plane of maximum connectivity.

Simulated porosity values were converted to permeability by using a transform equation derived from core analysis reports from the field (Figure 156):

$$k = 10^{\Phi \times 0.148 - 2.22} \quad (7)$$

The Δx and Δy were upscaled from 30.5 to 61 m (100 to 200 ft) and Δz was upscaled from 0.30 to 0.91 m (1 to 3 ft) for both stratigraphic and structural grids. The final grid contained 95 rows, 75 columns, and 38 layers. Table 16 gives the parameters used to create the model.

The geocellular model was able to successfully capture the lenticular geometry and northwest-southeast trending orientation of the porous and permeable bodies seen in this formation (Figure 157–Figure 160).

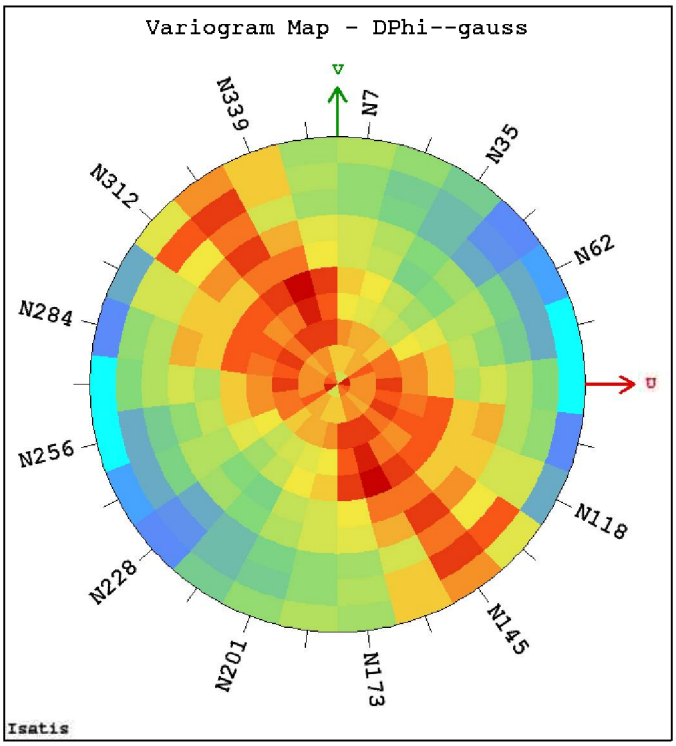

Figure 154 Semivariogram map from the combined log data set for the Carper sandstone at St. James Field. Warm colors indicate connectivity. A strong trend in the N145°E direction is clearly visible.

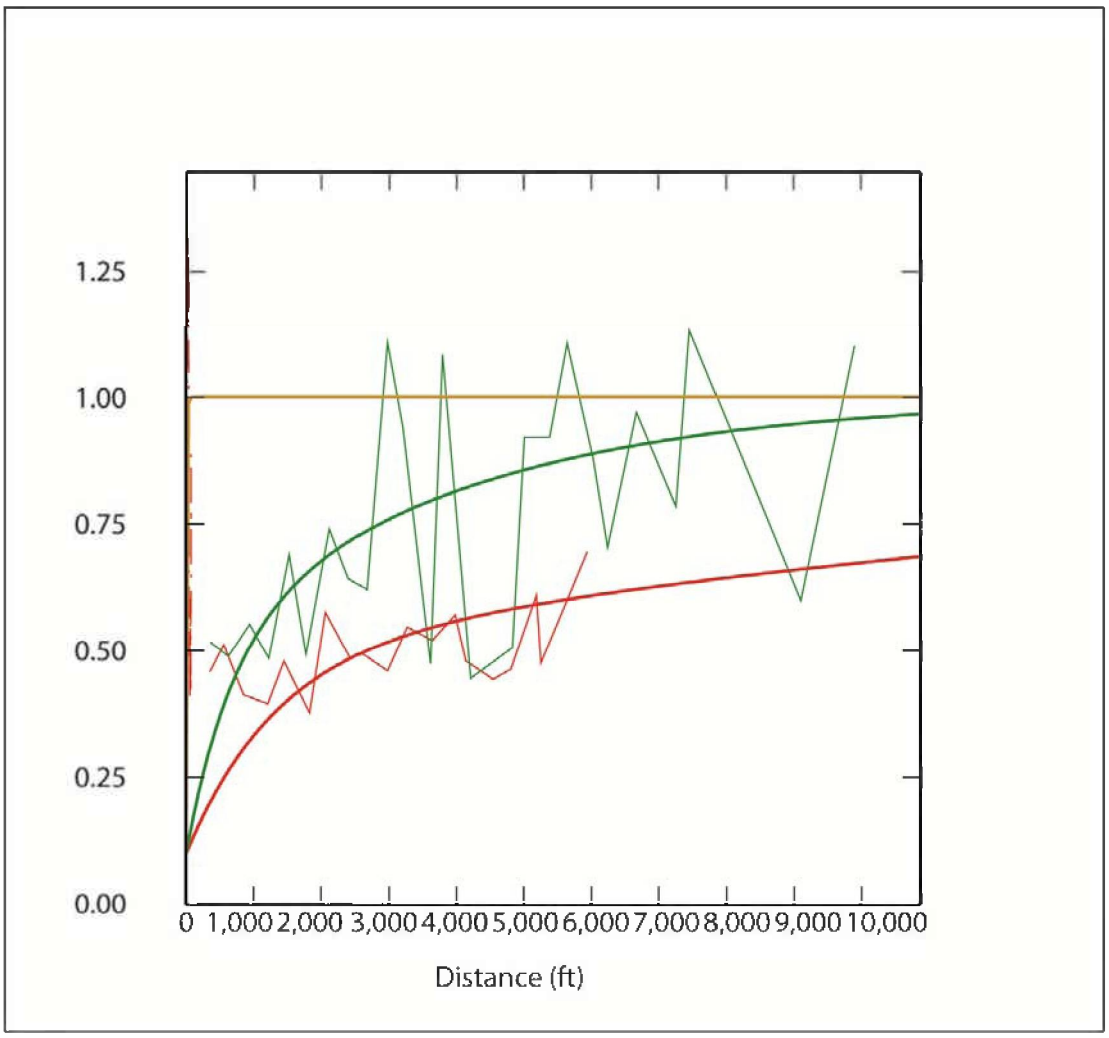

Figure 155 Directional experimental (thin lines) and model (thick lines) semivariograms for the turbidite model. The red lines are the semivariograms in the direction of maximum connectivity (N145°), and the green lines are the semivariograms normal to the direction of maximum connectivity (N55°). The significant difference in ranges between the two directions results in a model with elongated bodies oriented along the plane of maximum connectivity.

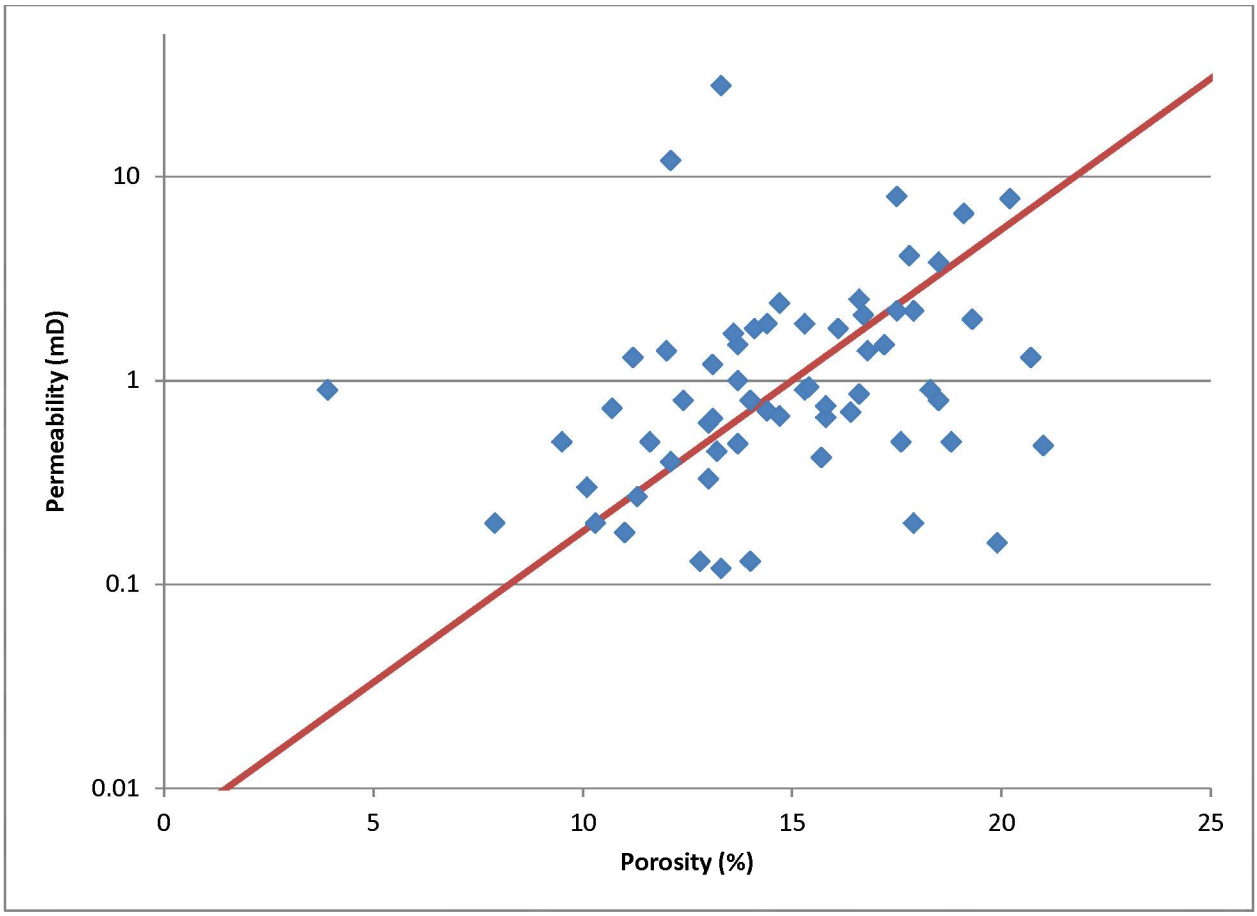

Figure 156 Plot of porosity (*x*-axis) vs. permeability (*y*-axis) from core analysis reports from the Carper Sandstone at St. James Field. The equation defining the line was used to transform simulated porosity values to permeability.

Table 16 Parameters for the turbidite geocellular model. The reservoir thickness, porosity, permeability, and pore space rows are the statistics after applying a 0.1% porosity cutoff and represent the higher quality portion of the formation.

Parameter	Value
Total Number of Grid Cells	2.71×10^5
x-direction	75
y-direction	95
z-direction	38
dx/dy (m [ft])	61 (200)
dz	0.9 (3)
Area (m^2 [ft^2])	2.65×10^7 (2.85×10^8)
Total volume (m^3 [ft^3])	9.20×10^8 (3.25×10^{10})
Reservoir thickness (min/max/mean) (m [ft])	12/32.9/21.35 (39/108/70.05)
Number of defined cells	1.71×10^5
Total defined volume (m^3 [ft^3])	5.81×10^8 (2.05×10^{10})
Depth (min/max) (m [ft])	759.9/825.7 (2,493/2,709)
Porosity(min/max/mean)	0.001/0.24/0.061/0.053
Total pore space	1.98×10^9
Permeability(min/max/mean) (cm^2 [mD])	9.86×10^{-14}/2.15×10^{-10}/5.92×10^{-13}/3.94×10^{-12} (0.01/21.77/0.06/0.40)
Reservoir porosity (min/max/mean)	0.00/0.24/0.10/0.03
Reservoir permeability(min/max/median/mean/st.d) (cm^2 [mD])	9.86×10^{-14}/2.15×10^{-10}/1.58×10^{-12}/2.96×10^{-12}/4.54×10^{-12} (0.01/21.77/0.16/0.3/0.46)
Reservoir pore space	2.05×10^9
k_z	9.86×10^{-14}/1.60×10^{-10}/3.94×10^{-13}/2.56×10^{-12} (0.01/16.19/0.04/0.26)
Reservoir k_z	9.86×10^{-14}/1.60×10^{-10}/8.87×10^{-13}/3.06×10^{-12} (0.01/16.19/0.09/0.31)

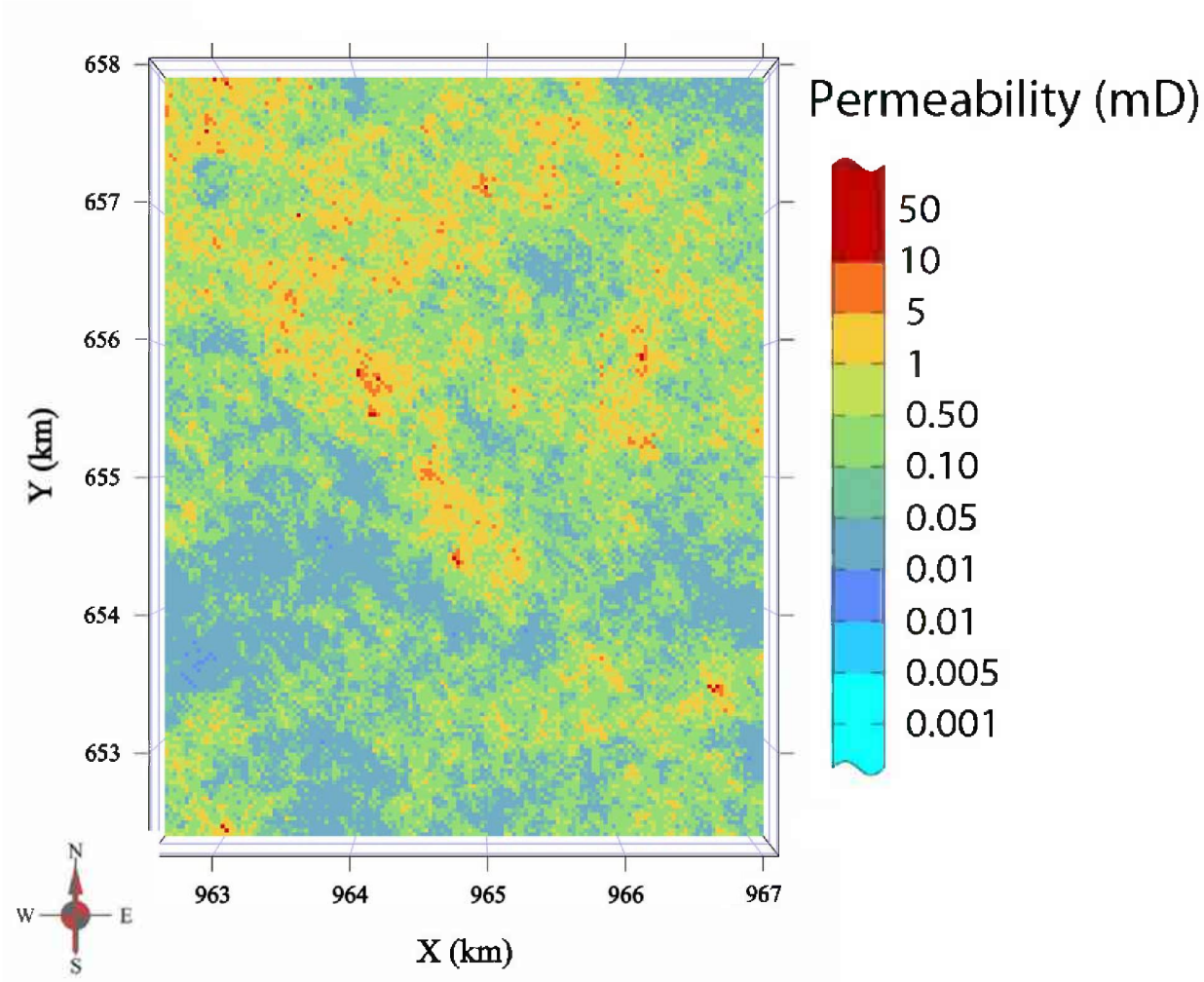

Figure 157 Distribution of permeability in the turbidite model. The layer is 12 m (39 ft) above the stratigraphic datum.

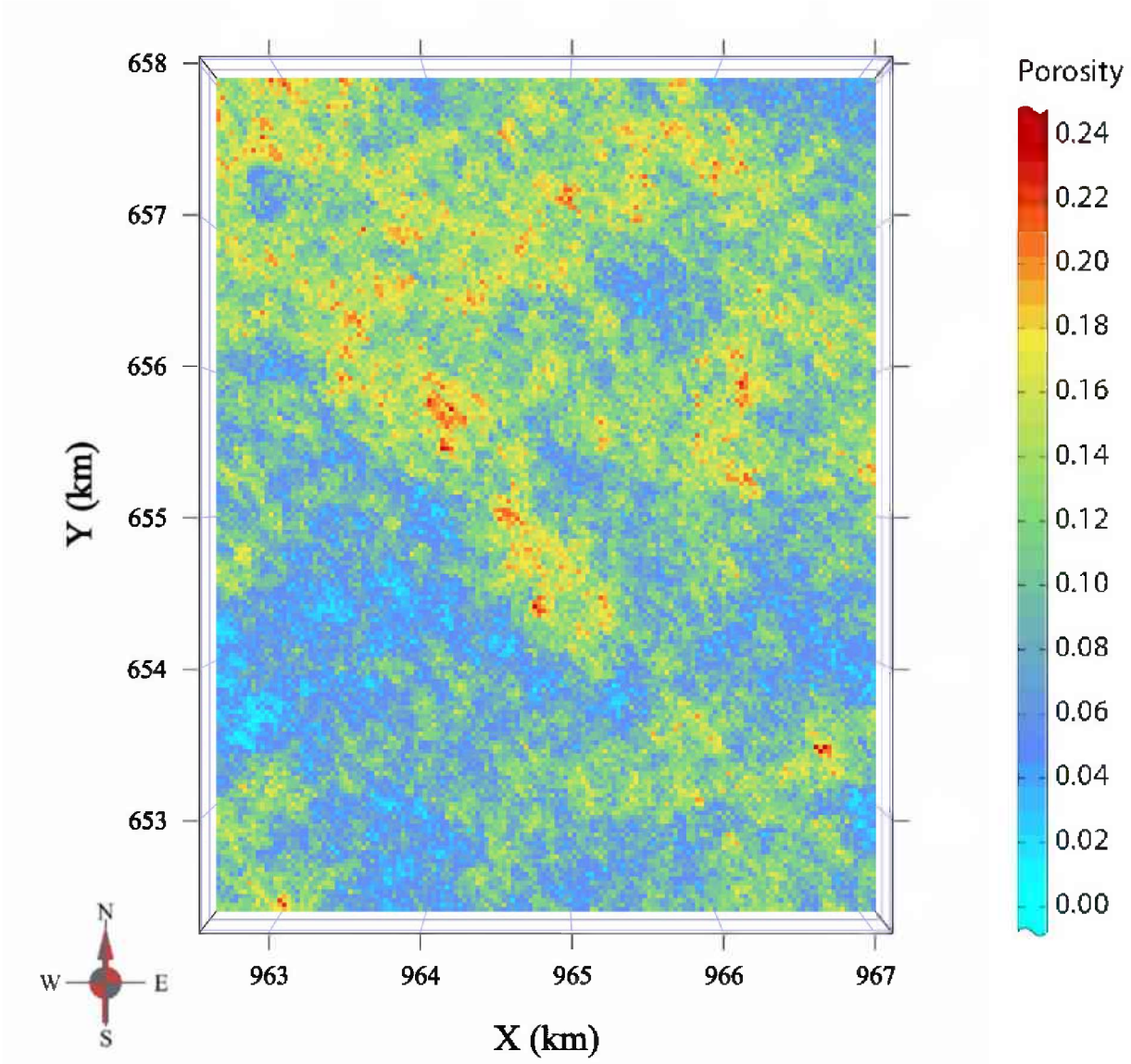

Figure 158 Distribution of permeability in the turbidite model. The layer is 12 m (39 ft) above the stratigraphic datum.

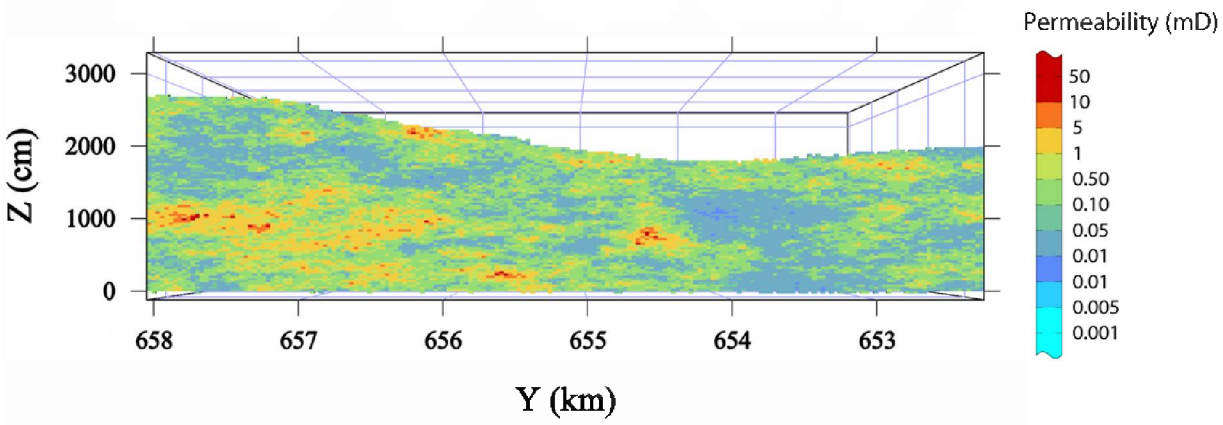

Figure 159 Side view of the permeability distribution for the turbidite model. The layer is the westernmost boundary.

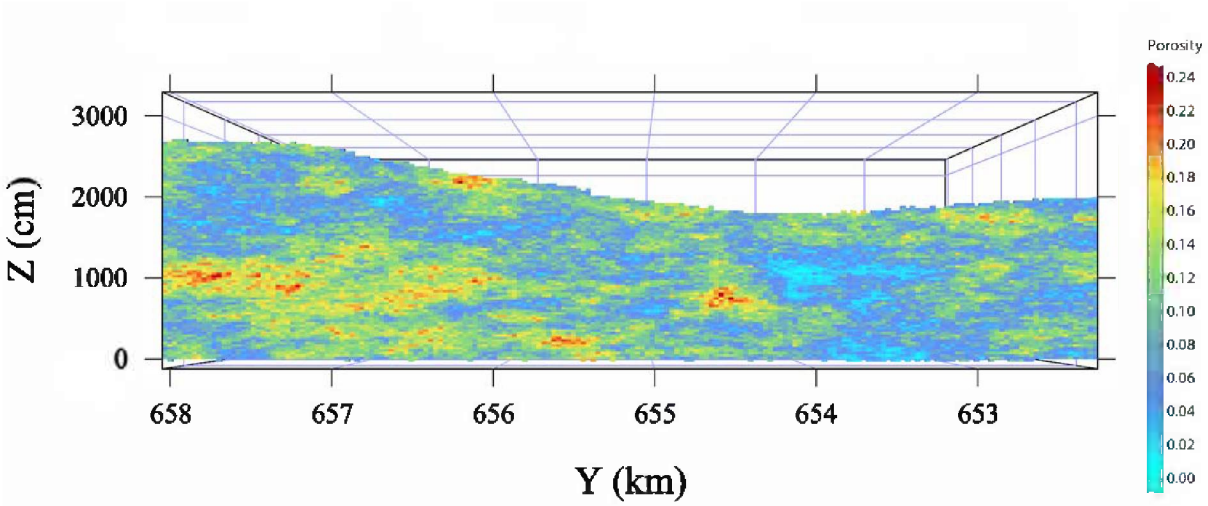

Figure 160 Side view of the permeability distribution for the turbidite model. The layer is the westernmost boundary.

Data Collected from LiDAR and Close-range Photogrammetry

As part of the geocellular modeling process, data was collected from outcrops using innovative field methods, and different methods were tested to better inform the geocellular modeling process. Data was collected from two outcrops using terrestrial-based LiDAR (Light Detection and Ranging) scanning and close-range photogrammetry. Outcrops offer a more complete picture of reservoir architecture that is unavailable through seismic and borehole data. Two outcrops were chosen that were considered excellent analogs of the different depositional environments being investigated. The innovative field techniques allowed the outcrops to be reconstructed digitally in three-dimensional form, resulting in a digital outcrop model (DOM) that could be manipulated and measured accurately. The DOMs could be viewed and interpreted by multiple geologists in a specialized visualization lab, eliminating the need to coordinate a large field trip with multiple participants. In addition, bedforms were delineated in the DOM and statistics and training images were generated to aid in the construction of the geocellular models.

Sites and Digital Outcrop Model Construction

Two sites were selected for study: Cagles Mill spillway and Anna Quarry (Figure 161).

Figure 161 Map showing the locations of two outcrop sites included in this study.

Cagles Mill spillway, Indiana, contains exposed Mansfield Formation (Pennsylvanian) beds that were deposited in a deltaic front system (Huff, 1985). The outcrop is an extensive exposure of interbedded sandstone and shale that thicken and thin over short distances and illustrates the

complex, compartmentalized architecture present in many oil-bearing formations in the ILB. The outcrop was selected because it was considered an excellent analog to the depositional environments represented by the Bridgeport B at Lawrence Field. Because of restrictions on transporting the terrestrial LiDAR scanner across state boundaries, close-range photogrammetry was used exclusively at Cagles Mill. Georeferenced ortho-photomosaics of the Cagles Mill exposures (based on stereophotography images taken during 2012 fieldwork) were generated using Sirovision software, and stratigraphic units were measured. Figure 162 shows a portion of the photomosaic for the north face of the spillway, with depositional units demarcated. The images that make up the photomosaic are georeferenced, permitting direct measurement of bed dimensions from the photomosaic. The accuracy of these measurements was field checked on a return visit to Cagles Mill in May 2013 and was found to be adequate, with an average error of 13%.

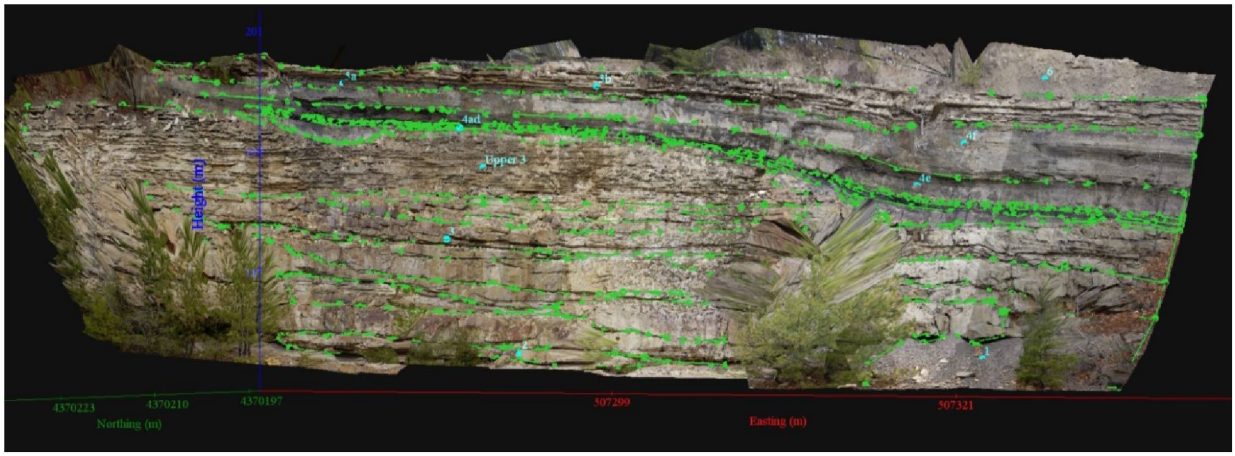

Figure 162 Photomosaic of the outcrop's north face at the Cagles Mill spillway with bedforms demarcated with green lines and labeled with light blue text. (Green points are anchor points used to generate lines.) A thick sequence of superposed point bars at the left and lower right is truncated by a shale and coal-filled channel, which is thickest at the upper right and thins laterally. A second point bar overlays the channel.

Anna Quarry, southern Illinois, contains exposed beds of Ste. Genevieve Limestone (Mississippian) beds with well-developed bodies of oolitic grainstone in the quarry walls. Multiple, stacked oolitic beds are present and measurement of the full lateral extent of the oolitic beds is possible. The outcrop is an excellent analog for the Ste. Genevieve at Johnsonville Consolidated. The terrestrial LiDAR was used in this case because of the distance between the outcrop and where work was permitted to take place (250 m [820 ft]) and brush obscured the camera setup stations. Multiple scans of the quarry wall were taken using the terrestrial LiDAR and control points were surveyed using a total station. Later the scans were reconstructed digitally using Polyworks software with each point in the cloud a measurement of the intensity of the light reflected. Thirteen oolitic beds were delineated on the point cloud using digital photos as an aid (Figure 163). Statistics were generated to be used with geocellular modeling.

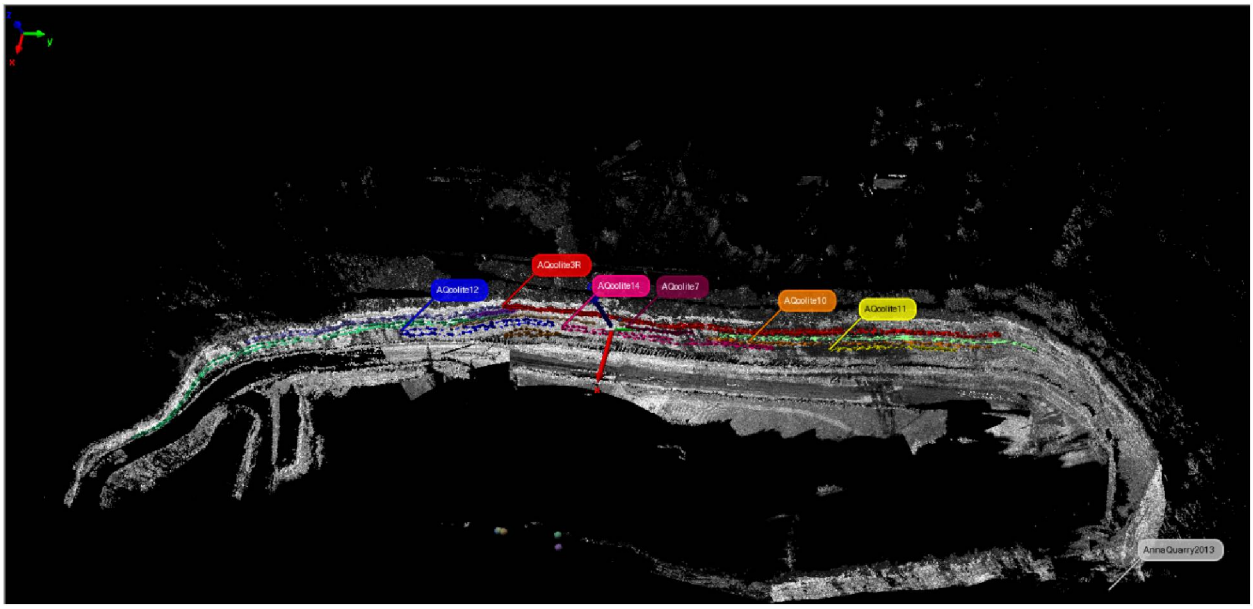

Figure 163 Point cloud of the Anna Quarry. Viewpoint is an oblique aerial view, looking downward at the quarry wall from the east. Multiple oolitic beds are outlined in color along the wall. No scale is provided but the quarry wall is approximately 85 m (280 ft) high and 1 km (0.6 mi) long.

Geocellular Modeling with Digital Outcrop Model

The main benefit of collecting the DOM of the two sites was to aid in development of the conceptual geologic model. Both outcrops serve as excellent analogs of their respective environments and collecting the data digitally enabled multiple geologists to study the outcrops in detail multiple times. The Cagles Mill outcrop is an excellent illustration of the manner in which sandstone bodies are deposited with shales and silty sandstones and form complex barriers and baffles between flow units. Anna Quarry illustrates the dimensions of oolitic beds in Ste. Genevieve Limestone and how they may coalesce to form larger units.

In addition to qualitative data, quantitative data was also extracted from the outcrops for use in geocellular models. The outcrop at Anna Quarry was selected for this purpose. Initial attempts to use the outcrop as a training image in multipoint statistics (MPS) simulations proved unsuccessful because the MPS method is designed for planar images than cross sections. Instead, the statistics generated from the DOM were used with object-based simulations and compared to the traditional, pixel-based simulations.

Statistics on oolitic beds (Table 17) gathered from the Anna Quarry DOM were used in nonconditional object-based simulations. These simulations create realizations of randomly placed oolitic beds with sizes governed by the length and thickness statistics taken from the outcrop data. The areas defined as oolitic beds are filled with porosity values typical of oolites, while the areas outside the oolitic beds are assigned an arbitrarily low value. Figure 164 compares the result of the geocellular model generated from the outcrop data to the model generated using well logs. In comparing the two, the geocellular model generated from the outcrop data more accurately defines the geometry of oolitic beds but lacks some of the internal variability found in the model generated from well logs. The geocellular model generated from

the outcrop could be improved by refining the distribution of porosity values within the oolitic beds or combining the outcrop data with the geophysical log data.

Table 17 Statistics generated from the oolitic beds delineated from the Anna Quarry DOM.

	Thickness (m [ft])	End-to-End Length (m [ft])	Area (m^2 [ft^2])	Perimeter (m [ft])	Aspect Ratio (Length: Thickness)	Area/Perimeter (m^2/m [ft^2/ft])
Mean	3.98 (13.1)	177 (581)	532 (5,730)	360 (1,180)	45.4	1.31 (4.30)
Standard Error	0.427 (1.40)	35.7 (117)	137 (1,480)	71.8 (235)	8.39	0.179 (0.588)
Median	3.74 (12.3)	139 (455)	419 (4,510)	291 (957)	47.9	1.14 (3.75)
Standard Deviation	1.54 (5.05)	129 (422)	495 (5,330)	259 (849)	30.3	0.646 (2.12)
Sample Variance	2.37 (25.5)	16,600 (178,000)	245,000 (2,840,000)	66,900 (720,000)	915	0.418 (4.49)
Kurtosis	0.282	0.373	0.376	0.423	–0.919	–0.759
Skewness	0.618	0.810	0.994	0.819	0.483	0.520
Range	5.47 (17.9)	438 (1,440)	1,590 (17,140)	880 (2,890)	88.9	2.02 (6.63)
Minimum	1.70 (5.56)	26.1 (85.6)	35.6 (383)	58.3 (191)	10.3	0.565 (1.85)
Maximum	7.17 (23.5)	464 (1,520)	1,630 (17,500)	939 (3,080)	99.3	2.58 (8.48)

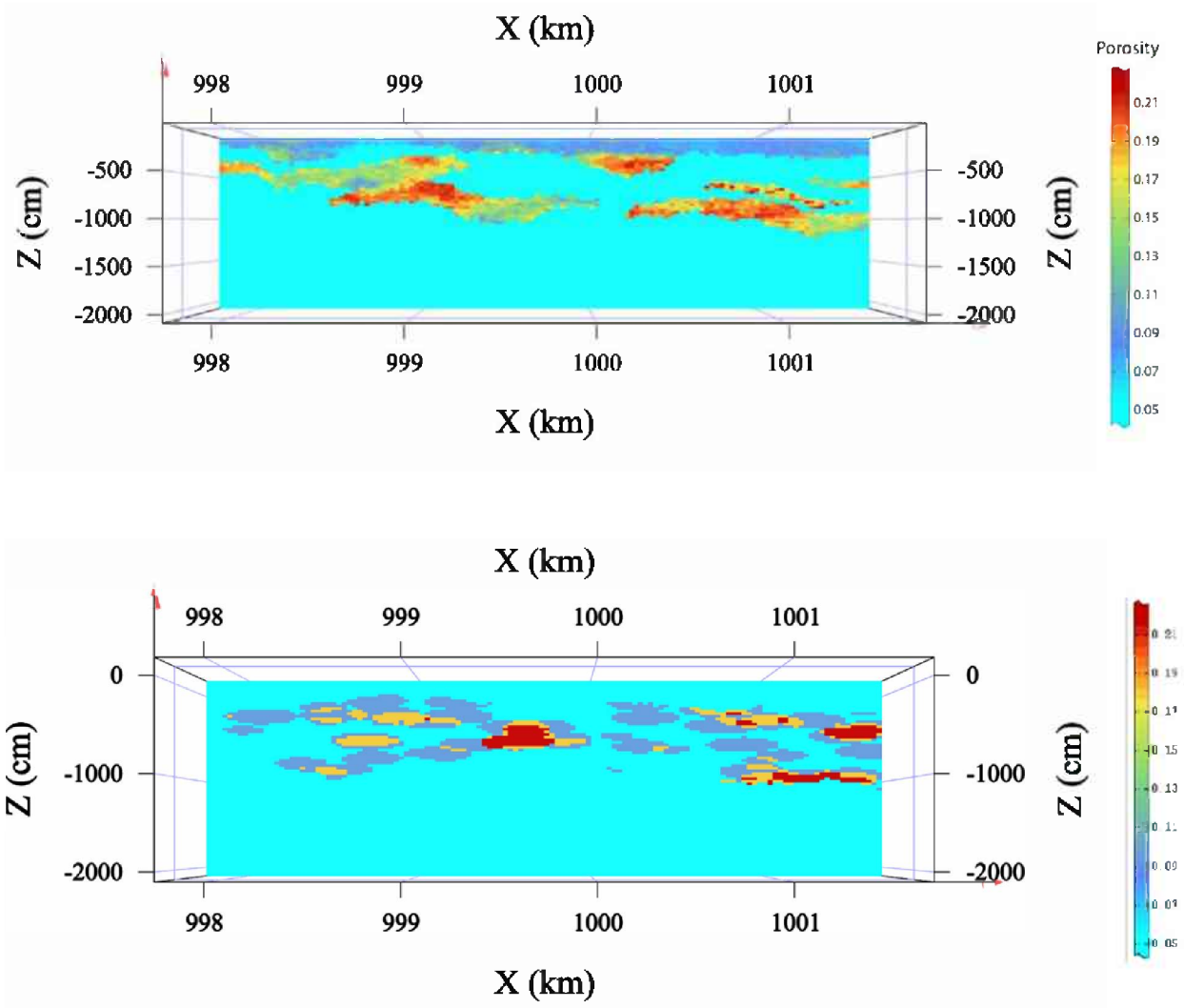

Figure 164 Side view of the porosity distribution for the geocellular model generated from well logs (top) and the model generated from outcrop data (bottom) to model oolitic beds. Both are taken from a row 1,250 m (4,100 ft) from the southern boundary and have 50× vertical exaggeration.

RESERVOIR SIMULATION

Reservoir simulations were conducted to evaluate the effects of depositional environment and injection strategies on CO_2 storage efficiency (E). Baseline results were compared with four different injection strategies to judge each's efficacy to maximize E. The baseline results are obtained from baseline simulation scenarios of CO_2 injection via a vertical well, perforated across the entire thickness of a formation, at multiple well locations. Landmark's Nexus software was used to conduct reservoir simulations in this project.

A series of reservoir simulations of CO_2 injection via vertical, horizontal, and deviated wells were conducted and storage efficiencies were estimated from simulation results. Because Nexus simulation software does not directly output values of E, a Geologic Storage Efficiency Calculator (GSECalc) that estimates E and other important reservoir parameters was developed (see Appendix 1).

Different injection, well completions, and plume management strategies that could be used to maximize the pore volume accessible by injected CO_2 were studied. The strategies considered include horizontal wells of varying descriptions (blanket completions, areal orientations, inclination, and lengths), dynamic completions, use of plume management wells, and development injection wells (The term "blanket" refers to fully perforating a well across its entire length). Parameters investigated in horizontal wells simulations include well length, well orientation, inclination, and vertical placement within the formation. Selective completions and dynamic completions were also simulated to evaluate their potential to improve storage efficiency. Methods to manage CO_2 plume movement within the subsurface via brine extraction and multi-well injection in open systems were also evaluated.

Initial Conditions

Upscaled geocellular models used as input in reservoir simulations are populated with permeability, porosity, reservoir thickness, well locations, and depth for each gridblock. The geocellular models described in the "Geocellular Models" section were used as input in the reservoir simulations. Even though some of the models were developed using data from oil fields, all models were 100% saturated with brine in the reservoir simulations. The following assumptions were made for all simulations:

1. Capillary pressures between CO_2 and water were not included.
2. To ensure storage efficiency was not influenced by model boundaries, all models boundaries were assigned an aquifer function to simulate an infinite formation.
3. General CO_2-brine relative permeability curves estimated from publicly available experimental data for sandstone and carbonate formations were used.
4. Pore pressure was maintained so that CO_2 had liquid like density.

In addition, only continuous CO_2 injection scenarios are studied during which no imbibition (hysteresis) of brine is anticipated. The initial temperature and pressure at the top of the formations were set at 32°C and 7,585 kPa (90°F and 1,100 psi; Table 18).

Table 18 Initial reservoir and fluid properties. Parameters: ρ_{wb}, stock tank water density; B_{wi}, water formation volume factor; μ_w, water viscosity; c_w, water compressibility; c_r, rock compressibility; and T_f, average formation temperature.

Property	Value
ρ_{wb}	1.1 g/cm^3 (68.7 lb/ft^3)
B_{wi}	1.01 rb/stb
μ_w	0.8 cP
c_w	3.0×10^{-6} psi^{-1}
c_r	5.0×10^{-6} psi^{-1}
T_f	32°C (90 °F)
P_{int}	7,585 kPa (1,100 psi)

Simulations were conducted using stratigraphic reservoir models attached to an infinite-acting analytical aquifer to eliminate the effects of structures and model boundaries on E: this ensures the models simulate the effects of depositional environment on E only. Geologic structures or closures, such as a dome, may have a strong effect on the volumetric storage efficiency of a reservoir, which is not related to depositional environment. Storage efficiency increases with the degree of confinement of the structure under the same reservoir conditions (IEAGHG, 2009). To further investigate the effect of structure on E and compare to simulations without structure, additional simulations using reservoir models with geologic structures were conducted to evaluate the effect of structures on E.

CO_2-Brine relative permeability data

Storage efficiency is dependent on the maximum saturation of CO_2 or the irreducible brine saturation, and one of the end points on the relative permeability curves. Consequently, storage efficiency is dependent on the choice of relative permeability data. A recent literature review by Burnside and Naylor (2014) on worldwide publicly available experimental data provided the foundation for estimating CO_2-brine relative permeability endpoints of sandstone and carbonate formations. However, there was no relative permeability data found specific to a depositional environment.

The CO_2-brine relative permeability curves for sandstone and carbonate reservoirs were estimated from experimental data of 48 rock samples obtained from locations in Canada, Japan, North Sea, United States, and United Kingdom (Table 19). All supercritical CO_2-brine relative permeability measurement experiments, except those of Perrin and Benson (2010) and Krevor et al. (2012), were conducted under unsteady-state conditions. Perrin and Benson (2010) and Krevor et al. (2012) were conducted under steady-state conditions.

Table 19 Sources of experimental date used to estimate general CO_2-brine relative permeability curves for sandstone and carbonate reservoirs.

Location	Number of samples		Source
	Sandstone	Carbonate	
Canada	22	13	Bennion and Bachu, 2008, 2010; Bachu, 2013
Japan	1	–	Shi et al., 2011a, b; Pentland et al., 2011a, b
North Sea	2	–	Shell, 2010
United Kingdom	2	–	Mackay et al., 2010
United States	6	–	Perrin and Benson, 2010; Krevor et al., 2012, Shi et al., 2011a, b; Pentland et al., 2011a, b
Australia	2	–	Perrin and Benson, 2010; Krevor et al., 2012

Bennion and Bachu (2008) grouped the experimental data in their study into five categories based on mean permeability (k) values, namely very low k, low k, mid k, high k, and very high k (Table 20 and Table 21). However, the study presented here grouped the experimental data, reported in Burnside and Naylor (2014), into the five groups proposed by Bennion and Bachu (2008) plus an additional category of commonly encountered permeability ranges (common k; Table 20 and Table 21) based on median (P_{50}), 10th percentile (P_{10}), and 90th percentile (P_{10}) probabilities. The data was grouped into categories because no correlation was found between the relative permeability characteristics of CO_2-brine systems for these rocks and other commonly measured rock properties, such as pore size, porosity, and permeability (Bachu, 2013). In addition, the categories provide a means to estimate relative permeability and run reservoir simulations when in-situ relative permeability data are unavailable. The parameters $S_{g,\,max}$, S_{gc}, and $k_{rg,\,max}$ in Table 20 represent the maximum CO_2 saturation, critical CO_2 saturation, and maximum relative permeability of CO_2, respectively.

The median (P_{50}, 50th percentile) value instead of the arithmetic mean of each category was used because it describes the central tendency and reduces the importance attached to the outliers in a given dataset. The 10th percentile (P_{10}) and 90th percentile (P_{90}) of the experimental data are also presented in Appendix 1. Table 22 provides a summary of relative permeability endpoints for both sandstone and carbonate with permeability between (9.86×10^{-13} and 4.93×10^{-9} cm^2 [0.1 md and 500 md]). The parameters n and m represent exponents of the Corey relative permeability function (Corey, 1954) for CO_2 and brine, respectively. The relative permeability endpoints and Corey's exponents data listed in Table 22 were used to generate CO_2-brine relative permeability curves.

Table 23 and Figure 165 and Figure **166** show the median end-point data and CO_2-brine relative permeability curves for sandstone and carbonate formations based on experimental data reported by Burnside and Naylor (2014). The parameters S_{wr} and $k_{rw,\,max}$ and in Table 23 represent the irreducible brine saturation and maximum relative permeability of brine (at residual CO_2 saturation), respectively. There are infinite combinations of relative permeability functions that can be used in models intended for general purpose. Relative permeability that was representative of all curves was used in anticipation of finding a method to normalize the storage efficiency E for the effect of relative permeability (see the "Storage Efficiency Normalization" section).

Table 20 Relative permeability endpoints P_{50} values for sandstone based on the analysis of 33 core samples worldwide.

Rock group	Number of samples	$k_{rg,\,max}$	$S_{g,\,max}$	S_{gc}
Very low k (<9.86 × 10^{-13} cm^2 [0.1 md])	4	0.4097	0.682	0.234
Low k (about 9.86 × 10^{-13} to 9.86 × 10^{-11} cm^2 [0.1 to 10 md])	6	0.3960	0.491	0.277
Mid k (about 9.86 × 10^{-11} to 9.86 × 10^{-10} cm^2 [10 to 100 md])	8	0.1994	0.528	0.288
High k (about 9.86 × 10^{-10} to 4.93 × 10^{-9} cm^2 [100 to 500 md])	9	0.1512	0.460	0.330
Very high k (> [500 md])	6	0.4768	0.584	0.300
Common k (about 9.86 × 10^{-13} to 4.93 × 10^{-9} cm^2 [0.1 to 500 md])	23	0.2349	0.510	0.297

Table 21 Relative permeability endpoints P_{50} values for carbonate based on the analysis of 13 core samples from western Canada.

Rock group	Number of samples	$k_{rg,\,max}$	$S_{g,\,max}$	S_{gc}
Very low k (<9.86 × 10^{-13} cm^2 [0.1 md])	1	0.5289	0.405	–
Low k (about 9.86 × 10^{-13} to 9.86 × 10^{-11} cm^2 [0.1 to 10 md])	3	0.5037	0.454	0.268
Mid k (about 9.86 × 10^{-11} to 9.86 × 10^{-10} cm^2 [10 to 100 md])	6	0.1047	0.516	0.207
High k (about 9.86 × 10^{-10} to 4.93 × 10^{-9} cm^2 [100 to 500 md])	3	0.0746	0.470	0.208
Common k (about 9.86 × 10^{-13} to 4.93 × 10^{-9} cm^2 [0.1 to 500 md])	12	0.1047	0.475	0.218

Table 22 Summary of relative permeability endpoints for both sandstone and carbonate with permeability between 9.86 × 10^{-13} and 4.93 × 10^{-9} cm^2 (0.1 and 500 md).

Rock type	Percentile	$k_{rg,\,max}$	$S_{g,\,max}$	S_{gc}	m	n
Sandstone (9.86 × 10^{-13} cm^2 < k < 4.93 × 10^{-9} cm^2 [0.1 md < k < 500 md])	P_{10}	0.0910	0.347	0.210	1.20	1.49
	P_{50}	0.2618	0.521	0.294	1.70	3.20
	P_{90}	0.5279	0.587	0.414	3.03	5.93
Carbonate (9.86 × 10^{-13} cm^2 < k < 4.93 × 10^{-9} cm^2 [0.1 md < k < 500 md])	P_{10}	0.0691	0.342	0.114	1.42	1.25
	P_{50}	0.1078	0.480	0.218	1.83	4.55

Table 23 Saturation and relative permeability end points.

Parameter	Sandstone	Limestone
S_{wr}	0.5	0.5
$k_{rw,max}$	1.0	1.0
S_{gc}	0.3	0.2
$k_{rg,max}$	0.25	0.25
m	2.0	2.0
n	3.0	4.0

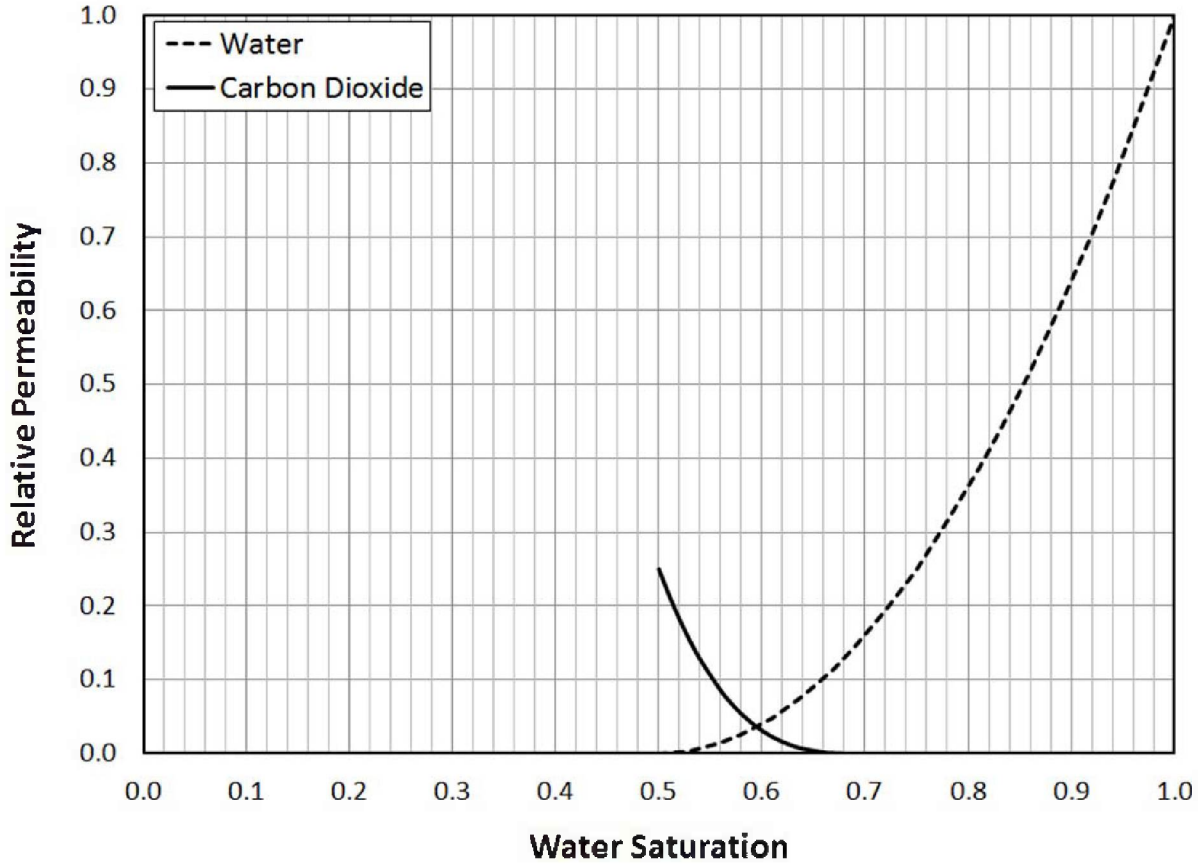

Figure 165 CO_2 and water relative permeability curves used for simulations in sandstone formations.

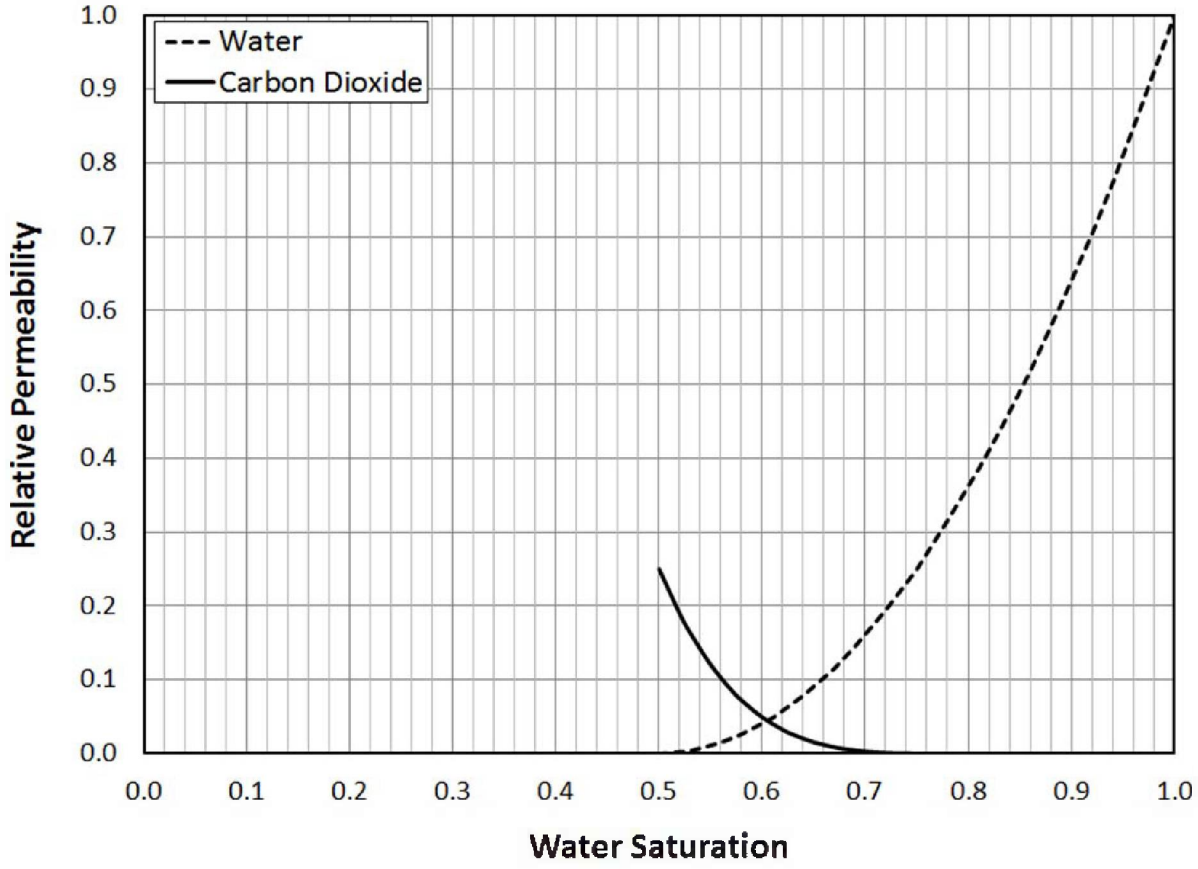

Figure 166 CO_2 and water relative permeability curves used for simulations in limestone formations.

Storage Efficiency Calculation

Most reservoir simulation programs (e.g., Landmark's Nexus software) currently do not directly output E. Thus, E must be calculated separately from the output using Eq. 8:

$$E = \frac{V_{CO_2}}{V_p(t)} \tag{8}$$

The V_{CO2} is the reservoir pore volume contacted by CO_2, i.e., gridblocks with CO_2 saturation greater than zero ($S_g > 0$). The reservoir volume available for storage, V_p (t), is dependent on the three-dimensional size and shape of the injected CO_2 plume, which changes over time. For this study, a geometric shape was assumed to estimate V_p (t). In plan view (x-y), three geometric shapes were used: circle, rectangle, and square. For one E calculation, the shape was applied for the entire thickness of the model. For all geometric shapes, the smallest size that encompasses the CO_2 plume in plan view is used:

$$\text{Circle: } V_p(t) = \pi\left(\frac{L_p}{2}\right)^2 h\phi \tag{9a}$$

$$\text{Rectangle: } V_p(t) = L_p W_p h\phi \tag{9b}$$

$$\text{Square: } V_p(t) = {L_p}^2 h\phi \tag{9c}$$

The parameters L_p, W_p, h, and Φ in Eqs. 9a, 9b, and 9c represent the plume length, plume width, thickness, and porosity of CO_2 contacted pore volume. Figure 167 shows the differences between the use of a circle, square, and rectangle for the same plume. The process of estimating storage efficiency can be further defined as static (E_s) or dynamic (E_d) storage efficiencies by having a constant or variable denominator in Eq. 8. The E_s represents the ratio between V_{CO2} and the total volume of reservoir available for storage (V_p [$t = t_{end}$]); the V_p ($t = t_{end}$) is a constant for all calculations of E. The E_d is the ratio between V_{CO2} and V_p (t), which changes with time. In order to track plume evolution, all estimations of E in this study were based on E_d.

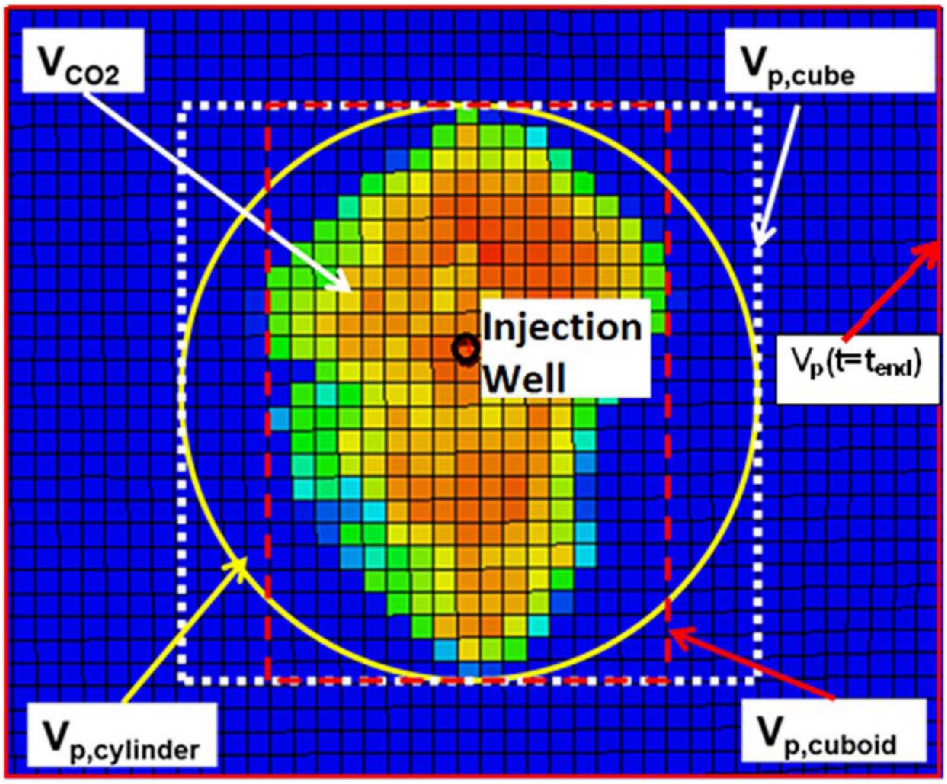

Figure 167 Illustration of the different methods used to estimate the available pore area for calculating E_A in Eqs. 9a, 9b, 9c. Warmer colors indicate higher CO_2 saturation and blue indicates water.

Preliminary Sensitivity Studies

Effect of Infinite-acting Aquifers

The outer boundaries of the depositional system models were infinite-acting to exclude outer boundary effects on estimated values of E. Attaching an infinite-acting aquifer to the reservoir model is a common way of achieving an infinite boundary. The Carter-Tracy (1960) and Fetkovich (1971) methods are generally used to model aquifer influx and outflux resulting from pressure perturbations at the outer edges of models. The Carter-Tracy analytical model was used to depict fluid flow in infinite-acting aquifers because it is easy to implement.

The water influx of a Carter-Tracy aquifer is a function of the dimensionless cumulative water influx and the aquifer parameters; the dimensionless water influx is a function of dimensionless time (t_d) and dimensionless pressure (P_d). For an infinite-acting aquifer, pressure perturbation

due to external boundary is zero or negligible. This is reflected in a default P_d vs. t_d table for an infinite aquifer implemented in the Nexus commercial simulator.

The key input parameters for the Carter-Tracy model are the aquifer capacity parameter, B, and the dimensionless time factor, t_0. The B defines the aquifer strength and has a unit of reservoir barrels per psi (rb/psi; Eq. 10). The t_d is a measure of the conductivity of an aquifer (Eq. 11). The equivalent reservoir length, r_o, is estimated using Eq. 12.

$$B = \frac{\phi h c_t \theta r_o^2}{\alpha_1} \tag{10}$$

$$t_0 = \frac{\alpha_2 k}{\phi \mu c_t r_o^2} \tag{11}$$

$$r_o = \sqrt{\frac{wl}{\pi}} \tag{12}$$

where, w is reservoir width (ft); l is model length (ft); ϕ is average porosity; h is aquifer thickness (ft); k is aquifer permeability (md); μ is brine viscosity (cp);
c_t is aquifer total compressibility (psi^{-1}); θ is angle subtended by the aquifer (radian [0–2π]);
r_o is equivalent reservoir radius (ft); α_1 is unit-dependent constant (5.61458 scf/rb); and α_2 is unit-dependent constant (0.006328 cp-scf/md-psi/day).

Aquifer properties can be estimated through direct measurement, history matching water influx, or material balance (Dake, 1978; Craft and Hawkins, 1991). The direct measurement and history matching approaches are impossible to implement in this study because both approaches require operational history data, which is unavailable.

Analytical Solution

The flow regime within an infinite-acting aquifer is transient, during which there is little to no external boundary effect. The bottomhole flowing pressure at the wellbore of an infinite-acting reservoir can be expressed follows (Ahmed and McKinney, 2004):

$$p_{wf} = p_i - \frac{162.6 q B \mu}{kh}\left[log\left(\frac{kt}{\phi \mu c_t r_w^2}\right) - 3.23\right]. \tag{13}$$

where,
p_{wf}, wellbore flowing pressure (psi);
p_i, initial reservoir pressure (psi);
q, well production rate (bbl/day);
B, formation volume factor of reservoir fluid (rb/stb);
μ, fluid viscosity (cP);
k, reservoir permeability (md);
h, average thickness (ft);
ϕ, porosity;
r_w, wellbore radius (ft);
t, time (hours); and
c_t, total compressibility (psi^{-1}).

During injection, q in Eq. 13 is replaced with "–q" which changes Eq. 13 to Eq. 14:

$$p_{wf} = p_i + \frac{162.6qB\mu}{kh}[\log\left(\frac{kt}{\phi\mu c_t r_w^2}\right) - 3.23]. \quad (14)$$

The above equation indicates that a plot of p_{wf} vs. t on a semilogarithmic scale would produce a straight line with an intercept of a and slope of m as described in Eqs. 15 and 16:

$$a = p_i + \frac{162.6qB\mu}{kh}[\log(\frac{k}{\phi\mu c_t r_w^2}) - 3.23]; \quad (15)$$

$$m = \frac{162.6qB\mu}{kh} \quad (16)$$

Carter-Tracy Analytical Aquifer Model

Reservoir properties may be considered reasonable estimates of aquifer properties because they may be of the same depositional environment. However, the Carter-Tracy aquifer function assumes homogeneity. A formation may be assumed to be infinite-acting if the simulated bottomhole flowing pressure (p_{wf}) of a well perforated within it reasonably matches that of an analytical solution. A series of reservoir simulations using homogeneous and heterogeneous geocellular models were conducted to determine (1) if a Carter-Tracy analytical aquifer with average reservoir properties (porosity and permeability) of a homogeneous model exhibits infinite-acting behavior, and (2) whether to use the arithmetic, geometric, or harmonic averaging method to estimate the permeability of the analytical aquifer surrounding a heterogeneous model so that the aquifer is infinite-acting.

A three-dimensional Cartesian grid with 80 × 100 × 75 cells, representing a formation that is 9,144 m (30,000 ft) long and 7,315 m (24,000 ft) wide with a thickness of 69 m (225 ft) was used. The arithmetic mean of the formation's porosity and permeability are 8.77% and 3.88 × 10^{-10} cm^2 (39.4 md). The formation is saturated with brine and is assigned an arbitrary initial pressure of 7,585 kPa (1,100 psi). Water was injected through a vertical well, completed from top to bottom of the reservoir at a rate of 1,333 m^3/d (8,386 bbl/d), which is above a 1,000 tonnes (1,102 tons) per day target. A radial Carter-Tracy analytical aquifer was attached to the edges of the model and the aquifer parameters were adjusted to create infinite-acting model boundaries (Table 24). The average porosity, average permeability, and thickness of the aquifer were equivalent to those of the formation.

Three representations of the formation were modeled: a homogeneous reservoir, vertically heterogeneous (layer) reservoir, and fully heterogeneous reservoir. The homogeneous model uses the average reservoir properties of the formation in all cells. The vertically heterogeneous model also uses average reservoir properties but by layers, i.e., all properties in each layer of the heterogeneous model are averaged. The fully heterogeneous model is equivalent to a vetted geocellular model of a strandplain formation. The porosity and permeability in the heterogeneous model vary from one gridblock to another. Reservoir properties (porosity, permeability, and thickness) of the analytical model were equivalent to those of the analytical aquifer to be modeled. A reasonable match between P_{wf} profiles of the reservoir simulation and analytical model indicates that the reservoir model is infinite-acting. Table 25 lists a set of analytical solution input data using a strandplain formation.

Table 24 Reservoir properties and Carter-Tracy parameters calculated using Eqs. 10–12 (1 psi^{-1} = 0.145 kPa^{-1}).

Parameter	Value	Type
ϕ	0.0877	Input
k	3.88×10^{-10} cm^2 (39.4 md)	Input
μ	1 cp	Input
c_t	8×10^{-6} psi^{-1}	Input
h	68.6 m (225 ft)	Input
r_o	4,613.378 m (15,135.75 ft)	Input
S	1	Input
B	40,470.87 rb/psi	Calculated
t_0	0.001551 1/days	Calculated

Table 25 Analytical solution input data of the strandplain formation (1 psi^{-1} = 0.145 kPa^{-1}).

Parameter	Value	Unit
k	3.88×10^{-10} (39.4)	cm^2 (md)
ϕ	0.877	–
h	68.6 (225)	m (ft)
μ	1	cp
q	1,333.45 (8,386.45)	m^3/d (bbl/d)
r_w	0.08 (0.25)	m (ft)
c_r	5×10^{-6}	1/psi
c_w	3×10^{-6}	1/psi
P_{int}	7,585 (1,100)	kPa (psi)
$T_{res,av}$	32 (90)	°C (°F)

Effect of Aquifer Permeability

Four simulation scenarios with different aquifer permeabilities were conducted to determine which scenario best depicts an infinite-acting formation. These scenarios represent a formation with no an aquifer, a formation with an aquifer of equivalent reservoir properties (base case), a formation with a weak aquifer, and a reservoir with a strong aquifer. The arithmetic average permeability of the reservoir and the aquifer are equal for the base case scenario (Table 26) and different for the other scenarios.

Figure 168 shows the P_{wf} for all four cases and the analytical solution. The P_{wf} of the base case closely matches the analytical solution while the other cases do not. The P_{wf} in the scenario with no aquifer starts to increase as the pressure front reaches the model's boundaries after approximately 10,000 hours (417 days) while that of the weak aquifer scenario reaches its boundaries at a later time. When the permeability of the aquifer is ten times greater than that of the reservoir, the P_{wf} starts to decrease when the pressure front reaches the model's boundaries because of a sharp contrast in conductivity between the formation and its surrounding aquifer. Results in Figure 168 suggest that a Carter-Tracy analytical aquifer surrounding a homogeneous formation exhibits infinite-acting behavior when assigned a permeability equivalent to the arithmetic average permeability of the formation.

Table 26 Homogeneous cases with various aquifer strengths.

Scenario	Reservoir Permeability (cm^2 [md])	Aquifer Permeability (cm^2 [md])
Base case	3.88×10^{-10} (39.4)	3.88×10^{-10} (39.4)
No aquifer	3.88×10^{-10} (39.4)	0
Weak aquifer	3.88×10^{-10} (39.4)	3.88×10^{-11} (3.94)
Strong aquifer	3.88×10^{-10} (39.4)	3.88×10^{-9} (394)

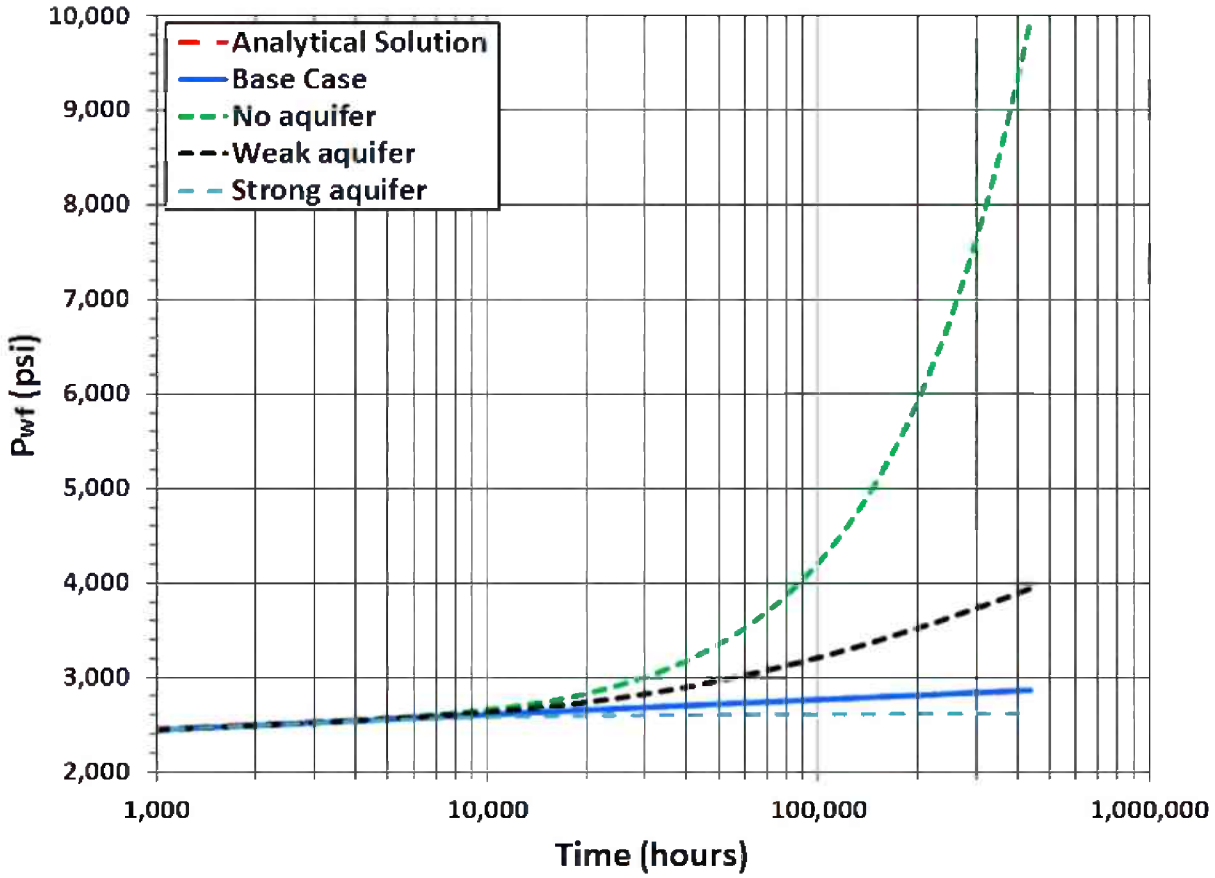

Figure 168 Effect of aquifer permeability (strength) on P_{wf} in a homogeneous formation.

Effect of B and t_0

Simulations were conducted to evaluate how the aquifer parameters B and t_0 affect P_{wf} by changing permeability and thickness, respectively. This is because B increases with formation thickness (Eq. 10) and t_0 increases with permeability (Eq. 11). The formation and surrounding aquifer were assumed to have similar average reservoir properties.

Table 27 shows the simulated scenarios. Figure 169 and Figure **170** compare the P_{wf} in different scenarios and their respective analytical solutions. The P_{wf} decreases as B or t_0 increase because a thicker and more permeable aquifer has greater capacity and conductivity, and thus releases

more pressure. The analytical solution matches the simulation at all levels, which again suggests the aquifer is infinite-acting as long as its petrophysical properties are equivalent to the arithmetic average of the formation it surrounds or is attached to (Figure 169 and Figure **170**).

Table 27 Homogeneous cases varying B and t_0.

Scenario	B (rb/psi [m^3/kPa])	t_0 (day^{-1})	k (cm^2 [md])	h (m [ft])
Base		0.001551	3.88×10^{-10} (39.4)	
Low t_0	40,470.87 (932.85)	0.000787	1.97×10^{-10} (20)	68.6 (225)
High t_0		0.01551	3.88×10^{-9} (394)	
Base	40,470.87 (932.85)			68.6 (225)
Low B	18,166.93 (418.75)	0.001551	3.88×10^{-10} (39.4)	30.8 (101)
High B	40,4708.7 (932.85)			685.8 (2,250)

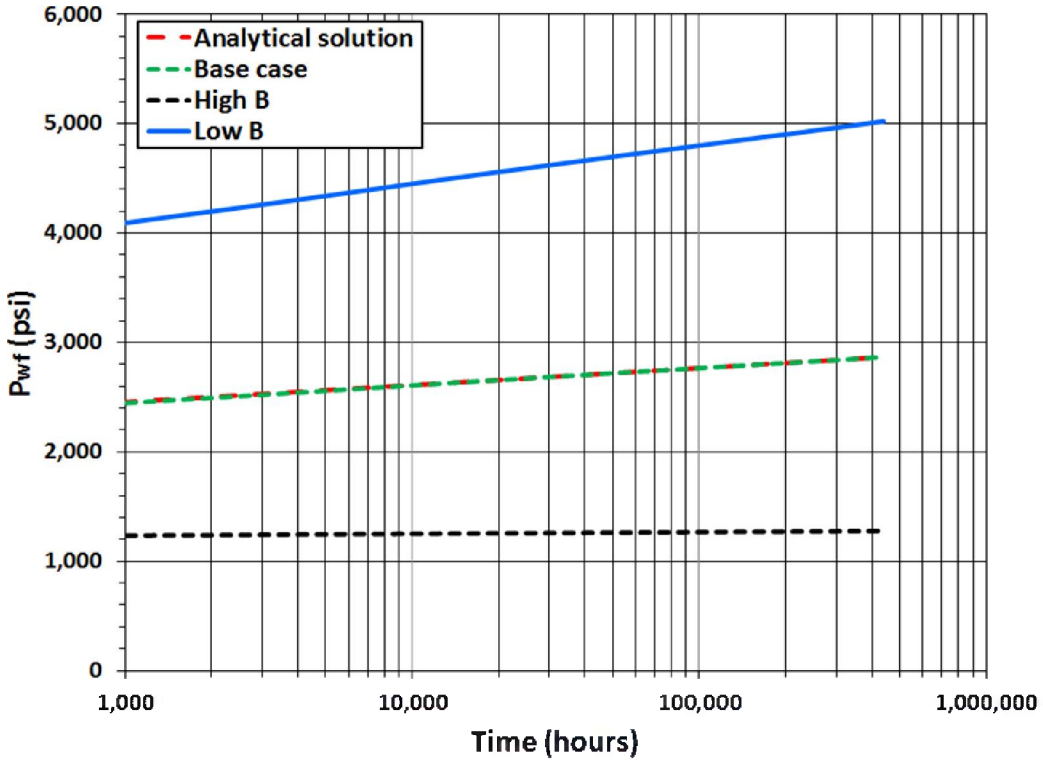

Figure 169 Effect of B on P_{wf} in a homogeneous formation.

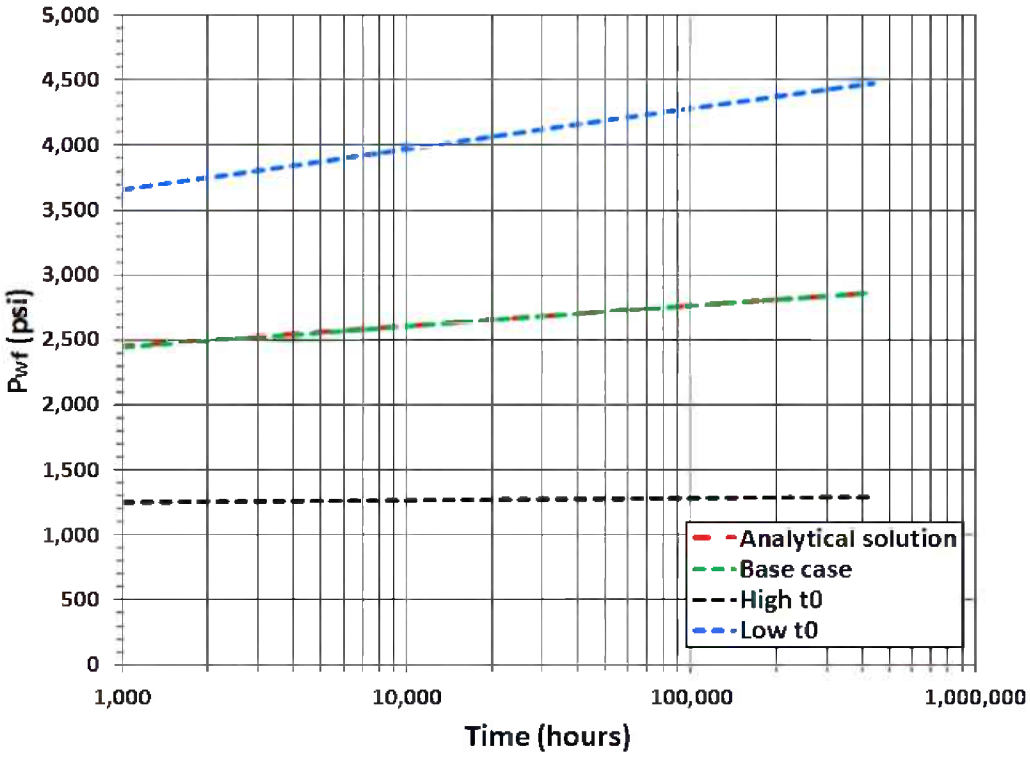

Figure 170 Effect of t_0 on P_{wf} in homogeneous formation.

Vertically Heterogeneous Reservoir

Three simulation scenarios were conducted to study the effect of reservoir-aquifer permeability contrast on the P_{wf} in a vertically heterogeneous reservoir. The average permeability of the reservoir is equivalent to the arithmetic mean of the layer permeabilities. The average permeabilities of the formation and surrounding aquifer for each scenario considered are presented in Table 28. The permeability of the aquifer for the base scenario is equivalent to the reservoir's average permeability. The aquifer's permeability is less than the average reservoir permeability for the weak aquifer scenario and greater for the strong aquifer scenario. Figure 171 compares the P_{wf} of the three cases to the analytical solution. The base scenario closely matches the analytical solution while the other scenarios do not. Results presented in Figure 171 suggest that the average reservoir properties can be used to model an infinite-acting aquifer attached to a vertically heterogeneous formation.

Table 28 Vertically heterogeneous cases with various aquifer strengths.

Scenario	Average Reservoir Permeability (cm^2 [md])	Aquifer Permeability (cm^2 [md])
Base case	1.06×10^{-9} (107.7)	1.06×10^{-9} (107.7)
Weak aquifer	1.06×10^{-9} (107.7)	1.06×10^{-10} (10.77)
Strong aquifer	1.06×10^{-9} (107.7)	1.06×10^{-8} (1077)

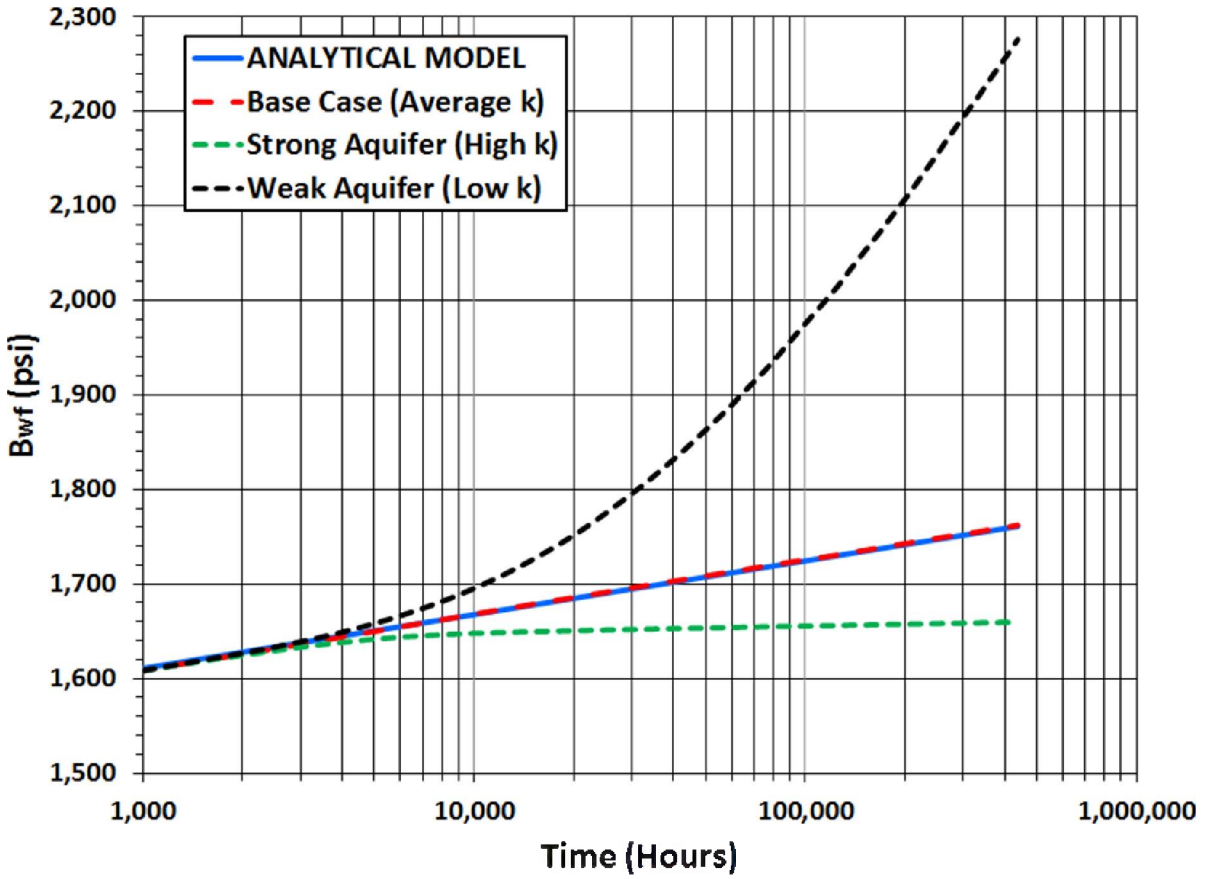

Figure 171 Effect of aquifer strength on P_{wf} in a vertically heterogeneous formation.

To better understand the connection between a vertically heterogeneous (layered) reservoir and a homogeneous reservoir, vertically heterogeneous models were added to previous homogeneous models (Table 27). Additional scenarios of vertically heterogeneous models with different permeability values in each layer of the formation and the permeability of the surrounding aquifer equivalent to the arithmetic mean of the layer permeabilities (homogenous aquifer) were also conducted.

Figure 172 and Figure **173** compare simulation results to the analytical model for different values of reservoir thickness (h) and permeability (k). Changes in h and k translate to changes in the capacity and conductivity of an aquifer surrounding a formation (Eqs. 10 and 11). Figure 172 and Figure **173** show the P_{wf} of simulations and analytical solution results for different values of h and k. The P_{wf} for the analytical solution, homogeneous formation, and vertically heterogeneous formations closely match each other; consequently, Carter-Tracy analytical aquifers attached to a vertically heterogeneous formation are infinite-acting when assigned average permeabilities equivalent to the arithmetic mean or weighted average permeabilities of the formations they surround (Figure 172 and Figure 173).

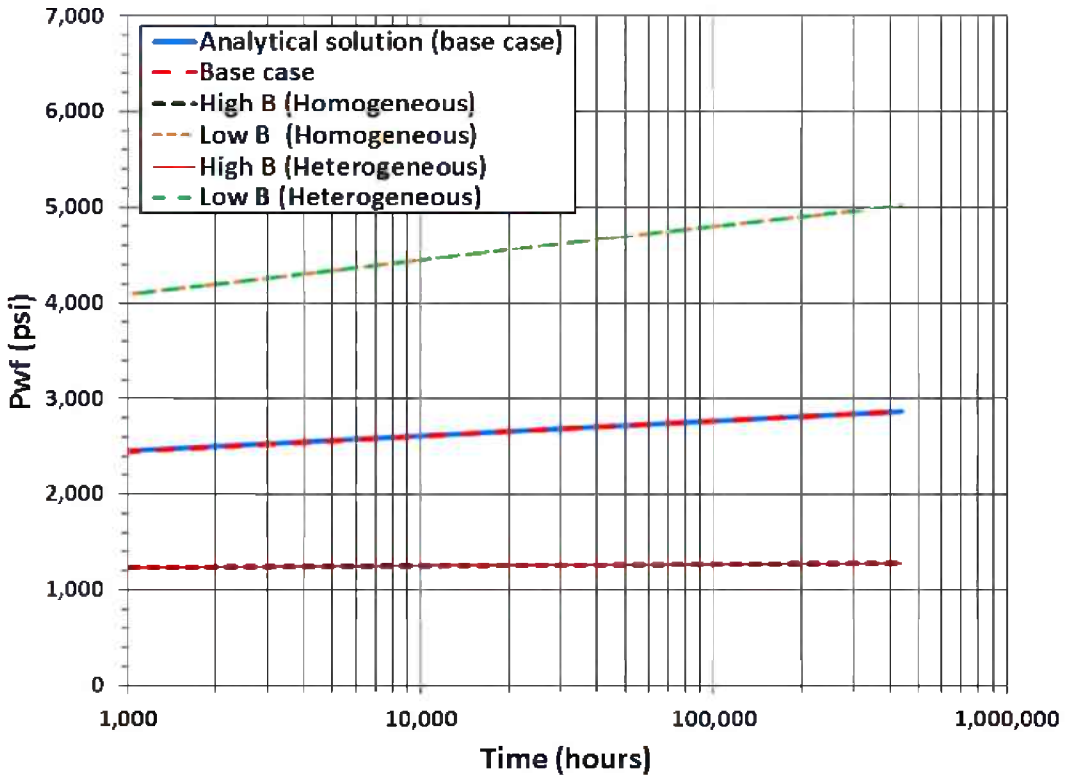

Figure 172 Effect of B on P_{wf} for homogeneous and heterogeneous formations.

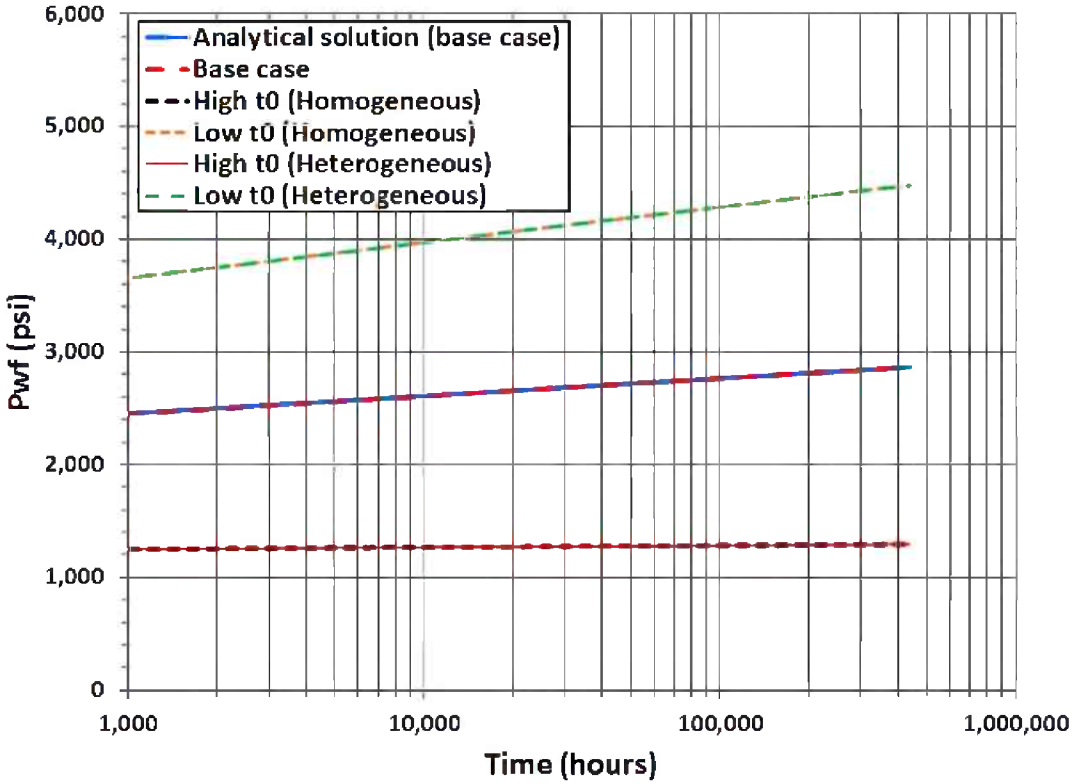

Figure 173 Effect of t_0 on P_{wf} for homogeneous and heterogeneous formations.

Fully Heterogeneous Reservoirs

The average permeability of a heterogeneous formation can be interpreted in terms of the effective permeability of a homogeneous reservoir that conducts the same flux over the same pressure drop (Warren et al., 1961). The most common permeability averaging methods include arithmetic average, harmonic average, and geometric average. The first two methods are derived from Darcy's equation (Darcy, 1856), which considers a system to comprise of parallel homogeneous layers or subunits. The weighted average is used when the flow direction is parallel to the layers. Permeability can be weighted by the thickness of the layers if the layers have unequal thickness, i.e., simple arithmetic average. Harmonic averaging is generally used when fluid flow is perpendicular to the layers (Ahmed and McKinney, 2004). A previous work by Cardwell and Parsons (1945) recommends arithmetic and harmonic averages as reasonable bounds of the effective permeability of a reservoir.

Average gridblock permeability is the geometric average of the directional permeabilities of that gridblock; average layer permeability is either the geometric or the harmonic average of all the gridblocks in that layer; and the average permeability of an entire model is either the geometric or the arithmetic average of the layer permeability. In scenarios where reservoir layers have the same thickness, weighted average becomes equivalent to arithmetic average. Considering the two bounds of permeability, arithmetic and harmonic averages, the average permeability of a reservoir can be calculated from gridblock to model scale (Table 29). The last column in Table 29 contains average permeability values of a heterogeneous formation estimated using different averaging methods at the gridblock, layer, and model scale.

The data in Table 29 was used to conduct six reservoir simulation scenarios to evaluate the effect of each permeability averaging method on P_{wf} (Figure 174). Results in Figure 174 indicate that a small change in reservoir permeability causes significant changes in the P_{wf}. None of the simulation results closely matched their corresponding analytical solutions. The smallest difference was achieved using Scenario 1 (arithmetic or weighted average method). The P_{wf} of the arithmetic average scenario fits well with a logarithmic trend line. The P_{wf} of the other scenarios all deviate upwards from the logarithmic trend line, there by exhibiting characteristics of a weaker aquifer.

Therefore, for a fully heterogeneous reservoir, a simple arithmetic or weighted average of formation permeability should be assigned to its surrounding aquifer function in order to model an infinite-acting system (formation plus aquifer). A semi-log plot of P_{wf} vs. t that produces a straight line with positive gradient indicates infinite-acting behavior, even though the P_{wf} of the numerical and analytical solutions of the heterogeneous model do not overlap each other. The P_{wf} of the numerical and analytical solutions of the heterogeneous model did overlap when the permeability of the latter was increased from 39.3 md to 42.0 md.

Table 29 Different methods of estimating the average permeability of a heterogeneous formation. As an example, the different methods are applied to an ILB formation with a strandplain depositional environment.

Scenarios	Gridblock	Layer	Entire Model	k (cm^2 [md])
1	Arithmetic	–	–	3.87×10^{-10} (39.29)
2	Geometric	Geometric	Arithmetic	3.55×10^{-10} (36.01)
3	Geometric	Geometric	Geometric	3.39×10^{-10} (34.38)
4	Geometric	Harmonic	Arithmetic	3.23×10^{-10} (32.74)
5	Geometric	Harmonic	Geometric	3.05×10^{-10} (30.94)
6	Harmonic	–	–	2.96×10^{-10} (29.97)

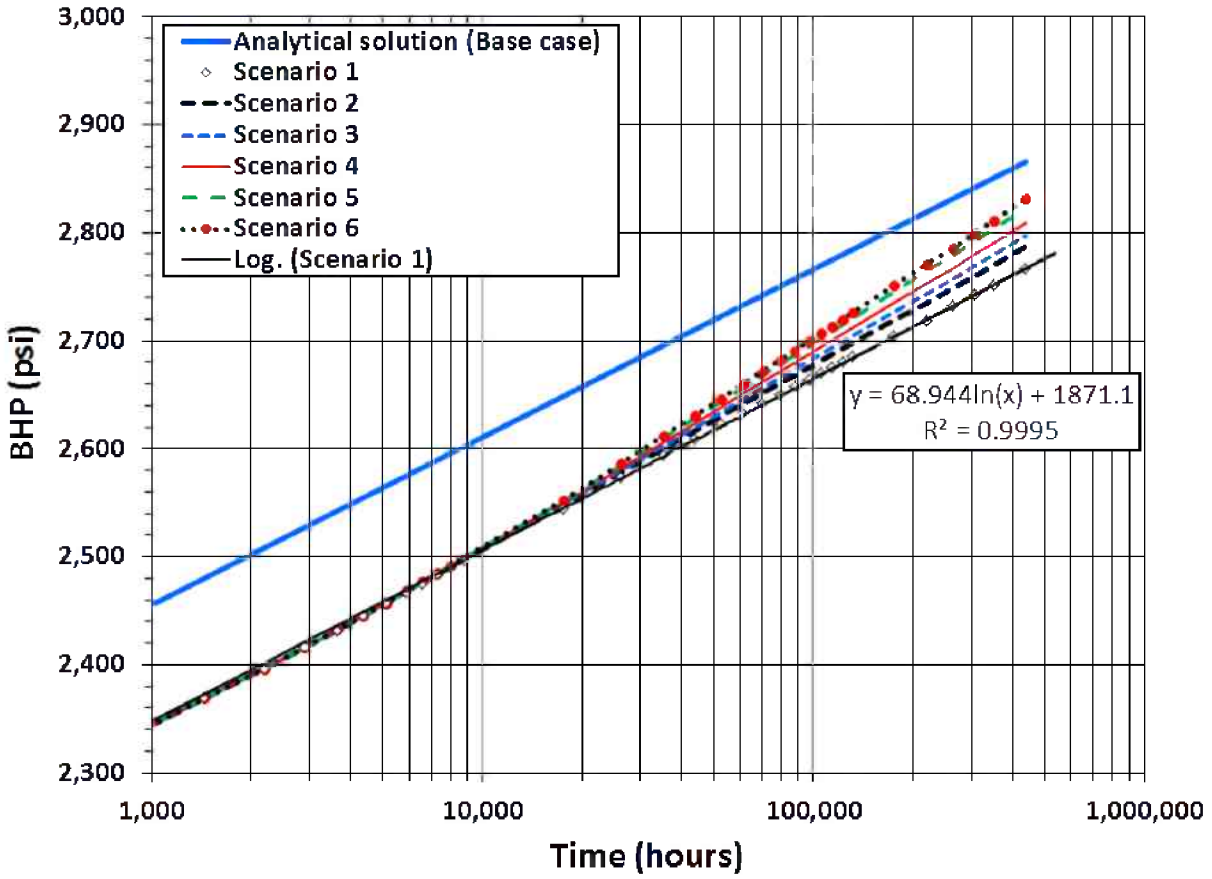

Figure 174 The P_{wf} of the different permeability averaging approaches compared to the analytical solution for a fully heterogeneous formation. All of the averaging methods predict P_{wf} lower than those of the analytical solution. Only the P_{wf} of the arithmetic mean curve is linear on the P_{wf} vs. log t plot. The average permeability of the analytical model is 39.3 md.

Effects of End-point Saturations and Relative Permeability (S_{wr}, S_{gc}, and $k_{rg,max}$)

The effects of end-point saturations and relative permeabilities on E were studied by conducting sensitivity on the irreducible water saturation (S_{wirr}), critical CO_2 saturation (S_{gc}), and the

maximum relative permeability of CO_2 using a heterogeneous model and vertical equilibrium relative permeability functions for water and CO_2. A value of one was assigned to the maximum relative permeability of water because the geologic formations in this study were assumed to be initially saturated (100%) with brine, i.e., zero initial CO_2 saturation.

The effect of each parameter was studied by conducting multiple simulation scenarios in which its value changes while those of other parameters are kept constant (Table 30, Table **31**, and Table **32**). Simulation results show that E decreases as S_{wirr} increases, which also corresponds to a reduction in the average CO_2 saturation within the contacted formation volume ($\bar{S}_g$; Table 31). Results in Table 33 show that E increases and $\bar{S}_g$ decreases as S_{gc} is increased. An increase in S_{gc} causes a corresponding drop in CO_2 mobility and thus results in an increase in E. Table 32 shows that E decreases as $k_{rg,\,max}$ increases.

Table 30 Effect of irreducible water saturation on E. The E_{rec}, E_{sqr}, E_{cyl} are storage efficiency calculated by the rectangle, square, and cylinder methods.

Scenario	S_{gc}	$k_{rg,\,max}$	E_{rec} (%)	E_{sqr} (%)	E_{cyl} (%)	$\bar{S}_g$
$S_{wirr} = 0.00$	0.25	0.5	9.4	7.1	9.0	0.76
$S_{wirr} = 0.35$	0.25	0.5	6.6	5.4	6.9	0.54
$S_{wirr} = 0.70$	0.25	0.5	3.9	2.9	3.7	0.27

Table 31 Effect of critical CO_2 saturation on E. The E_{rec}, E_{sqr}, E_{cyl} are storage efficiency calculated by the rectangle, square, and cylinder methods.

Scenario	S_{wirr}	$k_{rg,\,max}$	E_{rec} (%)	E_{sqr} (%)	E_{cyl} (%)	$\bar{S}_g$
$S_{gc} = 0.00$	0.35	0.5	2.9	2.7	3.4	0.60
$S_{gc} = 0.10$	0.35	0.5	5.7	4.7	6.0	0.51
$S_{gc} = 0.25$	0.35	0.5	6.6	5.4	6.9	0.54
$S_{gc} = 0.50$	0.35	0.5	8.1	6.3	8.0	0.57

Table 32 Effect of maximum CO_2 relative permeability on E. The E_{rec}, E_{sqr}, E_{cyl} are storage efficiency calculated by the rectangle, square, and cylinder methods.

Scenario	S_{gc}	S_{wirr}	E_{rec} (%)	E_{sqr} (%)	E_{cyl} (%)	$\bar{S}_g$
$k_{rg,\,max} = 0.20$	0.25	0.35	13	8.9	11	0.52
$k_{rg,\,max} = 0.35$	0.25	0.35	8.9	6.7	8.5	0.52
$k_{rg,\,max} = 0.50$	0.25	0.35	6.8	5.3	6.7	0.53

Reservoir Simulation Scenarios

Baseline Storage Efficiencies

Reservoir simulations of CO_2 injection were conducted to determine baseline E of eight different depositional environments. The baseline simulations involve injection via a vertical well, perforated across the entire vertical thickness of the formation. To avoid the choice of a well location that yielded a very high or low E, five simulation scenarios of different well locations were conducted. They included four locations at one-third the reservoir model's width from the center and one at the center of the reservoir grid; the baseline E was calculated as the arithmetic average of the E_s from simulations of these five locations.

In general, dynamic storage efficiency as a function of time for a given scenario of CO_2 storage shows E to approach a maximum value and stay relatively constant as CO_2 is injected over time (Figure 175). The time derivative of E ($\Delta E/[\Delta t]$) decreases over time and appears to approach zero as E approaches a constant value. The E of each simulation scenario was determined when its value is relatively unchanged.

Table 33 shows the ranges of E_d achieved using both stratigraphic and structural geocellular models of eight depositional environments studied. The fluvial deltaic and turbidite formations had the highest, and the shelf carbonate formation had the lowest baseline E values (Table 33).

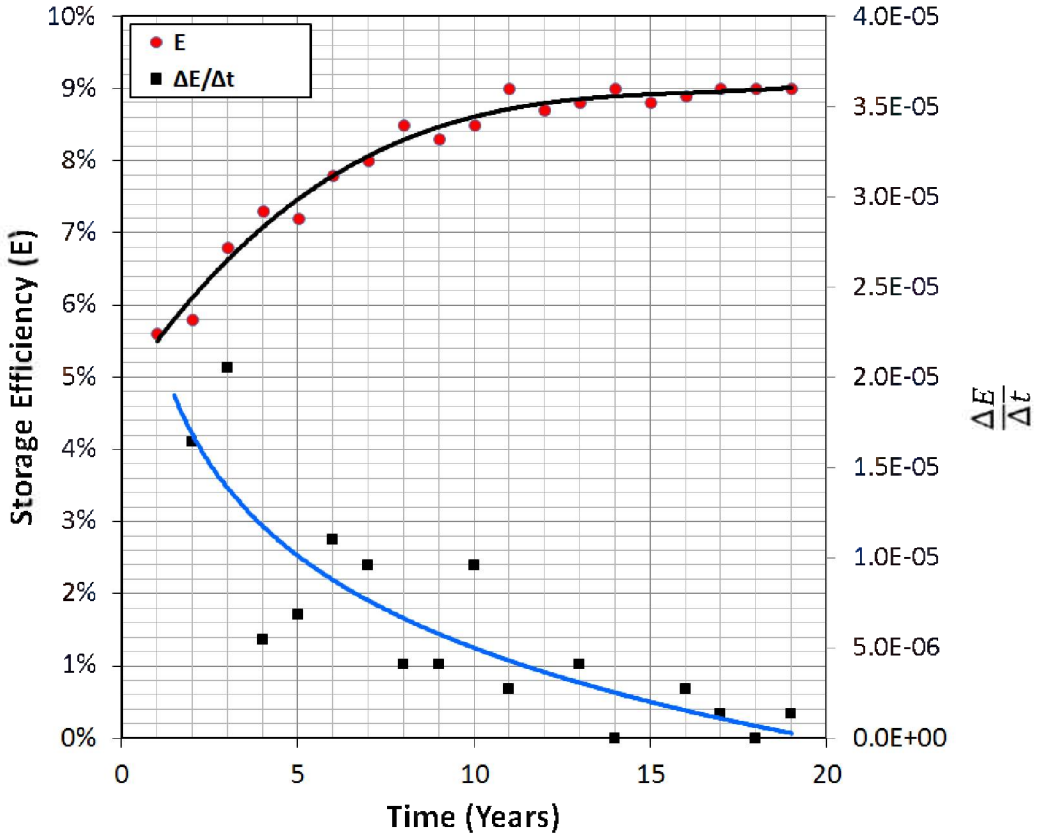

Figure 175 This is an example of a storage efficiency profile for CO_2 injection via a centrally located vertical well using a strandplain formation. Dynamic storage efficiency initially increases and then plateaus over time. The first derivative of *E* (dE/dt) decreases over time and approaches zero as *E* plateaus.

Table 33 The average baseline *E* of the depositional environments. A net increase in average baseline E is achieved when a structure is present (column 5).

Depositional Environment	Lithology	Baseline *E* (%)		
		Stratigraphic	Structural	% Change
Deltaic	Sandstone	14.8	15.8	6.5
Shelf clastic	Sandstone	10.1	13.2	30
Shelf carbonate	Limestone	5.27	6.04	15
Shelf carbonate	Dolomite	5.47	5.57	2.0
Fluvial deltaic	Sandstone	17.2	17.5	1.6
Strandplain	Sandstone	10.1	14.7	46
Reef	Limestone	12.9	13.1	2.1
Fluvial and alluvial	Sandstone	15.9	18.9	19
Turbidite	Sandstone	17.0	17.6	3.4

Effect of Geologic Structure

Geologic structures of the specific fields studied were removed from the geocellular models to ensure estimated storage efficiencies are functions of depositional environment only. The contribution of geologic structure to the overall storage efficiency was evaluated by conducting simulations using reservoir models with geologic structures (Table 33). The structure added to each of these depositional models was specific to the actual geologic formation from which each model was based. Varying degrees of structure were present. The increase in *E* based on storage ranged from 1.6% to 46% (Table 33).

Results in Table 33 suggest that the geologic structures contribute to a net increase in *E*. Three-dimensional views of the reservoir models revealed structures of different size, relief, and thickness. Large structures with low relief have large change in E compared to small structures with high relief. Good examples of formations with low and high reliefs from Table 33 are those of strandplain and shelf carbonate depositional environments, respectively. Figure 176 and Figure **177** show the CO_2 saturation distribution in structural reservoir models of strandplain and shelf carbonate formations.

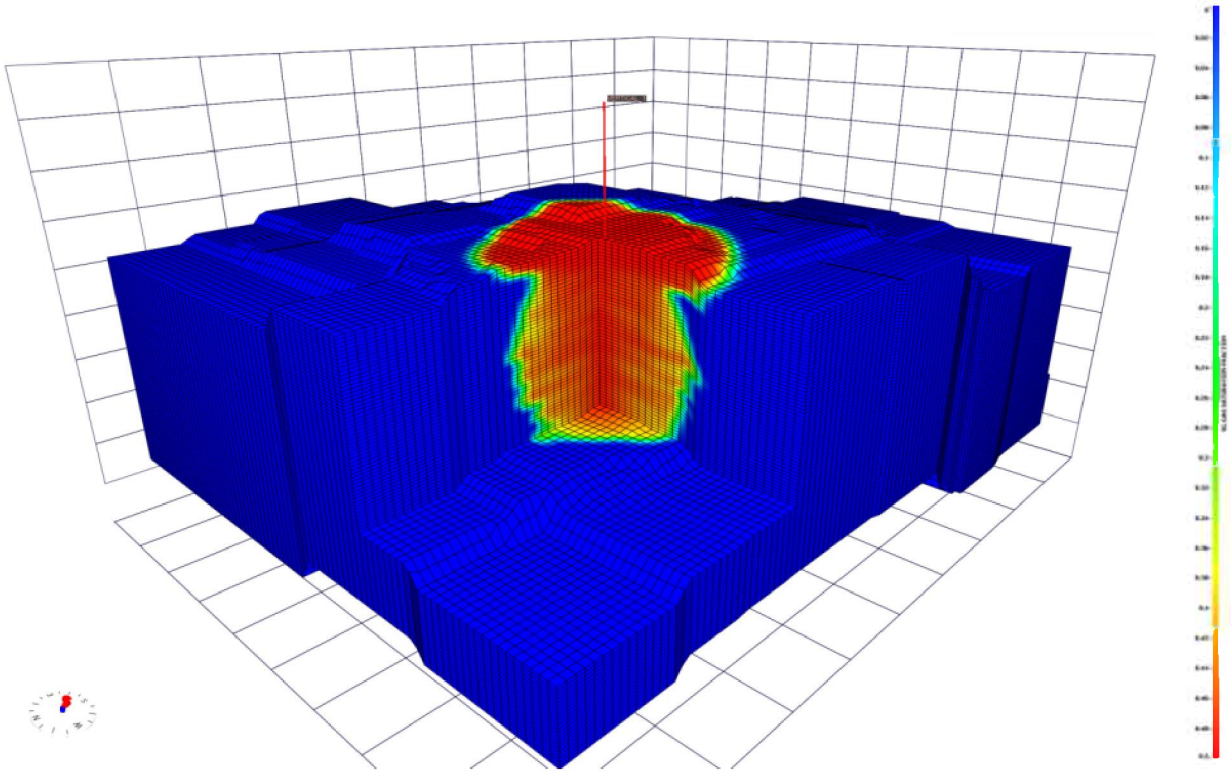

Figure 176 The CO_2 saturation distribution within the structure reservoir model of a strandplain formation. The model is 68.6 m (225 ft) thick and has a low relief structure. Warmer colors indicate higher CO_2 saturation and blue indicates water (Baseline E = 14.7%).

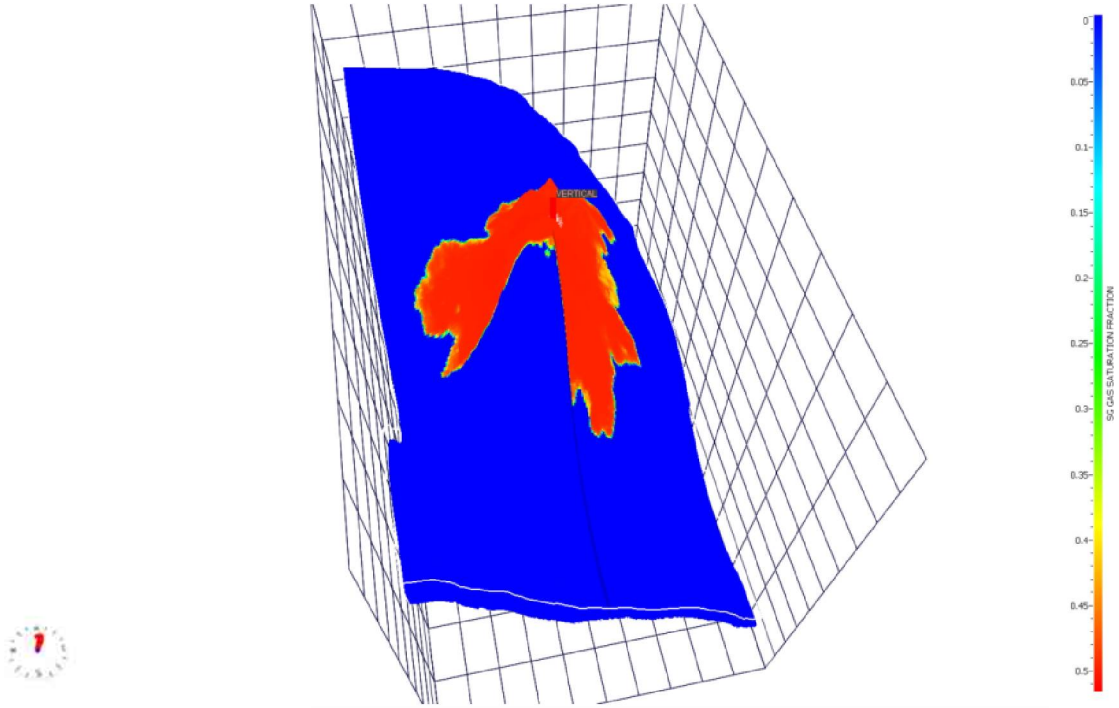

Figure 177 The CO_2 saturation distribution within the structure reservoir model of a shelf carbonate (dolomite) formation. The model is 21 m (69 ft) thick and has a high relief structure. Warmer colors indicate higher CO_2 saturation and blue indicates water (Baseline E = 5.57%).

Storage Efficiency Normalization

The baseline E ranges in Table 33 were normalized to reduce the dependency of storage efficiency on relative permeability. This is because the relative permeability of fluids competing for pore space change from formation to formation. Normalization methods that were tested include the following:

Equation	Comment	
$E_V = \frac{E}{\bar{S}_g}$;	Ratio of E to the average CO_2 saturation within contacted pore volume ($\bar{S}_g$).	(17)
$E_V = \frac{E}{\bar{S}_g}(k_{rg})_{S_g=\bar{S}_g}$;	Ratio of E to $\bar{S}_g$ multiplied by CO_2 relative permeability at S_g equal to $\bar{S}_g$.	(18)
$E_V = \frac{E(1-S_{wirr})}{\bar{S}_g}$;	Ratio of E to $\bar{S}_g$ multiplied by maximum CO_2 saturation ($S_{g,max}$ = 1-S_{wirr}).	(19)
$E_V = \frac{E(1-S_{wirr}-S_{gc})}{\bar{S}_g}$;	Ratio of E to $\bar{S}_g$ multiplied by the moveable CO_2 saturation (1-S_{wirr}-S_{gc})	(20)
$E_V = \frac{E(1-\bar{s}_g)}{\bar{S}_g}$;	Ratio of E to $\bar{S}_g$ multiplied by the average water saturation within CO_2 contacted pore volume ($\bar{S}_w = 1 - \bar{S}_g$).	(21)
$E_V = \frac{E(1-S_{wirr})}{\bar{S}_g - S_{gc}}$.	Product of E and maximum gas saturation ($S_{g,max}$) multiplied by the difference between $\bar{S}_g$ and the critical CO_2 saturation (S_{gc}).	(22)

Normalization with respect to average CO_2 saturation ($\bar{S}_g$) within the contacted formation volume (Eq. 17) worked best for a given maximum CO_2 relative permeability ($k_{rg,\,max}$). Eq. 17 best reduced the dependency of E on irreducible water saturation and critical gas saturation. The mean normalized baseline E, which is equivalent to the volumetric sweep efficiency (E_v), for each depositional environment, is presented in Table 34 and Figure 178. Table 34 also shows the standard deviation from the mean E_V, which ranges from 3.1% to 11.4% for the stratigraphic reservoir models. Results in Table 34 also suggest that geologic structures cause net increase in storage or volumetric sweep efficiency.

Table 34 Mean baseline E_V and standard deviation for each depositional environment.

Depositional Environment	E_V (%)				
	Stratigraphic		Structural		
	Mean	Standard deviation	Mean	Standard deviation	*% Change*
Deltaic	33.5	5.70	33.9	5.90	1.19
Shelf clastic	29.4	6.90	37.6	12.5	27.9
Shelf carbonate	15.9	4.10	17.6	5.60	10.7
	13.1	3.10	13.2	2.50	0.70
Fluvial deltaic	41.7	5.50	42.0	5.60	0.72
Strandplain	25.7	5.80	38.3	6.20	49.0
Reef	35.1	11.4	34.4	12.1	1.99
Fluvial and alluvial	34.4	7.90	39.0	8.10	13.4
Turbidite	42.5	11.3	43.4	11.1	2.12

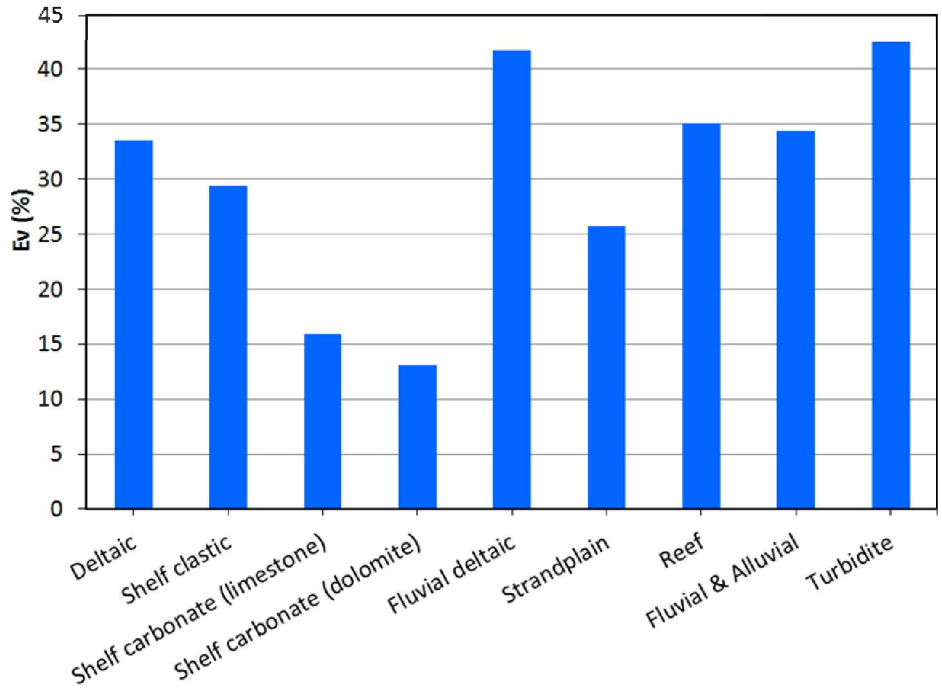

Figure 178 Bar chart showing the average E_V of eight depositional environments. The fluvial deltaic and turbidite depositional environment have the highest E_V while shelf carbonate (dolomite) has the lowest.

Efficiency Enhancement Strategies

Different well completions and orientations were evaluated to identify strategies that can be used to enhance E. The injection well orientations considered include horizontal wells and deviated wells, while the well completions strategies simulated include blanket completions, and selective completions. Detailed simulation results for each depositional environment are located in Appendix 1.

Horizontal Wells

A horizontal well is defined as a well or its segment drilled parallel to the bedding plane of a reservoir. Sufficiently long, horizontal wells provide large reservoir contact area and thereby improve well injectivity (Joshi, 1991). Multiple of simulations were conducted to investigate the effects of well depth, well length, and well orientation with respect to areal anisotropy on CO_2 storage efficiency.

Simulations of CO_2 injection via a horizontal well at different depths within the injection interval (top 20%, middle 20%, and bottom 20%) were performed. Simulation results indicate that placing horizontal wells within the bottom 20% interval of the formation is the most effective well placement approach to adopt for all eight depositional environments.

Before conducting any reservoir simulations, the average directional permeabilities of each model were estimated to determine the high and low permeability directions. The average permeability directions were aligned along the x- and y-directions of the reservoir grid. The x-direction corresponds to the east-west while the y-direction is equivalent to the north-south direction of the model. Then, two sets of reservoir simulations were conducted in which the horizontal well is placed along the x- and y-directions (Table 35). Each set consists of reservoir

simulation scenarios in which the horizontal well is located at the center of the model in one scenario and one-third its width from the center on both sides of the model's center (two scenarios). Results from the six simulation scenarios were compared to determine the best location to place horizontal wells when evaluating the effect of well length on E. Simulation results indicate that placing horizontal wells perpendicular to the high permeability direction of the formation is the most effective well placement approach to adopt for all eight depositional environments.

Placing a horizontal injection well perpendicular to the high permeability direction is analogous to using a similar well configuration to enhance drainage of hydrocarbons in naturally fractured reservoirs, as reported in Joshi (1991). Previous studies by Hutchinson (1959), Landrum and Crawford (1960), and Mortada and Nabor (1961) focused on the effect of directional permeability in a five-spot pattern flood and found areal displacement efficiency to be highest when the lines connecting producers and injectors are perpendicular to the maximum permeability direction.

Table 35 Simulation scenarios conducted to determine the best location for horizontal wells within a formation. Wells are placed at the bottom 20% interval of the models.

Scenario Number	Orientation	Well location	Comments
1	*x*-direction	Center	West and East locations are one-third model width from center location.
2		West	
3		East	
4	*y*-direction	Center	North and South locations are one-third model width from center location.
5		North	
6		South	

The effect of horizontal well length on E was also evaluated by conducting simulations in which well length is varied as a function of formation thickness, in order to estimate the optimum horizontal well length to achieve high storage efficiencies. An optimum well is defined here as the well length with the highest E_V value. The simulated well lengths were varied between five and 100 times the model thickness. The optimum well length was determined by comparing the E_V values of different simulated well length. The well length with the highest E_V was selected. Figure 179 shows two examples of the effect of well length on E_V; the wells were placed perpendicular to the high permeability direction and at the bottom 20% interval of the model.

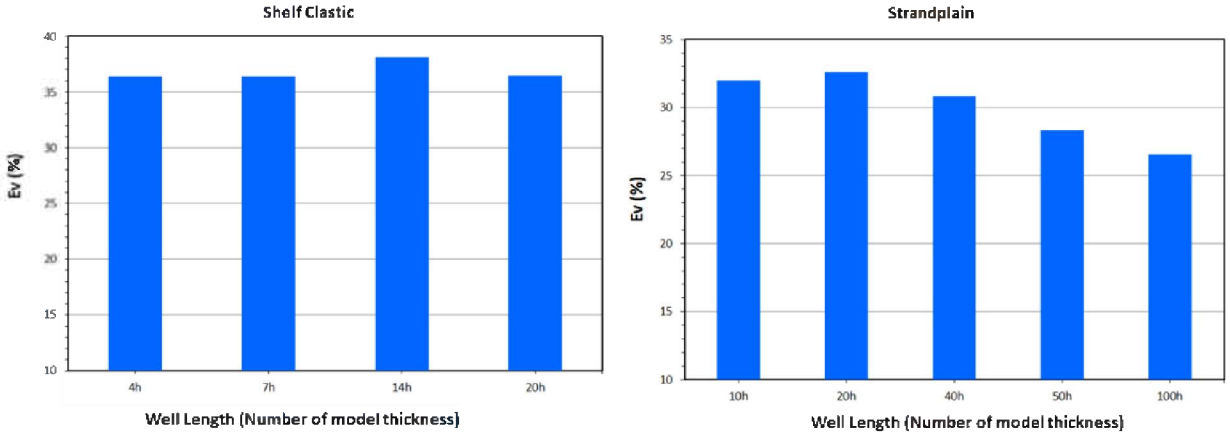

Figure 179 Change in E_V as a function of well length for shelf clastic (left) and strandplain (right) formations. The highest E_V well lengths are about 14 and 20 times the thicknesses (h) of the shelf clastic (141 ft) and strandplain (225 ft) models, respectively.

The optimum well lengths and relative difference in E_V for all the formations studied are presented in Table 36. Relative difference is defined as the percentage increase or decrease in E_V relative to the baseline E_V. With the exception of the shelf carbonate (limestone), the optimum well length for all the formations ranges between about 609.6 and 2,743 m (2,000 and 9,000 ft). Figure 180 compares the E_V values of the optimum horizontal well simulation scenarios to the baseline (vertical well) efficiency for each depositional environment. The shelf carbonate (limestone) formation has a short optimum well length because its model has a thick high permeability interval compared to its total thickness within which CO_2 preferentially flows into during injection. Results in Figure 180 and Table 36 suggest that E_V in the shelf clastic, shelf carbonate, strandplain, reef, fluvial and alluvial, and turbidite formations is significantly enhanced using horizontal wells. It can be inferred from Figure 180 and Table 36 that no increment in E_V can be achieved using a horizontal well in the fluvial deltaic model. In addition, the relative difference in E_V of most depositional environments is 20% and 40%.

Table 36 Most efficient horizontal well length for different depositional environments.

Depositional Environment	Average thickness (m [ft])	Well Length (m [ft])	% Relative difference in E_V
Deltaic	42.1 (138)	1,262 (4,140)	2.17
Shelf clastic	43 (141)	601.7 (1,974)	29.4
Shelf carbonate	21 (69)	126.2 (414.0)	18.6
	21 (69)	630.9 (2,070)	14.4
Fluvial deltaic	89.6 (294)	896.1 (2,940)	-0.852
Strandplain	68.6 (225)	1,372 (4,500)	24.7
Reef	52.1 (171)	2,606 (8,550)	63.7
Fluvial and alluvial	157 (515)	784.9 (2,575)	38.1
Turbidite	34.7 (114)	694.9 (2,280)	42.0

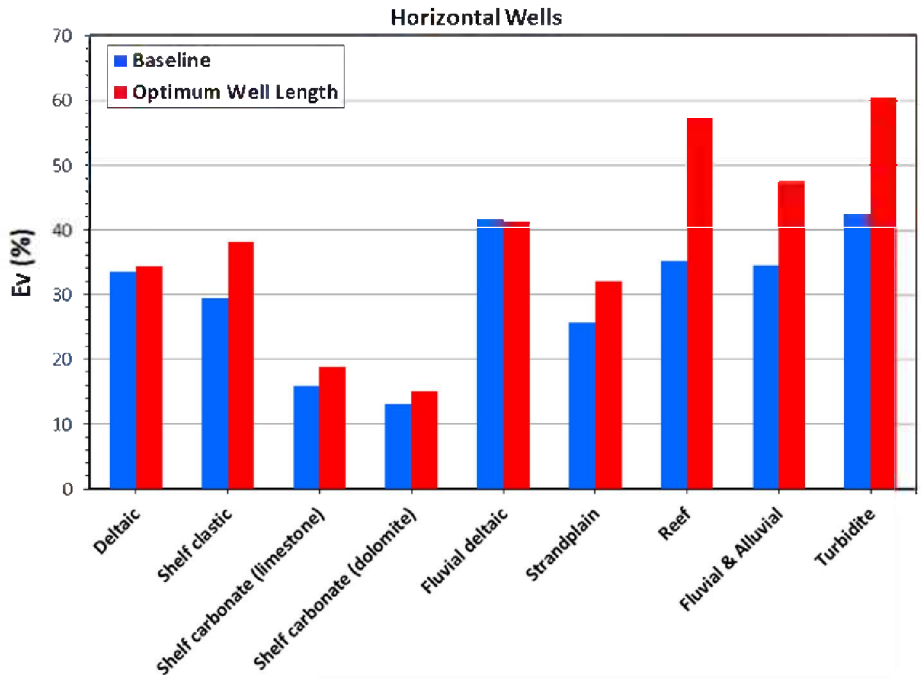

Figure 180 Comparison of the E_V for optimum horizontal well simulation scenarios to the baseline E_V.

Selective Completions

Selective completions involves perforating injection wells at targeted intervals within a formation. Dynamic completions involves sequential injection of CO_2 into different perforated intervals via a vertical, horizontal, or deviated well. "Blanket" completions may not be appropriate for injection in heterogeneous formations because injected CO_2 preferentially flow into high permeability intervals, thus by-passing low permeability intervals.

Different selective completions scenarios were simulated to determine an effective completions strategy that can be implemented to enhance E (Table 37). The effectiveness of each completions strategy was assessed by comparison of its estimated E_V value to that of the baseline E_V. The permeabilities of model layers were estimated as the arithmetic mean of the geometric mean of the x- and y-directional permeabilities (k_h) of all the gridcells in each layer. The model layers were also grouped into five or more intervals (20% of model thickness for formations less than 30.5 m [100 ft] and 10% of model thickness for formations greater than 61 m [200 ft] thick, respectively). The average horizontal permeability (k_h) for each interval is equivalent to the harmonic mean of the k_h for each layer. The classification of layers and intervals was based on each model's arithmetic average permeability. Layers or intervals having permeabilities greater than the average model permeability were considered high permeability layers or intervals and vice versa for low permeability layers and intervals (Table 37). The k_v/k_h ratio of each layer was calculated as the arithmetic mean of the ratio of the vertical permeability (k_v) to k_h of all layer gridcells.

Table 37 Simulation scenarios conducted to evaluate the effect of selective completions on *E*.

Scenario Number	Completions scenarios	Comments
1	Top 10-20%	Top 10-20% of model
2	Bottom 10-20%	Bottom 10-20% of model
3	High *k* layers	High k_h layers
4	Low *k* layers	Low k_h layers
5	High *k* intervals	High k_h intervals
6	Low *k* intervals	Low k_h interval
7	Low k_v/k_h layers	Low k_v/k_h layers

The simulation scenarios in Table 37 were conducted using vertical well locations that yielded the lowest and highest E_V in the baseline simulations. Figure 181 and Figure **182** compare the E_V of the seven simulation scenarios in Table 37 at the low and high baseline well locations to the lowest and highest baseline E_V for deltaic and fluvial and alluvial models (for reference the minimum, maximum, and average E_V values are shown). The E_V values at the high baseline well location are all lower than the highest baseline E_V. Only the E_V value for the high permeability layers simulation at the low baseline well location is greater than the lowest baseline E_V for deltaic model (Figure 181). The high permeability intervals and the bottom 10-20% simulation scenarios are greater than baseline E_V at both the low and high baseline well locations (Figure 182).

The E_V values of all seven scenarios at the low and high baseline well locations for all eight depositional environments were compared to their corresponding lowest and highest baseline E_V by calculating the relative differences between them. The scenario with the highest relative difference was selected as the most efficient completions strategy as shown in Table 38, for each depositional environment. The following conclusions can be drawn from the results in Table 38; (1) the bottom completions strategy is most efficient in shelf carbonate (limestone) and strandplain; (2) perforating at high permeability layers is most efficient in deltaic, shelf clastic, shelf carbonate (dolomite), and fluvial and alluvial; (3) perforating at low permeability layers is most efficient in fluvial deltaic and reef; (4) none of the seven completions strategies was more efficient than the blanket completions (baseline) E_V for turbidite; and (5) most of the increments in E_V were achieved at the low E vertical well locations (column 3, Table 38). The results in Table 38 also suggest that no completions strategy is most efficient for all the depositional environments but vary from one depositional environment to another. No clear conclusion can be drawn from these results because E_V was calculated based on total model thickness regardless of thickness of the perforated interval. Higher values of E_V may have been obtained if the CO_2-saturated thickness and not the total thickness of the models were used in E_V calculations. Overall, it may be concluded that a most likely change in E_V of 5—10% could be using the efficient completions strategies listed in Table 38.

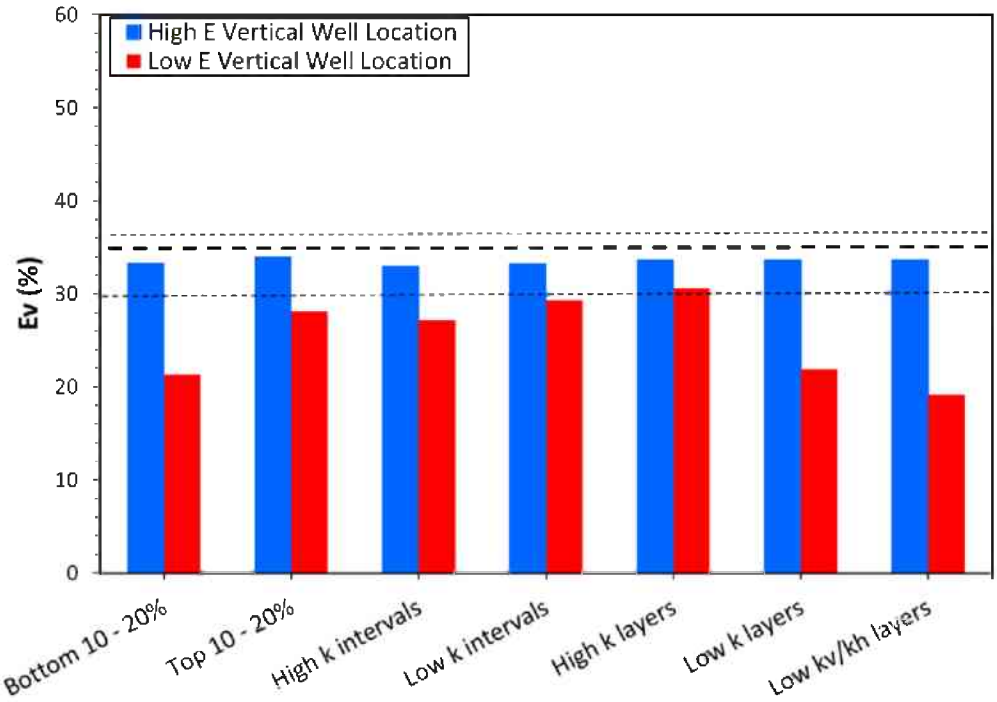

Figure 181 Comparison of the storage efficiencies of different completions strategies using the low E and high E vertical well locations for a deltaic model. The minimum, maximum, and average baseline E_V for the deltaic model are 30%, 37%, and 34%, respectively.

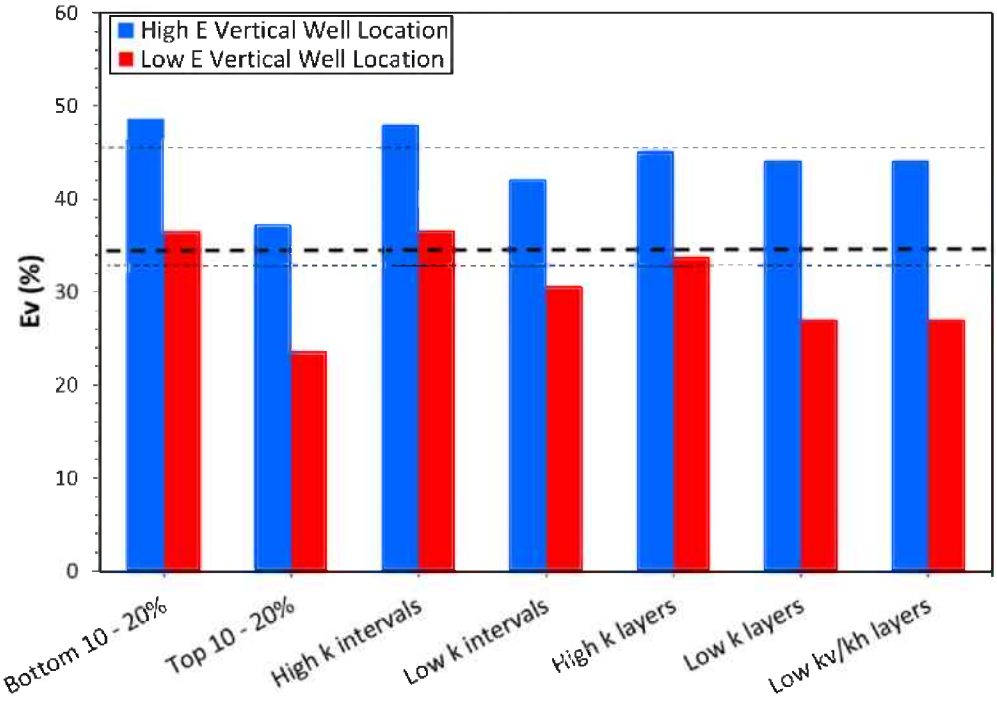

Figure 182 Comparison of the storage efficiencies of different completions strategies using the low E and high E vertical well locations for a fluvial and alluvial model. The minimum, maximum, and average baseline E_V for the fluvial and alluvial model are 33%, 45%, and 34%, respectively.

Table 38 Most effective selective completion strategies by depositional environment. None of the seven completions strategies were more efficient than the baseline E_V for the turbidite model.

Depositional environment	Most efficient completions strategy	Baseline E*	% Relative difference
Deltaic	High k layers	Low E	2.5
Shelf clastic	High k layers	Low E	11
Shelf carbonate (limestone)	Bottom 10 — 20%	Low E	7.4
Shelf carbonate (dolomite)	High k layers	Low E	34
Fluvial deltaic	Low k layers	Low E	4.5
Strandplain	Bottom 10 — 20%	Low E	1.1
Reef	Low k layers	High E	6.8
Fluvial and alluvial	High k intervals	Low E	11
Turbidite	None	None	—

*Baseline case yielding largest relative difference (column 4) for completions strategy of vertical wells.

Deviated Wells

Compartmentalized formations can be accessed via deviated, as opposed to multiple vertical or horizontal, wells, especially when communication between compartments is limited. Depending on the differences in burial depths, deviated wells can be used to penetrate these compartments. The inclination angle of the well is predetermined by the relative locations of compartments within a formation. Only the deltaic geocellular model clearly exhibited geologic features of a formation with limited communication between compartments, and thus was the only depositional environment considered for using deviated injection wells to enhance CO_2 storage efficiency. Table 39 presents four simulation scenarios conducted to evaluate the impact of deviated wells in a compartmentalized formation.

The blanket completions scenario involves completing the entire length of the deviated well. The high *k* intervals scenario involves completing the deviated well in the high permeability intervals only. In the low *k* intervals scenario, the deviated well is perforated in low permeability intervals only. In dynamic completions scenario, the deviated well is successively completed from the bottom to the top of the well for either all the high *k* or all the low *k* intervals, depending on whether the high *k* intervals or the low *k* intervals scenario has a greater E_V for that specific depositional environment.

Table 39 Simulation scenarios conducted to evaluate impact of selective and dynamic completions techniques on CO_2 storage efficiency for a deviated well.

Scenario Number	*Completions strategy*	*Comments*
1	Blanket completions	Perforate top to bottom of formation
2	High *k* intervals	Perforate high k_h intervals
3	Low *k* intervals	Perforate low k_h intervals
4	Dynamic completions	Successive completions

The E_V values for the blanket completions, high *k* intervals, and low *k* intervals scenarios were lower than that of the average baseline E_V of the deltaic model (Figure 183). The high *k* intervals scenario had a lower average E_v than the low *k* intervals scenario because low permeability portions of the formation are bypassed when CO_2 is injected through high permeability intervals (Figure 184); consequently, the dynamic completions simulation was conducted by successively perforating the deviated well at low *k* intervals. After CO_2 from injection into the bottom-most low *k* interval reached the upper and adjacent high *k* interval, the next overlying low *k* interval was completed.

The high E_v of the dynamic completions scenario in comparison to the other scenarios and the baseline E_V suggests that sequentially injecting at low permeability intervals, from bottom to top, is the most efficient completions strategy that can be adopted to maximize CO_2 storage efficiency in a compartmentalized formation. Figure 185 shows CO_2 plume distribution within a compartmentalized deltaic formation for Scenarios 3 and 4. The well is perforated in low *k* intervals. The CO_2 plume is more evenly distributed in dynamic completions scenario (Figure 185), which also confirms the results presented in Figure 183. Based on these results, the normalized E_v can be increased by about 6% (about 18% relative difference) using a deviated well with dynamic completions instead of using a vertical well in a compartmentalized deltaic formation.

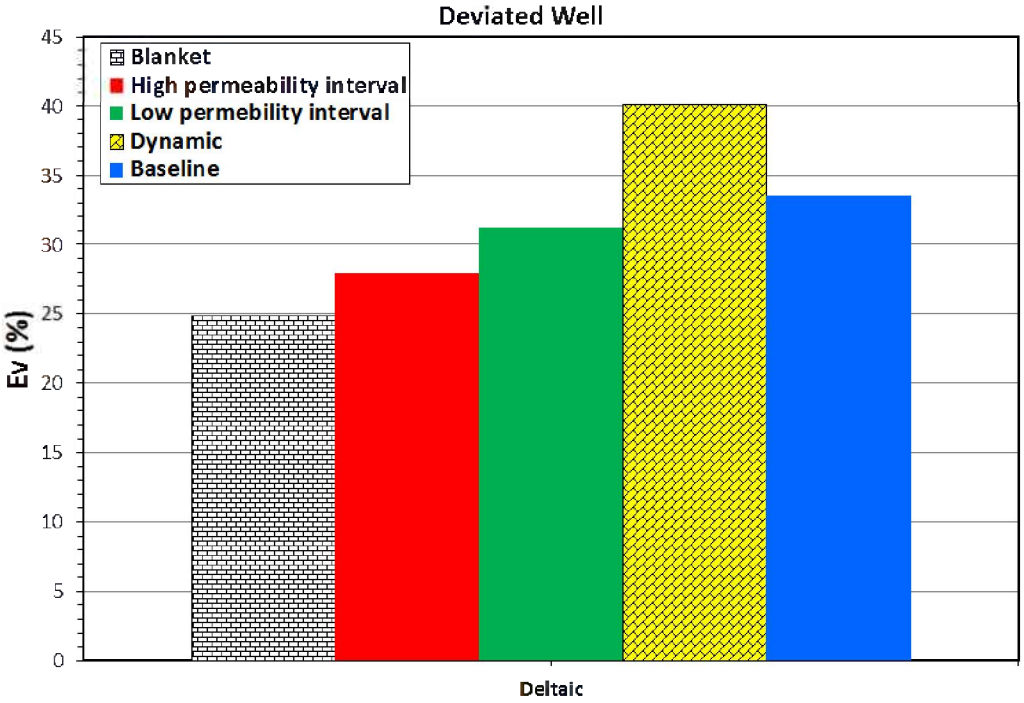

Figure 183 Selective completions scenarios of a compartmentalized deltaic reservoir model. Dynamic completions scenario (yellow) had the highest E_v. Baseline E_V is equivalent to the average E_V of five simulations with different vertical well locations.

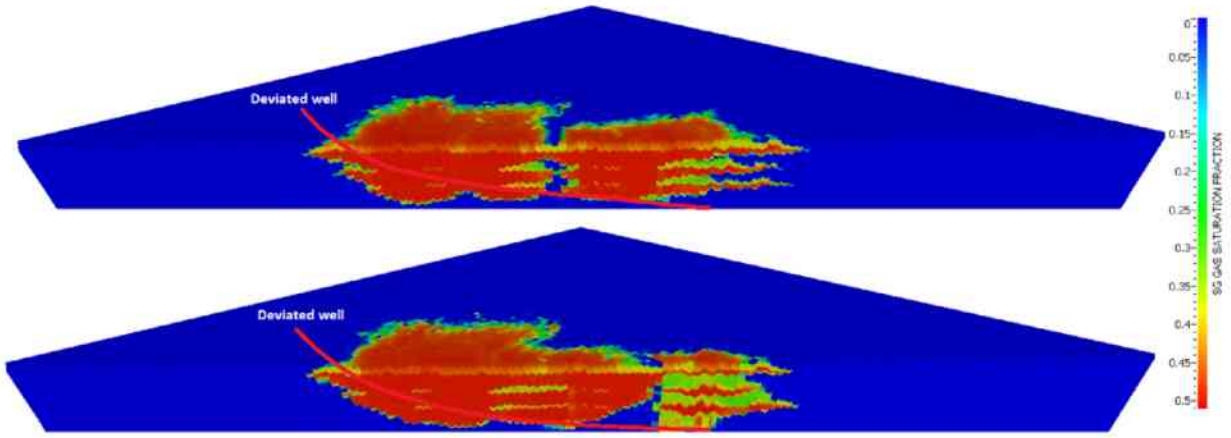

Figure 184 3-D cut-aways showing CO_2 plume distribution after *E* stabilizes (after 10 years of injection) for simulations in which the deviated well is perforated at high *k* intervals (top) and low *k* intervals (bottom) intervals. Warmer colors represent CO_2 saturations above zero. The E_V of the low *k* intervals simulation is greater than of the high *k* intervals simulation. Low permeability portions of the model's contacted pore volume are bypassed in the high *k* intervals simulation (top), which leads to a wider plume extent and lower sweep efficiency than in Scenario 3 (bottom).

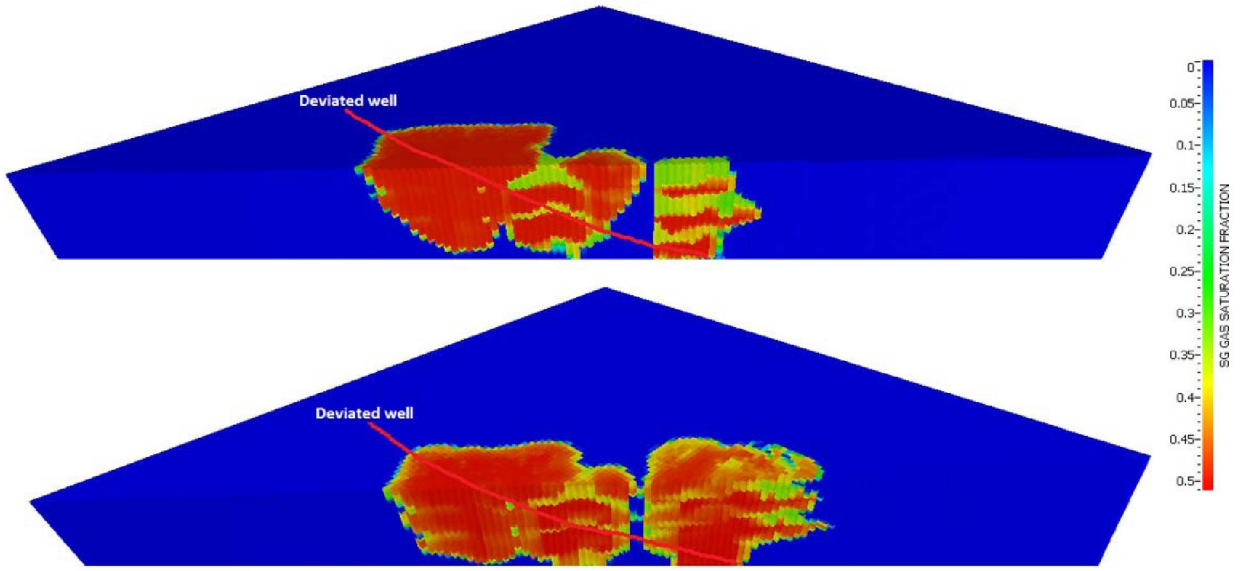

Figure 185 3-D cut-aways showing CO_2 plume distribution after *E* stabilizes (after 10 years of injection) for the low *k* intervals simulation (top) and dynamic completions simulation (bottom). Warmer colors represent CO_2 saturations above zero. The E_V of the dynamic completions simulation is greater than of the low *k* intervals simulation. The bypassed portions of the contacted pore volume around the center of the model are larger in the low *k* intervals simulation (top) than in the dynamic completions simulation.

Plume Management

Water Production (inverted five-spot)

A major challenge faced during CO_2 injection, especially in closed and semiclosed systems, is pressure buildup because of lack of connected pore space for displaced native brine to move (Frailey and Finley, 2011). Using peripheral wells to produce brine from the target formation increases the pore volume accessible for CO_2 storage.

Three scenarios (Table 40) consisting of an inverted five-spot well pattern with an injector at the center and four peripheral brine producers placed at distances equivalent to about one-third the width of the geocellular model. The P_{wf} of producers was constrained to 345 kPa (50 psi), which indicates that the wells were pumped i.e., very high water production rates. Two simulation scenarios involving water production with blanket completions (Scenario 1) and at the bottom interval of the model (Scenario 2) were conducted. These simulations were conducted to determine the better water production strategy between blanket completions and bottom completions by comparing their E_V values.

Table 40 Simulation scenarios conducted to evaluate effect of water production on *E*v.

Scenario	Completions strategy	System
1	Blanket completions	Open
2	Bottom completions	Open

The simulations were designed to shut in the producers once CO_2 breakthrough occurs, which are anticipated to occur at different times in a heterogeneous formation. Producers were shut in at CO_2 breakthrough to avoid CO_2 production. Figure 186 shows the water production well arrangement, which consists of a CO_2 injector with blanket completions (V1) surrounded by four peripheral producers (P1, P2, P3, and P4).
Figure 186 also shows plume extents and CO_2 saturation distribution over time in a deltaic model during a brine production for the blanket completions (top: left and right) and bottom completions scenarios (bottom: left and right). The plume size of blanket completions scenario is larger than that of bottom completions scenario. The average CO_2 saturation is higher for Scenario 2 (about 0.4 to 0.6) than Scenario 1 (about 0.3 to 0.5). Results in Figure 186 also show CO_2 to have breakthrough at all four producers (P1, P2, P3, and P4) in the blanket completions simulation as oppose to two producers (P2 and P3) in the bottom completions after seven years of injection which is supported by. Results in Figure 187 suggest that a higher E_V can be achieved by pumping brine from bottom completions than blanket completions in the deltaic model.

Figure 187 compares the E_V of eight depositional environments for blanket completions and bottom completions simulation scenarios to the normalized baseline E_V. The more efficient production well completions strategy between blanket completions and bottom completions for each depositional environment is presented in Table 41. The completions strategies were selected based on the relative difference between their E_V values and the normalized baseline E_V for each depositional environment. The completions strategy with the higher and nonzero relative difference was selected. No completions strategy was selected in cases where relative differences of both the blanket completions and bottom completions simulations are negative as

in the fluvial deltaic, strandplain, and reef models (Table 41). The following conclusions can be drawn from the results in Figure 187 and Table 41; (1) the E_V in shelf clastic and shelf carbonate (limestone) models can be increased by 10—25% using vertical production wells with blanket completions; (2) the E_V in deltaic, shelf carbonate (dolomite), fluvial and alluvial, and turbidite models can be increased by 2—20% using vertical production wells with bottom completions; and (3) the E_V values of the blanket completions and bottom completions simulations are lower than that of the normalized baseline E_V for fluvial deltaic, strandplain, and reef models.

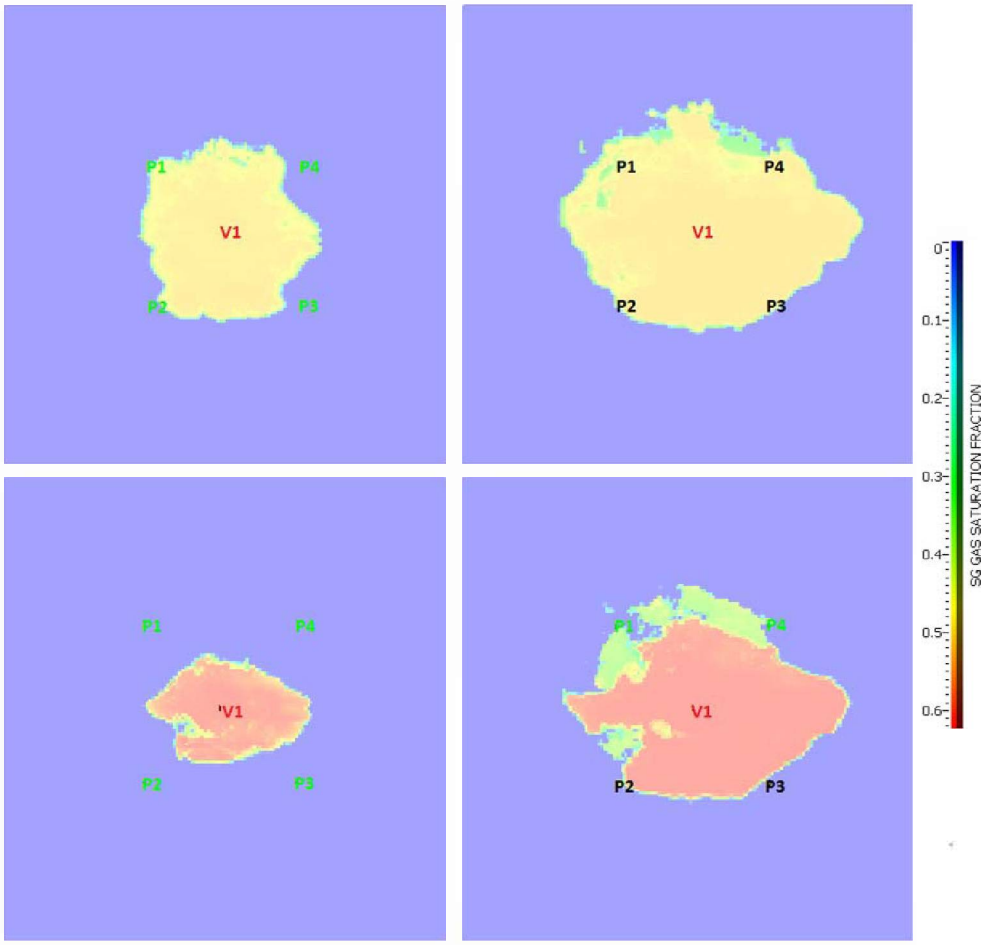

Figure 186 The CO_2 saturation distributions, production wells (P1–P4), and injection well (V1) over time for Scenario 1 (top: left and right images) and Scenario 2 (bottom: left and right images) using a deltaic model (top view). Plume distributions are all at layer 24 of 46. The images on the left are CO_2 saturation distributions before *E* stabilizes (after 3 years) and those on the right are CO_2 saturation distributions after *E* stabilizes (after 7 years). Red and green labels are active wells and black labels represent inactive producers. Warmer colors represent the CO_2 plume and cooler colors represent water-saturated portions of a formation.

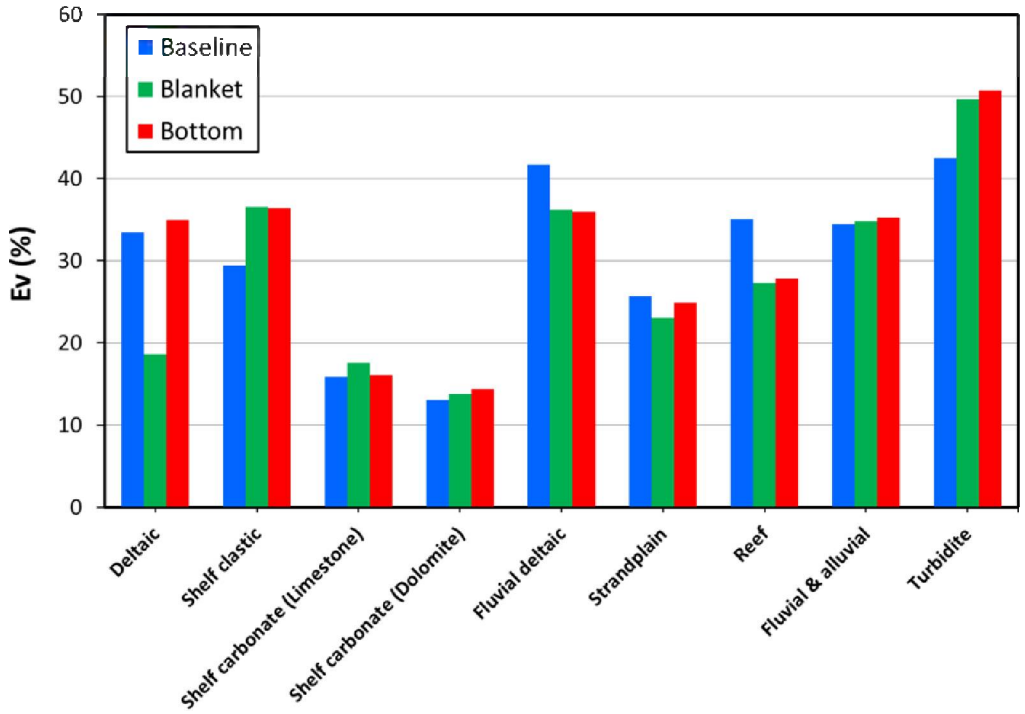

Figure 187 Comparison of the average E_v for each depositional environment of the blanket completions and bottom completions simulation scenarios to the average baseline (vertical well) E_V.

Table 41 Effective selective production well completions strategy by depositional environment for water production. None of the completions strategies were more efficient than the baseline E_V for the fluvial deltaic, strandplain, and reef models.

Depositional environment	Water production well completions strategy	% Relative difference
Deltaic	Bottom completions	4.4
Shelf clastic	Blanket completions	25
Shelf carbonate (limestone)	Blanket completions	11
Shelf carbonate (dolomite)	Bottom completions	10
Fluvial deltaic	None	—
Strandplain	None	—
Reef	None	—
Fluvial and alluvial	Bottom completions	2.4
Turbidite	Bottom completions	19

Multi-well Injection

A simple well pattern consisting of seven wells with similar arrangement to the water production scenarios described in the previous subsection was adopted. Figure 188 shows the well arrangements which consist of a CO_2 injection well with blanket completions (V1) surrounded

by four wells (P1, P2, P3, and P4) located one-third the model's width from V1. Wells P1, P2, P3, and P4 are also surrounded by four peripheral producers (P5, P6, P7, and P8) located two-thirds the model's width from V1.

Each simulation begins with CO_2 injection via V1 well with water production through wells P1, P2, P3, and P4 (top- left image in Figure 188). Wells P5, P6, P7, and P8 are initially inactive. When CO_2 breakthrough at P1, P2, P3, or P4 they are convert to injectors I1, I2, I3, or I4 and producers P5, P7, P8, or P6 are completed or activated (top-right and bottom-left images in Figure 188). Producers P1, P2, P3, and P4 are converted to injectors at CO_2 breakthrough to avoid production to the surface. The peripheral producers P5, P6, P7, or P8 are shut in when CO_2 breakthrough to avoid CO_2 production to the surface (bottom-right image in Figure 188).

Two scenarios of multi-well injection simulations were simulated for each depositional environment. One in which brine is produced using a vertical well with blanket completions (Scenario 1) and another with bottom completions (Scenario 2). Results of the blanket and bottom completions simulations were compared to the baseline E_V for each depositional environment (Figure 189).

The more efficient production well completions strategy between blanket completions and bottom completions for multi-well CO_2 injection by depositional environment is presented in Table 42. The completions strategies were selected based on the relative difference between their E_V values and the normalized baseline E_V. The completions strategy with the higher and nonzero relative difference was selected. No completions strategy was selected in cases where the relative differences of both the blanket completions and bottom completions simulations are negative as in the fluvial deltaic and strandplain models (Table 42). The following conclusions can be drawn from the results in Figure 187 and Table 42; (1) the E_V in deltaic, shelf carbonate (limestone and dolomite) and reef models can be increased by 20—60% using vertical production wells with blanket completions; (2) the E_V in shelf clastic, fluvial and alluvial, and turbidite models can be increased by 35—50% using vertical production wells with bottom completions; and (3) the E_V values of the blanket completions and bottom completions simulations are lower than that of the normalized baseline E_V for fluvial deltaic and strandplain models.

Figure 190 shows CO_2 saturation distribution of the blanket completions and bottom completions simulations (after storage efficiency stabilizes) in the shelf clastic model. The CO_2 saturation ranges are similar for both scenarios (about 0.30–0.45) but the plume of the bottom completions simulation is smaller than that of blanket completions simulation, which indicates that the bottom completions strategy is more efficient than the blanket completions strategy for the shelf clastic model; also in agreement with results in Figure 189 and Table 42.

Figure 191 shows the CO_2 saturation distribution of the blanket completions and bottom completions simulations in the reef model, after storage efficiency stabilizes. The CO_2 plume shapes of the blanket completions and bottom completions simulations rectangular and circular, respectively. The E_V of the blanket completions simulation (50%) is greater than that of the bottom completions simulation (34%). This is because a rectangle and square geometric shape (Eqs. 9b and 9c) better fit around the plume in the blanket completions simulation than the

bottom completions simulation. As a result, the average the efficiency, using all three methods for estimating V_p (Eqs. 9a, 9b, and 9c), in the blanket completions simulation is greater than that of the bottom completions simulation as shown in Figure 189.

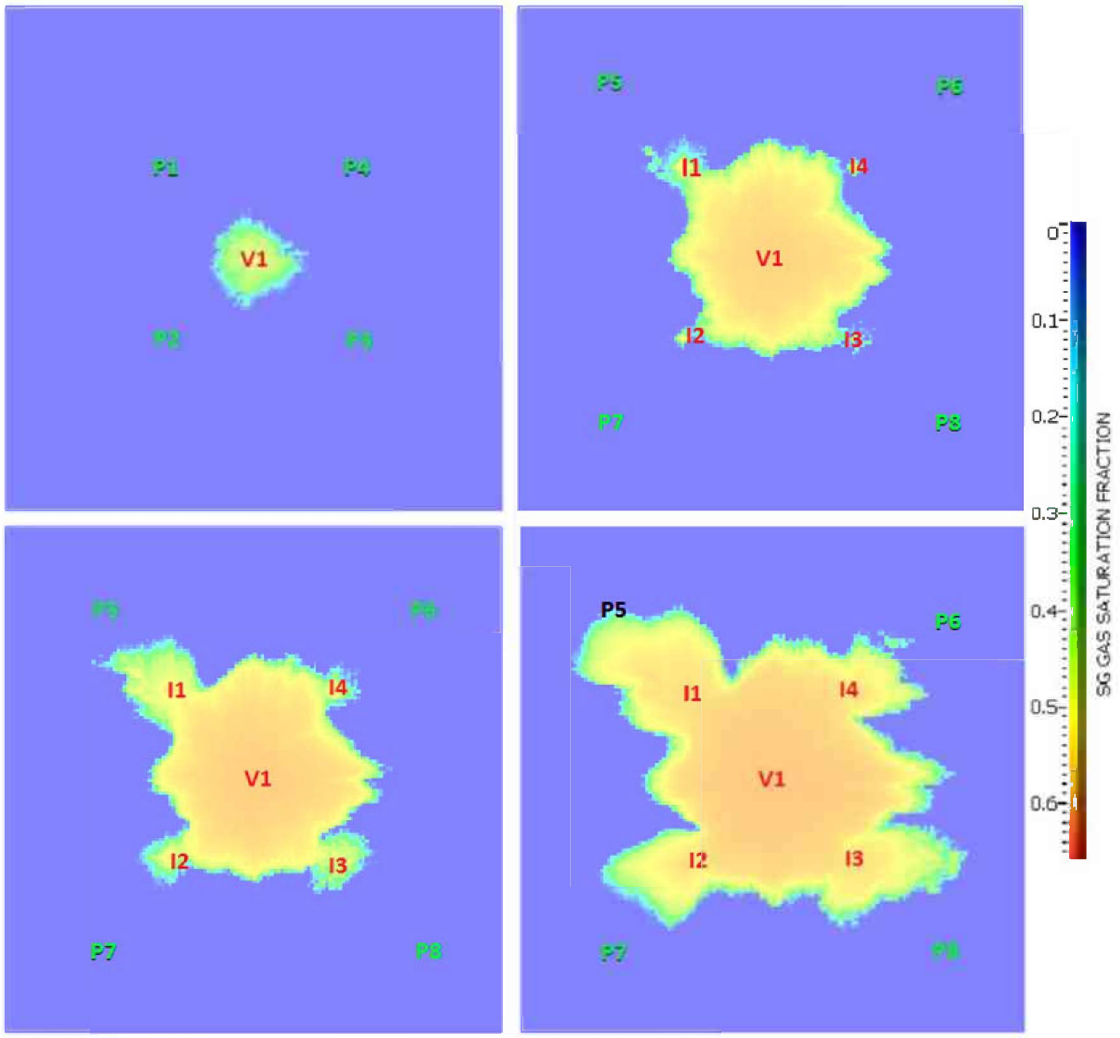

Figure 188 The CO_2 plume distribution during a multi-well injection scenario for a deltaic model (top view; layer 24 of 46). Warmer colors represent higher CO_2 saturations and cooler colors represent water-saturated portions of a formation. Red labels are active CO_2 injectors, green labels are active water producers, and the black label (bottom right image) represents a shut-in producer. At the beginning, CO_2 is injected via an injector at the center (V1), while brine is pumped from four surrounding producers (P1, P2, P3, and P4, top left). When CO_2 reaches the producers, they are converted to injectors (I1, I2, I3, and I4) and four additional peripheral producers become active (P5, P6, P7, and P8, top right). All nine wells are active before CO_2 reaches the peripheral producer (P5, bottom left), which is shut in when the CO_2 plume arrives at the well (bottom right).

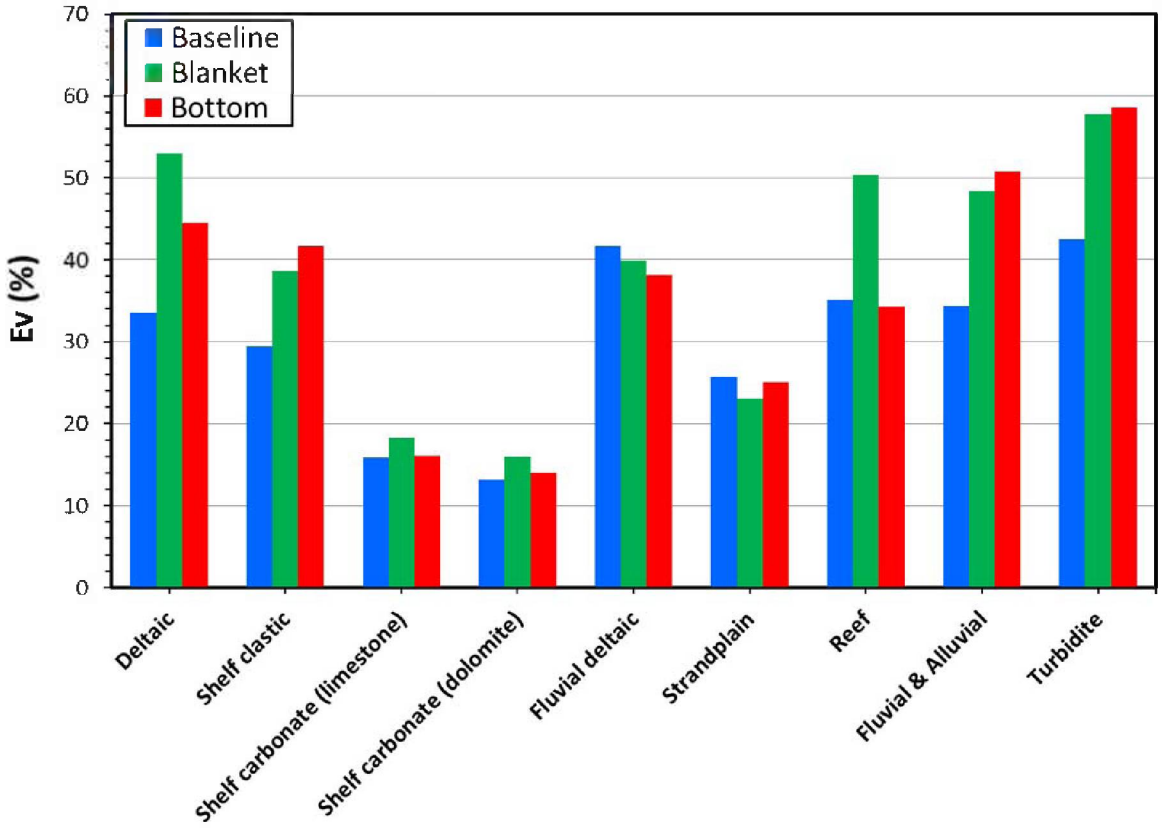

Figure 189 A comparison of multi-well injection to baseline simulation results by depositional environment.

Table 42 Effective production well completions strategy by depositional environment for multi-well CO_2 injection. None of the completions strategies were more efficient than the baseline E_V for the fluvial deltaic and strandplain models.

Depositional environment	Water production well completions strategy	% Relative difference
Deltaic	Blanket completions	58
Shelf clastic	Bottom completions	42
Shelf carbonate (limestone)	Blanket completions	15
Shelf carbonate (dolomite)	Blanket completions	22
Fluvial deltaic	None	—
Strandplain	None	—
Reef	Blanket completions	44
Fluvial and alluvial	Bottom completions	48
Turbidite	Bottom completions	38

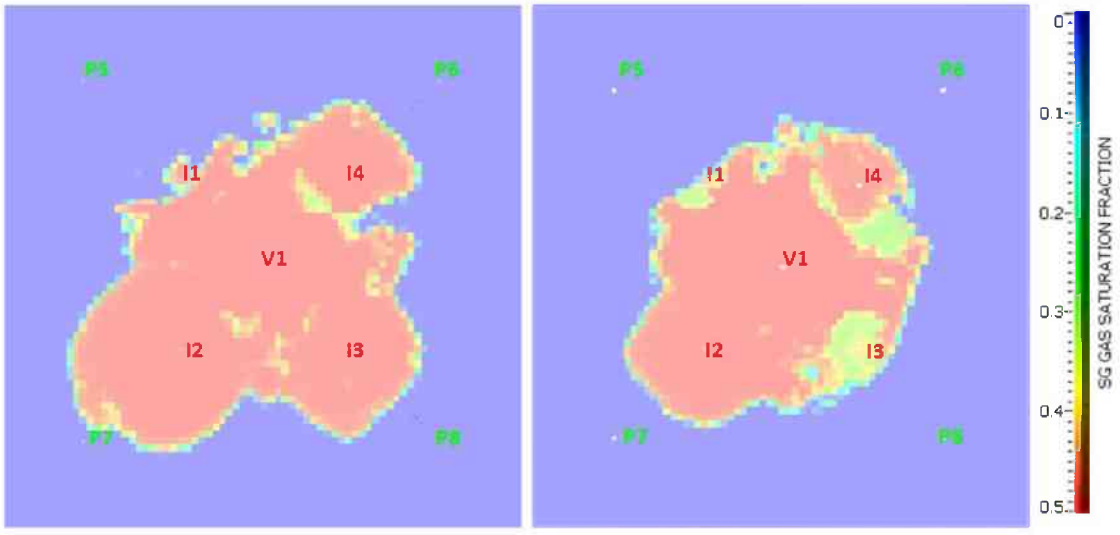

Figure 190 Top view of the CO_2 plume distributions, production wells (P5, P6, P7, and P8), and injection wells (V1, I1, I2, I3, and I4) for "blanket completions'' (left) and "bottom completions" (right) after E stabilizes for the shelf clastic model. Plume distributions are all at the same formation layer and depth. Red and green labels are active wells. Warmer colors represent the CO_2 plume and cooler colors represent water-saturated portions of a formation. The E_V of blanket completions simulation (39%) is less than that of the bottom completions simulation (42%).

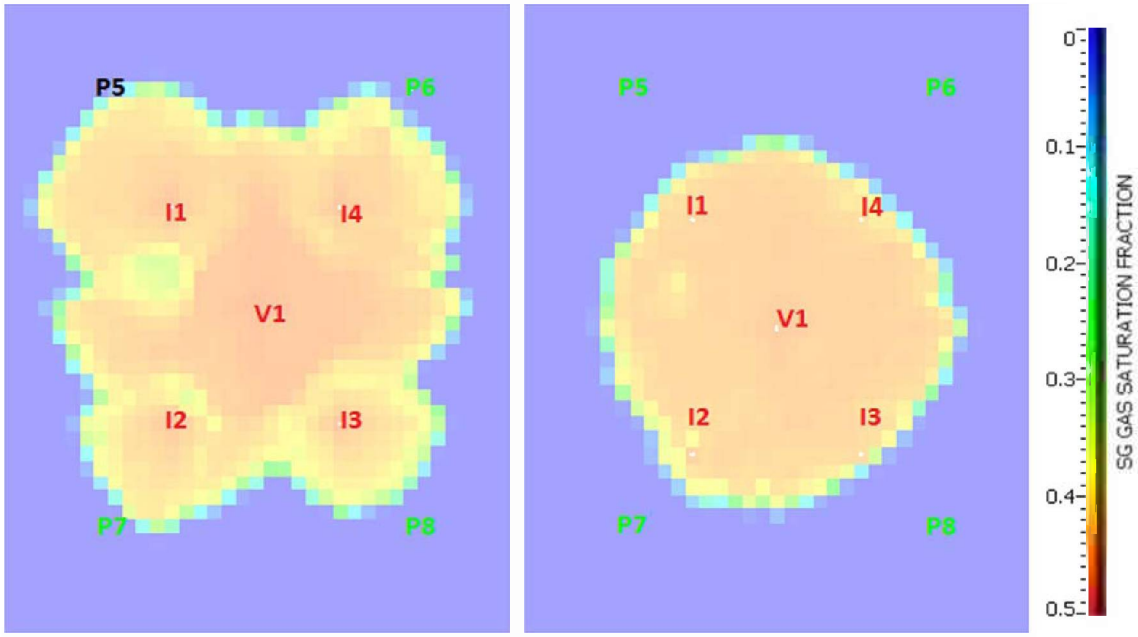

Figure 191 Top view of the CO_2 plume distributions, production wells (P5, P6, P7, and P8), and injection wells (V1, I1, I2, I3, and I4) for "blanket completions'' (left) and "bottom completions" (right) in the reef model. Plume distributions are all at the same formation layer and depth. Red and green labels are active wells and the black label represents a shut-in production well. Warmer colors represent the CO_2 plume and cooler colors represent water-saturated portions of a formation. The E_V of blanket completions simulation (50%) is greater than that of the bottom completions simulation (34%).

Discussion and Conclusions

The geologic characterization of eight Illinois Basin reservoirs was examined, taking into consideration the existing geologic and reservoir models. The result of this examination was a representative depositional model for each of the eight formation classes defined by DOE. Though these eight formation classes represent different depositional systems, the complexities and nuances of each class were noted. Specifically, ILB formations were matched to the dominant formation class; yet, the local geology of each reservoir exhibits strains of other depositional environments. While the geologic models were built around the representative environment, detailed studies of the reservoirs revealed that mixed depositional environments should be expected: a pure (end member) depositional environment is rare. Consequently, further studies based on these classes should take into consideration the context of the local geology, paying attention to the particular geologic forces at play. Based on the geologic characteristics identified here, each formation has a reservoir model that is used to predict the expected storage potential. The geological groundwork compiled in this report provides the basis for validating the reservoir models as reliable predictors of storage potential, and thus the corresponding storage potential expected in each of the DOE defined formation class.

Rankings of the depositional environments based on DOE identified CO_2 storage potential (NETL, 2010b) and baseline efficiencies (Table 34) are presented in Table 43. The depositional environments are ranked in decreasing order of storage potential and E_V. Figure 192 shows the baseline E_V ranges of each depositional environment. There is some overlap between the normalized baseline E_V ranges of the depositional environments except for shelf carbonate. The turbidite model has the highest baseline E_V but is classified as a medium storage potential depositional environment. On the other hand, the shelf carbonate is classified as a high storage potential depositional environment but it has the lowest baseline E_V. It can be concluded from the results in Table 43 that depositional environments of high storage potential do not necessarily have higher baseline E_V values than medium storage potential depositional environments or vice versa.

The baseline E_V can be enhanced by 20 — 40% using horizontal wells of optimum lengths ranging between 602 m (1974 ft) and 2,606 m (8,550 ft) (Table 36). The optimum well lengths vary from one depositional environment to another, and may vary between formations of similar depositional environment. As a result, conducting simulations to determine the optimum well length of candidate storage formations is recommended. A deviated well with dynamic completions at the lower permeability interval was used to enhance E_V in a compartmentalized deltaic formation by up to 18%. Figure 193 compares the storage efficiencies of the baseline, horizontal well, water production, and multi-well injection simulation scenarios for each depositional environment. No one injection strategy can maximize storage efficiency for all depositional environments.

The recommended completions strategy for each depositional environment is presented in Table 44. Some depositional environments have more than one recommended completions strategies because they are statistically equivalent. The horizontal well or multi-well injection (with water production via vertical wells with blanket completions) are the most efficient for all depositional systems, except fluvial deltaic in which vertical well with blanket completions is most efficient.

Table 43 Rankings of depositional environments according to the NETL (2010b) CO_2 storage potential and baseline efficiencies (vertical wells with blanket completions, average of five locations).

DOE Storage Potential[†]		Baseline scenarios		
Classification	***Depositional Environment***	***Rank***	***Depositional Environment***	***Normalized Baseline E_V (%)***
High potential	Deltaic	1	Turbidite	42.5
	Shelf clastic	2	Fluvial deltaic	41.7
	Shelf carbonate	3	Reef	35.1
	Strandplain	4	Fluvial and alluvial	34.4
	Reef	5	Deltaic	33.5
Medium potential	Fluvial deltaic	6	Shelf clastic	29.4
	Fluvial and alluvial	7	Strandplain	25.7
	Turbidite	8	Shelf carbonate	15.9/13.1[*]

[*] Shelf carbonate (limestone): 15.9% and shelf carbonate (dolomite): 13.1%.

[†] "The CO_2 storage classification is ranked in accordance to potential storage volume, which is controlled by the porosity and permeability of the reservoir material, frequency, and aerial extent of the different reservoir types." (NETL, 2010b).

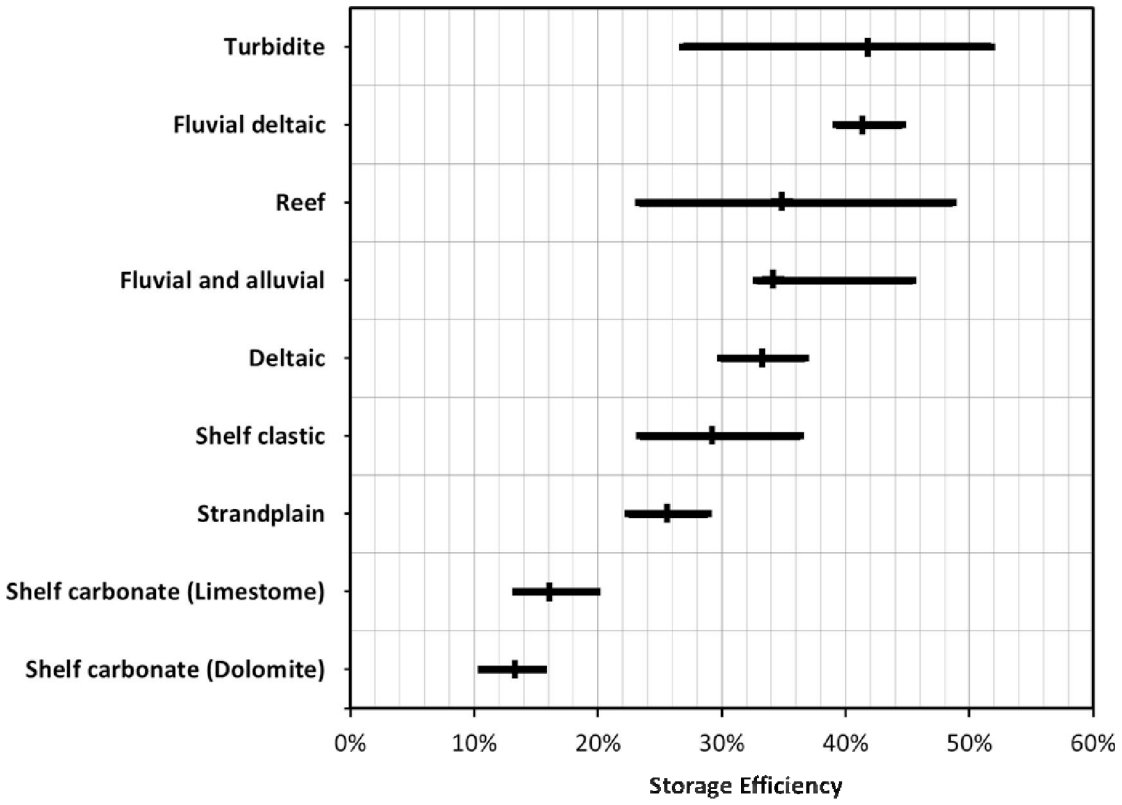

Figure 192 High and low with average normalized baseline E_V ranges of depositional environments arranged in descending order. Except for shelf carbonates, there is overlap between the E_V ranges of the depositional environments.

The lesson learned from simulation studies is that a single value or range of storage efficiencies cannot be applied to all depositional environments. Storage efficiency is strongly influenced by depositional environment and relative permeability, which was normalized using the average CO_2 saturation behind the plume front. The volumetric storage efficiency (normalized) ranges in Table 34 and Figure 192 can be used to estimate the storage efficiency of formations possessing different depositional environments. For example, the storage efficiency of a deltaic formation is equivalent to the product of the average CO_2 saturation within contacted formation pore volume and the average volumetric efficiency for the depositional environment (33.5%). The Geologic Storage Efficiency Calculator (GSECalc) tool provides estimates of the average CO_2 saturation from simulation data.

This study provides information that can be used to estimate the efficiency and storage capacity of geologic depositional environments, thus providing a means to assess formation, regional, and national CO_2 storage resource estimates, which is an integral component in the Carbon Utilization and Storage Atlas of the United States. Further study could consider the economic feasibility of the *E* enhancement strategies identified here.

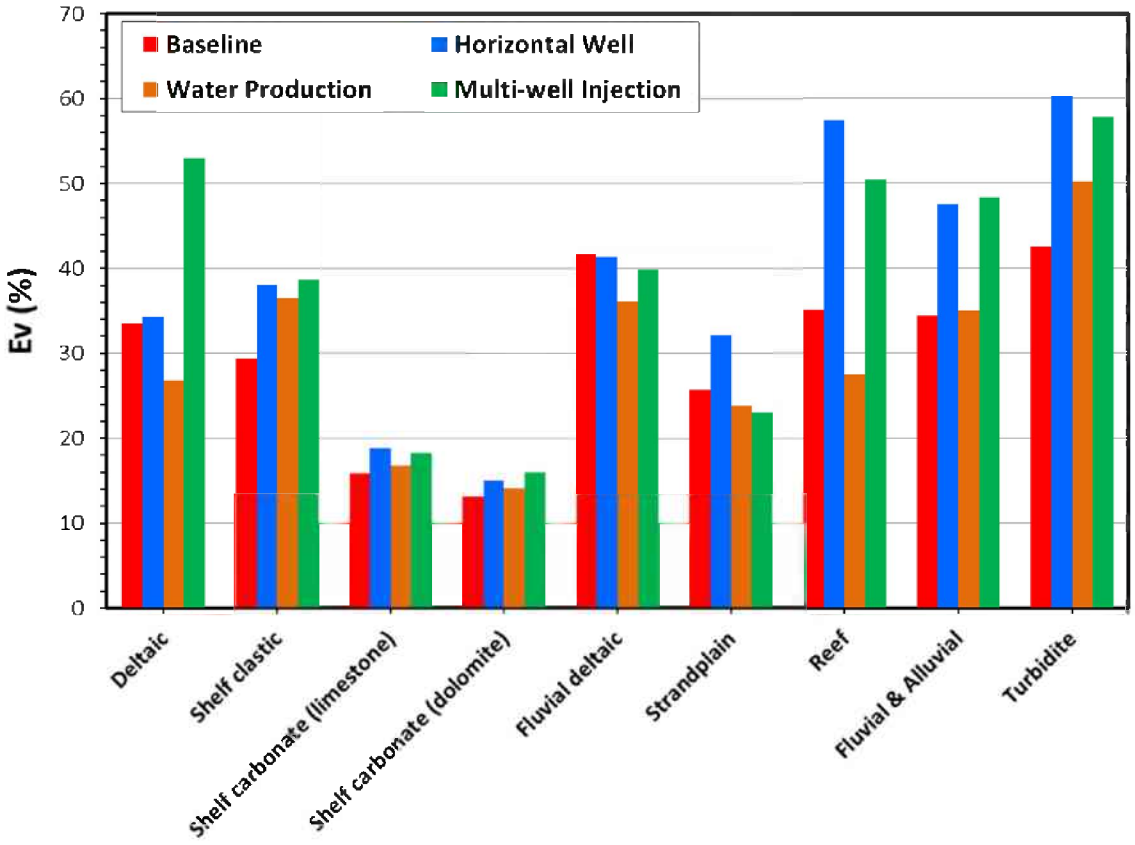

Figure 193 Comparison of E_V of different CO_2 injection strategies by depositional environment.

Table 44 Optimum CO_2 injection strategies by depositional environment. FD, multi-well injection; HW, horizontal well; VW, vertical well (baseline).

Depositional Environment	Lithology	Injection strategy
Deltaic	Sandstone	FD
Shelf clastic	Sandstone	FD/HW
Shelf carbonate	Limestone	HW/FD
	Dolomite	FD/HW
Fluvial deltaic	Sandstone	VW/HW/FD
Strandplain	Sandstone	HW
Reef	Limestone	HW
Fluvial and Alluvial	Sandstone	FD/HW
Turbidite	Sandstone	HW/FD

ACKNOWLEDGMENTS

This project (DE-FE0009612) is funded by the U.S. Department of Energy through the National Energy Technology Laboratory (NETL). Through a university grant program, Landmark Software (Nexus) was used for the reservoir and geologic modeling. As part of the university grant program, we acknowledge IHS for use of their Petra software.

REFERENCES

Adams, J. E. and M. L. Rhodes. 1960. "Dolomitization by Seepage Refluxion." *AAPG Bulletin* 44 (12): 1,912–1,921.

Ahmed, T. and P. D. McKinney. 2004. *Avanced Reservoir Engineering*. Burlington: Gulf Progessional Publishing.

Amaral, E. J. and W. A. Pryor. 1977. "Depositional Environment of the St. Peter Sandstone Deduced by Textural Analysis." *Journal of Sedimentary Research* 47 (1): 32–52.

Asquith, G. B. 1986. "Microporosity in the O'Hara Oolite Zone of the Mississippian Ste. Genevieve Limestone, Hopkins County, Kentucky, and its Implications for Formation Evaluation." *Carbonates and Evaporites* 1 (1): 7–12.

Bachu, S. 2013. "Drainage and Imbibition CO_2/Brine Relative Permeability Curves at in Situ Conditions for Sandstone Formations in Western Canada." *Energy Procedia* 37: 4,428–4,436. doi:10.1016/j.egypro.2013.07.001. http://linkinghub.elsevier.com/retrieve/pii/S1876610213010874

Baker, R. K. 1979. "The depositional environment of the Pennsylvanian upper Marchand sandstones, northern Caddo County, Oklahoma." In *Pennsylvanian sandstones of the Mid-Continent*, edited by N. J. Hyne, 195–219. Tulsa: Tulsa Geological Society.

Baker, S. E. and P. H. Carlisle. 1992. "Team Redevelopment a Success at Illinois' Tilden Reef Reservoir." *Oil and Gas Journal* 90: 82–88.

Bandy Jr., W. E. 1993. "Recognition on Wireline Logs and Mapping of Oolitic Facies in a Carbonate Sequence, Ste. Genevieve Limestone, Illinois Basin." In *Mississippian Oolites and Modern Analogs*, edited by B. D. Keith and C. W. Zuppann. Studies in Geology 35, 61–72. Tulsa: AAPG.

Barrows, M. H. and R. M. Cluff. 1984. "New Albany Shale Group (Devonian-Mississippian) Source Rocks and Hydrocarbon Generation in the Illinois Basin." In *Petroleum geochemistry and Basin Evaluation*, edited by G. Demaison and R. J. Murris. Memoir 35, 111–138. Tulsa: AAPG.

Bebout, D. G., W. A. White, C.M. Garrett, Jr., and T. F. Hentz, editors. 1992. *Atlas of Major Central and Eastern Gulf Coast Gas Reservoirs*. Austin: Bureau of Economic Geology.

Bebout, D. G., W. A. White, T. F. Hentz, and M. K. Grasmick, editors. 1993. *Atlas of Major Midcontinent Gas Reservoirs*. Austin: Bureau of Economic Geology.

Becker, L. E. 1974. *Silurian and Devonian Rocks in Indiana Southwest of the Cincinnati Arch*. Bulletin 50. Bloomington: Indiana Geological Survey.

Bell, A. H., E. Atherton, T. C. Buschbach, and D. H. Swann. 1964. *Deep Oil Possibilities of the Illinois Basin*. Circular 368. Champaign: Illinois State Geological Survey.

Bennion, D. B., and S. Bachu. 2008. "Drainage and Imbibition Relative Permeability Relationships for Supercritical CO_2/Brine and H_2S/Brine Systems in Intergranular Sandstone, Carbonate, Shale, and Anhydrite Rocks." *SPE Reservoir Evaluation & Engineering* (June): 487–496.

Bennion, D. B., and S. Bachu. 2010. "Drainage and Imbibition CO_2/Brine Relative Permeability Curves at Reservoir Conditions for Carbonate Formations." SPE 134028 presented at the SPE Annual Technical Conferences and Exhibition, Florence, Italy, September 9–22.

Bhattacharya, J. P. 2006. "Deltas." In *Facies Models Revisited* edited by H. W. Posamentier and R. G. Walker, 237–292. Tulsa: SEPM (Society for Sedimentary Geology).

Bird, K. J. 1998. "Northern Alaska Province (001)." *1995 National Assessment of United States Oil and Gas Resources—Results, Methodology, and Supporting Data*. U.S. Geological Survey Digital Data Series DDS-30, Release 2, one CD-ROM.

Blatchley, R. S. 1913. *The Oil Fields of Crawford and Lawrence Counties*. Bulletin 22. Champaign: Illinois State Geological Survey.

Bouma, A. H. 2000. "Fine-grained, Mud-rich Turbidite Systems: Model and Comparison with Coarse-grained, Sand-rich Systems." In *Fine-grained turbidite systems* edited by A. H. Bouma and C. G. Stone, 9–20. Tulsa: AAPG.

Bouma, A. H, P. Kuenen, and F. Shepard. 1962. *Sedimentology of some Flysch Deposits: A Graphic Approach to Facies Interpretation*. Amsterdam: Elsevier Publishing Company.

Boyd, R., R. Dalrymple, and B. A. Zaitlin. 1992. "Classification of Clastic Coastal Depositional Environments." *Sedimentary Geology* 80 (3–4): 139–150.

Boyd, R., R. Dalrymple, and B. Zaitlin. 2006. "Estuarine and incised-valley facies models." In *Facies Models Revisited* edited by H.W. Posamentier and R.G. Walker, 171–235. Tulsa SEPM (Society for Sedimentary Geology).

Bristol, H. M. 1974. *Silurian Pinnacle Reefs and Related Oil Production in Southern Illinois*. Illinois Petroleum 102. Champaign: Illinois State Geological Survey.

Burnside, N.M., and M. Naylor. 2014. "Review and Implications of Relative Permeability of CO_2/brine Systems and Residual Trapping of CO_2." *International Journal of Greenhouse Gas Control* 23 (April): 1–11. doi:10.1016/j.ijggc.2014.01.013.

Busch, D. A. 1974. *Stratigraphic traps in sandstones—exploration techniques*. Memoir 21. Tulsa: AAPG.

Buschbach, T. C. and D. C. Bond. 1974. *Underground Storage of Natural Gas in Illinois*. Illinois Petroleum 101. Champaign: Illinois State Geological Survey.

Buschbach, T. C. and D. R. Kolata. 1991. "Regional Setting of Illinois Basin." In *Interior Cratonic Basins*, edited by M. W. Leighton, D. R. Kolata, D. F. Olts and J. J. Eidel. Memoir 51, 29–55. Tulsa: AAPG.

Cardwell, W. T. and R. L. Parsons. 1945. "Average permeability of heterogeneous oil sands." *Trans* of AIME 160: 34–42.

Carter, R. D., and G. W. Tracy. 1960. "An Improved Method for Calculating Water Influx." *Trans. of AIME* 219: 415–417.

Cataconsinos, P. A., P. A. Daniels Jr., and W. B. Harrison III. 1991. "Structure, Stratigraphy, and Petroleum Geology of the Michigan Basin." In *Interior Cratonic Basins*, edited by M. W. Leighton, D. R. Kolata, D. F. Oltz and J. J. Eidel. Memoir 51, 561–601. Tulsa: AAPG.

Cazee, J. T. 2000. *Petroleum Exploration, Development, and Production in Indiana during 1999*. Mineral Economics Series 46. Bloomington: Indiana Geological Survey.

Charpentier, R. R. 1995. "Forest City Basin Province (056)." In *1995 National Assessment of United States Oil and Gas Resources—Results, Methodology, and Supporting Data*, edited by D. L. Gautier, G. L. Dolton, K. I. Takahashi, and K. L. Varnes. U.S. Geological Survey Digital Data Series DDS-30, Release 2, one CD-ROM.

Choquette, P. W. and R. P. Steinen. 1985. "Mississippian Oolite and Non-Supratidal Dolomite Reservoirs in the Ste. Genevieve Formation, North Bridgeport Field, Illinois Basin." In *Carbonate Petroleum Reservoirs*, edited by P. O. Roehl and P. W. Choquette, 207–225. New York: Springer-Verlag New York, Inc.

Clark, M. S., J. D. Melvin, R. K. Prather, and A. W. Marino. 1999. "Characterization of the Distal Margin of a Slope-Basin (Class-III) Reservoir, ARCO-DOE Slant Well Project, Yowlumne Field, California." In *Reservoir Characterization Recent Advances*, edited by R. Schatzinger and J. Jordan. Memoir 71, 21–28. Tulsa: AAPG.

Clifton, H. E. 1982. "Estuarine Deposits." In *Sandstone Depositional Environments* edited by P. A. Scholle, and D. Spearing. AAPG: 179–189.

Cluff, R. M. 1986. "Application of Modern Carbonate Sand Models to Oil and Gas Exploration, Mississippian Ste. Genevieve Limestone, Illinois Basin." In *Aux Vases and Ste. Genevieve Formations: A Core Workshop and Field Trip Guidebook*, edited by B. Seyler, 5–7: Illinois Geological Society; Illinois State Geological Survey; Southern Illinois University-Carbondale.

Cluff, R. M. and Z. Lasemi. 1980. *Paleochannel Across Louden Anticline, Fayette County, Illinois*. Illinois Petroleum 119. Champaign: Illinois State Geological Survey.

Cluff, R. M. and J. A. Lineback. 1981. "Middle Mississippian Carbonates of the Illinois Basin." Mt. Vernon, Illinois, Illinois Geological Society, April 23–24.

Cluff, R. M., M. L. Reinbold, and J. A. Lineback. 1981. *The New Albany Shale Group of Illinois*. Circular 518. Champaign: Illinois State Geological Survey.

Cole, R. D. and W. J. Nelson. 1995. *Stratigraphic Framework and Environments of Deposition of the Cypress Formation in the Outcrop Belt of Southern Illinois*. Illinois Petroleum 149. Champaign: Illinois State Geological Survey.

Collinson, C. 1967. "Devonian of the North-Central Region, United States." In *International Symposium on the Devonian System*. Reprint 1968-G, 933–971. Champaign: Illinois State Geological Survey.

Corey, A. T.1954. The Interrelation between Gas and Oil Relative Permeabilities, *Producers Monthly* (November): 38–41.

Coueslan, M. L., V. Smith, G. El-Kaseeh, J. Gilbert, N. Preece, L. Zhang, and J. Gulati. 2014. "Development and Implementation of a Seismic Characterization and CO_2 Monitoring Program for the Illinois Basin–Decatur Project." *Greenhouse Gas Science Technology* 4:626–644. doi: 10.1002/ghg

Craft, B. C. and M. F. Hawkins. 1991. *Applied reservoir engineering*. Second Edition, revised by Ronald E. Terry. Englewood Cliffs: Prentice Hall.

Dake, L.P. 1978. *Fundamentals of reservoir engineering*. Development in Petroleum Science, volume 8. Amsterdam: Elsevier.

Dalrymple, R. W. 1999. "Tide-dominated Deltas; Do They Exist or Are They All Estuaries?" In Annual Meeting Expanded Abstracts. AAPG: A29–A30.

Dalrymple, R. W., B. A. Zaitlin, and R. Boyd. 1992. Estuarine Facies Models: Conceptual Basis and Stratigraphic Implications. *Journal of Sedimentary Petrology* (62): 1,130–1,146.

Dapples, E. C. 1955. "General Lithofacies Relationships of St. Peter Sandstone and Simpson Group." *AAPG Bulletin* 39 (4): 444–467.

Darcy, H. 1856. Les Fontaines Publiques de la Ville de Dijon, Dalmont, Paris.

Davis, H. G. 1991. "Pre-Mississippian Hydrocarbon Potential of the Illinois Basin." In *Interior Cratonic Basins*, edited by M. W. Leighton, D. R. Kolata, D. F. Oltz and J. J. Eidel. Memoir 51. Tulsa: AAPG.

Devera, J. A. and G. H. Fraunfelter. 1988. "Middle Devonian Paleogeography and Tectonic Relationships East of the Ozark Dome, Southeastern Missouri, Southwestern Illinois and Parts of Southwestern Indiana and Western Kentucky." In *Devonian of the World*, edited by N. J. McMillan, A. F. Embry and D. J. Glass. Memoir 14, II, 181–196: Canadian Society of Petroleum Geologists.

Devera, J. A. and N. R. Hasenmueller. 1991. "Kaskaskia Sequence, Middle and Upper Devonian Series through Mississippian Kinderhookian Series." In *Interior Cratonic Basins*, edited by M. W. Leighton, D. R. Kolata, D. F. Olts and J. J. Eidel. Memoir 51, 113–123. Tulsa: AAPG.

Devera, J. A., W. J. Nelson, and R. D. Norby. 2011. "Middle Devonian Series through Mississippian System (Kaskaskia Sequence)." In *Geology of Illinois*, edited by D. R. Kolata and C. K. Nimz, 167–186. Champaign: Illinois State Geological Survey.

Dolton, G. L. 1995. "Michigan Basin Province (063)." In *1995 National Assessment of United States Oil and Gas Resources—Results, Methodology, and Supporting Data*, edited by D. L. Gautier, G. L. Dolton, K. I. Takahashi, and K. L. Varnes. U.S. Geological Survey Digital Data Series DDS-30, Release 2, one CD-ROM.

Dott Jr., R. H., C. W. Byers, G. W. Fielder, S. R. Stenzel, and K. E. Winfree. 1986. "Aeolian to Marine Transition in Cambro-Ordovician Cratonic Sheet Sandstones of Northern Mississippi Valley." *Sedimentology* 33 (3): 345–367.

Droste, J. B. and R. H. Shaver. 1985. "Comparative Stratigraphic Framework for Silurian Reefs-Michigan Basin to Surrounding Platforms." In *Ordovician and Silurian Rocks of the Michigan Basin and its Margins*, edited by K. R. Cercpne and J. M. Budai. Special Paper 4, 73–93. East Lansing: Michigan Basin Geological Society.

Droste, J. B. and R. H. Shaver. 1975. "Jeffersonville Limestone (Middle Devonian) of Indiana: Stratigraphy, Sedimentation, and Relation to Silurian Reef-Bearing Rocks." *AAPG Bulletin* 59: 393–412.

Droste, J. B. and R. H. Shaver. 1980. "Recognition of Buried Silurian Reefs in Southwestern Indiana: Application to the Terre Haute Bank." *Journal of Geology* 88 (5): 567–587.

Droste, J. B. and R. H. Shaver. 1987. *Upper Silurian and Lower Devonian Stratigraphy of the Central Illinois Basin.* Special Report 39. Bloomington: Indiana Geological Survey.

Droste, J. B., R. H. Shaver, and J. D. Lazor. 1975. "Middle Devonian Paleogeography of the Wabash Platform, Indiana, Illinois, and Ohio." *Geology* 3 (5): 269–272.

Elliot, L. A., and J. K. Warren. 1989. Stratigraphy and depositional environment of lower San Andres Formation in subsurface and equivalent outcrops: Chaves, Lincoln, and Roosevelt Counties, New Mexico. *American Association of Petroleum Geologists Bulletin* 73 (11): 1,307–1,325.

Fetkovitch, M. J. 1971. "A Simplified Approach to Water Influx Calculations-Finite Aquifer Systems." *J.Pet. Tech.*: 814–828.

Fisher, D. J. 1930. "Western Lawrence County Oil Field." Unpublished Manuscript, Illinois State Geological Survey, Champaign.

Flügel, E. 2010. *Microfacies of Carbonate Rocks: Analysis, Interpretation, and Application.* Berlin: Springer-Verlag.

Frailey, S. M., and R. J. Finley. 2011. "CO_2 plume management in saline reservoir sequestration." *Energy Procedia* 4: 4238–4245. doi: 10.1016/j.egypro.2011.02.372.

Frailey, S. M., I. G. Krapac, J. R. Damico, R. T. Okwen, and R. W. McKaskle. 2012a. CO_2 Storage and Enhanced Oil Recovery: Bald Unit Test Site, Mumford Hills Oil Field, Posey County, Indiana. J.H. Goodwin and C.C. Monson (Eds.). Illinois State Geological Survey, Open File Series 2012-5, 172 pp.

Frailey, S. M., T. M. Parris, J. R. Damico, R. T. Okwen, and R. W. McKaskle. 2012b. CO_2 Storage and Enhanced Oil Recovery: Sugar Creek Oil Field Test Site, Hopkins County, Kentucky. C.C. Monson and J.H. Goodwin (Eds.). Illinois State Geological Survey, Open File Series 2012-4, 234 pp.

Freiburg, J. T., D. G. Morse, H. E. Leetaru, R. P. Hoss, and Q. Yan. 2014. A Depositional and Diagenetic Characterization of the Mt. Simon Sandstone at the Illinois Basin - Decatur Project Carbon Capture and Storage Site, Decatur, Illinois, USA. Circular 583. Champaign: Illinois State Geological Survey.

Galloway, W. E. 1968. Depositional systems of the lower Wilcox Group, north-central Gulf Coast Basin. *Gulf Coast Association of Geological Societies Transactions* 18: 275–289.

Gautier, D. L., G.L. Dolton, K. I. Takahashi, and K. L. Varnes, eds. 1995. *1995 National Assessment of United States Oil and Gas Resources—Results, Methodology, and Supporting Data.* U.S. Geological Survey Digital Data Series DDS-30.

Gibson, A. C. 2001. "Three-Dimensional Geometries and Porosity Trends of Subsurface Ooid Shoal Hydrocarbon Reservoirs in the Mississippian Ste. Genevieve Formation of the Illinois Basin, USA." MS thesis, University of Illinois at Urbana-Champaign.

Gill, D. 1985. "Depositional Facies of Middle Silurian (Niagaran) Pinnacle Reefs, Belle River Mills Gas Field, Michigan Basin, Southeastern Michigan." In *Carbonate Petroleum Reservoirs*, edited by P. O. Roehl and P. W. Choquette, 121–139. New York: Springer-Verlag.

Goodman, A., A. Hakala, G. Bromhal, D. Deel, T. Rodosta, S. Frailey, M. Small, D. Allen, V. Romanov, J. Fazio, N. Huerta, D. McIntyre, B. Kutchko, and G. Guthrie. 2011. "U.S. DOE methodology for the development of geologic storage potential for carbon dioxide at the national and regional scale." *International Journal of Greenhouse Gas Control* 5 (4): 952–965.

Grammer, G. M. 2013. *An Integrated Approach to Characterization and Modeling of Carbonate Reservoirs*. AAPG Search and Discovery Article #50784.

Greb, S. F., R. T. Hendricks, and D. R. Chesnut Jr. 1993. *Fossil Beds of the Falls of the Ohio*. Special Publication 19. Series 11. Lexington: Kentucky Geological Survey.

Grube, J. 1992. *Reservoir Characterization and Improved Oil Recovery from Multiple Bar Sandstones, Cypress Formation, Tamaroa and Tamaroa South Fields, Perry County, Illinois*. Illinois Petroleum 138. Champaign: Illinois State Geological Survey.

Grube, J, and W. T. Frankie. 1999. *Reservoir Characterization and its Application to Improved Oil Recovery from the Cypress Formation (Mississippian) at Richview Field, Washington County, Illinois*. Illinois Petroleum 155. Champaign: Illinois State Geological Survey.

Hardie, L. A. 1987. "Dolomitization: A Critical View of some Current Views." *Journal of Sedimentary Petrology* 57 (1): 166–183.

Helpingstine, D., D. Williams, P. Caserotte, and S. Gustison. 2001. "Small-Scale 3-D Seismic Shoot Adds New Oil Reserves." *World Oil* September 2001: 94–95.

Huff, B. 1985. Stratigraphy and Depositional History of the Pennsylvanian Sequence Exposed at the Cagles Mill Spillway, Putnam County, Indiana. *Transactions of the Illinois Academy of Sciences* 78 (1 and 2): 33–48.

Huff, B. G. and B. Seyler. 2010. "Oil and Gas Geology." In *Geology of Illinois*, edited by D. R. Kolata and C. K. Nimz, 283–298. Champaign: Illinois State Geological Survey.

Hunter, R. E. 1993. "An Eolian Facies in the Ste. Genevieve Limestone of Southern Indiana." In *Mississippian Oolites and Modern Analogs*, edited by B. D. Keith and C. W. Zuppann. Vol. 35, 31–48. Tulsa: AAPG.

Hutchinson Jr., C. A. 1959. "Reservoir inhomogeneity assessment and control." *Pet. Eng.* (Sept.): B19–26.

International Energy Agency Greenhouse Gas R&D Programme (IEAGHG). 2009. *Development of storage coefficients for CO_2 storage in deep saline formations*. Report no. 2009/13.

James, N. P. 1983. "Reef Environment." In *Carbonate Depositional Environment*, edited by P. A. Scholle, D. G. Bebout and C. H. Moore. Vol. Memoir 33, 345–440. Tulsa: AAPG.

Jarvis, A., H. I. Reuter, A. Nelson, and E. Guevara. 2008. Hole-filled SRTM for the globe, version 4: available from the Consultative Group for International Agricultural Research-Consortium for Spatial Information SRTM 90m Database. http://srtm.csi.cgiar.org/

Jennings, Jr., J. W., and F. J. Lucia. 2003. "Predicting Permeability from Well Logs in Carbonates with a Link to Geology for Interwell Permeability Mapping." *SPE Reservoir Evaluation and Engineering* 6 (4): 215–225.

Joshi, S. D. 1991. *Horizontal Well Technology*. Tulsa: PennWell Books.

Krevor, S. C. M., R. Pini, L. Zuo, and S. M. Benson. 2012. "Relative permeability and trapping of CO_2 and water in sandstone rocks at reservoir conditions." *Water Resource Research* 48:W02532. doi.org/10.1029/2011WR010859.

Landrum, B. L., and P. B. Crawford. 1960. "Effect of directional permeability of sweep efficiency and production capacity." *Trans. of AIME* 219: 407–411.

Lasemi, Y., B. Seyler, Z. Lasemi, and Z. A. Khorasgani. 2010. *Sedimentology and Reservoir Characterization of the Silurian Deposits in the Mt. Auburn Trend of the Sangamon Arch, West-Central Illinois*. Circular 577. Champaign: Illinois State Geological Survey.

Lasemi, Y., D. Jahani, H. Amin-Rasouli, Z. Lasemi. 2012. Ancient Carbonate Tidalites. In *Principles of Tidal Sedimentology* edited by R. A. Davis and R. W. Dalrymple. Springer Science: 567–607.

Lasemi, Z. 2001. *Devonian and Mississippian Rocks: Stratigraphy and Depositional History*. Three-Dimensional Geologic mapping—A Pilot Program for Resource and Environmental Assessment in the Villa Grove Quadrangle, Douglas County, Illinois, edited by Z. Lasemi, R. C. Berg. Bulletin 106. Champaign: Illinois State Geological Survey.

Lasemi, Z., M. R. Boardman, and P. A. Sandberg. 1989. "Cement Origin of Supratidal Dolomite, Andros Island, Bahamas." *Journal of Sedimentary Petrology* 89 (2): 249–257.

Leetaru, H. 1996. *Reservoir Characteristics and Oil Production in the Cypress and Aux Vases Formations at Storms Consolidated Field in White County, Illinois*. Illinois Petroleum 150. Champaign: Illinois State Geological Survey.

Leetaru, H. E. and J. H. McBride. 2009. "Reservoir Uncertainty, Precambrian Topography, and Carbon Sequestration in the Mt. Simon Sandstone, Illinois Basin." *Environmental Geosciences* 16 (4): 235–243.

Leetaru, H. E. 2000. "Sequence Stratigraphy of the Aux Vases Sandstone: A major Oil Producer in the Illinois Basin. *AAPG Bulletin* 84 (3): 399–422.

Leonard, K. W. 1996. "Sequence Stratigraphy of the Lower Part of the Muscatatuck Group (Middle Devonian) in Southeastern Indiana." In *Paleozoic Sequence Stratigraphy—Views from the North American Craton*, edited by B. J. Witzke, G. A. Ludvigson and J. Day. Vol. Special Paper 306, 243–257. Boulder: Geological Society of America.

Lineback, J. A. 1966. *Deep-Water Sediments Adjacent to the Borden Siltstone (Mississippian) Delta in Southern Illinois*. Circular 401. Champaign: Illinois State Geological Survey.

Lineback, J. A. 1968. *Turbidites and Other Sandstone Bodies in the Borden Siltstone (Mississippian) in Illinois*. Circular 425. Champaign: Illinois State Geological Survey.

Long, D. G. F. 1978. Proterozoic Stream Deposits: Some Problems of Recognition and Interpretation of Ancient Sandy Fluvial Systems. In *Fluvial Sedimentology,* edited by A. D. Miall. 313–341. Canadian Society of Petroleum Geologist.

Lowenstam, H. A. 1946. *Marine Pool, Madison County, a New Type of Oil Reservoir in Illinois*. Report of Investigation 114. Champaign: Illinois State Geological Survey.

Lowenstam, H. A. 1949. *Niagaran Reefs in Illinois and their Relation to Oil Accumulation*. Report of Investigation 145. Champaign: Illinois State Geological Survey.

Lucia, F.J., 1999, *Carbonate Reservoir Characterization*. Springer-Verlag: Berlin.

Lumm, D. K. 1998. Subsurface Geometry and Petrography of Rock Units between the Beech Creek ("Barlow") Limestone (Pope Group) and the Springfield Coal (Carbondale Formation) across Part of the LaSalle Anticlinorium, Lawrence County, Illinois Vol. 1. Lexington: University of Kentucky.

Machel, H. G. and E. W. Mountjoy. 1986. "Chemistry and Environments of Dolomitization —A Reappraisal." *Earth-Science Reviews* 23 (3): 175–222.

Mackay, E., G. Pickup, and P. Olden. 2010. "Fate of CO_2: Rock mechanics, geochemistry and aquifer fluid flow." Presentation given at the CASSEM Conference, Edinburgh, October 4.

Manley, R. D., P. W. Choquette, and M. B. Rosa. 1993. "Paleogeography and Cementation in a Mississippian Oolite Shoal Complex: Ste. Genevieve Formation, Willow Hill Field, Southern Illinois Basin." In *Mississippian Oolites and Modern Analogs*, edited by B. D. Keith and C. W. Zuppann. Studies in Geology 35, 91–113. Tulsa: AAPG.

McBride, J. H. and D. R. Kolata. 2000. *A "new" Precambrian Geologic Province beneath the Illinois Basin, USA*. North-Central Section, 35th Annual Meeting. Geological Society of America.

McDurmitt, N. 1949. *Oil Accumulation in the Cypress Sandstone in the Herald Pool, White and Gallatin Counties, Illinois*. Circular 151. Champaign: Illinois State Geological Survey.

Meents, W. F. and D. H. Swann. 1965. *Grand Tower Limestone (Devonian) of Southern Illinois*. Circular 389. Champaign: Illinois State Geological Survey.

Middleton, G., and M. Hampton. 1973. Part I: Sediment Gravity Flows; Mechanics of Flow and Deposition. *SEPM* (Society for Sedimentary Geology).

Midwest Geological Sequestration Consortium (MGSC). 2005. *An Assessment of Geological Carbon Sequestration Options in the Illinois Basin*. DOE Contract DE-FC26-03NT41994. (Issued December 31, 2005.)

Midwest Geological Sequestration Consortium (MGSC). 2009. Enhanced Oil Recovery I: Loudon Single-Well Huff 'n' Puff. DOE Contract DE-FC26-03NT41994 (Issued December 31, 2009).

Morse, D. G. and H. L. Leetaru. 2003. Reservoir Characterization and 3D Models of Mt. Simon Gas Storage Fields in the Illinois Basin. Illinois State Geological Survey, Open File Series 2003-13, 148 p.

Morse, D. G., and H. E. Leetaru. 2005. Reservoir Characterization and Three-Dimensional Models of Mt. Simon Gas Storage Fields in the Illinois Basin. Circular 567. Champaign: Illinois State Geological Survey.

Mortada, M., and G. W. Nabor. 1961. "An approximate method for determining areal sweep efficiency and flow capacity in formations with anisotropic permeability." *Soc. Pet. Eng. J.* (Dec.): 277–286.

Moulton, G. F. 1925. *Further Contributions to the Geology of the Allendale Oil Field with a Revised Structure Map*. Reports of Investigations 7. Champaign: Illinois State Geological Survey.

National Energy Technology Laboratory (NETL). 2010a. *Carbon Sequestration Atlas of the United States and Canada*, third edition, US Department of Energy.

National Energy Technology Laboratory (NETL). 2010b. *Geologic Storage Formation Classification: Understanding Its Importance and Impacts on CCS Opportunities in the United States*. US Department of Energy, DOE/NETL 2010/1420.

National Energy Technology Laboratory (NETL). 2012. *Carbon Sequestration Atlas of the United States and Canada*, fourth edition, US Department of Energy.

Nelson, W. J. 1995. *Structural Features in Illinois*. Bulletin 100. Champaign: Illinois State Geological Survey.

Nelson, W. J., L. B. Smith, J. D. Treworgy, L. C Furer, and B. D. Keith. 2002. *Sequence Stratigraphy of the Lower Chesterian (Mississippian) Strata of the Illinois Basin*. Bulletin 107. Champaign: Illinois State Geological Survey.

Nelson, W. J., J. A. Devera, R. J. Jacobson, C. P. Weibel, L. R. Follmer, M. H. Riggs, S. P. Esling, E. D. Henderson, and M. S. Lannon. 1991. Geology of the Eddyville, Stonefort, and Creal Springs Quadrangles, Southern Illinois. Bulletin 96. Champaign: Illinois State Geological Survey.

New Mexico Bureau of Mines and Mineral Resources, Colorado Geological Survey, Utah Geological Survey, and Geological Survey of Wyoming. 1993. *Atlas of Major Rocky Mountain Gas Reservoirs*. New Mexico: New Mexico Bureau of Mines and Mineral Resources.

Norby, R. D. 1991. "Biostratigraphic Zones in the Illinois Basin." In *Interior Cratonic Basins*, edited by M. W. Leighton, D. R. Kolata, D. F. Oltz and J. J. Eidel. Memoir 51, 179–194. Tulsa: AAPG.

North, W. G. 1965. "Lower Devonian Stratigraphy of Illinois Interpreted from Well Log Data." MS thesis, Urbana-Champaign, University of Illinois.

North, W. G. 1969. *The Middle Devonian Strata of Southern Illinois*. Circular 441. Champaign: Illinois State Geological Survey.

Off, T. 1963. "Rhythmic Linear Sand Bodies Caused by Tidal Currents." *AAPG Bulletin* 47: 324–341.

Oltz, D. F. 1994. *Improved and Enhanced Oil Recovery in Illinois through Reservoir Characterization: Final Report for the Period June 1989 to December 1993*. DOE Report, DE-FG22-89BC14250 (Issued November 1994.).

Palmer, D. P. 1984. *Geologic Evaluation of Bridgeport Main Sand, Robins 102-B Project, Lawrence County, Illinois*. Littleton: Marathon.

Parrish, A. R. 2005. "A Detailed Reservoir Characterization of an Oolitic Hydrocarbon Reservoir in the Mississippian Ste. Genevieve Limestone at Sailor Springs East Field, Clay Co., IL." MS thesis, Indiana University.

Patton, J. B. and T. A. Dawson. 1955. "Stratigraphy." In *Sedimentation and Stratigraphy of the Devonian Rocks of Southeastern Indiana*, edited by H. H. Murray. Vol. Guidebook 8, 37–43. Indiana Geological Survey: Bloomington.

Pentland, C. H., R. El-Maghraby, A. Georgiadis, S. Iglauer, and M. J. Blunt. 2011a. "Immiscible displacements and capillary trapping in CO_2 storage." *Energy Procedia* 4: 4,969–4,976.

Pentland, C.H., R. El-Maghraby, S. Iglauer, and M. J. Blunt. 2011b. "Measurements of the capillary trapping of super-critical carbon dioxide in Berea sandstone." *Geophysical Research Letters* 38 (6): L06401.

Perkins, R. D. 1963. "Petrology of the Jeffersonville Limestone (Middle Devonian) of Southeastern Indiana." *Geological Society of America Bulletin* 74 (11): 1,135–1,354.

Perrin, J.-C., and S. M. Benson. 2010. "An experimental study on the influence of sub-core scale heterogeneities on CO_2 distribution in reservoir rocks." *Transport in Porous Media* 82 (1): 93–109.

Peterson, J. A. 1995. "Williston Basin Province (031)." In *1995 National Assessment of United States Oil and Gas Resources—Results, Methodology, and Supporting Data*, edited by D. L. Gautier, G. L. Dolton, K. I. Takahashi, and K. L. Varnes. U.S. Geological Survey Digital Data Series DDS-30, Release 2, one CD-ROM.

Pittman, E. D. 1989. *Petrogenesis and petrophysics of selected sandstone reservoirs of the Rocky Mountain region,* edited by E.B. Coalson and S. S. Kaplan, 245–254. Denver: Rocky Mountain Association of Geologists.

Pomar, L. 2001. Types of Carbonate Platforms: a Genetic Approach. *Basin Research* 13: 313–334.

Potter, P. E. 1956. *Subsurface Geology and Coal Resources of the Pennsylvanian System in Crawford and Lawrence Counties, Illinois*. Report of Investigations 193. Champaign: Illinois State Geological Survey.

Read, J. F. 1985. Carbonate Platform Facies Models. *AAPG Bulletin* 66: 860–879.

Reading, H. G., and M. Richards. 1994. Turbidite Systems in Deep-water Basin Margins Classified by Grain Size and Feeder System. *AAPG Bulletin* 78 (5): 792–822.

Rich, J. L. 1916. *Administrative Report and Economic and Geological Papers*. Bulletin 33. Champaign: Illinois State Geological Survey.

Rittenhouse, S. C. 2005. "Geological structure of the Mount Simon Sandstone in and around the Manlove gas storage field, Champaign County, Illinois: A geostatistical approach." MS thesis, Illinois State.

Schwalb, H. R. 1955. *Geneva (Middle Devonian) Dolomite in Illinois*. Circular 204. Champaign: Illinois State Geological Survey.

Seyler, B. 1986. *Aux Vases and Ste. Genevieve Formations: A Core Workshop and Field Trip Guidebook* Illinois Geological Society, Illinois State Geological Survey, Southern Illinois University-Carbondale.

Seyler, B., J. P. Grube, B. Huff, N. Webb, J. Damico, C. Blakley, V. Madhavan, P. Johanek, and S. Frailey. 2012. Reservoir Characterization of Bridgeport and Cypress Sandstones in Lawrence Field Illinois to Improve Petroleum Recovery by Alkaline-surfactant-polymer Flood, DOE Contract DE-NT0005664. (Issued December 21, 2012.)

Seyler, B., J. P. Grube, and Z. Lasemi. 2003. *The Origin of Prolific Reservoirs in the Geneva Dolomite (Middle Devonian), West-Central Illinois Basin*. Illinois Petroleum 158. Champaign: Illinois State Geological Survey.

Shaver, R. H., C. H. Ault, W. I. Ausich, J. B. Droste, A. S. Horowitz, W. C. James, S. M. Okla, C. B. Rexroad, D. M. Suchomel, and J. R. Welch. 1978. *The Search for a Silurian Reef Model Great Lakes Area*. Special Report 15. Bloomington: Indiana Geological Survey.

Shaw, T. H. and B. C. Schreiber. 1991. "Lithostratigraphy and Depositional Environments of the Ancell Group in Central Illinois: A Middle Ordovician Carbonate-Siliciclastic Transition." In *Mixed Carbonate-Siliciclastic Sequences*, edited by A. J. Lomando and P. M. Harris. Vol. 15. Tulsa: SEPM.

Shell. 2011. UK Carbon Capture and Storage Demonstration Competition. UKCCS-KT-S7.19-Shell-002, SCAL Report. Scottish Power CCS Consortium.

Shelby, J. M. 1980. Geologic and Economic Significance of the Upper Morrow Chert Conglomerates Reservoir of the Anadarko Basin. *Journal of Petroleum Technology* 32 (3): 489–495. SPE 7837-PA.

Shi, J.-Q., Z. Xue, and S. Durucan. 2011a. "Supercritical CO_2 core flooding and imbibition in Berea sandstone—CT imaging and numerical simulation." *Energy Procedia* 4: 5,001–5,008.

Shi, J.-Q., Z. Xue, and S. Durucan. 2011b. "Supercritical CO_2 core flooding and imbibition in Tako sandstone—influence of sub-core scale heterogeneity." *International Journal of Greenhouse Gas Control* 5 (1): 75–87.

Shirley, K. 2002. "Find Draws Illinois Basin Attention." *AAPG Explorer* July: 10–12.

Siever, R. 1951. The Mississippian-Pennsylvanian Unconformity in Southern Illinois. *AAPG Bulletin* 35 (3): 542–581.

Simms, M. 1984. "Dolomitization by Groundwater-Flow Systems in Carbonate Platforms." *Gulf Coast Association of Geological Societies Transactions* 34: 411–420.

Sloss, L. L. 1963. "Sequences in the Cratonic Interior of North America." *Geological Society of America Bulletin* 74 (2): 93–114.

Smith, D. G. 1976. "Effect of Vegetation on Lateral Migration of Anastomosed Channels of Glacial Meltwater River." *Geological Society of America Bulletin* 87 (6): 209–230.

Smith, L. B., A. Al-Tawil, and J. F. Read. 2001. "High-Resolution Sequence Stratigraphic Setting of Mississippian Eolianites, Appalachian and Illinois Basins." In *Modern and Ancient Carbonate Eolianites: Sedimentology, Sequence Stratigraphy, and Diagenesis*, edited by F. E. Abegg, P. M. Harris and D. B. Loope. Vol. 71, 167–181. Tulsa: Society for Sedimentary Geology.

Stevenson, D. L. 1964. *Carper Sand Oil Production in St. James, Wilberton, and St. Paul Pools, Fayette County, Illinois*. Circular 362. Champaign: Illinois State Geological Survey.

Sturm, S. 1982. Depositional environments and sandstone diagenesis in the Pennsylvanian Tyler Formation of southwestern North Dakota. In *Fourth International Williston Basin Symposium*, edited by J. E. Christopher and J. Kaldi, 251–262. Saskatchewan Geological Society Special Publication No. 6.

Swann, D. H. and A. H. Bell. 1958. "Habitat of Oil in the Illinois Basin." In *Habitat of Oil*, edited by L. G. Weeks, 447–472. Tulsa: AAPG.

Swann, D. H., J. A. Lineback, and E. Frund. 1965. *The Borden Siltstone (Mississippian) Delta in Southwestern Illinois*. Circular 386. Champaign: Illinois State Geological Survey.

Thomson, A. 1978. Petrography and diagenesis of the Hosston sandstone reservoirs at Bassfield, Jefferson Davis County, Mississippi. *Gulf Coast Geological Societies Transactions* 28: 651–664.

Udegbunam, E. O., and J. Grube. 1995. "Reservoir characterization and evaluation of oil productivity of Mississip[p]ian Cypress reservoirs of Lawrence Field." Illinois State Geological Survey, reprint.

Udegbunam, E. O., B. G. Huff, C. Kemppanien, and J. Morgan. 2001. *Integrated Geological and Engineering Study and Reservoir Simulation of the St. Peter Sandstone Gas Storage Reservoir at the Hillsboro Field, Montgomery County, Illinois*. Illinois Petroleum 156. Champaign: Illinois State Geological Survey.

US Geological Survey Geologic Carbon Dioxide Storage Resources Assessment Team (USGS). 2013. *National Assessment of Geologic Carbon Dioxide Storage Resources—Results*. Circular 1386. Virginia: US Geological Survey.

Ver Steeg, D. J. 1970. *Geologic Evaluation, Kimmel 118-K Test, Technical Service Project 62 02 008 07*. Littleton: Marathon.

Walker, R. G. and D. J. Cant. 1984. "Sandy Fluvial Systems." In *Facies Models*, edited by R. G. Walker, 71–89. Toronto: Geological Association of Canada.

Wanless, H. R., and J. M. Weller. 1932. Correlation and Extent of Pennsylvanian Cyclothems. Geological Society of America Bulletin 43 (4): 1,003–1,016.

Warren, J. E., F. F. Skiba, and H. S. Price. 1961. "An evaluation of the significance of pemeability measurements." *Journal of Petroleum Technology* 13 (8): 739–744. SPE 1641-G.

Warthin Jr., A. S. and G. A. Cooper. 1944. "Middle Devonian Subsurface Formations in Illinois." *AAPG Bulletin* 28: 1,519–1,527.

Weller, J. M. 1930. Cyclical Sedimentation of the Pennsylvanian Period and Its Significance. *The Journal of Geology* 38 (2): 97–135.

Whitaker, S. T. 1988. *Silurian Pinnacle Reef Distribution in Illinois: Model for Hydrocarbon Exploration*. Illinois Petroleum 130. Champaign: Illinois State Geological Survey.

Whitaker, S. T. and A. K. Finley. 1992. *Reservoir Heterogeneity and Potential for Improved Oil Recovery within the Cypress Formation at Bartelso Field, Clinton County, Illinois*. Illinois Petroleum 137. Champaign: Illinois State Geological Survey.

Whiting, L. L. and D. L. Stevenson. 1965. *The Sangamon Arch*. Circular 383. Champaign: Illinois State Geological Survey.

Willman, H. B., E. Atherton, T. C. Buschbach, C. Collinson, J. C. Frye, M. E. Hopkins, J. A. Lineback, and J. A. Simon. 1975. *Handbook of Illinois Stratigraphy*. Bulletin 95. Champaign: Illinois State Geological Survey.

Wilson, J. L. 1975. *Carbonate Facies in Geologic History*. Berlin: Springer-Verlag.

Workman, L. E. and T. Gillette. 1956. *Subsurface Stratigraphy of the Kinderhook Series in Illinois*. Report of Investigations 189. Champaign: Illinois State Geological Survey.

Xu, J. and B. Huff. 1995. *The Cypress Sandstone (Mississippian) Reservoir and its Recovery Potential at Xenia East Oil Field, Clay County Illinois*. Illinois Petroleum 147. Champaign: Illinois State Geological Survey.

Zaitlin, B. A., R. W. Dalrymple, and R. Boyd. 1994. "The stratigraphic organization of incised-valley systems associated with relative sea-level change." In Incised-Valley Systems: Origin and Sedimentary Sequences edited by R.W. Dalrymple, R. Boyd, and B.A. Zaitlin, 45–60. Tulsa: SEPM (Society for Sedimentary Geology).

APPENDIX 1: GSECALC AND WORLDWIDE PERMEABILITY DATA

Geologic Storage Efficiency Calculator (GSECalc)

Storage efficiency, E, is estimated from the reservoir grid and simulation output data using the following equation:

$$E = \frac{V_{inj}}{V_p} = \frac{\sum_{i=1}^{m} \Delta x_i \Delta y_i \Delta z_i \phi_i S_{g,i}}{\sum_{i=1}^{n} \Delta x_i \Delta y_i \Delta z_i \phi_i} \quad \text{(A1-1)}$$

where m represents the total number of gridblocks containing CO_2 with a saturation greater than the threshold value and n is the total number of gridblocks within a pore volume available for storage, which is defined by the CO_2 plume extent and method used to estimate available pore volume (see "Storage Efficiency Calculation" in the Reservoir Simulation section). The Δx_i, Δy_i, and Δz_i are the x, y, and z dimensions of a given gridblock, i. The φ_i is the gridblock porosity and $S_{g,i}$ represents the gridblock gas saturation. The above equation is applicable to gridblocks with CO_2 saturations greater than 0.0 or a specified threshold value.

Microsoft Access is a desktop database that incorporates data tables, coded procedures, and forms to direct user input and perform data analysis. The Access file is a single container with all the data and objects needed to make Access function. It can be copied and ran on any computer with Access 2010. Issues may arise in the embedded OLE (object linking and embedding) graph by switching among Access versions.

After importing reservoir modeling data into Access data tables, users input the data into forms that trigger queries to perform data analysis. Queries are coded procedures that describe how to perform analysis based on the formatted data tables. The results appear in tabular form, but exist only in memory until the query is closed. Query tables can be directly copied into a spreadsheet for further inspection or the query can be rerun as needed. Each time a query is run, it uses the data in the tables at the time of execution. Users can create their own queries, but changing any field or tables names will cause data analysis queries to fail.

Forms

There are five forms in the Access database to provide navigation and direct user input. The Main Menu (Figure A1-1) provides access to any of the forms in the database and a button to close the Access application. The five forms include Main Menu, Import Data, Gas Saturation Analysis, Statistics, and Delete Data Tables.

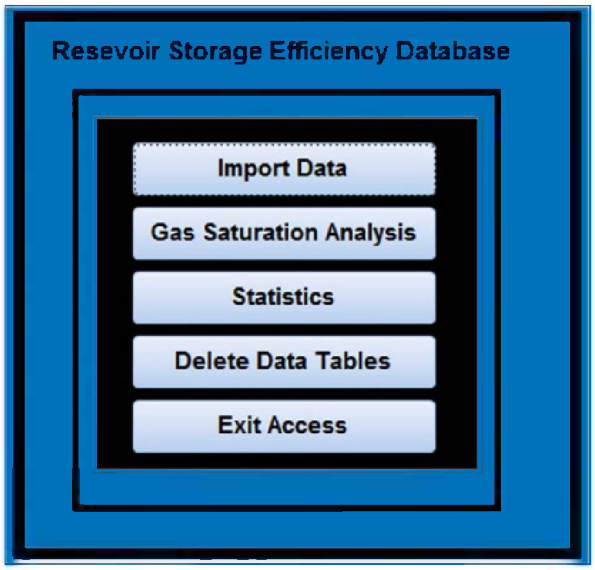

Figure A1-1 Database main menu.

Importing Data to Tables

Access has both data capacity and practical speed limitations using large datasets. The amount of data Access can store and analyze is limited by a 2 GB file size limit and by the rate queries will run on large datasets. The best strategy for maximizing database performance is to reduce the number of timesteps loaded from the recurring data file and, if possible, trim the grid if large numbers of grid cells are not saturated during injection. The more records that are added, the longer the data analysis will take. The database has been tested for up to 12 million records in the recurring data file.

Users are required to import two data files: an initialization or gridcell file and a recurring file containing data for each timestep. The field names within a data file should not be changed. All required fields listed below must be present in each file. The import code will ignore additional fields that are not needed to perform the data analysis.

Required fields

1. Initialization file (I, J, K, KX, KY, KZ, DXC, DYC, DZC, POR)
2. Recurring file (I, J, K, Time, Date, S_g, S_w, P, DENG, VISG)

Grid Importation

1. From the Main Menu, press the "Import" button to enter the Import interface (Figure A1-2).
2. Use the browse button to select the file name and path to either the target initialization or recurring data file.
3. After selecting the file name and path, choose the file type—either an initialization or recurring file.
4. Press "Import Data File" button. A message box will appear when the import process is complete. Do not attempt to do anything else in the database until the import message appears. While Access is processing the data, "Not Responding" may become visible at the top of the screen. Generally, this only means Access is too busy to respond.

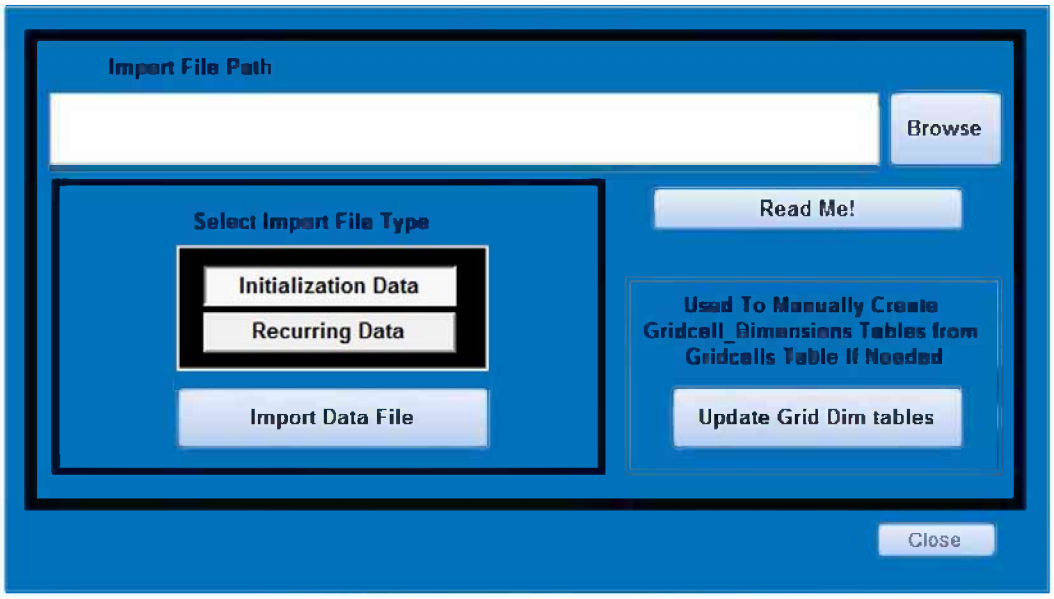

Figure A1-2 Import interface.

After importing both data files, the database should have a minimum of five tables to function. The Gridcell and Recurring_Data tables contain raw data generated when importing data files. Three additional tables, X_gridcell_Dimension, Y_gridcell_Dimension, and Z_gridcell_Dimension, are created immediately after the Initialization or gridcell data is imported. If they already exist, they will be overwritten as needed.

Data Analysis

Once the data is loaded, data analysis can be performed. Because the datasets are typically large for Access, the data analysis queries may take several minutes to run. Again, do not attempt to do anything else in the database until the analysis is complete. While Access is processing the data, "Not Responding" may become visible at the top of the screen. Generally, this only means Access is too busy to respond. Although the data is returned in tabular format, the data is not saved, it exists in temporary memory. Each time the query is run, it performs an analysis on the current data in the tables.

Gas Saturation Analysis

The following steps are required to perform gas saturation analysis (Figure A1-3):
1. Edit the gas saturation threshold if desired.
2. Select one of the five analysis options.
3. Press the "Run Analysis" button to perform the analysis.
4. Select the "Efficiency Graph" button to view CO_2 efficiency vs. time graphs (if the "Efficiency Analysis" option is selected).

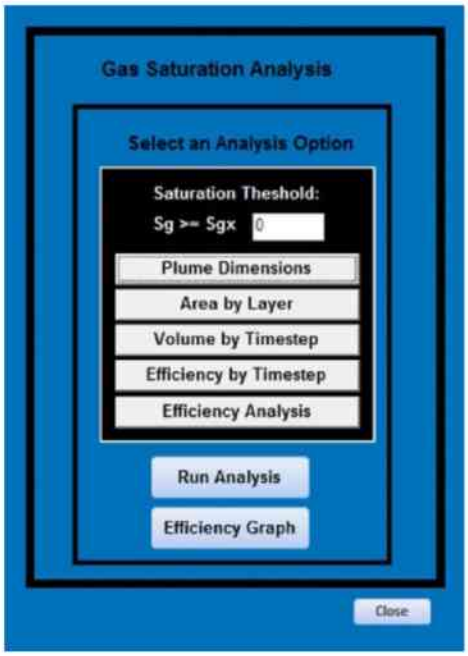

Figure A1-3 Gas saturation analysis interface.

Statistics

Analysis of reservoir data (permeability, porosity, pressure, density, and viscosity) requires the following steps (Figure A1-4):

1. Choose one of the nine reservoir parameters from the dropdown box.
2. Edit the gas saturation cutoff fraction if desired.
3. Select how to group the parameter by vertical grid layers.
4. Select the "Run Statistics" button to perform statistical analysis.

Fluid Saturation Distribution

1. Press the "Saturation Statistics By Timestep" button to view a table containing average saturations and densities of brine and CO_2 behind the plume front as a function of time.

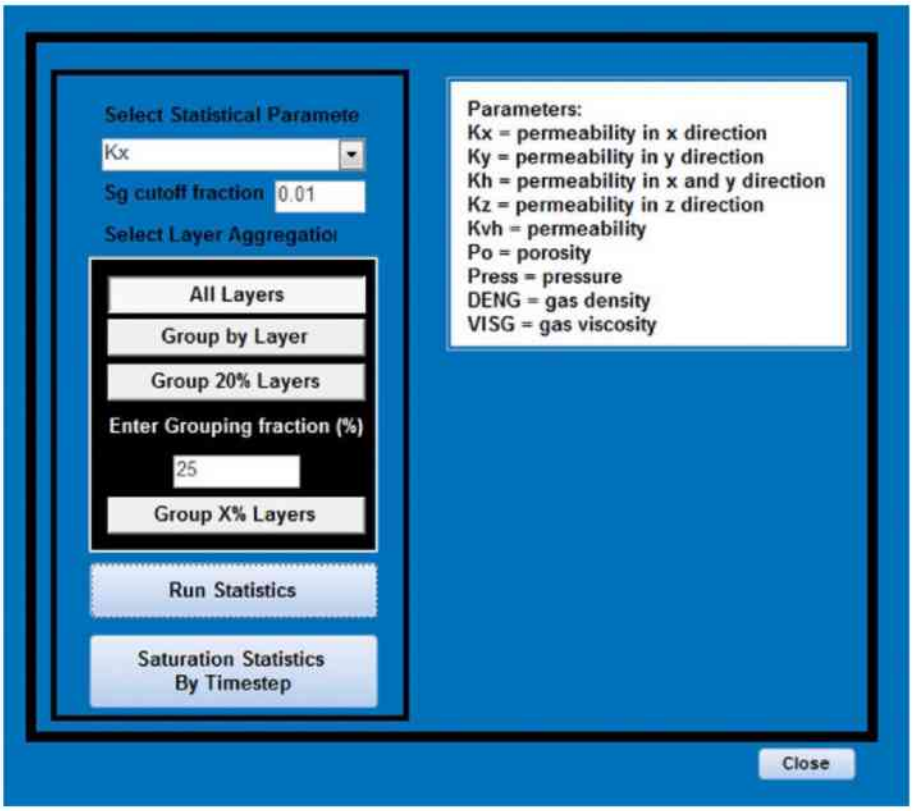

Figure A1-4 Statistics interface.

Deleting Data

Use the "Delete Table" button to remove data from the database (Figure A1-5). (Note: Before loading new data after each time a large amount of data is deleted, the database should be closed. As it closes, the database rewrites itself and frees up deleted memory. Failure to perform this task will cause the database to run slower and cause it to exceed file size restriction. The process can take a few minutes if the database is large).

After the database closes, open it again, and proceed to load data or perform analysis.

Figure A1-5 Interface for deleting data tables.

Exit Access

Select the "Exit Access" button from the Main Menu to close Access.

Worldwide publicly available CO_2-brine relative permeability experimental data

A recent literature review by Burnside and Naylor (2014) on worldwide publicly available experimental data provided the foundation for estimating CO_2-brine relative permeability endpoints of sandstone and carbonate formations. However, there was no relative permeability data found specific to a depositional environment. The CO_2-brine relative permeability curves for sandstone and carbonate reservoirs were estimated from experimental data of 50 rock samples obtained from locations in the North Sea, Canada, Japan, United States, and United Kingdom (Burnside and Naylor, 2014; Perrin and Benson, 2010; Krevor et al., 2011). The following tables list the data used to generate the estimates of storage efficiency for each depositional environment.

Table A1-1 Experimental relative permeability data of CO_2-brine system in sandstone (Revised after Burnside and Naylor, 2014).

Sample No.	ϕ (%)	k (cm^2 [md])	k_{rco2}	$S_{g,\,max}$	S_{gc}
1	11.7	7.99×10^{-13} (0.081)	0.5446	0.706	–
2	12.6	3.71×10^{-12} (0.376)	0.1156	0.341	–
3	12.5	2.66×10^{-11} (2.7)	0.3319	0.442	–
4	19.5	2.14×10^{-10} (21.7)	0.2638	0.577	0.297
5	15.3	3.51×10^{-12} (0.356)	0.526	0.803	0.102
6	16.1	2.09×10^{-10} (21.2)	0.129	0.575	0.253
7	17.2	1.54×10^{-8} (1,558.65)	0.0973	0.399	0.223
8	33.1	1.62×10^{-13} (0.0164)	0.4939	0.657	0.145
9	29	3.76×10^{-8} (3,812.36)	0.5735	0.618	0.421
10	14.5	6.41×10^{-10} (65)	0.0434	0.521	0.477
11	17.7	5.34×10^{-10} (54.2)	0.2733	0.534	0.459
12	23.6	5.29×10^{-9} (536.6)	0.0762	0.347	0.283
13	31.6	1.32×10^{-9} (133.9)	0.1461	0.558	0.383
14	11.5	7.39×10^{-12} (0.749)	0.5454	0.4345	0.3592
15	11.6	5.62×10^{-14} (0.0057)	0.2105	0.431	0.2339
16	11.9	2.49×10^{-9} (252.5)	0.1562	0.51	0.403
17	11.9	1.56×10^{-9} (157.8)	0.21	0.349	0.269
18	12.5	2.96×10^{-13} (0.03)	0.3255	0.725	0.519
19	17.6	1.02×10^{-9} (103.7)	0.1062	0.5103	0.382
20	16.2	6.81×10^{-10} (69.1)	0.0941	0.4041	0.2883
21	19.3	1.36×10^{-9} (137.9)	0.2597	0.346	0.238
22	14.8	6.91×10^{-10} (70.1)	0.405	0.4211	0.2256
23	27	5.46×10^{-10} (55.4)	0.135	0.43	0.28
24	18.7	3.25×10^{-9} (330)	–	0.313	0.21
25	22	4.40×10^{-9} (446)	–	0.85	0.35
26	20.3	4.24×10^{-9} (430)	0.063	0.38	–
27	18.2	4.44×10^{-10} (45)	0.608	0.566	–
28	22.1	9.01×10^{-9} (914)	0.38	0.55	0.31
29	28.3	1.14×10^{-11} (1.156)	0.3	0.59	0.33
30	24.4	7.40×10^{-11} (7.5)	0.46	0.54	0.21
31	23.6	2.17×10^{-9} (220)	–	0.46	0.31
32	–	–	0.08	0.62	0.38
33	–	–	0.061	0.443	0.283
34	26.3	2.02×10^{-8} (2,048)	0.96	0.67	0.38
35	26.9	1.01×10^{-8} (1,025)	0.92	0.7	0.29

Table A1-2 Experimental relative permeability data of CO_2-brine system for sandstone with optimized Corey's exponents. Corey's coefficient for brine, m; Corey's coefficient for CO_2, n (Bennion and Bachu, 2008; Bachu, 2013).

Sample No.	k (md)	Drainage cycle				Imbibition cycle			
		k_{rco2}	S_{wirr}	m	n	$k_{rw,\,max}$	S_{gc}	m	n
1	1.54×10^{-8} (1,558.65)	0.0973	0.601	1.33	4.34	0.5191	0.223	1.27	2.53
2	1.62×10^{-13} (0.0164)	0.4939	0.343	1.24	1.6	0.7683	0.145	1.15	2.25
3	3.76×10^{-8} (3,812.36)	0.5735	0.382	1.18	4.79	0.2437	0.421	1.01	2.67
4	6.41×10^{-10} (65.03)	0.0434	0.479	2.19	1.9	0.0257	0.477	1.35	3.09
5	5.35×10^{-10} (54.23)	0.2733	0.466	3.12	3.48	0.0278	0.459	1.01	1.94
6	5.29×10^{-9} (536.6)	0.0762	0.653	1.67	5.22	0.0741	0.283	2.55	3.9
7	1.32×10^{-9} (133.9)	0.1461	0.442	1.42	4.98	0.0931	0.383	2.11	1.67
8	7.39×10^{-12} (0.749)	0.5454	0.5655	1.75	3.73	0.0654	0.3592	2.03	1.15
9	5.62×10^{-14} (0.0057)	0.2105	0.569	1.45	3.89	0.3333	0.2339	1.25	3.01
10	2.49×10^{-9} (252.5)	0.1562	0.49	1.63	1.35	0.1549	0.403	1.38	1.29
11	1.56×10^{-9} (157.8)	0.21	0.651	4.54	3.74	0.2549	0.269	1.45	1.41
12	2.96×10^{-13} (0.03)	0.3255	0.275	1.21	5.48	0.1779	0.519	1.71	2.11
13	1.02×10^{-9} (103.66)	0.1062	0.4897	1.8	7	0.395	0.382	3	2.5
14	6.81×10^{-10} (69.11)	0.0941	0.596	1.5	4	0.3722	0.2883	4	1.78
15	1.36×10^{-9} (137.9)	0.2597	0.654	1.2	6.57	0.2424	0.238	2.12	1.2
16	6.91×10^{-10} (70.13)	0.405	0.579	1.15	1.81	0.1688	0.2256	1.05	1.45
17	3.51×10^{-12} (0.356)	0.526	0.197	1.3	1.7	0.905	0.102	1.2	1.2
18	2.09×10^{-10} (21.17)	0.129	0.425	1.2	1.3	0.267	0.253	1.9	4.5
19	2.66×10^{-11} (2.7)	0.3319	0.558	2.9	3.2	–	–	–	–
20	2.14×10^{-10} (21.72)	0.2638	0.423	1.7	2.8	0.365	0.297	2.1	4
21	3.71×10^{-12} (0.376)	0.1156	0.659	2.1	2.2	–	–	–	–
22	7.99×10^{-13} (0.081)	0.5446	0.294	1.8	5	–	–	–	–

Table A1-3 Experimental relative permeability data of CO_2-brine system for carbonate with optimized Corey's exponents (Bennion and Bachu, 2010).

Sample No.	k (cm^2 [md])	Drainage cycle				Imbibition cycle			
		k_{rco2}	S_{wirr}	m	n	$k_{rw,\,max}$	S_{gc}	m	n
1	1.77×10^{-13} (0.018)	0.5289	0.595	1.4	5.6	–	–	–	–
2	6.60×10^{-10} (66.98)	0.1883	0.569	1.4	2.1	–	–	–	–
3	5.35×10^{-10} (54.3)	0.1015	0.852	2.76	5.78	0.9165	0.045	6.25	1.72
4	4.53×10^{-10} (45.92)	0.1768	0.33	2.8	1.1	–	–	–	–
5	2.07×10^{-10} (21.02)	0.0999	0.492	2.7	4.6	0.55	0.218	2.1	4.4
6	7.34×10^{-10} (74.4)	0.1078	0.397	2.27	2.93	0.3821	0.207	1.01	2.56
7	1.52×10^{-9} (153.9)	0.1101	0.52	1.73	5.19	0.0249	0.356	2.25	2.76
8	3.67×10^{-9} (371.9)	0.0746	0.53	1.82	3.67	0.7888	0.131	2.53	1.57
9	3.49×10^{-9} (353.6)	0.0476	0.665	1.57	4.78	0.2727	0.208	1.17	2.89
10	6.44×10^{-10} (65.3)	0.0685	0.476	1.4	5.6	–	–	–	–
11	4.80×10^{-11} (4.87)	0.094	0.5963	1.83	5.44	0.0788	0.268	1.7	1.15
12	2.14×10^{-12} (0.217)	0.5037	0.546	1.56	1.16	0.0802	0.256	5.68	4.28
13	3.05×10^{-11} (3.09)	0.6117	0.2108	2.4	4.5	0.1346	0.4149	1.65	1.55

Table A1-4 Relative permeability and displacement characteristics with optimized Corey's exponents for sandstone based on the analysis of 22 core samples from western Canada.

Rock group	Number of samples	Drainage cycle				Imbibition cycle			
		$k_{rco2,\,max}$	S_{wirr}	m	n	$k_{rw,\,max}$	S_{gc}	m	n
Very low k ($<9.86 \times 10^{-13}$ cm^2 [0.1 md])	4	0.4097	0.319	1.35	4.45	0.3333	0.234	1.25	2.25
Low k (about 9.86×10^{-13} to 9.86×10^{-11} cm^2 [0.1 to 10 md])	4	0.4290	0.562	1.93	2.70	0.4852	0.231	1.62	1.18
Mid k (about 9.86×10^{-11} to 9.86×10^{-10} cm^2 [10 to 100 md])	6	0.1964	0.473	1.60	2.35	0.2179	0.293	1.63	2.52
High k (about 9.86×10^{-10} to 4.93×10^{-9} cm^2 [100 to 500 md])	5	0.1562	0.490	1.63	4.98	0.2424	0.382	2.11	1.41
Very high k ($>4.93 \times 10^{-9}$ [500 md])	3	0.0973	0.601	1.33	4.79	0.2437	0.283	1.27	2.67
Common k (about 9.86×10^{-13} to 4.93×10^{-9} cm^2 [0.1 to 500 md]))	15	0.2100	0.490	1.70	3.20	0.2424	0.297	1.90	1.67

Table A1-5 Relative permeability and displacement characteristics with optimized Corey's exponents for carbonate based on the analysis of 13 core samples from western Canada.

Rock group	Number of samples	Drainage cycle				Imbibition cycle			
		$k_{rco2,\,max}$	S_{wirr}	m	n	$k_{rw,\,max}$	S_{gc}	m	n
Very low k (<9.86 × 10^{-13} cm^2 [0.1 md])	1	0.5289	0.595	1.40	5.60	–	–	–	–
Low k (about 9.86 × 10^{-13} to 9.86 × 10^{-11} cm^2 [0.1 to 10 md])	3	0.5037	0.546	1.83	4.50	0.0802	0.268	1.70	1.55
Mid k (about 9.86 × 10^{-11} to 9.86 × 10^{-10} cm^2 [10 to 100 md])	6	0.1047	0.484	2.49	3.77	0.5500	0.207	2.10	2.56
High k (about 9.86 × 10^{-10} to 4.93 × 10^{-9} cm^2 [100 to 500 md])	3	0.0746	0.530	1.73	4.78	0.2727	0.208	2.25	2.76
Common k (about 9.86 × 10^{-13} to 4.93 × 10^{-9} cm^2 [0.1 to 500 md])	12	0.1047	0.525	1.83	4.55	0.2727	0.218	2.10	2.56

Table A1-6 Relative permeability endpoints P_{10} and P_{90} values for sandstone based on the analysis of 33 core samples worldwide.

Rock group	Percentile	k_{rco2}	$S_{g,\,max}$	S_{gc}
Very low k (<9.86 × 10^{-13} cm^2 [0.1 md])	P_{10}	0.2450	0.499	0.163
	P_{90}	0.5294	0.719	0.462
Low k (about 9.86 × 10^{-13} to 9.86 × 10^{-11} cm^2 [0.1 to 10 md])	P_{10}	0.2078	0.388	0.134
	P_{90}	0.5357	0.695	0.350
Mid k (about 9.86 × 10^{-11} to 9.86 × 10^{-10} cm^2 [10 to 100 md])	P_{10}	0.0789	0.416	0.242
	P_{90}	0.4659	0.578	0.466
High k (about 9.86 × 10^{-10} to 4.93 × 10^{-9} cm^2 [100 to 500 md])	P_{10}	0.0846	0.339	0.230
	P_{90}	0.2349	0.616	0.389
Very high k (>4.93 × 10^{-9} [500 md])	P_{10}	0.0868	0.373	0.253
	P_{90}	0.9400	0.685	0.401
Common k (about 9.86 × 10^{-13} to 4.93 × 10^{-9} cm^2 [0.1 to 500 md)	P_{10}	0.0910	0.347	0.210
	P_{90}	0.5279	0.587	0.414

Table A1-7 Relative permeability endpoints P10 and P90 for carbonate based on the analysis of 13 core samples from western Canada.

Rock group	Percentile	k_{rco2}	$S_{g,\,max}$	S_{gc}
Very low k (<9.86 × 10^{-13} cm^2 [0.1 md])	P_{10}	0.5289	0.405	–
	P_{90}	0.5289	0.405	–
Low k (about 9.86 × 10^{-13} to 9.86 × 10^{-11} cm^2 [0.1 to 10 md])	P_{10}	0.1759	0.414	0.258
	P_{90}	0.5901	0.722	0.386
Mid k (about 9.86 × 10^{-11} to 9.86 × 10^{-10} cm^2 [10 to 100 md])	P_{10}	0.0842	0.290	0.077
	P_{90}	0.1826	0.637	0.216
High k (about 9.86 × 10^{-10} to 4.93 × 10^{-9} cm^2 [100 to 500 md])	P_{10}	0.0530	0.362	0.146
	P_{90}	0.1030	0.478	0.326
Common k (about 9.86 × 10^{-13} to 4.93 × 10^{-9} cm^2 [0.1 to 500 md)	P_{10}	0.0691	0.342	0.114
	P_{90}	0.4722	0.663	0.368

APPENDIX 2: DETAILED SIMULATION RESULTS

Deltaic

Table A1-8 Baseline simulations.

Scenario	Case ID	E_{rec}, %	E_{cub}, %	E_{cyl}, %	$\bar{S}_g$	$E_{V,\,rec}$, %	$E_{V,\,sqr}$, %	$E_{V,\,cyl}$, %	$E_{V,\,avg}$, %	Standard deviation, %
Stratigraphic	Center	15.7	14.4	18.3	0.4672	33.6	30.8	39.2	34.5	4.3
	Non-center 1	16.5	10.5	13.4	0.4483	36.8	23.4	29.9	30.0	6.7
	Non-center 2	15.2	13.9	17.7	0.4286	35.5	32.4	41.3	36.4	4.5
	Non-center 3	16.0	9.5	12.1	0.419	38.2	22.7	28.9	29.9	7.8
	Non-center 4	17.1	14.2	18.0	0.4472	38.2	31.8	40.3	36.7	4.4
Structural	Center	17.0	15.6	19.8	0.4621	36.8	33.8	42.8	37.8	4.6
	Non-center 1	15.9	14.0	17.9	0.4672	35.1	30.3	38.7	34.7	4.2
	Non-center 2	17.6	11.2	14.3	0.4697	37.5	23.8	30.4	30.6	6.8
	Non-center 3	17.6	14.7	18.8	0.4651	37.8	31.6	40.4	36.6	4.5
	Non-center 4	18.3	10.7	13.6	0.4744	38.6	22.6	28.7	29.9	8.1

Table A1-9 Selective completions.

Scenario	Case ID	E_{rec}, %	E_{cub}, %	E_{cyl}, %	$\overline{S}_g$	$E_{V,rec}$, %	$E_{V,sqr}$, %	$E_{V,cyl}$, %	$E_{V,avg}$, %	Standard deviation, %
High E Well	Bottom interval (bottom)	14.8	13.3	16.9	0.4506	32.8	29.5	37.5	33.3	4.0
	Top interval (top)	15	13.6	17.4	0.4513	33.2	30.1	38.6	34.0	4.3
	High k interval (HKI)	14.7	13.2	16.8	0.4513	32.6	29.2	37.2	33.0	4.0
	Low k interval (LKI)	14.8	13.3	16.9	0.4512	32.8	29.5	37.5	33.2	4.0
	High k layers (HKL)	14.9	13.5	17.2	0.4513	33.0	29.9	38.1	33.7	4.1
	Low k layers (LKL)	14.9	13.5	17.2	0.4512	33.0	29.9	38.1	33.7	4.1
	Low k_v/k_h interval (Lk_{vh})	14.9	13.5	17.2	0.451	33.0	29.9	38.1	33.7	4.1
Low E Well	Bottom interval (bottom)	11.6	6	7.6	0.393	29.5	15.3	19.3	21.4	7.3
	Top interval (top)	15.7	8.7	11	0.4194	37.4	20.7	26.2	28.1	8.5
	High k interval (HKI)	15.2	8.4	10.7	0.42	36.2	20.0	25.5	27.2	8.2
	Low k interval (LKI)	16.4	9	11.5	0.4199	39.1	21.4	27.4	29.3	9.0
	High k layers (HKL)	16.8	9.2	11.8	0.4111	40.9	22.4	28.7	30.6	9.4
	Low k layers (LKL)	10	6	7.6	0.4071	24.6	22.4	18.7	21.9	3.0
	Low k_v/k_h	11.3	6.3	8	0.4463	25.3	14.1	17.9	19.1	5.7
Blanket completions	High E well	17.1	14.2	18	0.4472	38.2	31.8	40.3	36.7	4.4
	Low E well	15.2	13.9	17.7	0.4286	35.5	32.4	41.3	36.4	4.5

Table A1-10 Horizontal Wells. Average formation thickness, h.

Scenario	Case ID	E_{rec}, %	E_{cub}, %	E_{cyl}, %	$\bar{S}_g$	$E_{V,rec}$, %	$E_{V,sqr}$, %	$E_{V,cyl}$, %	$E_{V,avg}$, %	Standard deviation, %
Well horizontal location	X center	15.20	10.50	13.40	0.43	34.98	24.17	30.84	30.00	5.46
	X west	16.20	11.90	15.10	0.44	36.87	27.08	34.37	32.77	5.08
	X east	14.90	10.20	13.00	0.45	33.41	22.87	29.15	28.48	5.30
	Y center	13.30	9.60	12.20	0.43	30.68	22.15	28.14	26.99	4.38
	Y north	15.90	11.50	14.60	0.43	36.72	26.56	33.72	32.33	5.22
	Y south	15.20	13.10	16.70	0.45	33.97	29.27	37.32	33.52	4.04
Well vertical location	Top	14.00	9.60	12.30	0.44	31.69	21.73	27.84	27.09	5.02
	Middle	15.00	10.00	12.70	0.45	33.65	22.44	28.49	28.20	5.62
	Bottom	15.20	10.50	13.40	0.43	34.98	24.17	30.84	30.00	5.46
Well length	10h	15.50	13.00	16.60	0.45	35.09	29.43	37.58	34.04	4.18
	20h	15.50	13.20	16.80	0.44	34.82	29.65	37.74	34.07	4.09
	30h*	15.40	13.50	17.20	0.41	34.33	30.09	38.34	34.25	4.12
	50h	14.70	12.70	16.20	0.40	33.18	28.67	36.57	32.81	3.96
	75h	13.80	9.00	11.40	0.43	33.72	21.99	27.86	27.86	5.87

*Optimum well length

Table A1-11 Deviated wells.

Scenario	Case ID	E_{rec}, %	E_{cub}, %	E_{cyl}, %	$\overline{S}_g$	$E_{V,rec}$, %	$E_{V,sqr}$, %	$E_{V,cyl}$, %	$E_{V,avg}$, %	Standard deviation, %
Blanket completions	X center	11.4	7.5	9.6	0.4121	27.7	18.2	23.3	23.1	4.7
	Y center	14.6	11.0	14.0	0.4388	33.3	25.1	31.9	30.1	4.4
	Diagonal 45°	12.3	11.3	14.4	0.4361	28.2	25.9	33.0	29.0	3.6
	Diagonal 135°	7.9	5.9	7.5	0.4149	19.0	14.2	18.1	17.1	2.6
Intervals completions	High k	12.0	10.9	13.9	0.439	27.3	24.8	31.7	27.9	3.5
	Low k	13.5	12.2	15.6	0.4415	30.6	27.6	35.3	31.2	3.9
	Dynamic low k	16.1	15.0	19.2	0.4196	38.4	35.7	45.8	40.0	5.2

Table A1-12 Plume management.

Scenario	Case ID	E_{rec}, %	E_{cub}, %	E_{cyl}, %	$\overline{S}_g$	$E_{V,rec}$, %	$E_{V,sqr}$, %	$E_{V,cyl}$, %	$E_{V,avg}$, %	Standard deviation, %
Water Production	Blanket completions	9.1	8.5	10.9	0.5092	17.9	16.7	21.4	18.7	2.5
	Bottom completions	17.6	16.3	20.8	0.4537	38.8	35.9	45.8	40.2	5.1
	Bottom completions in a closed system	26.3	24.8	31.5	0.4476	58.8	55.4	70.4	61.5	7.9
Field Management	Blanket completions	22.4	19.6	25.0	0.4218	53.1	46.5	59.3	52.9	6.4
	Bottom completions	18.6	16.8	21.4	0.4257	43.7	39.5	50.3	44.5	5.4

Shelf Clastic

Table A1-13 Baseline simulations.

Scenario	Case ID	E_{rec}, %	E_{cub}, %	E_{cyl}, %	$\bar{S}_g$	$E_{V,rec}$, %	$E_{V,sqr}$, %	$E_{V,cyl}$, %	$E_{V,avg}$, %	Standard deviation, %
Stratigraphic	Center	12.7	11.4	14.5	0.3538	35.9	32.2	41.0	36.4	4.4
	Non-center 1	9.7	7.8	9.9	0.3376	28.7	23.1	29.3	27.1	3.4
	Non-center 2	12.8	7.1	9.1	0.3519	36.4	20.2	25.9	27.5	8.2
	Non-center 3	10.8	5.6	7.1	0.3351	32.2	16.7	21.2	23.4	8.0
	Non-center 4	11.5	9.8	12.4	0.344	33.4	28.5	36.0	32.7	3.8
Structural	Center	17.7	14.7	18.7	0.3628	48.8	40.5	51.5	46.9	5.7
	Non-center	12.8	6.6	8.4	0.3278	39.0	20.1	25.6	28.3	9.7

Table A1-14 Selective completions.

Scenario	Case ID	E_{rec}, %	E_{cub}, %	E_{cyl}, %	$\bar{S}_g$	$E_{V,rec}$, %	$E_{V,sqr}$, %	$E_{V,cyl}$, %	$E_{V,avg}$, %	Standard deviation, %
High *E* well	Bottom	9.4	8.6	11	0.325	28.9	26.5	33.8	29.7	3.8
	Top	7.1	6.9	8.9	0.3325	21.4	20.8	26.8	23.0	3.3
	HKI	12.6	11.5	14.6	0.357	35.3	32.2	40.9	36.1	4.4
	LKI	7.3	7.1	9.1	0.3318	22.0	21.4	27.4	23.6	3.3
	HKL	12.4	11.4	14.5	0.352	35.2	32.4	41.2	36.3	4.5
	LKL	7.3	7.1	9.1	0.3318	22.0	21.4	27.4	23.6	3.3
	LK_{vh}	9.7	9.3	11.9	0.3409	28.5	27.3	34.9	30.2	4.1
Low *E* well	Bottom	9.3	4.9	6.3	0.3265	28.5	15.0	19.3	20.9	6.9
	Top	7.9	4.3	5.4	0.3337	23.7	12.9	16.2	17.6	5.5
	HKI	12.4	6.3	8.1	0.3441	36.0	18.3	23.5	26.0	9.1
	HKL	12.4	6.3	8.1	0.3441	36.0	18.3	23.5	26.0	9.1
	LKI	8.1	4.4	5.5	0.3314	24.4	13.3	16.6	18.1	5.7
	LK_{vh}	9.5	5	6.4	0.3349	28.4	14.9	19.1	20.8	6.9
Blanket completions	High *E* well	12.7	11.4	14.5	0.3538	35.9	32.2	41.0	36.4	4.4
	Low *E* well	10.8	5.6	7.1	0.3351	32.2	16.7	21.2	23.4	8.0

Table A1-15 Horizontal wells.

Scenario	Case ID	E_{rec}, %	E_{cub}, %	E_{cyl}, %	$\overline{S}_g$	$E_{V,rec}$, %	$E_{V,sqr}$, %	$E_{V,cyl}$, %	$E_{V,avg}$, %	Standard deviation, %
Well horizontal location	X center	13.2	11.3	14.4	0.3563	37.0	31.7	40.4	36.4	4.4
	X west	11.2	8.7	11	0.3546	31.6	24.5	31.0	29.0	3.9
	X east	13.9	9.6	12.2	0.3493	39.8	27.5	34.9	34.1	6.2
	Y center	12.7	11.4	14.5	0.3571	35.6	31.9	40.6	36.0	4.4
	Y north	10.6	7.3	9.4	0.346	30.6	21.1	27.2	26.3	4.8
	Y south	11.6	7.7	9.8	0.3453	33.6	22.3	28.4	28.1	5.7
Well vertical location	Top	12.3	11.6	14.8	0.3577	34.4	32.4	41.4	36.1	4.7
	Mid	12.6	11.6	14.8	0.3574	35.3	32.5	41.4	36.4	4.6
	Bottom	12.7	11.4	14.5	0.3571	35.6	31.9	40.6	36.0	4.4
Well length	4h	12.7	11.6	14.8	0.358	35.5	32.4	41.3	36.4	4.5
	7h	12.6	11.6	14.8	0.3574	35.3	32.5	41.4	36.4	4.6
	14h	12.6	12.4	15.9	0.358	35.2	34.6	44.4	38.1	5.5
	20h	12.7	11.6	14.7	0.3565	35.6	32.5	41.2	36.5	4.4

Table A1-16 Plume management.

Scenario	Case ID	E_{rec}, %	E_{cub}, %	E_{cyl}, %	$\overline{S}_g$	$E_{V,rec}$, %	$E_{V,sqr}$, %	$E_{V,cyl}$, %	$E_{V,avg}$, %	Standard deviation, %
Water Production	Blanket completions	12.6	11.5	14.6	0.3528	35.7	32.6	41.4	36.6	4.5
	Bottom completions	12.7	11.4	14.5	0.3536	35.9	32.2	41.0	36.4	4.4
	Blanket completions in a closed system	16.4	14.5	18.5	0.3781	43.4	38.3	48.9	43.6	5.3
	Bottom completions in a closed system	16.6	14.9	19.0	0.3758	44.2	39.6	50.6	44.8	5.5
Field Management	Blanket completions	12.5	11.5	14.7	0.3335	37.5	34.5	44.1	38.7	4.9
	Bottom completions	13.5	12.8	16.3	0.3411	39.6	37.5	47.8	41.6	5.4

Shelf Carbonate (Limestone)

Table A1-17 Baseline simulations.

Scenario	Case ID	E_{rec}, %	E_{cub}, %	E_{cyl}, %	$\overline{S}_g$	$E_{V,rec}$, %	$E_{V,sqr}$, %	$E_{V,cyl}$, %	$E_{V,avg}$, %	Standard deviation, %
Stratigraphic	Center	7.1	4.2	5.4	0.3451	20.6	12.2	15.6	16.1	4.2
	Non-center 1	5.2	4.2	5.3	0.3363	15.5	12.5	15.8	14.6	1.8
	Non-center 2	6.0	3.1	4.0	0.3263	18.4	9.5	12.3	13.4	4.5
	Non-center 3	9.0	5.1	6.5	0.3449	26.1	14.8	18.8	19.9	5.7
	Non-center 4	5.2	3.9	4.9	0.3058	17.0	12.8	16.0	15.3	2.2
Structural	Center	7.7	4.6	5.9	0.3494	22.0	13.2	16.9	17.4	4.5
	Non-center 1	9.9	5.7	7.2	0.3485	28.4	16.4	20.7	21.8	6.1
	Non-center 2	6.0	3.3	4.1	0.3278	18.3	10.1	12.5	13.6	4.2

Table A1-18 Selective Completions.

Scenario	Case ID	E_{rec}, %	E_{cub}, %	E_{cyl}, %	$\overline{S}_g$	$E_{V,rec}$, %	$E_{V,sqr}$, %	$E_{V,cyl}$, %	$E_{V,avg}$, %	Standard deviation, %
High *E* well	Bottom	2.1	1.2	1.5	0.1498	14.0	8.0	10.0	10.7	3.1
	Top	8.1	4.6	5.8	0.371	21.8	12.4	15.6	16.6	4.8
	HKI	8.2	4.7	6	0.3211	25.5	14.6	18.7	19.6	5.5
	LKI	2.1	1.2	1.5	0.1498	14.0	8.0	10.0	10.7	3.1
	HKL	8.2	4.7	6	0.3211	25.5	14.6	18.7	19.6	5.5
	LKL	2.1	1.2	1.5	0.1498	14.0	8.0	10.0	10.7	3.1
	Kvh	8.1	4.6	5.8	0.371	21.8	12.4	15.6	16.6	4.8
Low *E* well	Bottom	2.6	1.2	1.5	0.1229	21.2	9.8	12.2	14.4	6.0
	Top	5.1	2.2	2.8	0.3013	16.9	7.3	9.3	11.2	5.1
	HKI	5.9	3.1	3.9	0.3272	18.0	9.5	11.9	13.1	4.4
Blanket completions	High *E* well	9	5.1	6.5	0.3449	26.1	14.8	18.8	19.9	5.7
	Low *E* well	6	3.1	4	0.3263	18.4	9.5	12.3	13.4	4.5

*HKL = HKI; LKI = Bottom; LKvh = top

Table A1-19 Horizontal wells.

Scenario	Case ID	E_{rec}, %	E_{cub}, %	E_{cyl}, %	$\bar{S}_g$	$E_{V,rec}$, %	$E_{V,sqr}$, %	$E_{V,cyl}$, %	$E_{V,avg}$, %	Standard deviation, %
Well horizontal location	X center	7.3	4.5	5.7	0.3443	21.2	13.1	16.6	16.9	4.1
	X west	7.4	4.8	6.1	0.3254	22.7	14.8	18.7	18.7	4.0
	X east	6.8	4.3	5.5	0.2987	22.8	14.4	18.4	18.5	4.2
	Y center	7.7	4.8	6.1	0.341	22.6	14.1	17.9	18.2	4.3
	Y north	6.3	3.5	4.5	0.3226	19.5	10.8	13.9	14.8	4.4
	Y south	6.3	4.3	5.5	0.3393	18.6	12.7	16.2	15.8	3.0
Well vertical location	Top	7.6	4.8	6.1	0.3463	21.9	13.9	17.6	17.8	4.0
	Mid	7	4.4	5.5	0.3243	21.6	13.6	17.0	17.4	4.0
	Bottom	7.7	4.8	6.1	0.341	22.6	14.1	17.9	18.2	4.3
Well length	6h	7.7	4.9	6.3	0.3352	23.0	14.6	18.8	18.8	4.2
	10h	7.7	4.8	6.1	0.341	22.6	14.1	17.9	18.2	4.3
	20h	7.1	4.6	5.8	0.3408	20.8	13.5	17.0	17.1	3.7
	30h	6.6	4.7	6	0.3376	19.5	13.9	17.8	17.1	2.9

Table A1-20 Plume management.

Scenario	Case ID	E_{rec}, %	E_{cub}, %	E_{cyl}, %	$\bar{S}_g$	$E_{V,rec}$, %	$E_{V,sqr}$, %	$E_{V,cyl}$, %	$E_{V,avg}$, %	Standard deviation, %
Water Production	Blanket completions	7.7	4.6	5.9	0.3451	22.3	13.3	17.1	17.6	4.5
	Bottom completions	6.9	4.1	5.3	0.3371	20.5	12.2	15.7	16.1	4.2
	Blanket completions in a closed system	11.6	10.9	13.9	0.3592	32.3	30.3	38.7	33.8	4.4
	Bottom completions in a closed system	12.8	11.4	14.5	0.3361	38.1	33.9	43.1	38.4	4.6
Field Management	Blanket completions	7.5	4.6	5.9	0.3283	22.8	14.0	18.0	18.3	4.4
	Bottom completions	6.9	4.1	5.3	0.3371	20.5	12.2	15.7	16.1	4.2

Shelf Carbonate (Dolomite)

Table A1-21 Baseline simulations.

Scenario	Case ID	E_{rec}, %	E_{cub}, %	E_{cyl}, %	$\bar{S}_g$	$E_{V,rec}$, %	$E_{V,sqr}$, %	$E_{V,cyl}$, %	$E_{V,avg}$, %	Standard deviation, %
Stratigraphic	Center	8.2	5.4	6.9	0.4399	18.6	12.3	15.7	15.5	3.2
	Non-center 1	6.4	4.1	5.2	0.4092	15.6	10.0	12.7	12.8	2.8
	Non-center 2	6.6	5.3	6.8	0.4152	15.9	12.8	16.4	15.0	2.0
	Non-center 3	5.9	3.0	3.8	0.3996	14.8	7.5	9.5	10.6	3.7
	Non-center 4	5.5	3.9	5.0	0.4107	13.4	9.5	12.2	11.7	2.0
Structural	Center	7.0	4.5	5.8	0.4223	16.6	10.7	13.7	13.7	3.0
	Non-center 1	7.3	4.1	5.2	0.4269	17.1	9.6	12.2	13.0	3.8
	Non-center 2	5.6	3.9	5.0	0.4189	13.4	9.3	11.9	11.5	2.1
	Non-center 3	6.4	4.4	5.6	0.4179	15.3	10.5	13.4	13.1	2.4
	Non-center 4	6.6	5.4	6.8	0.4252	15.5	12.7	16.0	14.7	1.8

Table A1-22 Selective completions.

Scenario	Case ID	E_{rec}, %	E_{cub}, %	E_{cyl}, %	$\overline{S}_g$	$E_{V,rec}$, %	$E_{V,sqr}$, %	$E_{V,cyl}$, %	$E_{V,avg}$, %	Standard deviation, %
High E well	Bottom	4.9	3.1	3.9	0.4478	10.9	6.9	8.7	8.9	2.0
	Top	6.4	4.1	5.2	0.4247	15.1	9.7	12.2	12.3	2.7
	HKI	7	4.5	5.7	0.4167	16.8	10.8	13.7	13.8	3.0
	LKI	4.9	3.1	3.9	0.4478	10.9	6.9	8.7	8.9	2.0
	HKL	7.2	4.6	5.8	0.4139	18.1	11.1	14.0	14.4	3.5
	LKL	5.1	3.3	4.2	0.4408	11.6	7.5	9.5	9.5	2.0
	LKvh	5.1	3.2	4.1	0.4413	11.6	7.3	9.3	9.4	2.2
Low E well	Bottom	4.7	3	3.8	0.4517	10.4	6.6	8.4	8.5	1.9
	Top	6.4	4.1	5.2	0.4247	15.1	9.7	12.2	12.3	2.7
	HKI	6.4	4.1	5.2	0.4247	15.1	9.7	12.2	12.3	2.7
	LKI	4.7	3	3.8	0.4517	10.4	6.6	8.4	8.5	1.9
	HKL	7.2	4.6	5.8	0.4148	17.4	11.1	14.0	14.1	3.1
	LKL	5.3	2.7	3.4	0.4089	13.0	6.6	8.3	9.3	3.3
	LKvh	5.1	3.2	4.1	0.4413	11.6	7.3	9.3	9.4	2.2
Blanket completions	High E well	8.2	5.4	6.9	0.4399	18.6	12.3	15.7	15.5	3.2
	Low E well	5.9	3	3.8	0.3996	14.8	7.5	9.5	10.6	3.7

Table A1-23 Horizontal wells.

Scenario	Case ID	E_{rec}, %	E_{cub}, %	E_{cyl}, %	$\overline{S}_g$	$E_{V,rec}$, %	$E_{V,sqr}$, %	$E_{V,cyl}$, %	$E_{V,avg}$, %	Standard deviation, %
Well horizontal location	X center	5.6	4.5	5.8	0.4092	13.7	11.0	14.2	13.0	1.7
	X west	7.5	4.2	5.4	0.3966	18.9	10.6	13.6	14.4	4.2
	X east	5.9	5.8	7.4	0.4121	14.3	14.1	18.0	15.4	2.2
	Y center	6.9	4.5	5.7	0.3984	17.3	11.3	14.3	14.3	3.0
	Y north	4.8	3	3.9	0.3917	12.3	7.7	10.0	10.0	2.3
	Y south	5.5	4.3	5.5	0.4269	12.9	10.1	12.9	11.9	1.6
Well vertical location	Top	5.3	4.5	5.8	0.4160	12.7	10.8	13.9	12.5	1.6
	Mid	5.6	4.6	5.8	0.4145	13.5	11.1	14.0	12.9	1.6
	Bottom	5.6	4.5	5.8	0.4092	13.7	11.0	14.2	13.0	1.7
Well length	10h	5.4	5.1	6.5	0.4345	12.4	11.7	15.0	13.0	1.7
	20h	5.9	5.5	7.1	0.4283	13.8	12.8	16.6	14.4	1.9
	30h	6	5.8	7.4	0.4262	14.1	13.6	17.4	15.0	2.0
	50h	6	5.8	7.4	0.4253	14.1	13.6	17.4	15.0	2.0
	75h	5.6	5.2	6.7	0.4218	13.3	12.3	15.9	13.8	1.8
	100h	5.7	5.3	6.8	0.4211	13.5	12.6	16.1	14.1	1.8
	150h	5.6	5.3	6.7	0.4185	13.4	12.7	16.0	14.0	1.8
	200h	5.4	5.1	6.5	0.4166	13.0	12.2	15.6	13.6	1.8
	250h	5.5	5.2	6.6	0.4157	13.2	12.5	15.9	13.9	1.8

Table A1-24 Plume management.

Scenario	Case ID	E_{rec}, %	E_{cub}, %	E_{cyl}, %	$\overline{S}_g$	$E_{V,rec}$, %	$E_{V,sqr}$, %	$E_{V,cyl}$, %	$E_{V,avg}$, %	Standard deviation, %
Water Production	Blanket completions	6.7	4.5	5.8	0.4124	16.2	10.9	14.1	13.7	2.7
	Bottom completions	6.9	4.5	5.8	0.4277	16.1	10.5	13.6	13.4	2.8
	Bottom completions in a closed system	8.3	6.2	7.9	0.4333	19.2	14.3	18.2	17.2	2.6
Field Management	Blanket completions	7.1	5.2	6.7	0.3975	17.9	13.1	16.9	15.9	2.5
	Bottom completions	6.9	4.5	5.8	0.4112	16.8	10.9	14.1	13.9	2.9

Fluvial Deltaic

Table A1-25 Baseline simulations.

Scenario	Case ID	E_{rec}, %	E_{cub}, %	E_{cyl}, %	$\overline{S}_g$	$E_{V,\,rec}$, %	$E_{V,\,sqr}$, %	$E_{V,\,cyl}$, %	$E_{V,\,avg}$, %	Standard deviation, %
Stratigraphic	Center	15.8	15.8	20.1	0.435	36.3	36.3	46.2	39.6	5.7
	Non-center 1	16.5	16.5	21.1	0.4086	40.4	40.4	51.6	44.1	6.5
	Non-center 2	18.2	17.3	22.0	0.4301	42.3	40.2	51.2	44.6	5.8
	Non-center 3	15.8	15.8	20.2	0.4400	35.9	35.9	45.9	39.2	5.8
	Non-center 4	13.3	13.3	16.9	0.3543	37.5	37.5	47.7	40.9	5.9
Structural	Center	15.5	15.5	19.7	0.4365	35.5	35.5	45.1	38.7	5.6
	Non-center 1	18.5	17.5	22.3	0.4350	42.5	40.2	51.3	44.7	5.8
	Non-center 2	16.0	16.0	20.4	0.443	36.1	36.1	46.0	39.4	5.7
	Non-center 3	16.4	16.4	20.8	0.4080	40.2	40.2	51.0	43.8	6.2
	Non-center 4	14.6	14.6	18.6	0.3671	39.8	39.8	50.7	43.4	6.3

Table A1-26 Selective completions.

Scenario	Case ID	E_{rec}, %	E_{cub}, %	E_{cyl}, %	$\overline{S}_g$	$E_{V,\,rec}$, %	$E_{V,\,sqr}$, %	$E_{V,\,cyl}$, %	$E_{V,\,avg}$, %	Standard deviation, %
High E well	Bottom	18.3	17.4	22.2	0.4308	42.5	40.4	51.5	44.8	5.9
	Top	18.2	17.3	22	0.4304	42.3	40.2	51.1	44.5	5.8
	HKI	18.2	17.3	22	0.4303	42.3	40.2	51.1	44.5	5.8
	LKI	18.3	17.4	22.2	0.4309	42.5	40.4	51.5	44.8	5.9
	HKL	18.5	17.2	22	0.4336	42.7	39.7	50.7	44.4	5.7
	LKL	18.2	17.3	22	0.4302	42.3	40.2	51.1	44.5	5.8
	LKvh	18.2	17.3	22	0.4308	42.2	40.2	51.1	44.5	5.8
Low E well	Bottom	13.3	13.3	16.9	0.3543	37.5	37.5	47.7	40.9	5.9
	Top	13.3	13.3	16.9	0.3564	37.3	37.3	47.4	40.7	5.8
	HKI	12.8	12.8	16.3	0.3567	35.9	35.9	45.7	39.2	5.7
	LKI	13.2	13.2	16.8	0.3536	37.3	37.3	47.5	40.7	5.9
	HKL	13.3	13.3	16.9	0.3561	37.3	37.3	47.5	40.7	5.9
	LKL	13.3	13.3	16.9	0.3534	37.6	37.6	47.8	41.0	5.9
	LKvh	13.3	13.3	16.9	0.3543	37.5	37.5	47.7	40.9	5.9
Blanket completions	High E well	18.2	17.3	22	0.4301	42.3	40.2	51.2	44.6	5.8
	Low E well	13.3	16.9	0.3543	37.53881	37.5	47.7	40.9	5.9	5.2

Table A1-27 Horizontal wells.

Scenario	Case ID	E_{rec}, %	E_{cub}, %	E_{cyl}, %	$\bar{S}_g$	$E_{V,rec}$, %	$E_{V,sqr}$, %	$E_{V,cyl}$, %	$E_{V,avg}$, %	Standard deviation, %
Well horizontal location	X center	13.6	12.9	16.5	0.4330	31.4	29.8	38.1	33.1	4.4
	X west	12.8	12.8	16.3	0.4044	31.7	31.7	40.3	34.5	5.0
	X east	11.6	11.6	14.8	0.3898	29.8	29.8	38.0	32.5	4.7
	Y center	12.5	12.5	15.9	0.3529	35.4	35.4	45.1	38.6	5.6
	Y north	13.2	13.2	16.9	0.3683	35.8	35.8	45.9	39.2	5.8
	Y south	17.9	17.9	22.8	0.4113	43.5	43.5	55.4	47.5	6.9
Well vertical location	Top	13.5	13.4	17	0.4472	30.2	30.0	38.0	32.7	4.6
	Mid	13	12.5	15.9	0.4438	29.3	28.2	35.8	31.1	4.1
	Bottom	13.6	12.9	16.5	0.433	31.4	29.8	38.1	33.1	4.4
Well length	10h*	16.5	16.5	21	0.4354	37.9	37.9	48.2	41.3	6.0
	20h	15.4	15.4	19.6	0.4338	35.5	35.5	45.2	38.7	5.6
	30h	14.7	14.7	18.7	0.4280	34.3	34.3	43.7	37.5	5.4
	75h	11.8	10.7	13.6	0.424	27.8	25.2	32.1	28.4	3.5
	100h	7.5	6.7	8.5	0.3526	21.3	19.0	24.1	21.5	2.6
	125h	5.4	5	6.4	0.3059	17.7	16.3	20.9	18.3	2.4

*Optimum well length

Table A1-28 Plume management.

Scenario	Case ID	E_{rec}, %	E_{cub}, %	E_{cyl}, %	$\bar{S}_g$	$E_{V,rec}$, %	$E_{V,sqr}$, %	$E_{V,cyl}$, %	$E_{V,avg}$, %	Standard deviation, %
Water Production	Blanket completions	14.6	14.6	18.6	0.4399	33.2	33.2	42.3	36.2	5.2
	Bottom completions	15.0	15.0	19.1	0.4458	33.6	33.6	42.8	36.7	5.3
	Bottom completions in a closed system	27.2	27.2	34.6	0.4301	63.2	63.2	80.4	69.0	9.9
Field Management	Blanket completions	15.1	15.1	19.2	0.4132	36.5	36.5	46.5	39.9	5.7
	Bottom completions	15.0	15.0	19.1	0.4297	34.9	34.9	44.4	38.1	5.5

Strandplain

Table A1-29 Baseline simulations.

Scenario	Case ID	E_{rec}, %	E_{cub}, %	E_{cyl}, %	$\bar{S}_g$	$E_{V,rec}$, %	$E_{V,sqr}$, %	$E_{V,cyl}$, %	$E_{V,avg}$, %	Standard deviation, %
Stratigraphic	Center	12.4	9.0	11.4	0.4050	30.6	22.2	28.1	27.0	4.3
	Non-center 1	12.6	9.6	12.2	0.3972	31.7	24.2	30.7	28.9	4.1
	Non-center 2	12.1	6.1	7.7	0.3836	31.5	15.9	20.1	22.5	8.1
	Non-center 3	12.5	7.2	9.2	0.3860	32.4	18.7	23.8	25.0	6.9
	Non-center 4	12.5	7.2	9.2	0.3860	32.4	18.7	23.8	25.0	6.9
Structural	Center	16.7	12.1	15.4	0.3846	43.4	31.5	40.0	38.3	6.2

Table A1-30 Selective completions.

Scenario	Case ID	E_{rec}, %	E_{cub}, %	E_{cyl}, %	$\bar{S}_g$	$E_{V,rec}$, %	$E_{V,sqr}$, %	$E_{V,cyl}$, %	$E_{V,avg}$, %	Standard deviation, %
High E well	Bottom	12.8	10.1	12.8	0.4178	30.6	24.2	30.6	28.5	3.7
	Top	12.2	9.7	12.3	0.4250	28.7	22.8	28.9	26.8	3.5
	HKI	12.8	10.1	12.8	0.4194	30.5	24.1	30.5	28.4	3.7
	LKI	12.8	10.1	12.8	0.4178	30.6	24.2	30.6	28.5	3.7
	HKL	12.8	10.1	12.8	0.4184	30.6	24.1	30.6	28.4	3.7
	LKL	12.2	9.7	12.3	0.4248	28.7	22.8	29.0	26.8	3.5
Low E well	Bottom	12.8	6.8	8.6	0.4131	31.0	16.5	20.8	22.8	7.5
	Top	11.9	6.4	8.2	0.4202	28.3	15.2	19.5	21.0	6.7
	HKI	12.8	6.8	8.6	0.4149	30.9	16.4	20.7	22.7	7.4
	HKL	12.8	6.8	8.6	0.4141	30.9	16.4	20.8	22.7	7.4
	LKI	12.1	6.2	8	0.4083	29.6	15.2	19.6	21.5	7.4
	LKL	11.8	6.2	7.9	0.4131	28.6	15.0	19.1	20.9	7.0
Blanket completions	High *E* well	12.6	9.6	12.2	0.3972	31.7	24.2	30.7	28.9	4.1
	Low *E* well	12.1	6.1	7.7	0.3836	31.5	15.9	20.1	22.5	8.1

Table A1-31 Horizontal wells.

Scenario	Case ID	E_{rec}, %	E_{cub}, %	E_{cyl}, %	$\overline{S}_g$	$E_{V,rec}$, %	$E_{V,sqr}$, %	$E_{V,cyl}$, %	$E_{V,avg}$, %	Standard deviation, %
Well horizontal location	X center	12	7.7	9.9	0.3490	34.4	22.1	28.4	28.3	6.2
	X west	12.7	7.9	10.1	0.3831	33.2	20.6	26.4	26.7	6.3
	X east	12.9	7.0	8.9	0.3057	42.2	22.9	29.1	31.4	9.9
	Y center	12.1	8.2	10.5	0.3811	31.8	21.5	27.6	26.9	5.1
	Y north	12.4	7.3	9.3	0.3832	32.4	19.1	24.3	25.2	6.7
	Y south	12.4	7.3	9.3	0.3832	32.4	19.1	24.3	25.2	6.7
Well length	10h*	14.2	10.3	13.1	0.3916	36.3	26.3	33.5	32.0	5.1
	20h	14.2	10	12.8	0.3786	37.5	26.4	33.8	32.6	5.6
	40h	13.4	8.9	11.3	0.3634	36.9	24.5	31.1	30.8	6.2
	50h	12.8	8.5	10.8	0.3782	33.8	22.5	28.6	28.3	5.7
	100h	10.3	6.5	8.2	0.3136	32.8	20.7	26.1	26.6	6.1

*Optimum well length

Table A1-32 Plume management.

Scenario	Case ID	E_{rec}, %	E_{cub}, %	E_{cyl}, %	$\overline{S}_g$	$E_{V,rec}$, %	$E_{V,sqr}$, %	$E_{V,cyl}$, %	$E_{V,avg}$, %	Standard deviation, %
Water Production	Blanket completions	10.8	9.1	11.7	0.4582	23.6	19.9	25.5	23.0	2.9
	Bottom completions	11.8	9.7	12.4	0.4541	26.0	21.4	27.3	24.9	3.1
	Blanket completions in a closed system	14.2	11.2	14.2	0.4555	31.2	24.6	31.2	29.0	3.8
	Bottom completions in a closed system	16.8	12.8	16.3	0.4457	37.7	28.7	36.6	34.3	4.9
Field Management	Blanket completions	9.9	8.6	11.0	0.4258	23.3	20.2	25.8	23.1	2.8
	Bottom completions	11.8	9.7	12.4	0.4515	26.1	21.5	27.5	25.0	3.1

Reef

Table A1-33 Baseline simulations.

Scenario	Case ID	E_{rec}, %	E_{cub}, %	E_{cyl}, %	$\overline{S}_g$	$E_{V,rec}$, %	$E_{V,sqr}$, %	$E_{V,cyl}$, %	$E_{V,avg}$, %	Standard deviation, %
Stratigraphic	Center	11.8	9.4	11.9	0.3959	29.8	23.7	30.1	27.9	3.6
	Non-center 1	16.1	12.1	15.4	0.3557	45.3	34.0	43.3	40.9	6.0
	Non-center 2	13.7	4.8	6.1	0.3516	39.0	13.7	17.3	23.3	13.7
	Non-center 3	13.7	10.1	12.9	0.3537	38.7	28.6	36.5	34.6	5.3
	Non-center 4	19.6	15.5	19.7	0.3754	52.2	41.3	52.5	48.7	6.4
Structural	Center	12.1	9.6	12.3	0.3961	30.5	24.2	31.1	28.6	3.8
	Non-center 1	16.0	12.0	15.3	0.3549	35.1	30.3	38.7	34.7	4.2
	Non-center 2	12.3	4.7	6.0	0.3601	34.2	13.1	16.7	21.3	11.3
	Non-center 3	14.0	10.3	13.1	0.3572	39.2	28.8	36.7	34.9	5.4
	Non-center 4	21.2	16.7	21.3	0.3776	56.1	44.2	56.4	52.3	7.0

Table A1-34 Selective completions.

Scenario	Case ID	E_{rec}, %	E_{cub}, %	E_{cyl}, %	$\overline{S}_g$	$E_{V,rec}$, %	$E_{V,sqr}$, %	$E_{V,cyl}$, %	$E_{V,avg}$, %	Standard deviation, %
High E well	Bottom	16.5	13	16.6	0.3651	45.2	35.6	45.5	42.1	5.6
	top	14.4	11.4	14.5	0.3620	39.8	31.5	40.1	37.1	4.9
	HKI	14.4	11.4	14.5	0.3620	39.8	31.5	40.1	37.1	4.9
	LKI	18.5	14.6	18.6	0.3705	49.9	39.4	50.2	46.5	6.2
	HKL	16.6	12.6	16.1	0.3665	45.3	34.4	43.9	41.2	5.9
	LKL	20	15.2	19.3	0.3725	57.2	43.5	55.2	52.0	7.4
	LKvh	17.9	14.1	18	0.3690	48.5	38.2	48.8	45.2	6.0
Low E well	Bottom	9.7	3.7	4.7	0.3622	26.8	10.2	13.0	16.7	8.9
	Top	10.1	3.9	4.9	0.3603	28.2	10.9	13.7	17.6	9.3
	HKI	9.4	3.6	4.6	0.3596	26.1	10.0	12.8	16.3	8.6
	HKL	10.5	4	5.1	0.3559	29.5	11.2	14.3	18.4	9.8
	LKL	10.8	4.1	5.2	0.3536	30.5	11.6	14.7	18.9	10.2
	LKvh	10.6	4	5.2	0.3581	29.6	11.2	14.5	18.4	9.8
Blanket completions	High E well	19.6	15.5	19.7	0.3754	52.2	41.3	52.5	48.7	6.4
	Low E well	13.7	4.8	6.1	0.3516	39.0	13.7	17.3	23.3	13.7

Table A1-35 Horizontal wells.

Scenario	Case ID	E_{rec}, %	E_{cub}, %	E_{cyl}, %	$\bar{S}_g$	$E_{V,rec}$, %	$E_{V,sqr}$, %	$E_{V,cyl}$, %	$E_{V,avg}$, %	Standard deviation, %
Well horizontal location	X center	22.3	16.2	20.6	0.3832	58.2	42.3	53.8	51.4	8.2
	X west	24.1	18.7	23.8	0.3817	63.1	49.0	62.4	58.2	8.0
	X east	26.7	14.7	18.7	0.3865	69.1	38.0	48.4	51.8	15.8
	Y center	22.3	18.6	23.7	0.392	56.9	47.4	60.5	54.9	6.7
	Y north	21.6	11.3	14.4	0.365	59.2	31.0	39.5	43.2	14.5
	Y south	21.4	18.9	24	0.3734	57.3	50.6	64.3	57.4	6.8
Well vertical location	Top	20.3	13.5	17.2	0.3857	52.6	35.0	44.6	44.1	8.8
	Mid	20.1	14	17.9	0.3838	52.4	36.5	46.6	45.2	8.0
	Bottom	22.3	16.2	20.6	0.3832	58.2	42.3	53.8	51.4	8.2
Well length	10h	17.9	14.4	18.4	0.3924	45.6	36.7	46.9	43.1	5.6
	15h	20.1	17.3	22.1	0.3982	50.5	43.4	55.5	49.8	6.1
	25h	23.1	17.1	21.8	0.3915	59.0	43.7	55.7	52.8	8.1
	30h*	25.6	17.1	21.7	0.3741	68.4	45.7	58.0	57.4	11.4
	35h	23.1	14.9	19	0.3566	64.8	41.8	53.3	53.3	11.5
	40h	20.9	12.9	16.4	0.3257	64.2	39.6	50.4	51.4	12.3

*Optimum well length

Table A1-36 Plume management.

Scenario	Case ID	E_{rec}, %	E_{cub}, %	E_{cyl}, %	$\bar{S}_g$	$E_{V,rec}$, %	$E_{V,sqr}$, %	$E_{V,cyl}$, %	$E_{V,avg}$, %	Standard deviation, %
Water Production	Blanket completions	11.3	9.1	11.5	0.39	29.0	23.3	29.5	27.3	3.4
	Bottom completions	11.9	9.1	11.6	0.4075	29.2	22.3	28.5	26.7	3.8
	Bottom completions in a closed system	18.6	12.7	16.1	0.4191	44.4	30.3	38.4	37.7	7.1
Field Management	Blanket completions	19.7	15.6	19.9	0.3653	53.9	42.7	54.5	50.4	6.6
	Bottom completions	13.9	10.7	13.6	0.3723	37.3	28.7	36.5	34.2	4.7

Fluvial and Alluvial

Table A1-37 Baseline simulations.

Scenario	Case ID	E_{rec}, %	E_{cub}, %	E_{cyl}, %	$\bar{S}_g$	$E_{V,rec}$, %	$E_{V,sqr}$, %	$E_{V,cyl}$, %	$E_{V,avg}$, %	Standard deviation, %
Structural	Center	18.3	16.9	21.6	0.4210	43.5	40.1	51.3	45.0	5.7
	Non-center 1	14.0	13.2	16.8	0.3933	35.6	33.6	42.7	37.3	4.8
	Non-center 2	17.4	9.9	12.7	0.4059	42.9	24.4	31.3	32.8	9.3
	Non-center 3	17.8	10.7	13.6	0.4087	43.6	26.2	33.3	34.3	8.7
	Non-center 4	18.1	16.3	20.7	0.4048	44.7	40.3	51.1	45.4	5.5

Table A1-38 Selective completions.

Scenario	Case ID	E_{rec}, %	E_{cub}, %	E_{cyl}, %	$\bar{S}_g$	$E_{V,rec}$, %	$E_{V,sqr}$, %	$E_{V,cyl}$, %	$E_{V,avg}$, %	Standard deviation, %
High *E* well	Bottom	19.9	18.1	23	0.4438	47.5	43.2	54.9	48.6	5.9
	Top	14.7	14.4	18.4	0.4472	34.6	33.9	43.3	37.3	5.2
	HKI	19.7	18	23	0.4113	46.7	42.7	54.6	48.0	6.0
	LKI	16.9	15.9	20.2	0.4044	40.3	37.9	48.1	42.1	5.4
	HKL	18.3	16.9	21.6	0.433	43.6	40.2	51.4	45.1	5.7
	LKL	15.7	15	19.2	0.4182	41.5	39.7	50.8	44.0	6.0
Low *E* well	Bottom	19.6	11.1	14.2	0.4438	47.8	27.0	34.6	36.5	10.5
	Top	13	6.9	8.8	0.4472	32.1	17.0	21.7	23.6	7.7
	HKI	19.4	11.3	14.4	0.4113	47.2	27.5	35.0	36.6	9.9
	LKI	16.2	9.2	11.8	0.4044	40.0	22.7	29.1	30.6	8.7
	HKL	17.7	10.4	13.3	0.433	43.3	25.4	32.5	33.8	9.0
	LKL	14.6	7.9	10	0.4006	36.5	19.7	25.0	27.0	8.6
Blanket completions	High *E* well	18.3	16.9	21.6	0.421	43.5	40.1	51.3	45.0	5.7
	Low *E* well	17.4	9.9	12.7	0.4059	42.9	24.4	31.3	32.8	9.3

*no LKVH completions

Table A1-39 Horizontal wells.

Scenario	Case ID	E_{rec}, %	E_{cub}, %	E_{cyl}, %	$\bar{S}_g$	$E_{V,rec}$, %	$E_{V,sqr}$, %	$E_{V,cyl}$, %	$E_{V,avg}$, %	Standard deviation, %
Well horizontal location	X center	16.9	12.2	15.6	0.4128	40.9	29.6	37.8	36.1	5.9
	X west	16	11.5	14.7	0.4084	39.2	28.2	36.0	34.4	5.7
	X east	15.1	10.9	13.9	0.4027	37.5	27.1	34.5	33.0	5.4
	Y center	16.3	14.4	18.4	0.4113	39.6	35.0	44.7	39.8	4.9
	Y north	15.9	11.6	14.8	0.4026	39.5	28.8	36.8	35.0	5.5
	Y south	17.1	12.6	16.1	0.4079	41.9	30.9	39.5	37.4	5.8
Well vertical location	Top	10	7.6	9.7	0.4334	23.1	17.5	22.4	21.0	3.0
	Mid	13.4	11.3	14.3	0.4192	32.0	27.0	34.1	31.0	3.7
	Bottom	16.3	14.4	18.4	0.4113	39.6	35.0	44.7	39.8	4.9
Well length	5h	13.5	13.4	17	0.4472	30.2	30.0	38.0	32.7	4.6
	10h	13	12.5	15.9	0.4438	29.3	28.2	35.8	31.1	4.1
	15h*	17.9	17.9	22.8	0.4113	43.5	43.5	55.4	47.5	6.9
	20h	12.8	12.8	16.3	0.4044	31.7	31.7	40.3	34.5	5.0

*Optimum well length

Table A1-40 Plume management.

Scenario	Case ID	E_{rec}, %	E_{cub}, %	E_{cyl}, %	$\bar{S}_g$	$E_{V,rec}$, %	$E_{V,sqr}$, %	$E_{V,cyl}$, %	$E_{V,avg}$, %	Standard deviation, %
Water Production	Blanket completions	14.0	13.0	16.6	0.4174	33.5	31.1	39.8	34.8	4.5
	Bottom completions	16.1	14.9	19.0	0.4071	39.5	36.6	46.7	40.9	5.2
	Bottom completions in a closed system	16.8	16.0	20.4	0.4084	41.1	39.2	50.0	43.4	5.7
Field Management	Blanket completions	18.4	17.3	22.1	0.3986	46.2	43.4	55.4	48.3	6.3
	Bottom completions	19.3	18.3	23.3	0.3999	48.3	45.8	58.3	50.8	6.6

Turbidite

Table A1-41 Baseline simulations.

Scenario	Case ID	E_{rec}, %	E_{cub}, %	E_{cyl}, %	$\bar{S}_g$	$E_{V,rec}$, %	$E_{V,sqr}$, %	$E_{V,cyl}$, %	$E_{V,avg}$, %	Standard deviation, %
Stratigraphic	Center	21.0	18.9	24.0	0.4115	51.0	45.9	58.3	51.8	6.2
	Non-center 1	18.3	14.1	18.0	0.3909	46.8	36.1	46.0	43.0	6.0
	Non-center 2	15.8	6.5	8.3	0.3792	41.7	17.1	21.9	26.9	13.0
	Non-center 3	21.6	16.3	20.8	0.4016	53.8	40.6	51.8	48.7	7.1
	Non-center 4	19.5	14.0	17.8	0.4048	48.2	34.6	44.0	42.2	7.0
Structural	Center	22.2	16.9	21.6	0.4039	55.0	41.8	53.5	50.1	7.2
	Non-center 1	19.8	14.2	18.1	0.4076	48.6	34.8	44.4	42.6	7.0
	Non-center 2	19.1	15.3	19.5	0.3971	48.1	38.5	49.1	45.2	5.8
	Non-center 3	16.2	7.0	8.9	0.3852	42.1	18.2	23.1	27.8	12.6
	Non-center 4	20.6	19.4	24.8	0.4230	48.7	45.9	58.6	51.1	6.7

Table A1-42 Selective completions.

Scenario	Case ID	E_{rec}, %	E_{cub}, %	E_{cyl}, %	$\overline{S}_g$	$E_{V,rec}$, %	$E_{V,sqr}$, %	$E_{V,cyl}$, %	$E_{V,avg}$, %	Standard deviation, %
High *E* well	Bottom	13.9	12	15.3	0.4177	43.5	43.5	55.4	47.5	6.9
	Top	15.1	12.8	16.3	0.4126	30.2	30.0	38.0	32.7	4.6
	HKI	17.5	14.6	18.6	0.4039	29.3	28.2	35.8	31.1	4.1
	LKI	13.8	11.6	14.7	0.4180	31.4	29.8	38.1	33.1	4.4
	HKL	17.9	14	17.9	0.395	35.8	35.8	45.9	39.2	5.8
	LKL	15.2	13	16.5	0.4109	31.7	31.7	40.3	34.5	5.0
	LKvh	15.4	13	16.6	0.4108	29.8	29.8	38.0	32.5	4.7
Low *E* well	Bottom	15.1	6.4	8.1	0.3834	39.4	16.7	21.1	25.7	12.0
	Top	15.8	6.9	8.8	0.4282	36.9	16.1	20.6	24.5	10.9
	HKI	15.3	6.6	8.4	0.3962	38.6	16.7	21.2	25.5	11.6
	LKI	15	6.4	8.1	0.3924	38.2	16.3	20.6	25.1	11.6
	HKL	15.4	6.5	8.3	0.3827	40.2	17.0	21.7	26.3	12.3
	LKL	15.4	6.4	8.2	0.3837	40.1	16.7	21.4	26.1	12.4
	LK_{vh}	15.1	6.3	8	0.3836	39.4	16.4	20.9	25.5	12.2
Blanket completions	High *E* well	21	18.9	24	0.4115	51.0	45.9	58.3	51.8	6.2
	Low *E* well	15.8	6.5	8.3	0.3792	41.7	17.1	21.9	26.9	13.0

Table A1-43 Horizontal wells.

Scenario	Case ID	E_{rec}, %	E_{cub}, %	E_{cyl}, %	$\bar{S}_g$	$E_{V,rec}$, %	$E_{V,sqr}$, %	$E_{V,cyl}$, %	$E_{V,avg}$, %	Standard deviation, %
Well horizontal location	X center	23.7	16.5	21	0.3987	59.4	41.4	52.7	51.2	9.1
	X west	24	20.3	25.8	0.4016	59.8	50.5	64.2	58.2	7.0
	X east	20.4	12.2	15.6	0.3963	51.5	30.8	39.4	40.5	10.4
	Y center	23	18.2	23.1	0.4006	57.4	45.4	57.7	53.5	7.0
	Y north	24.8	14.8	18.9	0.3969	62.5	37.3	47.6	49.1	12.7
	Y south	23.4	19.1	24.3	0.3960	59.1	48.2	61.4	56.2	7.0
Well vertical location	Top	21.7	15.9	20.2	0.4069	53.3	39.1	49.6	47.3	7.4
	Mid	22.4	16.2	20.6	0.4065	55.1	39.9	50.7	48.5	7.8
	Bottom	23.7	16.5	21	0.3987	59.4	41.4	52.7	51.2	9.1
Well length	10h	22.9	19.3	24.6	0.4051	56.5	47.6	60.7	55.0	6.7
	20h	23.6	20.2	25.8	0.4051	58.3	49.9	63.7	57.3	7.0
	30h	23.8	20.5	26.2	0.4051	58.8	50.6	64.7	58.0	7.1
	50h*	23.6	21.9	27.9	0.4053	58.2	54.0	68.8	60.4	7.6
	100h	23.1	17.6	22.4	0.3995	57.8	44.1	56.1	52.6	7.5
	150h	20.5	13.6	17.4	0.3847	53.3	35.4	45.2	44.6	9.0
	200h	16.2	9.9	12.7	0.3453	46.9	28.7	36.8	37.5	9.1

*Optimum well length

Table A1-44 Plume management.

Scenario	Case ID	E_{rec}, %	E_{cub}, %	E_{cyl}, %	$\bar{S}_g$	$E_{V,rec}$, %	$E_{V,sqr}$, %	$E_{V,cyl}$, %	$E_{V,avg}$, %	Standard deviation, %
Water Production	Blanket completions	20.9	16.8	21.4	0.3967	52.7	42.3	53.9	49.7	6.4
	Bottom completions	20.2	17.4	22.2	0.4066	49.7	42.8	54.6	49.0	5.9
	Bottom completions in a closed system	22.2	14.8	18.9	0.4081	54.4	36.3	46.3	45.7	9.1
Field Management	Blanket completions	24.3	19.1	24.3	0.3908	62.2	48.9	62.2	57.7	7.7
	Bottom completions	24.6	19.6	25.0	0.3936	62.5	49.8	63.5	58.6	7.6